

Fatigue Behaviour of Submerged Axially Loaded Grouted Connections

- Ermüdungsverhalten unter Wasser liegender
axial beanspruchter Grout-Verbindungen -

Von der
Fakultät für Bauingenieurwesen und Geodäsie
der
Gottfried Wilhelm Leibniz Universität Hannover
zur Erlangung des Grades eines

Doktors der Ingenieurwissenschaften
- Dr.-Ing. -

genehmigte Dissertation
von

Dipl.-Ing. Alexander Raba
geboren am 19.10.1982 in Achim.

2018

Doctoral Committee:

1. Examiner: Prof. Dr.-Ing. Peter Schaumann

2. Examiner: Prof. Dr.-Ing. Ludger Lohaus

Chairman: Prof. Dr.-Ing. Martin Achmus

Day of examination: 13.07.2018

Acknowledgements

The thesis in hands was mainly realised during my occupation as research associate at the Institute for Steel Construction of the Leibniz Universität Hannover.

First of all, I cordially thank Prof. Dr.-Ing. Peter Schaumann, head of the Institute for Steel Construction, for supervising my scientific work and being the first reviewer of my thesis. I sincerely appreciate the professional support and the space he gave me for my research as well as his trust in my professional skills. Letting me become part of his research team and benefit from its scientific achievements made this thesis possible in the first place. I thank Prof. Dr.-Ing. Ludger Lohaus, head of the Institute for Building Material Science, for undertaking the second review of my thesis. The support he gave me through technical discussions and the excellent collaboration in our joint research project were important parts in the realisation of this thesis. Further, I would like to thank Prof. Dr.-Ing. Martin Achmus for undertaking the chair of the doctoral committee and supporting the examination procedure.

Most parts of my investigations were carried out within the joint research project “GROWup - Grouted Joints for Offshore Wind Energy Converters under reversed axial loadings and up scaled thicknesses”. I am grateful for the support of the German Federal Ministry for Economic Affairs and Energy (BMWi) by funding this project (funding sign 0325290). I acknowledge the material supply of BASF and Densit and their accompaniment of the grouting processes. Moreover, I appreciate the technical discussions we had in meetings of the project’s advisory board. A special thanks goes to the technical staff of the Institute for Steel Construction, Karl-Heinz Hentschel, Christian Fricke, Dietmar Joseph and Katrin Lucher, for their support to realise the numerous experimental investigations and manufacturing new experimental equipment. In addition, I thank the technical team of the Institute for Building Material Science for assisting during the large-scale experiments.

I sincerely thank the team of the Institute for Steel Construction. By name, I would like to mention my former colleague Prof. Dr.-Ing. Stephan Lochte-Holtgreven who introduced me to the Institute for Steel Construction and the world of scientific research. Furthermore, I thank my former colleague Dr.-Ing. Anne Bechtel for the good collaboration in “GROWup”. I would like to particularly thank my colleagues Rasmus Eichstädt, Andre Stang and Joshua Henneberg for our technical discussions and their mental support. Moreover, I thank Rasmus Eichstädt and Joshua Henneberg for their detailed review of my thesis as well as their constructive criticism.

Last but not least, I thank my family and friends for their emotional support and unconditional motivation during the long time of elaborating my thesis.

Executive Summary

With conversion of the German supply system for electrical energy towards renewable resources, the demand for offshore wind farms significantly increases. For installation of wind turbines in the German North Sea, lattice substructures such as jackets are a possible design choice. These structures are usually fixed to their steel foundation piles via grouted connections, a structural detail consisting of one steel tube inserted into a second steel tube with larger diameter. The steel surfaces located inside the resulting annulus are equipped with shear keys and the annulus is filled with a grout material. The connection is located at mudline level in submerged conditions and is manufactured without sealing against water ingress. Due to the load bearing behaviour of the substructure, these grouted connections are predominantly axially loaded.

All currently available design approaches for the Fatigue Limit State of grouted connections are based on experimental tests which were carried out in dry ambient conditions. However, experimental investigations on the fatigue behaviour of concrete specimens in submerged conditions show an obvious reduction of fatigue capacity caused by interactions between specimens and the surrounding water. Corresponding degradation phenomena were also observed at foundations of onshore wind turbines. Objective of this thesis is to investigate the influence of water on the fatigue behaviour of predominantly axially loaded grouted connections.

In a first step, a set-up of tests on small-scale grouted connections in both, dry and wet ambient conditions, was realised. Besides the ambient condition, the influences of different grout layer thicknesses, different grout materials, the loading level as well as varied loading frequencies were investigated. In total, results from 78 small-scale specimens were evaluated. The tests showed a significant reduction of fatigue capacity caused by the interaction between connection and surrounding water. This effect was also influenced by the loading frequency.

In order to reassess these results for larger grouted connections, in a second step a test set-up of large-scale specimens for fatigue tests in submerged conditions was developed and implemented. The results of 4 large-scale specimens with two different grout layer thicknesses, two comparable grout materials as well as alternating and compression-compression loading were evaluated. Via comparison of the results to published experiments of comparable specimens tested in dry ambient conditions, the previously observed influence of water was confirmed for the larger scale.

In a third step, the experimental results were supplemented by numerical investigations. A modelling approach including detailed models with discrete shear keys was implemented. For the grout layer a non-linear material model, capable of tensile cracking by means of large plastic strains, was used. Furthermore, a fatigue design verification approach based on existing S-N curves for concrete was developed. The obtained results showed good agreement with the experiments.

In summary, a significant reduction of the fatigue capacity of axially loaded grouted connections caused by interaction with surrounding water was ascertained and the relevant parameters were identified. In addition, a numerical fatigue verification approach for the design of reliable grouted connections for application in submerged conditions was introduced.

Key words: Offshore wind energy, grouted connection, axial loading, fatigue, submerged, water

Kurzfassung

Die Umgestaltung der deutschen Energieversorgung zu vorwiegender Nutzung erneuerbarer Energiequellen erhöht den Bedarf an Offshore Wind Parks. Zur Installation von Windenergieanlagen in der deutschen Nordsee können aufgelöste Gründungsstrukturen verwendet werden. Diese Strukturen werden üblicherweise über Grout-Verbindungen mit ihren Gründungspfählen verbunden. Die Verbindung besteht dabei aus zwei ineinandergesteckten Rohren. Die Stahloberflächen im resultierenden Spalt werden mit Schubrippen ausgestattet und der Spalt wird mit Mörtel (Grout) gefüllt. Die Verbindung befindet sich auf Höhe des Meeresbodens und wird ohne Abdichtung gegen Wasser ausgeführt. Aufgrund des Tragverhaltens der Gründungsstruktur übertragen diese Verbindungen vorwiegend axiale Lasten.

Alle derzeit verfügbaren Bemessungsverfahren für den Grenzzustand der Ermüdung dieser Verbindungen basieren auf in trockener Umgebung durchgeführten Versuchen. Unter Wasser ausgeführte Versuche zum Ermüdungsverhalten von Betonproben zeigen einen deutlich reduzierten Ermüdungswiderstand aufgrund zusätzlicher vom Wasser erzeugter Degradationsphänomene. Ähnliche Schadensmechanismen wurden ebenfalls an den Fundamenten von Onshore Windenergieanlagen festgestellt. Im Rahmen dieser Dissertation wird der Einfluss von Wasser auf das Ermüdungsverhalten von axial beanspruchten Grout-Verbindungen untersucht und ein Numerik basiertes Bemessungsverfahren für Ermüdungsbeanspruchung unter Wasser erarbeitet.

Im ersten Schritt wurde ein Versuchsprogramm für kleinskalige Verbindungen in trockener und nasser Umgebung umgesetzt. Zusätzlich wurde der Einfluss von Spaltdicke, Grout-Material, Lastniveau und verschiedenen Belastungsfrequenzen untersucht. Insgesamt wurden 78 Versuchskörper ausgewertet. Die Ergebnisse zeigten eine signifikante Reduktion des Ermüdungswiderstands, bedingt durch Wechselwirkungen zwischen Verbindung und umgebendem Wasser.

Im zweiten Schritt wurden großskalige Ermüdungsversuche in nasser Umgebung realisiert. Es wurden Ergebnisse an 4 Versuchskörpern mit unterschiedlichen Spaltdicken und zwei Grout-Materialien sowie unter alternierenden und Druckschwelllasten erzielt und ausgewertet. Die Gegenüberstellung dieser Ergebnisse mit vergleichbaren publizierten Versuchen in trockener Umgebung bestätigte den zuvor beobachteten Wassereinfluss für großskalige Verbindungen.

In einem dritten Schritt wurden die Versuche durch numerische Simulationen ergänzt. Ein detaillierter Modellierungsansatz mit diskreten Schubrippen wurde beschrieben. Dabei kam ein nichtlineares Materialgesetz mit Zugfestigung für die Grout-Schicht zum Einsatz. Darüber hinaus wurde ein Bemessungsverfahren für den Grenzzustand der Ermüdung unter Verwendung existierender Ermüdungskurven für Beton vorgestellt. Die Simulationen zeigten gute Übereinstimmung mit den Versuchsergebnissen.

Zusammengefasst konnte eine signifikante Reduktion des Ermüdungswiderstands von axial beanspruchten Grout-Verbindungen aufgrund von Wechselwirkungen mit Wasser nachgewiesen und die maßgebenden Einflussparameter bestimmt werden. Zusätzlich wurde ein numerisches Verfahren zur Bemessung von Grout-Verbindungen für den Einsatz unter Wasser vorgestellt.

Schlagerworte: Offshore Windenergie, Grout-Verbindung, Axiallasten, Ermüdung, Wassereinfluss

Content

1	Introduction	1
1.1	Motivation	1
1.2	Objective	2
1.3	Structure	3
2	State of the Art.....	5
2.1	Introduction	5
2.2	Grouted connections in general	5
2.2.1	Geometry	5
2.2.2	Application	6
2.2.3	Installation	7
2.2.4	Manufacturing	9
2.2.5	Materials	10
2.2.6	Quality aspects.....	11
2.3	Loads and load bearing behaviour	12
2.3.1	Loads	12
2.3.2	Load bearing behaviour	14
2.3.3	Damage modes	16
2.3.4	Load displacement behaviour	17
2.4	Influence of selected parameters	20
2.4.1	Influence of water	20
2.4.2	Autogenous shrinkage	23
2.5	Ultimate Limit State (ULS) design approaches	23
2.5.1	General remark	23
2.5.2	Model 1	24
2.5.3	Model 2 – DNVGL-ST-0126 (2016).....	27
2.5.4	Model 3 – Schaumann et al. (2012).....	28
2.5.5	Ranges of applicability	30
2.6	Fatigue Limit State (FLS) design approaches	31
2.6.1	General remark	31
2.6.2	DIN EN ISO 19902 (2014).....	32
2.6.3	NORSOK N-004 (2013)	33
2.6.4	DNVGL-ST-0126 (2016)	33
2.6.5	Billington & Chetwood (2012).....	33
2.7	Numerical design approaches.....	34
2.7.1	General remark	34
2.7.2	Material models	34
2.7.3	Modelling.....	36

2.7.4	Fatigue Limit State (FLS).....	38
2.8	Discussion	39
2.8.1	Grouted connections in general	39
2.8.2	Loads and load bearing behaviour.....	40
2.8.3	Influence of selected parameters	40
2.8.4	Ultimate Limit State (ULS) design	41
2.8.5	Fatigue Limit State (FLS) design	41
2.8.6	Numerical design approaches.....	42
2.9	Summary and conclusion	42
3	Small-Scale Experiments.....	45
3.1	Introduction.....	45
3.2	Specimens	47
3.2.1	Geometry.....	47
3.2.2	Relation to current standards.....	48
3.2.3	Materials.....	48
3.2.4	Specimen preparation	49
3.3	Grout material property tests.....	50
3.3.1	Procedure.....	50
3.3.2	Results	50
3.3.3	Discussion	52
3.4	Ultimate Limit State (ULS) tests	52
3.4.1	Procedure.....	52
3.4.2	Evaluation of measurement data	53
3.4.3	Degradation behaviour	56
3.4.4	Comparison to analytical design approaches	58
3.4.5	Discussion	59
3.5	Fatigue Limit State (FLS) tests	60
3.5.1	Procedure.....	60
3.5.2	Evaluation of measurement data	61
3.5.3	Degradation behaviour	73
3.5.4	Discussion	81
3.6	Summary	84
4	Large-Scale Experiments	87
4.1	Introduction.....	87
4.2	Test set-up.....	88
4.2.1	Specimens.....	88
4.2.2	Measurement set-up	91
4.2.3	Load scenarios.....	92

4.3	Results	94
4.3.1	Grout material properties	94
4.3.2	Measurement results	99
4.3.3	Observed degradation behaviour	110
4.3.4	Analytical design approaches	113
4.4	Discussion	116
4.4.1	General remark	116
4.4.2	Degradation behaviour	116
4.4.3	Influence of autogenous shrinkage	119
4.4.4	Influence of the initial grout state	120
4.4.5	Influence of the grout layer thickness	121
4.4.6	Influence of the ambient condition (AC)	121
4.4.7	Influence of the loading scenario	122
4.4.8	Termination criteria (TC) for FLS tests	123
4.4.9	Applicability of analytical design approaches	123
4.5	Summary and conclusion	124
5	Numerical Investigations	127
5.1	Introduction	127
5.2	General approach	128
5.2.1	General remark	128
5.2.2	Numerical models	128
5.2.3	Material models	130
5.2.4	Calculation procedures	136
5.2.5	Fatigue verification	139
5.3	Results	143
5.3.1	Grout material validation	143
5.3.2	Small-scale tests	146
5.3.3	Large-scale tests	151
5.4	Discussion	163
5.4.1	Grout material parameters	163
5.4.2	Fatigue Limit State (FLS)	164
5.4.3	Autogenous shrinkage	166
5.4.4	Discrete cracks	167
5.4.5	Requirements for a standardisation	167
5.5	Summary and conclusion	169
6	Summary and Outlook	171
6.1	Summary	171
6.2	Outlook	173

Bibliography	175
Lists	185
List of Figures	185
List of Tables	191
Nomenclature	192
Appendix A – Small-scale test results	197
A.1 ULS results.....	198
A.2 FLS results – Geometry 1, Densit Ducorit S2	203
A.3 FLS results – Geometry 1, BASF Masterflow 9500	217
A.4 FLS results – Geometry 2, Densit Ducorit S2	226
A.5 FLS results – Geometry 2, BASF Masterflow 9500	229
Appendix B – Large-scale test results	233
B.1 Grout material properties	234
B.2 Hysteresis loops – laser data	235
B.3 Hysteresis loops – test rig data.....	237
Appendix C – Analytical design approaches	239
Appendix D – Numerical results.....	243
D.1 Small-scale - parameter studies.....	244
D.2 Large-scale – strain distributions	246
D.3 Large-scale – local stress distributions	247

1 Introduction

1.1 Motivation

With the aim to encourage the development of renewable energy supply systems, the German government passed the renewable energies law EEG (2000). In its current version (EEG (2017)) specific goals of a gross electrical power supply from renewable energies of 40 to 45 % in 2025 and at least 80 % in 2050 are stated. Offshore wind turbines, as shown in Figure 1.1, shall become one of the main resources in this converted energy supply system and expansion targets of 15.0 GW until 2030 are stated. At the end of 2017 a total cumulative electrical power of 5387.4 MW had been installed in the German North and Baltic Sea (Deutsche WindGuard GmbH (2018)). At an average turbine size of 6 MW this leaves a demand for ~1600 additional turbine installations until 2030 to meet the set expansion targets.



Figure 1.1: Two offshore wind turbines with jacket substructure located at the German offshore wind farm alpha ventus (© DOTI 2011 / alpha ventus, Photo: Matthias Ibeler)

The German offshore wind turbines are installed in an average water depth of ~29 m with a trend to deeper water of ~33 m in 2017 (Deutsche WindGuard GmbH (2018)). Lattice substructures such as jackets (see Figure 1.1) are a possible solution for water depth of 30 m and deeper. Moreover, for the time being they are the preferred substructure for offshore substations. Usually these substructures are bottom-fixed with steel piles, which are driven into the seabed. Substructure and foundation piles are connected by grouted connections. Due to the substructure's load bearing

behaviour, grouted connections in lattice substructures are predominantly axially loaded. This hybrid connection of steel tubes and a grout core is located in submerged conditions at mudline level without any sealing against water ingress.

Grouted connections for marine application were first developed and investigated for oil and gas platforms. For this purpose design approaches for Ultimate Limit State (ULS) and Fatigue Limit State (FLS) were elaborated. With emergence of offshore wind turbines, grouted connections and their corresponding design methods, developed for the oil and gas sector, were applied to offshore wind structures as well. However, the designs, the used materials as well as the acting loads of support structures for offshore wind turbines differ significantly to oil and gas platforms. In addition, to date the conducted experiments on grouted connections were carried out in dry ambient conditions, neglecting any possible influence of the surrounding water in real applications. In contrast, former research activities for marine concrete structures as well as damage cases of onshore foundations showed a significantly reduced fatigue capacity of cyclically loaded concrete in submerged conditions. This arose the question on a possible influence of water on the fatigue behaviour of axially loaded grouted connections in submerged conditions.

Within the scope of the joint research project “GROWup – Grouted Joints for Offshore Wind Energy Converters under reversed axial loadings”, funded by the German Federal Ministry for Economic Affairs and Energy (BMWFi, funding sign: 0325290), a series of small- and large-scale experiments was developed and conducted to investigate a possible influence of water. These experiments were the basis of the thesis in hands.

1.2 Objective

This thesis focuses on the influence of water on the fatigue behaviour of axially loaded grouted connections in submerged conditions. Prior to the research for this thesis, no experimental investigations on this topic, explicitly considering grouted connections, were published. Yet, investigations on the influence of water on the fatigue behaviour of plain concrete specimens as well as reinforced concrete beams can be found in the literature. Moreover, damage mechanisms caused by water, observed between steel mounting parts and surrounding concrete of foundations for onshore wind turbines, were published. Both, experimental investigations and real application damage mechanisms, showed a reduced fatigue capacity in submerged conditions. Hence, these results suggest an influence of water on the fatigue behaviour of submerged grouted connections.

The investigations described in the following were focused on axially loaded grouted connections. These connections can be found in lattice substructures. In case of bottom-fixed installations, for the time being grouted connections are without any alternative for lattice substructures. Moreover, in all currently relevant designs the connection is located in fully submerged conditions.

The major questions for the following investigations were:

- Is there a general influence of water on the connection’s fatigue behaviour?
- How should this influence be rated?
- Which phenomena are introduced by the water?
- How is the connection’s degradation behaviour?

- Are effects of the scale important in scaled experiments?
- Are there influences of the grout material?
- Are there influences of the load characteristic?
- How can this influence be considered in a design verification?

Intending to answer these questions, a methodology based on experimental and numerical investigations was developed and conducted in the scope of this thesis.

1.3 Structure

At the beginning, in **Chapter 2**, the current state of the art for axially loaded grouted connections and the effect of water to concrete structures is presented. After a detailed introduction of the connection and its practical application, the load bearing behaviour as well as known damage mechanisms are described. Subsequently, the currently standardised design approaches for ULS and FLS are presented and possible numerical approaches are described. Finally, open questions with a special focus on the influence of water are discussed and the detailed objectives for the following experimental and numerical investigations are stated.

The description of the experimental investigations begins with small-scale tests, presented in **Chapter 3**. After introduction of the specimen geometries and the used grout materials, the tests are described separately for ULS and FLS loading states. Each test description includes a presentation of the test set-up, the obtained results, a detailed discussion of the results and a comparison to analytical design approaches. The FLS tests include both, experiments in dry and wet ambient conditions. The Chapter closes with a summary of the major findings.

Chapter 4 focuses on the large-scale experiments. In the beginning the specimen geometries, the measurement set-up and the load scenarios for the fatigue tests in wet ambient conditions are introduced. Subsequently, general results, the measurement data as well as found damage patterns are described in detail. Moreover, analytical design approaches are applied to the large-scale geometries. The results are then discussed with a focus on typical characteristics and test parameters. Finally, the major findings and conclusions are summarised.

Numerical investigations are described in **Chapter 5**. At first the general modelling approach is presented with detailed information on the chosen material model for the grout layer. Moreover, a numerically based fatigue verification approach for axially loaded grouted connections in submerged ambient conditions is introduced. Afterwards, the results of a general material validation and for small- and large-scale geometries are presented and compared to selected experimental results. The subsequent discussion focuses on specific aspects for a numerical design approach. In the end, a summary of the major findings and conclusions is given.

Finally, the thesis ends in **Chapter 6** with a summary and an outlook on possible future research.

2 State of the Art

2.1 Introduction

The state of the art begins with introducing the basic idea of a grouted connection. This local perspective is then widened by adding more and more external aspects and requirements in order to realise an offshore application of this connection. Once a global perspective is reached and provides a general understanding of the connection, a historical review of all characteristic parameters and their influence on the connection, investigated prior to this thesis, is given. Subsequently, the current design methods, developed based on the beforehand described investigations, are introduced. Finally, based on the state of the art, the motivation for the research activities carried out in this thesis is derived.

2.2 Grouted connections in general

2.2.1 Geometry

The term ‘grouted connection’ is usually referred to a hybrid connection connecting steel tubes with use of grout material. In the field of offshore support structures, today the grouted connection is generally designed as depicted in Figure 2.1. A smaller tube named pile (index p) is placed inside a larger tube named sleeve (index s) and the resulting annulus is filled with a grout material (index g). The steel surfaces, facing the grout, are profiled with shear connectors, usually referred to as shear keys (index sk).

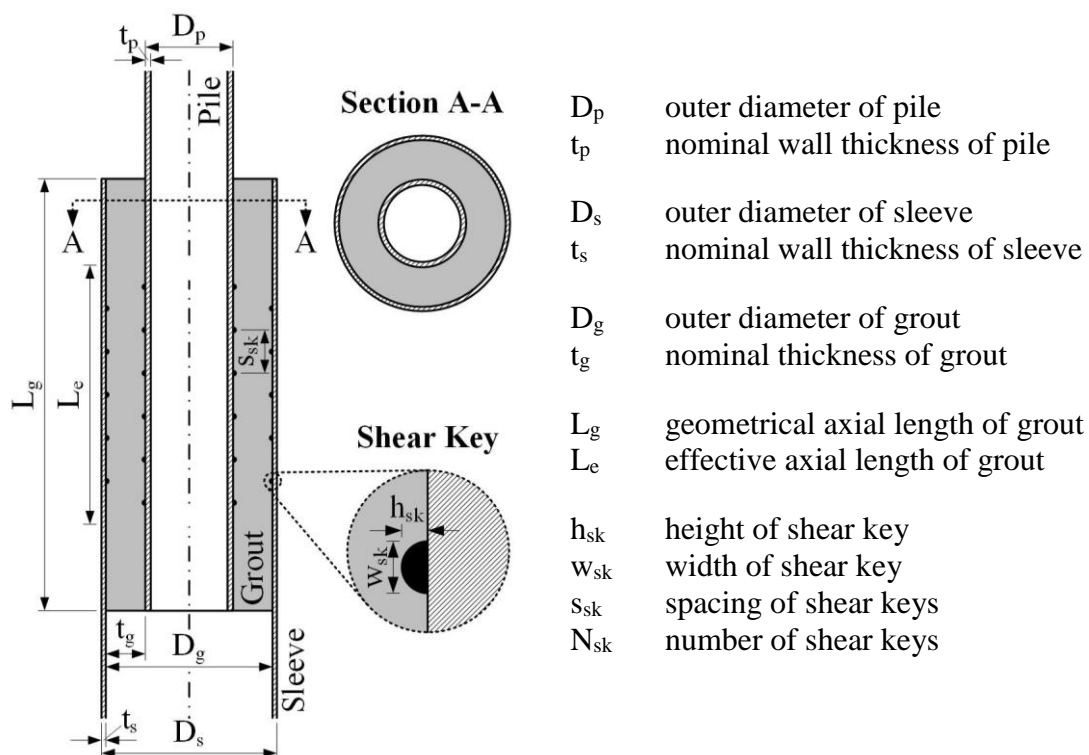


Figure 2.1: General geometry and geometrical parameters of a grouted connection in analogy to DIN EN ISO 19902 (2014)

The design of the connection depends on the geometrical parameters, outer diameter D and nominal wall thickness t of the steel tubes, which also specify D and t for the grout layer. The axial length of the grout layer L_g is limited by the overlapping length of the steel tubes. However, for load bearing purposes the effective axial length of the grout L_e is of greater importance because it takes into account non-load bearing features like sealings of the grout annulus and possible low quality grout material at the layer ends (see Section 2.2.2).

Today, in general shear keys are weld beads, applied onto the steel surfaces. They are characterised by height h_{sk} , width w_{sk} , spacing s_{sk} as well as number N_{sk} . Their geometry is usually assumed as a semi-circular or semi-elliptical profile. Concepts using circular or rectangular steel bars welded onto the steel surfaces as shown in Figure 2.6 are also available (see Karsan & Krahl (1984), Sele & Kjeoy (1989)). Grouted connections without shear keys are possible but only recommended for conical tubes (see DNVGL-ST-0126 (2016)). In the following, these plain pipe connections are only mentioned if they provide a better understanding of the respective context.

2.2.2 Application

Offshore support structures for wind turbines, substations as well as some oil and gas applications are usually bottom-fixed concepts (see WindEurope Business Intelligence (2018)). As shown in Figure 2.2 steel tubes are driven into the seabed to act as foundation and the support structure is connected to the driven tubes using grouted connections. The driven steel tubes are usually called piles or foundation piles.

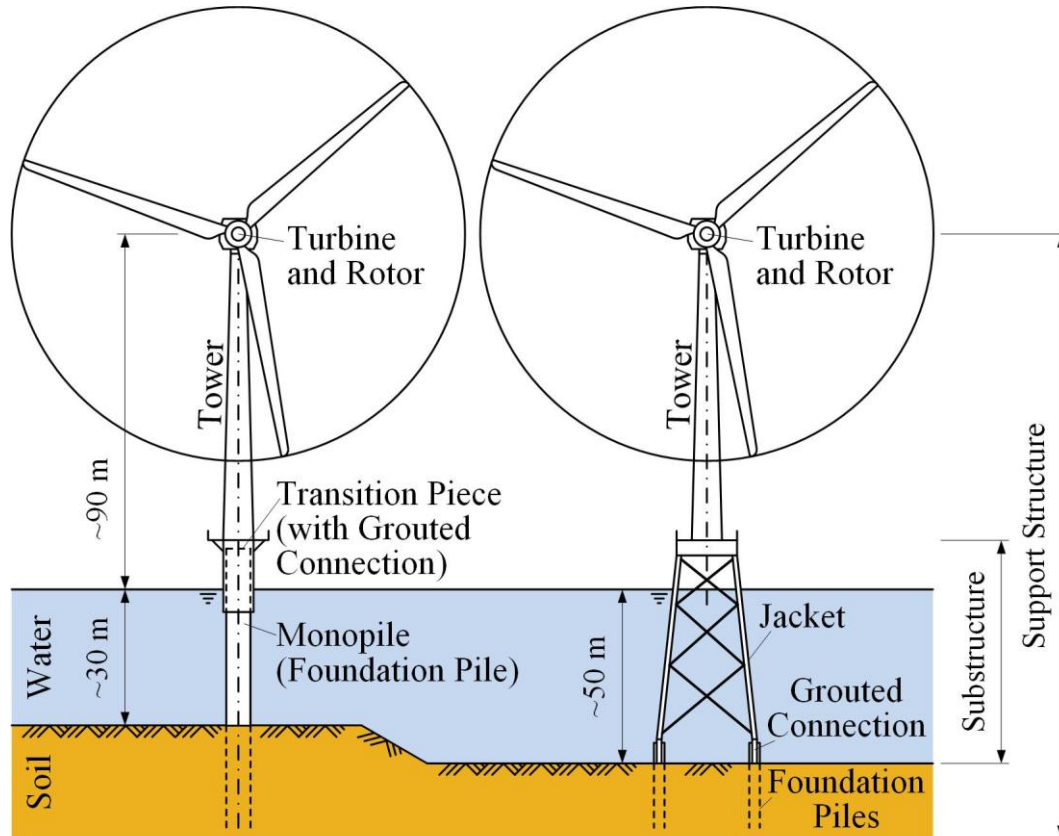


Figure 2.2: Typical support structures for offshore wind turbines and positions of grouted connections

Substructures made of steel are basically monopiles and lattice structures such as the jacket shown in Figure 2.2, with a market share according to WindEurope Business Intelligence (2018) of 81.7 % monopiles and 6.9 % jackets for wind turbines. In water depth up to ~30 m monopiles are the preferred substructure, while for deeper water up to ~50 m the jacket is mainly chosen (see 4COffshore (2018)). Other foundation concepts such as gravity based concrete structures, suction buckets or floating structures are available but, except for the gravity based foundation, are not yet used in a broader commercial application (see 4COffshore (2018)). Offshore substations are mainly founded on jacket substructures.

Based on experience from several research projects on substructures for offshore wind turbines, two simplified grouted connections representative for jacket substructures were developed at the Institute for Steel Construction. Figure 2.3 shows both grouted connections and their geometrical parameters. In the following investigations, which focus on grouted connections in jacket substructures, these connections were used as references.

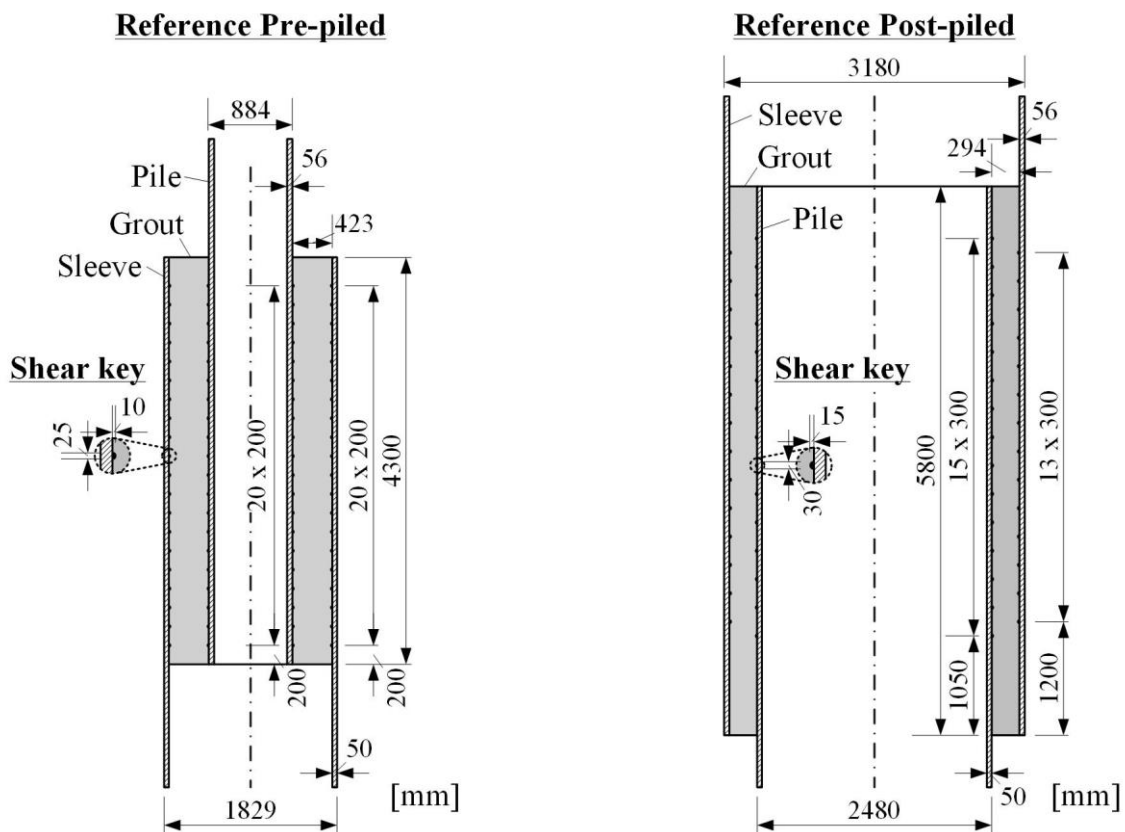


Figure 2.3: Geometry of simplified real grouted connections

2.2.3 Installation

Depending on the order of pile driving and substructure placing, two different installation procedures are possible. They influence how the grouted connection is connected to the substructure, as shown in Figure 2.4. A pre-piled installation, where the foundation piles are set first, is the typical procedure for monopiles. To use this procedure for lattice substructures, a driving template for a

correct positioning of the foundation piles is necessary. Once the foundation piles are set, the substructure can be placed and levelled on the foundation piles with hydraulic systems. In a post-piled installation procedure the substructure is simultaneously functioning as the pile driving template.

For the example of a jacket substructure possible connection options between substructure and grouted connection are shown in Figure 2.4 (see e.g., NORSOK N-004 (2013)). The grouted connection with the jacket leg inside the foundation pile is referred to as pin-pile connection, whereas the other two types are referred to as pile-sleeve connections. Independent of the connection between grouted connection and substructure, in the following the name declaration given in Figure 2.1, always indicating the outer steel tube as sleeve, is used.

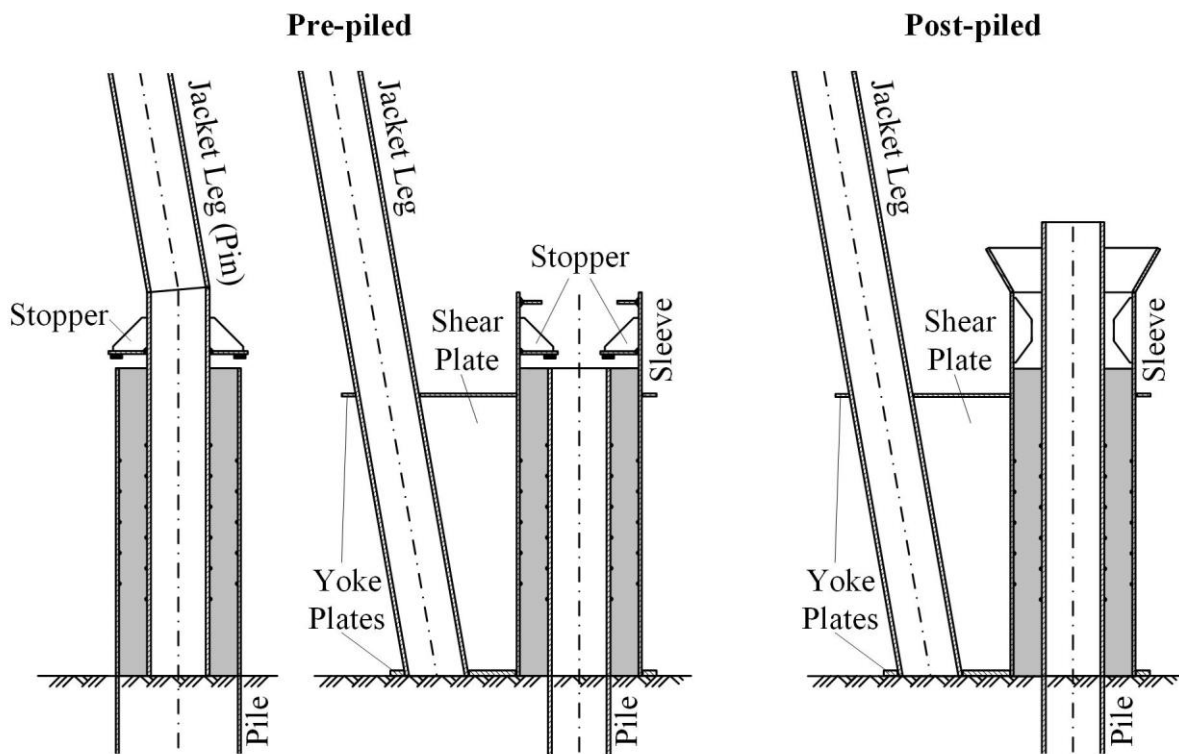


Figure 2.4: Schematic grouted connection designs for different installation procedures of jacket support structures

The main advantage of the grouted connection is its capability to compensate possible inclinations or eccentricities of the foundation piles. This capability is mainly defined by the thickness of the grout annulus t_g . For monopiles the grout layer thickness can be smaller because imperfections of only one foundation pile have to be compensated; this leads to grout layer thicknesses of 120 mm and less. In lattice substructures imperfections of three or more foundation piles must be compensated and therefore a thicker grout annulus between 300 and 500 mm is common.

The way in which a grouted connection is connected to the substructure influences the stress distribution in the steel parts. Hence, local variations of the steel tube thicknesses can be necessary, for example in the area of yoke plates (see Figure 2.4).

2.2.4 Manufacturing

Once the foundation piles are set and the support structure is placed and levelled, the lower end of the grout annulus is sealed (see Figure 2.5). In pin-pile connections (see Figure 2.4, left) the soil can be used as a natural sealing, whereas in pile-sleeve connections, the sealing is usually a rubber part installed before placing the support structure. Subsequently, the steel surfaces facing the grout annulus are cleaned from marine growth. The fresh grout is then pumped through multiple inlets at the lower end into the annulus. In this way the fresh grout material displaces the seawater inside the annulus and demixing of the grout due to free fall is prevented.

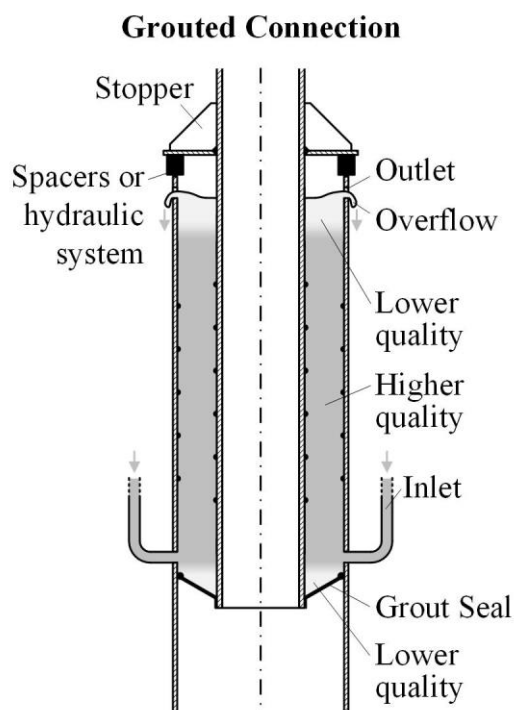


Figure 2.5: Schematic manufacturing process of a pre-piled grouted connection and in-situ quality of the grout material (acc. to Werner & Lohaus (2014))

When the fresh grout flows into the seawater, mingling in the boundary layer is possible and leads to a lower quality in the finally hardened grout (see e.g., Werner & Lohaus (2014), Werner (2017)). Moreover, the inlet tubes are usually prepared with a lubrication mix of pure cement paste, which is displaced by the fresh grout and spilled into the grout annulus where it influences the grout properties. In order to get high quality grout material in the main areas of the connection, the annulus is filled until a material overflow of high quality material is detected (see Figure 2.5).

After the filling process is completed, the fresh grout needs to harden until it reaches the desired design strength and thus, finalises the manufacturing process. Due to the in-situ curing, environmental loads can act on the grout before it reaches its desired strength. This loading process is referred to as early age cycling (see e.g., Tebbet & Billington (1985), Lohaus et al. (2014)) and it can influence the final load bearing capacity of the connection. Therefore, early age cycling shall be prevented or kept to a minimum during curing and possible effects shall be considered in design calculations (see e.g., DIN EN ISO 19902 (2014)).

Besides a high strength in the final application, the grout material shall meet additional requirements from the manufacturing process. A good flowability, plasticity and stability of the fresh grout is needed to ensure a reliable pumping process and a homogenous material distribution in the grout annulus. These characteristics have to be maintained during the whole filling process, which can last for several hours. After the filling process is completed, a quick stiffening and strength development is desired to reduce the effects of early age cycling as well as to allow a fast building process. Moreover, these characteristics shall be obtained at low water temperatures.

2.2.5 Materials

Steel

The material for the steel tubes has to withstand not only the structural loads but also extreme temperatures and the highly corrosive seawater environment. According to GL-COWT (2012) the recommended material strength is limited to fine grain steel grade S355. Hence, typical grouted connections are built with steel grades S235 and S355. For specific recommendations on toughness and mechanical or thermomechanical treatment usually reference is made to DIN EN 10025-4 (2005) and DIN EN 10225 (2009).

Regarding corrosion protection, the support structures are commonly coated in areas surrounded by air or in the splash zone. All submerged areas are left with non-treated surfaces. For these areas a cathodic corrosion protection system with sacrificial anodes is typical as described in DIN EN 12495 (2000).

Grout

In commercial applications for offshore support structures, grouted connections are filled with cementitious grout materials. In earlier oil and gas applications plain cements without aggregates were used, such as Ordinary Portland Cement (OPC), High Alumina Cements (HAC) or Oilwell B Cement (OIC). These materials were used in the earlier research on grouted connections as carried out by for example Billington (1978), Boswell L. F. & D'Mello (1986) or Lamport (1988). Benefit of these materials is the homogenous dry grout material, a simple mixing process and a good flowability of the fresh grout. A high rate of autogenous shrinkage and high temperatures during curing, caused by fast chemical reactions, are unfavourable. These high temperatures can lead to forced cracking of the hardened grout layer.

Today High Performance Grout (HPG) materials with aggregates of up to 6 mm diameter are common. These materials are characterised by significantly higher compressive strengths and elasticities compared to plain cement materials. Moreover, they are optimised for the specific offshore application, regarding for example a good flowability and fast strength development at low temperatures as well as small autogenous shrinkage. These materials are characterised by a low tensile strength compared to their compressive strength and a brittle failure behaviour. Adding fibres can improve the tensile strength but will come with a more challenging fresh material behaviour and requirements for the filling process (see Anders (2007)). Thus, for grouted connections in offshore wind applications the use of HPG without fibres is common.

Nevertheless, motivated mainly by lower costs for plain cement materials, current research activities focus on the possible applicability of OPC for offshore wind support structures (see Cotardo et al. (2017), Schaumann et al. (2018)).

2.2.6 Quality aspects

Steel surfaces

The condition of the steel surfaces facing the grout layer, directly influences the friction behaviour between steel and grout. Therefore, the surfaces must be free of mill scale, grease and loose materials, such as for example marine growth, before filling the grout. Coatings are unfavourable since investigations by Billington (1978) with epoxy coating showed a reduced interface strength and Domone & Jefferis (2005) state possible chemical interactions between grout and coating, which might lead to a weaker grout material.

Shear keys

The shear keys are welded onto the steel surface. Today, pure weld bead shear keys (see Figure 2.6, 3.) are preferred over bars welded onto the steel surfaces (see Figure 2.6, 1. and 2.). Therefore, depending on the shear key size, several layers have to be welded. As a result, the real profile of a shear key can look like Figure 2.6, 4. Notches between individual weld layers reduce the fatigue strength of a shear key. Moreover, in the expectable case of relative movements between shear key and grout the non-smooth surface might increase abrasion processes (see Section 2.3.3).

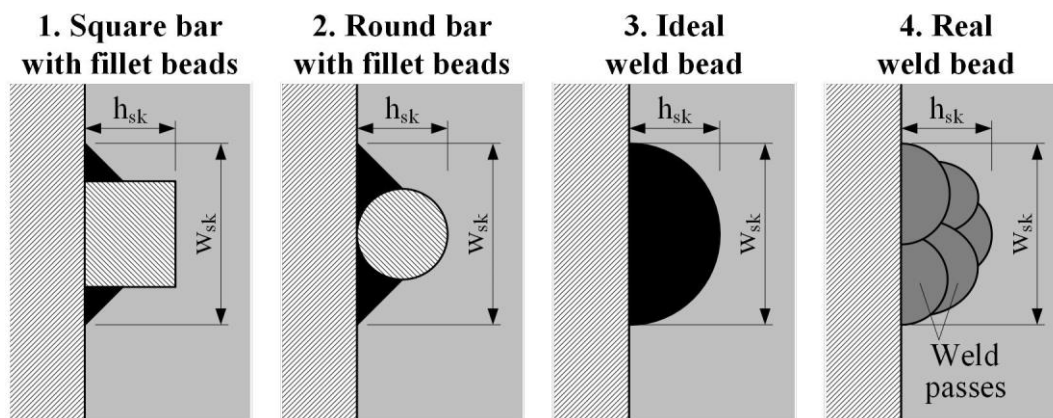


Figure 2.6: Possible shear key designs (1.-3.) acc. to Karsan & Krahl (1984) and DIN EN ISO 19902 (2014) and realistic weld bead shape (4.) acc. to GL-TN-GC (2013)

Grout material

As described in Section 2.2.4, the quality of the final grout material is influenced by the filling process. In the end regions of the grout annulus, grout material of poorer quality is expected due to mingling with seawater. Hence, these areas are excluded from the designated final load transfer. But also inside the remaining grout layer and in the interface between steel and grout, weaknesses are possible. Pumping interruptions during the filling process can lead to layers of pre-hardened grout, which might lead to imperfections and weaknesses in the final grout layer. Furthermore, for some materials segregation around the shear keys was observed, resulting in weaker material in

the main area of load application (see Werner (2017)). High temperature developments during curing, caused mainly by a rapid hardening process, can lead to forced cracking. Additionally, forced cracking is possible as a result of autogenous shrinkage.

2.3 Loads and load bearing behaviour

2.3.1 Loads

In support structures for offshore wind turbines grouted connections are mainly loaded by the dead weight of turbine and support structure as well as environmental loads such as wind and waves. Moreover, operational loads of the turbine, installation loads and accidental loads caused by for example failures in the turbine controller or ship impact (see Figure 2.7). For the design process, in standard IEC 61400-3 (2009) typical load cases for offshore wind turbines are defined.

Dependent on the type of substructure, the effects of loads (E) lead to different reaction loads (R) in the grouted connection, as shown in Figure 2.7. For lattice substructures, such as jackets, the reaction loads are predominantly axial and horizontal. Bending and torsional moments are split by the lever of the substructures footprint into force couples acting on all grouted connections, but local bending and torsion is still possible and depends on the substructure's stiffness. In contrast to grouted connections in jackets, in monopiles the connection has to transfer a significant amount of bending moments and therefore, is related to as predominantly bending loaded.

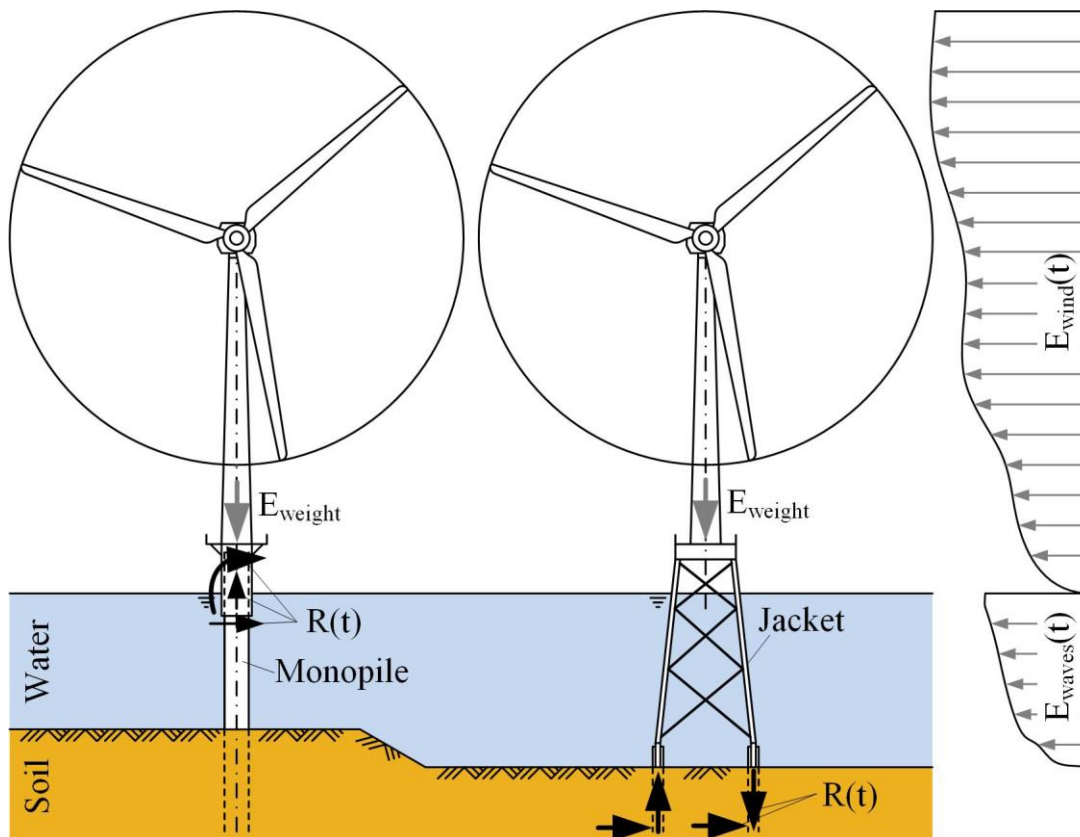


Figure 2.7: Schematic effects of loads (E) and reaction loads (R) in the grouted connections, depending on the type of substructure

Except for the dead weight, all loads are time variant. This leads to interactions between wind turbine and environment, such as aero- and hydrodynamic effects as well as soil-structure interactions. In combination with the individual setting of the turbine controlling system, these interactions influence the actual loads, acting on the support structure. A consideration of these effects for design purposes is possible by using coupled simulation software such as for example Bladed, WaveDyn or Poseidon. The latter developed at the Institute for Steel Construction, Leibniz Universität Hannover (see e.g., Böker (2010) and Dubois et al. (2016)).

For time invariant loads, as they are decisive for fatigue analysis, simulations with time series are common. In order to deal with the large amount of data from time series (see Figure 2.9, top right), simplifications are common. The time series can be split into individual load cycles and each load cycle can be characterised by certain properties as shown in Figure 2.8. With the help of counting algorithms such as the rainflow count (see Clormann & Seeger (1986)), all loads with a defined similarity are condensed in one class and reduced to number of load cycles N as well as their minimum and maximum load F_{\min} and F_{\max} . The results are stored in a Markov matrix.

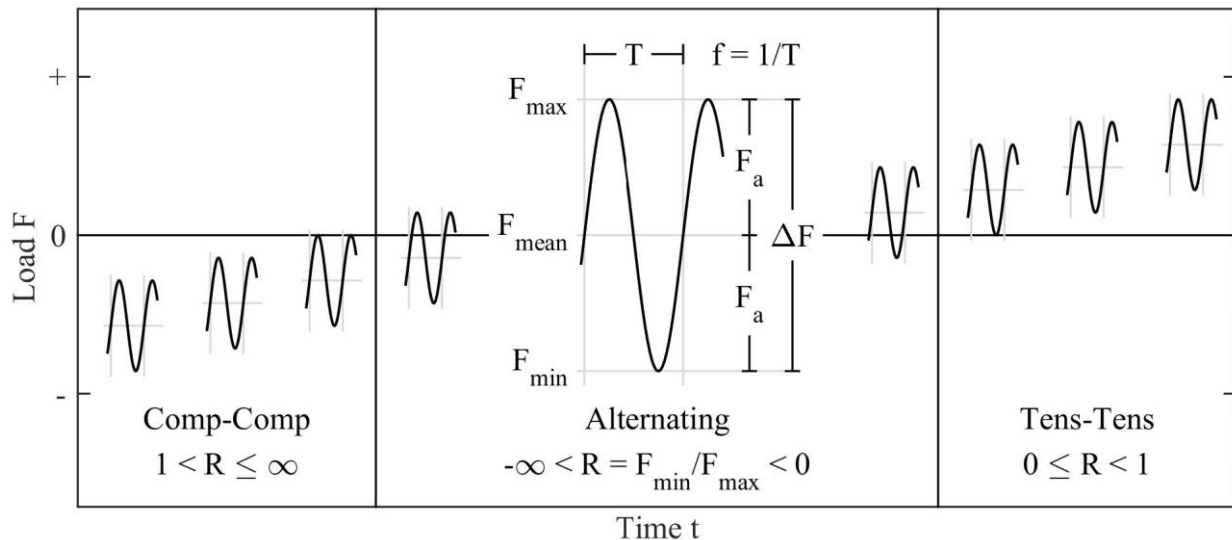


Figure 2.8: Characteristic properties of load cycles in analogy to Radaj & Vormwald (2007)

Figure 2.9 shows such simplified axial loads and corresponding numbers of load cycles for a typical grouted connection of a wind turbine with jacket substructure located in the German North Sea. Clearly visible is a mean offset due to dead weight and from load class 5 on pure compression-compression loads. The proportion between alternating and static loads is larger for offshore wind turbines than for oil and gas platforms, where static loads from dead weight are dominating.

Since the actual loads are influenced by the dynamic behaviour of the substructure, the most energetic loads acting on grouted connections are in phase with the substructure's first eigenfrequency. According to for example Schaumann et al. (2010b), Seidel & Foss (2006) and Rucker et al. (2012), typical first eigenfrequencies are ~ 0.22 Hz for monopiles and ~ 0.35 Hz for jackets.

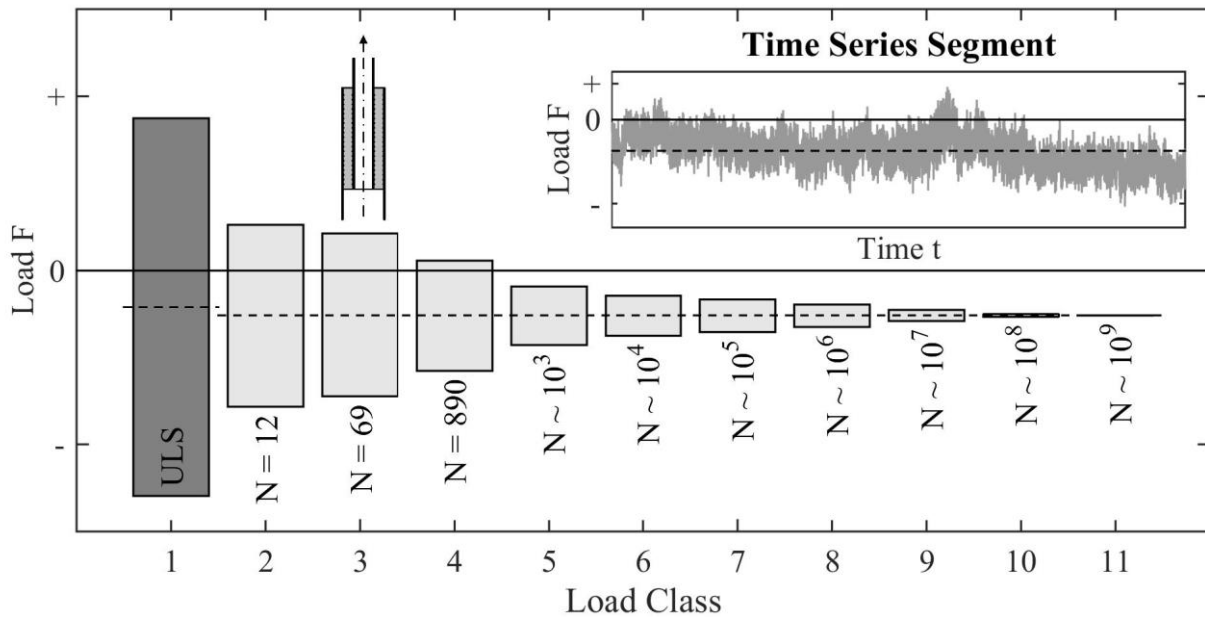


Figure 2.9: Classes of axial loads for a typical grouted connection of a wind turbine with jacket substructure located in the German North Sea and exemplary time series segment

2.3.2 Load bearing behaviour

The load transfer from pile to sleeve inside the connection depends on the type of load. Figure 2.10 shows the schematic load transfer for possible external loads. Horizontal loads are transferred by compressing the grout in the direction of loading. The steel tubes confine the grout layer and bear the load by tangential stresses. Due to the confinement in tangential direction a wider area of load transfer can be activated inside the grout layer. Bending moments are transferred similar to horizontal loads but the area of load transfer is concentrated at the grout layer's end regions and the areas are opposing each other (see Schaumann & Wilke (2007), Lotsberg et al. (2012)).

If no shear keys are applied, axial loads and torsional moments are transferred by friction and interlocking between grout and steel. The friction depends basically on surface irregularities and imperfections combined with lateral pressure (see Figure 2.12, right and Sele & Kjeoy (1989)). If both parts are missing, these loads cannot be transferred. Hence, designs with shear keys are recommended (see Schaumann et al. (2010c), Schaumann et al. (2013)). In early investigations Billington & Tebbet (1980) presumed adhesion to add further strength to the grout-steel interface. Nevertheless, tests by Sele & Seow (1988) focusing on adhesive bonds found only negligible effects of adhesion which was confirmed by investigations of Dallyn et al. (2016).

Shear keys interlock with the grout layer and change the load transfer mechanism significantly. Instead of a homogenous load transfer between steel and grout of plain pipe connections, the load transfer now localises at the shear key surface which faces the same direction as the load. The load is transferred from steel to grout via contact pressure and spreads into the grout layer. The opposing pressure propagation of a shear key on the pile and a shear key on the sleeve leads to high shear stresses along the diagonal between the shear keys (see Figure 2.10, left). For the grout segment between two shear planes Lamport (1988) introduced the term compression strut by analogy with the truss models, commonly used to explain the load bearing behaviour of reinforced concrete

structures. Horizontal loads, resulting from the inclination α of the shear plane, are borne by tangential stresses in the steel and grout parts. Likewise, in case of alternating axial loads the shear planes change their direction. In addition to the interlocking of shear keys and grout, surface friction as described for the plain pipe connections can also occur at the steel-grout interfaces (see e.g., Billington & Tebbet (1980)). Figure 2.10, left shows the load bearing behaviour of a grouted connection with circumferential shear keys for axial loads. In case of significant torsional moments vertical shear keys need to be applied as well (see NORSOK N-004 (2013), DNVGL-ST-0126 (2016)). Their load bearing behaviour is similar to the one of circumferential shear keys.

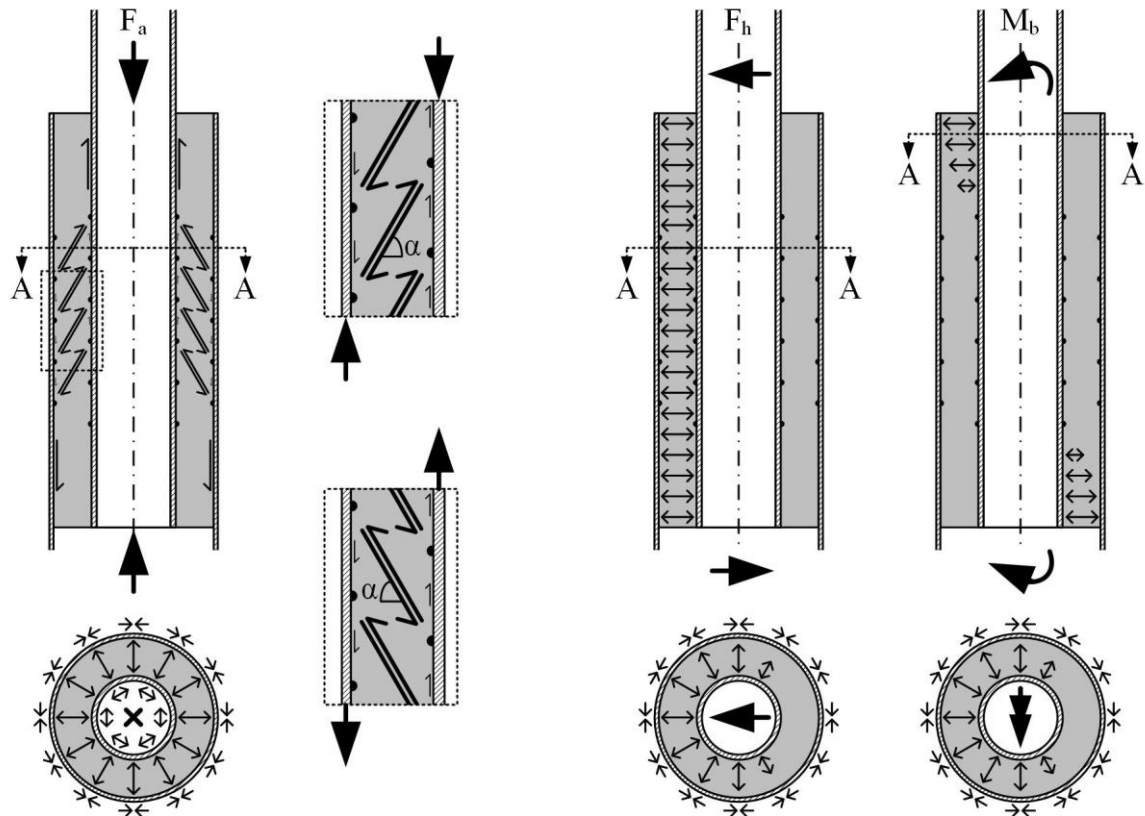


Figure 2.10: Schematic load transfer of grouted connections for axial (left), horizontal (centre) and bending (right) loads

The local interlocking behaviour between grout and shear key and consequently the local stresses are mainly influenced by the shear key geometry h_{sk} , w_{sk} and spacing s_{sk} (see e.g., Billington & Tebbet (1980), Forsyth & Tebbet (1988), Bechtel (2009), Raba (2010)).

In a real loading situation a combination of the described load parts is present. Hence, the real load bearing behaviour is also a superposition of the schematic load transfer mechanisms described before. In order to reduce the interaction of these individual mechanisms, for grouted connections with both, significant axial and bending loading, designs with shear keys located in the centre area of low bending stresses are recommended (see Schaumann & Wilke (2007)).

In the scope of this thesis only axial loading was investigated. Hence, the following descriptions focus on this particular loading situation.

2.3.3 Damage modes

Corresponding to the different load transfer mechanisms, diverse damage modes are conceivable, as shown in Figure 2.11. Grout crushing (1.) and diagonal shear cracking (2.) are the mostly observed failure modes and in the majority of cases they occur coincidentally.

For cementitious grouts without aggregates, Billington (1978) saw a combination of diagonal shear cracking 1 (2.) and grout crushing (1.). The diagonal shear cracks occurred between opposing shear keys under a certain inclination angle and aligned in the same direction as the applied load. Aritenang et al. (1990) reported an inclination angle of $\sim 45^\circ$ for similar grout materials. Bechtel (2016) found grout crushing (1.) and diagonal shear cracking 1 (2.) for HPG with varying inclination angles between $\sim 15^\circ$ and $\sim 62^\circ$.

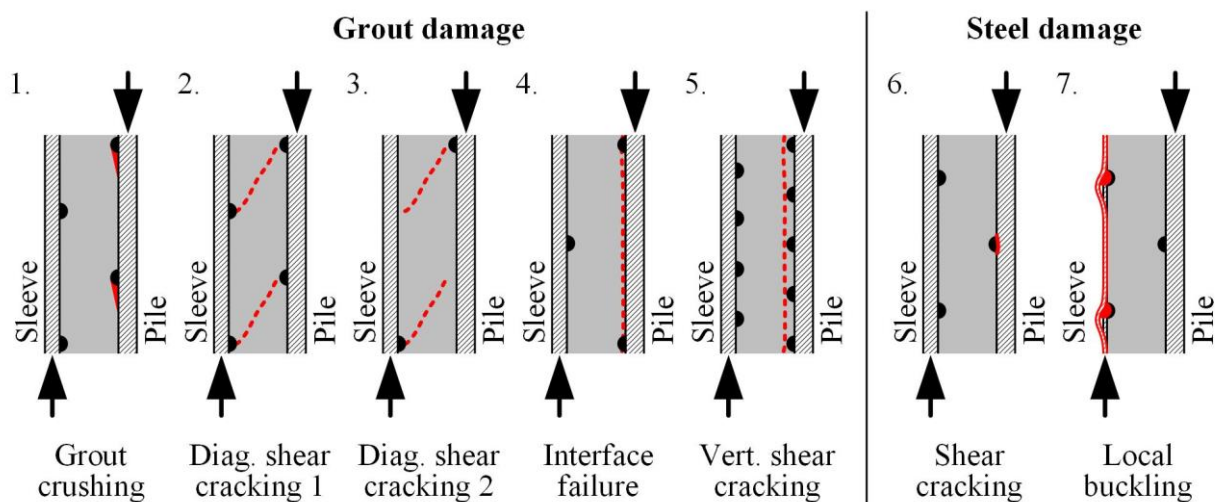


Figure 2.11: Schematic damage modes of grouted connections

Krahl & Karsan (1985) as well as Lamport (1988) reported diagonal shear cracks starting at one shear key and growing through the grout to the opposing plain surface (3.). The inclination angle of the shear cracks was similar to cracks occurring between shear keys. It can be concluded that the inclination angle is limited to a certain range and only within this range it is influenced by the shear key arrangement.

For high interlocking ratios h_{sk}/s_{sk} Krahl & Karsan (1985) as well as Forsyth & Tebbet (1988) presumed vertical shear damage of the grout to occur along the shear key tips (5.). However, corresponding test results are not published but limits for the interlocking ratio h_{sk}/s_{sk} are given in current design codes (see Section 2.5.5).

Steel damage modes can be shear damage of shear keys (6.) and local buckling of steel tubes in the area of shear keys (7.). Anders (2007) reported about sheared-off shear keys for small-scale specimens with rectangular shear keys. Local buckling at shear key positions was not observed in published tests. Both failure modes can be excluded by an appropriate design.

Besides these global damage modes local damage mechanisms are described by several authors. Sele & Kjeoy (1989) investigated the local frictional behaviour between plain steel and grout surface and stated the surface waviness δ to be decisive for the interlocking (see Figure 2.12, right).

In order to activate interlocking, a certain displacement between steel and grout is necessary, which activates lateral contact pressure and consequently friction. Depending on the surface strength, alternating loads can lead to abrasion and wedging. As a result the waviness and as a consequence the interlocking is reduced (see Schaumann et al. (2013), Dallyn et al. (2016)).

In static strength tests with constant loading direction, Krahl & Karsan (1985) found wedges of crushed grout material in front of the loaded shear key surfaces (see Figure 2.12, left). The length of the wedges was about four times the shear key height h_{sk} . At the unloaded side of the shear key voids occurred in the grout layer. Bechtel (2016) confirmed this behaviour for HPG materials.

In contrast to these observations, Aritenang et al. (1990) found grout crushing only in the circular shape of the shear keys. Conducting static strength tests with additional unloading procedures, the shear key movements led to a widening of the shear key groove in the grout layer (see Figure 2.12, centre).

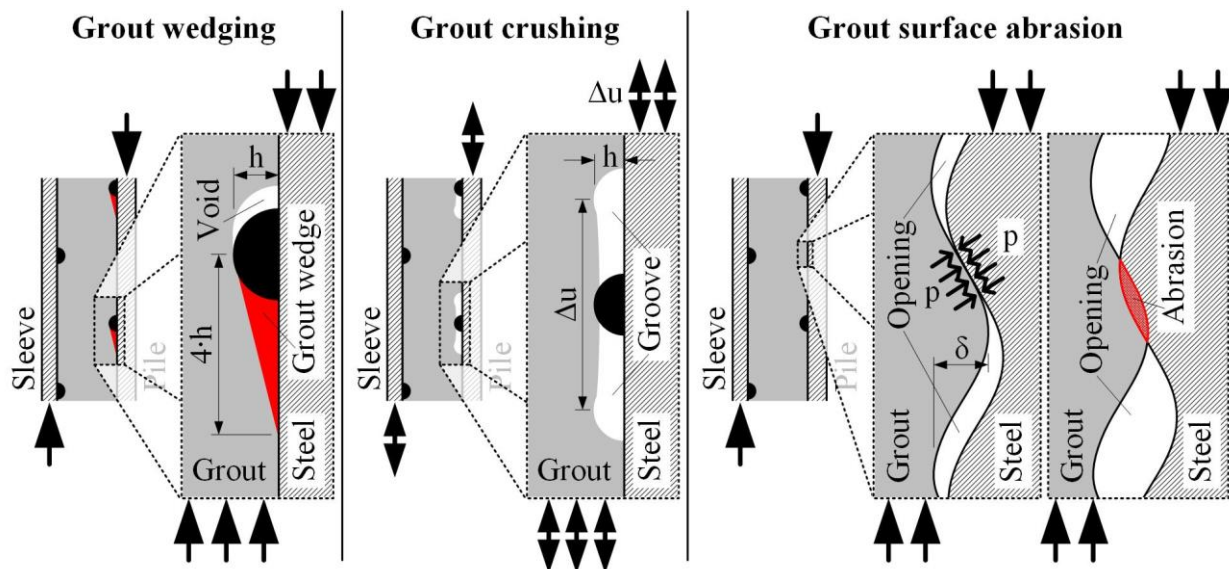


Figure 2.12: Schematic local damage mechanisms in grouted connections

2.3.4 Load displacement behaviour

Static loading

Figure 2.13 shows a typical load displacement curve of a quasi-static loaded grouted connection specimen published by Billington & Tebbet (1980) for plain cement grout, and for HPG published by Schaumann & Wilke (2006b). For plain cement grout the load displacement curve is smoothly losing stiffness with increasing load. After the static load bearing capacity F_{ULS} is reached, slippage occurs with a significant reduction of load bearing capacity. When the interlocking is restored, the load can be increased but to a decreasing level with every slippage phase. For the HPG material the initial load displacement behaviour is almost linear up to a loading level of $\sim 0.5 \cdot F_{ULS}$. After a pronounced kink, a further increase of load up to $1.0 \cdot F_{ULS}$ is possible but at a significantly lower stiffness. Once F_{ULS} is reached, the load bearing capacity reduces and large displacements occur. According to Schaumann & Wilke (2006b) the first kink is caused by a diagonal shear crack at the lower end of the connection. Further load displacement curves, confirming the described

behaviour, are published by for example Lamport (1988), Aritenang et al. (1990), Schaumann et al. (2008) and Schaumann et al. (2009). The results presented in both papers by Schaumann et al. show that with increasing grout material elasticity modulus and hence, more brittle material behaviour, the load displacement curve loses its smoothness.

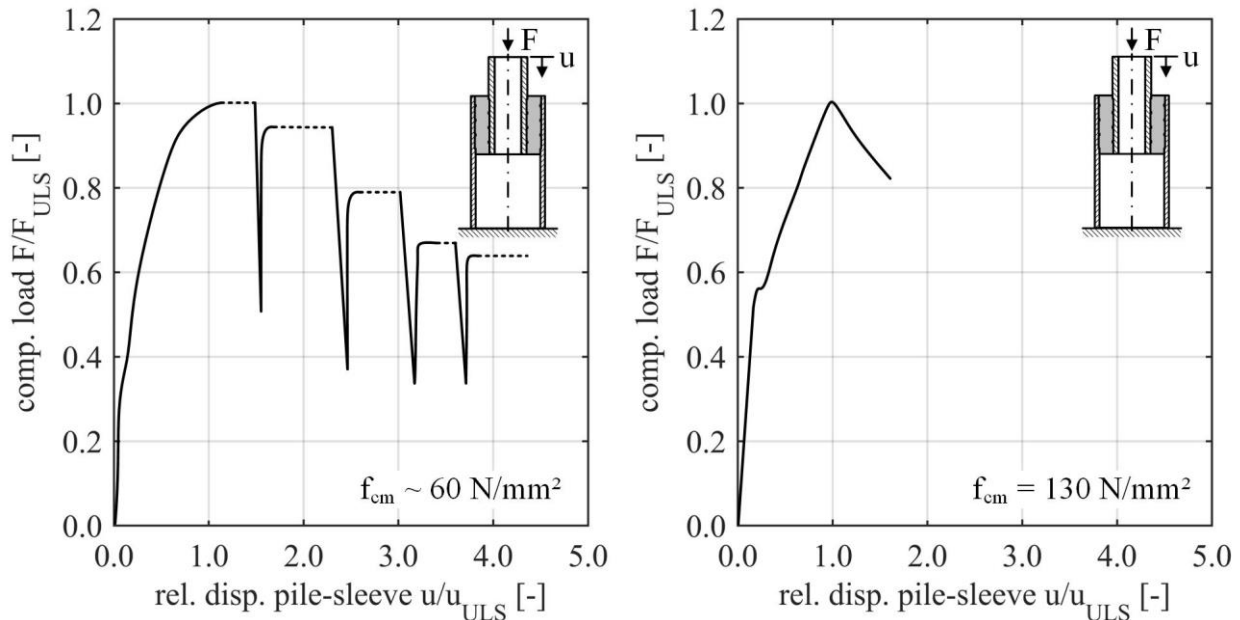


Figure 2.13: Schematic load displacement curve of a quasi-static loaded grouted connection with plain cement grout acc. to Billington & Tebbet (1980) (left) and with HPG acc. to Schaumann & Wilke (2006b) (right)

Fatigue loading

The load displacement behaviour under fatigue loading depends on whether the load is alternating or not. For the case of a pure compressive loading Schaumann et al. (2010a) observed an increase of relative mean displacement between pile and sleeve while the cyclic load displacement behaviour remained constant (see Figure 2.14, right). In contrast, for alternating loading Billington & Tebbet (1982) observed an almost unchanged relative mean displacement but an increasing displacement amplitude (see Figure 2.14, left). Moreover, the corresponding hysteresis showed a widening instead of a tilting behaviour observed for plain concrete (see e.g., Holmen (1979)). This means, the connection's stiffness remained constant but after load reversal, slipping occurred in the connection which led to impact loading on the shear key groove.

Comparing these results to the typical axial deformation behaviour of plain concrete cylinders, as described by Pfanner (2003) (see Figure 2.15, top left), shows certain similarities. During the first load cycles an initial settling process takes place, which is caused by micro-cracking in the grout layer. Subsequently, a phase of stable crack growth with a linear displacement increase per load cycle occurs. Finally, during the last load cycles the displacement rate increases due to matrix cracking until the specimen fails. However, Figure 2.14, right shows that for grouted connections the intermediate phase is not as stable as for concrete cylinders.

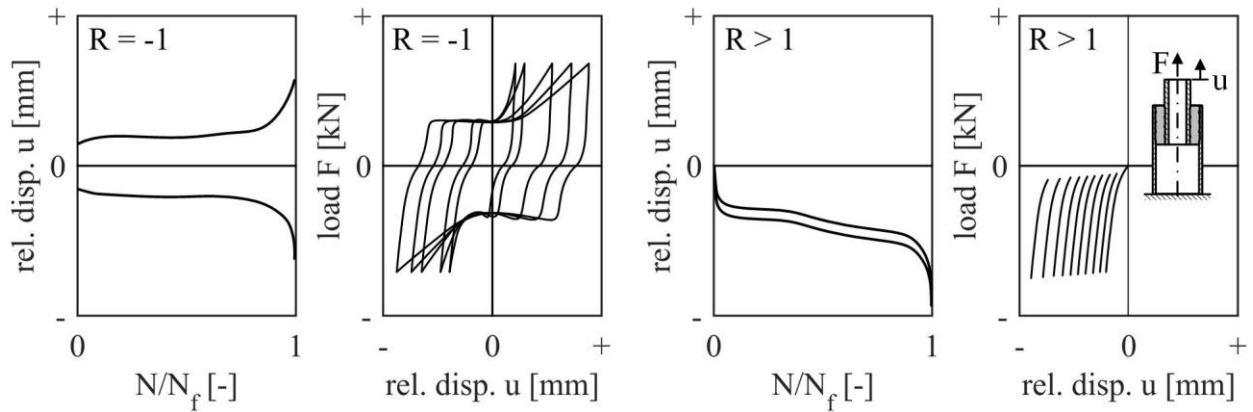


Figure 2.14: Schematic relative displacement evolution over number of normalised load cycles and corresponding hysteresis for alternating loads acc. to Billington & Tebbet (1982) (left) and for compression loads acc. to Schaumann et al. (2010a) (right)

In his research, Holmen (1979) evaluated the evolution of the elasticity modulus during testing (see Figure 2.15, bottom left). He observed a significant reduction during the whole test, which corresponds to a tilting hysteresis. For grouted connections such an evaluation was not carried out yet.

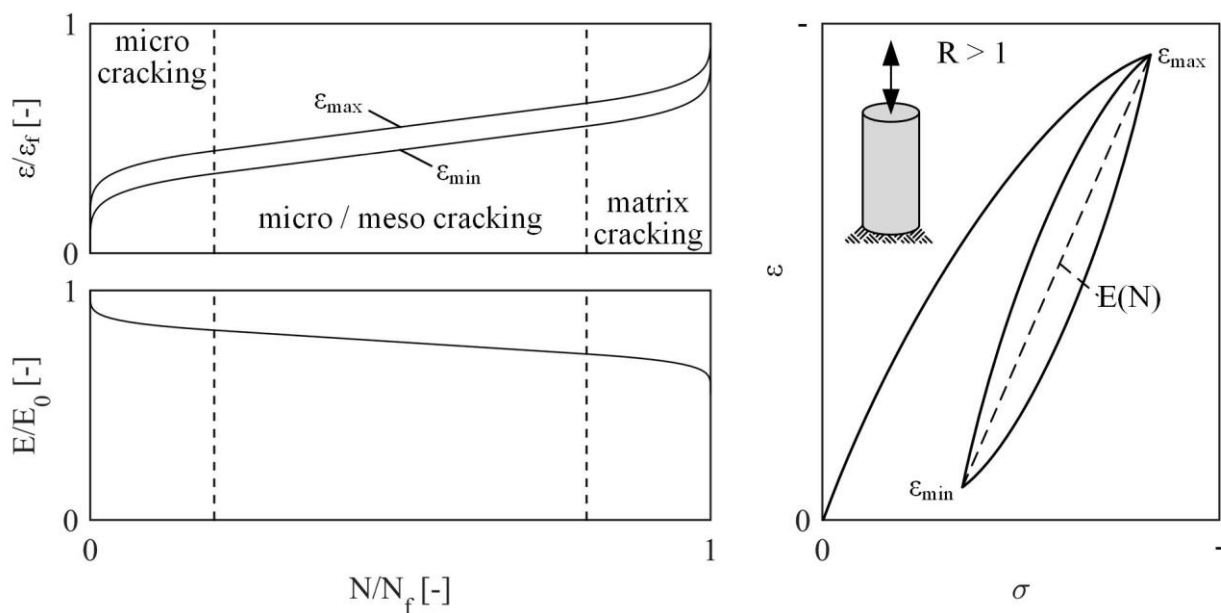


Figure 2.15: Schematic strain evolution over number of normalised load cycles of a concrete cylinder under cyclic compression and cracking phases acc. to Pfanner (2003) (top left), schematic reduction of elasticity modulus over number of normalised load cycles acc. to Holmen (1979) (bottom left) and schematic stress strain behaviour (right)

2.4 Influence of selected parameters

2.4.1 Influence of water

General influence

First investigations about the influence of water on the fatigue behaviour of reinforced concrete beams were carried out by Waagaard (1977). His specimens were 800 mm long reinforced concrete beams, tested under axial fatigue loading. As the author described, all specimens were pre-cracked. For the submerged specimens the author observed that the cyclic load led to a mechanism that pumped water through the crack and increased the deterioration of the crack surfaces. This behaviour resulted in a significant reduction of endurable load cycles for the tests carried out in submerged conditions. These observations were confirmed in later additional tests by Waagaard (1986).

Further investigations by Muguruma & Watanabe (1984), Muguruma & Watanabe (1986) and Nishiyama et al. (1987) covered axial compression-compression loaded cylinder specimens as well as 2400 mm long reinforced concrete beams in cyclic bending tests. The results confirmed a reduced fatigue capacity when tested in submerged ambient conditions. Muguruma & Watanabe (1984) also saw a dependency between concrete density and number of endurable load cycles, where a higher density reduced the difference between dry and wet ambient condition results. Additionally, the authors investigated the influence of different curing conditions. After initial curing in a water basin for all specimens, they took some specimens for further curing in dry conditions. Afterwards, they tested dry curing and dry testing (DA), dry curing and wet testing (DW) as well as wet curing and dry testing (WA). The lowest number of endurable load cycles was observed for DW, whereas the results for WA were in between DW and DA. Real grouted connections of lattice substructures are cast, cured and loaded in submerged conditions. Unfortunately, a corresponding combination WW was not covered by the authors.

Nygaard et al. (1992) investigated normal and lightweight aggregate concrete cylinders with diameters of 50, 100 and 450 mm in compression-compression fatigue tests. Besides tests in wet and dry ambient conditions, the authors also conducted tests on sealed specimens. In general the results for wet ambient conditions showed the lowest number of endurable load cycles and therefore confirmed the previously described investigations of other authors. For sealed specimens, the resulting endurable load cycles were in between wet and dry ambient conditions but closer to the wet ambient condition results. The authors explained this behaviour with the water ingress gradient. For sealed and wet ambient conditions the water ingress gradient is comparable, while for dry ambient condition specimens the water saturation decreases towards the surfaces. In addition, the size of the specimen's diameter influenced the fatigue behaviour. With increasing diameter, the influence of the ambient condition was reduced. Again, the authors used the water ingress depth as explanation. The water ingress depth depends on the time the specimen can soak in water. While the specimens are cured in a water basin, a natural saturation level is reached. Afterwards, in the tests the cyclic load pumps the water in and out of the specimen. In relation to the specimens diameter the boundary layer depth influenced by pumping is getting smaller with increasing diameter. Nygaard et al. (1992) assumed a depth of 10 mm to be the limit for the influenced boundary layer. However, it must be mentioned that the specimens with smaller diameters of 50 and 100 mm were

loaded with a loading frequency of 1 Hz while the 450 mm diameter specimens were loaded with a loading frequency of 0.5 Hz. Moreover, only an average of two specimens per parameter set-up was tested. The authors expected no influence of the loading frequency. However, as described in the next Section other investigations showed a significant influence of the loading frequency for tests in wet ambient conditions. Hence, the physical mechanism described by Nygaard et al. (1992) seems to be plausible but a corresponding experimental proof is needed.

Soerensen (2011) extended the research with the commercial grout material for offshore applications BASF Masterflow 9500. This material had a compressive strength of ~ 140 N/mm². He investigated cylinders of 60 mm diameter and 120 mm length in dry and submerged ambient conditions in axial compression-compression tests. His results confirmed a reduced number of endurable load cycles also for HPG material. However, his results showed a significant scatter.

Latest investigations were carried out by Hümme (2013), Hümme (2015) and Hümme et al. (2016) for grout and plain concrete cylinder specimens tested in dry and wet ambient conditions under compression-compression loading. The results confirmed a reduced fatigue capacity for specimens tested in submerged conditions. Hümme (2015) observed spalling of the surface and loose grout particles blurring the surrounding water. He also described that water ingress in surface defects and surface imperfections washes out loose particles. Moreover, Hümme (2015) expects water pressure caused by crack closing to cause additional tensile stresses and leading to faster deterioration.

Loading frequency

In Waagaard (1986) the author extended his prior experiments with investigations on different loading frequencies. Using the same concrete beam specimen as described before, loading frequencies of 0.2, 1 and 3 Hz were realised. In addition, the influence of compression-compression and compression-tension loading was examined. The results showed an increase of endurable load cycles with increasing loading frequencies. For loading frequencies of 0.2 and 1 Hz this behaviour was also enhanced when compression-tension loading was applied.

Investigations by Soerensen (2011) comprised tests with 0.35, 5 and 10 Hz in both ambient conditions. The submerged specimens showed an increase of endurable load cycles correlating with an increasing frequency. He explained this phenomenon by the flow velocity of the water inside the cracks. A low flow velocity, resulting from a low loading frequency gives, the water more time to soak deeper into the grout surfaces. When the load direction changes, a thicker layer of water saturated pores is compressed and probably damaged by water overpressure.

Loading frequencies of 1 and 10 Hz were investigated for standard concrete specimens by Hümme et al. (2016) and for high-strength grout by Hümme (2015). The results confirmed the prior observations that in submerged ambient conditions higher frequencies lead to more endurable load cycles.

Water pressure

Waagaard (1986) also investigated the influence of water pressure. For the investigated pressures of 0, 7 and 14 bar he found no significant influence on the fatigue behaviour. As explanation he pointed out that the deterioration is caused by a pumping mechanism as described before and is therefore not influenced by water pressure. Hence, it can be concluded that for typical water depths of bottom fixed offshore wind turbine installations, the influence of water pressure on grouted connections can be neglected (~3 to ~5 bar).

Pre-cracking

Most of the specimens used by Waagaard (1977) and Waagaard (1986) were initially pre-cracked. The influence of pre-cracking showed only a slight reduction in endurable load cycles. The author assumed that imperfections of the specimens' surfaces lead to cracked states after a few load cycles. Consequently, all specimens can be assumed to have been pre-cracked.

Salinity

For wet ambient conditions Waagaard (1986) and Nygaard et al. (1992) used seawater with a natural amount of salt. Muguruma & Watanabe (1984), Soerensen (2011) and Hümme et al. (2016) used tap water for their tests. Tests combining both fatigue tests in tap and seawater were carried out on reinforced concrete beams for example by Katwan (1988). In his dissertation Katwan (1988) described that salt influences the concrete passivity and leads to faster corrosion of the reinforcement bars. This behaviour resulted in less endurable load cycles for tests carried out in seawater. Moreover, chemical reactions between concrete and chlorides are possible, which may reduce the concrete strength. These processes depend on the mixture of the concrete, the type of aggregates and the type of available chlorides as well as possible other chemical components of the surrounding water. Consequently, the salinity of water influences concrete or grout strength on a long-term scale but a general statement on the significance of this effect is hardly possible.

Experience from application

Besides the previously described research results, experiences from practical applications of cyclically loaded concrete in wet ambient conditions also showed an influence of the water on the fatigue behaviour of concrete. Publically available are for example information about damage cases of onshore wind turbines as described by Bosse (2008) and Bosse (2009). In the affected turbines, the connection between steel tower and concrete foundation was realised by a steel segment casted into the foundation. The interface between steel and concrete was cyclically loaded and not sealed against ingress of water. As a result, water was pumped through the interface by the turbines cyclic motions and led to severe deterioration of the concrete surface facing the steel segment. Flushed concrete particles were found on top of the foundation around the interface. As a renovation measure, Bosse (2008) recommended a bitumen sealing of the interface, which was later realised.

2.4.2 Autogenous shrinkage

During the hydration process of cement mixtures, chemical reactions occur between cement and water. During this process cement gel filled pores in the mixture need to be filled with an adequate amount of water for a complete chemical reaction. If less water is available, the pores dry out and thus, their volume is reduced. This effect is called autogenous shrinkage and depends prevalingly on the water content of the mixture and the chemical reaction. In contrast, drying shrinkage depends mainly on the boundary conditions. Autogenous shrinkage can only be influenced by the water cement ratio and chemical additives in the mixture. On a global scale also the amount of aggregates in the mix influence the shrinkage deformation because the aggregates do not participate in the chemical reaction and hence do not shrink. In summary, less water and fewer aggregates lead to larger autogenous shrinkage deformations.

Billington (1978) investigated autogenous shrinkage for OPC and HAC cement on sealed cylinder specimens. He observed shrinkage between ~ 0.1 and ~ 0.2 % after 28 days of curing, which corresponds to ~ 1000 and ~ 2000 $\mu\text{m}/\text{m}$. In his summary he assumed no significant influence of autogenous shrinkage on the load bearing behaviour and capacity of grouted connections with shear keys.

For the commercial grout BASF Masterflow 9500 Soerensen (2011) found a negligible amount of autogenous shrinkage deformations but did not provide numerical values. The material's manufacturer states that autogenous shrinkage for BASF Masterflow 9500 is less than 100 $\mu\text{m}/\text{m}$ at 20°C (see BASF Construction Chemicals (2010)).

Weicken (2013) and Weicken & Lohaus (2014) investigated grouting mortar for offshore applications and found that autogenous shrinkage was completed within the first ~ 7 days of curing. In Weicken (2013) the author measured autogenous shrinkage of up to 780 $\mu\text{m}/\text{m}$ at 20°C .

Particular investigations about autogenous shrinkage effects on the fatigue behaviour of grouted connections are not yet carried out.

2.5 Ultimate Limit State (ULS) design approaches

2.5.1 General remark

Currently, there are three basic load bearing models for predominantly axially loaded grouted connections coincidentally established. Model 1 considers a homogenised interface shear stress acting at the decisive steel-grout interface. For the connection shown in Figure 2.1 this is the interface between pile and grout. The idea goes back to plain pipe grouted connections, where the interface stress results from the applied load divided by the interface area. Within this model the influence of shear keys is covered as an increased interlocking between steel and grout. Model 2 is an advanced version of Model 1 based on the local scale of load per shear key. Model 3 is based on the idea of compression struts occurring between shear keys, as depicted in Figure 2.10. Therefore, the applied load is divided into parts per compression strut and the load bearing capacity per compression strut is calculated.

Subsequently, the individual approaches are described per publication, focusing on axial loads only. For a better comparability the original approaches are modified by means of consistent indices in this thesis and geometric parameters according to Figure 2.1. Only approaches, described in currently valid codes and technical notes, are included. The Model 1 design approach of the former code DNV-OS-J101 (2013) and its history is not covered. This approach included surface friction as part of the connection's load bearing capacity. After a large series of damages in grouted connections designed on friction capacity only (see Schaumann et al. (2010c)), this approach was withdrawn. A different approach on the compression strut Model 3 given in GL-TN-GC (2013) is also excluded from the description since it is not yet established as a general approach.

2.5.2 Model 1

Effects of actions

For the Model 1 approach the effects of actions σ_a from axial loads F_a are calculated according to Equation (2.1) (see Figure 2.1 for geometric parameters). As described before, the resulting stress σ_a is not influenced by shear keys and therefore constant throughout the whole interface.

$$\sigma_a = \frac{F_a}{\pi \cdot D_p \cdot L_e} \quad (2.1)$$

API RP 2A-WSD (2007)

Equation (2.2), which represents a linear relation between cube compressive strength f_{cu} and interface bond strength f_{ba} , was derived by Karsan & Krahl (1984). In total, results from 44 plain pipe and 73 shear key connection tests, partly from the authors and partly from other research projects including data from Billington & Tebbet (1980), were considered for evaluation. The line described by Equation (2.2) is a lower boundary of all test results and, as stated by the authors, an arbitrary safety margin. Hence, the calculated f_{ba} can be interpreted as a design value. Equation (2.2) is included in the American API RP 2A-WSD (2007) recommended practice document, which was valid until 2014.

$$f_{ba} = 0.138 + 0.5 \cdot f_{cu} \cdot \frac{h_{sk}}{s_{sk}} \quad (2.2)$$

The final utilisation ratio can be calculated according to Equations (2.3) and (2.4) including a material safety factor γ_m .

$$f_d = \frac{f_{ba}}{\gamma_m} \quad (2.3)$$

$$U_g = \frac{\sigma_a}{f_d} \leq 1.0 \quad (2.4)$$

OTO 2001/016 (2002)

In contrast to the previous approach, in his earlier research Billington (1978) found a parabolic relation between cube compressive strength f_{cu} and interface bond strength f_{bu} . Moreover, he saw an influence of the stiffness relations between steel and grout parts. To include this behaviour in the design equations he introduced the stiffness factor K shown in Equation (2.5), which is calculated from the individual slendernesses D/t of the connection's individual parts and the corresponding elastic moduli E .

$$K = \left[\left(\frac{D_p}{t_p} \right) + \left(\frac{D_s}{t_s} \right) \right]^{-1} + \frac{E_g}{E_s} \cdot \left(\frac{D_g}{t_g} \right)^{-1} \quad (2.5)$$

Billington & Tebbet (1980) derived the characteristic interface bond stress f_{buc} given in Equation (2.6). They considered 64 static test results from plain pipe and shear key equipped specimens. Besides the stiffness factor K , also a coefficient C_L , to account for a slightly reduced load bearing capacity with increasing L/D_P ratio, and a surface condition factor C_S , to account for different interlocking conditions, are included in the equation. Today Equation (2.6) is available in the current British OTO 2001/016 (2002) report as well as an alternative to the previously described approach in API RP 2A-WSD (2007).

$$f_{buc} = K \cdot C_L \cdot \left(9 \cdot C_S + 1100 \cdot \frac{h_{sk}}{s_{sk}} \right) \cdot f_{cu}^{0.5} \quad (2.6)$$

The strength check can be carried out according to Equation (2.4) with f_{buc} instead of f_d .

DIN EN ISO 19902 (2014)

In 1994 a group of experts was set up to revise the design approaches of that time (see Harwood et al. (1996)). After screening more than 600 test results from several research projects, also including the data basis and test results of Karsan & Krahl (1984), the authors decided to take 193 of these results into account for their evaluation.

In the investigated test results the authors found two different failure modes. The first one was sliding at the steel grout interface (see Figure 2.11, 4.). This failure mode was covered by the previously described design approaches. In addition, the results of Forsyth & Tebbet (1988) showed a second failure mode of diagonal shear cracking in the grout matrix (see Figure 2.11, 2. and 3.) for smaller shear key spacings s_{sk} .

For the first failure mode in older publications the term bond strength was used to include effects of adhesion, but later evaluations by Harwood et al. (1996) could not find a significant influence of adhesion and hence the authors proposed the term 'interface shear strength'. Starting from Equation (2.6), the authors introduced Equation (2.7) for calculation of the interface shear strength $f_{g,sliding}$.

$$f_{g,sliding} = C_p \cdot \left[2 + 140 \cdot \left(\frac{h_{sk}}{s_{sk}} \right)^{0.8} \right] \cdot K^{0.6} \cdot f_{cu}^{0.3} \quad (2.7)$$

In the new equation the surface condition coefficient C_s as well as a coefficient C_L for the L/D_P ratio was not included anymore. Beforehand, Forsyth & Tebbet (1988) found a non-linear relation between shear key density h_{sk}/s_{sk} and the interface strength, which was not covered correctly by the older C_s parameter. Moreover, on the basis of the broader data base Harwood et al. (1996) could not confirm an influence of the L/D_P ratio. Instead a parabolic scale parameter C_P , relying on the pile diameter D_P , was introduced (see Equation (2.8)). Furthermore, in the broader data base the influence of h_{sk}/s_{sk} , K and f_{cu} was found to be smaller than derived for Equation (2.6). Hence, exponents for these parameters were introduced or modified.

$$C_p = \begin{cases} \left(\frac{D_p}{1000} \right)^2 - \left(\frac{D_p}{500} \right) + 2 & D_p \leq 1000 \text{ mm} \\ 1.0 & D_p > 1000 \text{ mm} \end{cases} \quad (2.8)$$

As described by Harwood et al. (1996), from a certain range of shear key density h_{sk}/s_{sk} on, grout matrix failure becomes decisive. The limit is stated as $h_{sk}/s_{sk} \sim 0.06$. The derived Equation (2.9) for grout matrix failure is today included in DIN EN ISO 19902 (2014), DNVGL-ST-0126 (2016) and NORSOK N-004 (2013).

$$f_{g,shear} = \left[0.75 - 1.4 \cdot \left(\frac{h_{sk}}{s_{sk}} \right) \right] \cdot f_{cu}^{0.5} \quad (2.9)$$

The final strength check according to Equation (2.4) must be carried out for the decisive failure mode which can be obtained according to Equation (2.10).

$$f_g = \min(f_{g,sliding}; f_{g,shear}) \quad (2.10)$$

Moreover, the design strength f_d defined in DIN EN ISO 19902 (2014) includes not only a material safety factor γ_m but also a reduction factor k_{red} to account for a reduced material strength due to early age cycling (see Section 2.2.4).

$$f_d = \frac{f_g \cdot k_{red}}{\gamma_m} \quad (2.11)$$

NORSOK N-004 (2013)

For the interface shear strength $f_{g,sliding}$ Det Norske Veritas AS (2013) modified Equation (2.7) with a slightly different consideration of the scale influence. The new Equation (2.12) was later included in NORSOK N-004 (2013) as well as DNV-OS-J101 (2014) and DNVGL-ST-0126 (2016). The data basis for this modification is not publically described.

$$f_{g,sliding} = \left[\frac{800}{D_p} + 140 \cdot \left(\frac{h_{sk}}{s_{sk}} \right)^{0.8} \right] \cdot K^{0.6} \cdot f_{cu}^{0.3} \quad (2.12)$$

The grout matrix strength shall be calculated according to Equation (2.9). The strength check can be carried out according to Equations (2.10), (2.3) and (2.4). Possible influences of early age cycling are not considered in NORSOK N-004 (2013).

2.5.3 Model 2 – DNVGL-ST-0126 (2016)

General remark

The design approach for predominantly axially loaded grouted connections described in DNVGL-ST-0126 (2016) is based on the previously described design approach by Det Norske Veritas AS (2013) included in NORSOK N-004 (2013). Though, instead of the effective overlapping length of the grout layer L_e , in the DNVGL approach the interface strength is determined for the area of one shear key spacing s_{sk} multiplied by the number of shear keys N_{sk} . This provides the benefit that areas without shear keys do not contribute to the calculated global load bearing capacity of the connection.

Effects of actions

The effects of action for axial loads F_a are calculated according to Equation (2.13) which is similar to Equation (2.1) but instead of the effective grout layer length L_e , the number of shear keys N_{sk} is considered. The result is the load $F_{V1,Shk,d}$ per circumferential shear key.

$$F_{V1,Shk,d} = \frac{F_{a,d}}{\pi \cdot D_p \cdot N_{sk}} \quad (2.13)$$

Resistance

The calculation of interface shear strength $f_{g,sliding}$ is the same as given in Det Norske Veritas AS (2013) and stated in Equation (2.12). The grout matrix strength is the same given in Equation (2.9). The final axial strength per shear key $F_{V1,Shk,cap,d}$ (see Equation (2.14)) is then calculated from the decisive strength f_g (see Equation (2.10)) per shear key spacing s_{sk} and a material safety factor γ_m .

$$F_{V1,Shk,cap,d} = \frac{f_g \cdot s_{sk}}{\gamma_m} \quad (2.14)$$

The utilisation ratio follows in Equation (2.15).

$$U_g = \frac{F_{V1,Shk,d}}{F_{V1,Shk,cap,d}} \leq 1.0 \quad (2.15)$$

In DNVGL-ST-0126 (2016), early age cycling is considered as a general limitation of movements during curing to a maximum of 1 mm.

2.5.4 Model 3 – Schaumann et al. (2012)

General remark

The compression strut based design approach is presented in its latest formulation as described by Schaumann et al. (2012). The model was introduced by Lamport (1988) and later adjusted by Anders (2007). In addition to the data base used by Harwood et al. (1996), Schaumann et al. (2012) validated their approach also with test results from Lamport (1988) and Anders (2007). Figure 2.16 visualises the basic idea of this approach.

Effects of actions

For this approach the resistance is calculated as axial load bearing capacity of the connection. Thus, instead of effects of actions the connection's axial load can be used for the strength check.

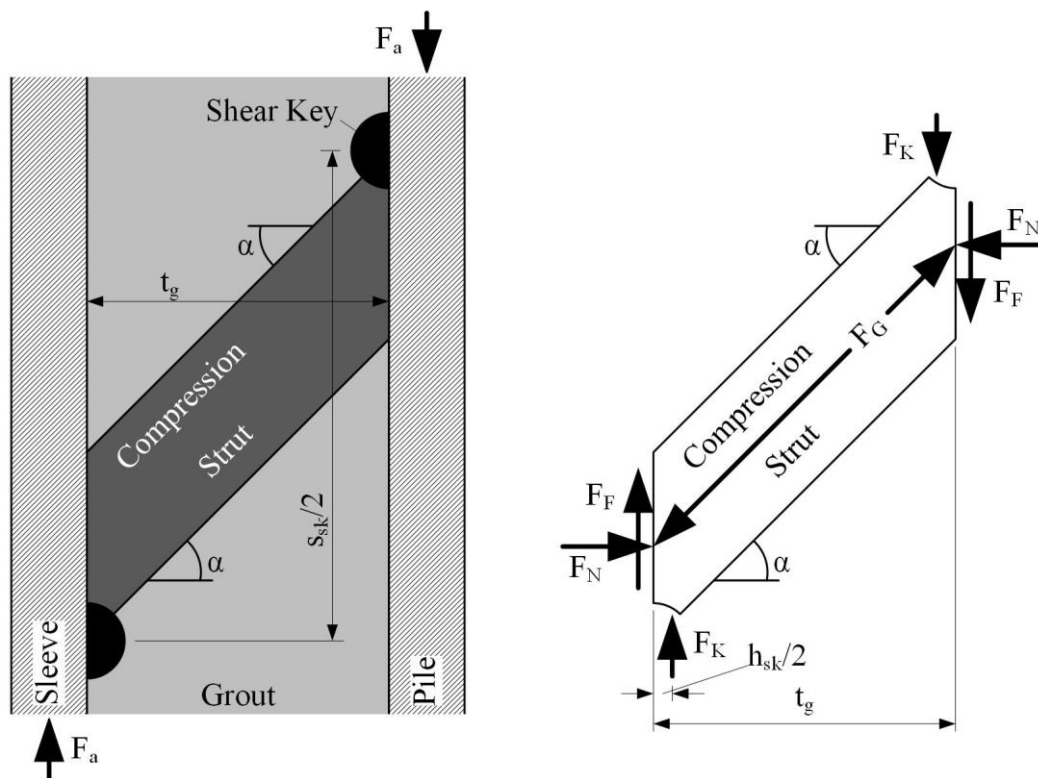


Figure 2.16: Compression strut model and corresponding free body diagram acc. to Schaumann et al. (2012)

Resistance

The load bearing capacity of one compression strut consists of a vertical part F_K and a horizontal part F_N . Accordingly, the load bearing capacity of a grouted connection is the sum of F_K and F_N multiplied by the number of shear keys N_{sk} as described by Equation (2.16).

$$F_{ges} = (F_K + F_N) \cdot N_{sk} \cdot y \cdot \left(\frac{h_{sk}}{s_{sk}} \right)^x \quad (2.16)$$

The vertical part F_K given in Equation (2.17) is calculated as grout capacity multiplied by the simplified load application area of one shear key. To take into account the confining influence of the surrounding steel tubes and the resulting higher capacity of the grout, the grout capacity f_{cu} is raised by a confinement factor κ multiplied with the yielding limit of the weakest steel part (see Equation (2.18)). For the confinement factor κ Schaumann et al. (2012) recommend a value of 3 in analogy to Johansson & Akesson (2001).

$$F_K = [f_{cu} + \kappa \cdot \sigma_{lat}] \cdot h_{sk} \cdot \pi \cdot (D_p + h_{sk}) \quad (2.17)$$

$$\sigma_{lat} = \min \left[\left(\frac{f_y \cdot 2 \cdot t_p}{D_p} \right); \left(\frac{f_y \cdot 2 \cdot t_s}{D_s} \right) \right] \quad (2.18)$$

The horizontal part F_N given in Equation (2.19) depends on F_K , the strut inclination angle α as well as the surface friction coefficient μ .

$$F_N = \frac{F_K \cdot (t_g - h_{sk})}{[t_g \cdot (\tan \alpha - \mu)]} \quad (2.19)$$

According to Anders (2007) the connection's load bearing capacity is non-linearly correlated to the number of shear keys N_{sk} . In test results he saw less contribution per shear key to the overall capacity F_{ges} with increasing number of shear keys. Therefore, he introduced a correction term depending on the h_{sk}/s_{sk} ratio (see Equation (2.16)). The best correlation with his test results were obtained with the parameters $x = -0.628$ and $y = 0.141$.

The utilisation ratio can be calculated according to Equation (2.20). A safety concept with corresponding safety factors is not defined for this approach.

$$U_g = \frac{F_a}{F_{ges}} \leq 1.0 \quad (2.20)$$

In contrast to the latest formulations of Model 1 and 2, the previously described Equations cover only the compression strut failure, which corresponds to grout matrix failure in terms of Model 1 and 2. Krahl & Karsan (1985) and Forsyth & Tebbet (1988) assumed an additional failure mode for closely spaced shear keys, where the grout matrix fails between two shear keys on the same surface (see Figure 2.17). In order to exclude this failure mode, Schaumann et al. (2012) proposed a limit for h_{sk}/s_{sk} , considering the vertical shear strength of the grout (see Equation (2.21)).

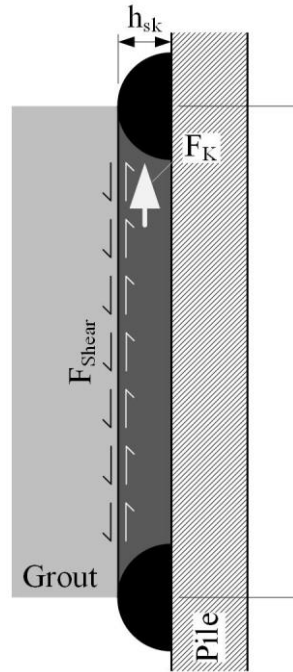


Figure 2.17: Model for vertical shear failure acc. to Schaumann et al. (2012)

$$\max\left(\frac{h_{sk}}{s_{sk}}\right) \leq \frac{(0.5 \cdot v \cdot f_{cu}) \cdot (D_p + 2 \cdot h_{sk})}{[f_{cu} + \kappa \cdot \sigma_{lat}] \cdot (D_p + h_{sk})} \quad (2.21)$$

2.5.5 Ranges of applicability

The previously described design approaches were developed on the basis of a similar set of test results. Therefore, the authors defined certain ranges of applicability given by the parameter ranges covered in the corresponding tests. Table 2.1 shows all ranges of applicability, as they are defined in the three major design codes DIN EN ISO 19902 (2014), NORSOK N-004 (2013) and DNVGL-ST-0126 (2016). The missing limitation for f_{cu} in DNVGL-ST-0126 (2016) is emphasised, since it allows to use this approach for high strength grouts. Moreover, in DNVGL-ST-0126 (2016) a minimum value for the shear key spacing s_{sk} is given. This limit prevents an overlay of deformations in the steel tubes, due to local bending caused by the shear keys.

The comparison between the ranges of applicability and the parameters of the reference structures show that for both selected reference structures the grout strength f_{cu} as well as the stiffness K exceed the ranges. Moreover, the reference pre-piled connection has a more compact pile and grout layer.

Table 2.1: Ranges of applicability for current design codes

			ISO 19904	N-004	DNVGL-ST-0126	Reference Pre-piled	Reference Post-piled
20.0 ≤	f_{cu}	[N/mm ²] ≤ 80.0	√	√		140.0 !	140.0 !
20.0 ≤	D_p/t_p	[-] ≤ 40.0	√	√		15.8 !	49.6
		≤ 60.0			√		
30.0 ≤	D_s/t_s	[-] ≤ 140.0	√	√	√	36.5	56.8
10.0 ≤	D_g/t_g	[-] ≤ 45.0	√	√	√	4.1 !	10.4
1.0 ≤	L_e/D_p	[-] ≤ 10.0	√	√	√	3.9	2.1
1.5 ≤	w_{sk}/h_{sk}	[-] ≤ 3.0	√	√	√	2.5	2.0
5.0 ≤	h_{sk}	[mm]			√	10.0	15.0
0.0 ≤	h_{sk}/s_{sk}	[-] ≤ 0.1	√	√	√	0.05	0.05
	h_{sk}/D_p	[-] ≤ 0.012	√	√	√	0.011	0.006
	D_p/s_{sk}	[-] ≤ 16.0	√	√		4.420	8.3
1.0 ≤	$s_{sk} / \min \left[\begin{array}{l} 0.8 \cdot \sqrt{D_p/2 \cdot t_p} \\ 0.8 \cdot \sqrt{D_s/2 \cdot t_s} \end{array} \right]$	[-]			√	1.6	1.5
	C_p	[-] ≤ 1.5	√	√		1.013	1.0
	K	[-] ≤ 0.02	√	√		0.066 !	0.033 !

2.6 Fatigue Limit State (FLS) design approaches

2.6.1 General remark

Design approaches for the Fatigue Limit State (FLS) of grouted connections are available as structural member considerations, not describing the local effects inside the connection but the global fatigue behaviour. In general, fatigue failure of the grout layer is decisive and is mainly influenced by local load application at the shear keys (see Harwood et al. (1996)). The following design approaches are closely related to the ULS design approaches described before. They are based on stress ratio S between acting axial interface stress σ_a and the connection's ULS capacity f_g (see Equation (2.22)).

$$S = \frac{F_{\max}}{F_{\text{ULS}}} = \frac{\sigma_a}{f_g} \quad (2.22)$$

The resulting damage D (see Equation (2.23)) is calculated according to Palmgren-Miner's linear damage hypothesis as ratio between number of endurable load cycles $N_R(S)$ and number of acting load cycles $N_E(S)$.

$$D = \sum \frac{N_E(S)}{N_R(S)} \quad (2.23)$$

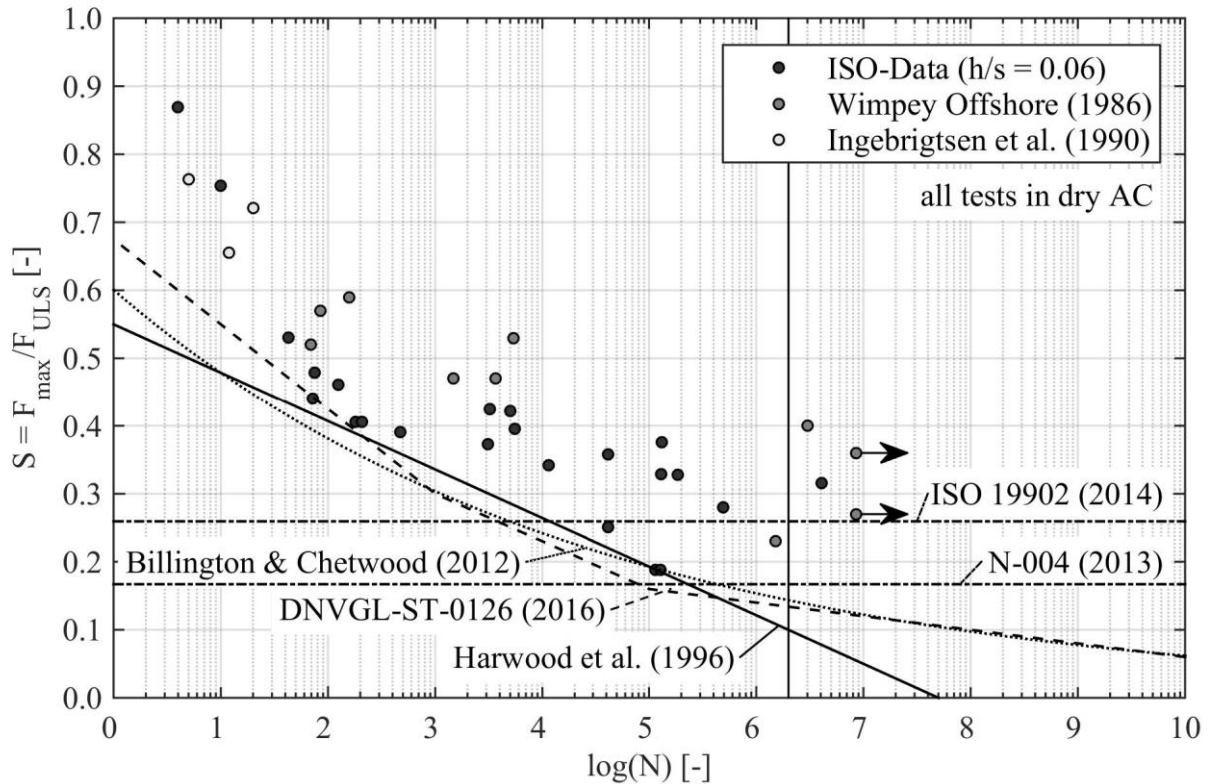


Figure 2.18: Characteristic S-N curves for fatigue design approaches of current design standards and corresponding test results (calculations for pre-piled reference structure)

Figure 2.18 shows all of the subsequently described fatigue design approaches for pure axial loads and if necessary calculated with parameters taken from the reference grouted connection for a pre-piled substructure (see Figure 2.3). In addition, fatigue test results for grouted connections with shear keys and alternating loads ($R = -1$) are included.

2.6.2 DIN EN ISO 19902 (2014)

Harwood et al. (1996) found no fatigue damage in plain pipe connections when loaded below their ultimate capacity. Evaluations of fatigue tests with alternating loads ($R = -1$) on grouted connections with shear keys showed slipping after load reversal (see Figure 2.14, left). The slipping occurred at loads above the connection's frictional capacity and led to impact loading on the shear key groove. The authors concluded that fatigue damage was caused only by the impact load and stated that for loads below the frictional capacity no fatigue damage would occur. This simplified fatigue design approach, neglecting the number of applied load cycles, is given in Equation (2.24) and available via DIN EN ISO 19902 (2014).

$$f_{g,FLS} = C_p \cdot 2 \cdot K^{0.6} \cdot f_{cu}^{0.3} \quad (2.24)$$

However, the early investigations by Yamasaki et al. (1980) showed significant fatigue damage at load levels below the frictional capacity for plain pipe connections. Moreover, Ingebrigtsen et al. (1990) found significant fatigue damage for shear key connections in compressive loading ($R \rightarrow \infty$) tests, which showed that impact loads are not the only mechanism causing fatigue.

For fatigue loads above the plain pipe connection's capacity, Harwood et al. (1996) proposed an S-N curve described by Equation (2.25) and shown in Figure 2.18 (solid line).

$$S_{\text{design}} = 0.75 - 4 \cdot \frac{h}{s} - \frac{\log(N)}{14} \quad (2.25)$$

2.6.3 NORSOK N-004 (2013)

Similar to DIN EN ISO 19902 (2014) a fatigue limit is presented in NORSOK N-004 (2013). However, different to the DIN EN ISO 19902 (2014) approach, a further reduction is possible to consider effects of bending moments. Equation (2.26) provides the connection's axial fatigue limit load $P_{f,Rd}$ including a reduced interface strength $f_{g,sliding}$ and a reduction factor for bending moments C_{PMred} , which is 1 for pure axial loading. Compared to the DIN EN ISO 19902 (2014) approach, this leads to a $\sim 2/3$ lower fatigue limit for pure axial loads.

$$P_{f,Rd} = \frac{0.3 \cdot f_{g,sliding} \cdot D_p \cdot L_e}{\gamma_M} \cdot C_{PMred} \quad (2.26)$$

2.6.4 DNVGL-ST-0126 (2016)

Within DNVGL-ST-0126 (2016) a three part logarithmic S-N curve is described, which is given here in Equation (2.27) and shown in Figure 2.18 (dashed line).

$$\begin{aligned} \log(N) &= 5.400 - 8 \cdot S & S \geq 0.30 \\ \log(N) &= 7.286 - 14.286 \cdot S & 0.16 < S < 0.30 \\ \log(N) &= 13.000 - 50 \cdot S & S \leq 0.16 \end{aligned} \quad (2.27)$$

2.6.5 Billington & Chetwood (2012)

The logarithmic S-N curve of Harwood et al. (1996) leads to high calculated damage values D for low load levels S . Billington & Chetwood (2012) stated that the actual fatigue contribution of small stress ratios is negligible and hence the older approach is to conservative. Derived from the same data basis as Harwood et al. (1996), they proposed a new S-N curve given in Equation (2.28) and shown in Figure 2.18 (dotted curve). However, for load cycle numbers above $\sim 10^7$, no test results are available and thus in the area with the biggest difference between the Harwood et al. (1996) and the Billington & Chetwood (2012) curves, experimental proof for both approaches is missing.

$$S_{\text{design}} = 10^{-0.2214 - 0.0987 \cdot \log(N)} \quad (2.28)$$

2.7 Numerical design approaches

2.7.1 General remark

Besides the aforementioned analytical design methods, for the time being numerical methods are state of the art for the design of grouted connections. Documents like the DNVGL-RP-0419 (2016) describe several options for the implementation of numerical models. First numerical approaches were published shortly after the first test results (see e.g., Chilvers (1984)). Since then the computational methods and capabilities have extensively improved and expanded. The following description focuses on the latest developments.

2.7.2 Material models

Grout

Grout materials are characterised by a high compressive strength and a significantly lower tensile strength (see Figure 2.19). In uniaxial tensile loading the material shows a constant tangential stiffness (E_{cm}) and a sudden loss of load bearing capacity without significant prior plastic strains. Once the tensile strength f_{ctm} is exceeded the material is split by tensile cracks. Contrarily, in compressive loading plastic strains occur almost from the beginning and increase towards the compressive strength f_{cm} . Once the compressive strength is exceeded, the material's strength slowly reduces.

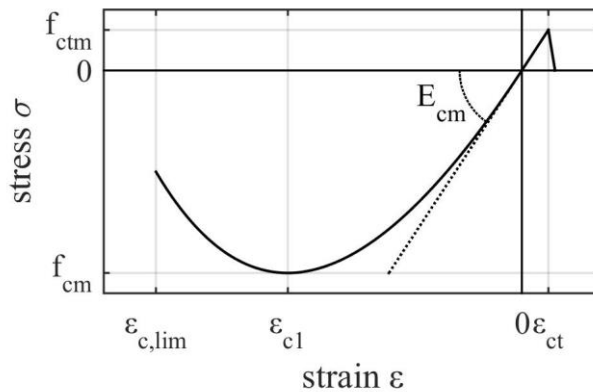


Figure 2.19: Schematic uniaxial stress-strain relation for grout material

Investigations on normal and high performance concrete (HPC) (see e.g., Kupfer et al. (1969), Dahl (1992), Grünberg et al. (2007), Göhlmann (2008), Speck (2008)), with bi- and tri-axial loading showed an improved material strength for multiaxial static stress states. Further investigations by Grünberg et al. (2007) and Göhlmann (2008) proved this behaviour for low cycle fatigue. According to the authors, for load cycle numbers of $N > 10^8$ the positive effect of multiaxial stress states starts to invert towards a significantly reduced material strength.

Commonly used for modelling concrete in numerical simulations is the spatial Drucker-Prager (DP) yield criterion, shown in Figure 2.20 (blue lines). The yield surface is a cone, rotationally

symmetric to the hydrostatic axis and can be defined for compression (solid line) or tension (dashed line). Hence, the yield surface is independent of uni-, bi- or tri-axial stress states. Advantage of this yield surface is the simple description by two parameters, which can be obtained from the material's tensile and compressive strength.

Spatial yield surfaces with improved concrete like characteristics are described in the literature (see e.g., Speck (2008)). These yield surfaces are defined by up to five parameters and not all of these parameters can be obtained from standard material property tests. For plain HPC under multiaxial loading, Speck (2008) developed an advanced yield criterion based on the four parameter Ottosen (1977) yield criterion (see Figure 2.20, orange line) and showed good compliance with experimental investigations. Likewise Schaumann & Lochte-Holtgreven (2013) used the Ottosen (1977) yield criterion for a material formulation for HPG materials at multiaxial loading and also showed good compliance with experimental results of other authors such as for example Dahl (1992).

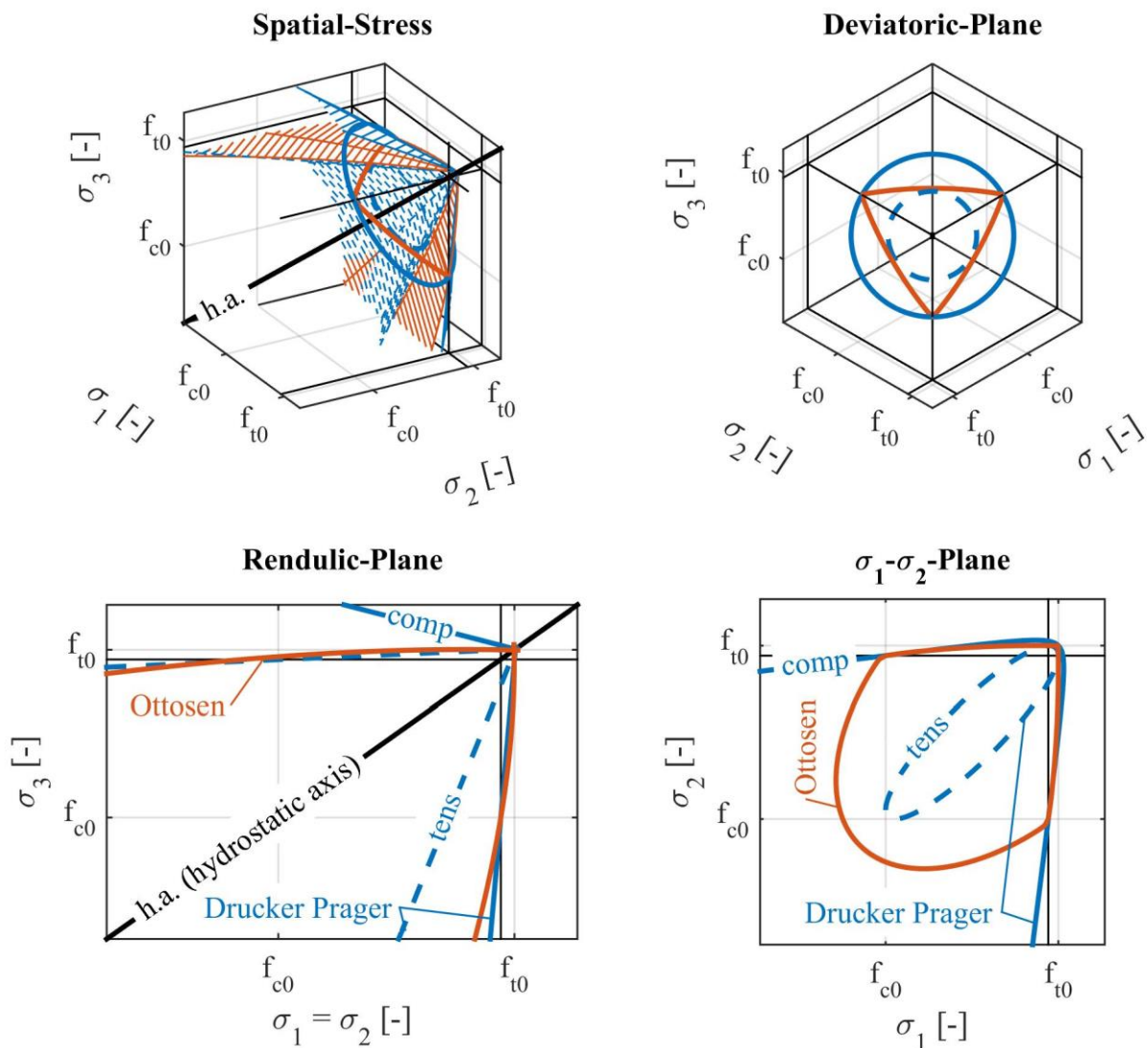


Figure 2.20: Yield surfaces according to Drucker & Prager (1952) and Ottosen (1977)

A comparison between the DP and the Ottosen yield surface show good agreement for uniaxial stress states (see Figure 2.20). However, in multiaxial stress states DP over- (compression, solid

line)) or underestimates (tension, dashed line) the material strength. More advanced formulations based on DP are available, usually referred to as Extended-Drucker-Prager (EDP). These formulations allow a non-linear yield surface description in both, the Rendulic-plane as well as the deviatoric-plane and hence give an improved representation of the multiaxial concrete material behaviour.

In commercial finite-element software non-linear material approaches with tensile cracking capabilities are available. Widely used for scientific purposes is the “Concrete Damaged Plasticity” (CDP) model in the finite element software Abaqus. This material model is a combination of approaches by Lubliner et al. (1989) and Lee & Fenves (1998), who used DP as a basis and thus CDP is also a form of EDP. However, in contrast to the usual formulations of EDP, the CDP material model includes the capability of a local stiffness reduction in order to cover tensile cracking behaviour of the material. Further details of the CDP are described in Section 5.2.3.

Steel

For modelling steel properties, linear elastic or bilinear material models based on Mises (1913) yield criterion are usually used. For cyclic loading these materials can be extended with isotropic or kinematic hardening capabilities. More advanced material models capturing cyclic material behaviour such as Chaboche (1989) are also available.

2.7.3 Modelling

Global approaches

To include grouted connections in simulations of complete substructures, often modelling approaches without discrete shear keys are used. In order to reduce the numerical effort, the steel parts are modelled with shell elements while the grout layer is modelled with volumetric elements. The contact between steel and grout is rigid on the whole surface or discretely fixed at the shear key positions. Consequently, these models reduce the influence of grouted connections in axial direction to shear deformations of the grout layer.

In these approaches, the grout material is usually described by material models such as DP (see e.g., Lochte-Holtgreven (2013), Schaumann et al. (2013)) or EDP (see e.g., Wilke (2014), Bechtel (2009)). A detailed design verification of the grouted connection based on this modelling approach is not recommendable since the grout’s stress state is highly simplified. However, calculated local forces can be used for more detailed investigations of the grouted connection.

Local approaches

For a design verification of a grouted connection with shear keys more detailed models are necessary (see DNVGL-RP-0419 (2016)). These models are usually built with volumetric elements for both steel and grout parts which leads to large amounts of degrees of freedom. Hence, various approaches to reduce the computational effort were published.

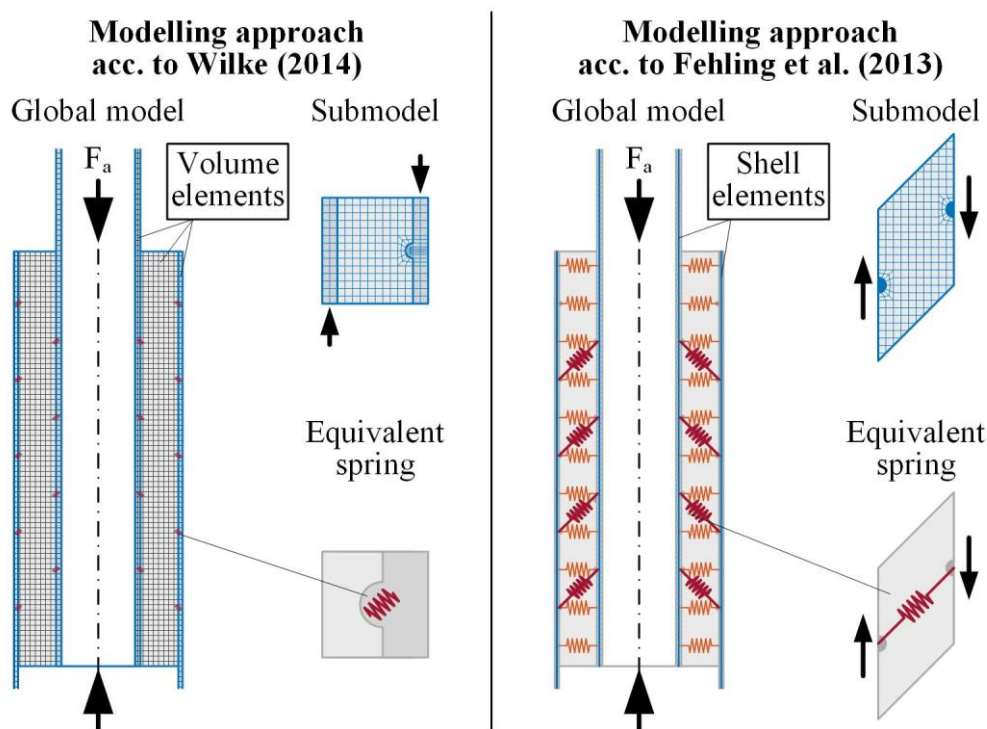


Figure 2.21: Schematic representation of two simplified numerical modelling approaches for grouted connections

Voßbeck et al. (2013) presented a model with shell elements for the steel parts and volumetric elements for the grout layer. The interaction between steel and grout was realised by discrete coupling at the shear key positions. Moreover, the grout material was modelled using a linear elastic material model. To compensate the deficits of a missing cracking capability of the material, the authors modelled discrete horizontal cracks at the shear key positions. Though, this approach does not cover the local stress distribution around the shear keys. Moreover, the arrangement with horizontal cracks is questionable because comparable experimental results are not published. Likewise, Löhning & Muurholm (2013) presented a model with discrete horizontal cracks and linear elastic material behaviour. In contrast to Voßbeck et al. (2013) their model was built with volumetric elements for the steel and grout parts and included discrete shear keys. Thus, a more detailed stress distribution in the grout layer could be determined, however with linear elastic material models.

An approach to simplify the interaction between steel and grout was described by Wilke (2014) (see Figure 2.21, left). Therefore, the interlocking stiffness between shear key and grout layer is determined in an extra model and the shear keys in the grouted connection model are then substituted by springs with non-linear characteristic. The grout layer is modelled using the EDP material model. This approach improves the connection's numerical deformation behaviour compared to global approaches but does not describe the local stress distribution around the shear keys.

A different simplification approach was published by Fehling et al. (2013) (see Figure 2.21, right). Similar to the approach of Wilke (2014), the authors used two separate models. The first model described a compression strut segment to determine the general load displacement behaviour. In the second model the steel parts were implemented with shell elements and the grout layer was modelled with spring elements representing the individual compression struts (strut and tie model).

This approach allowed the use of a complex non-linear material model for the compression strut behaviour and had low computational effort.

Detailed models including discretely modelled shear keys and solely volumetric elements were published for example by Lochte-Holtgreven (2013), Mittelstaedt et al. (2014) and Bechtel (2016). Bechtel (2016) used the EDP material model, while Schaumann & Lochte-Holtgreven (2013) recommended their novel material model based on the Ottosen (1977) yield surface. Mittelstaedt et al. (2014) used the finite element software ATENA which provides a non-linear material model with cracking capability using the yield criterion of Menetray & Willam (1995) (see Cervenka et al. (2016)). The models of these three authors show the most detailed stress distribution around the shear keys but at the same time cause the highest computational effort.

2.7.4 Fatigue Limit State (FLS)

For a design verification against fatigue failure usually the effects of actions are compared with fatigue related resistance values. The effects of actions are usually condensed via counting methods into representative load spectra with corresponding numbers of applied load cycles N_E (see Figure 2.9). For these load spectra the structural response of the grouted connection is calculated in a numerical simulation using one of the priorly described modelling approaches (see Section 2.7.3). Afterwards the local stresses are compared to the material's fatigue resistance, which is usually described by an S-N curve (see Figure 2.22). Based on the S-N curve, the number of endurable load cycles N_R per load spectrum can be obtained. And finally, with Palmgren-Miner's linear damage hypothesis (see Equation (2.23)), the resulting damage D can be calculated as sum of the ratio between number of acting N_E and number of endurable load cycles N_R per load spectrum.

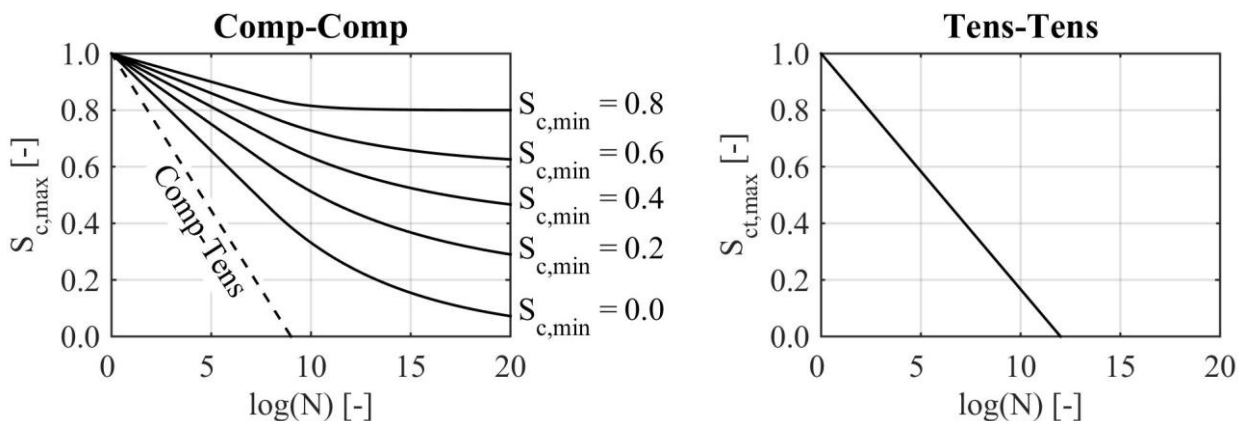


Figure 2.22: S-N curves for concrete and different loading ratios acc. to MC2010 (2013)

Lochte-Holtgreven (2013) used the uniaxial S-N curves given in MC1990 (1993) for his numerical investigations. Bechtel (2016) chose the newer uniaxial S-N curves given in MC2010 (2013) (see Figure 2.22). In contrast, Fehling et al. (2013) recommended the S-N curves from DNV-OS-C502 (2012). However, the authors showed no comparison between experimental and numerical results for grouted connections.

By definition, the described fatigue verification approach includes a few simplifications, worth mentioning. Reducing the acting loads via a counting method deletes the load sequence information. Additionally, the quasi-static numerical calculations per load spectrum start from a user defined connection state. It can be assumed that the structural response of an un-cracked grout layer is different to one with several shear cracks, as they can be expected to occur (see Section 2.3.3). Consequently, identical load spectra can be assumed to cause different levels of damage in dependence of the current state of the connection. These effects should be considered in the numerical calculation in order to increase the accuracy of the results.

In order to cover the aforementioned missing effects in a numerical simulation and moreover include the specific material behaviour in multiaxial stress states, Göhlmann (2008) described a different fatigue verification approach for concrete. In his implementation he linked the yield surface of Willam & Warnke (1974) with S-N curve based damage variables. According to the size of the damage variables the yield surface is narrowed down with each applied load cycle. Failure occurs when the calculated stresses exceed the yield surface. His numerical results showed good agreement with multiaxial test results. This description allows a detailed investigation of the material deformations under cyclic loading and takes into account effects from the load sequence. Lochte-Holtgreven (2013) implemented this approach in combination with the Ottosen (1977) yield criterion and calculated numerical S-N-curves for bi- and tri-axially loaded concrete specimens. His results showed good agreement with experimental results from the literature. Similar to Göhlmann (2008), he used the uniaxial S-N curves given in MC1990 (1993) to calculate the damage variables. However, for this approach a calculation of each applied load cycle is necessary in order to cover sequence effects and benefit from this approach.

Instead of the yield surface, Bechtel (2016) implemented an approach described by Pölling (2000) which reduces the elastic modulus according to the damage variable. Her damage calculations were based on the uni-axial S-N curves given in MC2010 (2013).

2.8 Discussion

2.8.1 Grouted connections in general

This thesis focuses on predominantly axially loaded grouted connections, which are always equipped with shear keys (see Section 2.2.1 and Section 2.2.2). Dependent on the installation procedure (see Section 2.2.3) the grout layer thickness is chosen to provide enough space to compensate possible imperfections. In order to avoid demixing of the fresh grout material the connections are filled from the lower end (see Section 2.2.4). For the time being, HPG materials especially designed for offshore applications are usually used (see Section 2.2.5).

The presented reference structures (see Figure 2.3) represent typical grouted connections for offshore wind turbines. Nevertheless, these designs exceed the ranges of applicability of currently standardised design approaches for ULS (see Section 2.5) and FLS (see Section 2.6). Hence, their validity for current designs is questionable. This applies in particular to the grout material strength as well as the grout layer thickness (see Section 2.5.5).

2.8.2 Loads and load bearing behaviour

Time-varying loads acting on grouted connections in lattice substructures are in the range of ~50 % of the design ULS load for low cycle fatigue and below 1 % for high and very high cycle fatigue (see Section 2.3.1). The high load levels are expected to cause the major fatigue degradation. In the low cycle fatigue range alternating loads are expectable, while in the high and very high cycle fatigue range compression-compression loads are typical. For jacket substructures the frequency of fatigue relevant loads for the grouted connection is usually in the range of 0.3 to 0.4 Hz.

The known load bearing behaviour of grouted connections (see Section 2.3.2) was derived from a combination of measuring the connection's behaviour during loading (see Section 2.3.4) and analysing the resulting damage patterns (see Section 2.3.3). The dominating degradation mechanisms in dry ambient conditions are diagonal shear cracking and grout crushing in front of the loaded shear key surfaces.

2.8.3 Influence of selected parameters

Influence of water

Based on the description given in Section 2.4.1, the influence of wet ambient conditions on the fatigue behaviour of grout and concrete specimens can be summarized as follows. It must be considered that all described tests were carried out on material specimens, primarily cylinder specimens, as well as reinforced concrete beams. None of these specimens include confinement effects, as they are present in grouted connections.

All investigations showed a significantly reduced number of endurable load cycles for wet ambient conditions compared to dry ambient conditions. The results were loading frequency dependent, whereby a higher frequency led to more endurable load cycles. The observed damage mechanisms revealed spalling of the specimens' surface caused by water overpressure in pores inside the specimens. Moreover, pumping mechanisms were observed, pumping water through cracks and leading to transport of loose particles as well as further deterioration of the crack surfaces and reduced friction inside cracks. Besides these effects, theories were described considering the water ingress depth to influence the deterioration speed. Additionally, a correlation between grout or concrete material density and deterioration speed was found, where a higher density and therefore a reduced water ingress led to more endurable load cycles. Influences of water pressure on the described fatigue behaviour are negligible.

In summary, the described influences of water can be expected to be also relevant for the fatigue behaviour of grouted connections.

Autogenous shrinkage

As described in Section 2.4.2, autogenous shrinkage must be expected for all cement based materials. In a grouted connection, autogenous shrinkage of the circular grout layer might cause detachment of the outer grout surface from the sleeve and a pre-stressing of the inner grout steel interface. Moreover, tangential stresses caused by restrained shrinkage deformations due to the pile can result in radial cracking of the grout layer. These cracks will release the pre-stress in the

pile grout interface. In axial direction autogenous shrinkage deformations are obstructed by the circumferential shear keys. This will lead to axial tensile stresses in the grout layer close to the shear key tips and initial crack formation can occur. The size of the autogenous shrinkage deformations depends on the grout material characteristics but also on the size of the grout layer.

Consequently, a pre-cracked grout layer state caused by autogenous shrinkage can be expected for grouted connections. This state depends on the grout material as well as the grout layer's geometry. In submerged ambient conditions, the initial cracks and possible detachments in grout steel interfaces ease the ingress of water and thus influence the interaction between water and grouted connection.

2.8.4 Ultimate Limit State (ULS) design

The described evolution of current design approaches for the ULS (see Section 2.5) showed that with taking additional test results into account, modifications of the approach became necessary. All Equations of Model 1 and 2 were developed from regression analysis of test results. Model 3 includes correction terms based on regression analyses as well. Already Sele & Seow (1988) saw a lack of physical background in the approach of Billington & Tebbet (1980) and the evolution progress underlines this statement.

For the stated ranges of application and pure axial loading the design approaches are validated. Nevertheless, since the actual mechanical and physical effects in the connection are not covered in detail, extending the range of applicability to new geometrical parameters and grout materials, must be validated with corresponding tests.

2.8.5 Fatigue Limit State (FLS) design

The previously presented fatigue design approaches (see Section 2.6) are obtained from fatigue tests with pure axial loads and a loading ratio of $R = -1$. This loading ratio can be expected to be a worst case scenario, since most fatigue loads are in the compression regime, as visible in Figure 2.9 and stated by Harwood et al. (1996).

The simplified fatigue limit approaches of Harwood et al. (1996) and the one given in NORSOK N-004 (2013) are quite conservative in the low cycle fatigue range but might overestimate the fatigue capacity in the very high cycle fatigue range. The justification for this approach given by Harwood et al. (1996) is questionable. Nevertheless, assuming a fatigue load distribution as shown in Figure 2.9, high loads correspond with a low number of cycles and if these loads fulfil the conservative approach, high cycle loads might be significantly smaller.

The three load cycle dependent approaches are comparable up to $\sim 10^5$ load cycles. For higher load cycles the approaches of Billington & Chetwood (2012) and DNVGL-ST-0126 (2016) are still comparable, but it shall be emphasized that the curve shape after 10^7 load cycles is not confirmed by any test results. Different from S-N curves for raw material (see e.g., MC2010 (2013)), the presented approaches are lower boundaries of the test results and not statistically derived curves with specific failure probabilities.

Finally, it is emphasized that none of the presented fatigue design approaches considers an influence of water on the fatigue capacity of grouted connections.

2.8.6 Numerical design approaches

Even though, several numerical investigations on grouted connections have been carried out, an approach with general applicability is not yet defined. Main challenge of the numerical investigation of grouted connections is to find an optimum between level of detail of the numerical model and computational effort. Thus, the level of detail is not only influenced by the geometrical implementation and mesh properties but also by the chosen material models. While for the steel behaviour simple material models are usually sufficient, the non-linear and spatial stress state dependent behaviour of grout demands a complex material model. The corresponding material parameters are challenging to define and solving these complex material equations in the numerical simulation can increase the computational effort. Moreover, for the evaluation of the numerical results, options with different levels of detail are possible.

2.9 Summary and conclusion

The general characteristics of grouted connections, their application and their manufacturing procedure were introduced. Moreover, their load bearing and degradation behaviour as known from laboratory tests in dry ambient conditions was presented. A detailed description of influences of water identified for the fatigue behaviour of submerged concrete specimens as well as reinforced concrete beams was given. Furthermore, currently standardised design approaches for the ULS and FLS of grouted connections were described. In addition, published possibilities for numerical design approaches were summarised. Finally, the state of the art was discussed.

Based on the presented state of the art, the following demands for the subsequently described experimental and numerical investigations were defined.

- **Specimen geometries**

Two scales of specimens shall be developed. At first, small-scale specimens are intended to find the major parameters which influence the fatigue behaviour of submerged grouted connections and to realise a large number of samples for a statistical evaluation. At second, large-scale specimens shall be investigated to proof the previously found phenomena for larger grouted connections and evaluate a possible scale effect. Both sizes of specimens are supposed to include two different grout layer thicknesses. Besides assessing an expectable influence of the grout layer thickness on the load bearing behaviour, this will allow to investigate thickness influences on autogenous shrinkage. Intended to allow reference to existing small-scale test results, the small-scale geometries shall follow the corresponding publications. The large-scale geometries shall be designed in accordance with the introduced reference structures and also follow prior investigations.

- **Grout materials**

The specimens shall be filled with commercial HPG materials to cover realistic material behaviour for offshore applications. Different material strengths shall be investigated in the small-scale specimens. This might allow to extend the range of application for currently

standardised design approaches. The filling process shall be designed in accordance with real applications, but with a dry grout annulus to reduce possible influences of a submerged filling process.

- **Loads**

The applied loads shall be limited to pure axial loading in order to exclude superposition effects of combined loading and allow a focused analysis of the load bearing and degradation behaviour. Moreover, different loading levels are supposed to be investigated to identify possible load level related changes in the degradation behaviour and to realise a Fatigue Limit State. Furthermore, the loads shall be varied in their loading frequency to investigate expectable effects when loaded in submerged ambient conditions. The loading frequency range to be investigated shall cover a realistic range. In addition, investigations with different loading ratios R are intended to find further possible influences.

- **Influence of water**

In order to investigate the influence of water, experiments with dry and wet ambient conditions shall be developed. In addition, these experiments are supposed to consider different loading frequencies to allow an evaluation of expectable effects. Water pressure comparable to real application water depth will not be realised since its effect can be considered as negligible. Likewise, the experiments can be executed with tap water instead of realistic seawater.

- **Degradation behaviour**

Prior to each experiment the initial state of the grout layer shall be evaluated especially regarding autogenous shrinkage. During the experiments the load bearing and deformation behaviour of the specimens is supposed to be documented. Therefore, a suitable measurement set-up has to be applied, this shall be in reference to other published experimental results. After completion of the mechanical tests, dismantling the specimens will give insights on the degradation behaviour of the grout layer as well as the interfaces between grout and steel. In combination with the measurement data, the observed damage patterns will allow a detailed analysis of the connections' fatigue behaviour.

- **Standardised ULS and FLS design approaches**

Main focus of this thesis is the fatigue behaviour of grouted connections. Nevertheless, for developing the experimental investigations the previously described ULS design approaches will be used as a tool to estimate the specimens' ultimate capacities. By implication, this will allow a later comparison between calculation-based expectations and the observed experimental behaviour. Thus, a coarse evaluation of the ULS design approaches and their applicability for the specimen properties will be possible. Similar to the ULS design approaches, the presented FLS design approaches will be used as a tool to develop suitable fatigue experiments. Later on, a comparison between calculated and experimental results will allow an evaluation of the FLS design approaches and their applicability for the investigated specimen properties.

- **Numerical design approaches**

Based on the described options for numerical simulations of grouted connections a numerical design approach shall be developed. The description shall include detailed information on modelling a grouted connection, a suitable material model to cover the complex characteristics of grout material as well as a method to evaluate the numerically calculated results regarding fatigue. Afterwards, the numerical results can be compared to experimental results and thus the proposed design approach can be validated for the fatigue behaviour of submerged grouted connections.

3 Small-Scale Experiments

3.1 Introduction

Typical grouted connections in offshore support structures have tube diameters and grout lengths of several meters. Investigating the connection's load bearing and fatigue behaviour in a laboratory environment at real-scale comes with large efforts, if even possible. Small-scale tests enable to investigate numerous set-ups and parameters at comparably low financial costs and with conventional hydraulic testing rigs. Therefore, the small-scale test set-up described in this Chapter was developed.

Main objective of the small-scale tests was to investigate the influence of surrounding water on the fatigue behaviour of the connection. Based on this objective and open questions of the state of the art, the following parameters were chosen for investigation.

- **Grout layer thickness**
In order to evaluate the influence of the grout layer thickness two different grout layer thicknesses were investigated. It was expected that a thicker grout layer would reduce the specimen's stiffness and therefore its load bearing capacity.
- **Grout material**
Two grout materials with different compressive strength were chosen to investigate the influence of the material's strength. It was expected that a higher compressive strength would lead to a higher load bearing capacity but conceivably to a lower fatigue strength due to more brittle material behaviour.
- **Test procedure**
A quasi-static loading for the Ultimate Limit State (ULS) capacity and an alternating loading with constant amplitude for the Fatigue Limit State (FLS) were chosen.
- **Ambient condition (AC)**
Since the influence of water was going to be investigated, dry and wet AC were realised. It was expected that a wet AC would lead to a reduced fatigue capacity.
- **Loading level**
Usually a reduced load level increases the fatigue capacity. Moreover, this parameter was investigated not only to quantify the influence of the loading level but also to see possible correlations with the influences of water. Two loading levels, each normalised to the specimens ULS capacity, were investigated.
- **Loading frequency**
As known from the state of the art, a positive influence of an increased loading frequency could be expected for fatigue tests in wet ambient conditions. Hence, the loading frequency was varied between 0.3 Hz, representing a realistic loading frequency under offshore loading conditions, and 10 Hz as a preferable loading frequency for laboratory fatigue tests.

• **Degradation behaviour**

Prior tests (see Section 2.3.3) showed a typical degradation behaviour with grout crushing in front of the shear keys and diagonal grout cracking due to high shear stresses. This behaviour was going to be expected for these tests as well.

Based on the described objectives and the rules for design of experiments according to Kleppmann (2013), the parameter set-up given in Figure 3.1 was elaborated.

Specimen Geometry	Filling Material	Test Procedure	Ambient Conditions	Loading Conditions		No. Tests	Results
				$\frac{F_{max}}{F_{ULS}}$	f [Hz]		
Geom 1 $t_g = 22.50$ mm shear keys	Densit Ducorit S2 ($f_c = 90$ N/mm ²)	ULS	dry			3	$F_{ULS}, F(u)$
		FLS	dry	0.5	5.0	3	$N, u(F)$
			wet	0.5	10.0	3	
					5.0	3	
					2.0	3	
					1.0	3	
	0.3	3					
	0.2	5.0	3				
	1.0	3					
	BASF Masterflow 9500 ($f_c = 140$ N/mm ²)	ULS	dry			3	$F_{ULS}, F(u)$
		FLS	dry	0.5	5.0	3	$N, u(F)$
			wet	0.5	5.0	3	
1.0					3		
5.0					3		
1.0					3		

Figure 3.1: Set-up for small-scale grouted connection tests

3.2 Specimens

3.2.1 Geometry

First small-scale specimens were developed at the Institute for Steel Construction in close collaboration with the Institute for Building Material Sciences, both Leibniz Universität Hannover, within the research project “ForWind – Work Package 5: Life-cycle assessment of support structures” by Schaumann & Wilke (2006a) and Anders (2007). As stated by Lochte-Holtgreven (2013) and Wilke (2014), the specimens were designed to focus on the grout material behaviour in a three dimensional stress state caused by axial loading and the resulting confinement by the surrounding steel tubes. The specimens were equipped with shear keys, in order to get a defined interlocking between steel and grout. Due to the specimen’s small dimensions, the shear keys were CNC turned from the tube surfaces instead of being welded on to the surfaces. Moreover, the shear keys were rectangular shaped instead of a half ellipse as usual for welded shear keys. In order to exclude failures like yielding or buckling, the steel tubes were dimensioned with a low slenderness. This means that they were not true to scale to real grouted connections. Schaumann et al. (2009), Keindorf (2010) and Wilke (2014) also investigated a geometry without shear keys. By virtue of its unpredictable load bearing capacity, relying only on surface roughness and imperfections, which are defined by the manufacturing process, this geometry was excluded from the following investigations.

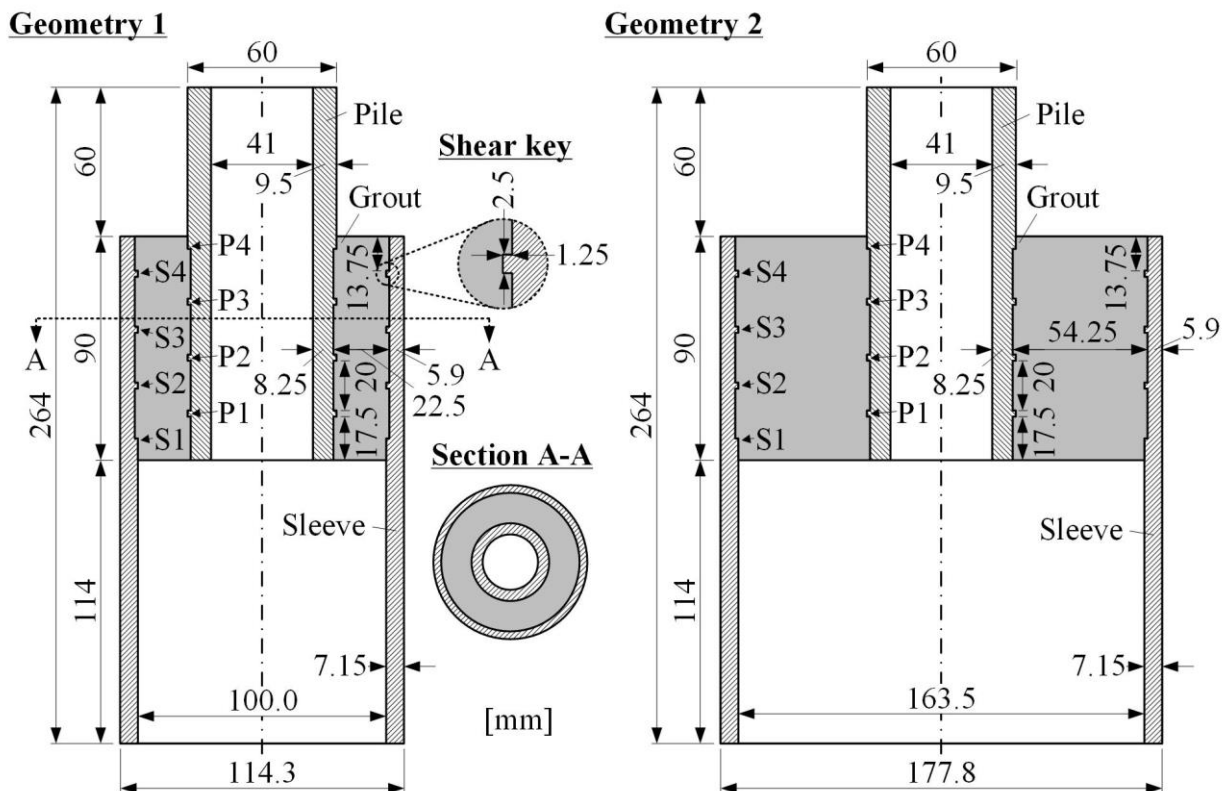


Figure 3.2: Geometry of the two small-scale grouted connection specimens

For the experiments presented in this thesis, the two small-scale geometries shown in Figure 3.2 were developed based on the specimen by Schaumann & Wilke (2006a). Geometry 1 was similar to the geometry of Schaumann & Wilke (2006a) but revised with minor modifications for a simpler

production and an improved reproducibility. Prior investigations with a comparable geometry were also performed by Anders (2007), Keindorf (2010), Lochte-Holtgreven (2013) and Wilke (2014). Geometry 2 had a larger grout layer thickness caused by a modified sleeve diameter.

3.2.2 Relation to current standards

As mentioned before, the specimens' steel tubes were characterised by a low slenderness compared to real structures. Therefore, the specimens were not to scale to real connections. Table 3.1 shows the ranges of applicability of current design methods from different standards as well as the geometric characteristics of the two real-scale reference structures (see Figure 2.3) and the two small-scale specimen geometries (see Figure 3.2). The geometries of both specimens show more similarity with the pre-piled structure than with the post-piled. Especially the grout layer slenderness is comparable, whereas the slendernesses of pile and sleeve are only half as large compared to the reference pre-piled connection. As a result the steel tubes are much stiffer and the confinement stress can be expected to be higher than in a real connection. This can increase the load bearing capacity of the specimens due to the improved grout material strength in a multiaxial stress state (see Section 2.7.2).

Table 3.1: Ranges of applicability for ISO 19902, N-004 and DNVGL-ST-0126 and parameters of the small-scale specimens, exceeding values are highlighted

			Reference Pre-piled	Reference Post-piled	Geom 1	Geom 2
f_c	[N/mm ²]	\geq 20 \leq 80	140.0	140.0	90.0 140.0	90.0 140.0
D_p/t_p	[-]	\geq 20 \leq 40 \leq DNVGL: 60	15.8	49.6	7.0	7.0
D_s/t_s	[-]	\geq 30 \leq 140	36.6	56.8	19.4	30.1
D_g/t_g	[-]	\geq 10 \leq 45	4.1	10.4	4.6	3.1
L_c/D_p	[-]	\geq 1 \leq 10	3.9	2.1	1.6	1.6
w_{sk}/h_{sk}	[-]	\geq 1.5 \leq 3.0	2.5	2.0	2.0	2.0
h_{sk}	[mm]	\geq 5.0	10.0	15.0	1.3	1.3
h_{sk}/S_{sk}	[-]	\leq 0.100	0.050	0.050	0.056	0.056
h_{sk}/D_p	[-]	\leq 0.012	0.011	0.006	0.022	0.022
D_p/S_{sk}	[-]	\leq 16.000	4.420	8.267	2.556	2.556
C_p	[-]	\leq 1.500	1.013	1.000	1.888	1.888
K	[-]	\leq 0.020	0.078	0.033	0.080	0.091

3.2.3 Materials

The steel parts were turned out of seamless standard steel tubes (RO 60.3x11, RO 114.3x8.8, RO 177.8x8.8) in a CNC lathe. The tubes had a material strength of structural steel grade S355.

With the aim of investigating the influence of the grout material strength on the load bearing behaviour of the connection, two grout materials with different uniaxial compressive strength were chosen. Both materials were commercial grout products for offshore applications from ITW Densit ApS and BASF Construction Chemicals. According to the manufacturers, Densit Ducorit S2 (DDS2) had a uniaxial compressive strength of $f_c = 90 \text{ N/mm}^2$ whereas BASF Masterflow 9500 (BM95) had $f_c = 140 \text{ N/mm}^2$. More mechanical properties are given in Table 3.2. Both materials were fine grain grouts with a maximum aggregate size of $\sim 5 \text{ mm}$ and a mixing water amount between 7 and 8 % by weight.

Table 3.2: Mechanical properties of the two grout materials given by the manufacturers (ITW Densit ApS (2012); BASF Construction Chemicals (2010))

	Densit Ducorit S2 (DDS2)	BASF Masterflow 9500 (BM95)	Material specimen shape
f_c [N/mm ²]	90.0	140.0	Cube 75x75x75 mm
f_t [N/mm ²]	6.0	8.6	
f_{bt} [N/mm ²]	n/a	18.4	Prism 160x40x40 mm
E_c [N/mm ²]	40'000	50'900	Cylinder 150x300 mm
ν [-]	0.18	n/a	
ρ [kg/m ³]	2385	n/a	

3.2.4 Specimen preparation

The steel parts were produced by a local steel works company. In preparation for the grouting process the steel tubes were degreased and the surfaces, later facing the grout, were checked with a tactile surface roughness measuring system according to DIN EN ISO 4287 (2010). As shown in Figure 3.3 for all specimens the arithmetic average roughness R_a values were within the lower range of expectation for turning machining given in DIN 4766-2 (1981).

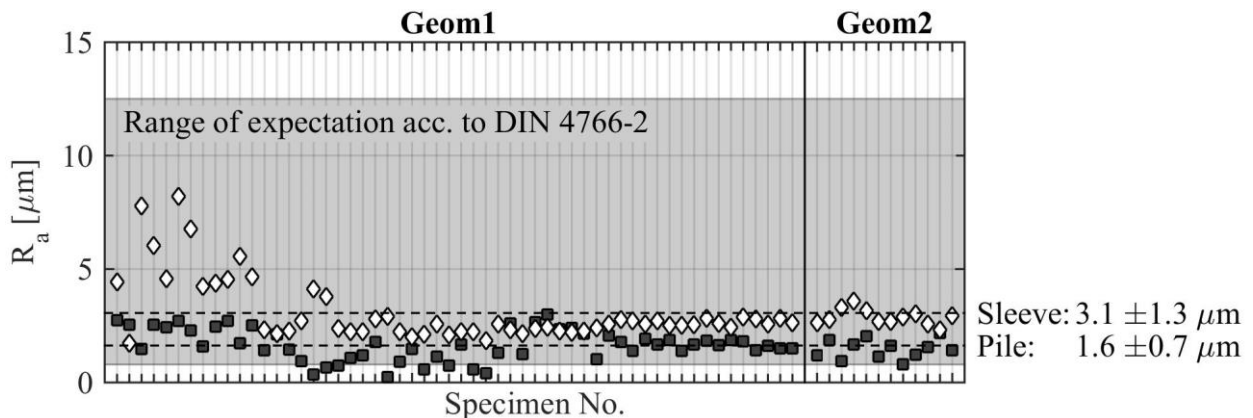


Figure 3.3: Measured surface properties of small-scale specimens

Afterwards, the tubes were plugged on a plastic formwork (see Figure 3.4). The formwork ensured a centring of the tubes and sealed the lower end of the grout section. Subsequently, the specimens were filled with fresh grout material and then covered with foil, which slowed down the drying process and reduced shrinkage of the grout material. After 24 hours the plastic formwork was removed and the specimens were stored in a water basin filled with fresh water at room temperature. The specimens stayed in the water basin until they were tested. After 28 days of curing the

ultimate static capacity F_{ULS} of three specimens was determined in ULS tests (see Section 3.3.3). Afterwards, the FLS tests (see Section 3.5) started at varying curing ages.

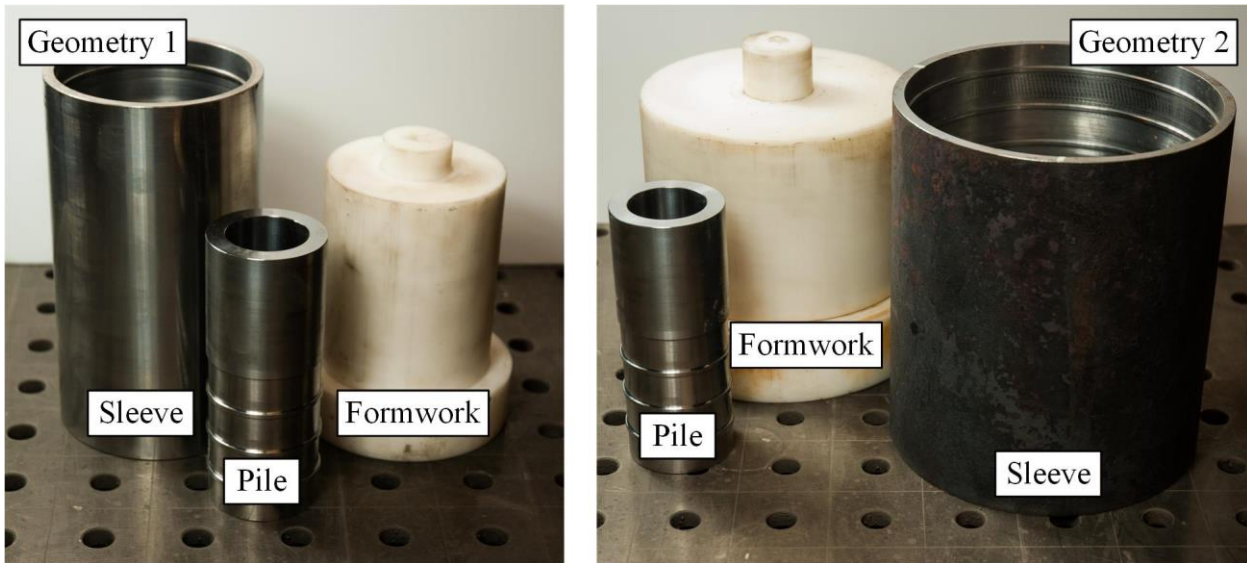


Figure 3.4: Blank steel pieces and formwork of the two specimen geometries

3.3 Grout material property tests

3.3.1 Procedure

During production of the specimens, the quality of the grout material was monitored by the Institute for Building Materials Science (IfB), Leibniz Universität Hannover. Besides slump tests on the day of production, material strengths and stiffnesses at several ages were documented. In the course of the investigations, three batches were produced for each material at different times.

3.3.2 Results

The results of the accompanying grout material strength tests after 28 days are presented in Figure 3.5 (see Schaumann & Raba (2015b)). The dark grey bars show the properties according to the manufacturers and the coloured bars show results for different material batches. Each bar represents the mean value and the brackets at the top represent the 95 % confidence interval (CI) based on a Student's t distribution.

Except for the tensile strength f_t the actual strength of DDS2 was always higher than given by the manufacturer. Whereas the actual strength of BM95 was in the range of the value given by the manufacturer or slightly lower. In addition to the reference strength after 28 days, the strength evolution over age is of interest. Since the small-scale specimens in the FLS tests were tested at different ages, the strength evolution might have influenced the achieved test results. Figure 3.6 shows the grout material strength evolution over age of the specimen for both materials and different batches of production. When assuming the strength evolution according to MC2010 (2013) as reference, both materials showed a regular strength evolution with few negligible outliers.

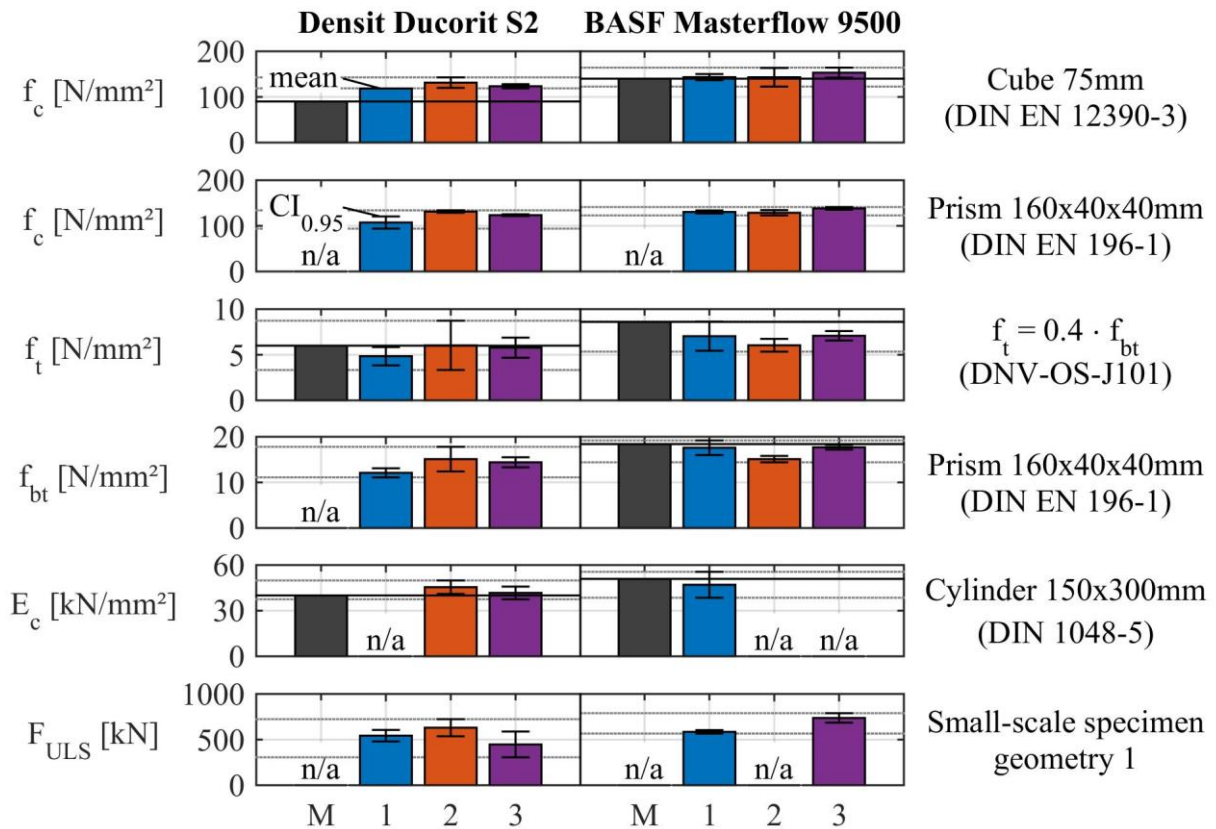


Figure 3.5: Grout material properties according to manufacturer (M) and accompanying material test batches (1-3) at an age of 28 days (Schaumann & Raba (2015b))

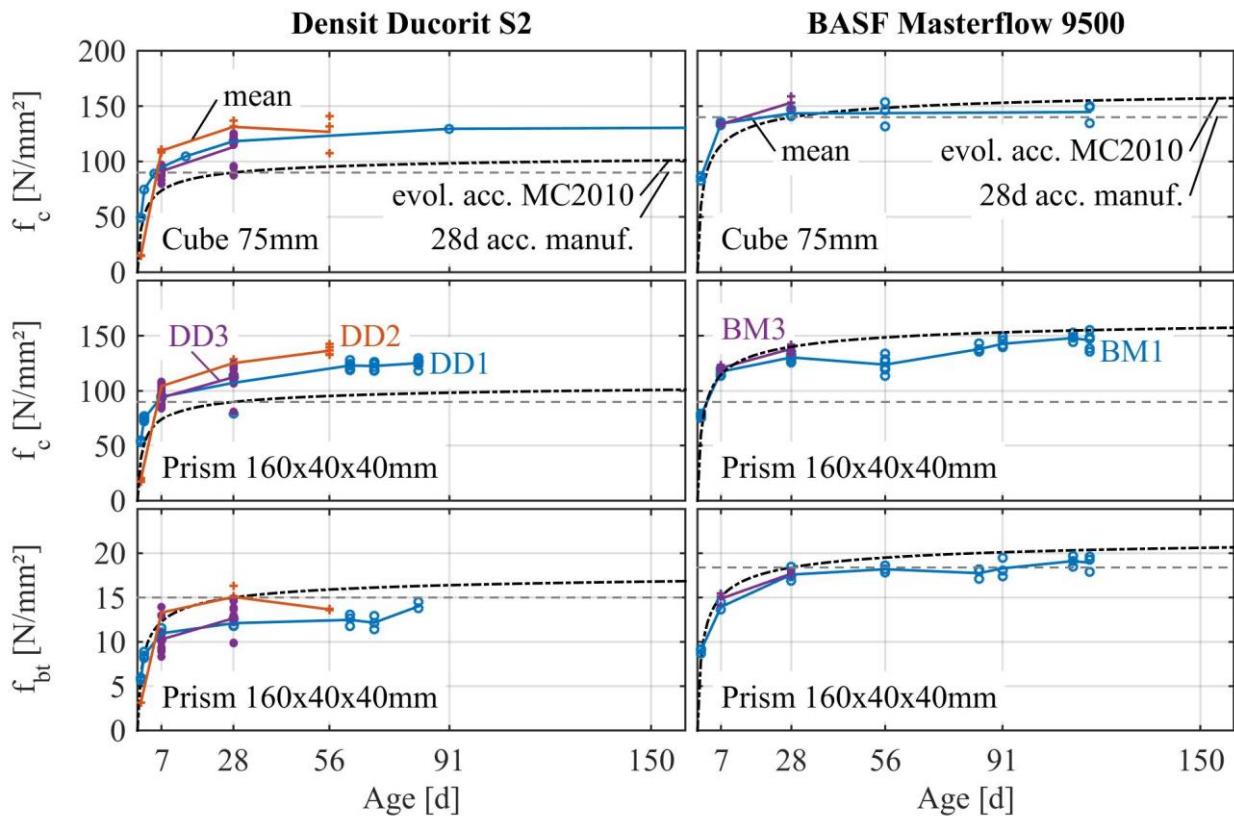


Figure 3.6: Grout material strength evolution

In correspondence with the aforementioned results, for DDS2 a clearly higher compressive strength f_c as given by the manufacturer is visible, while the bending tensile strength f_{bt} is overestimated by the manufacturer. However, it has to be considered that the f_{bt} evolution according to MC2010 (2013) is calculated using $f_t = 0.4 f_{bt}$ since the manufacturer does not provide a f_{bt} value. BM95 shows a better accordance with the MC2010 (2013) evolution prediction and reaches comparable strengths f_c and f_{bt} as given by the manufacturer.

3.3.3 Discussion

The reference strength after 28 days was more alike for both materials than expected according to the material product sheets from the manufacturers (ITW Densit ApS (2012); BASF Construction Chemicals (2010)). Moreover, since the confidence intervals were overlapping, a statistically significant difference of the material strengths could not be identified. Consequently, on one hand the expected influence of the grout material strength could not be evaluated based on the achieved test results. However on the other hand, the test results of both materials could be treated as one sample in the following evaluations of the fatigue test results, with reasonable caution regarding possible other material differences.

The FLS tests started at different grout material ages, in total the small-scale specimens covered an age range of 33 to 197 days (see Appendix A). This corresponds to a theoretical strength difference of 12 % according to MC2010 (2013). The actual scatter of F_{ULS} after 28 days (see Figure 3.5) was in a similar range while the scatter of number of endurable load cycles of the FLS tests (see Figure 3.25) was larger. A correlation between grout material age and number of endurable load cycles was not observed. Hence, the influence of the grout strength evolution after an age of 28 days was neglected in the following evaluations.

3.4 Ultimate Limit State (ULS) tests

3.4.1 Procedure

The small-scale ULS tests were conducted after 28 days of grout curing to determine the ultimate capacity of the specific specimen-grout combination. The tests delivered the maximum applicable quasi-static load F_{ULS} and the deformation behaviour. This characteristic value was used as a reference value for the later FLS tests. Additionally, with these results the production quality of the specimens was evaluated.

The small-scale ULS tests were carried out in the test rig shown in Figure 3.7. The test rig consisted of a servo-hydraulic cylinder with a maximum load capacity of 1 MN and an axial hinge to realise pure axial loads in the specimen. During the displacement controlled tests the specimens were compressed with a displacement application speed of 0.2 mm/min. The tests were terminated after a displacement of at least 8 mm was applied since the major degradation occurred in the first ~3 mm of displacement (see Section 3.4.2).

During the tests the relative compression of the specimen was measured with three lasers that were placed circumferentially at 0°, 120° and 240° angle of the specimen. The lasers had a measuring range of 10 mm. With the measurement data of the three lasers the mean displacement along the

central axis u_{Laser} was calculated and used for evaluation. Moreover, the displacement of the hydraulic cylinder u_{Rig} was measured with a rotary potentiometer and the applied load F was measured with a load cell.

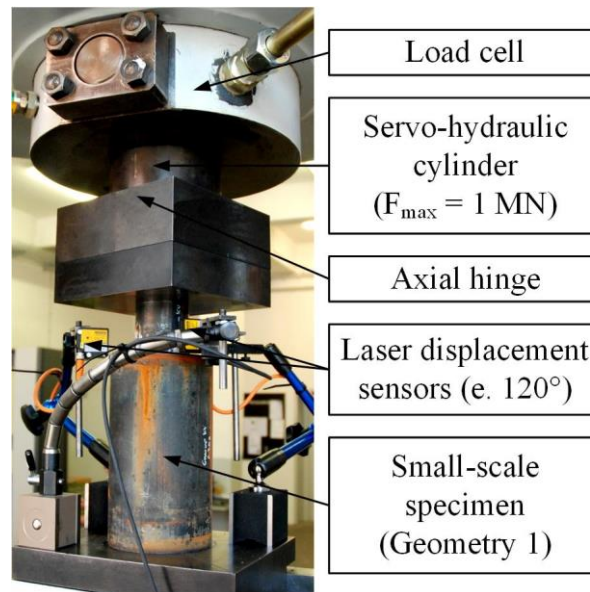


Figure 3.7: Test rig for quasi-static tests

3.4.2 Evaluation of measurement data

Figure 3.8 and Figure 3.9 show the typical load-displacement curve of small-scale ULS test with Geometry 1 and Geometry 2 respectively. After initial settlements, caused by microscopic imperfections of the grout layer around the shear keys and on the contact surfaces between test rig and steel parts of the specimen, three different ranges of displacement behaviour are visible.

The elastic range (1) is characterised by a nearly linear load-displacement behaviour. After a first kink (F_{slip}) the specimen's stiffness decreases significantly and the plastic range (2) begins. This range is then characterised by a non-linear load-displacement behaviour. It ends at the point of the ultimate load bearing capacity (F_{ULS}). Subsequently, the post failure range (3) begins which is characterised by a persistent loss of load bearing capacity.

Within the elastic range the load-displacement data between 0.1 and $0.4 \cdot F_{\text{ULS}}$ were used to calculate the elastic stiffness K of each specimen (see Figure 3.8) by applying a linear regression to these data points. Afterwards, the elastic stiffness K was used to estimate the zero point free of initial imperfections for each specimen and the load-displacement data were adjusted accordingly.

Additionally, both Figures show the load-displacement data for both measuring systems, laser (u_{Laser}) and potentiometer (u_{Rig}). It is clearly visible that the potentiometer, which is measuring not only the displacement between specimen footing and load application plate but also additional elastic deformations within the test rig, records a lower stiffness. Hence, all following evaluations mainly focus on laser data.

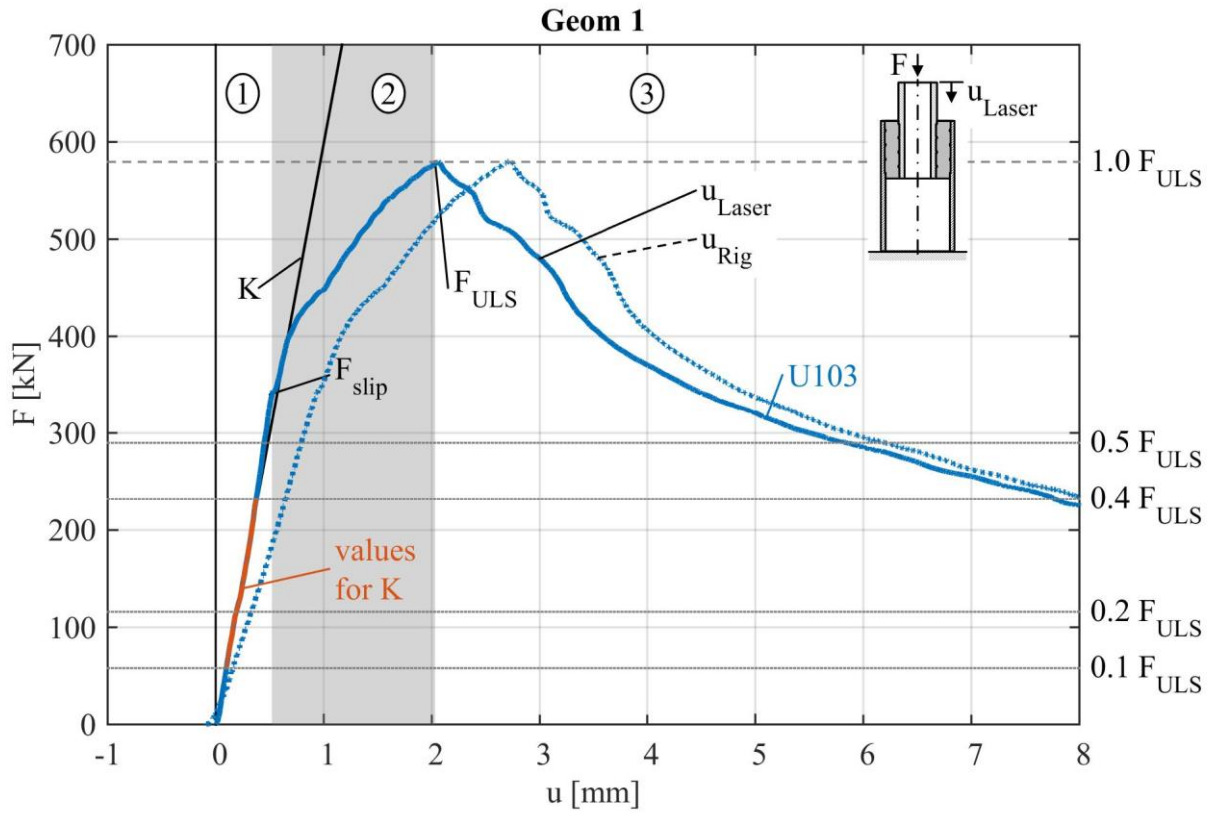


Figure 3.8: Schematic load-displacement curve of a small-scale ULS test with Geometry 1

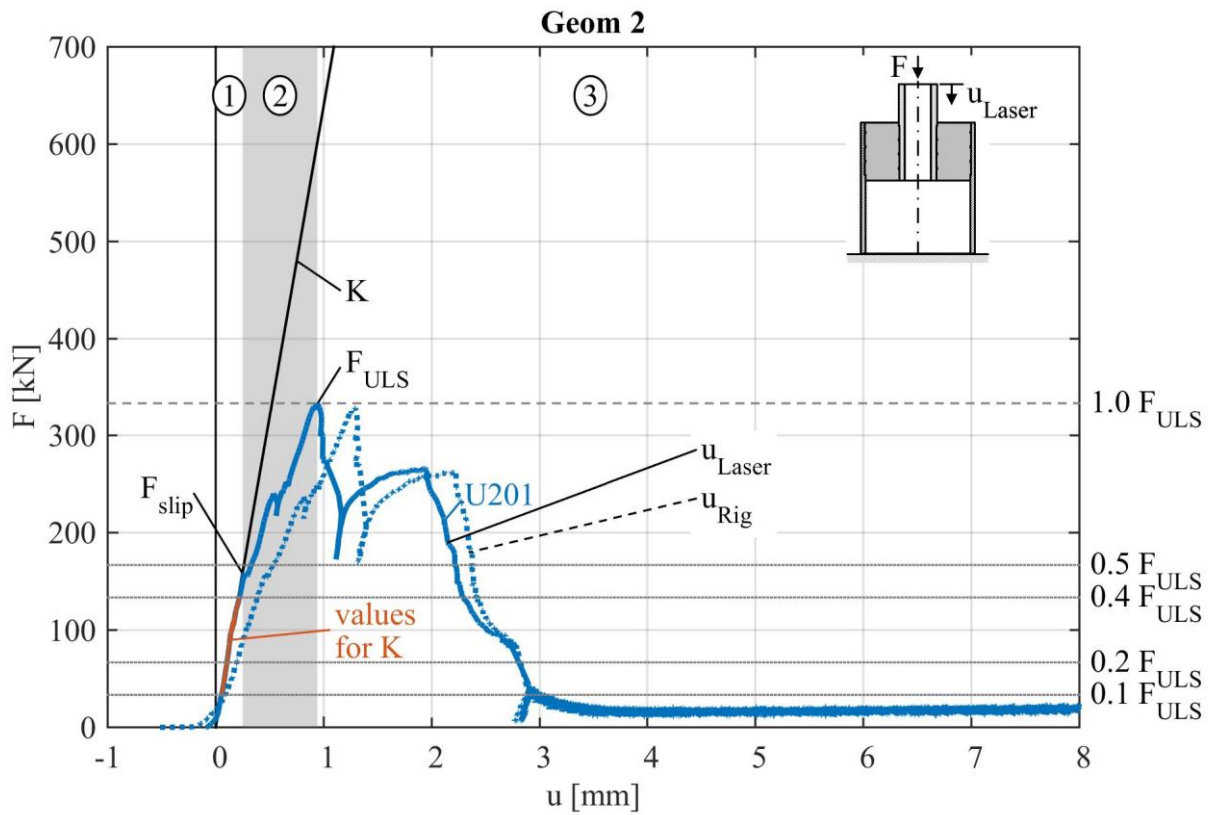


Figure 3.9: Schematic load-displacement curve of a small-scale ULS test with Geometry 2

Figure 3.10 shows the results of all small-scale ULS tests. The upper plot shows the load bearing capacities distinguished between F_{ULS} and F_{slip} as well as the corresponding mean values (dotted

lines). In general both materials gave similar results for F_{slip} , with minor influence of the production batch. This corresponds with the scatter of the material strength properties given in Figure 3.5. For F_{ULS} the scatter is much wider, which is most pronounced for batch DD3. BM95 delivered slightly higher F_{slip} and significantly higher F_{ULS} values (see Table 3.3). Geometry 2 delivered about half the load bearing capacity of Geometry 1.

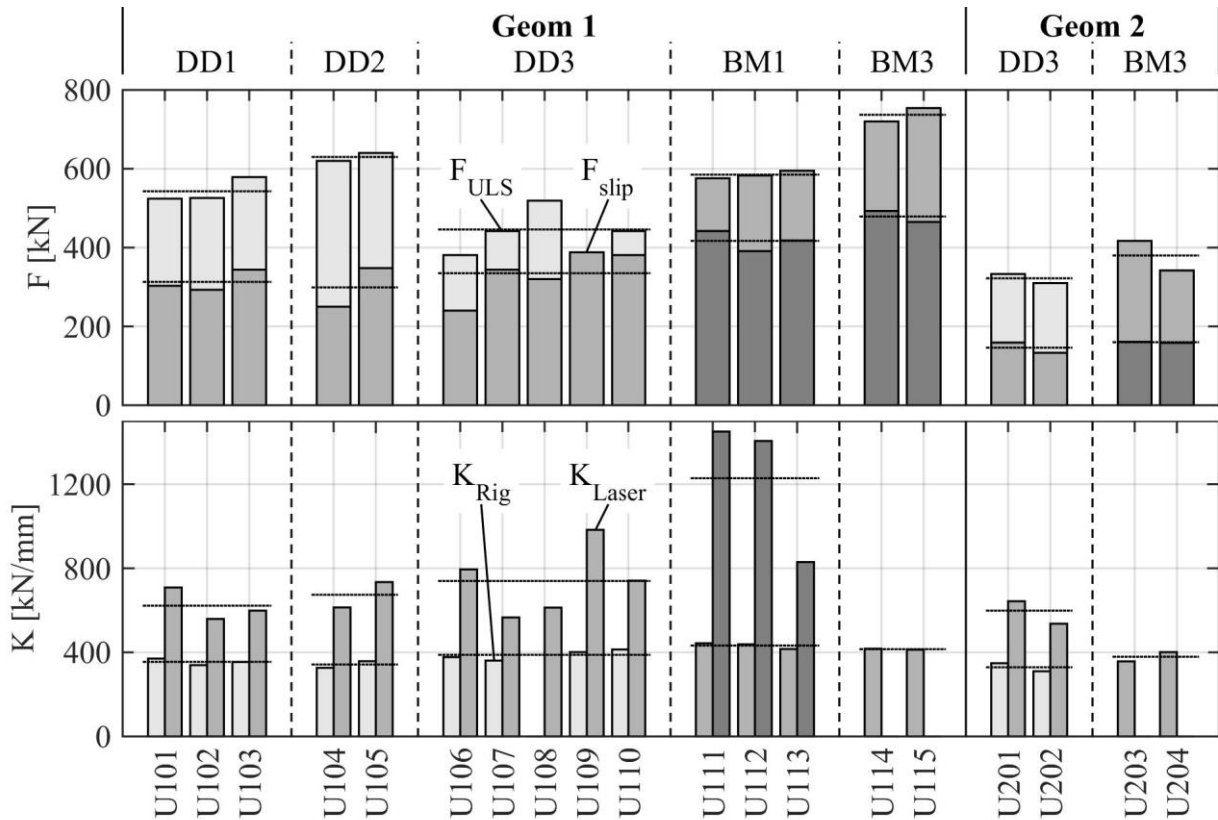


Figure 3.10: Summarised results of the ULS tests

Table 3.3: Summarised load bearing capacities compared between grout material and specimen geometry

	f_c [N/mm ²]	Geom 1			Geom 2			Geom 1 / Geom 2	
		F_{slip} [kN]	F_{ULS} [kN]	$F_{\text{slip}} /$ F_{ULS}	F_{slip} [kN]	F_{ULS} [kN]	$F_{\text{slip}} /$ F_{ULS}	F_{slip}	F_{ULS}
DDS2	116.3	321.2	519.2	0.62	146.0	322.0	0.45	0.45	0.62
BM95	144.1	441.8	646.0	0.68	159.5	380.0	0.42	0.36	0.59
BM / DD	1.24	1.38	1.24		1.09	1.18			

The lower plot of Figure 3.10 shows the elastic stiffness K of the specimens, determined by a linear regression applied to the measurement data between 0.1 and $0.4 \cdot F_{\text{ULS}}$ (see Figure 3.8 and Figure 3.9). This range was chosen to exclude initial settlements below $0.1 \cdot F_{\text{ULS}}$ and scatter of F_{slip} above $0.4 \cdot F_{\text{ULS}}$ from the evaluation. The left bar represents the stiffness derived from the potentiometer measurement K_{Rig} , the right shows the stiffness derived from the laser measurement K_{Laser} . As mentioned before, the stiffness K_{Rig} is significantly lower due to additional deformations of the

test rig within the measuring length. Additionally, the difference of K_{Rig} between the grout materials is not as pronounced as for K_{Laser} (see Table 3.4). In general the stiffer BM95 led to a stiffer specimen and the smaller grout layer (Geom 1) also increased the specimens' stiffness.

Table 3.4: Summarised stiffness compared between grout material and specimen geometry

	E_c [N/mm ²]	Geom 1		Geom 2		Geom 2 / Geom 1	
		K_{Rig} [kN/mm]	K_{Laser} [kN/mm]	K_{Rig} [kN/mm]	K_{Laser} [kN/mm]	K_{Rig} [kN/mm]	K_{Laser} [kN/mm]
DDS2	43'567	366.8	691.3	329.2	589.7	0.90	0.85
BM95	47'567	425.5	1228.7	n/a	n/a	n/a	n/a
BM / DD	1.09	1.16	1.78	n/a	n/a		

3.4.3 Degradation behaviour

After the ULS tests were completed, the specimens were cut and opened to inspect the grout layer and its damage patterns. Figure 3.11 shows two opened specimens with small (left) and large (right) grout layer thickness, showing the typical damage patterns. Both specimens showed diagonal shear cracks in the grout layer.

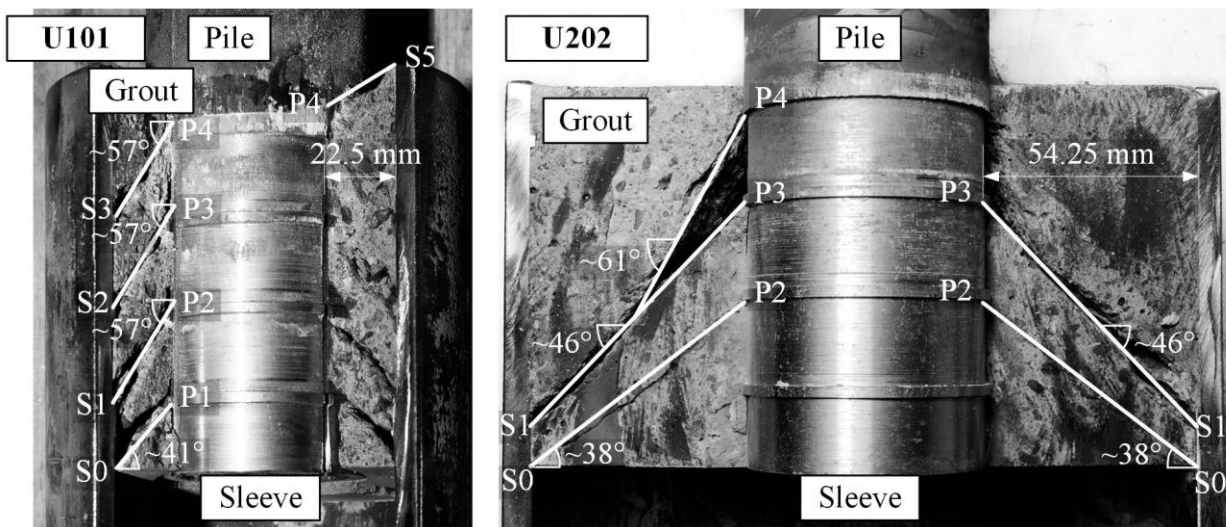


Figure 3.11: Damage patterns of ULS specimens with different grout layer thickness

For the quasi-static load and the small grout layer, two different cracks are visible. The lowest crack occurred between shear key P1 and the lower end of the grout at the sleeve surface S0, with an orientation angle of $\sim 41^\circ$. The three other cracks occurred between one shear key on the sleeve surface and the next higher shear key on the pile surface (S1 – P2, S2 – P3, S3 – P4) showing the same orientation angle of $\sim 57^\circ$. The specimen with large grout layer showed a similar damage pattern but the diagonal shear cracks occurred between different shear key pairs. The lowest crack occurred between the lower end of the grout S0 and shear key P2 with an orientation angle of $\sim 38^\circ$. The next crack occurred between shear key S1 and P3 with an orientation angle of $\sim 46^\circ$. And an additional crack occurred between P4 and the aforementioned crack. Compared to Geometry 1, the cracks skipped the lowest shear key on the pile surface (S0 – P2, S1 – P3) but showed comparable orientation angles.

Besides the diagonal shear cracks, grout crushing in front of the loaded surface of each shear key and corresponding voids in the size of the measured final displacement behind the shear keys were found (see Figure 3.12).

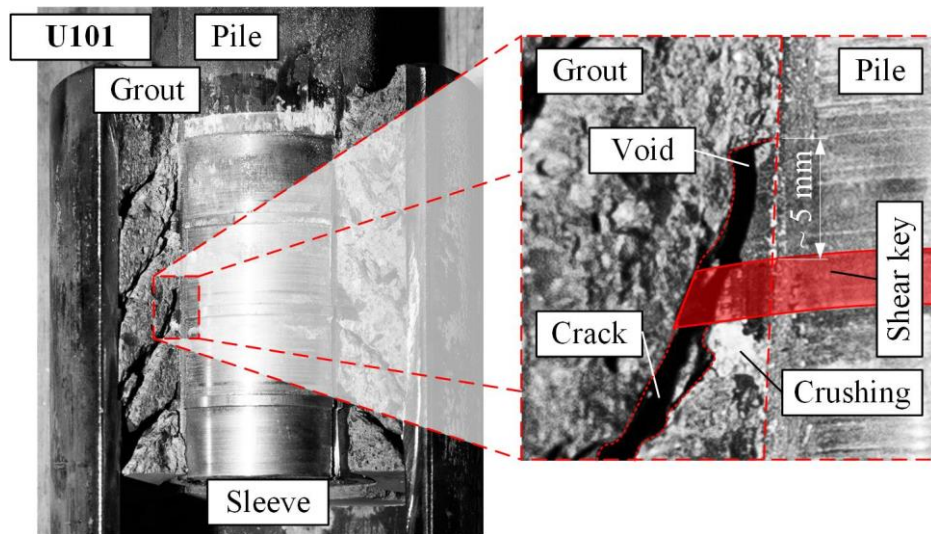


Figure 3.12: Damage patterns at shear key of ULS specimen

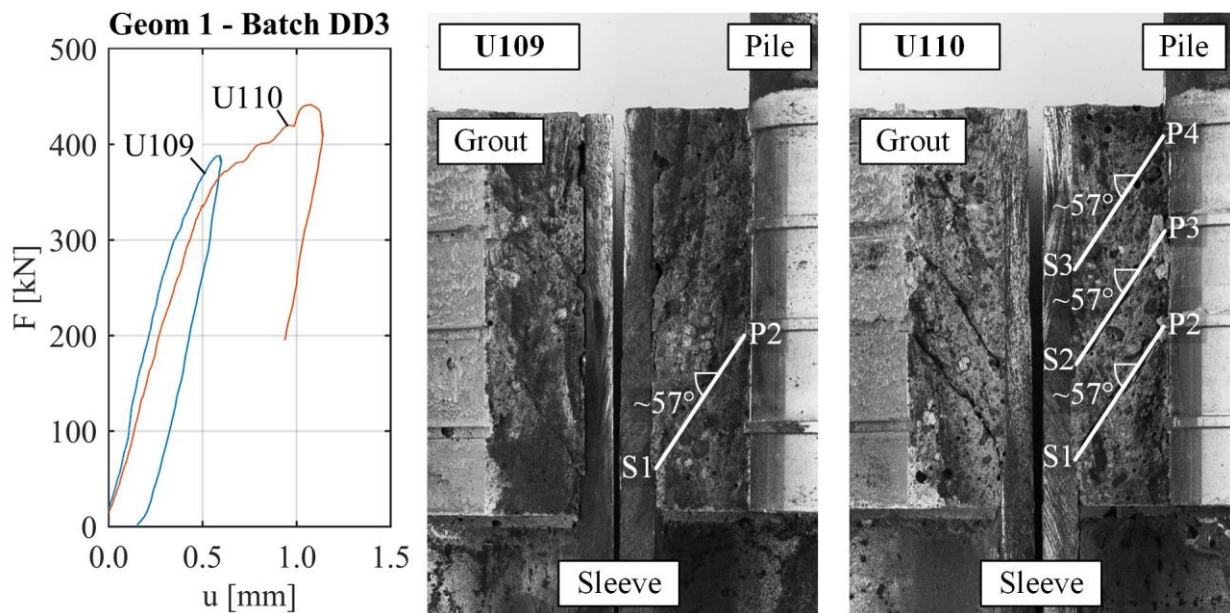


Figure 3.13: Load-displacement results of ULS step test (left) and damage pattern at different load levels (right)

Figure 3.13 shows the results of two ULS tests which were terminated after the first kink (F_{slip}) occurred in the load displacement curve (U109) and after the ultimate capacity (F_{ULS}) was reached (U110). The opened specimens showed the damage patterns at these transitions between the ranges defined in Figure 3.8. The first transition was induced by cracking of the highest loaded diagonal shear surface. Further the second transition was induced by completed cracking of all diagonal shear surfaces. This cracking behaviour corresponds to the observations of Anders (2007), Schumann et al. (2009), Keindorf (2010) and Wilke (2014).

3.4.4 Comparison to analytical design approaches

Based on the design approaches described in Section 2.5 the characteristic ULS capacities of the small-scale specimens were calculated. In Figure 3.14 the analytical results are compared to the test results for F_{ULS} and in Figure 3.15 to F_{slip} . Within the calculations not only the characteristic material properties given by the manufacturers but also the material properties obtained from self-conducted tests (see Figure 3.5) were considered.

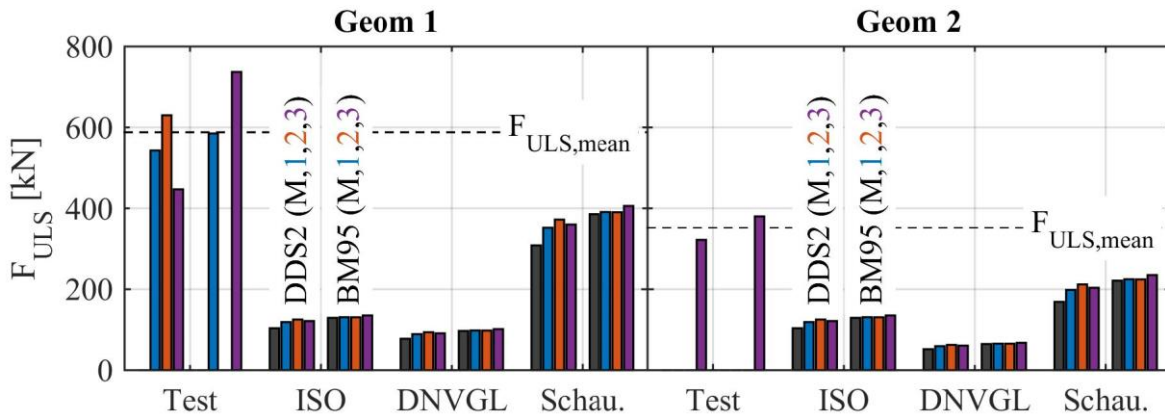


Figure 3.14: Characteristic load bearing capacities F_{ULS} measured in tests and calculated F_{ULS} for different material batches (1,2,3) according to current design methods

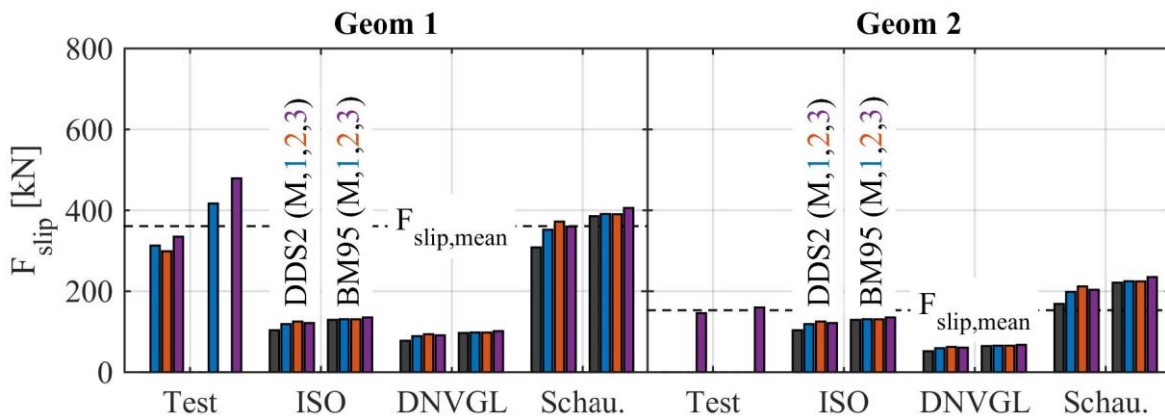


Figure 3.15: Characteristic load bearing capacities F_{slip} measured in tests and calculated F_{ULS} for different material batches (1,2,3) according to current design methods

All design methods give lower load bearing capacities F_{ULS} for Geometry 2 with the larger grout layer and thus correspond to the trend of the test results. The approach described in DIN EN ISO 19902 (2014) is based on the bonding stress model (see Section 2.5.2) considering the effective grout layer length to be load transferring. In contrast to that the approach given in DNVGL-ST-0126 (2016) depends on the number of shear keys (see Section 2.5.3). Therefore, the DNVGL-ST-0126 (2016) equations give the lowest load bearing capacities between 15 and 20 % of the measured F_{ULS} . With the equations from DIN EN ISO 19902 (2014) slightly higher load bearing capacities between 20 and 27 % are calculated. However, even the equations by Schaumann et al. (2012) underestimate the measured F_{ULS} values by 20 to 40 %. When comparing the analytical values with the measured F_{slip} (see Figure 3.15) the equations of DNVGL-ST-0126 (2016) and DIN EN ISO 19902 (2014) still give a load bearing capacity of 20 to 40 % of F_{slip} while the equations by Schaumann et al. (2012) overestimate F_{slip} by up to 25 %.

3.4.5 Discussion

Based on the test results described beforehand, the general load bearing behaviour of the small-scale specimens under quasi-static load can be described as follows. After initial settlements are overcome, both materials behave linear elastic. Therefore, the specimen behaves almost linear elastic. At a load level of about $0.5 \cdot F_{ULS}$ of the specimen, a diagonal shear crack evolves between shear keys S1 and P2 for Geometry 1 (see Figure 3.13 and Figure 3.16, left) and between S1 and P3 for Geometry 2 (see Figure 3.16, right), F_{slip} is reached. Afterwards the stiffness of the specimens reduces significantly and the remaining diagonal shear surfaces start to crack. The diagonal shear cracks are oriented between 38° and 61° (see Figure 3.11). At F_{ULS} all diagonal shear cracks except for the lowest one are fully evolved (see Figure 3.16) and the remaining load bearing capacity reduces with simultaneously increasing displacements. The relative displacement, which occurs after F_{ULS} is reached, can be traced back to grout crushing in front of the loaded shear key surfaces and diagonal shear cracking of the lowest shear surface.

As shown in Figure 3.16 the final crack pattern leads to five separated grout parts for Geometry 1. Once the crack S1-P2 has developed, loads induced by shear keys P1 and P2 can only be transferred via friction between grout and sleeve. Since the diagonal shear crack between the grout layer's lower end and P1 evolves after F_{ULS} is reached, a certain amount of friction must be activated in the interface between grout and sleeve. Nevertheless, after crack S1-P2 has evolved the main loads are induced by shear keys P3 and P4 and transferred to the sleeve via compression.

For Geometry 2 the final cracking pattern leads to three separated grout parts. The cracking chronology can be assumed to be similar to Geometry 1. Once shear crack S1-P3 has evolved the main loads are induced by shear key P4.

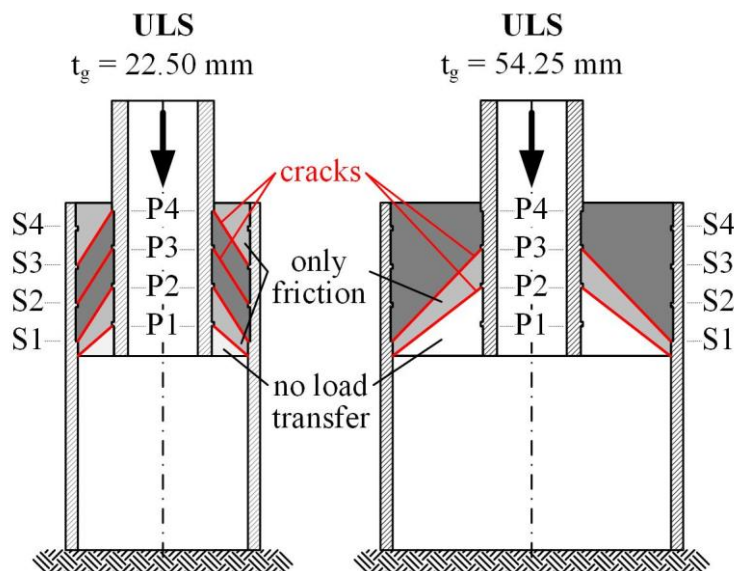


Figure 3.16: Schematic cracking behaviour of small-scale specimens in ULS tests

A comparison between the obtained F_{ULS} capacities (see Table 3.3) and the load bearing mechanism described beforehand, explains the significant reduction of load bearing capacity for the larger grout layer. The ratio of two mainly active shear keys in Geometry 1 versus one in Geometry 2 corresponds to a reduction of F_{ULS} to almost 60 %. The difference to 50 % (1/2 active shear keys)

can be traced back to a significantly larger surface area between grout and sleeve for the second lowest grout part and hence, a larger friction capability increasing the load share of shear key P3.

Even though the investigated specimens exceed certain ranges of applicability of currently standardised analytical design approaches (see Section 3.2.2), these approaches give conservative characteristic load bearing capacities F_{ULS} and acceptable F_{slip} values.

Finally, F_{slip} seems to be the more appropriate value for the load bearing capacity of the small-scale specimens since the scatter of non-elastic range 2 and F_{ULS} (see Figure 3.8) is much higher than for the elastic range 1 and F_{slip} . Though, in correspondence with the tradition of grouted connection tests (see Chapter 2), the further evaluation is carried out in reference to F_{ULS} .

3.5 Fatigue Limit State (FLS) tests

3.5.1 Procedure

The fatigue behaviour is decisive for the durability of grouted connections. Thus, small-scale fatigue tests were conducted subsequent to the ULS tests. The test-rig for the small-scale FLS tests is shown in Figure 3.17. It consisted of a servo-hydraulic cylinder with a dynamic loading capacity of 380 kN up to a loading frequency of 10 Hz and an axial hinge to exclude bending loading due to possible eccentric positioning of the specimen. The specimens were positioned in a water basin, which allowed dry and wet (fresh water) ambient conditions (AC).

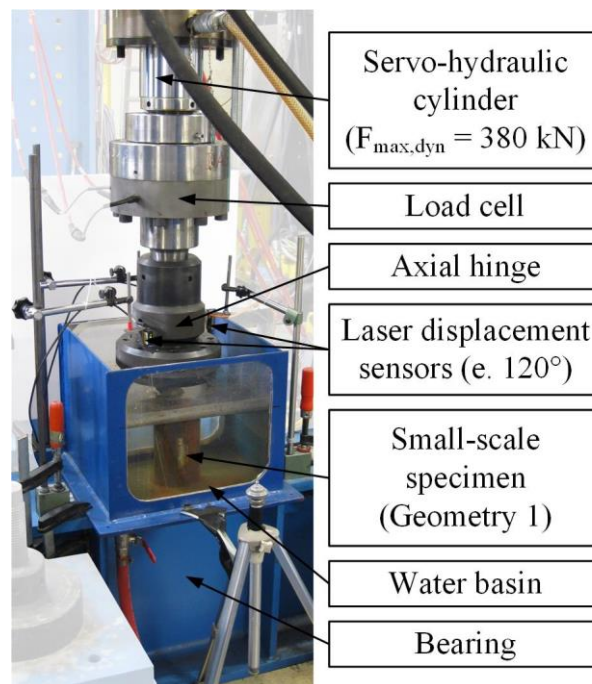


Figure 3.17: Test rig for the fatigue tests

The tests were conducted until two million load cycles were applied (runner), or failure of the specimen, characterised by a sudden and significant increase of relative displacement between pile and sleeve (Δu).

Similar to the ULS measurement set-up, the applied load F was measured with a load cell, and the specimen's displacement u was measured with lasers positioned at 0° , 120° and 240° angle circumferential to the specimen.

Additionally, during selected tests an automated photography system was installed for documentation of possible grout flushing. The system shown in Figure 3.18 consisted of a DSLR-camera facing towards a studio flash with a softbox. So, only the contour of the specimen was photographed. The remote trigger was set for an optimum between number of pictures, memory card capacity and expected test duration. In general about 3000 pictures were taken per test.

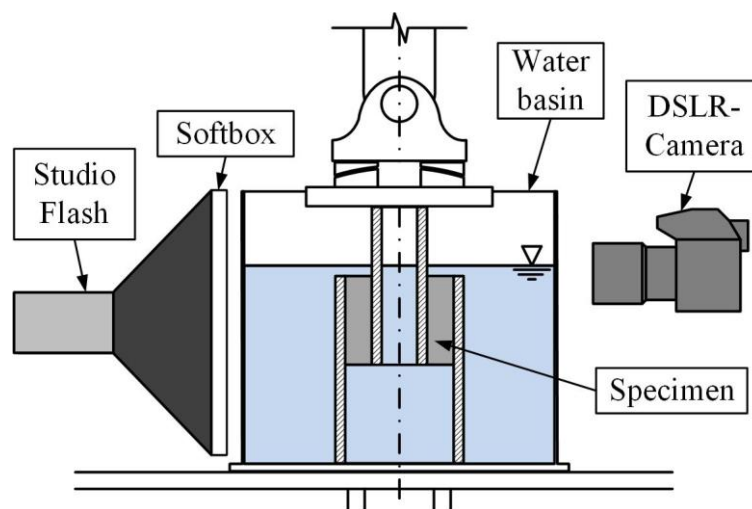


Figure 3.18: Automated photography system

3.5.2 Evaluation of measurement data

General remark

In the following, only chosen samples of all 49 evaluated small-scale fatigue tests are presented. Purpose is to illustrate the fatigue behaviour of the specimen and the influencing parameters. All test results can be looked up in Appendix A.

Influence of FLS test rig

While evaluating the measurement data of the fatigue tests, implausibly high mean displacements were identified. Therefore, additional tests regarding the test rig were conducted. The test set-up was similar to the fatigue tests (see Section 3.5.1) but with a steel block instead of a grouted connection specimen. As shown in Figure 3.19, eight load scenarios with incrementally increased loads were applied. Each load scenario consisted of 2'000 load cycles, a constant loading ratio of $R = 20$ and a loading frequency of $f = 5$ Hz. Pure compressive loads were applied.

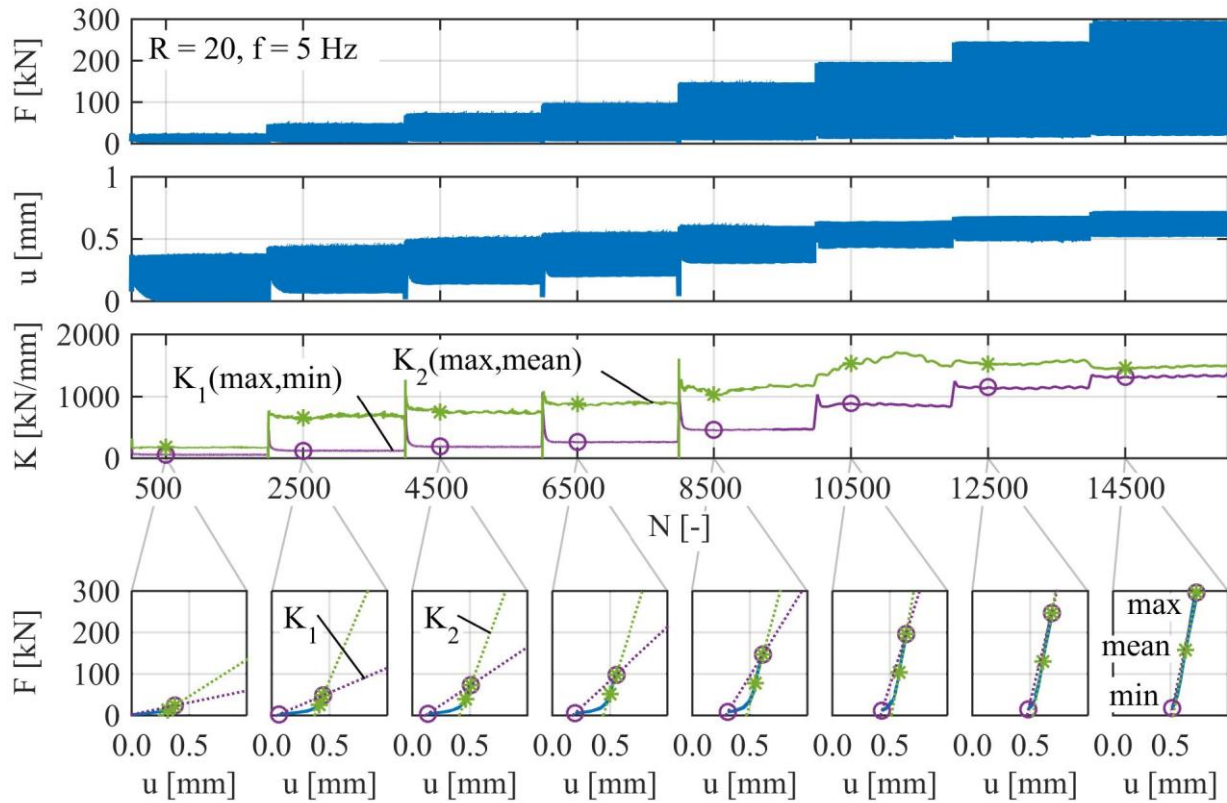


Figure 3.19: Measurement of rig stiffness with dummy

The measured displacement range $\Delta u = u_{\max} - u_{\min}$ decreased with increasing load range $\Delta F = F_{\max} - F_{\min}$ (see Figure 3.19) which cannot be explained by the specimen's stiffness. As visible in the load-displacement plots, at loads below $F \sim 50$ kN, larger relative displacements occurred than above $F \sim 50$ kN. Figure 3.20 shows the test rig set-up and the position of the laser sensors. According to this set-up, the lasers measured the summarised displacements of load application plate, specimen (i.e. steel tubes, grout layer, contact surface between steel and grout), water basin floor and bearing. Due to the cut-off behaviour of the large displacements, the water basin floor was identified to cause this non-linearity.

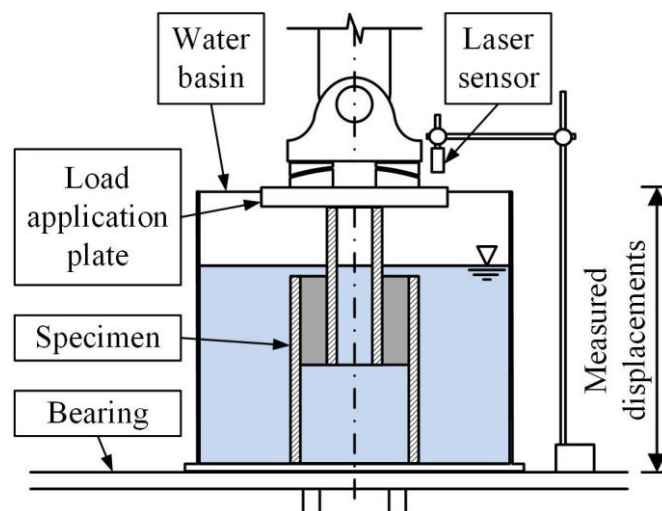


Figure 3.20: FLS test rig and range of measured displacement

While manufacturing, the water basin walls were welded onto the relatively thin floor ($t = 12$ mm). The resulting welding distortions caused a bulging of the basin floor and therefore a gap between basin floor and bearing. At low load levels, firstly this gap was closed and hence the basin floor added additional elasticity to the range of measured displacements.

For the evaluation of the measured data this meant two major problems. Firstly, the measured mean displacement was shifted to a higher value. Secondly, the displacement range Δu was contaminated and thus also the secant stiffness of the hysteresis. Therefore, the following approach was elaborated to solve the problem and was applied to all FLS test results.

Usually, the secant stiffness K of a hysteresis is calculated according to:

$$K_1(\text{max, min}) = \frac{F_{\text{max}} - F_{\text{min}}}{u_{\text{max}} - u_{\text{min}}} \quad (3.1)$$

For the presented data a new secant stiffness K_2 was defined using the hysteresis mean values (see Equation (3.2)) instead of the min values, since they were less influenced by the observed non-linearities (see Figure 3.19).

$$K_2(\text{max, mean}) = \frac{F_{\text{max}} - F_{\text{mean}}}{u_{\text{max}} - u_{\text{mean}}} \quad (3.2)$$

As visible in Figure 3.19, the secant stiffness K_2 is almost free of non-linearities for load levels of 200 kN and above. Hence, with the suggested approach a stiffness evaluation of the FLS tests was possible at least for the mentioned load levels.

For the shifted mean values, the false initial displacement u_0 was determined by calculating the distance between the measured zero and the K_2 predicted zero of the first hysteresis (see Figure 3.21).

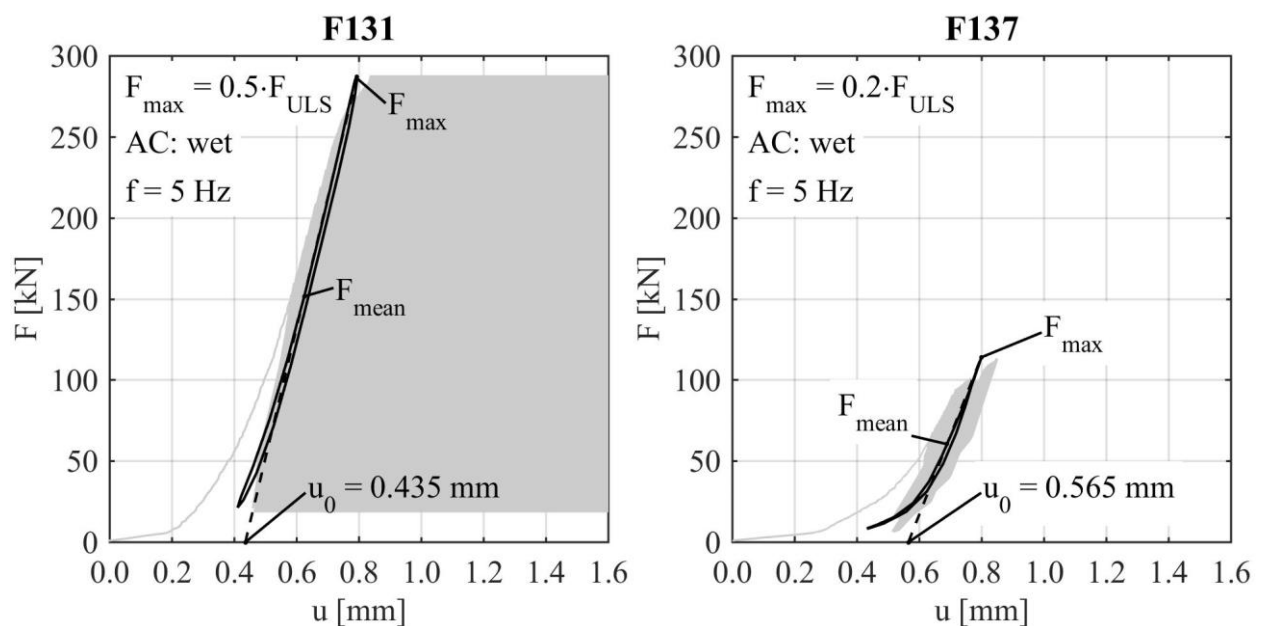


Figure 3.21: Initial displacement correction approach

Termination criteria (TC) for FLS tests

For specimens loaded at $0.2 \cdot F_{ULS}$ the termination criteria (TC) runner (see Figure 3.22) and Δu (see Figure 3.23), as defined prior to the tests (see Section 3.5.1), did not apply. Exemplarily shown for specimen F137 in Figure 3.24, the specimen's displacement showed only a short constant phase in between the first $\sim 5\%$ of applied load cycles. Subsequently, the displacement increased at a more or less constant rate.

As described in the previous Section, the measured data contain the summarised displacement of load application plate, specimen (i.e. steel tubes, grout layer, contact surface between steel and grout), water basin floor and bearing. The deformations of load application plate, steel tubes and bearing can be expected to be linear elastic and therefore time invariant. Hence, they are negligibly small in relation to the magnitude of the measured data. Deformations of the water basin floor were subtracted as aforementioned. Consequently, the measured displacements can be associated with the deformation of grout layer and contact surface between steel and grout.

On the one hand, no sudden loss of load bearing capacity appeared at a loading level of $0.2 \cdot F_{ULS}$ and the specimen could still bear the applied load. But on the other hand, the pile was constantly sinking into the sleeve. Considering the content of the measured displacements, this behaviour is equivalent to a significant degradation of the grout layer and its contact surfaces. This load bearing behaviour cannot be assessed as serviceable and thus, a third TC (u_{max}) was defined for a mean displacement of $u_{min}(N) = 8 \text{ mm}$.

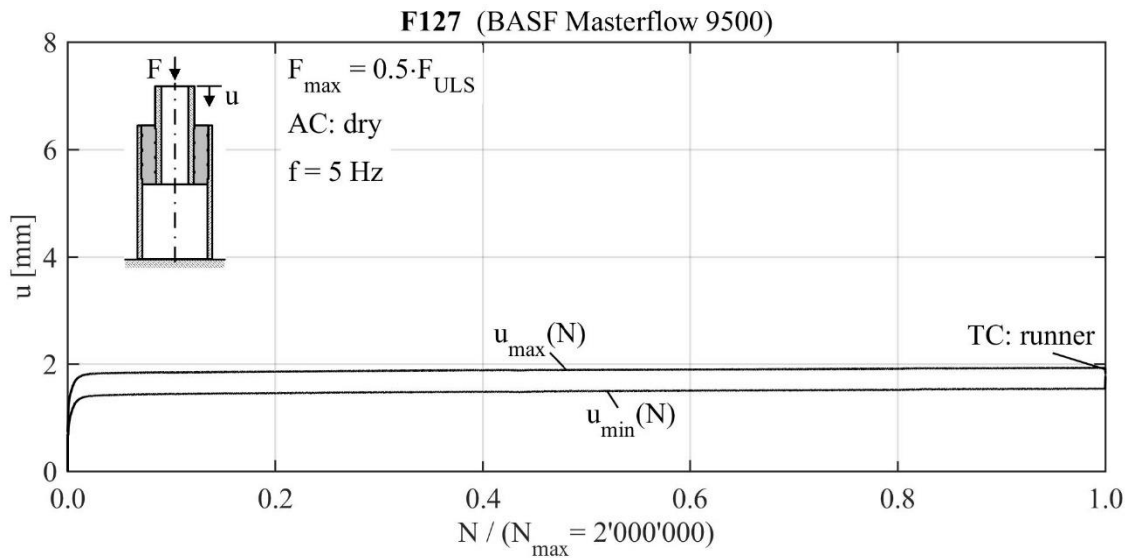


Figure 3.22: Test results of specimen F127 with termination criterion runner

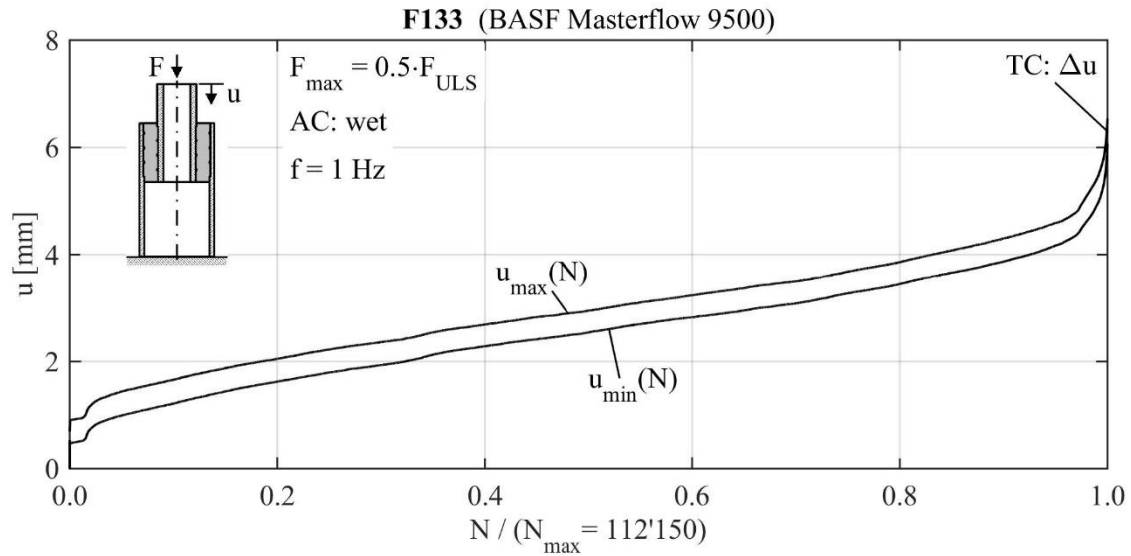


Figure 3.23: Test results of specimen F133 with termination criterion Δu

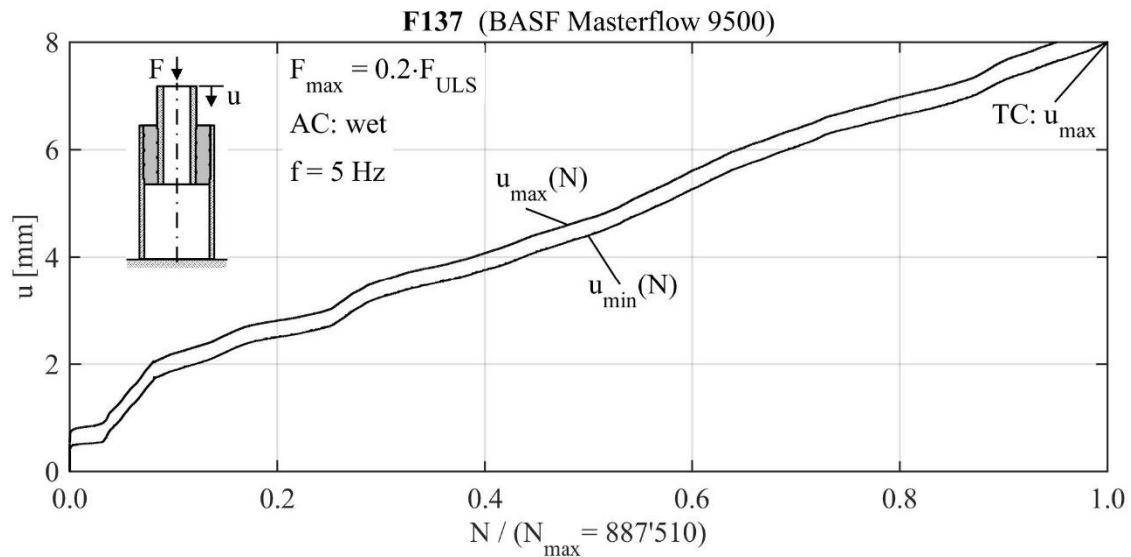


Figure 3.24: Test results of specimen F137 with termination criterion u_{\max}

Number of endurable load cycles

Considering the previously defined TC, the number of endurable load cycles for each FLS specimen could be determined from the measurement data. Figure 3.25 shows a corresponding S-N plot for all small-scale FLS tests with Geometry 1. While specimens tested in dry AC at $F_{\max} = 0.5 \cdot F_{\text{ULT}}$ and $f = 5.0 \text{ Hz}$ were runners (grey diamond), specimens tested at identical loading conditions but in wet AC failed (TC: Δu) at an average of 50'000 load cycles (red dots). Hence, loading a specimen in wet AC significantly reduces the number of endurable load cycles.

Furthermore, a load reduction from $0.5 \cdot F_{\text{ULT}}$ down to $0.2 \cdot F_{\text{ULT}}$ (red dots) in wet AC led to an average test termination (TC: u_{\max} and runner) after 1.4 million load cycles. Accordingly, as expected, a load reduction extends the number of endurable load cycles.

Finally, reducing the loading frequency down to $f = 1.0 \text{ Hz}$ (green crosses) and further down to $f = 0.3 \text{ Hz}$ (blue stars) in wet AC at $F_{\max} = 0.5 \cdot F_{\text{ULT}}$ also extended the number of endurable load

cycles up to an average of $N = 230'000$ (TC: Δu). Based on the results presented in Figure 3.25 as well as additional results for $f = 10.0$ Hz and $f = 2.0$ Hz, the frequency dependent S-N curve given in Figure 3.25 was developed and first presented in Schaumann & Raba (2015a).

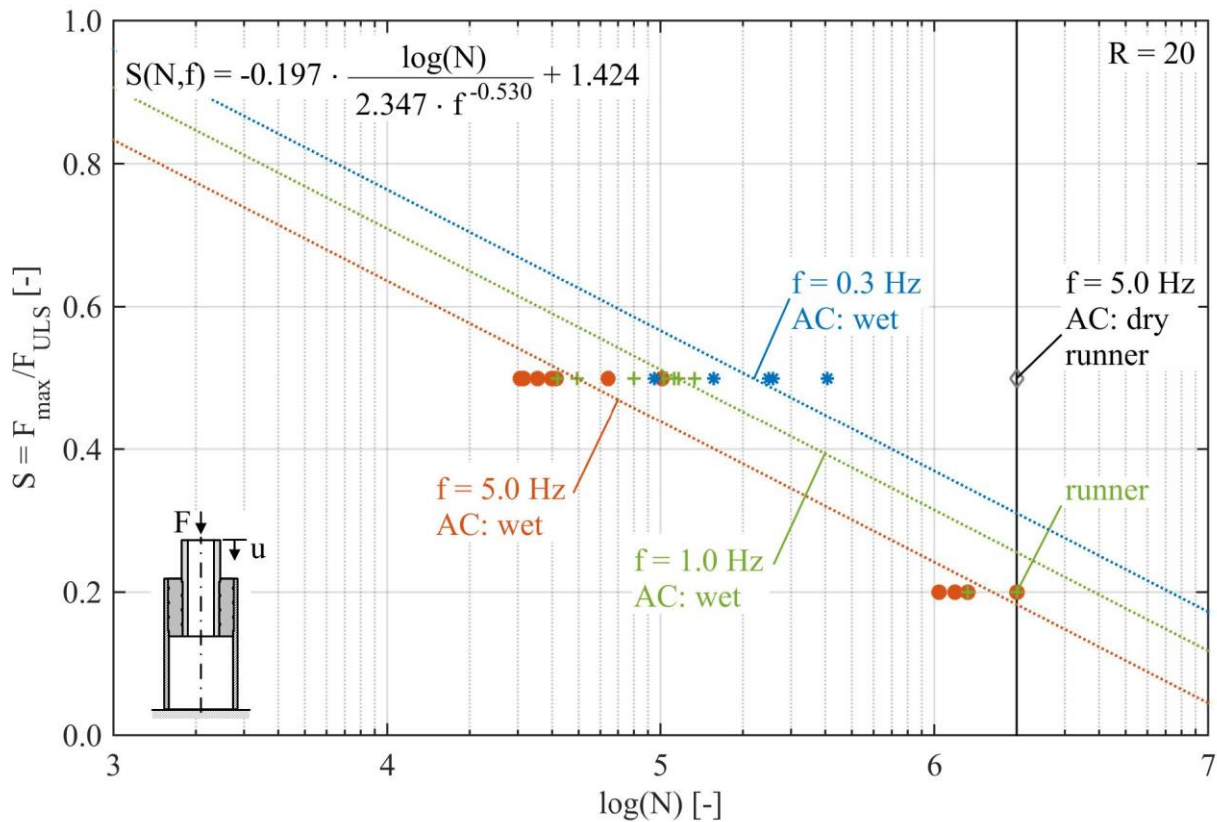


Figure 3.25: S-N plot of small-scale test results for different AC and loading frequencies in analogy to Schaumann & Raba (2015a)

It must be emphasized that the slope of the S-N curves is a proposition based on the results for 5.0 Hz. As mentioned before, the results obtained at $F_{\max} = 0.2 \cdot F_{\text{ULS}}$ are based on TC u_{\max} , while those obtained at $0.5 \cdot F_{\text{ULS}}$ are based on TC Δu . For a sudden loss of load bearing capacity the number of endurable load cycles is expected to be larger at $0.2 \cdot F_{\text{ULS}}$.

In Figure 3.26 the number of endurable load cycles for both geometries at identical loading conditions are presented. For the larger grout layer, three of four specimens tested in dry AC were runners. The one specimen that failed at about 350'000 load cycles can be rated as outlier since the difference between the numbers of load cycles is highly significant. In wet AC the specimens with the larger grout layer failed (TC: Δu) at an average of 15'000 load cycles. Consequently, a larger grout layer leads to a reduced number of endurable load cycles. From the presented results, a grout layer thickness dependent S-N curve, given in Figure 3.26, was derived.

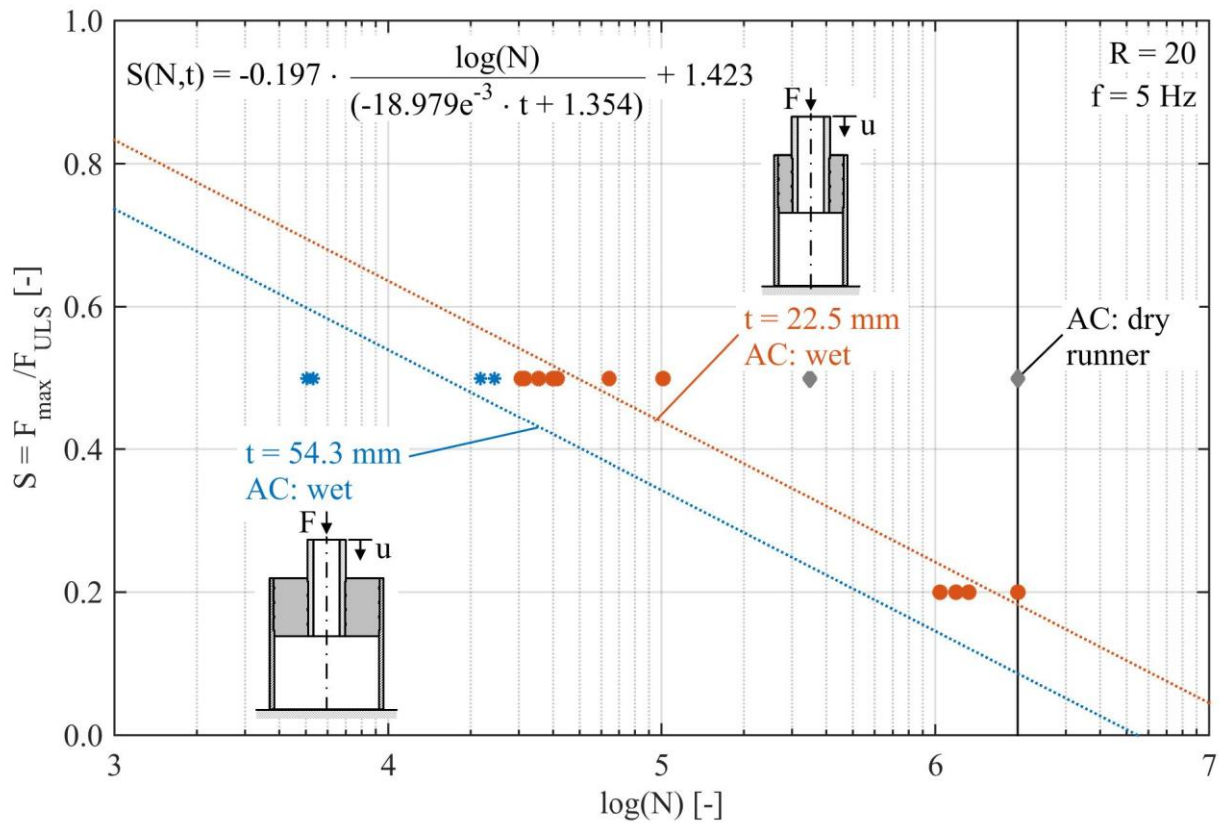


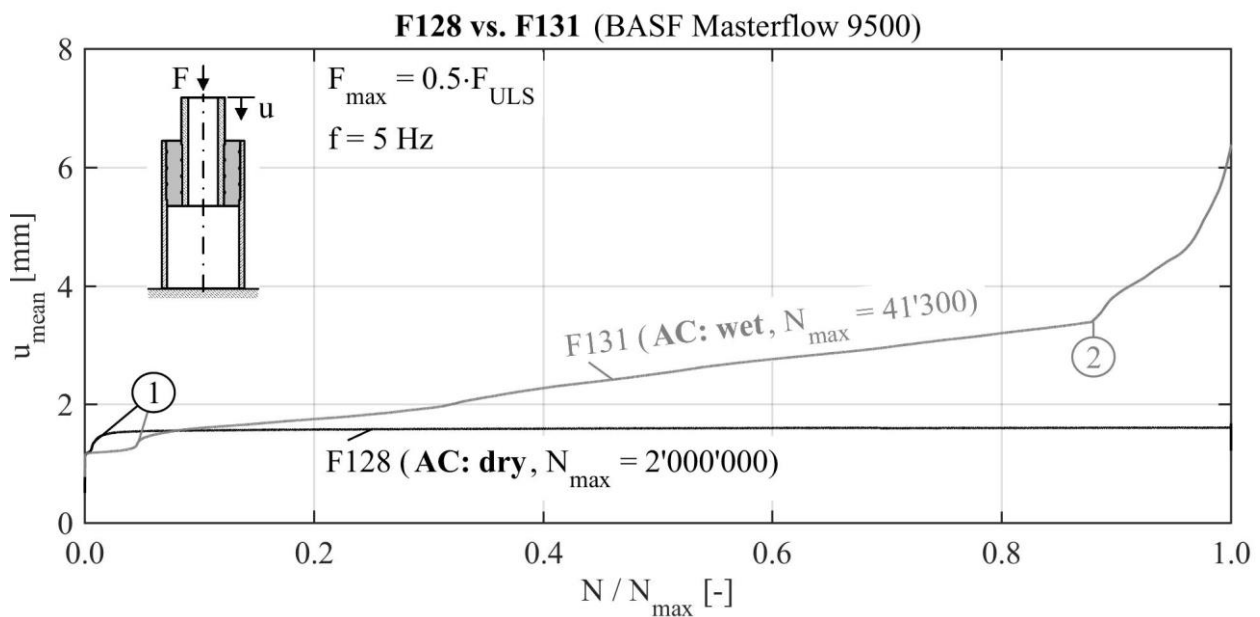
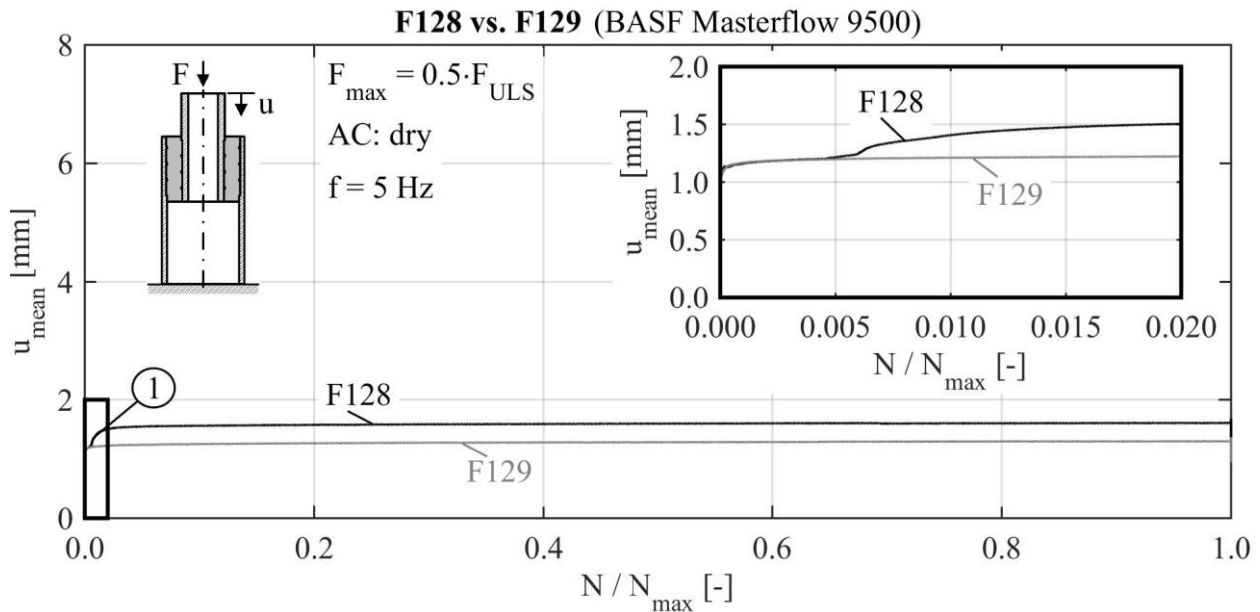
Figure 3.26: S-N plot of small-scale test results for different AC and grout layer thickness

Load cycle dependent deformation behaviour

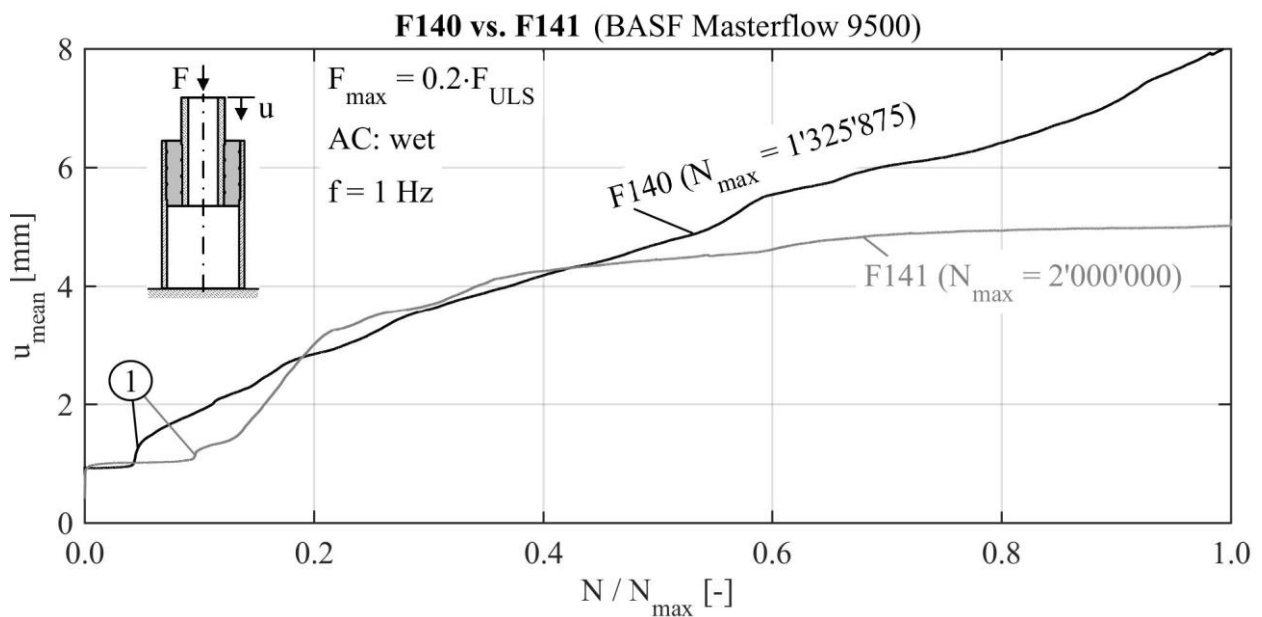
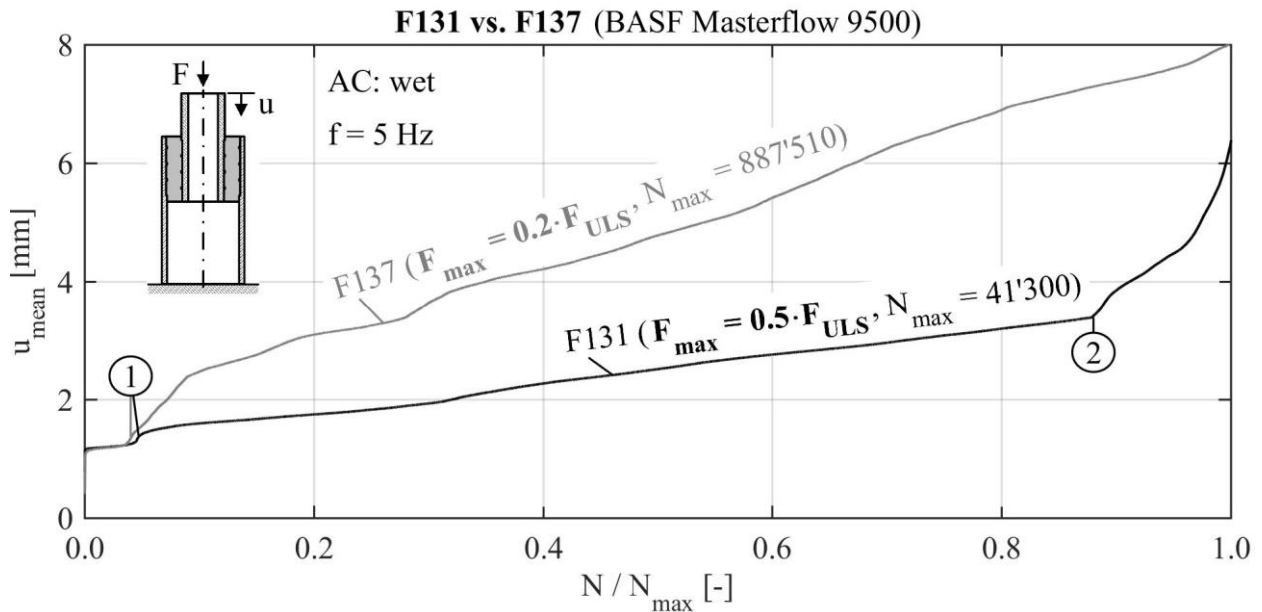
In the following Section the deformation behaviour in dependency of the number of applied load cycles is described in detail, based on selected measurement data which show characteristic behaviour. The full set of measurement data can be found in Appendix A.

Figure 3.27 shows the measured mean deformation for two specimens tested in dry AC with identical loading conditions of $0.5 \cdot F_{\text{ULS}}$. Both specimens reached two million load cycles and the tests were terminated by TC runner. Likewise, both specimens showed a slight change in their load deformation behaviour during the first $\sim 0.2\%$ of applied load cycles. This change was observed in all tests independent of grout material, geometry and loading condition. While specimen F129 showed no additional change in its load deformation behaviour for the further test, specimen F128 showed a significant additional offset at $\sim 0.6\%$ of applied load cycles marked with 1 in Figure 3.27. After stabilising at $\sim 2\%$ of applied load cycles, both specimens showed a constant load deformation behaviour until the test was terminated.

In Figure 3.28 specimen F128 is compared to specimen F131 where the test set-up varied only regarding the AC. The deformation of specimen F131, tested in wet AC, showed the previously described initial offset marked 1. Different to specimen F128, the deformation of F131 increased constantly after a first kink (1) occurred. Additionally, a second kink (2) in the deformation curve is visible within the last $\sim 20\%$ of applied load cycles.



In Figure 3.29 the deformation behaviour of specimen F131 is compared to specimen F137, which was loaded at $0.2 \cdot F_{ULS}$. Both deformation curves show the typical kink 1 in the beginning of the test and afterwards a constant increase of deformation. Different to specimen F131, no second kink was observed for specimen F137. In addition to that, test F131 was terminated by TC Δu and test F137 by TC u_{max} .



The specimens F140 and F141 were filled with the same grout material and tested in identical loading conditions as well as equal AC. Nevertheless, similar to specimens F128 and F129, their deformation behaviour shown in Figure 3.30 varied. Both deformation curves show the initial kink 1 in the beginning and the deformation increase afterwards. But the deformation behaviour of specimen F141 stabilised after ~70 % of applied load cycles at a significantly high mean offset of ~5 mm and the test was terminated by TC runner. In contrast to that the deformation of specimen F140 kept increasing and the test was terminated by TC u_{max} .

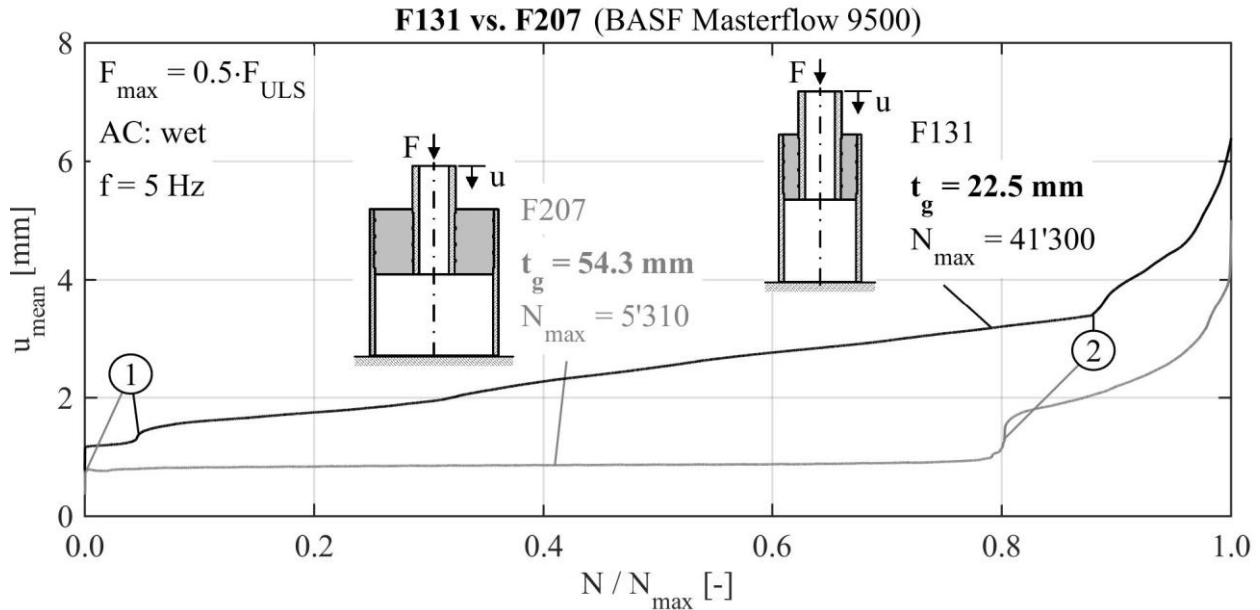


Figure 3.31: Deformation behaviour of two specimens with different grout layer thickness

Finally, Figure 3.31 shows the deformation behaviour of specimens F131 and F207. Both specimens were tested with same loading conditions and AC but varied in their grout layer thickness. For the larger grout layer the initial kink 1 was not as pronounced as for the smaller one. Moreover, F207 tested in wet AC showed a constant load deformation behaviour until kink 2 occurred. The second kink led to a higher offset than observed for the smaller grout layer. Both specimen tests were terminated by TC Δu .

Behaviour of the secant stiffness

In Section 3.5.2, the calculation for the reassessed secant stiffness K_2 of the hysteresis was described. This calculation was applied to all FLS test results. Three of these results for K_2 and the corresponding u_{mean} values are exemplarily shown in Figure 3.32. Even though, for specimens F131 and F137 a load cycle dependent increase of mean deformation was recorded, the secant stiffness stayed constant. This behaviour is in contrast to the findings of for example Holmen (1979) and Oneschkow (2016) for plain concrete specimens, for which a slight decrease of the secant stiffness was registered during the last applicable load cycles. The elastic properties of the grout layer stayed constant during the tests. Hence, neither degradation processes can be detected by evaluating the connections hysteresis secant stiffness, nor can an upcoming failure (TC Δu) of the connection be predicted.

In Figure 3.33 for the grout material DDS2 and in Figure 3.34 for the grout material BM95, the distributions of all K_2 curves are visualised as box plots and their mean values are connected by a dashed line. Additionally, the corresponding F_{max} values are plotted as dotted line. When comparing the two lines, a proportional correlation between K_2 and F_{max} is visible, meaning a low F_{max} leads to a low K_2 .

This behaviour can be explained by the influence of the test rig as described beforehand. Even though the influence was significantly reduced, a visible amount of the non-linear test rig behaviour remained in the measurement data. Since the lower load F_{min} was defined to be fixed to F_{max}

by a ratio of $R = 20$, a low F_{\max} leads to a low F_{\min} . As visible in Figure 3.21 the non-linear influence is higher at lower loads. Hence, also secant stiffness K_2 is lower due to the test rig influence. It can be assumed that the secant stiffness is not influenced by the grout layer degradation. Moreover, an influence on K_2 from the grout layer thickness cannot be determined.

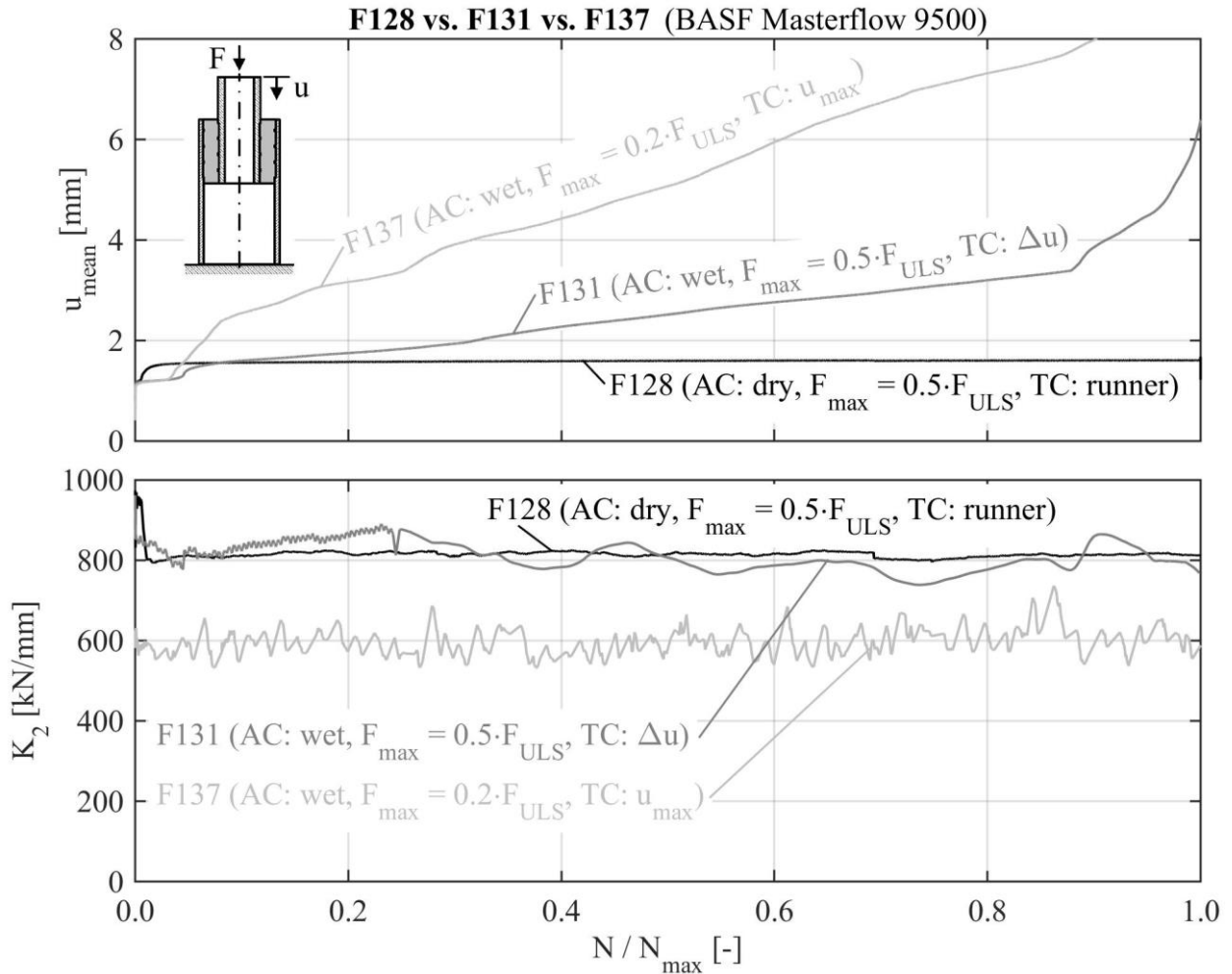


Figure 3.32: Secant stiffness behaviour of three specimens with different loading conditions and AC

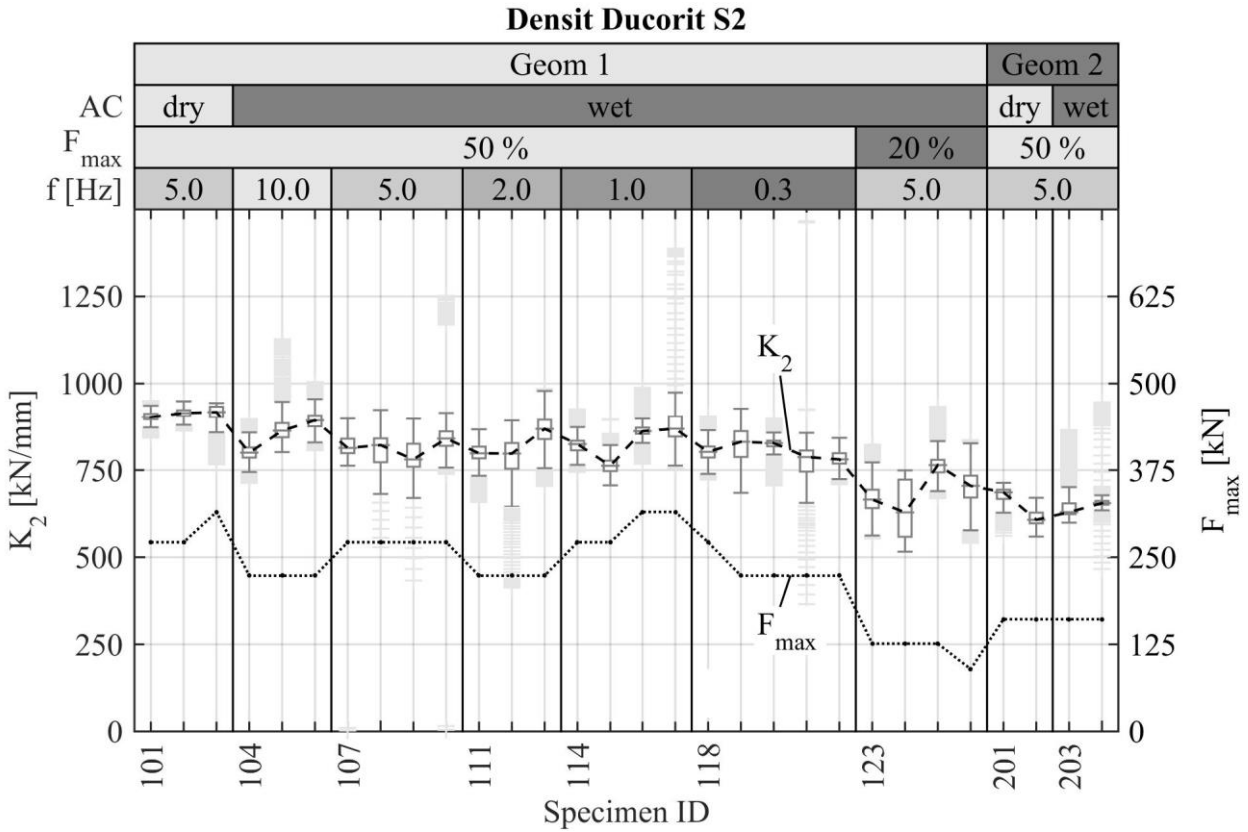


Figure 3.33: Distribution of stiffness K_2 for small-scale specimens with DDS2

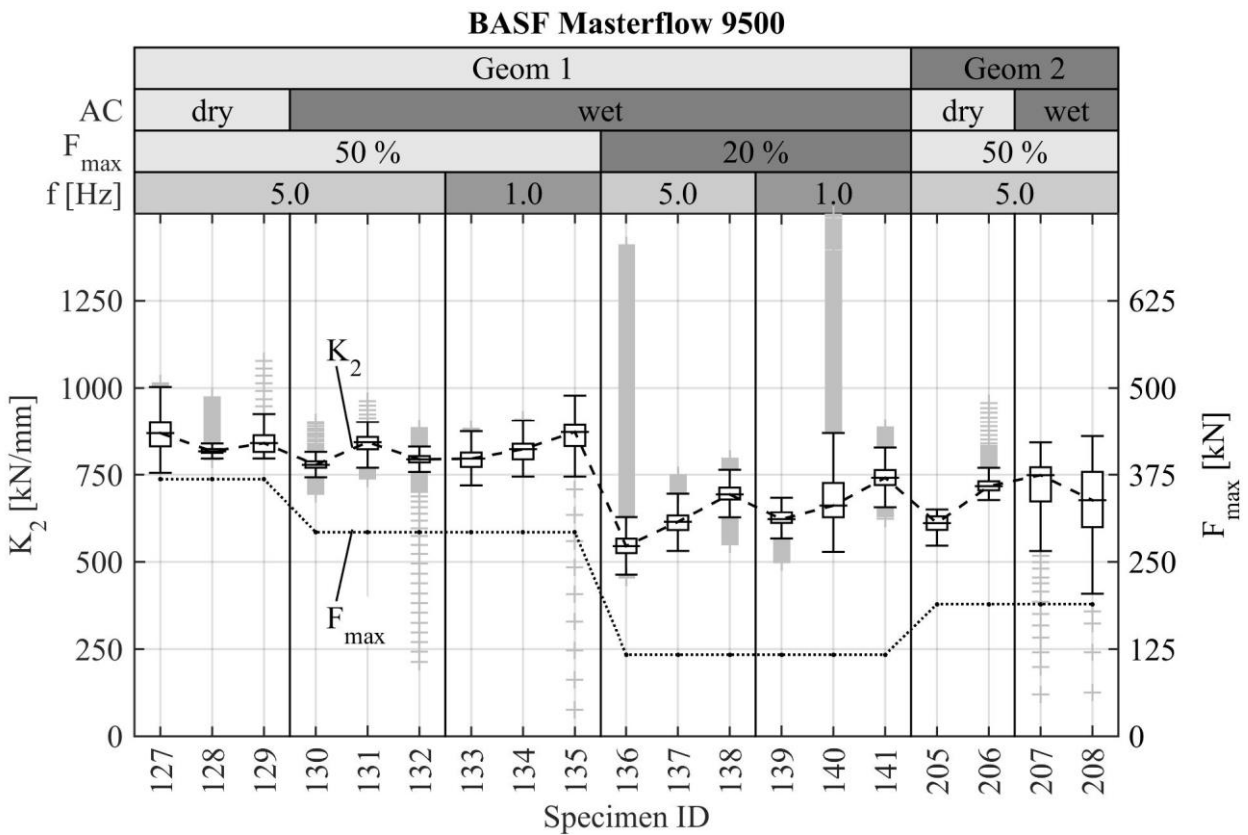


Figure 3.34: Distribution of stiffness K_2 for small-scale specimens with BM95

3.5.3 Degradation behaviour

Grout particle flushing

During the tests grout particle flushing was observed as exemplarily shown in Figure 3.35. The grout particles mainly accumulated on top of the grout layer surface. Due to the particle size and water movements caused by the cyclic load application, particles were also spread in the water of the water basin (see Figure 3.35, image sequence bottom). Consequently, no mass or volume determination was possible.

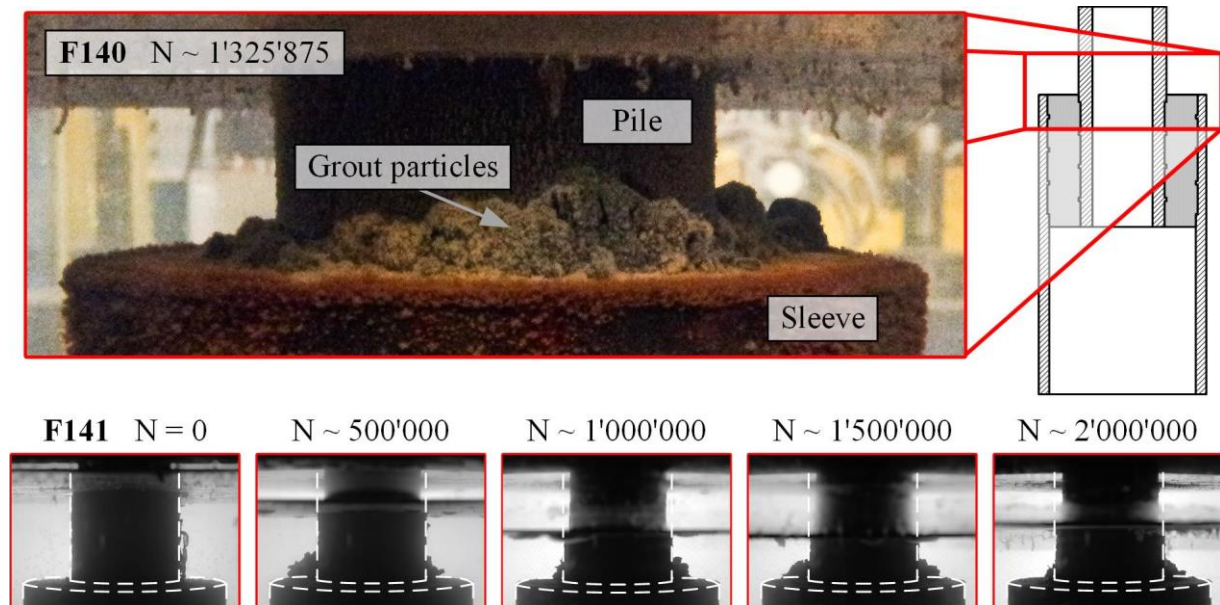


Figure 3.35: Grout particle flushing observed during FLS tests

The observed flushing intensity always correlated with the measured relative deformations between pile and sleeve. Hence, the most flushing was observed in the FLS tests at $0.2 \cdot F_{ULS}$ loading level. These specimens endured the most load cycles and simultaneously showed the highest relative deformations.

Dismantled specimens

As done before in the ULS tests, the FLS specimens were cut and opened after the tests were completed, to analyse the resulting damage patterns. Figure 3.36 shows the damage patterns of two specimens with different grout layer thickness, both tested in dry AC.

For Geometry 1 (left) a diagonal shear crack between the lower end of the grout layer S0 and shear key P1 with an orientation angle of $39^\circ - 42^\circ$ degrees is visible. Moreover, a second diagonal shear crack is visible between shear keys S1 and P2 with an orientation angle of $\sim 56^\circ$. Both cracks are fully cracked but still closed. This damage pattern is comparable to the damage pattern of the ULS tests regarding the crack position and orientation angle (see Section 3.4.3). All six FLS test specimens with Geometry 1 tested in dry AC showed the same damage pattern, except for specimen F129 which showed only the lowest crack (see Table 3.6). Further damage patterns are not visible.

For Geometry 2 (right), only one diagonal shear crack between shear keys S1 and P2 with an orientation angle of $21^\circ - 45^\circ$ is visible. A second crack occurred between P3 and S1 also with an orientation angle of $\sim 45^\circ$. Further damage patterns are not visible.

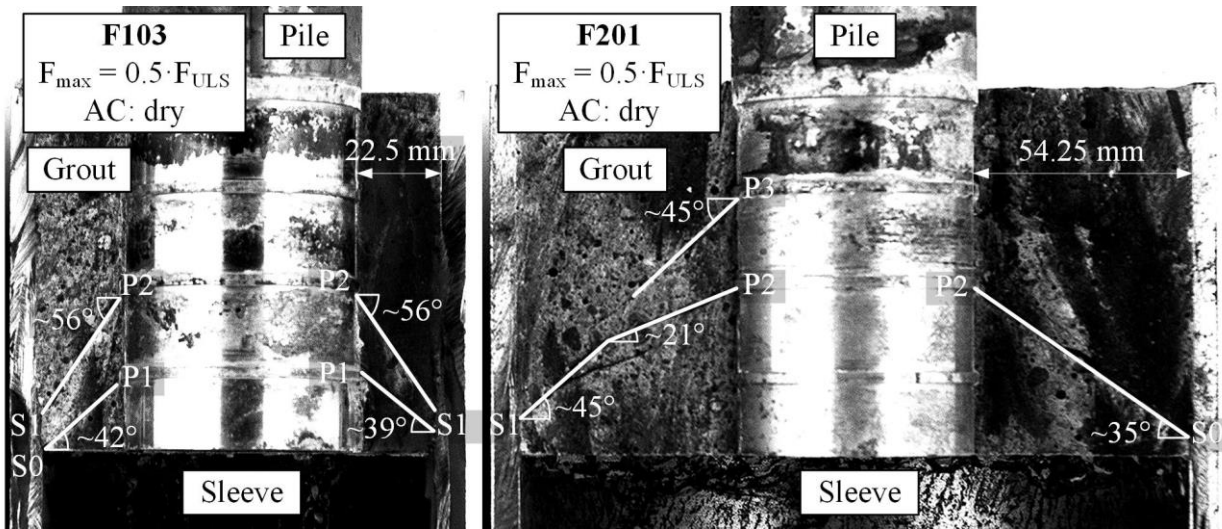


Figure 3.36: Damage patterns of FLS specimens with different grout layer thickness tested in dry ambient conditions

Figure 3.37 shows the damage patterns of two specimens tested in wet AC at a loading level of $0.5 \cdot F_{ULS}$ and a loading frequency of 5 Hz. Specimen F130 shows a similar damage pattern compared to specimen F103 tested in dry AC, albeit the cracks of F130 are opened and abrasion of the grout material is visible. Additionally, grout particles are adhesive to the pile surface between the upper shear keys. For specimen F207 a similar damage pattern is visible. Two diagonal shear cracks evolved between shear keys S0-P2 and S1-P3 both with orientation angles of $\sim 39^\circ$. Both cracks are opened and show abrasive wear of the grout surfaces. Additionally, a crack between shear key P4 and the centre of the lower diagonal shear crack is visible. Moreover, grout particles in front of shear key P4 are visible.

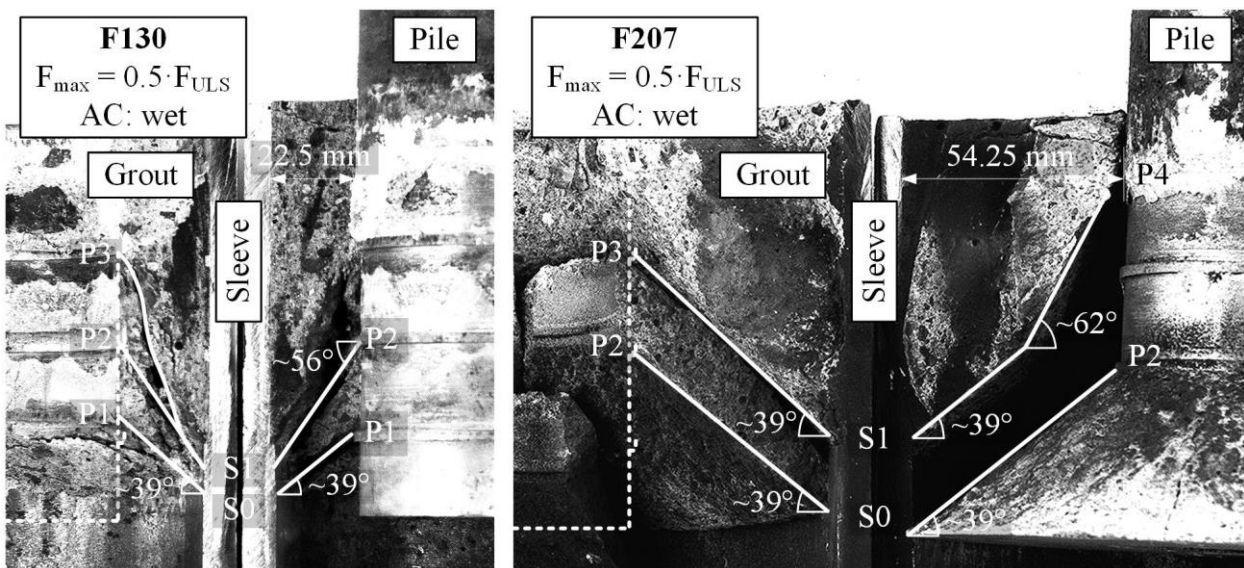


Figure 3.37: Damage patterns of FLS specimens with different grout layer thickness tested in wet ambient conditions

In Figure 3.38 two specimens F140 and F141 with Geometry 1, both tested with identical loading conditions and AC but showing different failure modes are presented. In Specimen F140 a diagonal shear crack between shear key S1 and P2 with an orientation angle of $\sim 56^\circ$ is visible but no additional cracks in the upper grout part. The test was terminated by TC u_{\max} , which means the deformation growth after the diagonal shear crack evolved was caused by a sliding between pile and grout. In contrast, specimen F141 shows only one diagonal shear crack between shear key S0 and P1 with an orientation angle of $\sim 39^\circ$. The grout surface at shear key P1 has an offset of ~ 2.5 mm to the upper shear key surface and the shear key groove in the grout layer is about ~ 5 mm wide, which means it widened by ~ 2.5 mm during the test.

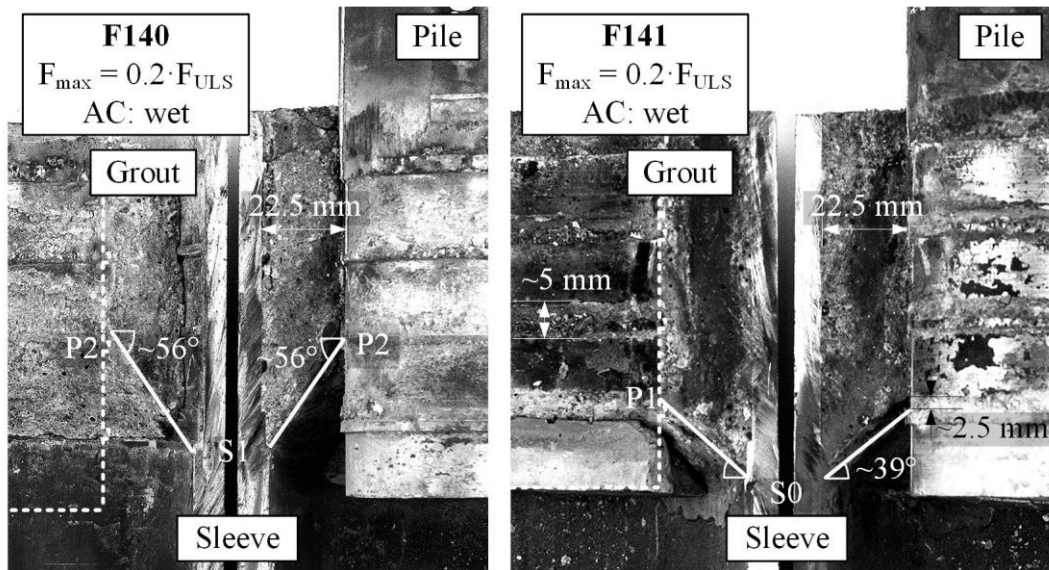


Figure 3.38: Damage patterns of FLS specimens with different failure modes tested in wet ambient conditions

The positions of visible cracks for all small-scale specimens are summarised in Table 3.5 for Geometry 1 and grout material DDS2, in Table 3.6 for Geometry 1 and grout material BM95 and in Table 3.7 for Geometry 2 and both grout materials.

For Geometry 1 regardless of the used grout material, a kink 1 in the displacement curve was observed. In addition, a diagonal shear crack between shear key S0 and P1 had evolved in all but specimen F129. However, since kink 1 is differently pronounced in the displacement curves, a correlation between kink 1 and diagonal shear crack S0 and P1 can be assumed, indicated by blue coloured boxes in the following tables.

Also in all tests carried out at a loading level of $0.5 \cdot F_{ULS}$, a diagonal shear crack between shear key S1 and P2 was observed but a correlating kink in the displacement curves is missing. Hence, this crack seems to be of minor importance for the specimen's load displacement behaviour.

However, kink 2 seems to be correlated to diagonal shear cracks occurring between shear keys S1 and P3. Corresponding boxes are coloured red.

At the lower load level of $0.2 \cdot F_{ULS}$, the degradation mechanisms changed from shear cracking to grout crushing. Neither diagonal shear cracks between shear keys S1 and P2, nor kink 2 was observed for these specimens.

Similar observations were made for Geometry 2 specimens but with different diagonal shear crack positions. Kink 1 is correlated to cracks between shear keys S0 and P2 and kink 2 to cracks between shear keys S1 and P3. As described before, the cracks in the larger grout layer show similar orientation angles as in specimen 1, which led to different shear key couples.

Table 3.5: Overview of damage patterns of small-scale FLS test specimens with Geometry 1 and grout material DDS2

Id	Geom.	Material	Test procedure					u(N)		Visible Cracks					
			AC	F_{max}	f	N	TC	kink		S0		S1		S2	S3
			[-]	[-]	[Hz]	[-]		1	2	P1	P2	P2	P3	P3	P4
F101	1	Ducorit S2	dry	0.5	5.0	2000000	run	x		x		x			
F102	1	Ducorit S2	dry	0.5	5.0	2000000	run	x		x		x			
F103	1	Ducorit S2	dry	0.5	5.0	2000000	run	x		x		x			
F104	1	Ducorit S2	wet	0.5	10.0	16685	Δu	x		x		x		x	x
F105	1	Ducorit S2	wet	0.5	10.0	32435	Δu	o		o		x		x	x
F106	1	Ducorit S2	wet	0.5	10.0	60937	Δu	x	x	x		x	x		
F107	1	Ducorit S2	wet	0.5	5.0	64125	Δu	o		x		x		x	
F108	1	Ducorit S2	wet	0.5	5.0	31392	Δu	x	x	x		o	x		
F109	1	Ducorit S2	wet	0.5	5.0	35307	Δu	x	o	x		x		x	
F110	1	Ducorit S2	wet	0.5	5.0	101221	Δu	x	x	x		x	x	x	
F111	1	Ducorit S2	wet	0.5	2.0	142148	Δu	x		o		x			
F112	1	Ducorit S2	wet	0.5	2.0	204282	Δu	x		x		x			
F113	1	Ducorit S2	wet	0.5	2.0	65298	Δu	o	x	x		x	x		
F114	1	Ducorit S2	wet	0.5	1.0	102735	Δu	x	x	o		o	x	x	
F115	1	Ducorit S2	wet	0.5	1.0	116482	Δu	x	x	o		x	x		
F116	1	Ducorit S2	wet	0.5	1.0	49349	Δu	x	o	x		x	x		
F117	1	Ducorit S2	wet	0.5	1.0	80146	Δu	x	x	x		x	x		
F118	1	Ducorit S2	wet	0.5	0.3	156307	Δu	x	x	x		x	x		
F119	1	Ducorit S2	wet	0.5	0.3	248450	Δu	x	x	o		x	x	x	x
F120	1	Ducorit S2	wet	0.5	0.3	95250	Δu	x	x	o		x		x	x
F121	1	Ducorit S2	wet	0.5	0.3	407951	Δu	x	x	x		x			
F122	1	Ducorit S2	wet	0.5	0.3	258350	Δu	o		o		x			
F123	1	Ducorit S2	wet	0.2	5.0	2000000	run	x		x					
F124	1	Ducorit S2	wet	0.2	5.0	2000000	run	x		x					
F125	1	Ducorit S2	wet	0.2	5.0	1038739	u_{max}	x		x					
F126	1	Ducorit S2	wet	0.2	5.0	1188273	u_{max}	o		o					
								x definite evaluation							
								o possible evaluation							

Table 3.6: Overview of damage patterns of small-scale FLS test specimens with Geometry 1 and grout material BM95

Id	Geom.	Material	Test procedure					u(N)		Visible Cracks							
			AC	F _{max} [-]	f [Hz]	N [-]	TC	kink		S0		S1		S2		S3	
								1	2	P1	P2	P2	P3	P3	P4		
F127	1	Masterflow	dry	0.5	5.0	2000000	run	x		x		x					
F128	1	Masterflow	dry	0.5	5.0	2000000	run	x		x		x					
F129	1	Masterflow	dry	0.5	5.0	2000000	run			x							
F130	1	Masterflow	wet	0.5	5.0	30700	Δu	x	o	x		x	x			x	
F131	1	Masterflow	wet	0.5	5.0	41300	Δu	x	x	x		x	x				
F132	1	Masterflow	wet	0.5	5.0	39837	Δu	x	x	o		x	x				
F133	1	Masterflow	wet	0.5	1.0	112150	Δu	x	o	x		x	x				
F134	1	Masterflow	wet	0.5	1.0	41800	Δu	x	x	o		x	x		x		
F135	1	Masterflow	wet	0.5	1.0	132923	Δu	o		x		x					
F136	1	Masterflow	wet	0.2	5.0	1190005	u _{max}	o		x							
F137	1	Masterflow	wet	0.2	5.0	887510	u _{max}	x		x							
F138	1	Masterflow	wet	0.2	5.0	1277251	u _{max}	x		o							
F139	1	Masterflow	wet	0.2	1.0	2000000	run	x		x							
F140	1	Masterflow	wet	0.2	1.0	1325875	u _{max}	x		x							
F141	1	Masterflow	wet	0.2	1.0	2000000	run	x		x							
								x definite evaluation o possible evaluation									

Table 3.7: Overview of damage patterns of small-scale FLS test specimens with Geometry 2

Id	Geom.	Material	Test procedure					u(N)		Visible Cracks							
			AC	F _{max} [-]	f [Hz]	N [-]	TC	kink		S0		S1		S2		S3	
								1	2	P1	P2	P2	P3	P3	P4		
F201	2	Ducorit S2	dry	0.5	5.0	2000000	run	x			x						
F202	2	Ducorit S2	dry	0.5	5.0	2000000	run	x			x						
F203	2	Ducorit S2	wet	0.5	5.0	24393	Δu	x	x		x		x				
F204	2	Ducorit S2	wet	0.5	5.0	21743	Δu	x	x		x		x				
F205	2	Masterflow	dry	0.5	5.0	2000000	run	x			x						
F206	2	Masterflow	dry	0.5	5.0	348245	Δu	x	x		o		x				
F207	2	Masterflow	wet	0.5	5.0	5310	Δu	x	x		x		x				
F208	2	Masterflow	wet	0.5	5.0	5050	Δu	x	x		x		x				
								x definite evaluation o possible evaluation									

X-ray computed tomography

In addition to conventional dismantling of the completely tested specimens to inspect the fractured grout layer, X-ray computed tomography (CT) as a non-destructive imaging method was applied to one specimen.

CT is a combination of basic X-ray imaging and the computed blending of numerous X-ray images, taken at different positions in relation to the specimen (see Cierniak (2011)). For a CT-scan a specimen is placed between an X-ray transmitter and an X-ray receiver. X-rays pass through the specimen and are attenuated by the irradiated matter. The energy of the X-rays and the elemental composition of the specimen influence the strength of attenuation. The resulting energy difference between transmitter and receiver provides information about the material in-between the beam path. Usually, the measured energy density is visualised as a grey-scale, where white indicates a high attenuation and black indicates little attenuation. By taking images at different angles around the specimen and in different positions of height, spatial information about the specimen's internal structure are obtained. Via computational algorithms the images are finally combined to a spatial model. Due to the fact that only the attenuation strength is measured, materials become more distinguishable in the resulting image if they differ more in their elemental composition. For the grouted connection specimen the interesting matters are air, grout and steel which are different enough to become distinguishable in a CT-scan. The theoretical size resolution of a scan depends on the acceleration voltage of the tube and the size of the detector. Moreover, the size resolution is influenced by the specimen's properties and possible artifacts.

In the course of the small-scale grouted connection tests, one specimen tested in an FLS test (AC: wet) was scanned to evaluate the serviceability of CT-scans for grouted connections. The CT-scan was carried out at the Institute for Multiphase Processes at Leibniz Universität Hannover. Figure 3.39 shows the CT-scanner set-up. It was a third generation X-ray CT, consisting of a fan beam X-ray tube, with a maximum acceleration voltage of 420 kV and a line detector with 1024 photo-diodes.

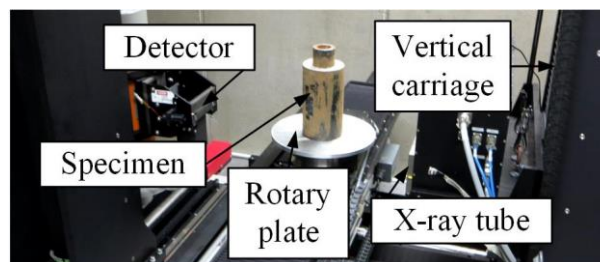


Figure 3.39: CT-scanner set-up

Figure 3.40 shows the resulting spatial model of CT-scan data of a small-scale specimen. The figure includes six vertical cutting planes, showing the interior of the specimen. Based on the energy density, steel parts were coloured in black. Shear keys are clearly visible on the inner steel surfaces.

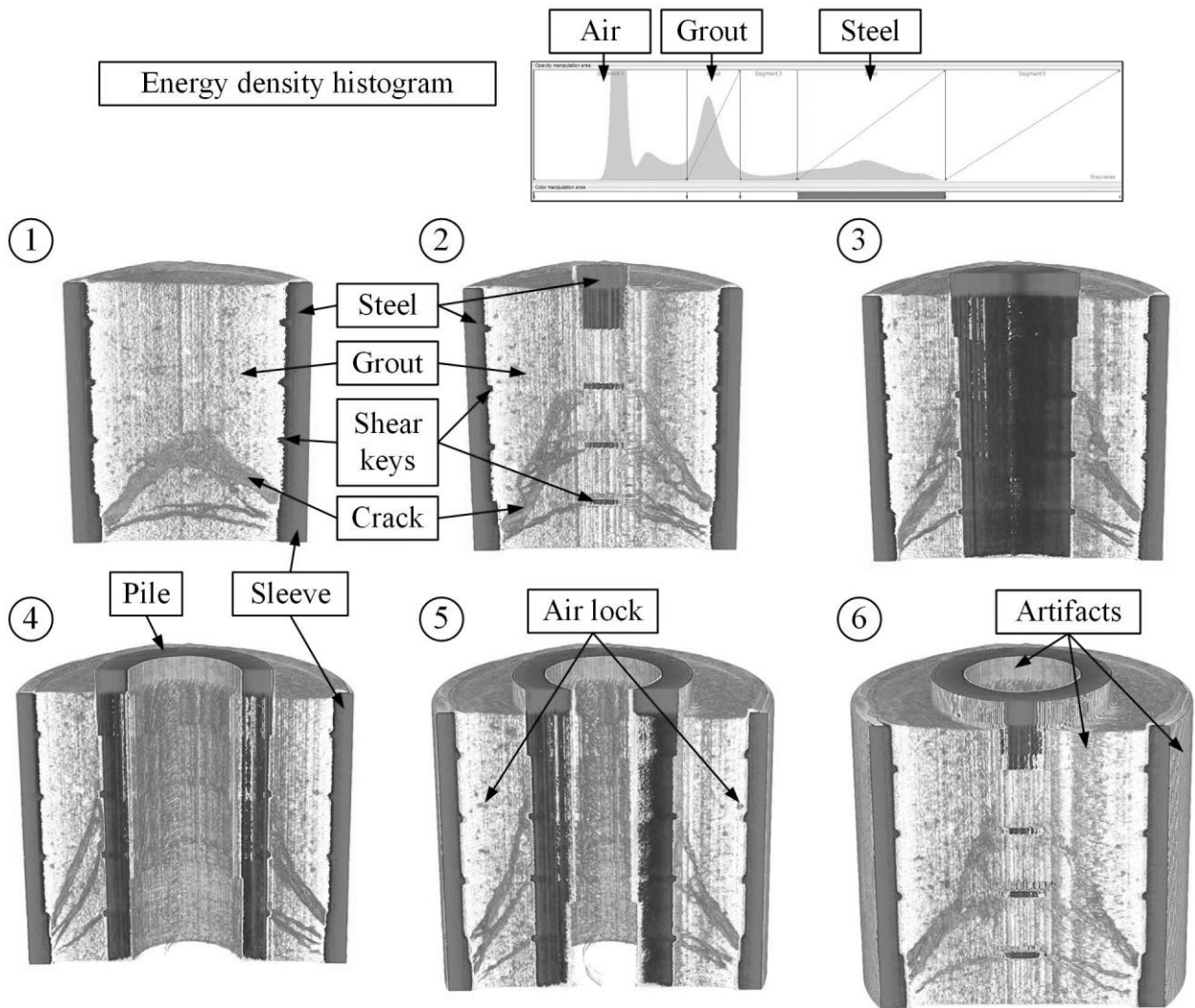


Figure 3.40: Spatial model of CT-scan data of a small-scale specimen from an FLS test showing six vertical cutting planes, steel parts are coloured in black

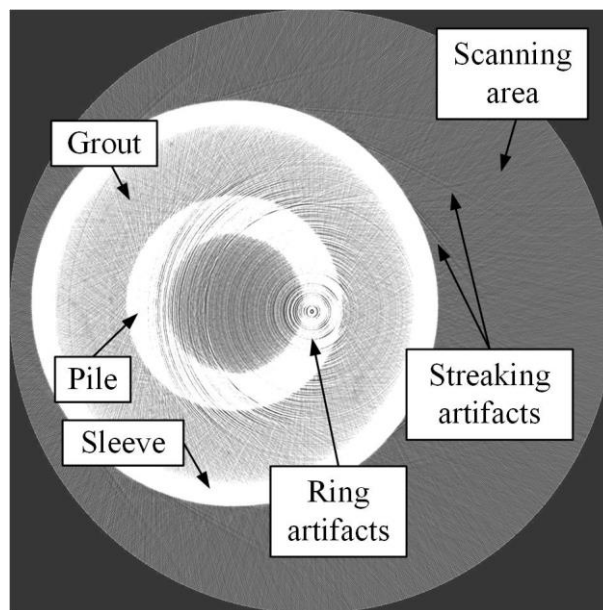


Figure 3.41: CT-scan slice showing typical artifacts

Prior to evaluating the visual impression of the grout section, it is important to have a look at possible artifacts of the CT-scan method. According to Barrett & Keat (2004) several artifacts can occur in a CT-scan of which two typical artifacts can be found in the grouted connection data. Figure 3.41 shows one slice of the CT-scan at the upper end of the grout section. In the centre of the scanning area, ring artifacts are clearly visible. According to Barrett & Keat (2004) ring artifacts result from an uncalibrated detector. Before scanning the grouted connection specimen, the detector was calibrated with a phantom which reduced the ring artifacts but could not completely remove them. In addition, the specimen was placed eccentric to the centre of the scanning area to avoid an overlay of the ring artifacts with the cylindrical geometry. In Figure 3.40 vertical lines are visible which result from the ring artifacts. The second artifact, visible in Figure 3.40, leads to the grey coloured steel surfaces outside of the sleeve and inside of the pile.

Despite these artifacts, Figure 3.40 gives a good visual impression of the cracks in the grout section. Corresponding to the cut specimens, diagonal shear cracks evolved between shear keys on the opposing steel surfaces. However, the additional information from the CT-scan is the spatial spread of the cracks. A comparison between the different cutting planes reveals that the, on a meso scale inhomogeneous, grout material leads to an arbitrary crack evolution. Ramification is possible and can cause a merging of separate cracks into one crack.

Conclusively, CT-scans of grouted connections allow a non-destructive insight to the connection, providing qualitative information about the condition of the grout. Therefore, this method can be a helpful tool in scientific applications. Nevertheless, for this specific case no further CT-scans were carried out since the cut specimens were classified as sufficient for the desired evaluation of the fracture patterns. Comparison to analytical design approaches

Figure 3.42 shows fatigue test results which were used to derive several structure S-N-curves that can be found in the current standards as well as in the literature (see Section 2.6). Additionally, the results of the presented small-scale grouted connection fatigue tests are shown (coloured dots). Even though, fatigue tests conducted in wet ambient conditions (AC) delivered significantly lower numbers of endurable load cycles compared to similar tests in dry AC, all test results are above the S-N-curves, except for the simplified fatigue limit described in DIN EN ISO 19902 (2014). However, it has to be kept in mind that the presented tests were conducted with a loading ratio of $R = 20$ while the other test results are from $R = -1$ tests. A loading ratio of $R = 20$ is more favourable and hence leads to a higher number of endurable load cycles. Moreover, the obtained results for wet AC and a loading level of $0.2 \cdot F_{ULS}$ were accompanied with large deformations of the specimens, as described beforehand. A general statement on the applicability of these S-N curves for submerged grouted connections cannot be made on the presented small-scale test results.

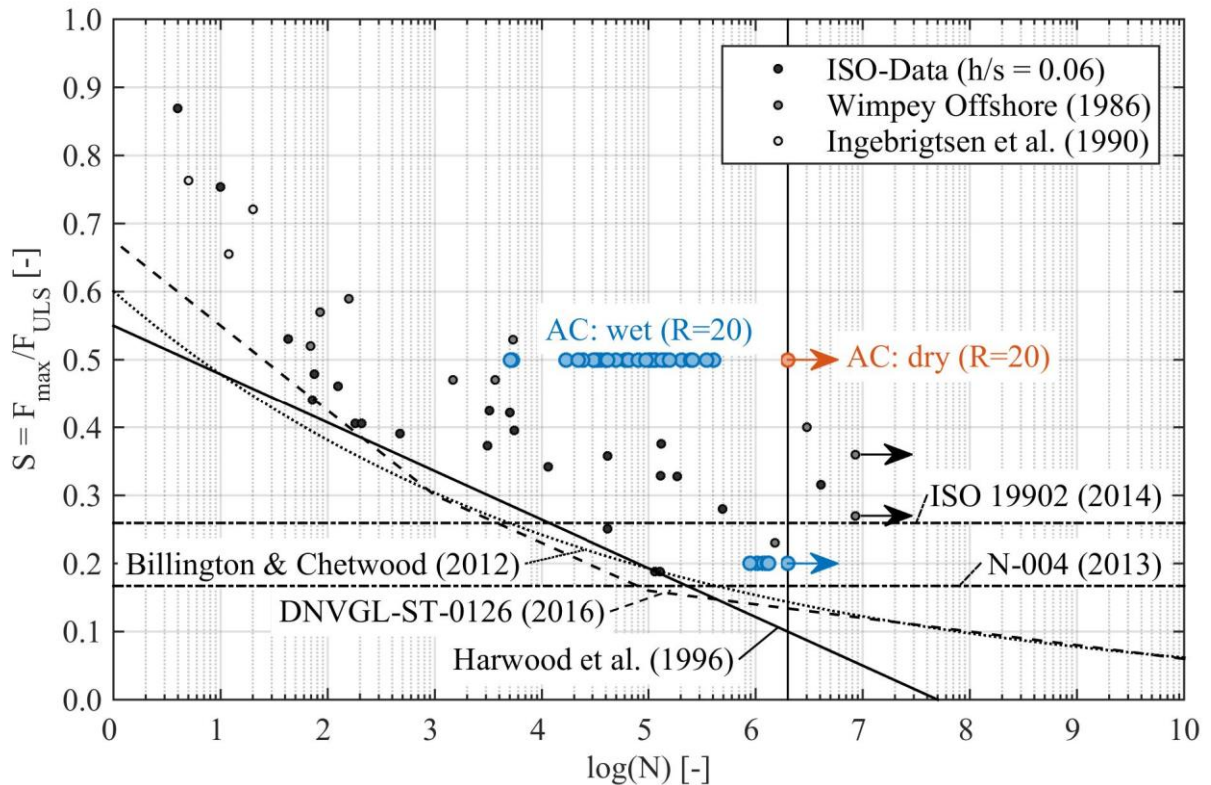


Figure 3.42: Characteristic analytical fatigue design for grouted connections according to current design methods and comparison with small-scale fatigue test results

3.5.4 Discussion

General remark

Considering the previously described test results, the degradation behaviour of the small-scale specimens under cyclic loading can be summarised as follows for individual parameters.

Influence of maximum compressive load

At a loading level of $0.5 \cdot F_{ULS}$, all tests carried out in wet AC were terminated by TC Δu , which means a total loss of load bearing capability. The damage patterns showed diagonal shear cracks between the grout layer's lower end and shear key P1 as well as between shear keys S1 and P2 (see Figure 3.43). Moreover, in some cases cracks between shear keys S1 and P3 were observed. Above the highest shear crack, large voids were found due to grout crushing and flushing which were responsible for the final failure of the connection. This damage pattern is a mix of the ULS damage pattern described in Section 3.4.5 and fatigue related grout crushing.

At a loading level of $0.2 \cdot F_{ULS}$ the number of endurable load cycles increased and two different load degradation behaviours were observed. Some specimens showed a pronounced offset of mean displacement after kink 1 was visible. This offset stayed constant until the test was terminated by TC runner. The corresponding damage pattern showed a diagonal shear crack between the lower end of the grout layer and shear key P1. No significant grout crushing was visible. For the other

specimens also kink 1 was observed in the displacement curves but afterwards the mean displacement constantly increased until the tests were terminated by TC u_{\max} . The corresponding damage pattern showed a diagonal shear crack between the lower end of the grout layer and shear key P1 but also significant voids above this crack caused by grout crushing and flushing. Based on the schematic cracking behaviour shown in Figure 3.43, centre, it can be assumed that crushing is the major degradation mechanism which occurred at a load level of $0.2 \cdot F_{\text{ULS}}$.

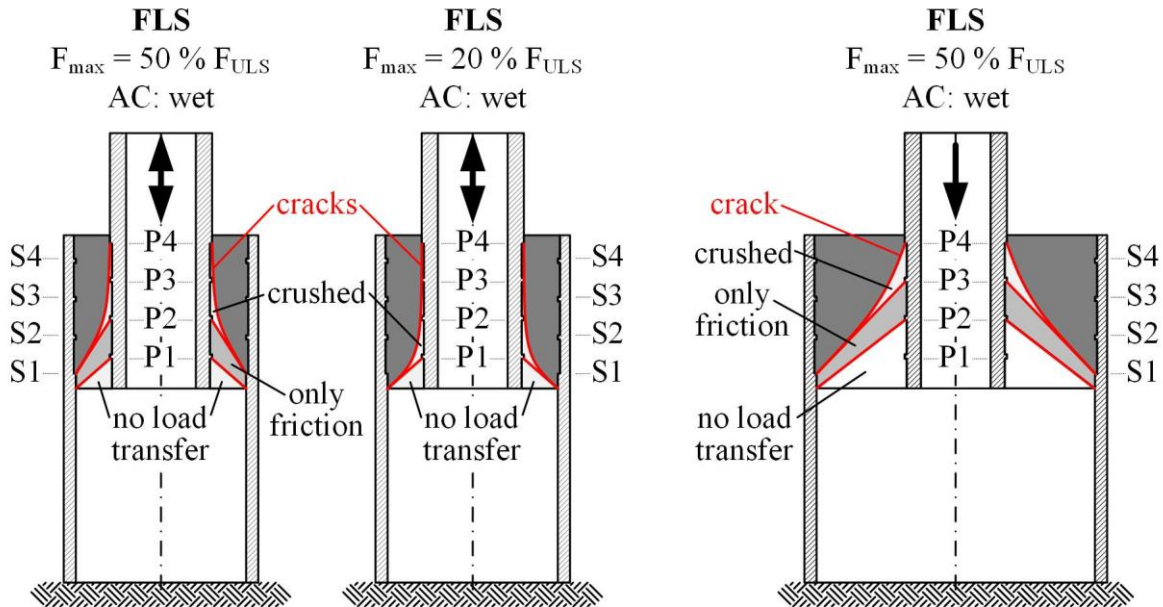


Figure 3.43: Schematic cracking behaviour of small-scale specimens in FLS tests

Comparing the described degradation behaviour leads to the conclusion that at low load levels the concentrated load application in front of the loaded shear key surfaces leads to grout crushing and transport of crushed grout particles results in a constantly increasing mean displacement. When increasing the load, the overall grout matrix receives higher loads which causes crushing and shear cracking to evolve at the same time. The result is a much more brittle failure at smaller displacements.

Influence of the ambient condition (AC)

The comparison between FLS tests carried out in dry and wet AC shows a significant reduction of endurable load cycles in wet AC. All tests carried out in dry AC were runners and showed only one diagonal shear crack between the grout layer's lower end and shear key P1. Significant local grout crushing was not visible. For all fatigue tests carried out in wet AC, particle flushing was observed during the tests and large voids of removed grout particles were found later in the damage patterns. Hence, the influence of the AC can be summarised as follows. Water invades the interface between steel and grout, where cyclic movements lead to a pumping mechanism. Particles of crushed grout are flushed out which reduces the grout volume and keeps the degradation process sustained. Moreover, for the small-scale specimens the water reduces the grout material's fatigue strength. A possible reason is water ingress in the grout surfaces, which leads to spalling as described for example by Hümme (2015) (see Section 2.4.1). Moreover, micro cracks induced by the rectangular shear key shape might grow faster due to surface abrasion caused by water circulating

inside the crack as for example described by Waagaard (1977) (see Section 2.4.1). If the assumption by Nygaard et al. (1992) regarding a water ingress depth of about 10 mm is correct (see Section 2.4.1), the small grout layer of only 22.5 mm thickness is almost fully soaked in water. This can explain the mixed degradation behaviour of cracking and crushing at a loading level of $0.5 \cdot F_{ULS}$.

Influence of grout layer thickness

In both geometries diagonal shear cracks were observed at orientation angles between 21° and 62° , with the main orientation angle of Geometry 1 being $\sim 56^\circ$ and of Geometry 2 being $\sim 39^\circ$. The orientation angle was influenced by the shear key positioning but its main orientation is predefined by the mechanical properties of the grout material. Hence, a larger grout layer led to diagonal shear cracks evolving between different shear key couples than in the smaller grout layer. For the two investigated grout layer thicknesses, this led to a similar cracking pattern of Geometry 1 and 2 at identical loading conditions. However, the cracking pattern leads to only one mainly loaded shear key in Geometry 2, while two shear keys remain loaded in Geometry 1 (see Figure 3.43).

Influence of loading frequency

As shown in Figure 3.25 a reduced loading frequency leads to more endurable load cycles. This behaviour can be explained by the grout flushing process. A higher frequency leads to higher pumping speed. Hence, the grout particles are flushed out faster and the grout crushing process is increased. Remarkably, the observed influence of the loading frequency for the small-scale grouted connection is contradictory to the results other researchers found for plain grout material specimens (see Section 2.4.1). Soerensen (2011) explained a reduced fatigue behaviour at higher frequencies with less time for the water to ingress in the specimen. Consequently, the ingress depth is smaller and the spalling process induced by water in the boundary layer is reduced. For the small-scale specimens, it can be concluded that the pumping process is the main influence on the specimens' fatigue behaviour. Further deterioration mechanisms caused by water seem to be less important.

Stiffness evolution

It was shown that the secant stiffness K_2 of the hysteresis is only influenced by the mechanical properties of the grout material. A degradation of the stiffness could not be determined. As described in Section 2.3.4, Holmen (1979) for example observed a reduction of the secant stiffness in micro crack phase 1 and macro crack phase 3. Thus, the secant stiffness evolution was expected to help predicting an upcoming failure of the grouted connection. This could not be confirmed by the obtained results. For the plain concrete cylinders that Holmen (1979) investigated, the applied load is homogeneously beared by the full structure. Inhomogeneities in the local stress distribution and the final damage pattern of the specimens are caused by the local arrangement of cement and aggregates. In contrast to this, for the small-scale specimens tested here, the damage pattern is localised to the diagonal shear cracks and the grout crushing in front of the loaded shear key surfaces. Hence, the grout layer is split into individual parts, each keeping its elastic properties. Furthermore, the final failure of the specimens tested in wet AC was caused by grout crushing and flushing of the grout particles due to the water. As a consequence, the final degradation happens

in the interface between steel and grout, which is significantly different to the failure of the specimens of Holmen (1979).

3.6 Summary

In the previous Chapter small-scale grouted connection specimens with differing sleeve diameter and consequently differing grout layer thickness were introduced. In a series of both, ULS and FLS tests, these specimens were extensively investigated. The resulting measurement data as well as the final damage patterns of all specimens were systematically evaluated. Finally the main load bearing and fatigue behaviour was summarised and compared to the state of the art. In the following, the individual results for the parameters defined at the beginning of this Chapter are summarised.

- **Grout layer thickness**

A larger grout layer thickness led to a reduced load bearing capacity F_{ULS} and a lower specimen stiffness. Reason for this behaviour, was a reduced number of activated shear keys due to diagonal shear cracks occurring at a similar orientation angle but between different shear key couples for different grout layer thicknesses. This behaviour was observed in both ULS and FLS tests.

- **Grout material**

In contrast to the material properties given by the manufacturers, the two chosen grout materials were statistically more alike than desired. In the ULS tests the slightly weaker grout material led to slightly lower load bearing capacities F_{ULS} . For the other material a higher specimen stiffness and a more brittle cracking behaviour was observed. In the FLS tests no significant differences between the two materials were visible.

- **Test procedure**

Quasi-static loading in the ULS tests led to distinct diagonal shear cracks and afterwards to grout crushing. In contrast to that, in wet AC FLS tests grout crushing and flushing become the decisive damage mechanism. Moreover, shear cracking was observed at lower load levels than in the ULS tests. This behaviour confirmed a reduced grout material strength under fatigue loading.

- **Ambient condition (AC)**

For both geometries, a wet AC in the FLS tests led to significantly reduced numbers of endurable load cycles. Reasons were described in detail in Section 3.5. Overall the most important effect of the water was a pumping mechanism caused by cyclic movements between steel and grout. The pumped water then flushed out crushed grout particles and reduced the grout layers volume around the shear keys. This behaviour led to constantly increased relative mean displacements between pile and grout.

- **Loading level**

As expected, a reduced loading level corresponded with an extended number of endurable load cycles in FLS tests. In addition to that, the loading level influenced the fatigue degradation behaviour. At low load levels, grout crushing in front of loaded shear key surfaces became decisive, while at higher load levels a combination of grout crushing and diagonal shear cracking was observed.

- **Loading frequency**

Contrary to findings from the literature, a reduced loading frequency led to an extended number of endurable load cycles. This was explained by slowed down spalling processes acting on the grout but speed up pumping of water and flushing of grout particles.

- **Degradation behaviour**

The typical grout crushing and diagonal shear cracking behaviour known from prior tests was confirmed by the small-scale investigations. The comparison between ULS and FLS cracking patterns confirmed also a reduced material strength for the grout layer when cyclically loaded.

4 Large-Scale Experiments

4.1 Introduction

The large-scale specimens were designed to scale to real connections and thus overcome this shortcoming of the previously described small-scale tests (see Section 3.2). Further objective of the large-scale tests was to verify the previously found influence of surrounding water on the fatigue behaviour of grouted connections and the resulting degradation mechanisms. A test set-up with four submerged large-scale specimens (W1 – W4) described in this Chapter was developed and carried out. Based on the objective for the large-scale tests and the results of the small-scale specimens, the following parameters were chosen to be investigated.

- **Ambient condition (AC)**

The results of the small-scale tests showed a significant reduction of endurable load cycles for tests carried out in wet AC. This influence was also expected for the large-scale tests. Four wet AC tests (W1-W4) were carried out in the framework of this thesis. Results of two dry AC tests (D1 and D2) published by Bechtel (2016) were used as reference to investigate the influence of the AC.
- **Loading scenario**

With increased loading level an increase of degradation was expected. Moreover, the loading ratio R was modified in the tests to investigate the influence of alternating and pure compression loads. Exaggerated degradation was expected for alternating loads.
- **Grout layer thickness**

A thicker grout layer was expected to reduce the specimen's stiffness as well as its load bearing capacity. Two different grout layer thicknesses were chosen for investigation.
- **Grout material**

Two different commercial grout materials were used. Due to their similar mechanical properties, no significant influence on the load bearing as well as the fatigue behaviour was expected.
- **Degradation behaviour**

For the large-scale tests a similar degradation behaviour, as seen in prior tests as well as in the small-scale fatigue tests, was expected. This behaviour was characterised by grout crushing in front of the loaded shear key surfaces in combination with grout particle flushing due to water as well as diagonal shear cracking.
- **Termination criterion (TC)**

Usually the termination criterion for fatigue tests is a sudden loss of load bearing capacity of the specimen. In the small-scale fatigue tests carried out in wet AC, large relative displacements were measured while the load bearing capacity was sustained. A similar behaviour was expected for the large-scale tests.

Materials

The steel tubes were standard profiles according to DIN EN 10210-2 (2006) with a steel grade of S355. Both material certificates from the supplier as well as external strength tests carried out at the Institute for Materials (IW), Leibniz Universität Hannover confirmed the steel grade and found a mean yield strength of $f_y = \sim 450 \text{ N/mm}^2$ (see Bechtel (2016)).

The specimens were filled with two different commercial grout products characterised by the mechanical properties given in Table 4.1. Changing the material between tests W2 and W3 became necessary because BASF Masterflow 9500 (BM95) was not available at the time of preparation. Densit Ducorit S5 (DDS5) was chosen as a substitute because it has almost identical mechanical properties according to the manufacturers. Both materials were fine grain grouts with a maximum aggregate size of 5 mm and a mixing water amount between 7 and 8 % by weight.

Table 4.1: Mechanical properties of the two grout materials given by the manufacturers (ITW Engineered Polymers (2016), BASF Construction Chemicals (2010))

	BASF Masterflow 9500 (BM95)	Densit Ducorit S5 (DDS5)	Material specimen shape
f_c [N/mm ²]	140.0	130.0	Cube 75x75x75 mm
f_t [N/mm ²]	8.6	7.0	
f_{bt} [N/mm ²]	18.4	18.0	Prism 160x40x40 mm
E_c [N/mm ²]	50'900	55'000	Cylinder 150x300 mm
ν [-]	n/a	0.19	
ρ [kg/m ³]	n/a	2440	
Specimen	W1, W2, D1, D2	W3, W4	

Manufacturing

The steel parts were manufactured at the local steel works company G+F Strate GmbH, Hannover by assembling steel tubes and adapter flanges as well as applying the weld bead shear keys. Afterwards, the specimens' geometries were checked at the Institute for Steel Construction. In addition, the steel surfaces facing the grout were cleaned from rust and mill scale by using wire brushes and angle grinders with flap discs. Finally, the surfaces showed a level of purity according to grade Sa 2 as defined in DIN EN ISO 8501-1 (2007). This was checked with a tactile surface roughness measuring system according to DIN EN ISO 4287 (2010). The real shear key geometry shown in Figure 4.2 corresponded accurately to the idealised half circle of the design descriptions (see Figure 4.1).

The grouting was conducted inside the test rig to ensure a precise fit between hardened specimen and the rig as well as to ensure a millimetre precise overlapping position. The grout annulus's lower end was sealed by a plate and the fresh grout was filled in through an inlet located about 10 cm above the sealing. In order to exclude unquantifiable influences of a reality like submerged grouting process, the grout annulus was dry during the grouting process. The performance of grout materials in submerged grouting processes and their final material properties are described for example by Werner & Lohaus (2014).

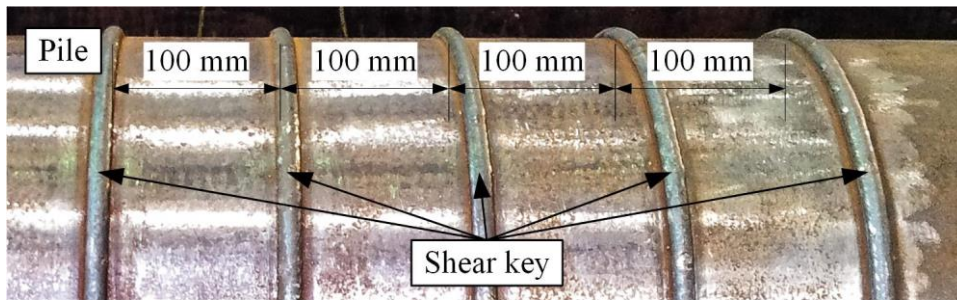


Figure 4.2: Exemplary geometry of real shear keys

The grout material was prepared from 8 x 25 kg bags per batch, each dry mixed for 2 minutes and then wet mixed for 8 minutes. The dry grout to water weight ratio was between 7.00 and 7.25 for BM95 and 6.50 and 7.00 for DDS5. The grout material was filled in with a conveying pump (PFT ZP 3 XL) through a 10 m long 2 inch hose. Before producing the fresh grout, a lubrication mix of plain cement (CEM I 42,5 R) was pumped through the hose and disposed before the hose was attached to the specimen.

In parallel to the grouting, standardised material tests were conducted to evaluate the quality of the fresh material. Moreover, the whole grouting process was supervised by consultants of the material manufacturers who were involved in all material related decisions. In addition to that, plain grout material specimens were produced to monitor the strength evolution and obtain the mechanical properties at the beginning of each large-scale test.

After a minimum of 24 h the specimens were removed from the test rig and stored at room temperature for at least 28 days before the FLS tests started. During this curing and waiting phase the grout layer surfaces were kept wet at all time to avoid dry shrinkage.

Water system

To realize a submerged ambient condition in the tests, the specimens were filled with water. Therefore, the sleeve was sealed at the bottom by a steel plate and extended atop of the grout section forming a water collar (see Figure 4.3). From an inlet inside the top adapter the water was filled in, and by an outlet in the pile above the grout section the water poured into the water collar. Two outlets in the water collar allowed a circulation. However, the water supply was set to a minimum speed to keep a constant water level, but not to create a stream. About 24 hours prior to the tests the specimens were filled with water to let the grout soak.

Since grout particle flushing was expected, a filter basin was developed, containing two filter stages of 106 μm and 250 μm for specimens W1 and W2 and 28 μm and 106 μm for specimens W3 and W4 as well as a sedimentation tank (see Figure 4.3). The filter basin was the last part in the water system before the plughole.

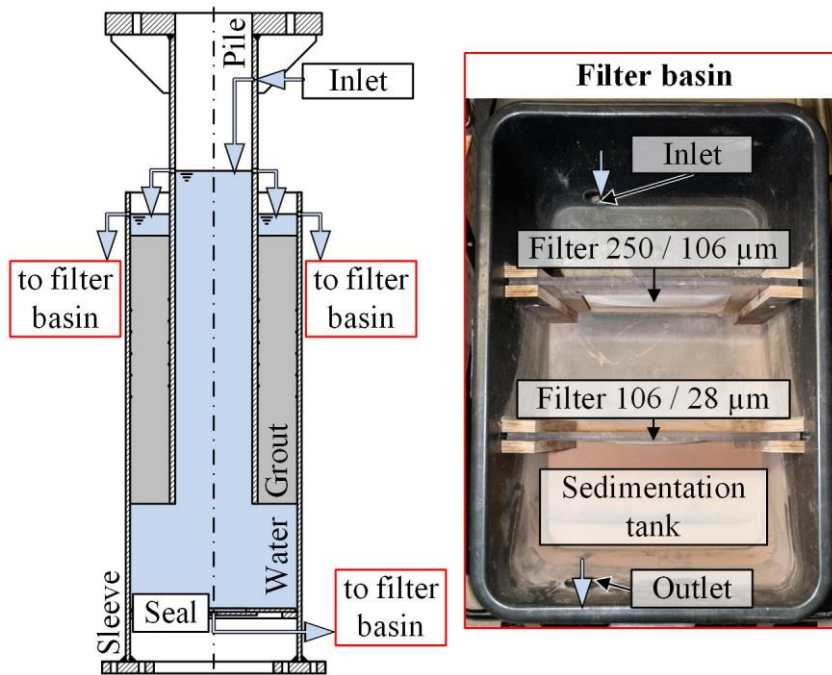


Figure 4.3: Schematic water system and filter basin

4.2.2 Measurement set-up

The measurement set-up was based on the descriptions by Bechtel (2016) and adapted to the modified test set-up, especially caused by the water filled specimens. Additionally, the measuring set-up was supplemented between test W2 and W3, based on the previously obtained test results. Bechtel (2016) based her measurement set-up on numerical simulations, therefore it was expected to be representative and choosing her set-up as basis allowed a direct comparison between test results obtained in dry and wet ambient conditions.

The measuring transducers were divided into the categories: evaluation relevant and test safety as well as measurement plausibility relevant. In Figure 4.4 the test safety relevant transducers are indicated with dotted lines. Those were a potentiometer measuring the deformation of the test rig u_{Ri} and three lasers positioned at 120° intervals circumferential of the specimen, measuring the deformation of the lower specimen adapter u_{Ad} . While u_{Ri} was expected to be zero during the test, u_{Ad} was expected to represent the load related deformation of the adapter without any load cycle dependent alteration. For plausibility checks, the displacement of the hydraulic cylinder u_{TR} was measured inside the test rig and the deformation of the specimen u_{SP} , including the ring flanges connecting the specimens with the test rig, was measured with a second potentiometer. For evaluation purposes the applied load F_{TR} was measured via a translation of the applied hydraulic pressure inside the test rig. Moreover, three lasers positioned at 120° intervals were measuring the relative displacement between pile and sleeve u_{PS} , and for specimens W3 and W4 additional lasers, also positioned at 120° intervals, were measuring the relative displacement between sleeve and grout u_{SG} . The set-up was completed by strain gauges positioned at 120° intervals at several heights, measuring the axial strain at the steel surfaces. The vertical positions were chosen to investigate the load transfer from pile to sleeve by the shear keys. At level 1 ($\epsilon_{ax,1}$) and level 9 ($\epsilon_{ax,9}$) the strains were expected to represent the applied load F_{TR} , and in between the strains were expected to increase from close to zero at level 2 ($\epsilon_{ax,2}$) up to the full strain at level 9 ($\epsilon_{ax,9}$). The

vertical grid was refined for specimens W3 and W4 to realise a higher resolution for the load transfer.

All transducers were recorded with a sampling rate of 50 Hz. In order to reduce the amount of measurement data, a specific recording scheme was used. During the tests the number of applied load cycles was automatically detected from the measurement data. For each load cycle the minimum and maximum values of each transducer were stored. In Addition to that, for each 100 load cycles all data of 5 load cycles were recorded. Thus, the amount of data to be stored could be reduced by more than 1/10.

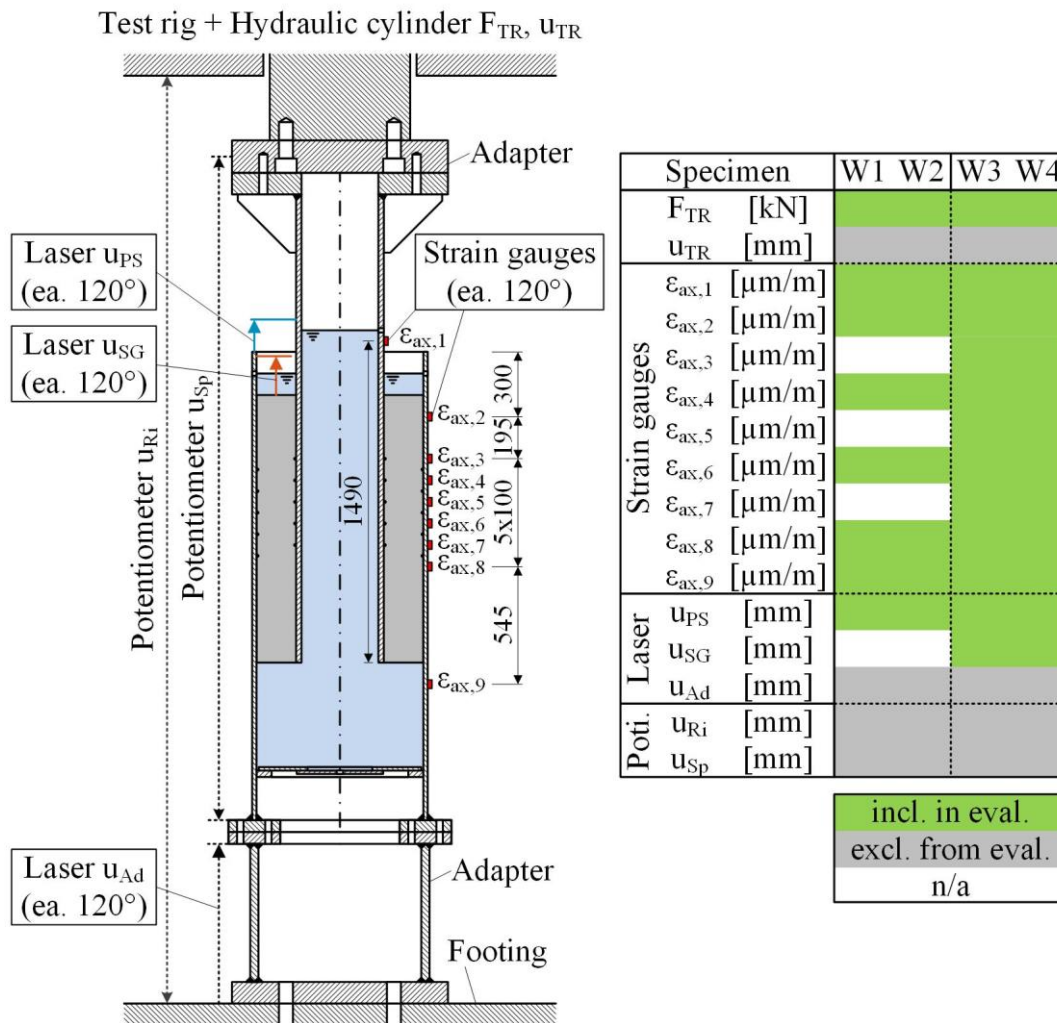


Figure 4.4: Measurement set-up for large-scale specimens exemplarily for geometry 1

4.2.3 Load scenarios

Goal of the fatigue tests was to investigate both, the load displacement behaviour under cyclic loading as well as the degradation behaviour of the grout layer. Hence, the load levels had to be chosen low enough to avoid ULS or low cycle fatigue failure but high enough to provoke damage of the grout layer. Moreover, limitations of the test rig and the connection of the specimen to the test rig had to be considered. The tests were carried out in a hydraulic test rig manufactured by INSTRON and located at the Institute for Building Material Sciences, Leibniz Universität Hannover. Capabilities of the test rig were alternating loads up to ±8 MN at loading frequencies of up to

2 Hz. For the bolted connection between pile and hydraulic cylinder the limit for tensile loads was 3 MN.

Based on the ULS and FLS design approaches described in DIN EN ISO 19902 (2014) and DNV-OS-J101 (2014), Bechtel (2016) carried out a load bearing capacity estimation for the two specimen geometries (see Figure 4.1). In addition to that, industrial project partners provided axial reference loads for the reference grouted connection of a jacket substructure located in 30 m water depth (see Figure 2.3). The loads were calculated on the basis of IEC 61400-3 (2009), where design load case (DLC) 6.1 gave the decisive ULS loads and DLC 1.2 was chosen for fatigue load calculations.

Considering these data, Bechtel (2016) derived a load scenario of seven load stages with incrementally increased loads as shown in Figure 4.5, right. The load scenario started with three load stages of alternating loads with a load ratio of $R = -1$ and then changed to pure compression loads with $R \rightarrow \infty$. The load levels were uniformly defined for both geometries, thereby leading to lower utilisation ratios for geometry 2 compared to geometry 1. The first six load stages were applied each for 100'000 load cycles followed by load stage 7 with 15'000 load cycles. When a specimen survived load stage 7, Bechtel (2016) additionally repeated load stage 3 to see possible influences of pre-damage.

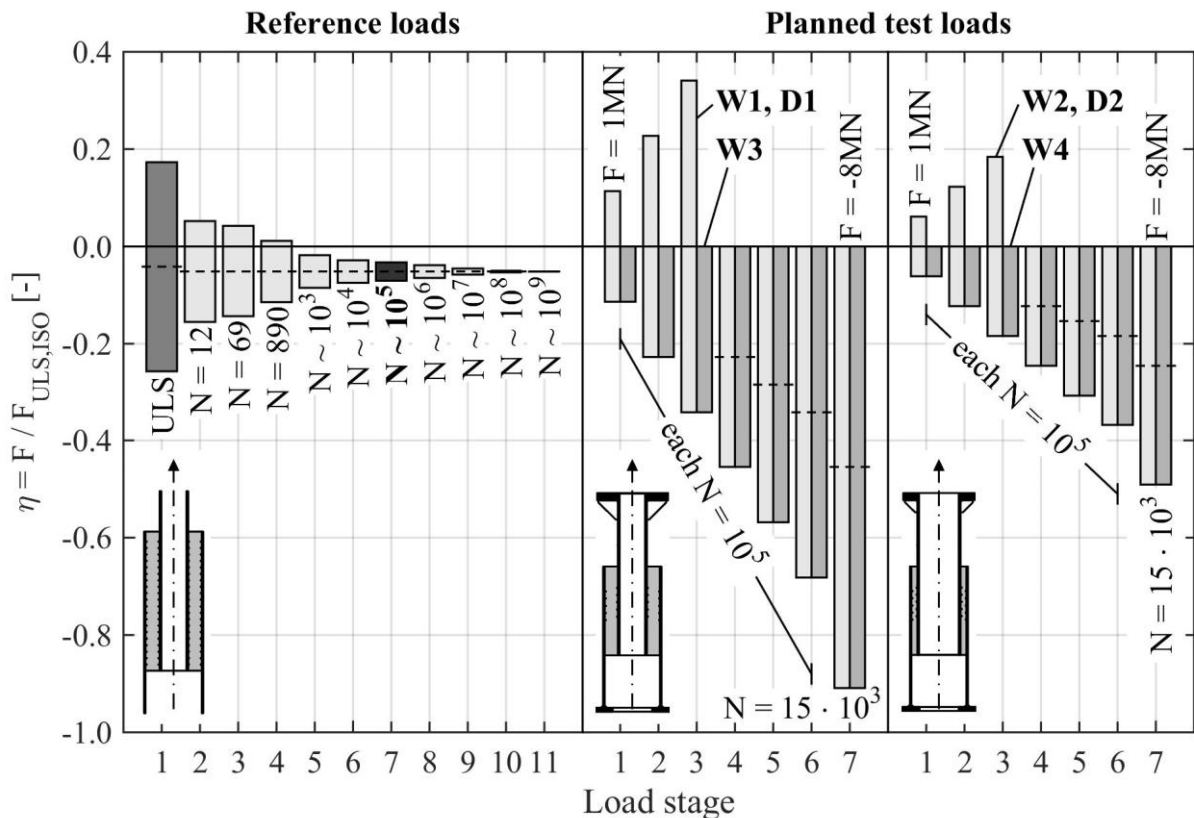


Figure 4.5: Load scenarios for large-scale fatigue tests in analogy to Bechtel (2016)

As the reference loads in Figure 4.5, left show, alternating loads with a loading ratio of $R = -1$ are not likely for a realistic loading situation but they represent a worst-case scenario. Usually, in real structures fatigue loads with large numbers of load cycles are pure compression loads.

When comparing the utilisation ratios η for each load stage and the different connections (see Figure 4.5), a much larger characteristic utilisation of the test specimens than for the reference connection is clearly visible. This impression becomes more obvious, when comparing the η of real loads for $N = 10^5$ load cycles with the η of the experimental loads.

For the described load scenario, three of Bechtel's four specimens reached load stage 7 with only slight changes in the load displacement behaviour. However, significantly damaged grout layers were found in the opened specimens. Thus, even though the chosen load levels are comparably high, Bechtel's results proofed that they were accurately chosen to reach the defined target of a fatigue damage.

For the wet AC tests W1 and W2, the load scenarios of Bechtel were applied in order to allow a direct comparison between dry and wet AC. Due to the specific damage pattern caused by alternating loads (see Section 4.4.2) and the fact that real fatigue loads are mainly pure compression, the load scenarios were adapted for the wet AC tests W3 and W4, to similar compressive load levels but without applying any tensile loads (see Figure 4.5, right).

4.3 Results

4.3.1 Grout material properties

Strength evolution

The results from the plain grout material tests (see Section 4.2.1) are shown in Figure 4.6 for BM95 and in Figure 4.7 for DDS5. On the left hand side of the Figures the strength evolution over age is shown. The strength evolution prediction according to MC2010 (2013) is presented by a dash dotted line. For both materials the strength evolution is regular and in comparable range with the prediction. In the bar plots on the right hand side of the Figures, the mean strength values after 28 days and at the first day of each test are given. Moreover, the corresponding 95 % t-test confidence intervals (CI) are presented.

Figure 4.8 shows an overview of the mechanical grout material properties at the beginning of each test except for the elastic modulus, which was measured after 28 days. Moreover, the corresponding 95 % confidence intervals (CI) are depicted. The CIs of all results are intersecting, hence a statistically significant difference between the mechanical properties or a significant influence of the material age at the beginning of the fatigue tests is not provable.

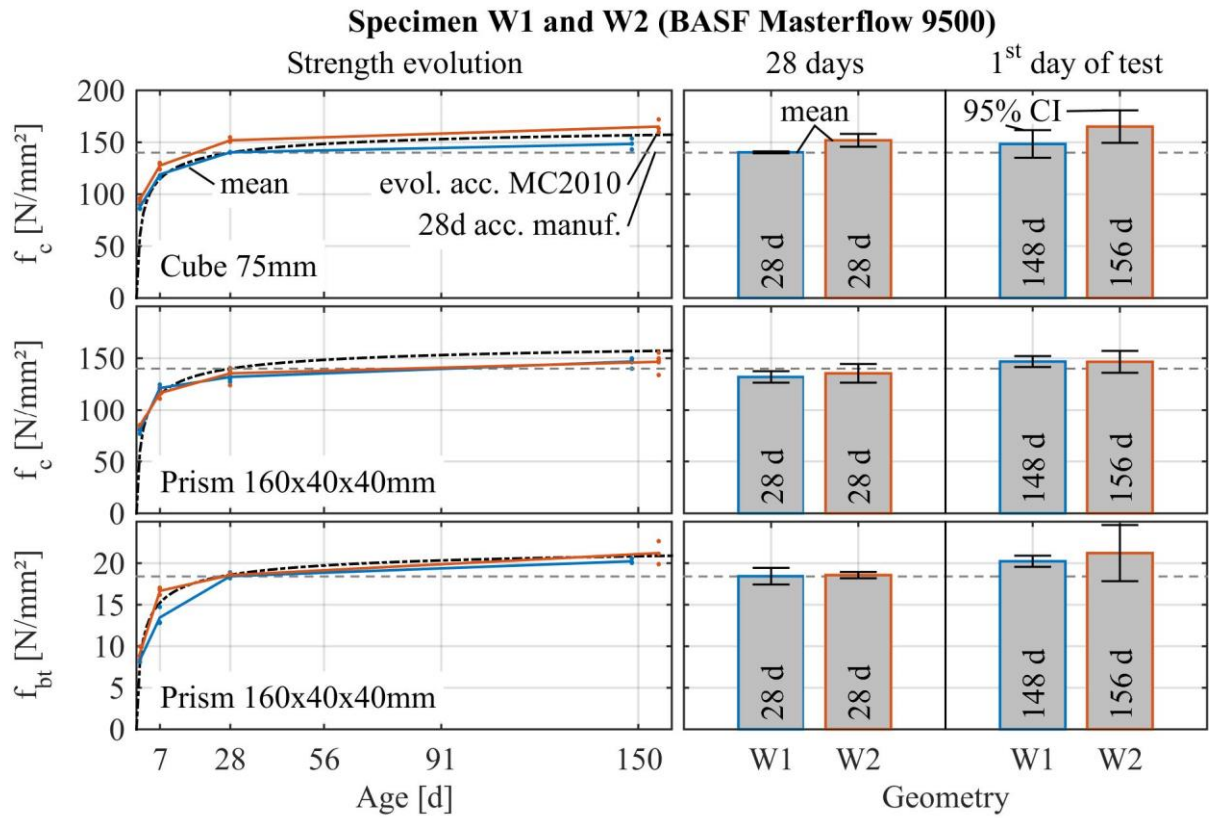


Figure 4.6: Grout material strength evolution of specimens W1 and W2 (left) and strength properties at first day of test (right), all samples taken before grout pump.

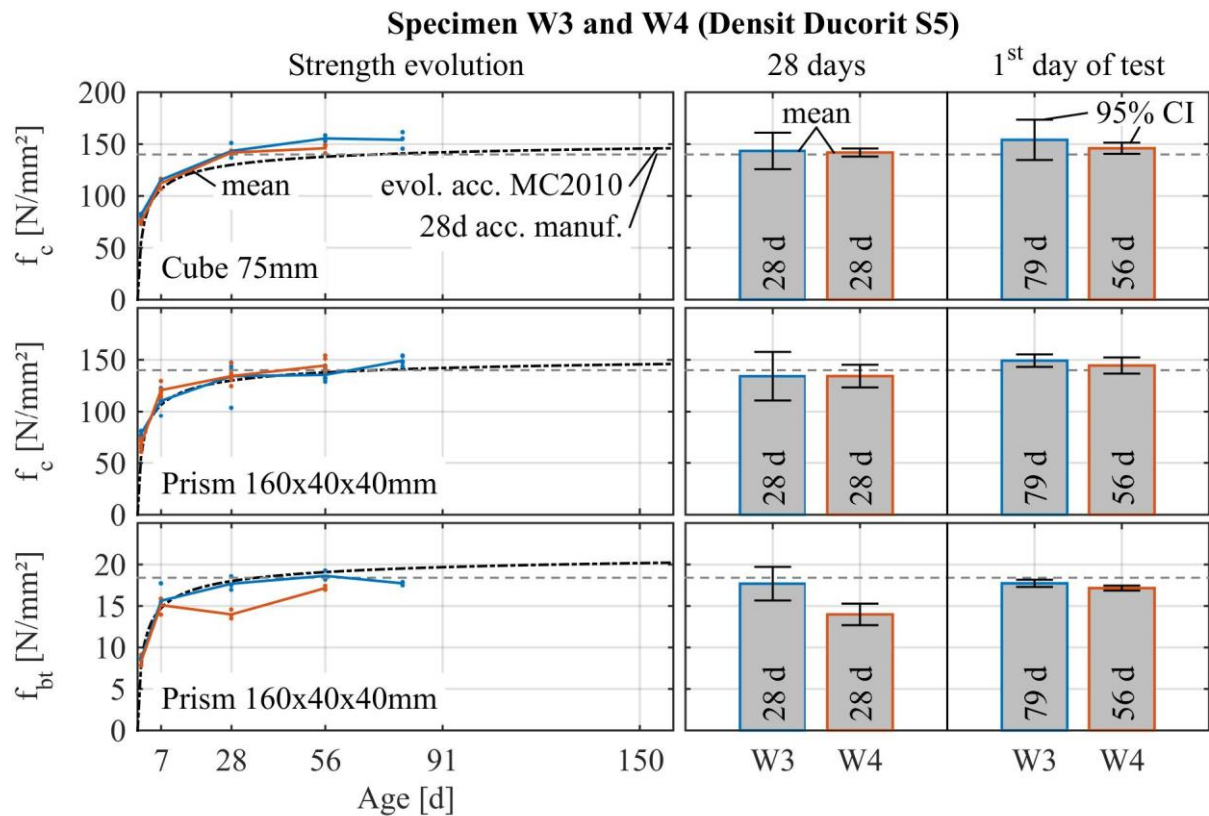


Figure 4.7: Grout material strength evolution of specimens W3 and W4 (left) and strength properties at first day of test (right), all samples taken before grout pump.

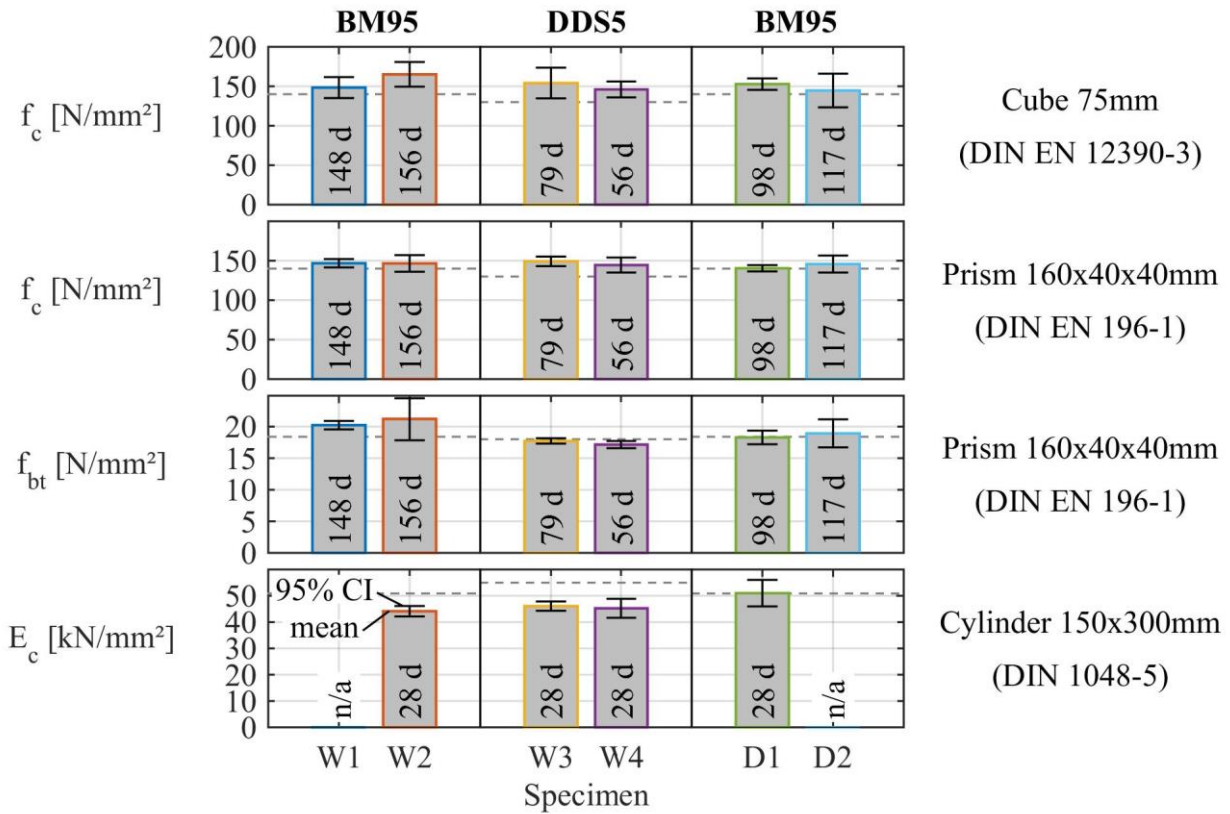


Figure 4.8: Mechanical grout material properties at beginning of each test, values for specimens D1 and D2 from Bechtel (2016)

Fresh grout

For the fresh BM95 filled into specimen W1 deviations from the optimum fresh grout behaviour were observed. In Figure 4.9, showing the resulting slump flow diameters for all four tests with BM95, the articulated variations are visible. Test W1 showed the lowest slump flow which was slightly increased by additional water after the second batch. During the grouting process of specimen W1 slightly higher ambient and preparation water temperatures of about 1-2°K were measured.

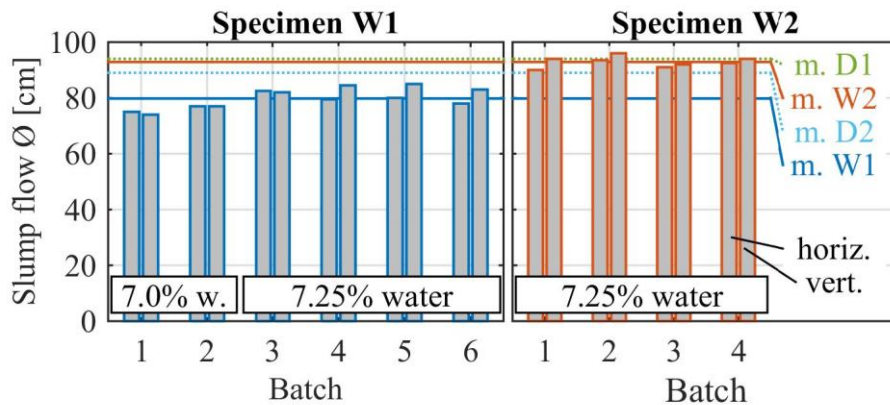


Figure 4.9: Slump flows of BM95 measured according to SVB-Richtlinie (2003)

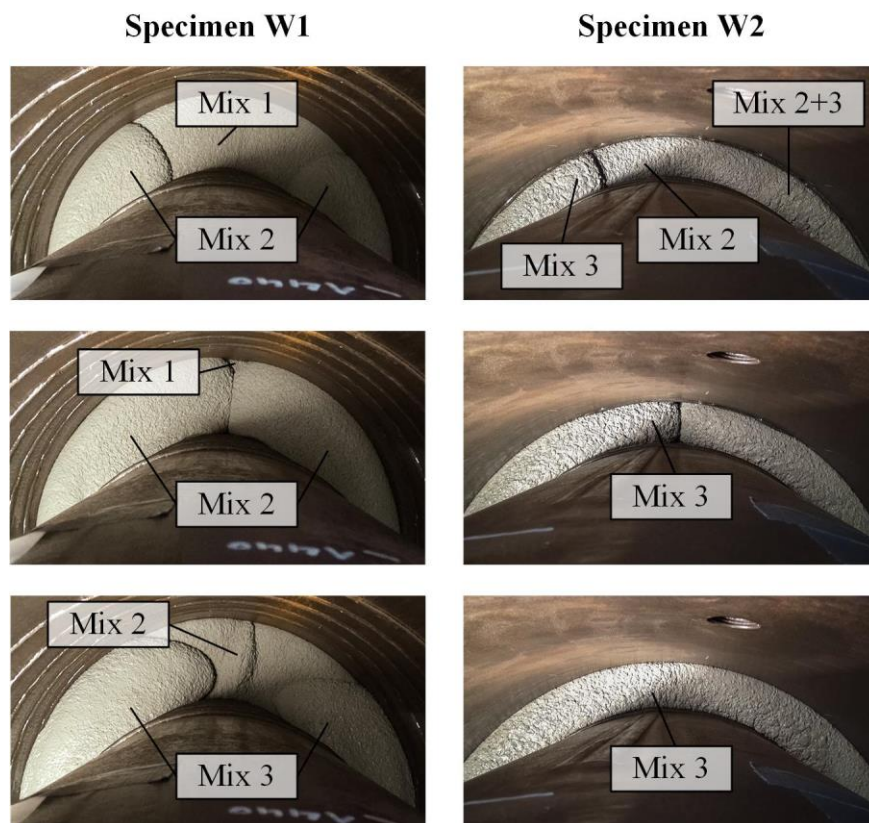


Figure 4.10: BM95 behaviour during filling process of specimens W1 and W2

In agreement with the accompanying material manufacturer's advisor, the fresh grout material was filled into the specimen. Figure 4.10 shows snapshots of the filling process. Despite the fact that both specimens were filled from below, for specimen W1 (left) the new mixtures did not equally elevate the already filled material. Instead the new mix rose through a funnel around the inlet and flowed around the pile on top of the older material layer. In specimen W2 (right) the different mixes homogenised while in specimen W1 (left) each mix formed an individual layer with a visible boundary, which not seamlessly homogenised. Due to these observations, weak spots in the grout section of specimen W1 were expected. Irregular deviations for the fresh DDS5 grout were not observed.

Hardened grout

In this Section material related grout layer properties are described as they were visible before the tests started as well as they were afterwards found in the dismantled specimens. Load related deterioration and damage is described in Section 4.3.3.

For both specimens W3 and W4, filled with DDS5 grout material, radial cracks were visible before the fatigue tests started. For the thicker grout layer two cracks at approximately 180° circumferential of the specimen and for the thinner grout layer three cracks at approximately each 120° were found.

As expected from the fresh grout behaviour, the grout layer of specimen W1 had significant material related deficits as shown in Figure 4.11. In the top left picture the full grout layer is visible after a segment of the sleeve was taken off. The inhomogeneous mixing behaviour of the fresh

grout led to weak surfaces between each mix layer, as highlighted in red. A reliable interlocking was not established in these interfaces and the individual parts could be easily separated by hand. Compared to fresh brittle cracks, the weak surfaces showed less clear colours and less cracked aggregates (see Figure 4.11 centre). Interestingly, no interaction between water and the weak surfaces was perceptible.

Moreover, a large amount of air pores was found in the grout parts, as visible in Figure 4.11, bottom right. The largest pores were of similar size as the aggregates. Especially at the mix layer boundaries, the amount of pores increased and changed also into areas of segregation. In some areas, this segregation was right below the shear keys on the pile surface (see Figure 4.11 bottom left). Nevertheless, the fresh grout showed a regular air pore content of about 2.5 %.

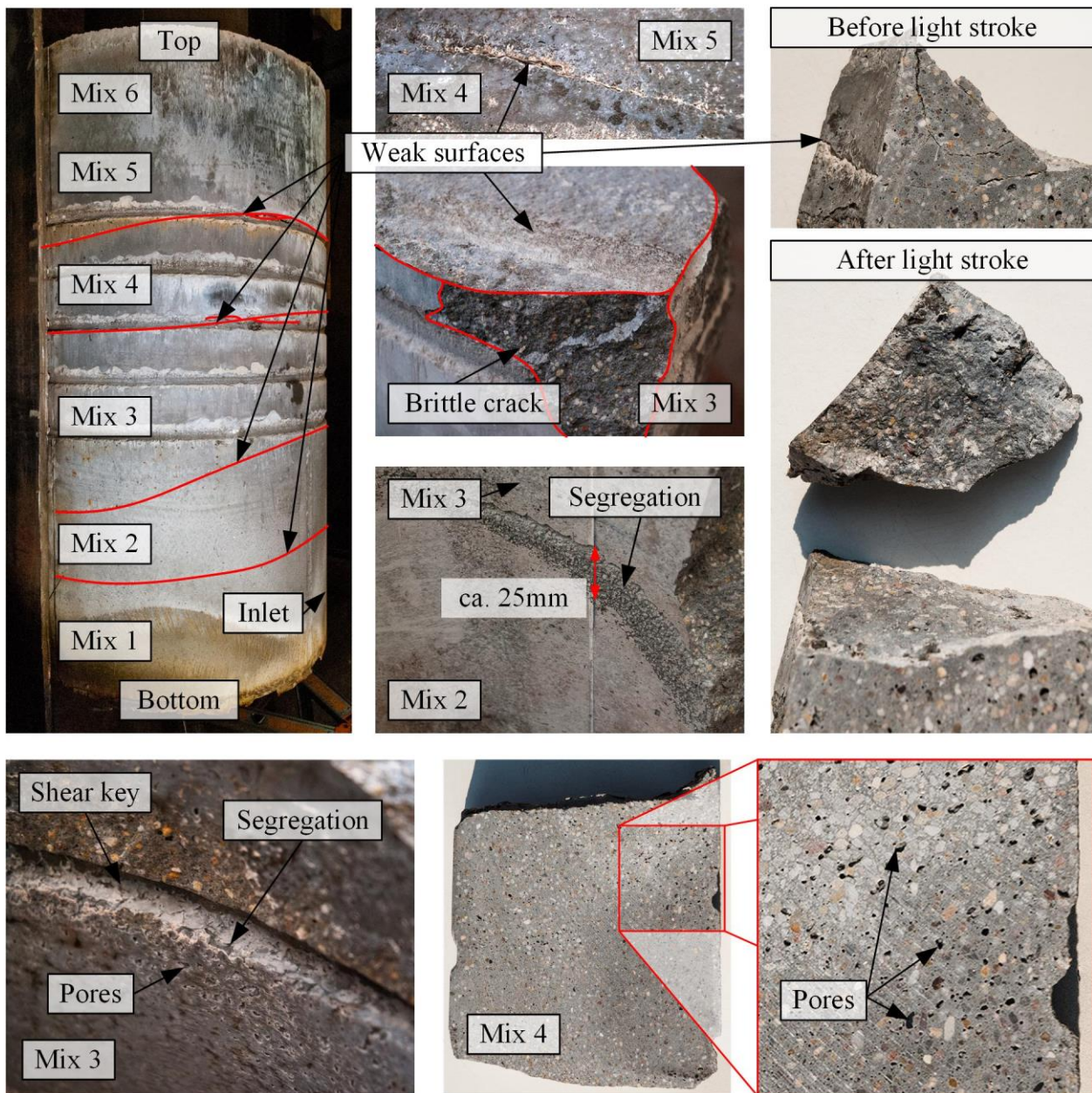


Figure 4.11: Compilation of material quality related weak spots in specimen W1

Investigations by Werner (2017) showed demixed grout material at the boundary layer due to the filling process. This behaviour led to almost pure cement below the shear keys. Consequently, the material in this highly loaded area had less strength and stiffness. However, in none of the four specimens demixing of this kind was observed.

4.3.2 Measurement results

General remark

The following evaluation includes results from the four large-scale tests carried out in wet AC (W1-W4) as well as two test results from Bechtel (2016) which were determined under similar test conditions but in dry AC (D1 and D2). Table 4.2 gives an overview of the large-scale tests.

Table 4.2: Overview of large-scale test results

Test	Geometry	t_g [mm]	Grout material	Ambient condition	Failure acc. to TC	Reference
W1	1	183.3	BASF	wet	LS1	(Bechtel (2016))
W2	2	81.5	Masterflow 9500		LS1	
W3	1	183.3	Densit	wet	LS1	
W4	2	81.5	Ducorit S5		LS2	
D1	1	183.3	BASF	dry	LS7	
D2	2	81.5	Masterflow 9500		LS7	

Measuring inaccuracy

Before evaluating the measurement data in detail, a general view on possible measuring inaccuracies and uncertainties is taken. As described before, the tests were carried out load controlled; hence the applied load F is the reference value and all other measured values are correlated to F and are influenced by the structural behaviour of the specimen.

Therefore, the first uncertainty is the deviation between the intended load level F_{target} and measured real load F_{real} in the test rig (see Figure 4.12). The mean standard deviation of F_{real} in tests W1 to W4 is $\sigma \sim 0.6\%$. In all four tests F_{real} is on average ~ 10 kN smaller than F_{target} which corresponds to a mean deviation of $\sigma \sim -0.7\%$. The mean standard deviation of F_{real} corresponds to $\sim 0.12\%$ of the test rig's total cyclic load range.

The next uncertainties are the displacement measurements carried out using lasers. These data are directly influenced by the degradation behaviour of the specimen; therefore an evaluation of possible uncertainties based on the obtained measurement data like done for F_{real} is not possible. The laser manufacturer states a linearity deviation of 0.03 mm, the smallest mean Δu_{PS} measured per load cycle is 0.10 mm. Hence, the possible inaccuracy can amount to 30 % at this load level. At loads ≥ 3 MN the inaccuracy can amount to $\leq 7.5\%$. In contrast to that the measured mean displacement between pile and sleeve u_{PS} grew up to 25 mm. At this displacement value the possible inaccuracy corresponds to $\sim 0.12\%$.

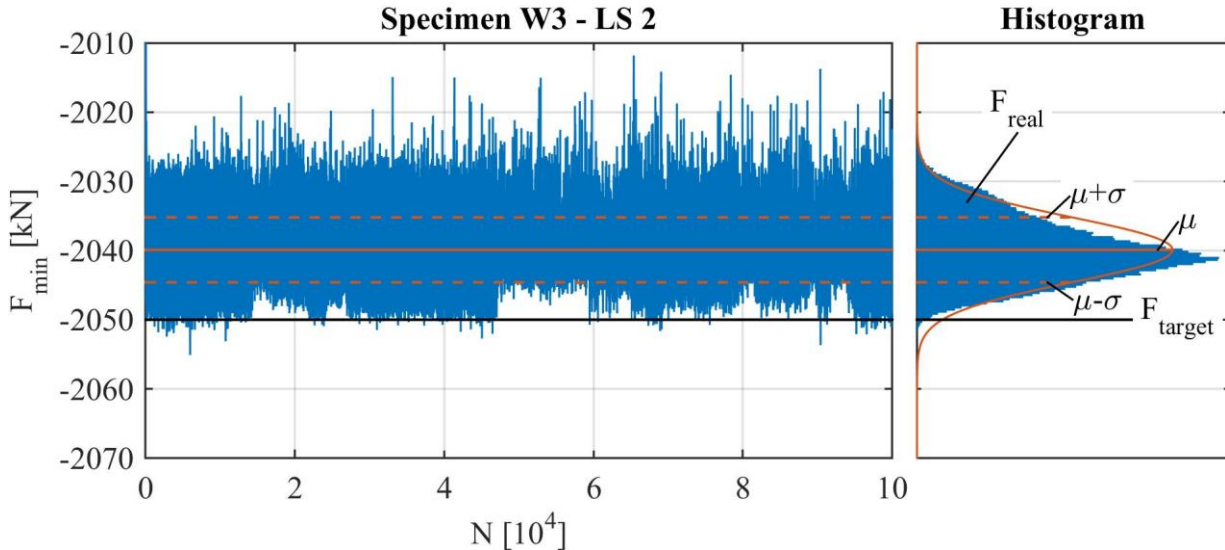


Figure 4.12: Example of the distribution of measured load peaks per load cycle

The last uncertainties are the strain measurements. The strain gauges at level 1 and 9 (see Figure 4.4) can be expected to be directly related to F_{real} according to Equation (4.1). Each of the parameters in Equation (4.1) has its own probability distribution. While the applied load F and consequently the axial strain ε_{ax} are variable during each test, the material parameter elastic modulus of steel E_s and the geometrical parameters sleeve diameter D_s and sleeve thickness t_s are assumed to be constant for each specimen but variable between specimens.

$$\varepsilon_{\text{ax}} = \frac{F}{E_s \cdot A_s} = \frac{F}{E_s \cdot (D_s - t_s) \cdot t_s \cdot \pi} \quad (4.1)$$

To separate the inherent noise from $\varepsilon_{\text{real}}$, F_{real} can be transformed into $\varepsilon_{\text{target}}$ according to Equation (4.1) and then be subtracted from the measured strain values in level 1 and level 9. As a result $\varepsilon_{\text{real}}$ shows an average standard deviation of $\sigma \sim 4.2\%$. A drift of the strain gauge measurement values was not visible.

The influence of the other parameters is estimated using a Monte-Carlo simulation. The cross sectional values D_s and t_s are regulated in DIN EN 10210-2 (2006) where a deviation of $D \pm 10$ mm and $t \pm 10\%$ is permissible. Assuming a normal distributed production output with a precision $> 95\%$, the standard deviation for t_s is $\sigma \sim 5.0\%$ and for D_s is $\sigma \sim 1.2\%$. For the elastic modulus E_s the Joint Committee on Structural Safety (2001) estimates a standard deviation of $\sigma \sim 3.0\%$ and a log-normal distribution. In a Monte-Carlo simulation with a constant force F and distributed material and geometric parameters, a standard deviation of $\sigma \sim 5.0\%$ for ε_{ax} is determined. Further including the inherent noise of $\varepsilon_{\text{real}}$ as well as the standard deviation of F_{real} , the Monte-Carlo simulation leads to an overall standard deviation of $\sigma \sim 6.4\%$. This value is a measure for the possible uncertainty when comparing the results from two specimens.

Relative displacement behaviour

Figure 4.13 up to Figure 4.17 show the relative displacement behaviour over number of applied load cycles of all large-scale specimens, including the data from Bechtel (2016). The data from Bechtel are used as reference in the later discussion (see Section 4.4) but not described in detail.

The relative displacement is measured via lasers between pile and sleeve u_{PS} and additionally for specimens W3 and W4 as relative displacement between sleeve and grout u_{SG} (see Figure 4.4). Each box represents one load stage with the corresponding F_{min} and F_{max} values stated on top. Different to the planned seven load stages (see Figure 4.5), the evaluation shows only four load stages because, in none of the tests carried in wet AC, more than the first four load stages were applied.

The relative displacement behaviour of specimen W1 shown in Figure 4.13 is dominated by a significant deformation increase in both tensile and compressive direction right from the beginning of the test. Within the last ~ 20 % of load stage 1 the increase accelerates. Moreover, at the end of load stage 1 the Δu_{PS} amounts to ~ 5 mm.

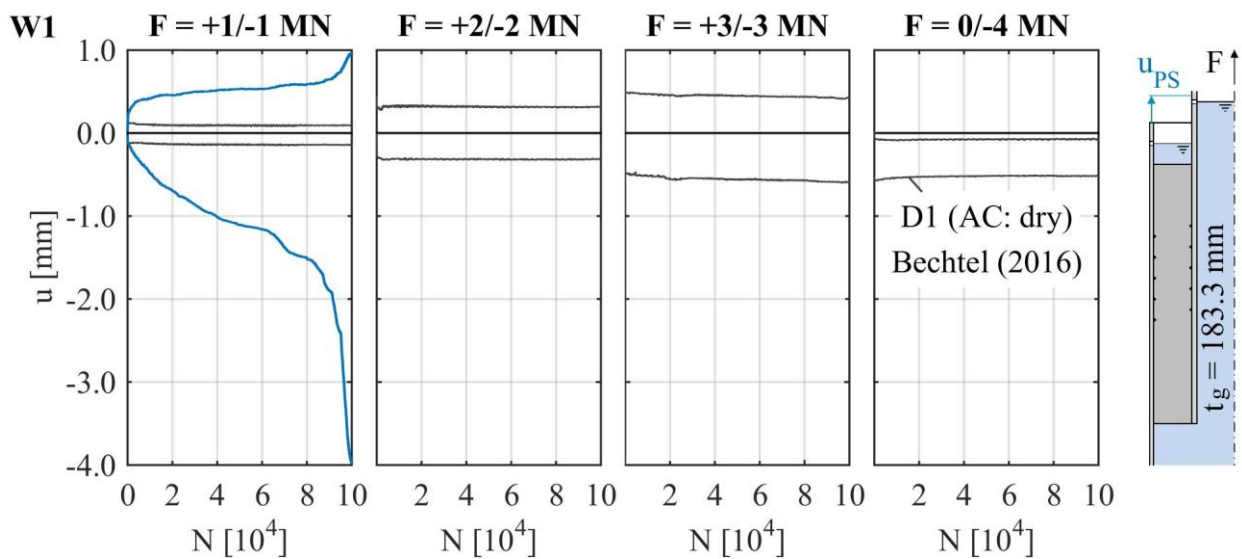


Figure 4.13: Relative displacement behaviour of specimens W1 and D1

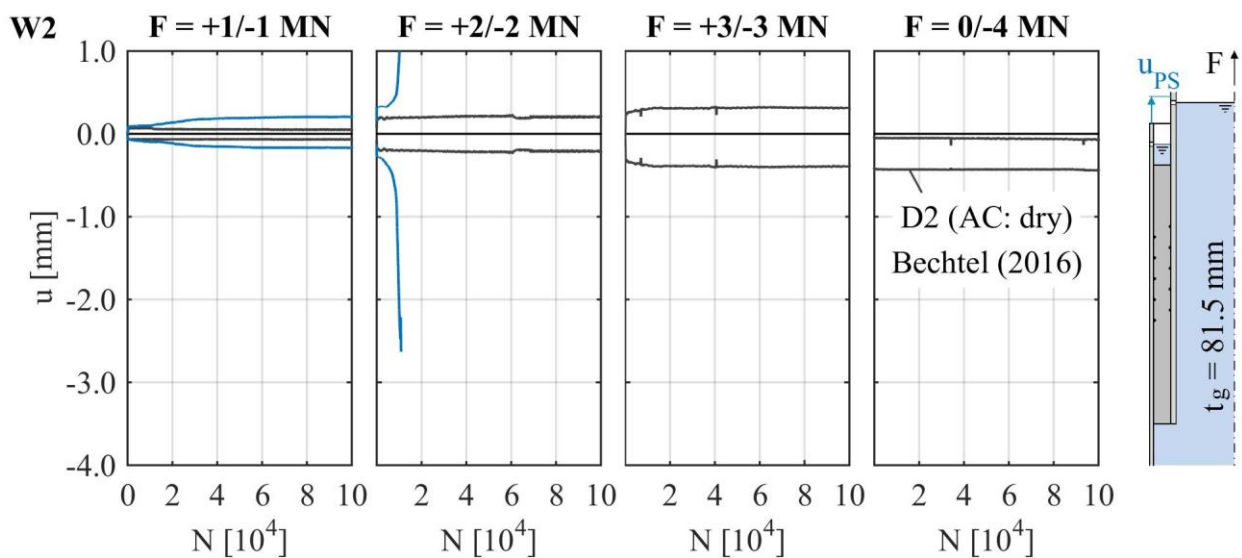


Figure 4.14: Relative displacement behaviour of specimens W2 and D2

After load stage 1 was completed the specimen was declared to have failed but the test was continued at the same load level of load stage 1 until 200'000 load cycles were reached. During the

test it was observed that relative displacement occurred mainly in the interface between sleeve and grout, as shown in Figure 4.13.

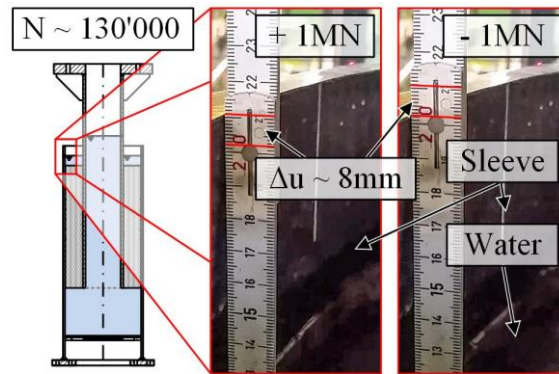


Figure 4.15: Relative displacement between sleeve and grout of specimen W1

For specimen W2 the initial Δu_{PS} in load stage 1 widens up to $\Delta u_{PS} \sim 0.38$ mm and stabilises after $\sim 0.4 N_{max}$ (see Figure 4.14). In load stage 2 the relative displacement range widens rapidly after $\sim 10^7$ load cycles. At this point the specimen was declared to have failed. Similar to specimen W1, the relative displacement occurred mainly in the interface between grout and sleeve. However, specimen W2 endured higher load levels than specimen W1.

Due to the previously described relative displacements, mainly observed between grout and sleeve, specimens W3 and W4 were equipped with additional lasers to measure the relative displacement at this interface (see Figure 4.4).

For specimen W3 an initial downslide in the first load stage is visible but less pronounced than for specimen W1 (see Figure 4.16). After about 40 % of load cycles the displacement stabilises. Within load stage 2 the relative displacement shows a pronounced kink at ~ 20 % of applied load cycles. After this kink a significant downslide with a total displacement of $u_{PS} \sim 25$ mm at the end of the load stage occurs. Even though the specimen was still capable of bearing the applied load, it was declared to have failed due to its large relative mean displacement.

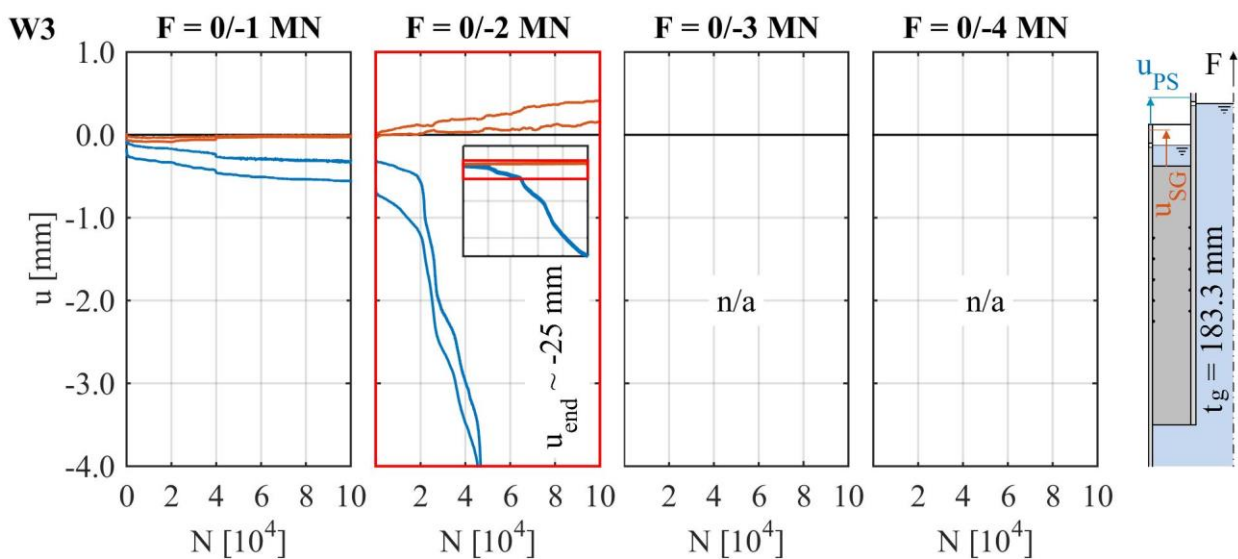


Figure 4.16: Relative displacement behaviour of specimen W3

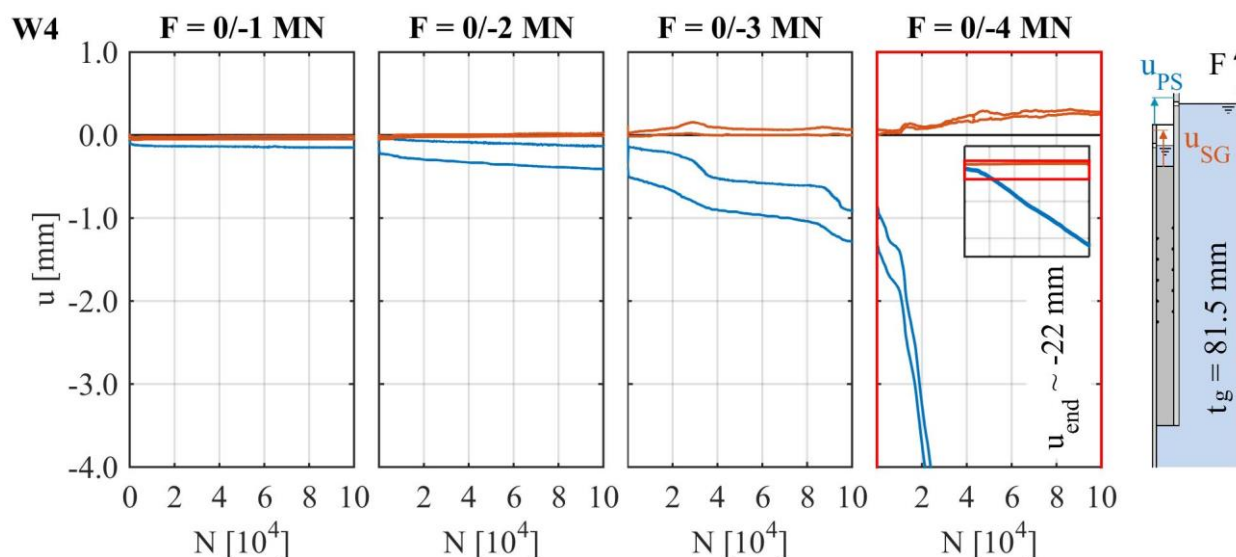


Figure 4.17: Relative displacement behaviour of specimen W4

For specimen W4 no significant downslope is visible in load stage 1 (see Figure 4.17). A slight downslope occurs in load stage 2 and increases in the further load stages. After load stage 4 a total displacement of $u_{PS} \sim 22$ mm is detected. At this point the specimen was declared to have failed, due to its large relative mean displacement. Clear kinks in the displacement curve are visible in load stage 3 at $\sim 35\%$ and $\sim 90\%$ applied load cycles as well as in load stage 4 at $\sim 10\%$ applied load cycles. Likewise to the previous results, specimen W4 with the smaller grout layer endures higher load levels with less relative displacement than specimen W3. Contrary to the results from specimens W1 and W2, the relative displacement in specimens W3 and W4 occurred mainly between pile and grout.

In order to reduce the amount of information from the displacement measurements and to allow a simpler comparison between the test results, linear regression analysis was applied to the mean relative displacement as well as to the displacement range, exemplarily shown for specimen W4 in Figure 4.18 and Figure 4.19. The slope m of the linear function gives the mean relative displacement rate, respectively the displacement range rate and thus is a measure for the degradation behaviour. The analysis results for the specimens W1-W4 as well as for the specimens D1 and D2 from Bechtel (2016) are given in Table 4.3.

A comparison between the linear regression and the actual displacement data in load stage 3 and 4 in Figure 4.18 show that the linear approach cannot cover the individual kinks in the displacement curves. Nevertheless, linear regression analysis applied to displacement measurement data is a practically appropriate way to evaluate the general displacement increase.

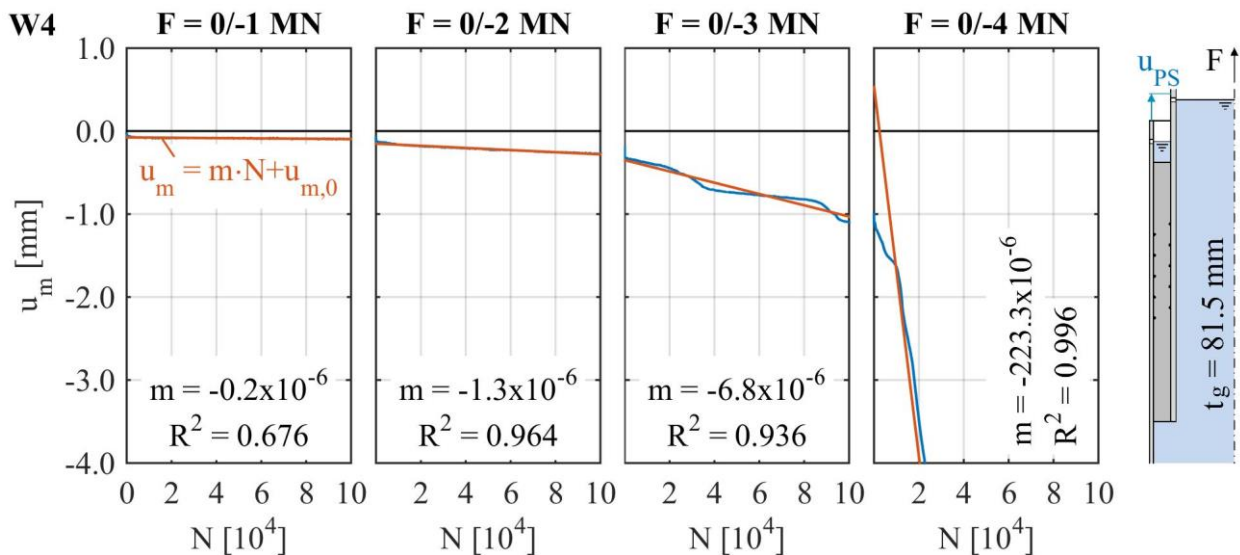


Figure 4.18: Regression analysis of mean displacement behaviour of specimen W4

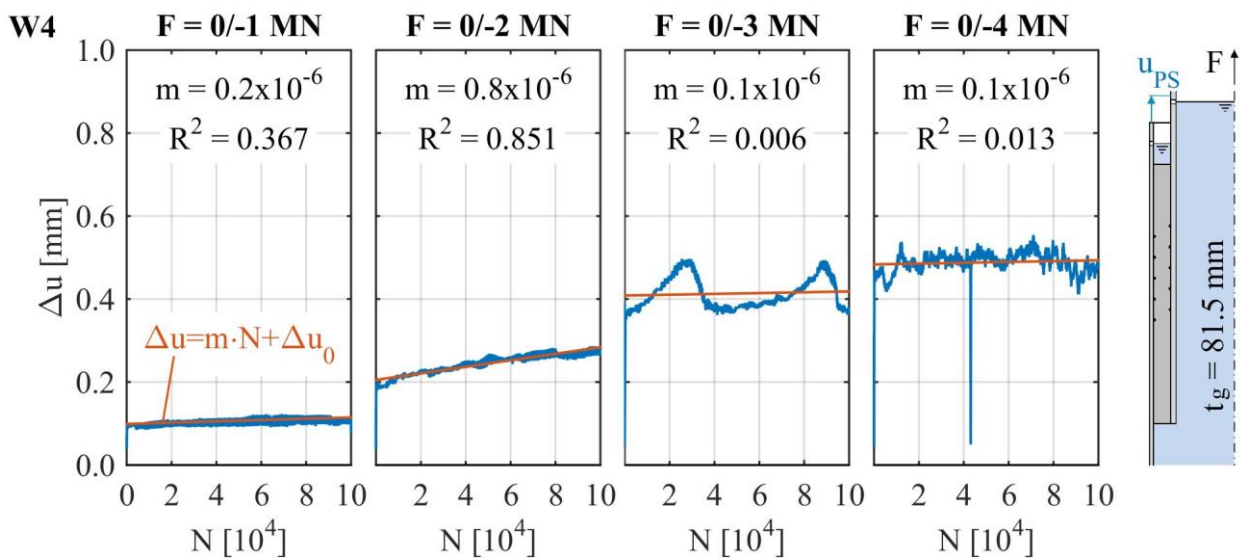


Figure 4.19: Regression analysis of displacement range behaviour of specimen W4

Table 4.3: Overview of mean displacement rate and displacement range rate

Specimen		LS1	LS2	LS3	LS4	LS5	LS6	LS7	LS8
$m(u_m)$ [mm/ 10^6 N]	W1	-8.8							
	W2	0.1	-44.0						
	W3	-2.6	-280.2						
	W4	-0.2	-1.3	-6.8	-223.3				
	D1	-0.2	-0.1	-0.7	0.2	-0.2	-0.1	-12122.9	
	D2	-0.1	0.0	0.0	-0.1	-0.2	-0.3	-39.3	-3.4
$m(\Delta u)$ [mm/ 10^6 N]	W1	24.5							
	W2	1.9	213.2						
	W3	1.0	0.5						
	W4	0.2	0.8	0.1	0.1				
	D1	0.1	-0.1	0.2	-0.2	0.0	-0.8	-2420.6	
	D2	-0.1	0.2	0.6	-0.1	0.1	0.0	1.9	-4.8

The results for specimens D1 and D2 in Table 4.3 show small slopes below $1 \text{ mm}/10^6 \text{ N}$ in similar ranges with even alternating signs for the first 6 load stages. In load stages 7 and 8 the slope increases significantly, which corresponds to the specimens' degradation behaviour described by Bechtel (2016). For specimen W1 both displacement rates are already much larger than $1 \text{ mm}/10^6 \text{ N}$ in load stage 1, same for load stage 2 of specimen W2. Moreover, the displacement range rate of specimen W2 is larger than $1 \text{ mm}/10^6 \text{ N}$ in load stage 1. For specimen W3 the mean displacement rate exceeds $1 \text{ mm}/10^6 \text{ N}$ already in load stage 1 and for specimen W4 in load stage 2.

Stiffness degradation

The hysteresis loops of selected specimens are shown and discussed in this Section. All other hysteresis loops are available in Appendix B. As visible in Figure 4.20, for each load stage a hysteresis loop at beginning (blue), middle (red) and end (green) of the load stage is shown. Additionally, the mean secant stiffness for the tensile (K_t) and the compressive (K_c) branch are shown (black dashed line). Generally, the x and y axis are scaled in a way that identical secant stiffnesses show the same graphical slope for different loading levels, otherwise the axis tick labels are printed in bold letters. To exclude the non-linear slope change around the zero crossing from calculating the secant stiffness, the inner $\pm 20 \%$ of the force F are neglected. All calculated secant stiffnesses are summarised in Table 4.4.

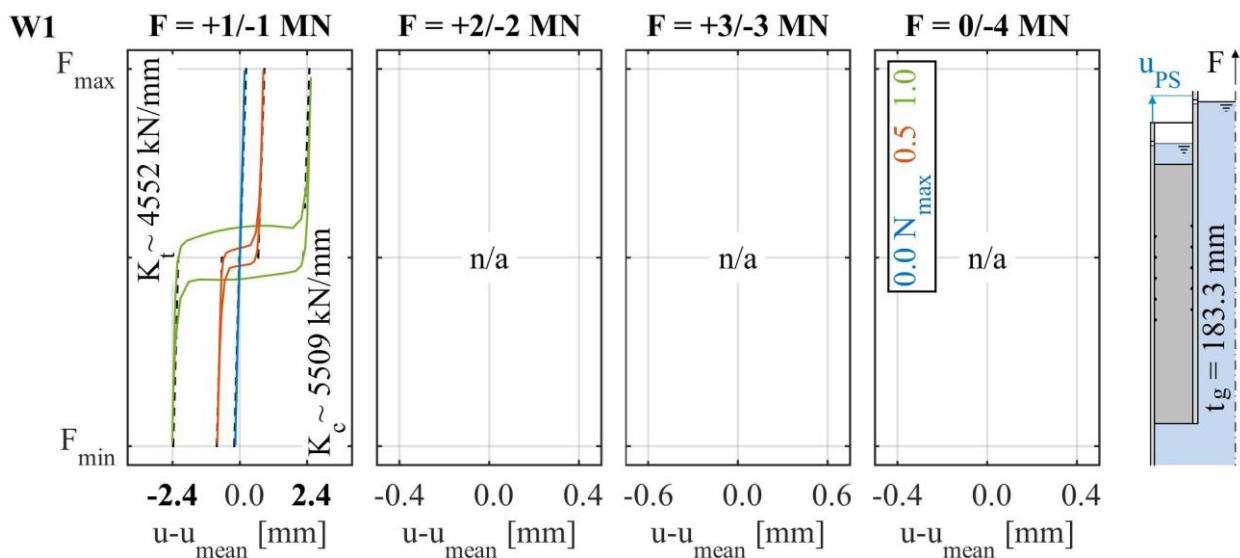


Figure 4.20: Hysteresis loops of specimen W1

Representative for alternating loads, the results of specimen W1 are shown in Figure 4.20. The slope of the lower and upper ends of the hysteresis branches is almost constant during the load stage. However, around the zero crossing a bubble opens up during the test. The width of this bubble corresponds to the measured displacement range shown in Figure 4.13. A similar behaviour is also visible for specimen W2.

Figure 4.21 shows the results of specimen W3, which are representative for pure compressive loads. Similar to the results of specimen W1 only a slight change in the specimen's stiffness can be ascertained. In contrast to specimen W1 only slight opening of the hysteresis loops in load stage 2 is visible for specimen W3.

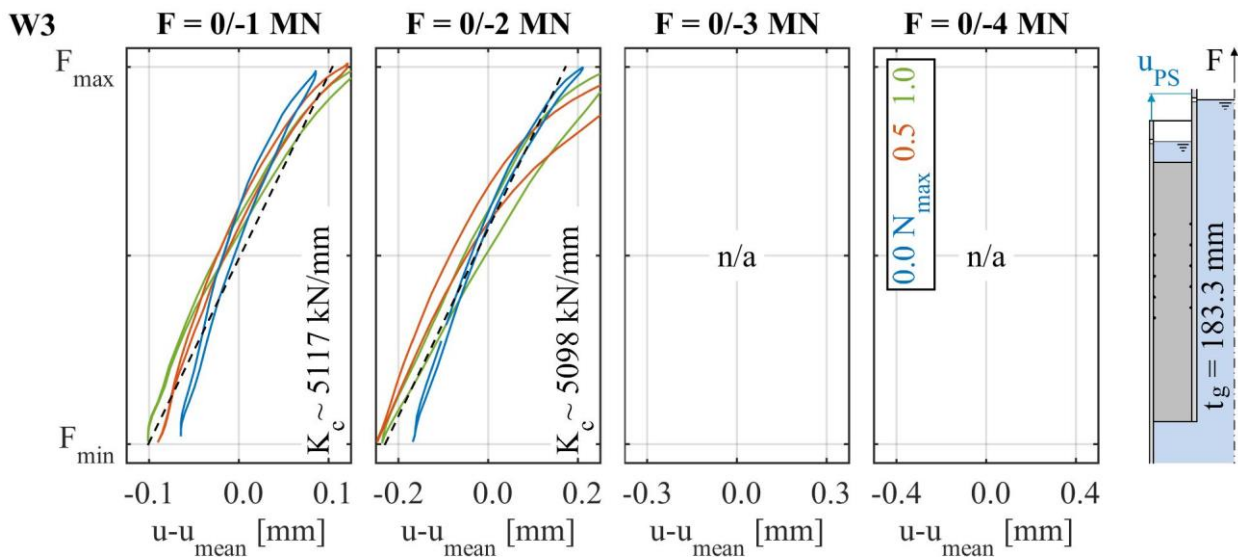


Figure 4.21: Hysteresis loops of specimen W3

As stated in Section 4.3.2 the displacements measured in load stages 1 and 2 must be expected to be highly influenced by the displacement lasers' linearity deviation. Thus, the calculated secant stiffnesses are only suitable for a qualitative evaluation. In general, geometry 2 shows a larger stiffness by a factor of ~ 2 , the tensile stiffness K_t is lower than the compressive stiffness K_c , and a trend of a slightly lower stiffness at higher loading levels is visible.

Table 4.4: Overview of calculated mean secant stiffnesses of large-scale specimens

		Geometry 1			Geometry 2			Geom 1 / Geom 2
		W1	W3	Mean	W2	W4	mean	
K_t [kN/mm]	LS 1	4552		4552	8600		8600	0.53
	LS 2				7911		7911	
	LS 3							
	LS 4							
	mean	4552		4552	8256		8256	
K_c [kN/mm]	LS 1	5509	5117	5313	14929	10954	12942	0.41
	LS 2		5098	5098	11061	10317	10689	
	LS 3					10250	10250	
	LS 4					9171	9171	
	mean	5509	5108	5308	12995	10173	11584	

Strain distribution

The strain measurements at different heights of the connection represent the load transfer from pile to sleeve. The uppermost strain gauge (see Figure 4.4, $\epsilon_{ax,1}$) measures the nominal strain in the pile, while the lowest strain gauge (see Figure 4.4, $\epsilon_{ax,9}$) measures the nominal strain in the sleeve. Both strain values are directly related to the applied load F (see Section 4.3.2). All strains measured in between are influenced by the load transfer into the sleeve.

Figure 4.22 to Figure 4.25 show the strain distributions measured for specimens W1 to W4. Each line, more specifically data point, represents the mean value of a range of 20 % applied load cycles

per load stage. Similar to the previous data plots, each box represents one load stage. The x axis is scaled in a way that the strains corresponding to F_{\min} and F_{\max} of each load stage give the same graphical impression.

For specimen W1 (see Figure 4.22) the strain distribution changes only slightly during the first load stage at $h = 845$ mm. After ~ 20 % of applied load cycles the strain at this measurement height is slightly reduced. The strain distribution in specimen W2 (see Figure 4.23) changes for compressive loading in load stage 1 in the middle section of the grout layer to a more linear strain distribution. Further slight changes are visible in load stage 2.

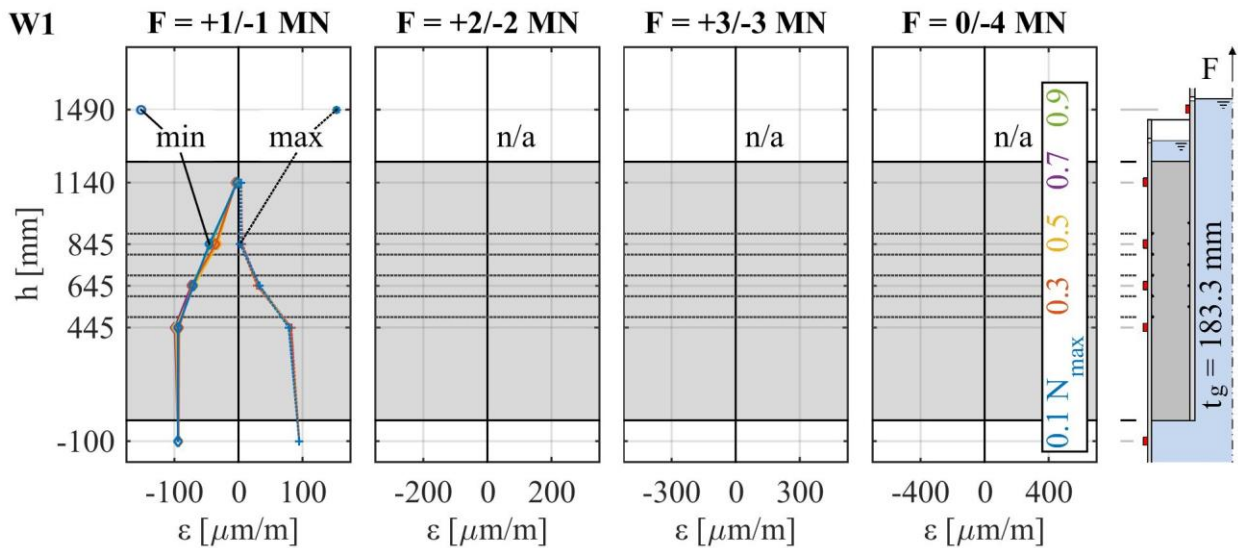


Figure 4.22: Strain distribution in specimen W1

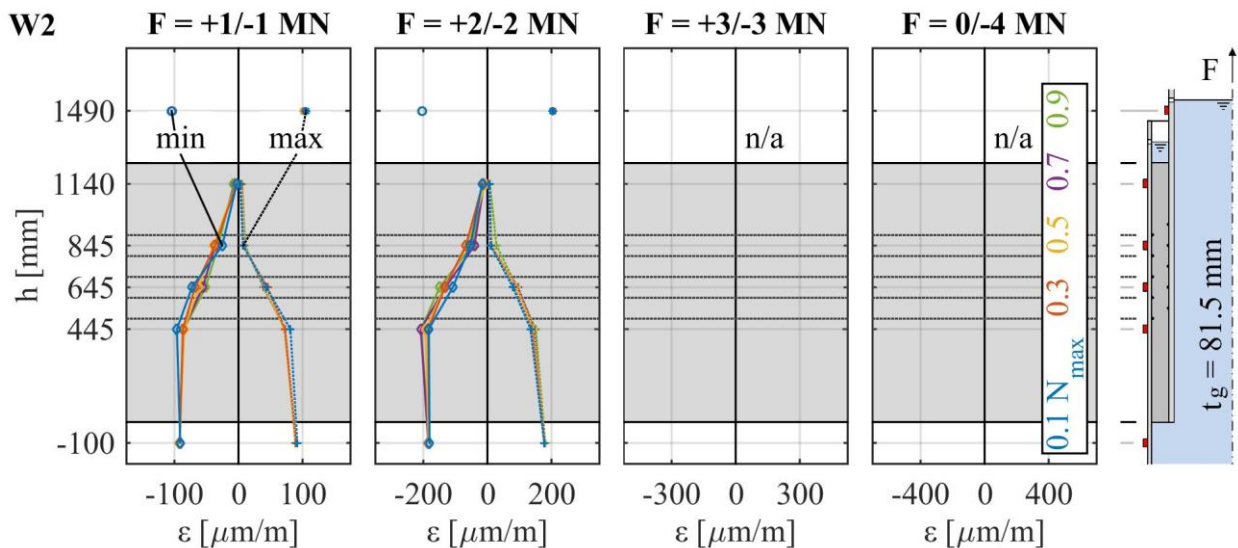


Figure 4.23: Strain distribution in specimen W2

The strain distribution along the sleeve of specimen W3 is given in Figure 4.24. Clearly visible is a redistribution in the first load stage, leading to less strains in the upper and more strains in the lower grout layer section. After about 40 % of the applied load cycles the strain distribution stabilises. At this time the strains at $h = 945$ mm are reduced to almost zero. It is also remarkable that the strain gauges at $h = 445$ mm and $h = 545$ mm measure almost the same strain level during the

load stage. In the second load stage a strain redistribution is visible between the two lowest shear keys after about 20 % of applied load cycles. Moreover, strains higher than the nominal strain in the sleeve were measured in this area.

During the first load stage, the strain distribution of specimen W4 shown in Figure 4.25 is constant. In load stage 2 the strain gauge at $h = 945$ mm shows a significantly reduced strain compared to load stage 1. Moreover, in the same load stage, a strain redistribution is visible in the lower region of the grout layer, leading to larger strains in the upper region of the connection. In load stage 3 a further strain redistribution is visible during the first ~ 50 % of applied load cycles. This redistribution ends with less strains in the upper grout layer region and higher strains at $h = 445$ mm. Finally, in load stage 4, a redistribution back to larger strains in the upper grout layer region is visible.

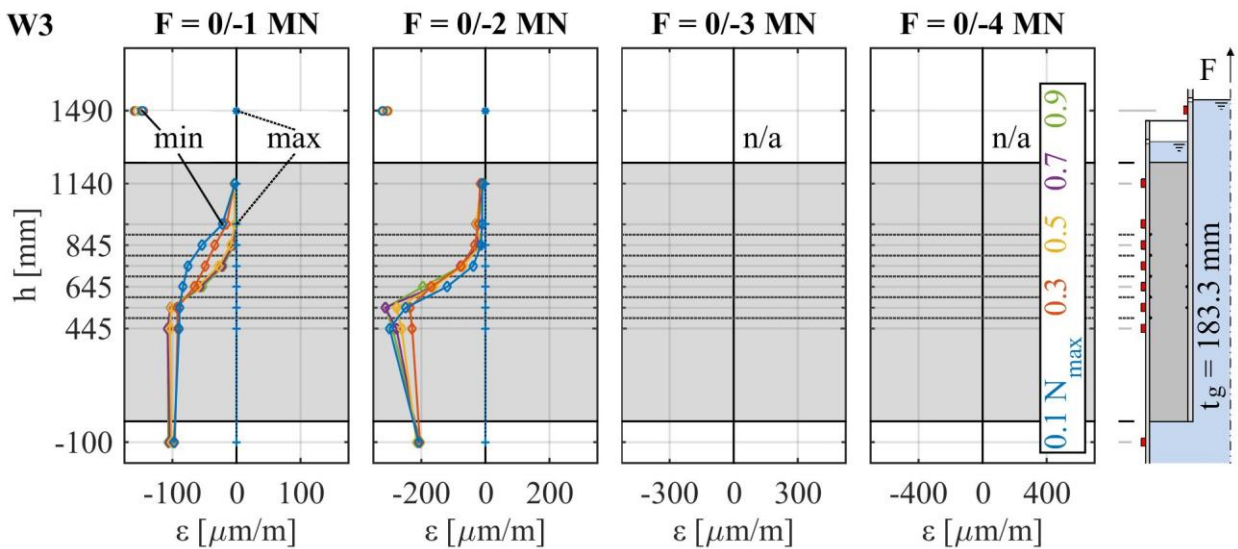


Figure 4.24: Strain distribution in specimen W3

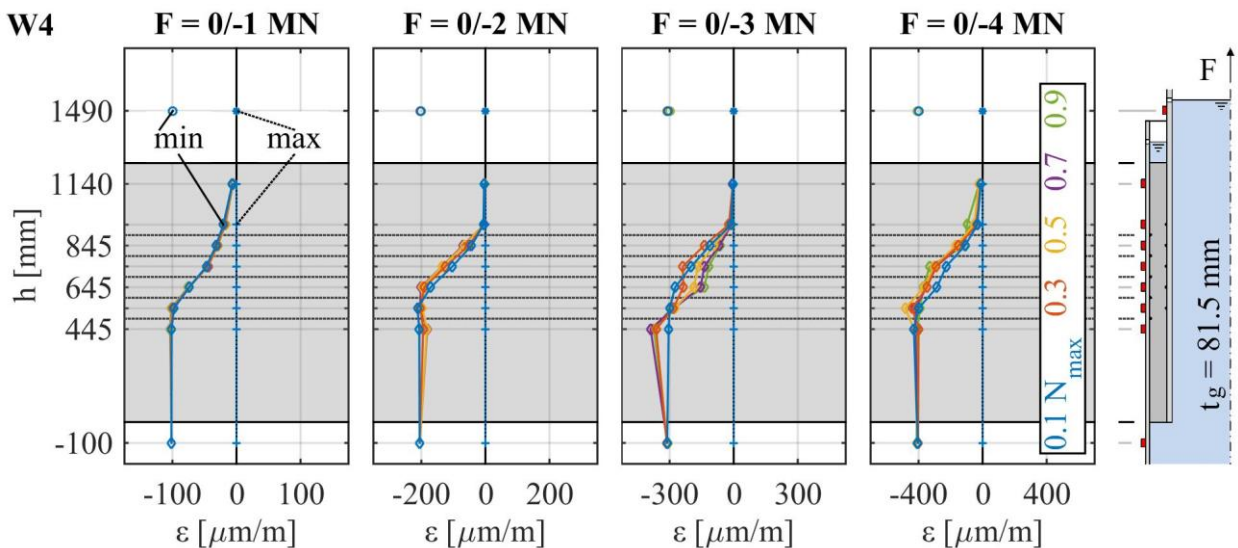


Figure 4.25: Strain distribution in specimen W4

Further measurement data

In Figure 4.26 the load control curve F , the resulting impulse rate dp and the load-displacement curve for specimens W1 and W2 are plotted at the beginning and the end of each load scenario. Considering the load curve of specimen W1, a plateau is visible at the end of the load stage. For specimen W1 this plateau corresponds to a nearly doubled impulse rate. For specimen W2 the impulse rate also increases but with less amount.

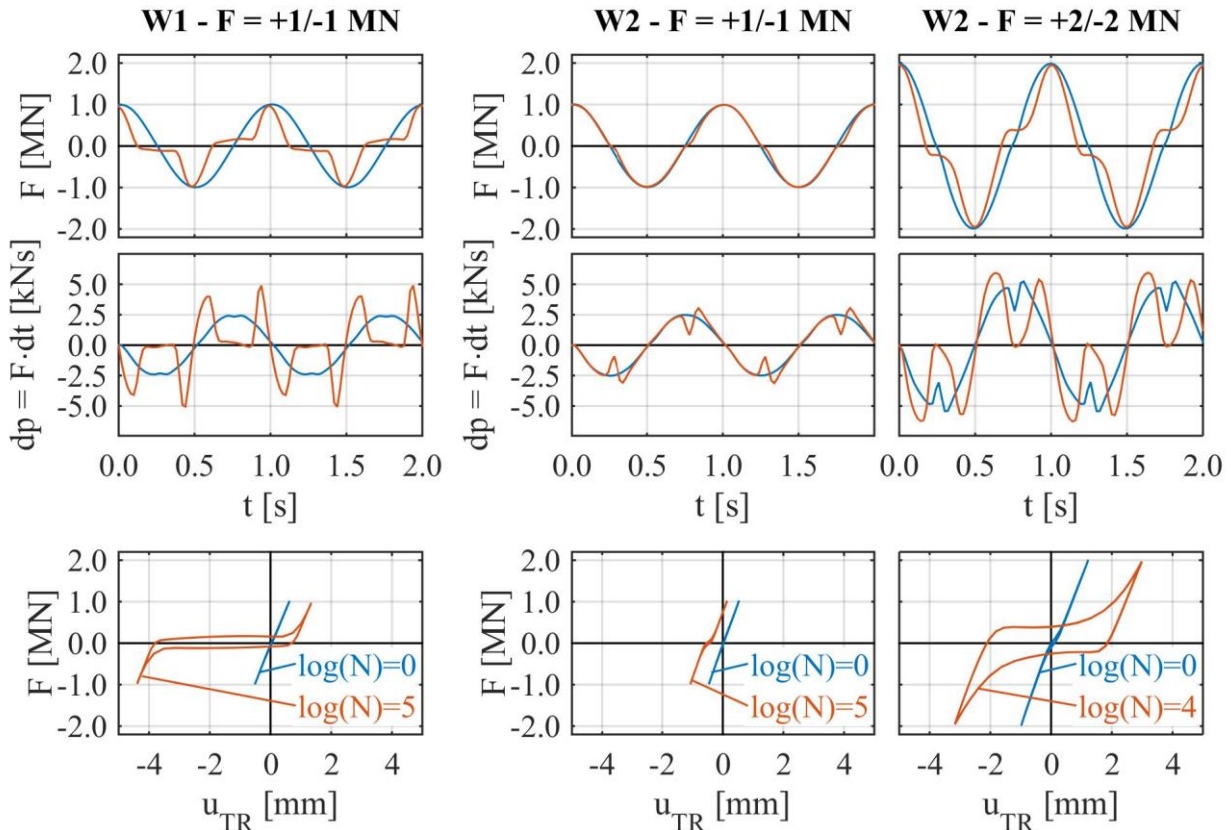


Figure 4.26: Load control curve of test rig for specimens W1 and W2 (top), resulting impulse rate dp (middle) and load-displacement curve (bottom)

In Figure 4.27 the measured load F and the measured displacement of the test rig's cylinder during the start-up process for specimen W4 is shown. These data were obtained while the hydraulic system was switched to high pressure mode. A tensile load impulse is visible with a maximum tensile load of ~ 1800 kN, which is close to the load level of the second load stage (see Figure 4.5). Moreover, the load speed is about 5000 kN/s which is slightly slower than the intended load speed of load stage 1 (e.g., $dF/dt(\pm 1 \text{ MN}, 1 \text{ Hz}) \sim 6300$ kN/s). The load-displacement curve in Figure 4.27, right shows an offset for F at the end of the load impulse, which corresponds to a plastic deformation caused by the load impulse. For specimen W3 similar measurement data were recorded. The load impulse was not intended for neither of the specimens.

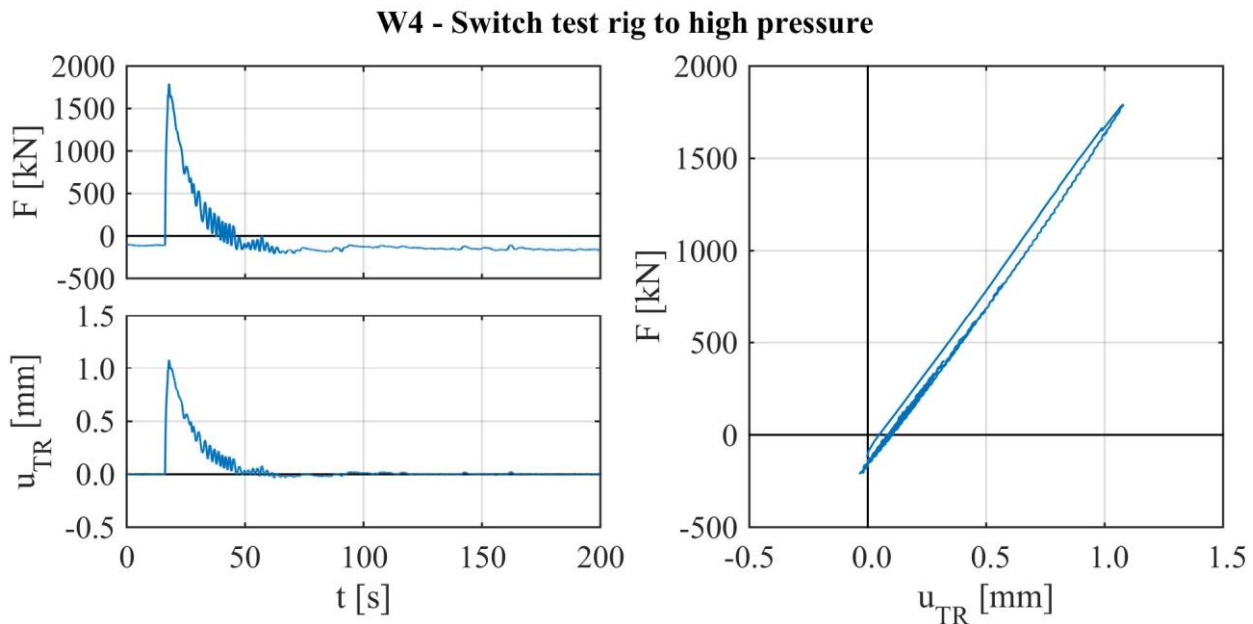


Figure 4.27: Load control curve while switching to high pressure for specimen W4 (top left), resulting displacement (bottom left) and load-displacement curve (right)

4.3.3 Observed degradation behaviour

Grout particle flushing

Figure 4.28 gives an overview of flushed grout particles observed for specimens W1 and W2. For specimen W1 a much larger amount of flushed particles was found compared to specimen W2. The particles of specimen W1 were mainly accumulated in the filter basin (see Figure 4.28, left) and inside the specimen on top of the water seal (see Figure 4.28, top centre). In the filter basin, the largest amount was attested in the sedimentation tank with a particle size of less than $106\ \mu\text{m}$. It can be assumed that an undetermined amount of particles was flushed through the plughole without being attested. The particles collected for specimen W1 had a total weight of about 1 kg and a powdery consistency.

For specimen W2 only little amounts of grout particles were attested, mainly on top of the grout layer around the pile grout interface (see Figure 4.28, bottom right). In the filter basin only minor particle amounts were attested mainly in the sedimentation tank. Likewise for specimen W1, it can be assumed that an indeterminate amount of particles was flushed through the plughole without being attested.

For specimens W3 and W4 flushed grout particles were found mainly on top of the grout layer as shown in Figure 4.29. The grout particle layer in specimen W3 was approximately 2 cm thick and almost homogeneously spread. In contrast to that, the grout particle layer in specimen W4 was unevenly spread due to the local water flow inside the narrow collar caused by the water system. Still, the amount of flushed grout particles was approximately identical, which corresponds to the maximum displacement measured for both specimens (see Figure 4.16 and Figure 4.17). Due to the observation from specimen W1 and W2 the filter size was reduced to $28\ \mu\text{m}$ (see Section 4.2.1) but only minor amounts of flushed particles were found in the sedimentation tank of the filter.

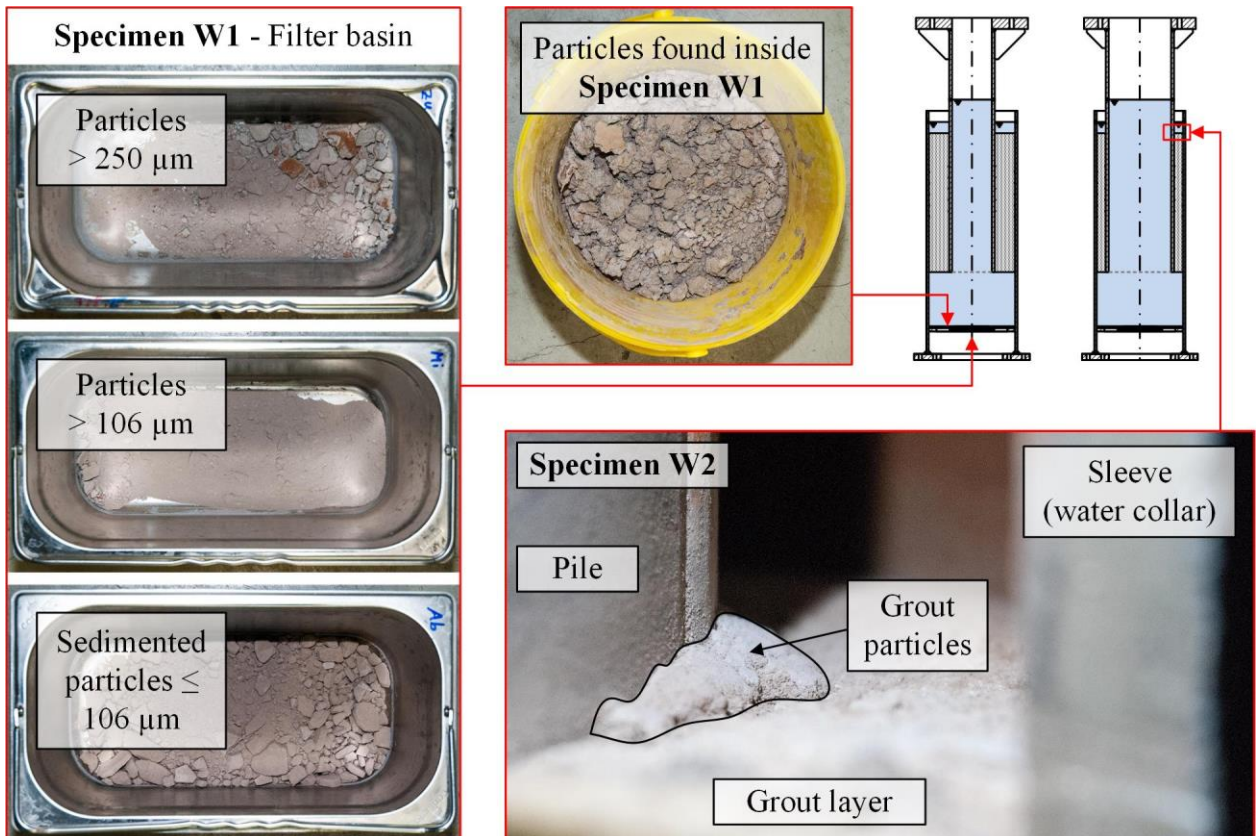


Figure 4.28: Compilation of grout particle flushing observations in specimens W1 (top and left) and W2 (bottom right)

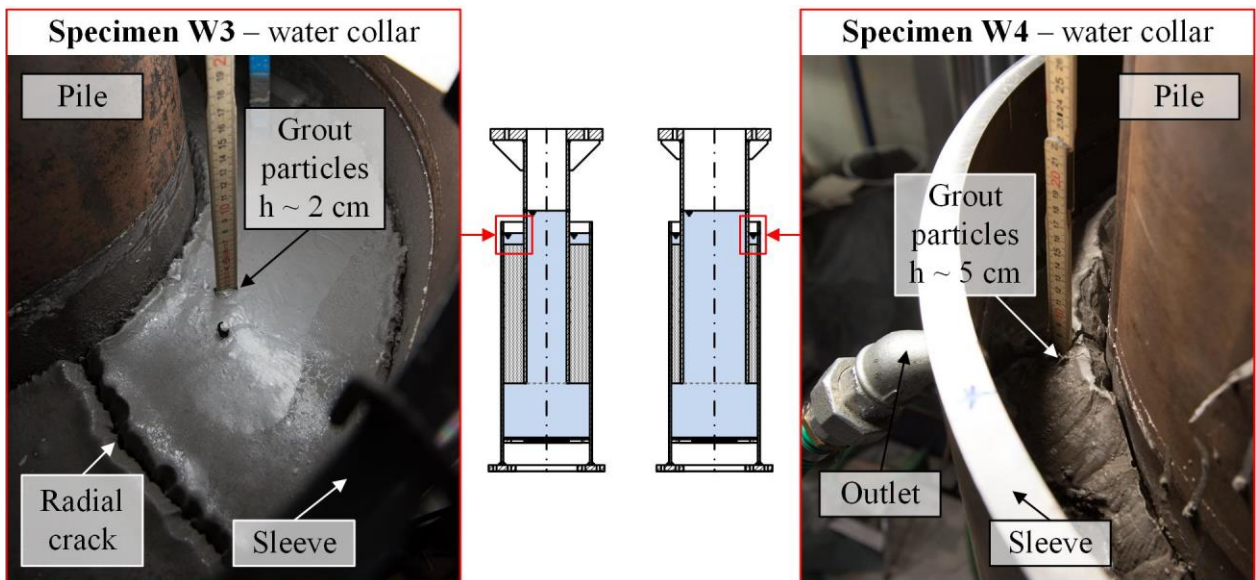


Figure 4.29: Compilation of grout particle flushing observations in specimens W3 (left) and W4 (right)

Grout crushing and cracking

In specimen W1 the grout layer showed only material related cracks, as described in Section 4.3.1. In the interface between sleeve and grout, widened shear key grooves were found. In Figure 4.30, top middle, exemplarily the shear key groove of shear key S1 in specimen W1 is shown. The width of the groove is widened from the shear key width $w_{sk} = 12$ mm up to 20 mm. Similar degradation

was found for the other shear key grooves facing the sleeve of specimen W1. In contrast to that no grout crushing was found around the shear keys on the pile.

A downward pointing diagonal shear crack was found between shear keys S1 and P1 of specimen W2 (see Figure 4.30 and Figure 4.34). This crack had an orientation angle of $\sim 37^\circ$. Furthermore, an upward pointing diagonal shear crack was found between shear keys S2 and P1. This crack had also an orientation angle of $\sim 37^\circ$. Similar to specimen W1, widened shear key grooves were found in the grout layer facing the sleeve.

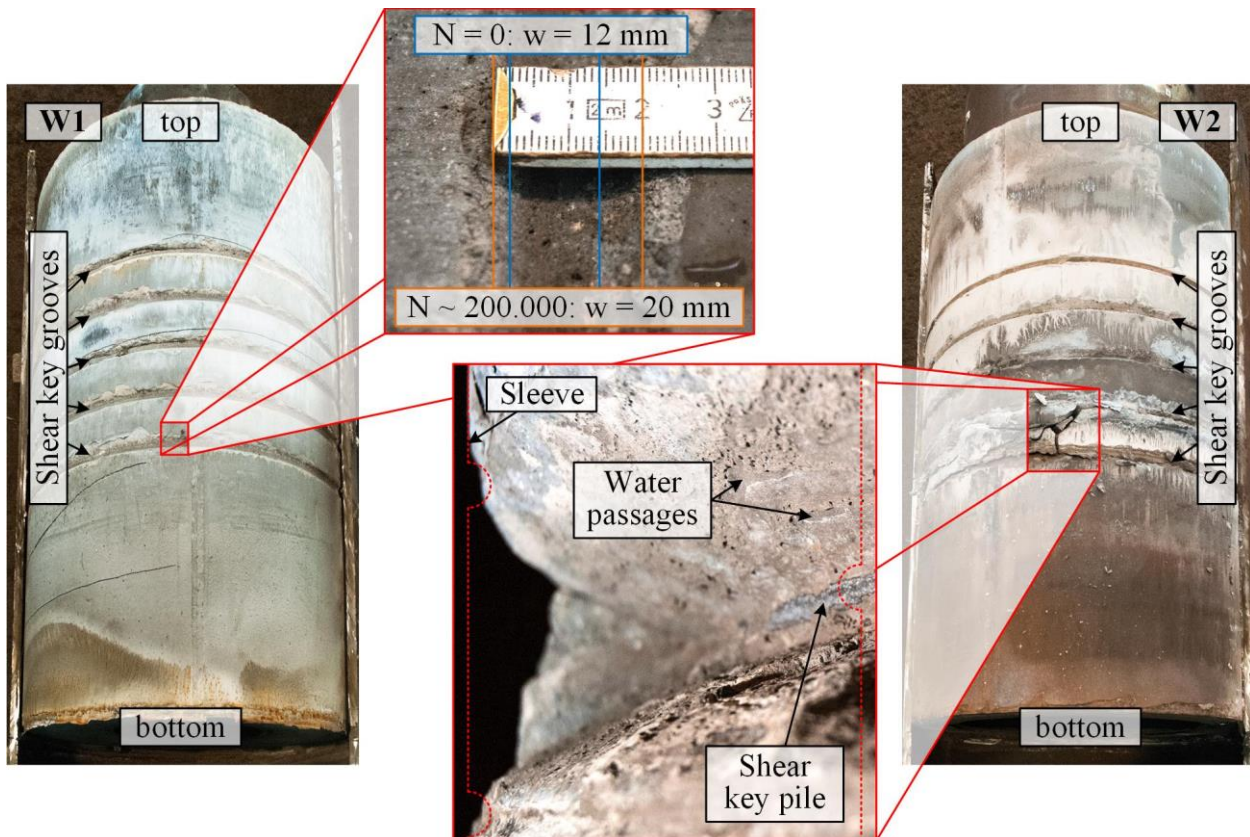


Figure 4.30: Compilation of major degradation mechanisms found in dismantled specimens W1 (left) and W2 (right)

As visible in Figure 4.31, left and Figure 4.34, a downward pointing diagonal shear crack was found in specimen W3 between shear keys S1 and P2 with an orientation angle of $\sim 37^\circ$. This crack was open with an approximate distance between the crack surfaces of ~ 25 mm. Additional downward pointing cracks with no measurable opening were visible between shear keys S4-P5 with an orientation angle of $\sim 37^\circ$ and S1-P3 with an orientation angle of $\sim 56^\circ$. A horizontal crack was visible starting from shear key P5 and ending at the inner sleeve surface. Moreover, an upward pointing diagonal shear crack was found between shear keys S5-P4 with an orientation angle of $\sim 16^\circ$. Voids in the grout layer were visible at the pile facing grout surface above shear keys P3 to P5 with a void length of ~ 25 mm. All cracks started in the upper region of the voids respectively the widened shear key grooves. On the crack surfaces of the crack S1-P1, flushed grout particles had accumulated and were also found in the voids of the shear key grooves, described beforehand.

In specimen W4 a downward pointing diagonal shear crack was found between shear keys S1 and P1 with an orientation angle of $\sim 37^\circ$ (see Figure 4.31 and Figure 4.34). This crack was open with

an approximate axial distance between the crack surfaces of ~ 22 mm. Further shear cracks with no significant opening and orientation angles of $\sim 37^\circ$ were visible between shear keys S2-P2, S4-P4 and S5-P5. A diagonal shear crack between shear keys S1 and P2 with an orientation angle of $\sim 67^\circ$ was found. Additionally, an upward pointing diagonal shear crack was found between shear keys S4-P3 with an orientation angle of $\sim 37^\circ$. An almost horizontal crack was found starting at shear key P5 and ending at the inner sleeve surface. Similar to specimen W3, voids in the grout layer were found above the shear keys P2 to P5 at the pile facing grout surface. The voids had a length of ~ 22 mm. All cracks started in the upper region of the widened shear key grooves. Similar to specimen W3, flushed grout particles had accumulated on the surfaces of shear crack S1-P1 and flushed grout particles were found in the voids of the shear key grooves.

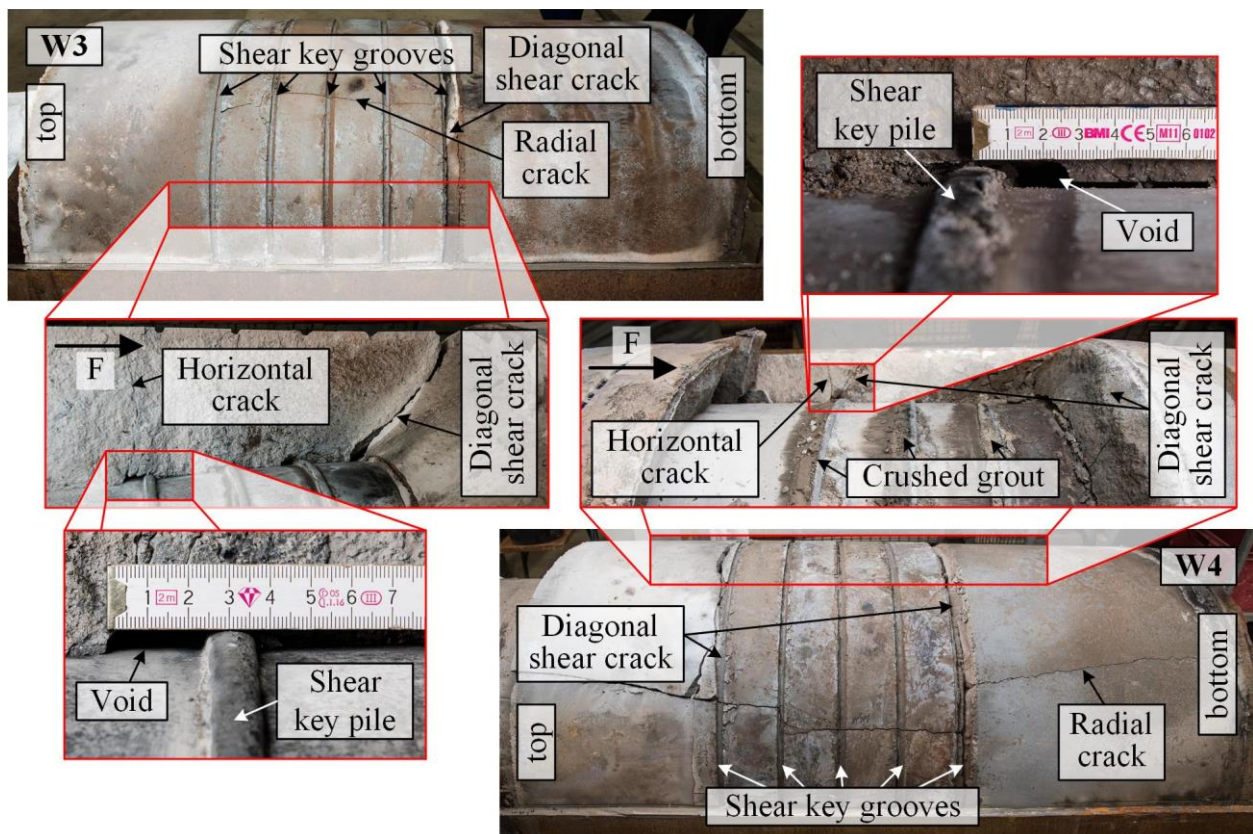


Figure 4.31: Compilation of major degradation mechanisms found in dismantled specimens W3 (left) and W4 (right)

4.3.4 Analytical design approaches

Relation to current standards

Table 4.5 shows the typical ranges of applicability of current design standards (see Section 2.5.5). The reference structures pre and post-piled (see Figure 2.3) exceed the ranges of applicability for grout material compressive strength f_{cu} , pile slenderness D_p/t_p , grout slenderness D_g/t_g and stiffness K . Geometry 1 is characterised by values comparable to the reference pre-piled grouted connection and geometry 2 by values comparable to the reference post-piled. Hence, the specimen geometries exceed the ranges of applicability for the same parameters as the reference structures.

Table 4.5: Ranges of applicability for DIN EN ISO 19902 (2014), NORSOK N-004 (2013) and DNVGL-ST-0126 (2016) and parameters of the large-scale specimens

				Reference Pre-piled	Reference Post-piled	Geom 1	Geom 2
f_{cu}	[N/mm ²]	\geq \leq	20 80	140.0	140.0	140 / 130	140 / 130
D_p/t_p	[-]	\geq \leq	20 60	15.8	49.6	16.3	24.4
D_s/t_s	[-]	\geq \leq	30 140	36.6	56.8	40.7	40.7
D_g/t_g	[-]	\geq \leq	10 45	4.1	10.4	4.2	9.5
L_e/D_p	[-]	\geq \leq	1 10	3.9	2.1	3.1	2.0
w_{sk}/h_{sk}	[-]	\geq \leq	1.5 3.0	2.5	2.0	2.0	2.0
h_{sk}	[mm]	\geq	5.0	10.0	15.0	6.0	6.0
h_{sk}/s_{sk}	[-]	\leq	0.100	0.050	0.050	0.060	0.060
h_{sk}/D_p	[-]	\leq	0.012	0.011	0.006	0.015	0.010
D_p/s_{sk}	[-]	\leq	16.000	4.420	8.267	4.064	6.100
C_p	[-]	\leq	1.500	1.013	1.000	1.352	1.150
K	[-]	\leq	0.020	0.078	0.033	0.075	0.041

Ultimate Limit State (ULS) capacity

In Section 2.5 different design approaches to calculate the ULS capacities of the large-scale specimens are presented. Figure 4.32 shows the results of these approaches for the large-scale specimen geometries and the used grout materials. For DDS5 slightly lower ULS capacities are calculated because of the grout material's slightly lower compressive strength (see Table 4.1). The lowest capacities follow from the approach given in DNVGL-ST-0126 (2016). The highest capacities are calculated with the approach of Schaumann et al. (2012) (see Section 2.5.4). The large difference between the results from the DIN EN ISO 19902 (2014) approach and the DNVGL-ST-0126 (2016) approach is caused by the shear key arrangement with shear keys in the connection's centre. The DIN EN ISO 19902 (2014) approach takes into account the grout layer length while in the DNVGL-ST-0126 (2016) approach only the area with shear keys is considered.

The black dashed line shows a load level of 8 MN which is the highest planned load in the load scenarios according to Figure 4.5. To both specimens D1 and D2 of Bechtel (2016) tested in dry AC this loading level was applied in the fatigue tests. Assuming that the fatigue capacity is usually lower than the ULS capacity, the calculated ULS capacities according to DIN EN ISO 19902 (2014) and Schaumann et al. (2012) are in accordance with the obtained test results.

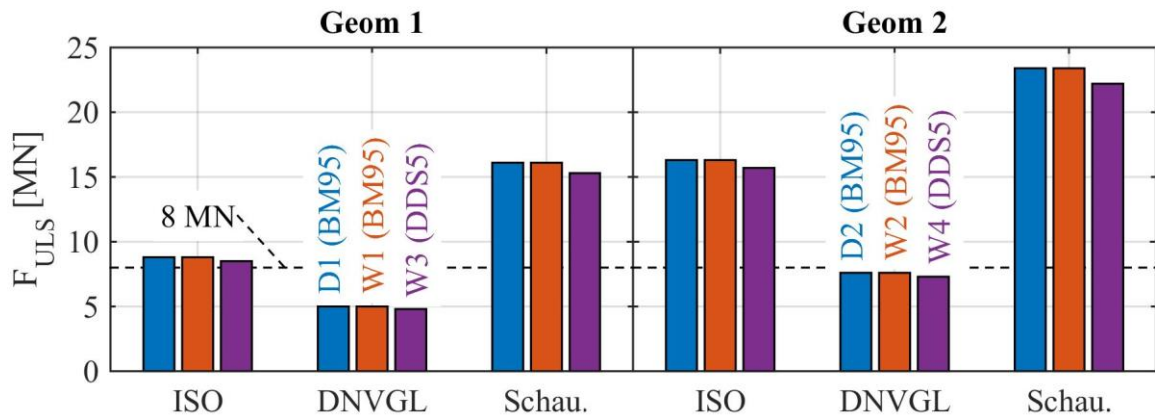


Figure 4.32: Characteristic ULS capacities for the large-scale specimen geometries and grout materials calculated according to current design methods

Fatigue Limit State (FLS) capacity

Based on the FLS design approaches described in Section 2.6 the fatigue load levels for a single load stage of $N = 100'000$ load cycles are calculated and presented in Figure 4.33. Moreover, the highest loads endured by the specimens in the fatigue tests are shown. Clearly visible is the large ratio of ~ 8 for F_{FLS} between wet AC (W1-W4) and dry AC (D1, D2) tests.

For the dry AC tests the FLS capacity is assumed to be between 6 and 8 MN since 6 MN was the last load stage where 100'000 load cycles were applied. It has to be kept in mind that in addition already 5 load stages with lower loads but also 100'000 load cycles were applied. These load stages have presumably caused additional degradation. For the wet AC tests, the highest load stages with little degradation and little relative displacement (see Section 4.3.2), were chosen as FLS capacity.

A comparison between the test results and the calculated FLS capacities shows conservative results of all approaches for dry AC tests. In contrast, for the wet AC tests only the approach given in DNVGL-ST-0126 (2016) provides FLS capacities in the range of the test results. This impression is strengthened when considering that all design approaches are defined for the worst loading case of $R = -1$. Despite this good agreement, a validation of the S-N curves' slope is not possible with the obtained results because only $N = 100'000$ load cycles were investigated and the load sequence is neglected.

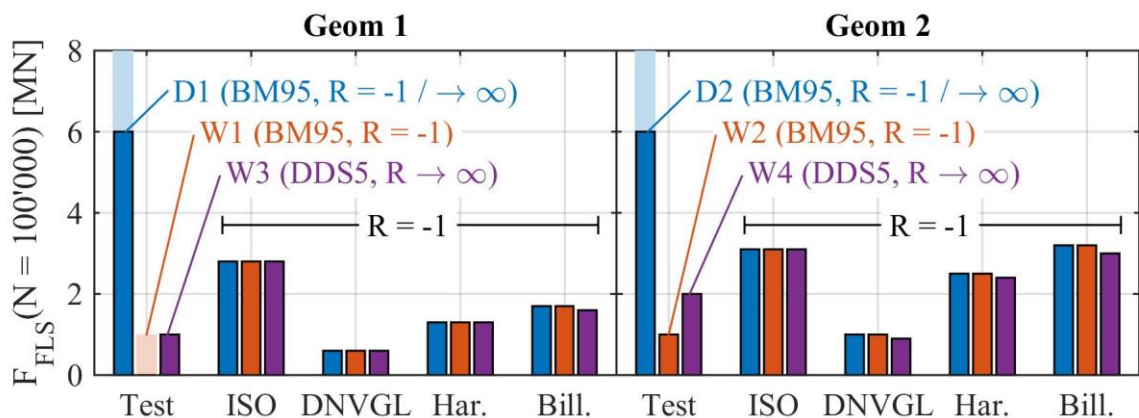


Figure 4.33: Characteristic FLS capacities for the large-scale specimen geometries and grout materials calculated according to current design methods

4.4 Discussion

4.4.1 General remark

In the following Section the degradation behaviour of each individual specimen is elaborated considering the previously described measurement data and damage patterns. An overview of the observed damage modes found in the dismantled specimens is given in Figure 4.34. Afterwards, the influence of specific parameters and boundary conditions is discussed and the test results are compared to current standards.

4.4.2 Degradation behaviour

Specimen W1

The degradation of specimen W1 was governed by grout crushing and flushing of crushed particles in the interface between sleeve and grout (see Figure 4.34, left). This is proven by the widened shear key grooves facing the sleeve, which were found in the dismantled specimen and the grout particle flushing observed during the test (see Section 4.3.3). The final width of the shear key grooves (see Figure 4.30) corresponds to the relative displacement range measured between sleeve and grout (see Figure 4.15).

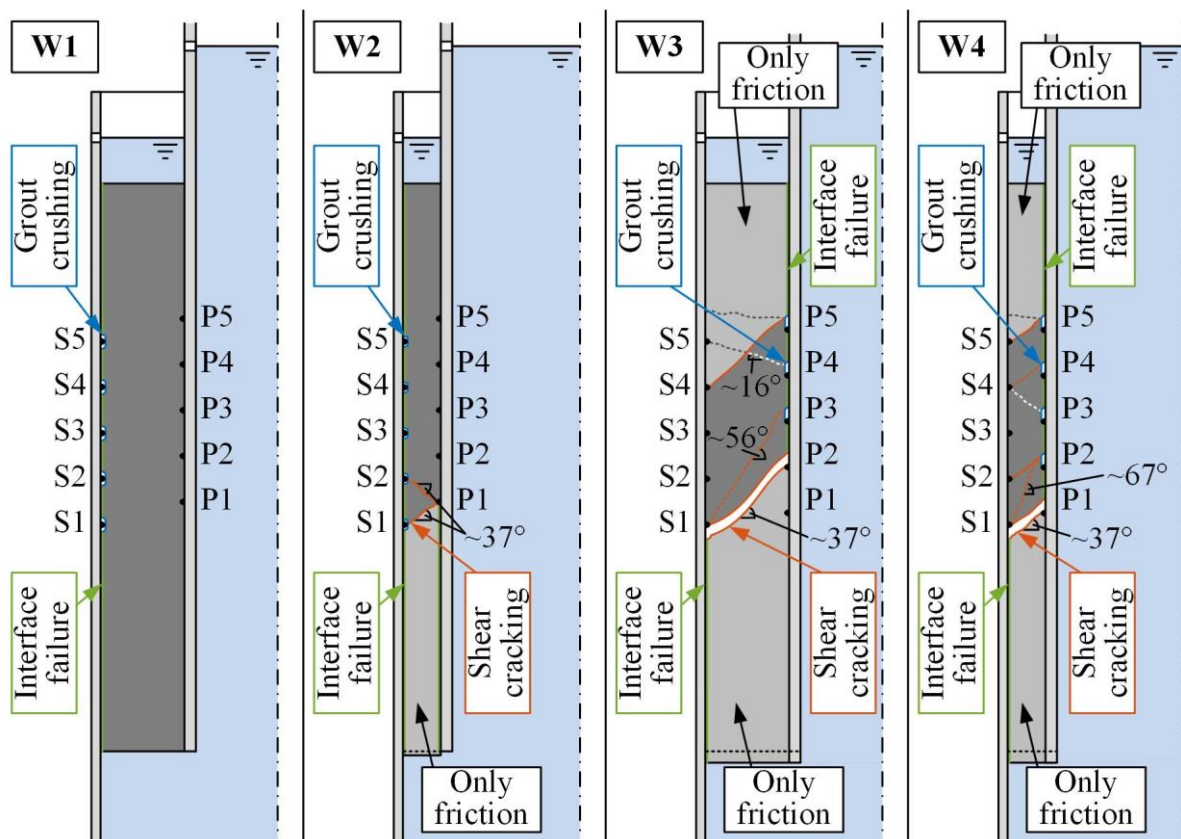


Figure 4.34: Overview of damage modes found in the grout layers of the specimens

Moreover, the relative displacement range corresponds to the width of the bubble in the hysteresis loop shown in Figure 4.20. The fact that the slope of the ends of the hysteresis loops does not change during one load stage in combination with the growing bubble around the zero crossing

leads to the conclusion that the degradation behaviour is primarily a local phenomenon. It occurs around the shear keys, more specifically being caused by the shear keys. The shear key applies its load to the grout via contact pressure. Once the local stresses exceed the grout material's compressive strength, the material is crushed. The crushed particles are then removed and flushed out of the connection by the water which is pumped through the interface due to relative cyclic movements between grout and steel. In case of alternating loads, this crushing process occurs at both sides of a shear key and leads to a connection backlash.

The load transfer between grout and steel is a combination of dominating contact pressure at the loaded shear key surface and, if activatable, additional friction in between the shear keys (see Section 2.3.2). In case of connection backlash and alternating loads, after crossing zero, a reversed load can be transferred only via friction until the shear key is again in contact with the grout surface. Hence, once the stiction capability is exceeded, a load increase causes an accelerated relative movement between grout and steel. The result is a load impulse when the shear key closes contact with the grout. It must be assumed that this impulse increases the grout crushing process. Similar observations were made by other researchers for fatigue tests with alternating loads in dry AC (see Section 2.3.3 and Section 2.3.4). In accordance with this description, the impulse rate derived from the load control curve (see Figure 4.26) shows an increase with a growing amount of connection backlash. Thus, it can be concluded that once the form fitted interlocking between grout and shear key is damaged, the degradation process increases at alternating loads. For a fatigue resistant connection this behaviour must be prevented.

The strain distribution for specimen W1 (see Figure 4.22) is more or less stable. This corresponds to the crack free grout layer (see Figure 4.34, left), which causes an active load transfer via all shear keys. The deviations can be explained by a slightly irregular grout crushing and flushing process.

Specimen W2

For specimen W2 a similar degradation behaviour to specimen W1 can be assumed and proven by the found damage modes (see Figure 4.34, centre left) as well as the measurement data (see Figure 4.14). Different to specimen W1, the large displacement increase started in load stage 2, which can be explained by a higher load bearing capacity of specimen geometry 2.

Furthermore, diagonal shear cracks were found in the dismantled specimen W2 (see Figure 4.34, centre left). The downward pointing shear crack causes a loss of load transfer capability of shear key P1 for compressive loads. However, since the degradation behaviour is localised at the grout-sleeve interface this crack will not significantly influence the degradation behaviour. On the contrary, the upward pointing shear crack deactivates the load transfer capabilities of shear key S1 and S2 for tensile loads. Furthermore, with this crack, for compressive loads, shear key S1 can only be activated via contact pressure in the surfaces of shear crack S2-P1. If the surfaces get worn down by for example circulating water, contact pressure gets uncertain.

The strain distribution of specimen W2 shows no significant redistribution in both load stages (see Figure 4.23). Based on these data, it can be assumed that the cracks evolved in the last phase of load stage 2 and reduced the number of active shear keys. As a result, the load per active shear key

increased and led to a faster degradation. This assumption can be proven by the sudden increase of relative displacement in the last phase of load stage 2 shown in Figure 4.14.

Specimen W3

In specimen W3, the main degradation occurred at the shear key grooves facing the pile in combination with a diagonal shear crack between shear key S1 and P2 (see Figure 4.34, centre right). Before the tests, radial cracks were found which were assigned to autogenous shrinkage (see Section 4.3.1 and Section 4.4.3). The local degradation mechanism around the shear keys can be expected to be similar to the one described for specimen W1.

The diagonal shear crack between shear keys S1 and P2 almost deactivates shear keys P1 and P2 for transferring compressive loads because the lowest grout part can only transfer loads to the sleeve via friction after this crack evolved (see Figure 4.34, centre right). Hence, the load on shear keys P3 to P5 increases. Similar to that, the upper diagonal shear crack deactivates the load transfer capabilities of shear keys S4 and S5. The strain distribution given in Figure 4.24 shows a redistribution of strains in the beginning of the first load stage. The strain gauge at $h = 945$ mm measures a strain reduction to almost zero during the first 40 % of load stage 1. This behaviour can be explained by the occurrence of shear crack S4-P5. The fact that no significant strain difference is measured between the strain gauges at $h = 445$ mm and $h = 545$ mm can be explained by an already fully evolved shear crack S1-P2 in the beginning of load stage 1.

The relative displacement behaviour of specimen W3 (see Figure 4.16) shows a degradation phase during the first 40 % of load stage 1. Afterwards, the displacement behaviour stabilises. Based on the aforementioned cracking behaviour, it can be concluded that the local grout stresses of load stage 1 cause only minor grout crushing in front of the loaded shear key surfaces. Nevertheless, in load stage 2 the relative displacement increases from the beginning and significantly accelerates after about 20 % of load stage 2. This also corresponds to the described cracking behaviour and the reduction of active shear keys on the pile.

As described in Section 4.3.2, a tensile load impulse was accidentally applied to the specimen before the first fatigue load stage due to inconsistencies in the test-rig control system. The horizontal crack starting at shear key P5 as well as the upward pointing diagonal shear crack between shear keys S5 and P4 can be traced back to this tensile load impulse.

Specimen W4

Similar to specimen W3, the degradation of specimen W4 was governed by grout crushing and flushing at shear keys in the pile-grout interface (see Figure 4.34, right), likewise was the cracking behaviour. Even though, the inclination angles of the diagonal shear cracks are similar, the shear key couples involved in individual shear cracks in specimen W4 are different to the ones in specimen W3. As a result, shear crack S1-P1 deactivates only shear key P1 for compressive loads and so does shear crack S5-P5 for shear key S5.

During load stage 1 the relative displacement measurements (see Figure 4.17) as well as the strain distribution along the sleeve (see Figure 4.25) show no considerable change. While the strain

gauge at $h = 945$ mm detects significant strains during load stage 1, almost no strains are measured at this height in load stage 2. This can be explained by the occurrence of shear crack S5-P5, which deactivates shear key S5 for compressive loads (see Figure 4.34, right). Moreover in load stage 2, a slight increase in the relative displacement measurements is visible as well as further strain redistribution from the lower grout area to the upper grout area during the first ~ 40 % of applied load cycles. The redistribution might be explained by the diagonal shear cracks S1-P1 and S2-P2. In load stage 3 the relative displacement measurements show a clear kink at ~ 35 %. Similar to that, a strain redistribution in the area of the lower shear keys is visible leading to more strain at $h = 445$ mm. This might be caused by the diagonal shear crack between shear keys S1-P2. In load stage 4 another kink is visible at ~ 15 % of load cycles in the relative displacement behaviour and afterwards a significant deformation increase occurs. Since several cracks were found in the grout layer of specimen W4 and the measured strain redistributions are not as pronounced as for other specimens, assigning individual cracks to measured events is tainted with some uncertainties.

Particle flushing

In all previously discussed specimens grout particle flushing was observed. As described in Section 4.3.3 the found grout particles can be smaller than $28 \mu\text{m}$, which means they fit through cracks which are hardly visible. Since the grout particles are found in several positions in the specimens and the assumption that particles are also flushed through the plughole, only a qualitative evaluation is possible. The largest amounts of flushed particles are found for specimens W3 and W4 and the smallest amount is found for specimen W2. This corresponds to the measured final relative displacements (see Section 4.3.2) as well as the size ratios of the widened shear key grooves (see Section 4.3.3). Hence, it can be concluded that the major part of flushed grout particles originates from the shear key grooves. The described findings on where the flushed particles are found suggest that grout particles are mainly flushed in the opposite direction of the load.

4.4.3 Influence of autogenous shrinkage

While the mechanical properties of the applied grout materials are almost similar (see Section 4.3.1), the comparison of the specimen test results show a significant difference. The degradation behaviour of specimens W1 and W2 filled with BM95 is located at the shear key grooves facing the sleeve, while the degradation behaviour of specimens W3 and W4 filled with DDS5 is located at the shear key grooves facing the pile. Moreover, specimens W3 and W4 show more diagonal shear cracks but also almost horizontal cracks (see Figure 4.34).

Theoretically, assuming a perfectly form fitted grout layer, one unified shear key geometry and a same number of shear keys on each steel part, the load application surface of the shear keys on the pile is smaller due to the piles smaller diameter. Hence, the grout in front of the loaded shear key surfaces at the pile has to bear higher loads, and as a result the first degradation should occur in this interface. Based on the observed degradation behaviour of specimens W1 and W2 it must be assumed that the load application area of the shear keys on the sleeve of these specimens is smaller than on the pile. A plausible explanation is autogenous shrinkage.

As described in Section 2.4.2 autogenous shrinkage usually occurs in cement based grout materials. During the curing process autogenous shrinkage leads to a reduction of grout volume. As a

consequence, the grout layer shrinks on to the pile and tangential tensile stresses evolve in the grout layer. While these tensile stresses are lower than the grout materials tensile strength, the interface between pile and grout gets pre-stressed and more friction in the areas between the shear keys can be activated and participate in the load transfer. As a result, less stress is localised at the shear keys. Though, at the interface between sleeve and grout, the shrinkage leads to a gap. Thus, no friction can be activated in this interface and the contact area between grout and shear key gets smaller. Once the tangential tensile stresses in the grout layer exceed the grout material's tensile strength, radial cracks evolve and release the pre-stress. Consequently, the grout parts can evenly position in the grout annulus and the load bearing behaviour returns closer to its initial state.

For BM95 the manufacturer states autogenous shrinkage of $<100 \mu\text{m/m}$ (see BASF Construction Chemicals (2010)), while DDS5 shows up to $\sim 147 \mu\text{m/m}$ according to the manufacturer (see ITW Densit ApS (2012)). This ratio can explain the radial cracks that were found in specimens W3 and W4 before the tests and the reason that no radial cracks were found in specimens W1 and W2 (see Section 4.3.1). The fact that segregated grout material full of voids was found below the shear keys of specimen W1 but no grout degradation was observed in these areas (see Figure 4.11, bottom left), suggests the presence of pre-stresses at this interface.

In addition to the radial shrinkage movement, the grout layer also shrinks in axial direction. This movement is impeded by the shear keys. Thus, in front of the shear key tips tensile stresses must be expected which might cause a pre-cracked state solely from autogenous shrinkage. This explains why the grout layer of specimens W3 and W4 filled with DDS5 was more likely to crack.

As a result, autogenous shrinkage significantly influences the load bearing behaviour of a grouted connection by means of form-fitted interlocking between steel and grout, pre-stressing of the pile-grout interface as well as possible pre-cracking.

4.4.4 Influence of the initial grout state

In the previous Section, autogenous shrinkage is esteemed to have a major influence on the load bearing behaviour of grouted connections and consequently on their degradation behaviour. Additionally, during production of specimen W1 a less favourable behaviour of the fresh grout material was observed (see Section 4.3.1). In accordance to this behaviour, the final grout layer of the dismantled specimen showed material related deficits. However, neither the final mechanical grout material properties nor the specimen's degradation behaviour shows weaknesses which can clearly be attributed to these material deficits. In case of the material segregation found below the shear keys on the pile surface, the autogenous shrinkage related pre-stressing of this interface is beneficiary (see Section 4.4.3). For the sleeve interface, no segregation could be attested. Though, it has to be kept in mind that areas of segregated material around the shear keys could have been fully removed by the connection's degradation behaviour.

While other researchers observed crack growth and crack surface deterioration due to water being pumped through the crack (see Section 2.4.1), the weak surfaces found in specimen W1, which can be classified as initial cracks, showed no considerable interaction with water or abrasive wear. This leads to the assumption that the influence of surrounding water is only significant in areas of high stresses in the grout layer.

Thus, a general statement on the influence of the initial grout state is not possible. Of course, in the highly stressed areas around the shear keys, the grout material should be free of deficits.

4.4.5 Influence of the grout layer thickness

Theoretically a grouted connection with a thicker grout layer can be expected to have a lower axial stiffness because a thicker grout layer can bear higher shear deformation at an equal stress state. The secant stiffnesses, derived from the relative displacement measurements (see Table 4.4), confirm this presumption. Yet, this cannot explain a higher load bearing or fatigue capacity of a thinner grout layer. Based on the observed degradation behaviour, additional influences of the grout layer thickness must be assumed. For a more specific evaluation it is necessary to differentiate the observed specimen behaviour for each grout material.

For specimens W1 and W2 filled with BM95, assumably a major influence for the degradation behaviour was the initial grout layer deformation caused by autogenous shrinkage (see Section 4.4.3). Since the sleeve geometry is identical for both grout layer thicknesses, the stresses in the grout-sleeve interface can be presumed identical. Yet, the autogenous shrinkage deformation in radial direction can be assumed to be smaller for the thinner grout layer of specimen W2. Thus, for this specimen a larger contact area between shear keys and grout at the sleeve surface can be expected, which leads to lower stresses in front of the loaded shear key surfaces. This can explain the higher load bearing and fatigue capacity observed for specimen W2 compared to specimen W1.

The DDS5 filled specimens W3 and W4 not only showed local crushing but also significant shear cracking. As described in Section 4.4.2, the diagonal shear cracks deactivate shear keys on the pile for transfer of compressive loads. For the thicker grout layer two of five shear keys are deactivated by the lowest diagonal shear crack, while for the thinner grout layer the lowest crack deactivates only one of five shear keys. Moreover, as described in Section 4.4.3, the autogenous shrinkage behaviour of DDS5 can be expected to cause initial cracking at the shear key tips and consequently crack growth at lower load stages than for specimens W1 and W2. Therefore, once the diagonal shear cracks are evolved and deactivated certain shear keys (see Section 4.4.2), the load per active shear key increases. The larger number of active shear keys in the thicker grout layer of specimen W4 explains the specimen's higher load bearing and fatigue capacity compared to specimen W3. However, this particular behaviour is caused by the specific shear key arrangement of the used specimens and is not generally valid for the influence of the grout layer thickness in grouted connections. In future investigations on influences of the grout layer thickness, the shear key spacing should be related to the grout layer thickness.

4.4.6 Influence of the ambient condition (AC)

A comparison of the relative displacement measurements of specimens W1 (see Figure 4.13) and W2 (see Figure 4.14) to the corresponding specimens D1 and D2 tested by Bechtel (2016) in dry AC, shows a significant increase of relative displacement at identical load levels in wet AC tests. Furthermore, the wet AC test specimens were declared to have failed in earlier load stages due to large relative displacements between pile and sleeve. In contrast to that, the dry AC specimens showed an almost constant load displacement behaviour (see Figure 4.13 and Figure 4.14) and

failed with a sudden loss of load bearing capacity (see Bechtel (2016)). Thus, it can be concluded that the fatigue capacity of grouted connections in wet AC is significantly lower than in dry AC.

As described beforehand the degradation behaviour in wet AC is mainly a combination of grout crushing and flushing of crushed grout particles by water. Bechtel (2016) as well as others (see Section 2.3.3) found crushed grout in front of the loaded shear key surfaces of specimens tested in dry AC. Thus, since these particles are held in place by the surrounding grout, they could still participate in the load transfer mechanism. Hence, the major influence of wet AC, which can be proven by the large-scale fatigue tests, is grout particle flushing due to water being pumped through the steel-grout interfaces.

Additional influences of water described by other researchers (see Section 2.4.1) such as grout spalling due to water ingress in the boundary layer, might also be valid for the large-scale specimens. However, proving this behaviour with the presented measurement data (see Section 4.3.2) and damage patterns (see Section 4.3.3) is not possible.

In order to design a fatigue resistant grouted connection for application in wet AC, the following two solutions are possible. The first solution is to seal the connection against water and thus inhibit the pumping process. This will enable to benefit from the aforementioned high structural capacities in dry AC. However, finding an appropriate sealing system and prove its long-term reliability will be challenging. And the second solution is a reduction of permissible fatigue loads to prevent local grout crushing.

4.4.7 Influence of the loading scenario

Specimens W1 and W2 were loaded with alternating loads with a load ratio of $R = -1$ (see Figure 4.5). In contrast to that, specimens W3 and W4 were loaded with pure compressive loads of $R \rightarrow \infty$.

The pure compressive load (specimens W3, W4) caused a downward relative movement between pile and grout (see Figure 4.16 and Figure 4.17) and widening of the shear key grooves (see Figure 4.34). This degradation behaviour can be evaluated as indulgent, since it does not lead to a sudden failure of the whole connection nor to a large relative displacement range.

For alternating loads (specimens W1, W2) a different behaviour was observed. As described in detail for specimen W1 (see Section 4.4.2), the widening of the shear key grooves leads to a connection backlash and hence an instable load bearing behaviour with large relative displacement ranges (see Figure 4.16). Moreover, the impulsive contact closure between shear key and grout after load reversal, accelerates the degradation behaviour significantly. This behaviour is unfavourable for a support structure and must be prevented.

Finally, when considering autogenous shrinkage effects as well as possible grout deformations caused by early age movements, an initial connection backlash is likely to be expected. As a result, it is recommended to limit the fatigue relevant loads to pure compressive or pure tensile loads.

4.4.8 Termination criteria (TC) for FLS tests

Fatigue tests, carried out on grout material cubes, are usually terminated by bursting specimens which are no longer able to carry the applied load, thus the TC for the test is obvious. In the small-scale tests (see Chapter 3.5.2) a similarly definite behaviour was observed for specimens tested in wet AC at high load levels. In contrast to that, for low load levels the small-scale specimens showed a downslide behaviour with sustained load bearing capacity, which was likewise observed for the large-scale specimens W3 and W4 tested in wet AC. To compare these results to S-N-curves a suitable TC needs to be defined.

Based on the degradation behaviour observed in the four large-scale tests and in the tests from Bechtel (2016) (see Section 4.4.6), a fatigue failure should not only be defined as a loss of load bearing capacity but also as a loss of elastic structural behaviour. Thus, increasing relative displacements between grout and steel, as they were measured in all fatigue tests from a certain load stage on, should not be permissible for a fatigue safe grouted connection. As elaborated in Section 4.4.2, the relative displacement is mainly caused by grout crushing in front of the loaded shear key surfaces and removal of the crushed particles by water being pumped through the interface, leading to a widened shear key groove. For pure compressive or pure tensile loads a certain relative displacement might be acceptable but the damage caused by alternating loads will significantly increase with any widening of the shear key groove. Hence, if alternating loads cannot be excluded from acting on the connection, no degradation of the shear key groove should be permissible. Yet, if loads can be limited to pure compression or pure tension, the allowable size of relative displacement depends on the global support structure and its load bearing behaviour. This corresponds to the recommendation given in Section 4.4.7.

For the presented results, the approach of evaluating the linear regression slope for both mean deformation and deformation range as described in Section 4.3.2 is an adequate measure to define failure. The corresponding results are given in Table 4.2. However, a sufficient period of time has to be measured for this approach.

4.4.9 Applicability of analytical design approaches

The comparison of geometrical parameters to real-scale reference structures given in Table 4.5 shows a good agreement regarding diameters, slendernesses and shear key arrangements. Hence, the large-scale specimens can be classified as being to scale to real-scale connections. Moreover, the comparison of geometrical parameters to the ranges of applicability for current design approaches shows the same exceeding parameters for both large- and real-scale connections.

For the large-scale specimens no ULS tests were carried out. Nevertheless, it can be expected that the connections' actual ULS capacities are above the highest loads applied in the FLS load scenarios (see Figure 4.5). The dry AC tests from Bechtel (2016) were carried out up to 8 MN compressive load, which is in the range of the ULS capacity calculated according to DIN EN ISO 19902 (2014) for geometry 1 (see Figure 4.32). Moreover, the calculations show a higher ULS capacity for the thinner grout layer, which corresponds to the FLS test results (see Section 4.4.5). Based on these results, it can be assumed that both ULS design approaches according to DIN

EN ISO 19902 (2014) and DNVGL-ST-0126 (2016) give good results for the investigated geometries. However, the difference to the actual ULS capacities cannot be evaluated.

Contrary to the ULS capacities, only the FLS results calculated according to the DNVGL-ST-0126 (2016) approach are in good agreement with the wet AC test results. But it has to be kept in mind that the calculations do not include sequence effects and that they represent only one point on the S-N curve. Consequently, the FLS design approaches cannot be validated.

4.5 Summary and conclusion

In a series of four fatigue tests carried out in wet ambient conditions the influence of surrounding water on the fatigue behaviour of grouted connections was investigated. Two large-scale specimen geometries with different grout layer thickness were used. The specimens' geometries were to scale to real-scale reference grouted connections. Besides the varying geometries, two different grout materials as well as two different loading scenarios were investigated. Results of two comparable large-scale specimens tested in dry ambient conditions were taken from the literature.

The described findings lead to the conclusion that the fatigue behaviour of the large-scale specimens tested in wet AC was governed by the combination of grout crushing in front of the loaded shear key surfaces and flushing of crushed grout particles out of the connection by water pumped through the steel-grout interface. Diagonal shear cracking was important in cases where it reduced the number of active shear keys and thus influenced the load per shear key. Moreover, autogenous shrinkage influenced the initial grout layer shape at the beginning of loading and hence the interlocking between steel and grout as well as the initial cracking state of the grout layer. This led to a significantly lower fatigue capacity.

For the investigation parameters defined prior to the test, the following conclusions were made.

- **Ambient condition (AC)**

The comparison between four wet AC fatigue tests and two dry AC tests showed a significant reduction of endurable load cycles in wet AC. This corresponded to the expectations and the results from the small-scale tests. Main degradation mechanism in the large-scale specimens was the previously described combination of grout crushing and particle flushing as well as shear cracking.

- **Loading scenario**

Two different loading scenarios with alternating ($R = -1$) and pure compressive ($R \rightarrow \infty$) loading levels were applied to the specimens. As expected a higher loading level led to increased degradation in wet AC. Alternating loads showed a significantly worse damage behaviour than pure compressive loads due to connection backlash and resulting impulse loading on the shear key grooves.

- **Grout layer thickness**

Two different grout layer thicknesses were investigated. As expected the thicker grout layer led to larger grout deformations and hence a lower specimen's stiffness. Moreover, the results showed a lower fatigue capacity for the specimens with thicker grout layer. This

corresponded to the expectations and the results from the small-scale tests. Main reason for this behaviour was diagonal shear cracking and the resulting number of active shear keys participating in the load transfer.

- **Grout material**

Two grout materials with comparable mechanical properties were used for each specimen geometry. Unlikely, the materials led to significantly different degradation behaviour. Owing to different autogenous shrinkage behaviour, the initial grout layer deformations were different and caused damage in different grout-steel interfaces. It is concluded that autogenous shrinkage should be considered in the design approach.

- **Degradation behaviour**

After the fatigue tests were finished, the specimens were dismantled and the damage patterns of the grout layer were analysed. The described findings led to the conclusion that the fatigue behaviour of the large-scale specimens tested in wet AC was governed by a combination of grout crushing in front of the loaded shear key surfaces and flushing of the crushed grout particles due to water being pumped through the grout-steel interfaces. Diagonal shear cracking was important in cases where it reduced the number of active shear keys and therefore increased the load per active shear key.

- **Termination criterion (TC)**

As expected from the results of the small-scale tests, the large-scale fatigue tests carried out in wet AC did not lose their load bearing capacity but showed large relative displacements in the degraded grout-steel interface. Additionally, for alternating loads a growing connection backlash was observed. Consequently, failure of the connection due to alternating loads was defined as an increasing relative displacement range between steel and grout and for pure compressive loads as an increasing relative displacement between steel and grout. For real applications alternating loads shall be excluded and the permissible relative displacement due to degradation shall be defined from a holistic support structure analysis.

5 Numerical Investigations

5.1 Introduction

With the small-scale (see Chapter 3) and large-scale tests (see Chapter 4) for the first time load bearing and degradation behaviour of grouted connections in wet ambient conditions (AC) was investigated experimentally. The numerical investigations described in this Chapter were performed to generate more information for understanding and explaining the observed behaviour and develop a fatigue verification approach for grouted connections located in wet AC. Therefore, the following investigations were carried out in the scope of this thesis:

- **Development and validation of numerical models**
First of all numerical models for the various specimen geometries had to be implemented. According to the state of the art (see Section 2.7), several approaches with different grades of detail regarding the geometry, the material models and the numerical mesh are possible. Objective was to develop models which were able to show detailed local stress states and give a good representation of the grout material's brittle behaviour.
- **Influence of autogenous shrinkage**
Based on both, measurement data as well as damage patterns found in the large-scale experiments (see Chapter 4), a significant influence of autogenous shrinkage on the load bearing and degradation behaviour of grouted connections was assumed. Numerical investigations with different rates of autogenous shrinkage were carried out to clarify this influence.
- **Influence of cracks**
To investigate the influence of cracks on the load bearing and degradation behaviour of grouted connections two different approaches were combined. Generally, for the grout layer a material model, capable of tensile cracking, was chosen. In addition, investigations with discretely modelled cracks, based on the damage patterns found in the experiments (see Section 3.5.3 and Section 4.3.3), were carried out and compared to the experimental results.
- **Development and validation of a fatigue verification approach for wet AC**
Based on the hypothesis that local grout crushing in front of the loaded shear key surfaces must be prevented in order to exclude the main influence of water on the fatigue behaviour of grouted connections in wet AC, a fatigue verification approach was developed. Afterwards, this approach was applied to the various small- and large-scale specimen geometries and validated by comparison to the experimental results (see Chapter 3 and Chapter 4).

5.2 General approach

5.2.1 General remark

The numerical models of small- and large-scale specimens differ in regard to their geometry, their applied load and the data used for evaluation. Thus, a summarised description of the general numerical modelling approach is given in the following. For the simulations the commercial finite element software Abaqus/CAE 2016 was used.

5.2.2 Numerical models

Geometry

Both small- and large-scale specimens are rotationally symmetric with respect to their geometry as well as their loading and boundary conditions. Thus, the numerical models were reduced to a two-dimensional cutting plane with rotational symmetric boundary conditions, which reduced the numerical effort substantially (see Figure 5.1).

Both steel tubes were modelled with extensions from the grout layer in order to exclude influences of boundary conditions from the grout area. As described before, the local stress state at the shear keys is decisive for the fatigue behaviour of grouted connections. Hence, the shear keys were geometrically modelled with idealised shapes to cover the local behaviour following the numerical approaches of Lochte-Holtgreven (2013) and Bechtel (2016) (see Section 2.7.3).

Interaction

In both grout-steel interfaces, surface-to-surface contact interaction was applied. The contact behaviour in normal direction was defined as hard contact allowing no penetration of the contact surfaces but separation after contact closure. In tangential direction the contact behaviour was defined as Coulomb friction with a friction coefficient μ and a penalty contact algorithm.

In recently performed numerical investigations on grouted connections a friction coefficient of $\mu = 0.4$ was commonly used. This value was proven by experimental investigations of Fehling (1990) and Lotsberg et al. (2013) and was recommended in the DNV-OS-J101 standard until 2013. Wilke (2014) found the best accordance between numerical simulations and experimental data for $\mu = 0.56$. In the latest version of DNVGL-ST-0126 (2016) a friction coefficient of $\mu = 0.7$ is recommended. For hydro lubricated grout-steel interfaces also Dallyn et al. (2016) observed a friction coefficient of $\mu = 0.7$. However, it can be expected that water in the grout-steel interface reduces friction and moreover in both, dry and wet ambient conditions, friction is reduced over time due to abrasion and wear (see e.g., Schaumann et al. (2013)). Hence, if not stated otherwise a friction coefficient of $\mu = 0.4$ was used in the numerical simulations.

Mesh

All parts of the numerical model were meshed with predominantly quadrilateral stress elements with linear integration order and axisymmetric stress formulation (CAX4). In areas where triangular shaped elements were needed, CAX3 elements were used. Reduced integration elements

were not used because, despite activated hourglass control, this element type led to severe hourglassing in the contact areas. The size of the elements was investigated for each geometry in a sensitivity study.

Boundary conditions

The lower end of the sleeve was fixed in axial direction. The rotational symmetric boundary conditions were included in the chosen element type.

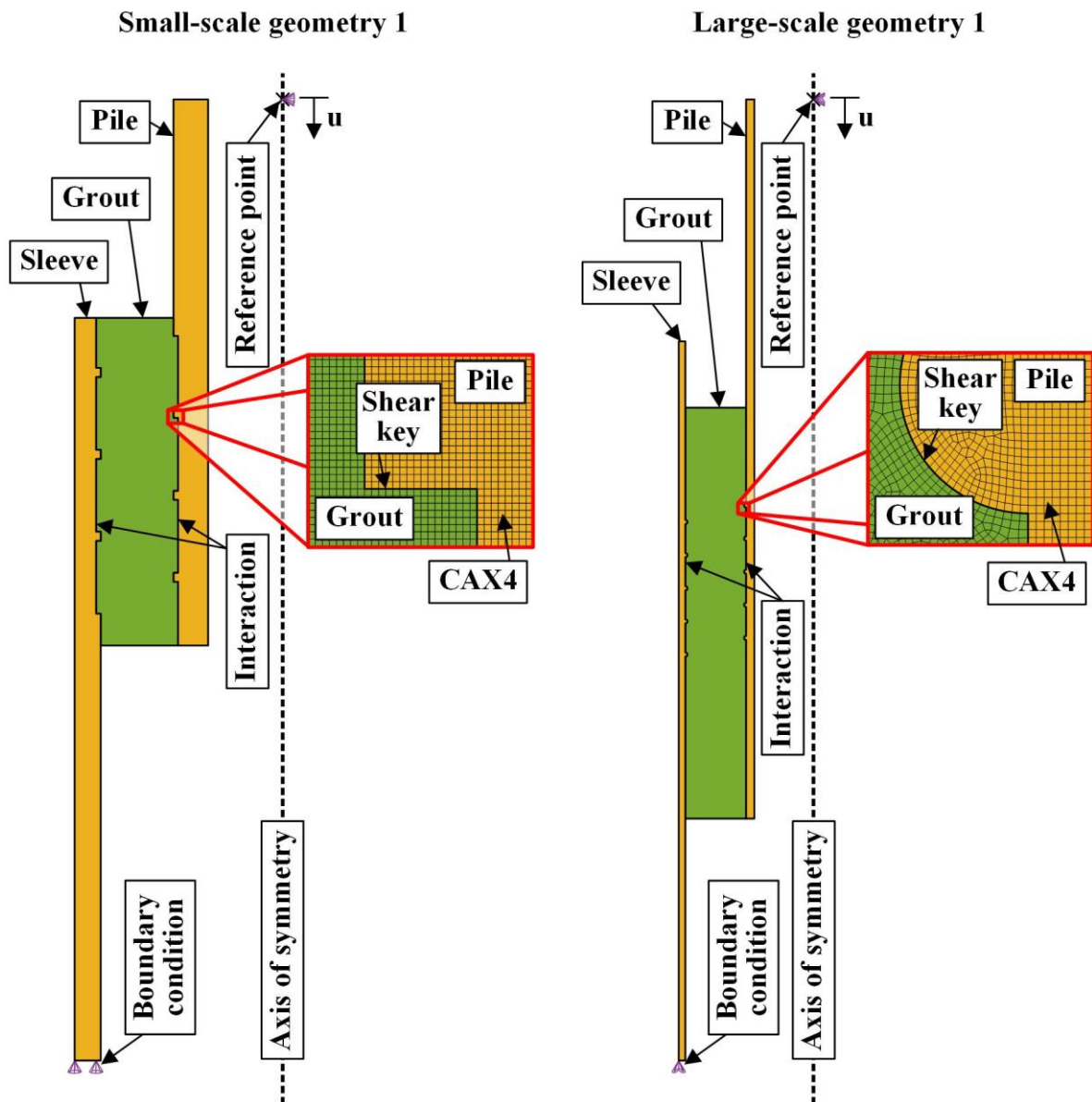


Figure 5.1: Rotational symmetric finite element models of small- and large-scale specimens with geometry 1

Loading

The upper end of the pile was connected to a reference point on the centre axis via multi point constraints with beam characteristics (see Figure 5.1). During the calculation, the reference point

was incrementally displaced. The calculated reaction force of the reference point corresponds to the force applied via the test rig in the experiments.

5.2.3 Material models

Grout

General remark

The grout material was modelled using the Concrete Damaged Plasticity (CDP) material model available in the Abaqus finite-element software. In the following Section, the material law is introduced, the necessary material parameters are described and ways to estimate reasonable parameter values are shown.

Elastic behaviour

The elastic behaviour was defined by elastic modulus E and Poisson's ratio ν . For both parameters values were provided by the material manufacturers. Moreover, the elastic modulus was also obtained in material tests accompanying both small- and large-scale tests (see Section 3.3 and Section 4.3.1).

When actual data were not available, Equation (5.1) from MC2010 (2013) was used to estimate the Poisson ratio.

$$\nu = 0.20 \quad (5.1)$$

To calculate the elastic modulus from the material's mean compressive strength f_{cm} , Equation (5.2) is given in MC2010 (2013). In this Equation a factor α_E for the effect of different types of aggregates is included, which is in the range of 0.7 and 1.2. For the measured material properties a mean $\alpha_E \sim 0.9$ gave the best compliance.

$$E_{ci} = 21'500 \cdot \alpha_E \cdot \left(\frac{f_{cm}}{10} \right)^{1/3} \quad (5.2)$$

where:

α_E	factor for effect of types of aggregate
$f_{cm} = f_{ck} + \Delta f = f_{ck} + 8$	mean compressive strength
f_{ck}	characteristic compressive strength

Compressive behaviour

Figure 5.2 shows a schematic stress-strain relation with stresses normalised to the mean compressive strength f_{cm} . The dotted line represents a linear elastic behaviour defined by the mean elastic modulus E_{cm} while the black curve represents the total strain ϵ_c according to Equation (5.3) from MC2010 (2013). For the CDP definition in Abaqus the inelastic uniaxial stress-strain relation is needed, which is the difference between elastic and total strain (see Equation (5.3)).

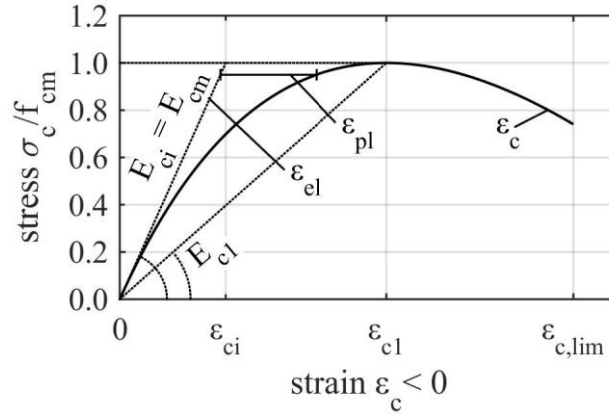


Figure 5.2: Schematic uniaxial stress-strain relation acc. to MC2010 (2013)

$$\varepsilon_c = \varepsilon_{el} + \varepsilon_{pl} \quad (5.3)$$

$$\frac{\sigma_c}{f_{cm}} = - \left(\frac{k \cdot \eta - \eta^2}{1 + (k-2) \cdot \eta} \right) \quad (5.4)$$

where:

σ_c compressive stress

$\eta = \frac{\varepsilon_c}{\varepsilon_{c1}}$ normalised strain

$k = \frac{E_{ci}}{E_{c1}}$ plasticity number

Tensile behaviour

The tensile behaviour in CDP is described by the mean tensile strength f_{ctm} and the subsequent crack opening width w . As Figure 5.3 shows, the crack opening is defined as ratio between tensile cracking energy G_F and mean tensile strength f_{ctm} . According to MC2010 (2013) the cracking energy can be calculated with Equation (5.5).

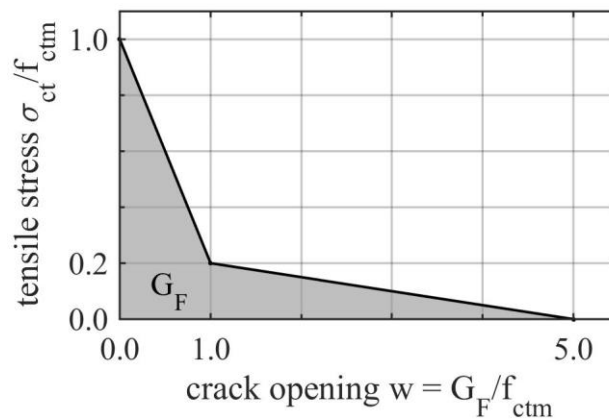


Figure 5.3: Stress-crack opening relation for uniaxial tension acc. to MC2010 (2013)

$$G_F = 0.073 \cdot f_{cm}^{0.18} \quad (5.5)$$

If the mean tensile strength of a grout material is not provided by the manufacturer or available from tests, Equation (5.6) from MC2010 (2013) can be used.

$$f_{ctm} = \begin{cases} 0.3 \cdot (f_{cm} - 8)^{2/3} & \text{if } f_{cm} \leq 58.0 \text{ N/mm}^2 \\ 2.12 \cdot \ln(1 + 0.1 \cdot f_{cm}) & \text{if } f_{cm} > 58.0 \text{ N/mm}^2 \end{cases} \quad (5.6)$$

In cases where only flexural tensile strength values are available $f_{ctm,fl}$ can be transferred into f_{ctm} via Equation (5.11).

$$f_{ctm} = \alpha_{fl} \cdot f_{ctm,fl} \quad (5.7)$$

where:

$$\alpha_{fl} = \frac{0.06 \cdot h_b^{0.7}}{1 + 0.06 \cdot h_b^{0.7}} \quad \text{conversion factor}$$

$$h_b \quad \text{prism depth in mm}$$

Yield surface

The aforementioned compressive and tensile material behaviour is valid for uniaxial loading conditions. The spatial elastic material behaviour of CDP is described by a yield surface according to Lubliner et al. (1989) given in Equation (5.8).

$$F(\boldsymbol{\sigma}) = \frac{1}{1-\alpha} \cdot \left(\sqrt{3 \cdot J_2} - \alpha \cdot I_1 + \beta \cdot \langle \sigma_{\max} \rangle - \gamma \cdot \langle -\sigma_{\max} \rangle \right) \quad (5.8)$$

where:

$$\alpha = \frac{f_{b0}/f_{c0} - 1}{2 \cdot f_{b0}/f_{c0} - 1}$$

$$\beta = \frac{f_{c0}}{f_{t0}} \cdot (1 - \alpha) - (1 + \alpha)$$

$$\gamma = \frac{3 \cdot (1 - K_c)}{2 \cdot K_c - 1}$$

$$\langle \hat{\sigma}_{\max} \rangle = \frac{1}{2} \cdot \left(\left| \hat{\sigma}_{\max} \right| + \hat{\sigma}_{\max} \right) \quad \text{Macauley-bracket}$$

Moreover, in the Abaqus implementation of CDP, the uniaxial strength values f_{c0} and f_{t0} are defined as functions of plastic strains, using the previously described uniaxial compressive and tensile stress-strain relations.

To define the yield surface the biaxial to uniaxial compressive strength ratio f_{b0}/f_{c0} as well as the shape parameter K_c must be set. If no plastic strains are defined, f_{b0}/f_{c0} corresponds to the biaxial compressive strength f_{2c} as defined in MC2010 (2013). Figure 5.4 shows the Lubliner et al. (1989) yield surface with two different parameter sets for f_{2c} and K_c and without plastic strains. A smaller K_c value allows higher deviatoric stresses at predominantly uniaxial loading states and equal hydrostatic stress level (see Figure 5.4, top left). This behaviour is typical for brittle materials. While

Lubliner et al. (1989) recommend a value of $K_c = 2/3$ for concrete, Speck (2008) recommends values < 0.5 for UHPC. In the Abaqus implementation K_c must be greater 0.5 because the concave yield surface cannot be solved by the used numerical implementation. For f_{t0}/f_{c0} Dahl (1992) recommends a value of 1.16 for normal concrete while Speck (2008) found values of 1.09 for concrete class C70/85 and higher.

Due to the Macaulay-bracket operation the parameter β is active in the mixed and pure tensile stress domain while γ is active only in the tri-axial compression domain. Hence, the parameter K_c influences only the shape of the yield surface in tri-axial compression. As described in Section 5.2.4 the chosen calculation approach includes the initial yield surface state. Since the acceptable fatigue stresses are limited to values according to Equation (5.8), stress states close to the yield surface will not be reached. As a result, the influence of K_c and f_{t0}/f_{c0} seems negligible. Nevertheless, sensitivity studies were carried out on both parameters (see Section 5.3.1).

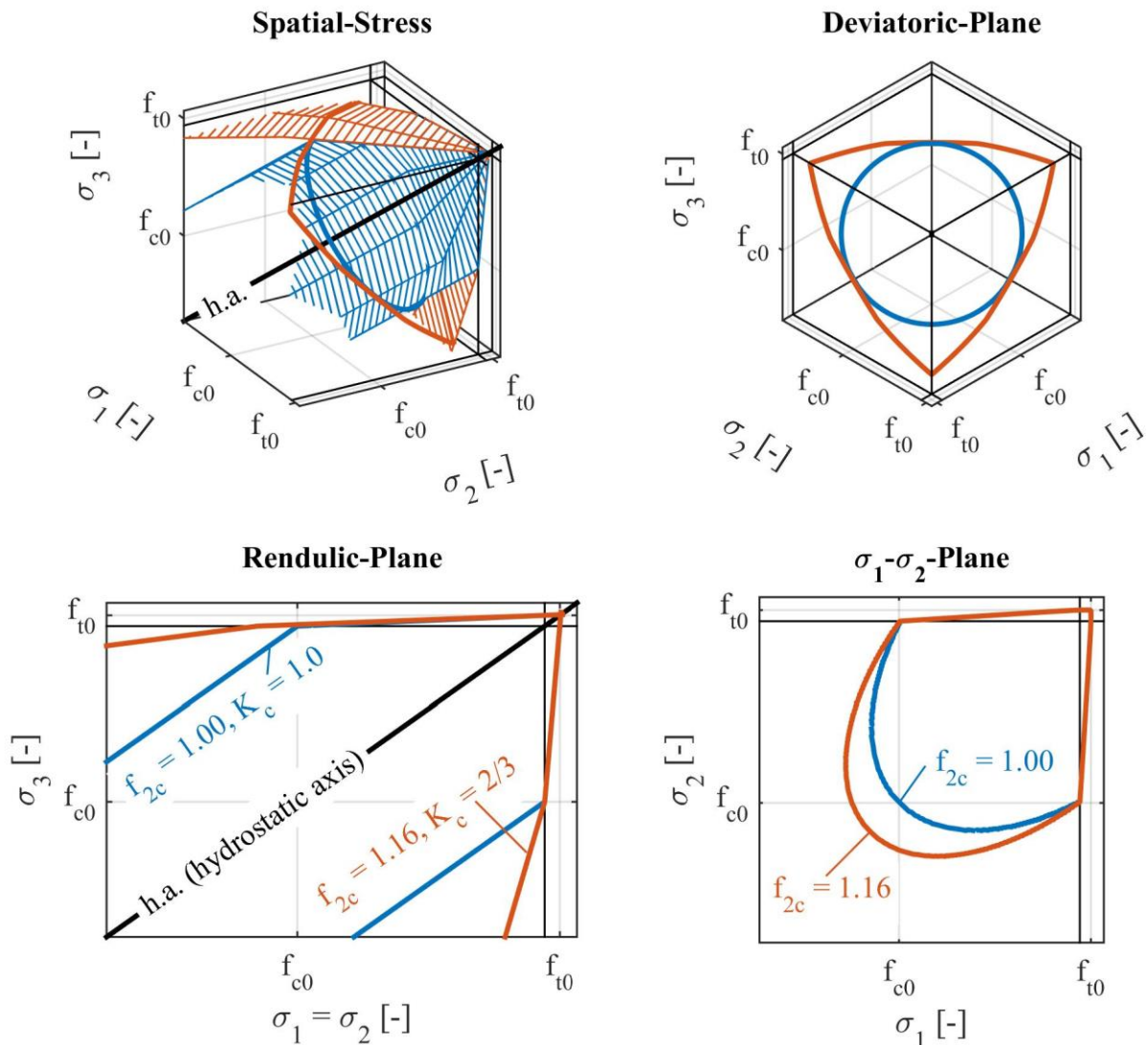


Figure 5.4: Concrete damaged plasticity yield surfaces according to Lubliner et al. (1989) with different parameter sets and no plastic strains

Flow potential

Lee & Fenves (1998) extended the yield criterion of Lubliner et al. (1989) (Equation (5.8)) with a plastic flow potential given in Equation (5.9) and Equation (5.10). The flow potential is described as a hyperbolic Drucker-Prager yield surface and is represented in Figure 5.5.

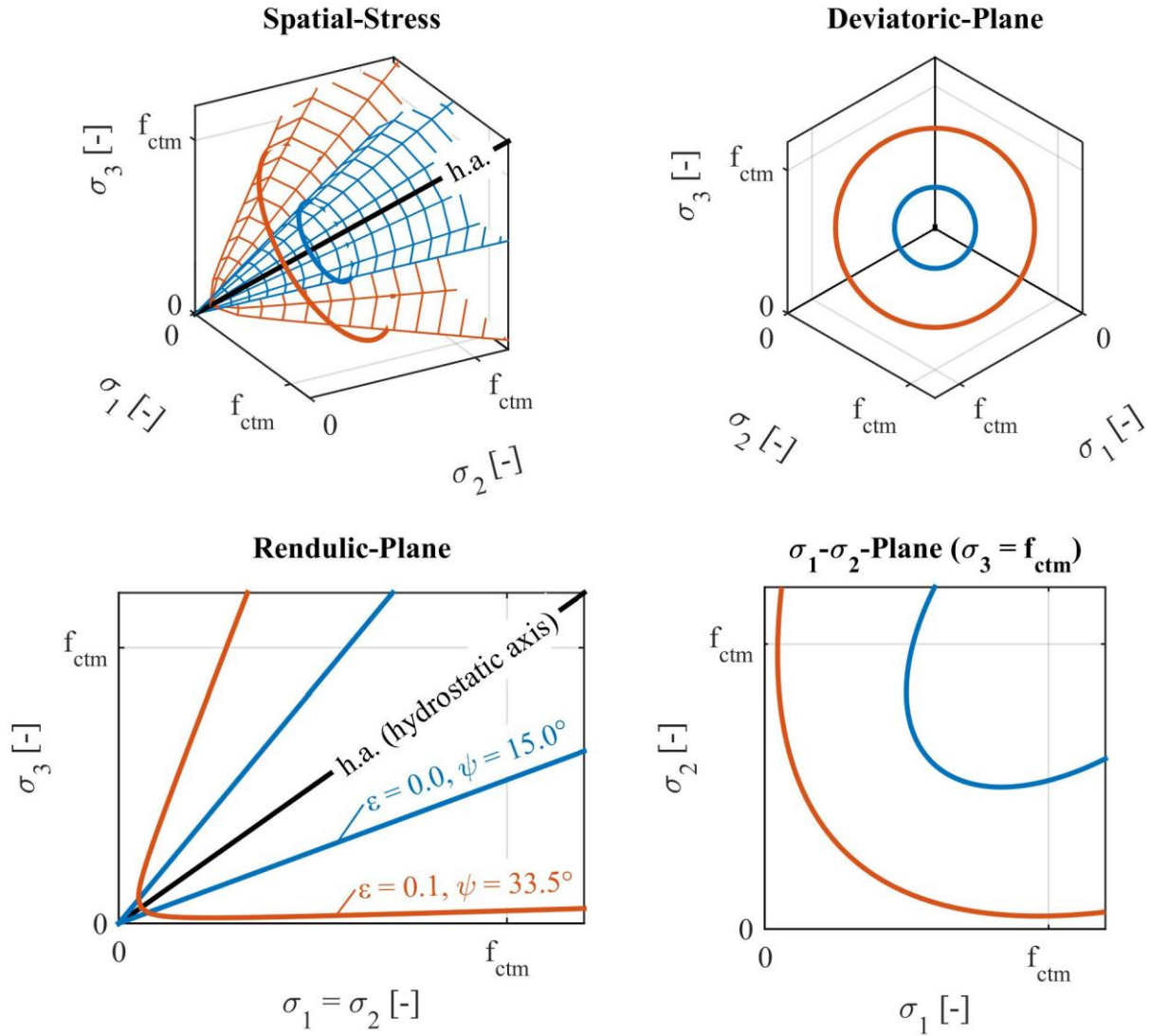


Figure 5.5: Concrete damaged plasticity flow potential according to Lee & Fenves (1998) with two different parameter sets

$$\dot{\varepsilon}_{pl} = \dot{\lambda} \cdot \frac{\partial G(\bar{\sigma})}{\partial \bar{\sigma}} \quad (5.9)$$

$$G = \sqrt{(\varepsilon \cdot f_{ctm} \cdot \tan(\psi))^2 + \rho^2} - \xi \cdot \tan(\psi) \quad (5.10)$$

where:

- ψ dilatancy angle
- ε eccentricity

The dilatancy angle ψ shapes the width of the flow potential and is a measure for the material's volumetric change after cracking. Oñate et al. (1988) recommend values of $8^\circ \leq \psi \leq 15^\circ$ for normal concrete. For the eccentricity a default value of 0.1 is recommended (Dassault Systèmes (2015)). Since the flow potential influences the material behaviour after tensile cracking, both parameters ψ and ε must be chosen with care. A sensitivity study was carried out for both parameters (see Section 5.3.1).

Viscoplastic regularization

Since the tensile cracking behaviour or more precisely the viscous flow of cracked elements is highly local, singularities in the numerical model can occur and cause convergence problems. Hence, the CDP formulation also includes a viscoplastic regularization parameter μ whose effect is described in Equation (5.11). This parameter allows crack induced viscoplasticity to spread over a larger area and smoothen the numerical singularity. Starting with $\mu = 1e-6$ this value was incrementally increased until convergence of the individual calculation was possible.

$$\dot{\varepsilon}_v^{pl} = \frac{1}{\mu} (\varepsilon^{pl} - \varepsilon_v^{pl}) \quad (5.11)$$

Expansion

In order to investigate autogenous shrinkage behaviour, equivalent thermal loads were applied to the grout layer. The grout material's thermal expansion behaviour was described with a thermal expansion coefficient α_T according to Equation (5.12). Since this value is just a tool for numerical purposes a further look on influences of moisture on this parameter was neglected.

$$\alpha_T = 10 \cdot 10^{-6} \text{ 1/K} \quad (5.12)$$

Table 5.1: Used material parameters for grout

	Small-scale		Large-Scale				
	DDS2	BM95	W1 BM95	W2	W3 DDS5	W4	
f_{cm} [N/mm ²]	116.3	143.0	140.3	151.9	143.4	141.9	Exp
$f_{ctm,fl}$ [N/mm ²]	13.0	16.4	18.4	18.6	17.7	14.0	Exp
f_{ctm} [N/mm ²]	5.8	7.3	8.1	8.2	7.8	6.2	MC
E_{cm} [N/mm ²]	43'567	51'000	44'133	44'133	46'066	45'245	Exp
ν_c [-]	0.18	0.20	0.20	0.20	0.19	0.19	Man / MC
G_F [N/mm]	0.172	0.179	0.179	0.179	0.178	0.178	MC
ψ [-]	33.5						
ε [-]	0.1						
f_{b0}/f_{c0} [-]	1.16						
K_c [-]	0.667						

Summary

With the priorly described set of Equations from MC2010 (2013), it is possible to estimate all necessary material parameters for the uniaxial definition of the CDP material model from the grout

material's compressive strength f_{cm} . All chosen material parameters are summarised in Table 5.1. If possible, the parameters were obtained from experimental data (Exp). Otherwise, they were taken from manufacturers' data sheets (Man) or calculated with MC2010 (2013) equations (MC) as described before. CDP specific parameters were investigated in sensitivity studies (see Section 5.3.1).

Steel

For the steel parts two different material models were investigated. The first one was purely elastic, just considering the elastic modulus E and Poisson ratio ν . The second one was a bilinear material model with kinematic hardening, also considering the yield stress f_y and a hardening modulus H (see Table 5.2). Sensitivity studies showed that in the range of permissible fatigue stresses in the grout, plastic strains in the steel parts are negligible. Hence, only the linear elastic material model was used for further investigations.

Table 5.2: Used material parameters for steel

E [N/mm ²]	210'000.0
ν [-]	0.3
f_y [N/mm ²]	355.0
H [N/mm ²]	21'000.0

5.2.4 Calculation procedures

General remark

The calculations were carried out displacement controlled with incremental displacement increase and numerous data output steps. This procedure gave the most stable calculations.

Mesh sensitivity

The precision of numerical simulations depends significantly on the mesh density. Especially in areas of harsh geometrical changes, such as at the root and tip of the shear key (see Figure 5.6), a finer mesh leads to more accurate results. Furthermore, non-linearities due to plastic material behaviour are influenced by the mesh density. At the same time, these local changes can cause severe singularities with implausible calculation results. In order to find an optimum between mesh density and credible results, a mesh sensitivity study was carried out for each numerical model. The size of the square elements was chosen as fraction of the shear key height h_{sk} . The influence of the element size was evaluated for the distribution of the minimum principal stresses of the grout along the loaded shear key surfaces (see Figure 5.6). For a simple visual detectability, the nodal stress results were plotted along the nodal's x coordinate.

Models with varying element sizes (deviation factor ~ 0.1), developed with the aim of reducing the necessary numerical effort, showed high influence on the cracking behaviour of the CDP material model and thus on the local stress states. Consequently, only meshes with high homogeneity and very low element size deviation were used.

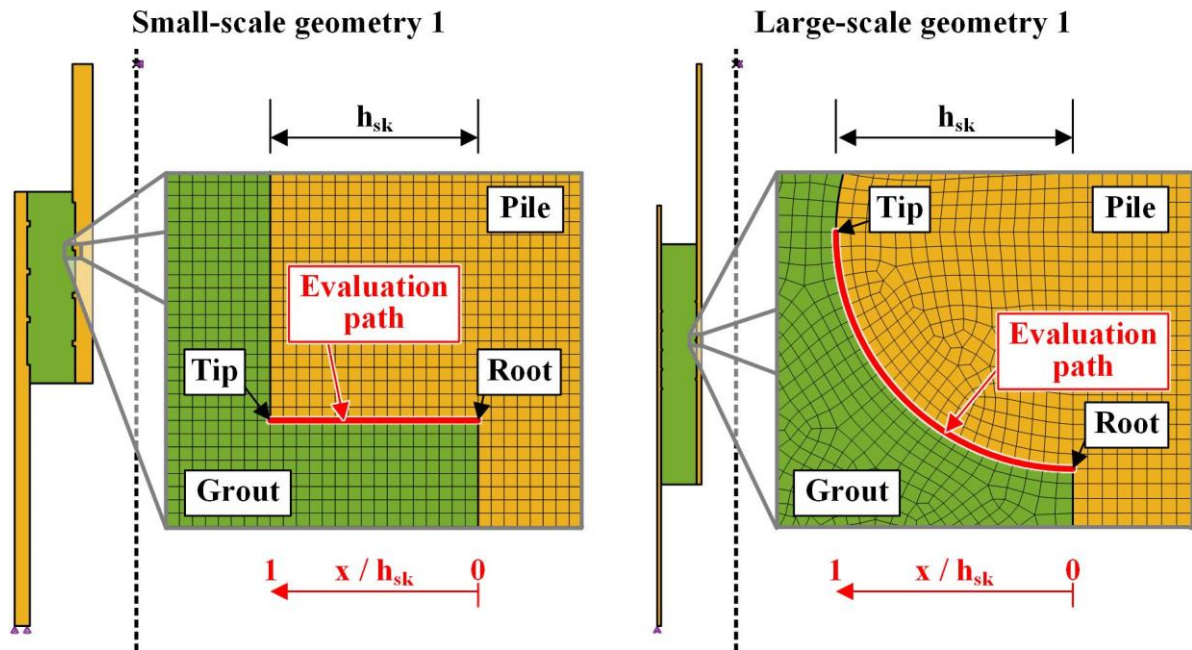


Figure 5.6: Local mesh at shear key and evaluation path for stresses and sensitivity analysis

Discrete cracks

During the numerical investigations a quasi-static stress state was calculated which corresponds to the connections behaviour during the first load cycle. Hence, neither crack growth due to cyclic loading and material fatigue nor cracking processes related to load application speeds could be considered. Consequently, the cracking capability of the CDP material model was limited to crack initiation.

For both small- and large-scale specimens typical cracking patterns were found in the dismantled specimens (see Section 3.4.3 and Section 4.3.3). In the final discussion it was assumed that these cracks caused a redistribution of load share per shear key and deactivated specific shear keys from the load transfer. In order to verify this assumption, numerical simulations with discretely modelled cracks were carried out. Therefore, the grout layer was cut into several individual parts. For calculations with autogenous shrinkage, equivalent thermal load cases the crack surfaces were bonded during the thermal load case and afterwards the bond was deactivated. This prevented fatigue related cracks from opening because of autogenous shrinkage.

Autogenous shrinkage

As described in Section 2.4.2 autogenous shrinkage heavily depends on the chosen grout material. Deformations of up to $-780 \mu\text{m/m}$ for grouting mortar (Weicken (2013)) and up to $-2000 \mu\text{m/m}$ for cement slurries (Billington (1978)) are described in the literature. Before testing the large-scale specimens, radial cracks were found in the grout layers filled with DDS5 (see Section 4.4.3). These cracks were ascribed to be caused by autogenous shrinkage deformations. For the specimens filled with BM95 no radial cracks were found before the tests were carried out. The damage behaviour differed significantly between the two filling materials. The specimens filled with BM95 failed at the interface between grout and sleeve, while the specimens filled with DDS5 failed at the interface

between pile and sleeve. Numerical investigation on the influence of autogenous shrinkage were conducted to give more insights.

In MC2010 (2013) Equation (5.13) is given to estimate the amount of autogenous shrinkage for a material of certain compressive strength f_{cm} and at a specific age t .

$$\varepsilon_{cbs}(t) = -\alpha_{bs} \left(\frac{0.1 \cdot f_{cm}}{6 + 0.1 \cdot f_{cm}} \right)^{2.5} \cdot \left[1 - \exp(-0.2 \cdot \sqrt{t}) \right] \cdot 10^{-6} \quad (5.13)$$

where:

$\alpha_{bs} = 600 \dots 800$ coefficient for cement type

t age in days

In combination with thermal shrinkage as described in Equation (5.14) the autogenous shrinkage deformations can be transferred into an equivalent thermal load case as stated in Equation (5.15).

$$\varepsilon_T = \alpha_T \cdot \Delta T \quad (5.14)$$

$$\varepsilon_T = \varepsilon_{cbs}(t)$$

$$\Delta T = \frac{-\alpha_{bs} \left(\frac{0.1 \cdot f_{cm}}{6 + 0.1 \cdot f_{cm}} \right)^{2.5} \cdot \left[1 - \exp(-0.2 \cdot \sqrt{t}) \right] \cdot 10^{-6}}{\alpha_T} \quad (5.15)$$

Table 5.3: Autogenous shrinkage values for different grout materials

	Specimens (acc. to MC2010 (2013))				BASF Construction Chemicals (2010)	ITW Densit ApS (2012)	Weicken (2013)
	W1	W2	W3	W4			
Grout Material	BM95	BM95	DDS5	DDS5	BM95	DDS5	
T [d]	148	156	79	56			
f_{cm} [N/mm ²]	149	165	154	146			
α_{bs}	600	600	600	600			
$\varepsilon_{cbs}(t)$ [$\mu\text{m}/\text{m}$]	-235	-254	-219	-197	-100	-147	-780
α_T [1/K]	$10 \cdot 10^{-6}$						
ΔT [K]	-23.5	-25.4	-21.9	-19.7	-10.0	-14.7	-78.0

Table 5.3 summarises the autogenous shrinkage values for the large-scale specimens, calculated according to MC2010 (2013). Moreover, it states the values given by the manufacturers. Different to the calculated values, BASF Construction Chemicals (2010) states an autogenous shrinkage value of $<100 \mu\text{m}/\text{m}$ which is proven by investigations of Soerensen (2011). Also ITW Densit ApS

(2012) specifies a lower shrinkage value than calculated for DDS5. In contrast to that, Weicken (2013) found an autogenous shrinkage value of $780 \mu\text{m}/\text{m}$ for a comparable high strength grout material. In the numerical investigations the influence of autogenous shrinkage was investigated with the aforementioned shrinkage values.

5.2.5 Fatigue verification

General remarks

The decisive degradation process ascertained in the submerged small- and large-scale fatigue tests is the local crushing of grout material in front of the load transferring shear key surfaces (see Chapter 3 and Chapter 4). Water inside the interface between steel and grout is pumped through the interface by the load induced relative movement of steel and grout parts and as a consequence, the loose grout particles are flushed out of the connection. As a result the load displacement behaviour of the connection becomes unreliable. To exclude this water related degradation process and design a fatigue resistant grouted connection for submerged application, the local grout crushing must be prevented. Hence, to evaluate the fatigue resistance of a grouted connection design, the local stresses in the grout layer around the shear keys must be evaluated regarding their fatigue relevance.

Based on the priorly described hypotheses, a fatigue verification approach was developed. Main goal of the fatigue verification approach was to allow an accurate and robust calculation procedure. The schematic procedure given in Figure 5.7 is a further development of approaches described by Wilke (2014), Lochte-Holtgreven (2013) and Bechtel (2016). One major adjustment is the use of a highly discretized finite-element model with shear keys and the focused evaluation of compressive stresses at the grout contact area towards the shear key (see Figure 5.7, 5). In the following, the underlying procedure for each of the six parts in Figure 5.7 is described.

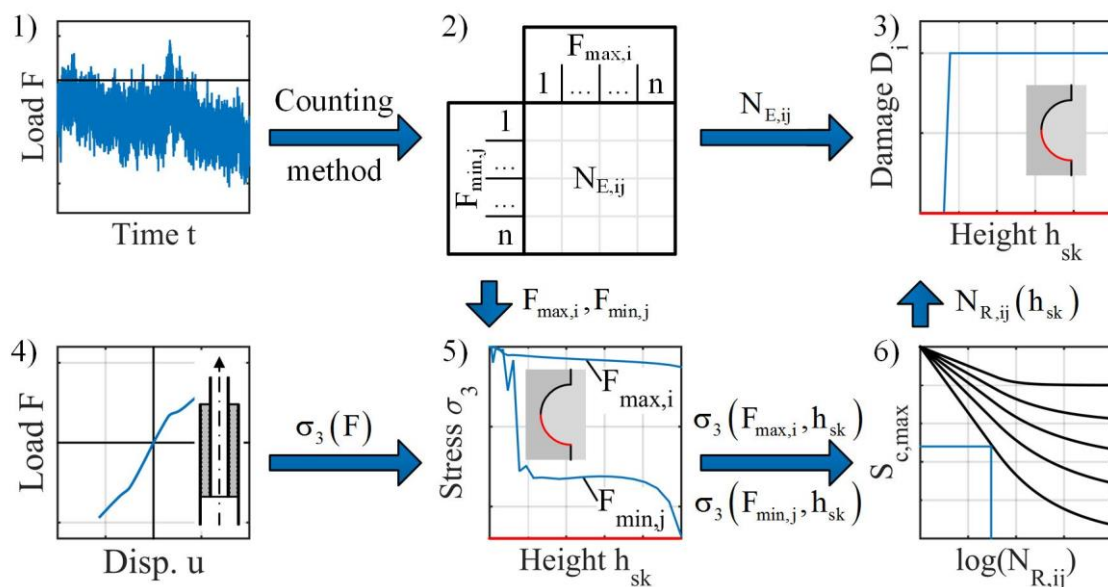


Figure 5.7: Schematic representation of the fatigue verification approach

Actions

First step of the verification approach is to transfer and reduce the time series of loads acting on the grouted connection (see Figure 5.7, 1) via an appropriate counting method into classes of similar load levels and corresponding numbers of load cycles. The result is a Markov matrix (see Figure 5.7, 2). This procedure reduces the amount of load data to a smaller set with equal information but sacrifices the load sequence.

Load bearing behaviour

The local stress distribution around the shear keys is assumed to be decisive for the connection's fatigue behaviour in wet AC. Moreover, the load share per shear key can be expected to be influenced by the cracking state of the whole grout layer. Hence, a numerical model for fatigue verification of the specimens must describe the complete grout layer, include discretely modelled shear keys and utilise an appropriate material model which covers the nonlinear stress-strain behaviour of grout. A corresponding modelling approach and an appropriate material model are described in Section 5.2.2 and Section 5.2.3. Such a model is characterised by a large amount of degrees of freedom.

In order to reduce the computational effort, a quasi-static finite element calculation is carried out for each possible set of material parameters, cracking states, autogenous shrinkage rates and load directions. The applied load is incrementally increased up to the highest expectable load level. The result is a load-stress relation for the grout layer (see Figure 5.7 4).

Effects of actions

Acting loads and load bearing behaviour are combined by evaluating the load-stress relation obtained from the numerical simulations for each load level of the Markov matrix. From these data the grout layer's minimum principal stress distribution in front of each loaded shear key surface is extracted (see Figure 5.7, 5). It can be expected that in the area of load transfer the minimum principal stress is decisive for the grout material's fatigue behaviour.

Figure 5.8, left shows an exemplary minimum principal stress distribution along the loaded shear key surface. Stress distributions for two load stages (LS) are depicted. Towards the shear key tip ($x/h_{sk} = 1.0$) the grout material is cracked and hence only small and inhomogeneously distributed stresses are visible in the crack influenced area (gray background). At the shear key root ($x/h_{sk} = 0.0$) a stress singularity is visible, which is caused by the geometrical notch in the numerical model. The main load transfer between shear key and grout is realised via compressive contact. Hence, for the further evaluation of the compressive stresses, the stresses in the crack influenced area as well as the model related singularity must be excluded. The size of the crack influenced area varies for each shear key and grouted connection geometry. Thus, it is not possible to define a universally valid evaluation path for the fatigue verification.

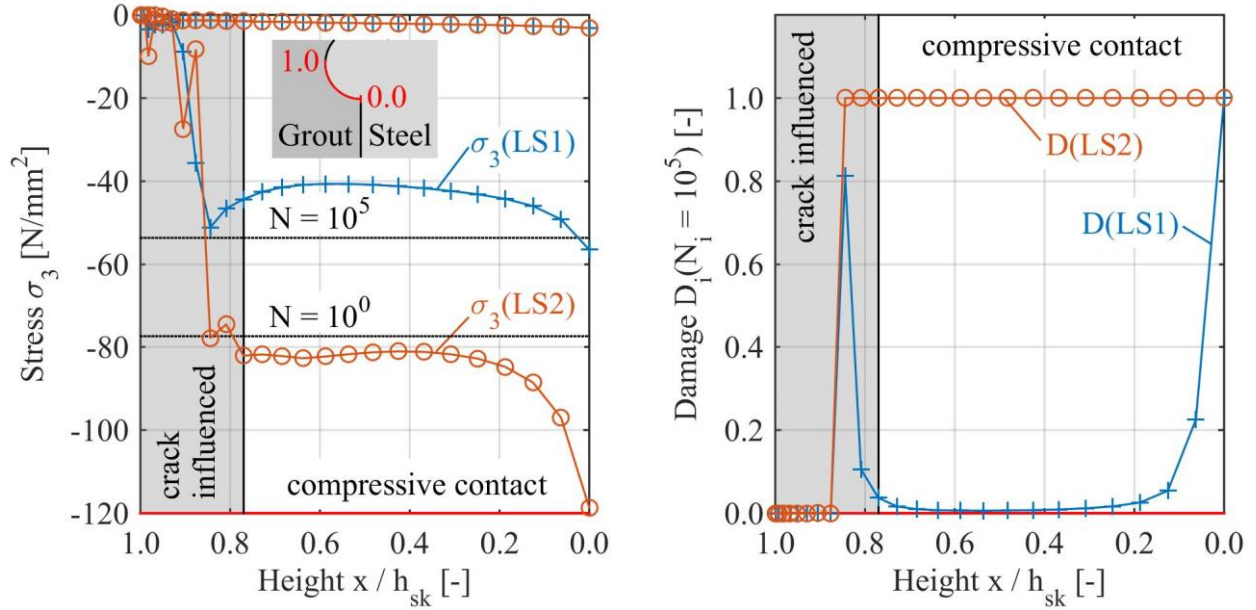


Figure 5.8: Exemplary minimum principal stress distribution along the loaded shear key surface for two load stages (left) and corresponding damage estimation (right)

Number of endurable load cycles

The obtained minimum principal stresses for minimum and maximum load of a load class are compared to the uniaxial compression-compression S-N curves of MC2010 (2013). Therefore, the local stresses calculated for each load class extreme values ($\sigma_{c,\max}$, $\sigma_{c,\min}$) are normalised to the compressive fatigue strength $f_{ck,\text{fat}}$ according to Equation (5.16) up to Equation (5.18).

$$S_{c,\max,ij} = \frac{|\sigma_{c,\max,ij}|}{f_{ck,\text{fat}}} \quad (5.16)$$

$$S_{c,\min,ij} = \frac{|\sigma_{c,\min,ij}|}{f_{ck,\text{fat}}} \leq 0.8 \quad (5.17)$$

$$f_{ck,\text{fat}} = \beta_{cc}(t) \cdot 0.85 \cdot f_{ck} \cdot \left(\frac{1-f_{ck}}{400} \right) \quad (5.18)$$

where:

$\sigma_{c,\max}$ maximum compressive stress

$\sigma_{c,\min}$ minimum compressive stress

$$\beta_{cc}(t) = \exp \left\{ s \cdot \left[1 - \left(\frac{28}{t} \right)^{0.5} \right] \right\}$$

t concrete age in days at beginning of fatigue loading

s coefficient depending on strength class of cement

The number of endurable load cycles $N_{R,ij}$ is then calculated according to Equation (5.19) up to Equation (5.22). The resulting S-N curve is shown in Figure 2.22 and Figure 5.7, 6.

$$\log(N_{1,ij}) = \frac{8}{(Y_{ij} - 1)} \cdot (S_{c,max,ij} - 1) \quad (5.19)$$

$$\log(N_{2,ij}) = 8 + \frac{8 \cdot \ln(10)}{(Y_{ij} - 1)} \cdot (Y_{ij} - S_{c,min,ij}) \cdot \log\left(\frac{S_{c,max,ij} - S_{c,min,ij}}{Y_{ij} - S_{c,min,ij}}\right) \quad (5.20)$$

$$Y_{ij} = \frac{0.45 + 1.8 \cdot S_{c,min,ij}}{1 + 1.8 \cdot S_{c,min,ij} - 0.3 \cdot S_{c,min,ij}^2} \quad (5.21)$$

$$\log(N_{R,ij}) = \begin{cases} \log(N_{1,ij}) & \text{if } \log(N_{1,ij}) \leq 8 \\ \log(N_{2,ij}) & \text{if } \log(N_{1,ij}) > 8 \end{cases} \quad (5.22)$$

Damage estimation

Subsequently, the expectable damage for each evaluated node is calculated according to Palmgren-Miner's linear damage hypothesis (see Equation (5.23)).

$$D = \sum_{ij} \frac{N_{E,ij}}{N_{R,ij}} \leq 1.0 \quad (5.23)$$

where:

D	fatigue damage
$N_{E,ij}$	number of acting stress cycles at a given stress level
$N_{R,ij}$	number of endurable cycles at a given stress level

The right plot of Figure 5.8 shows the corresponding damage distribution for the stress values shown left and $N = 10^5$ load cycles. The damage is calculated according to the previously described fatigue verification approach with damage values limited to a maximum of one.

For load stage 1 the stress peaks at the shear key root ($x/h_{sk} = 0.0$) and at $x/h_{sk} \sim 0.82$ are in the range of the fatigue limit stress for $N = 10^5$ applied load cycles. Consequently, the calculated damage is in the range of one, while for the rest of the compressive contact area the calculated damage is nearly zero. For the fatigue evaluation of the local stress distribution it is assumed that grout material crushing occurs when a damage value of one is reached. However, for a material removal leading to a displacement offset between steel and grout, damage must be one at all nodes in the area of compressive contact. This assumption takes into account that stress peaks are removed during cyclic loading and the stress distribution homogenises.

5.3 Results

5.3.1 Grout material validation

Plasticity

Before conducting numerical investigations the yield surface of CDP was compared to the Ottosen (1977) yield surface, which is highly recommended for modelling grout materials under multiaxial stress states by Lochte-Holtgreven (2013) and for HPC by Speck (2008). Figure 5.9 shows both yield surfaces. In general, the Lubliner et al. (1989) surface is a little bit smaller but the general shape of both yield surfaces is quite similar. Hence, assuming the Ottosen (1977) yield surface to give the best representation of grout material behaviour, the CDP material model can be rated as a slightly conservative alternative.

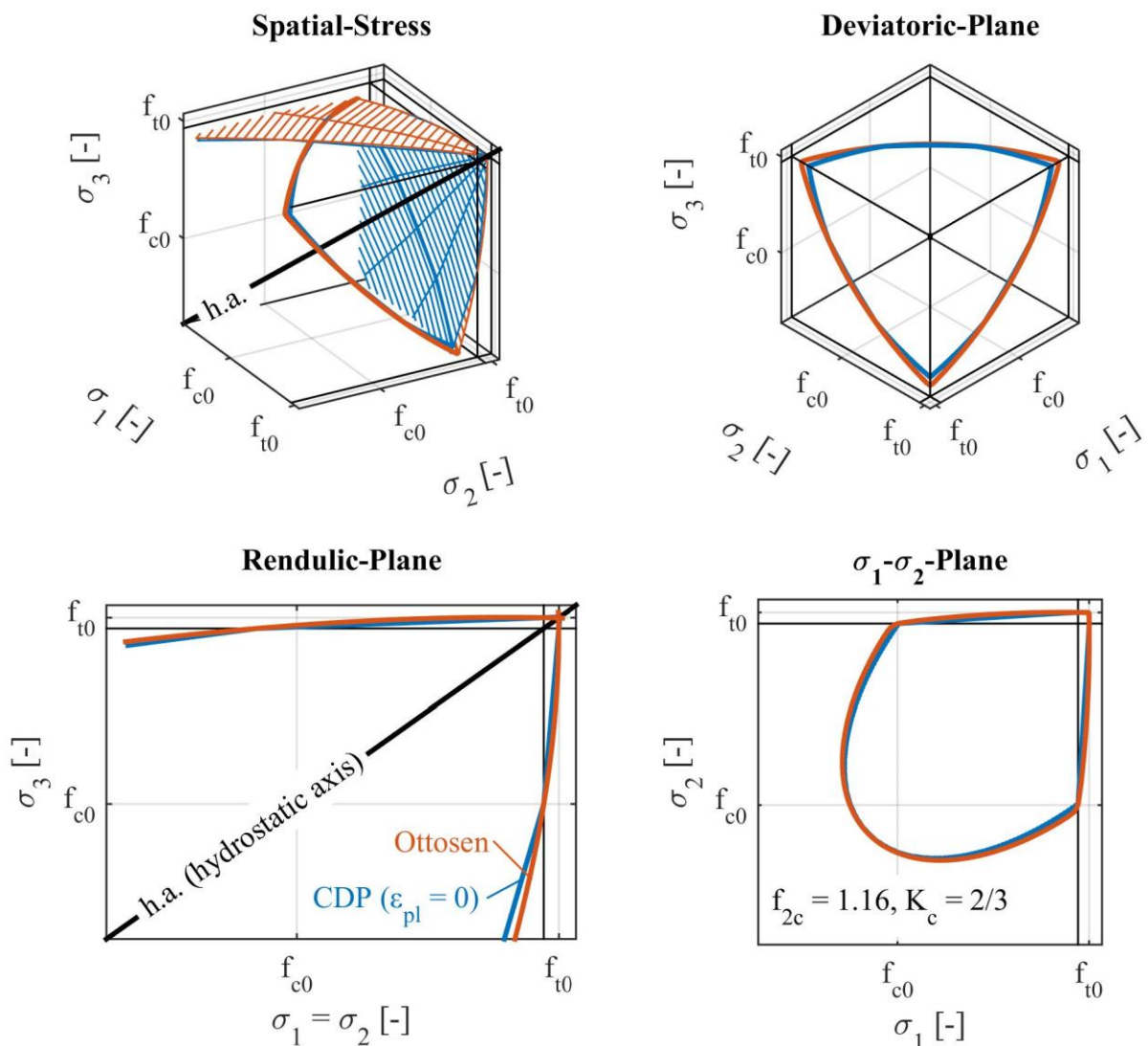


Figure 5.9: Concrete damaged plasticity yield surface according to Lubliner et al. (1989) compared to the yield surface according to Ottosen (1977)

Compressive behaviour

According to Equation (5.4), the ratio between the secant stiffness for the strength peak E_{c1} and the mean tangent stiffness E_{cm} gives the plasticity number k which is a measure for a material's uniaxial brittleness. Usually this value is not provided by the material manufacturer nor is it obtained from the common material tests. In MC2010 (2013) values for concrete are given, which are plotted as gray dots in Figure 5.10. By a logarithmic regression these discrete values can be translated into Equation (5.24). Grout materials are usually more brittle which is represented by the blue dot, obtained from the stress-strain relation published by Lochte-Holtgreven (2013) for a DDS5 prism (see Figure 5.11). To include this higher brittleness in the plasticity number the author of this thesis proposes a linear correction given in Equation (5.25) and represented by the blue curve in Figure 5.10.

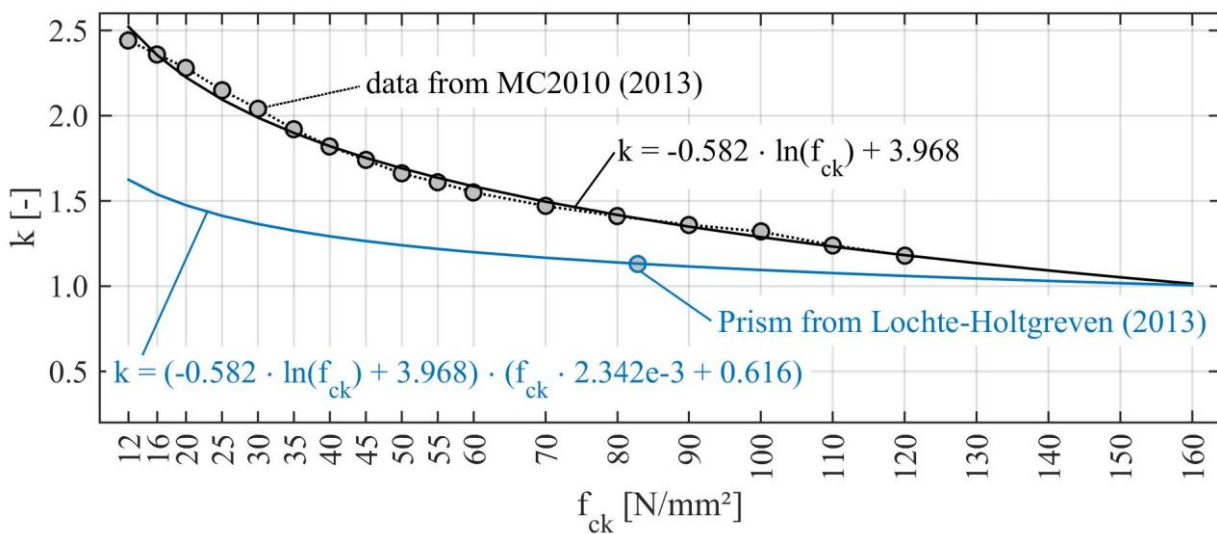


Figure 5.10: Nonlinear regression for plasticity number k acc. to MC2010 (2013) and linear correction proposal for brittle grout materials

$$k = \frac{E_{ci}}{E_{c1}} \sim -0.582 \cdot \ln(f_{ck}) + 3.968 \quad \text{for concrete} \quad (5.24)$$

$$k = (-0.582 \cdot \ln(f_{ck}) + 3.968) \cdot (f_{ck} \cdot 2.342e-3 + 0.616) \quad \text{for brittle grout} \quad (5.25)$$

With the proposed plasticity number k , a uniaxial stress-strain relation according to Equation (5.4) was calculated and used for the CDP definition. The numerical result was compared to a test result published by Lochte-Holtgreven (2013) for a DDS5 prism. Figure 5.11 shows the numerical model (left) as well as the comparison of results (right). The accordance between numerical and experimental results is very satisfying and the chosen approach to set up the uniaxial stress-strain relation was used for all following numerical investigations.

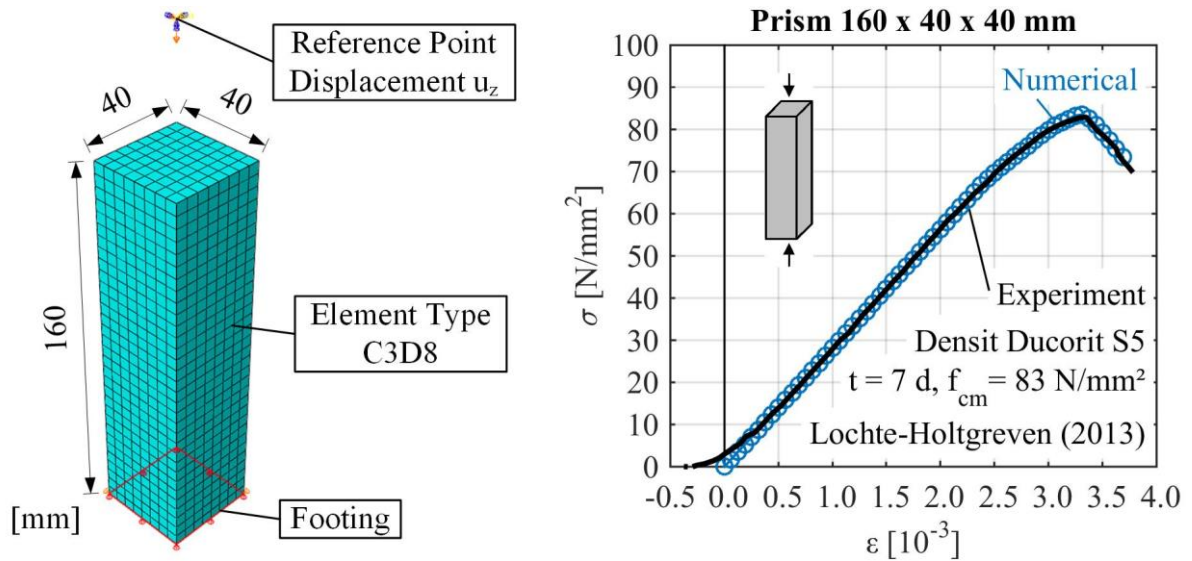


Figure 5.11: Numerical model of grout prism (left) and comparison of numerical results with experimental results from Lochte-Holtgreven (2013) (right)

Material parameters

Additional to the theoretical evaluation of material parameter influences in Section 5.2.3, sensitivity studies were carried out using the small-scale geometry 1. All results are shown in Appendix D. Only the dilatation angle ψ of the flow potential showed a significant influence in the load range of interest.

Figure 5.12 shows the maximum principal stress distribution along the loaded shear key surface of shear key P1. With increasing dilatation angle, the material’s cracking behaviour becomes more localised towards the shear key tip, leading to significantly different stress distributions.

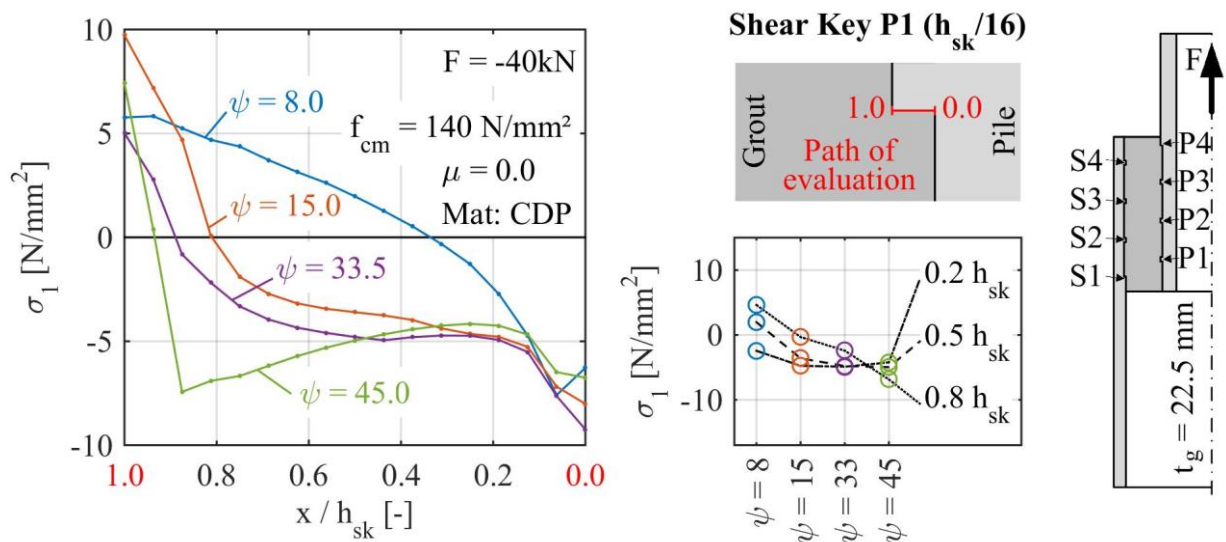


Figure 5.12: Local numerical maximum principal stress results at loaded shear key surface for small-scale geometry 1 with different dilatation angles

In Figure 5.13 the maximum plastic strain distributions of the grout, calculated with different dilatation angles, are compared to the cracking pattern observed in experimental tests. With a dilatation angle of $\psi = 8.0^\circ$ the cracking tends to vertical shear cracks in the upper grout section. This behaviour was not observed in the experimental ULS tests. Similar to that, the steeper crack calculated with $\psi = 15.0^\circ$ was not observed in any experimental tests. The best compliance between experimental and numerical results was achieved with $\psi = 33.5^\circ$. This value was used for all further investigations.

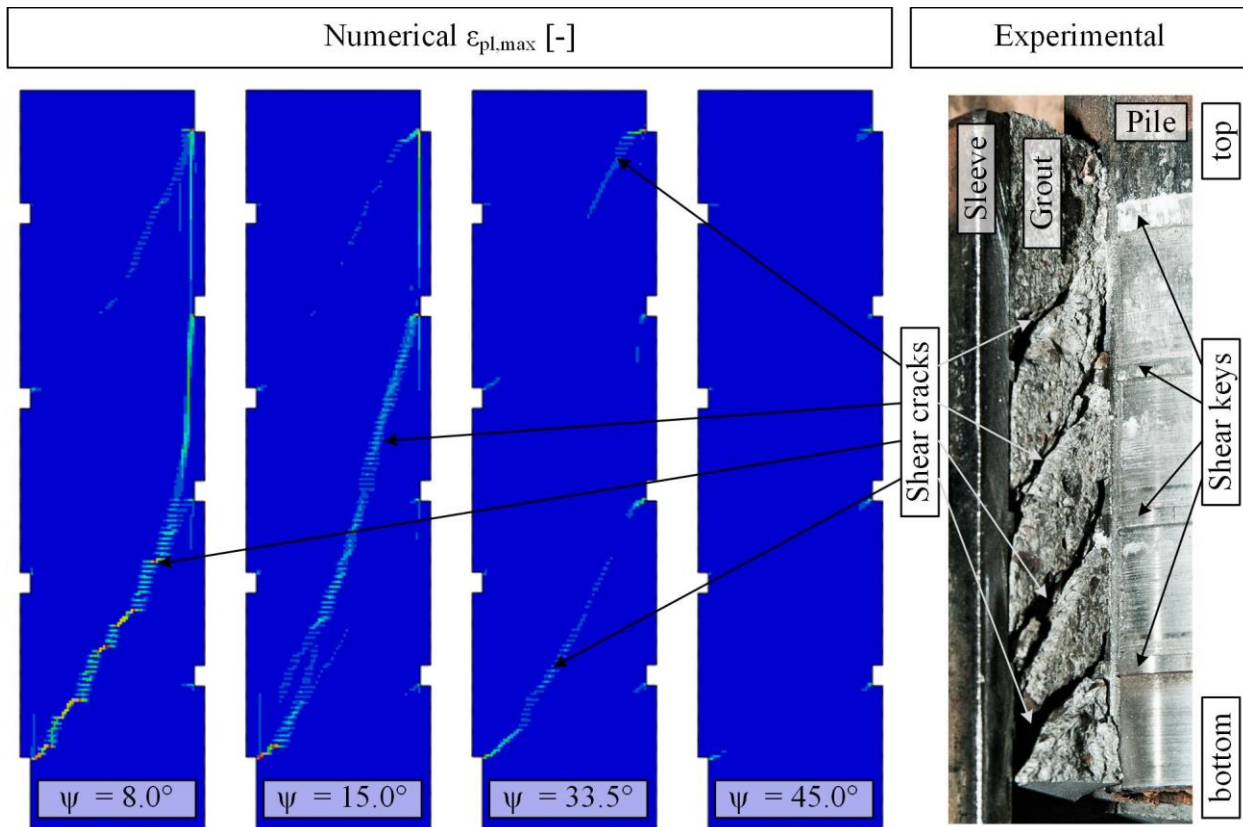


Figure 5.13: Comparison between experimental cracking pattern (right) and numerical plastic strains calculated with different dilatation angles (left)

5.3.2 Small-scale tests

Mesh sensitivity

Figure 5.14 shows the local minimum principal stress σ_3 at the loaded surface of shear key P4 for specimen geometry 1. It is clearly visible that a finer mesh leads to increasing stresses towards the ends of the path of evaluation caused by the harsh geometrical changes. Hence an evaluation of stresses at the ends of the path is not recommendable. The comparison of maximum stresses for $0 < x/h_{sk} < 1$ shows sufficiently converging stresses for a mesh density of $h_{sk}/16$ and finer. Consequently, all following numerical investigations for the small-scale geometries were carried out with a mesh density of $h_{sk}/16$.

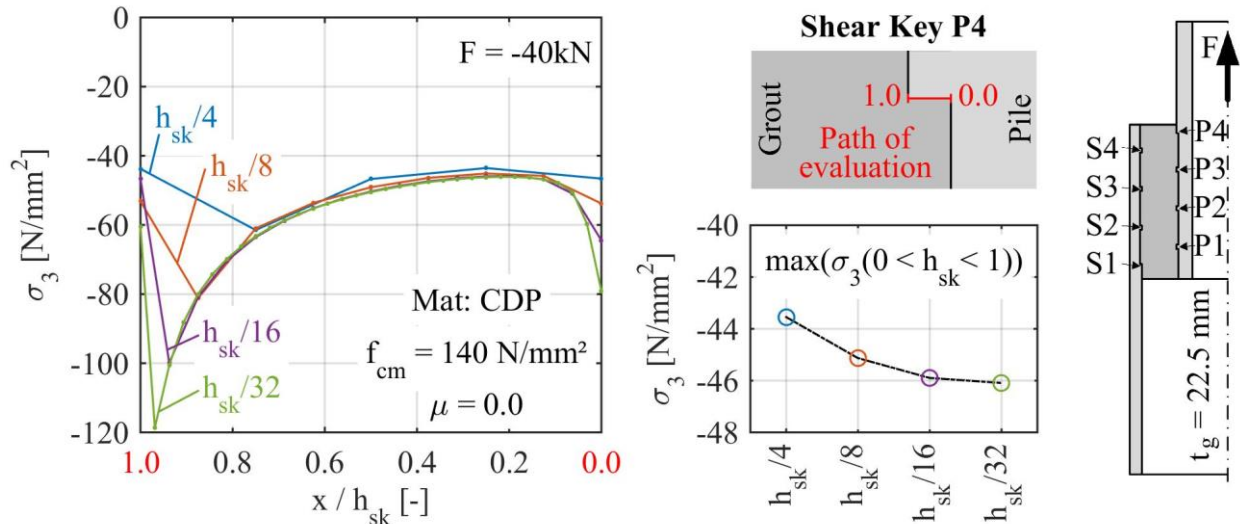


Figure 5.14: Local numerical minimum principal stress results at loaded shear key surface for small-scale geometry 1 with different mesh densities

Influence of non-linear material

In Figure 5.15 the local minimum principal stress σ_3 results for linear elastic (LIN) and concrete damaged plasticity (CDP) material models for the grout material are shown. Except from the stress distribution towards the shear key tip ($1.0 h_{sk}$) the linear elastic material model gives about 8 N/mm^2 lower stress results at a load of $F = -40 \text{ kN}$. Main reason is the materials tensile behaviour in this area. While the linear elastic material shows tensile stresses above 100 N/mm^2 (see Figure 5.16), the concrete damaged plasticity material plasticized. Moreover, Figure 5.15 shows results obtained with a bilinear material model (BIL) for steel. Since no differences between LIN and BIL are visible, in this case a linear material model seems sufficient for steel.

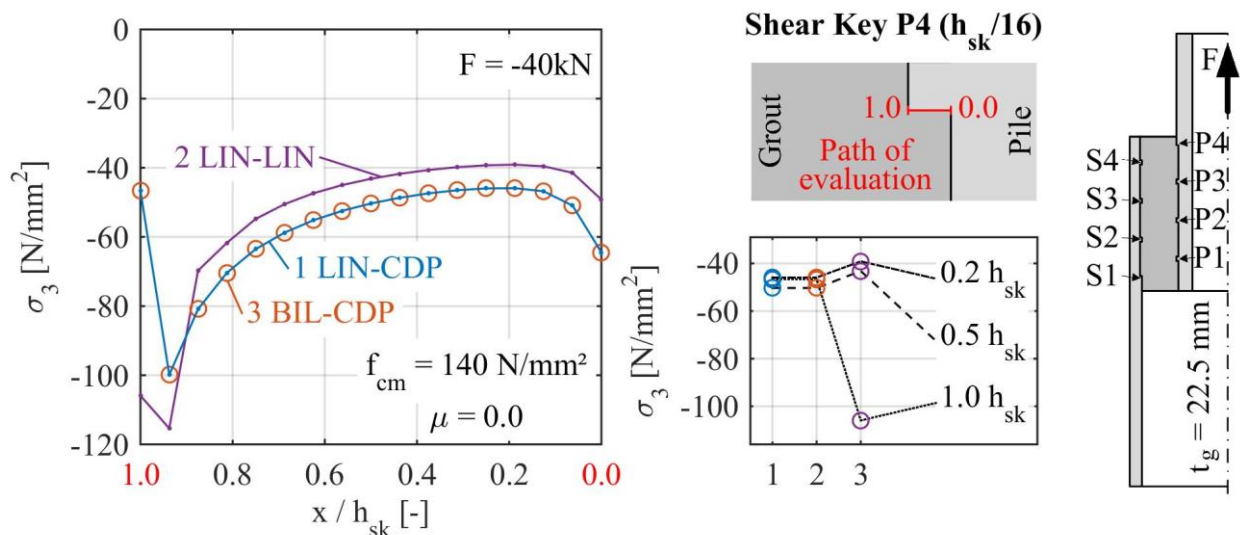


Figure 5.15: Local numerical minimum principal stress results at loaded shear key surface for small-scale geometry 1 with different material models for the grout

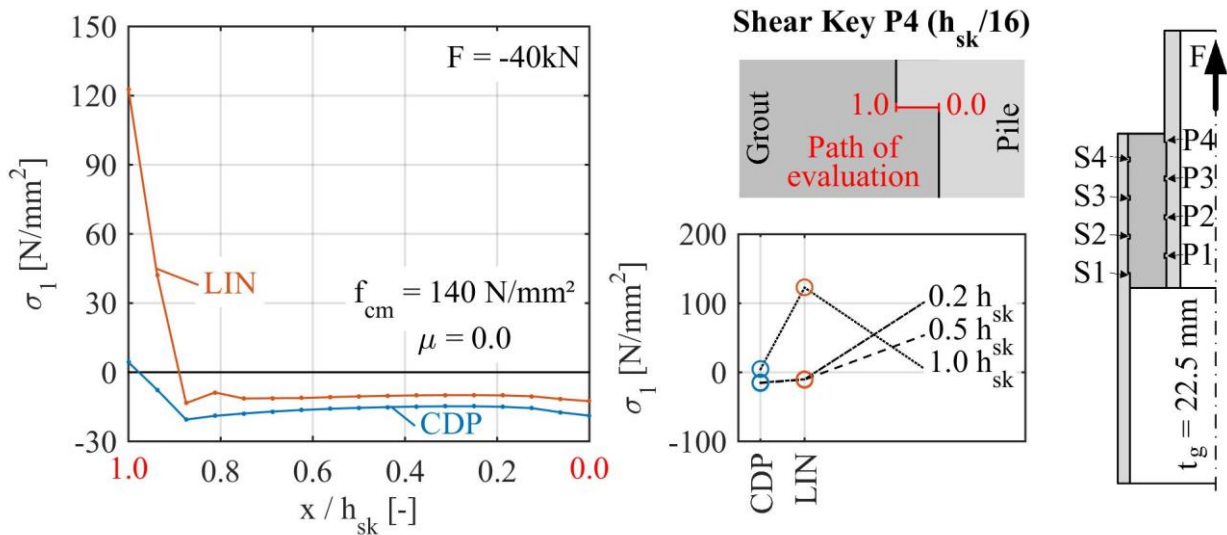


Figure 5.16: Local numerical maximum principal stress results at loaded shear key surface for small-scale geometry 1 with different material models for the grout

Discrete cracks

Figure 5.17 shows the stress distribution for three different models. The first model is without cracks (0crk, blue line), the second model includes a crack between the lower end of the grout layer and shear key P1 (1crk, orange line) and the third model includes an additional crack between shear key S1 and P2 (2crk, purple line). A significant impact of the cracks on the load share per shear key on the pile is clearly visible. The first crack deactivates shear key P1 and the second crack deactivates shear key P2. As a result, the load share on shear keys P3 and P4 almost doubles. In contrast to that, the shear keys on the sleeve are only slightly influenced by the cracks. These results proof the assumptions made in Chapter 3 for the load bearing behaviour of a cracked grout layer.

Autogenous shrinkage

The minimum principal stress distributions for different autogenous shrinkage load cases are presented in Figure 5.18. The results calculated without autogenous shrinkage (blue line) show a slight increase along the pile shear keys towards shear key P4. A similar increase is visible for the sleeve shear keys towards shear key S1. With introduction of an autogenous shrinkage equivalent load of $\Delta T = -10$ K (orange line) this global distribution is inverted, leading to highest load shares at shear keys P1 and S4. A further increase of the thermal load to $\Delta T = -78$ K (purple line) increases the load share on shear key P1 and S4 and almost removes the load share on shear keys P3, P4 and S1, S2. Moreover, the stresses at shear key S4 cause an inhomogeneous stress distribution caused by autogenous shrinkage related cracking in the CDP material model.

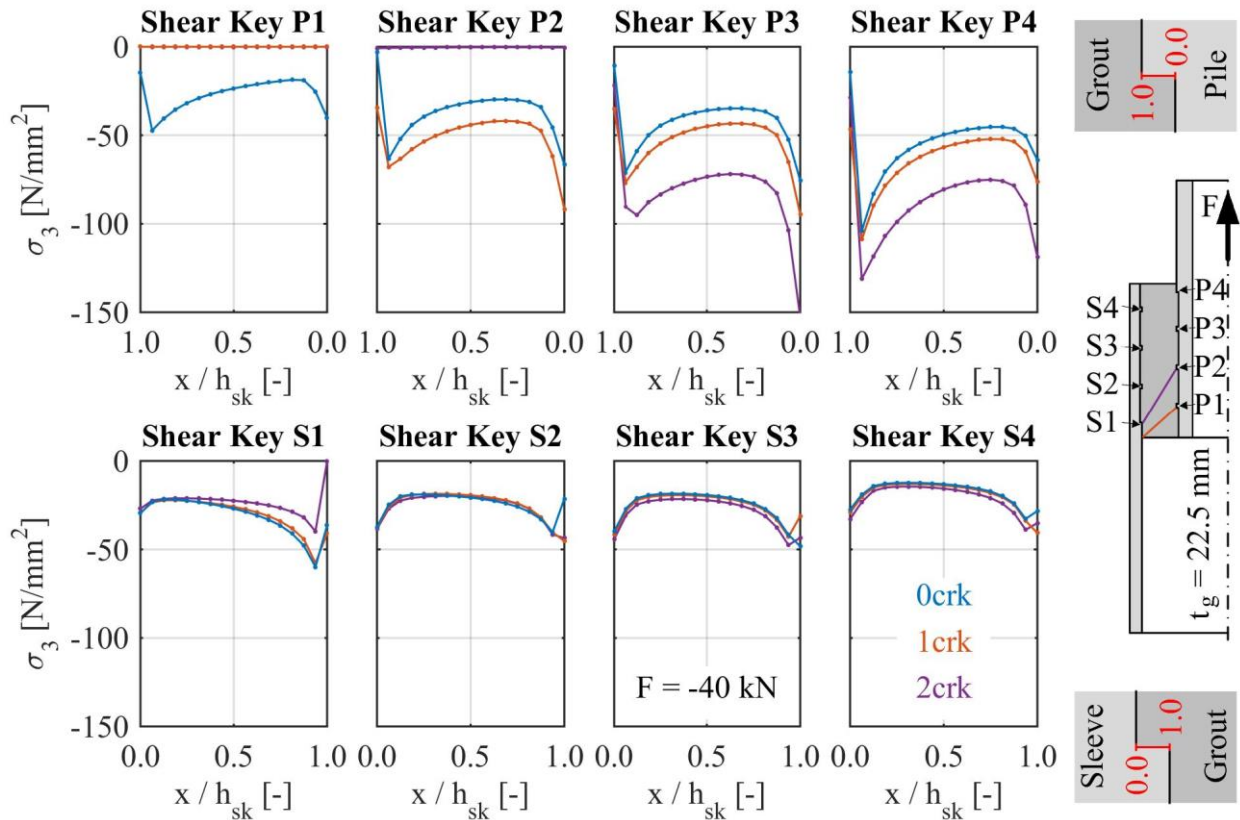


Figure 5.17: Local numerical minimum principal stress results at loaded shear key surface for small-scale geometry 1 with discrete cracks

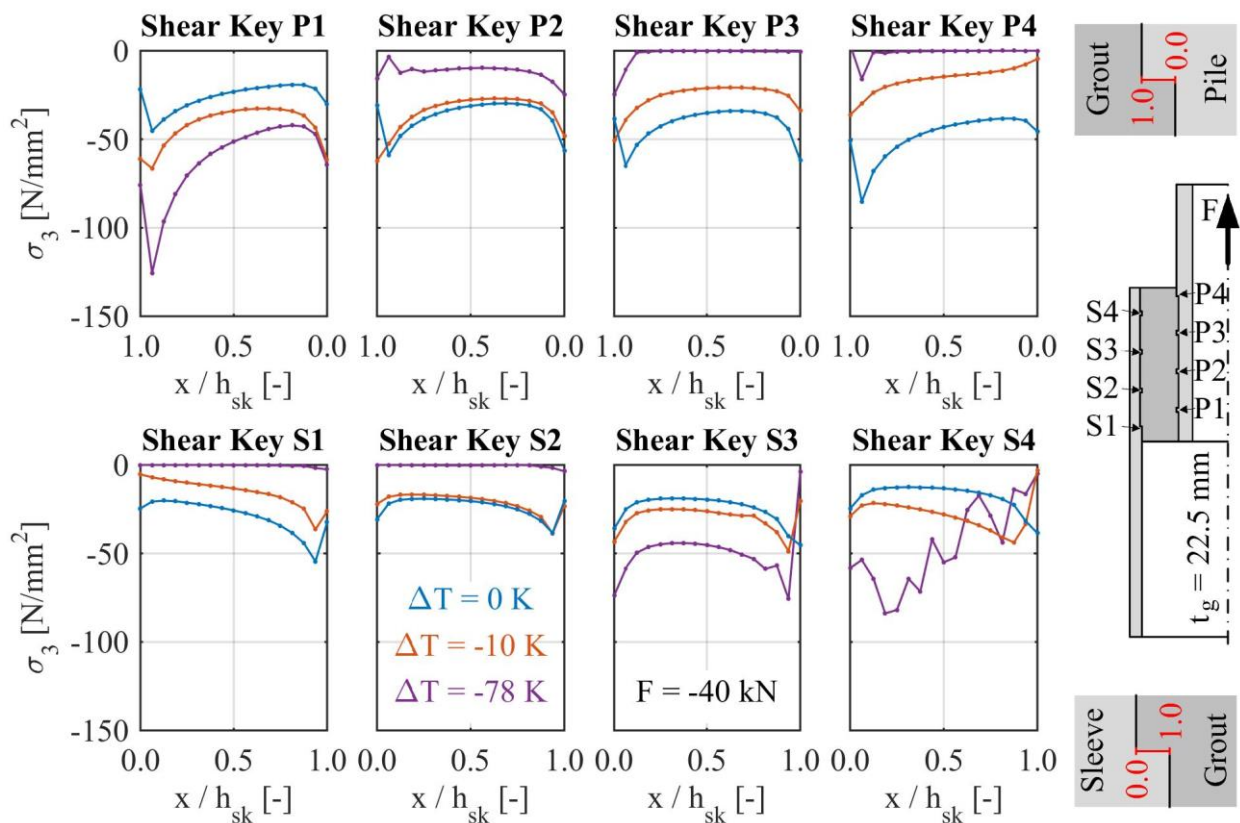


Figure 5.18: Local numerical minimum principal stress results at loaded shear key surface for small-scale geometry 1 with different autogenous shrinkage rates

Fatigue Limit State (FLS) capacity

Based on the previously described fatigue verification approach (see Section 5.2.4) numerical fatigue calculations were carried out for both small-scale geometries (see Figure 3.2), considering the actual material properties (see Table 5.1) and an uncracked as well as cracked grout layer. Since both values can be rated as singularities, the evaluation of stresses along the shear key height excluded the values at both, the shear key root ($h_{sk} = 0.0$) and tip ($h_{sk} = 1.0$).

Figure 5.19 and Figure 5.20 show the experimental results for both small-scale geometries and fatigue curves for different cracking states. Different to a usual S-N-plot for concrete, instead of the normalised load level $S = F_{max}/F_{ULS}$ the y axis shows the not normalised load F_{max} . This is necessary because for the time being a standardised approach to obtain F_{ULS} from a numerical calculation is not available and hence a reasonable normalisation of the numerical results is not possible.

For both geometries the numerical fatigue curves are considerably lower than the experimental results. While for the uncracked grout layer (solid lines) both specimen geometries show similar fatigue capacities, discrete cracks (dashed lines) reduce the fatigue capacity significantly by a factor of $\sim 1/3$ for geometry 1 and $\sim 2/3$ for geometry 2.

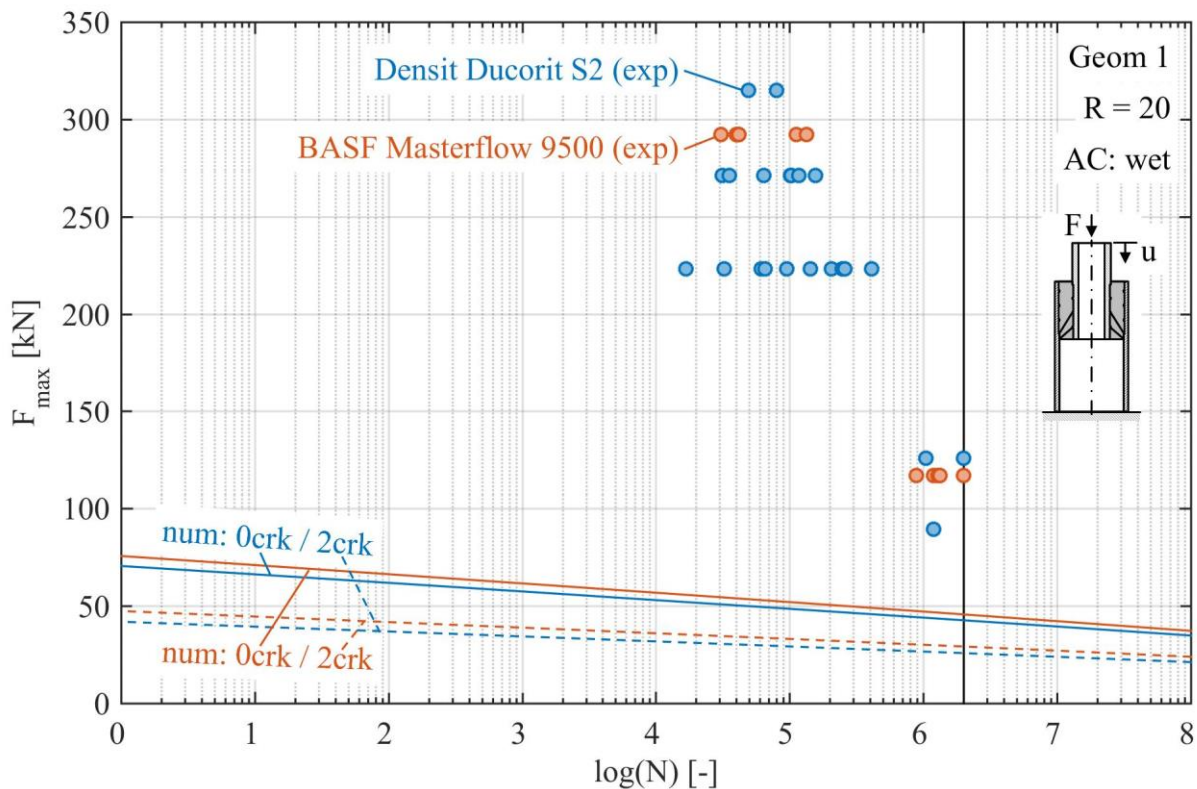


Figure 5.19: F-N diagram with experimental and numerical results for small-scale geometry 1, different grout materials and discrete cracks

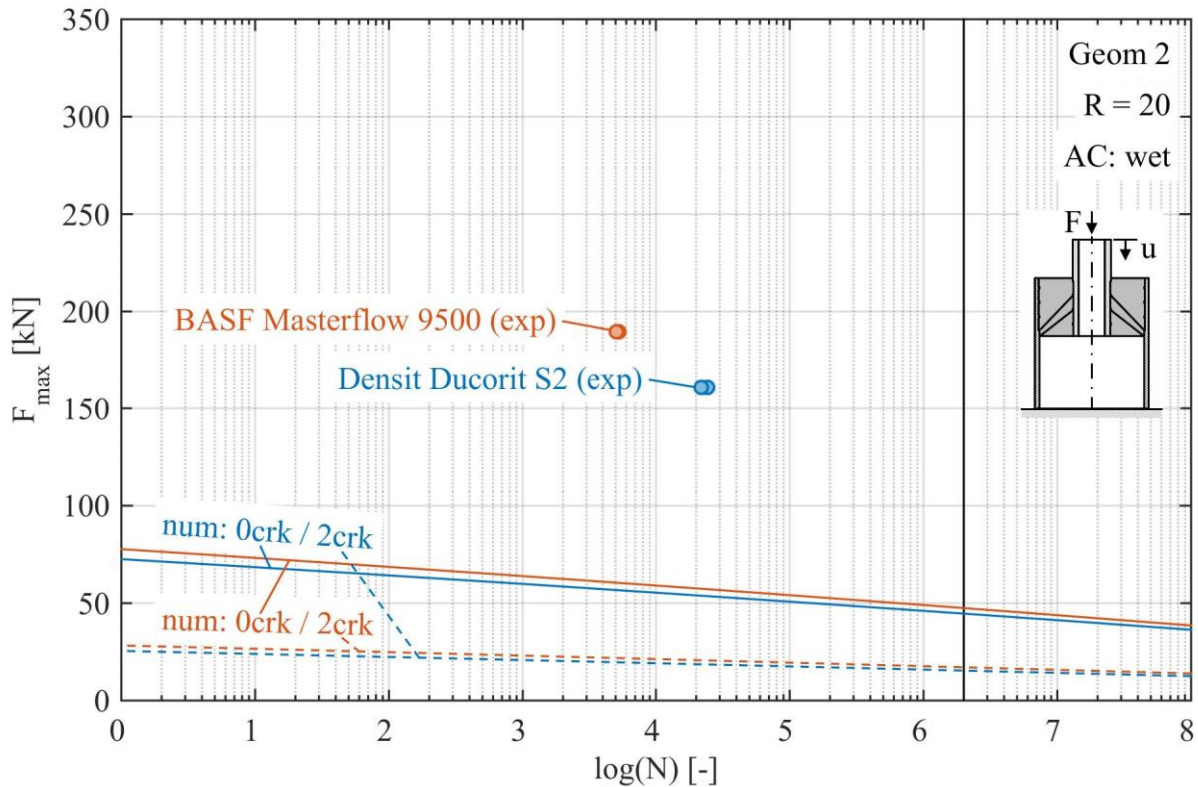


Figure 5.20: F-N diagram with experimental and numerical results for small-scale geometry 2, different grout materials and discrete cracks

5.3.3 Large-scale tests

Mesh sensitivity

In Figure 5.21 the local minimum principal stress σ_3 results at the loaded surface of shear key P5 for specimen geometry 1 are shown. A finer mesh leads to increasing stresses towards the shear key root ($h_{sk} = 0.0$). Around the shear key tip ($h_{sk} = 1.0$), a finer mesh leads to more non-linear material behaviour and a smaller minimum principal stress due to cracking. The stress distributions become more similar from a mesh density of $h_{sk}/8$ upwards. Moreover, a clear plateau of compressive load application is visible between 0.0 and $0.7 \cdot h_{sk}$. Comparing the maximum value of σ_3 in this area shows a converging behaviour from $h_{sk}/8$ upwards. Consequently, all following numerical investigations for the large-scale geometries were carried out with a mesh density of $h_{sk}/16$ to include a small safety margin for the autogenous shrinkage calculations where stress concentrations occur (see e.g., Figure 5.30).

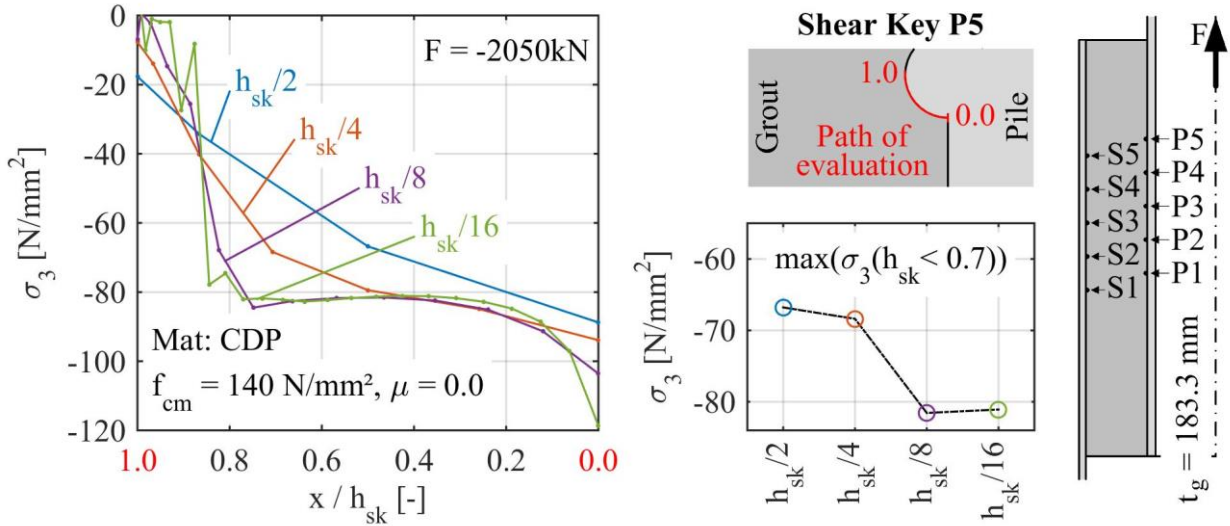


Figure 5.21: Local numerical minimum principal stress results at loaded shear key surface for large-scale geometry 1 with different mesh densities

Strain distribution

Specimen W1

In Figure 5.22 the axial strain distribution at the pile ($h = 1490$ mm) and along the sleeve ($h = -100$ mm to 1140 mm) is depicted as mean value of each 20 % of applied load cycles per load stage. Besides the measured data from the experiments (black line), numerical results without autogenous shrinkage (blue line) and with autogenous shrinkage deformation equivalent to a thermal load of $\Delta T = -10$ K (orange line) are presented. A better compliance between experimental results and the results with autogenous shrinkage throughout the whole load stage is clearly visible.

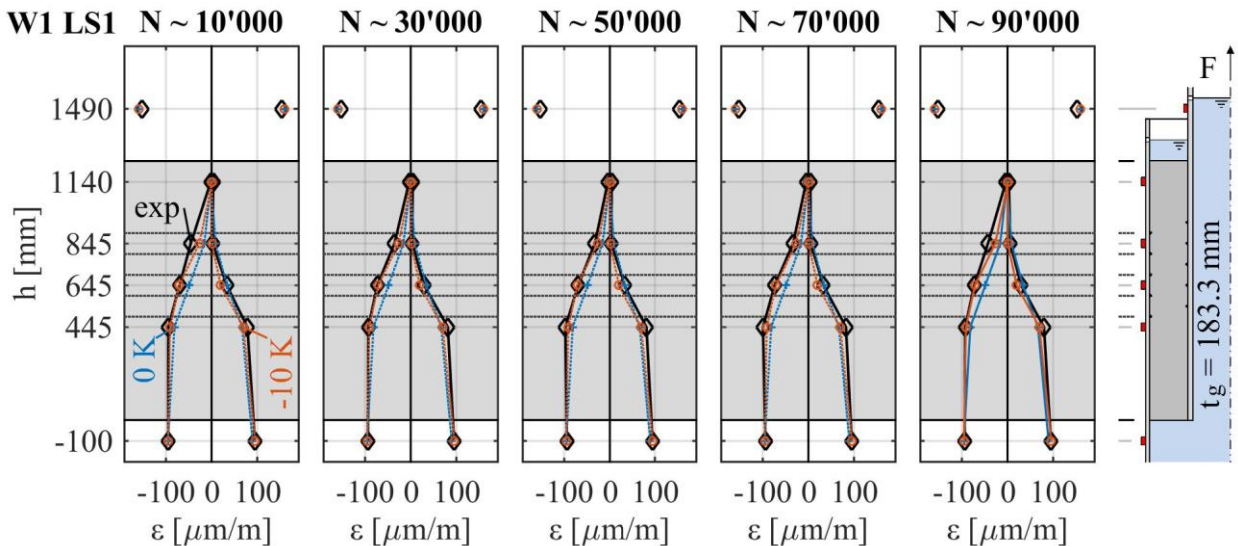


Figure 5.22: Axial strain distribution from numerical calculations and strain measurements in specimen W1 LS1 for different measures of autogenous shrinkage

Specimen W2

The axial strain distribution from experimental and numerical investigations for specimen W2 at load stage 1 is shown in Figure 5.23. Best agreement is visible between experimental (black line) and numerical results with an autogenous shrinkage equivalent thermal load of $\Delta T = -10$ K (orange line). This behaviour is constant during the whole load stage 1.

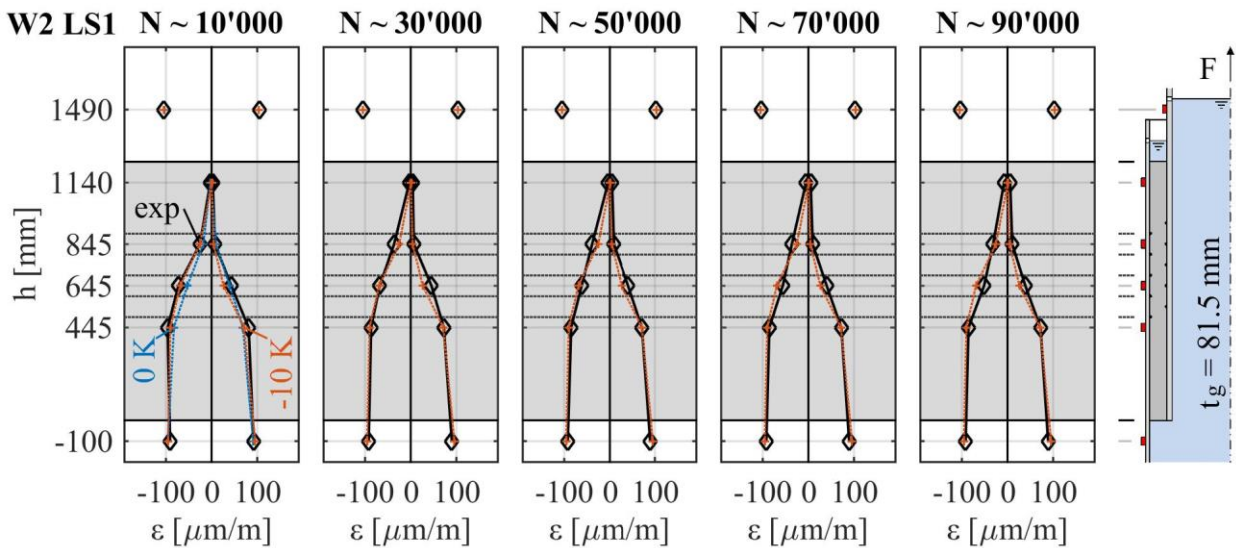


Figure 5.23: Axial strain distribution from numerical calculations and strain measurements in specimen W2 LS1 for different autogenous shrinkage rates

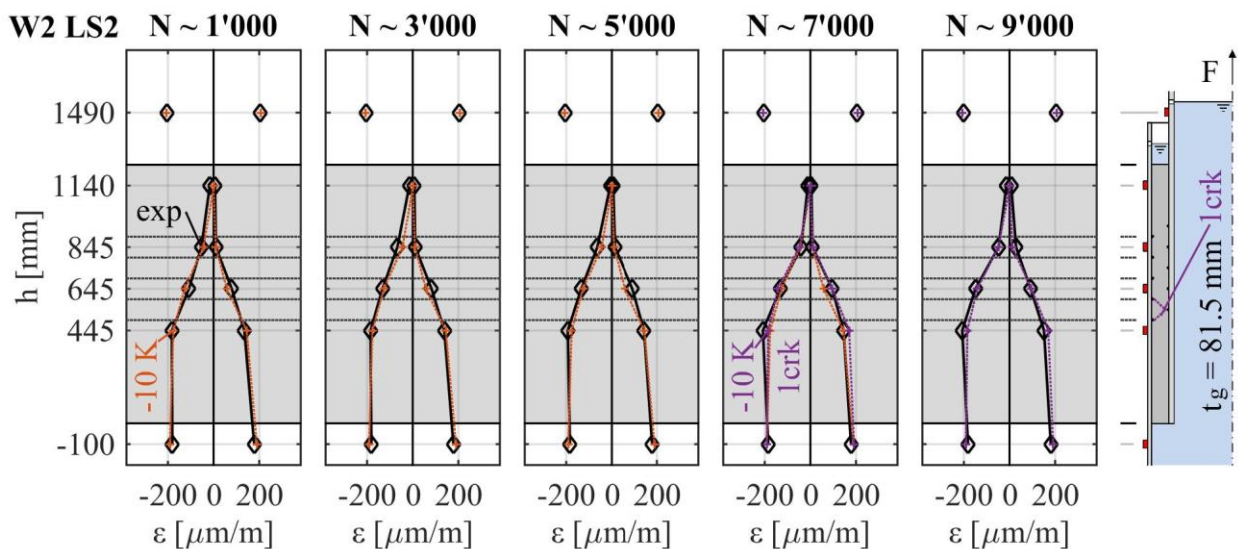


Figure 5.24: Axial strain distribution from numerical calculations and strain measurements in specimen W2 LS2 for different cracking states

In the dismantled specimen W2 diagonal shear cracks were found in the lower grout area between shear keys S1-P1 and S2-P1 (see Section 4.3.3). Figure 5.24 shows the axial strain distribution for specimen W2 with uncracked (orange line) and cracked (purple line) grout layer for load stage 2. During the first ~60 % of applied load cycles, the numerical results with autogenous shrinkage deformations equivalent to a thermal load of $\Delta T = -10$ K and without discrete cracks are in good

agreement with the experimental results. For the last ~40 % a better compliance to the experimental results is achieved with discrete cracks.

Specimen W3

Figure 5.25 and Figure 5.26 show the axial strain distribution from experimental results of specimen W3 as well as from numerical investigations with different rates of autogenous shrinkage and with different states of discrete cracks in the grout layer. In the beginning of load stage 1 (see Figure 5.25) the best compliance between experimental (black line) and numerical results is found for autogenous shrinkage deformations equivalent to a thermal load of $\Delta T = -15$ K and without discrete cracks (orange line). At $N \sim 30'000$ applied load cycles, a better agreement with experimental data can be obtained for a calculation without autogenous shrinkage and a first crack in the lower area of the grout layer (purple line). Subsequently, at $N \sim 50'000$ applied load cycles the compliance is improved when comparing experimental results to numerical results without autogenous shrinkage and a second crack (green line). Especially the strain value at $h = 945$ mm is significantly influenced by the second crack.

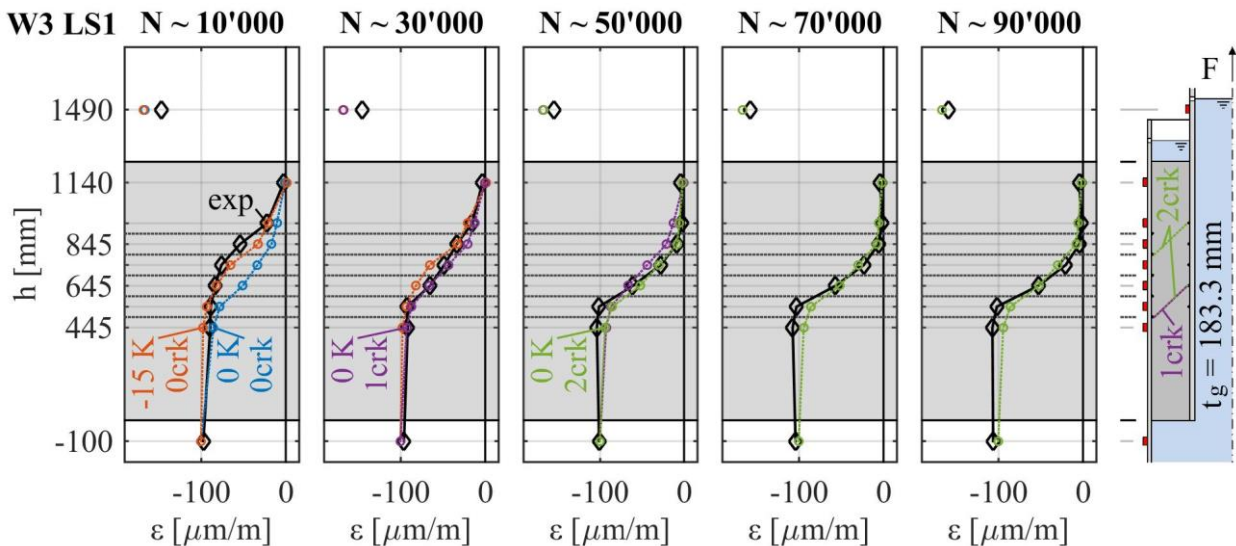


Figure 5.25: Axial strain distribution from numerical calculations and strain measurements in specimen W3 LS1 for different cracking states and shrinkage rates

For load stage 2 (see Figure 5.26) good compliance between experimental and numerical results is not possible with the chosen numerical models for the strain gauge positions between $h = 445$ mm and $h = 645$ mm. Nevertheless, the introduction of a third diagonal shear crack between shear keys S1 and P3 (red line) slightly increases the strain at $h = 445$ mm and decreases the strain at $h = 545$ mm, which might correspond to the experimental strain data in the beginning of load stage 2.

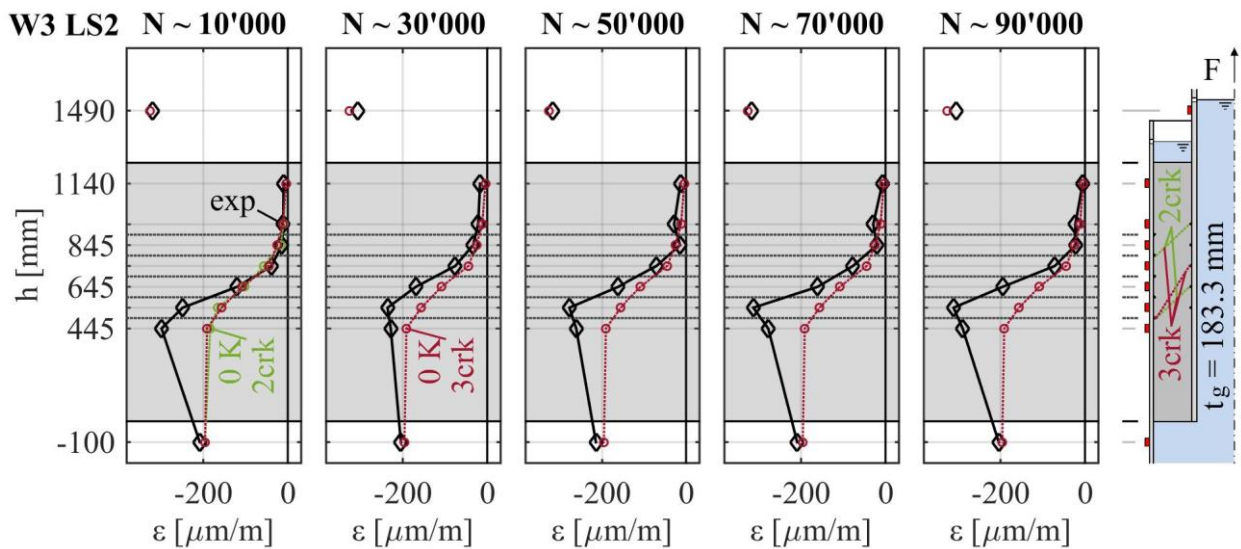


Figure 5.26: Axial strain distribution from numerical calculations and strain measurements in specimen W3 LS2 for different cracking states

Specimen W4

During load stage 1 the axial strain distribution given in Figure 5.27 shows good agreement between experimental data (black line) and numerical results with an autogenous shrinkage equivalent thermal load of $\Delta T = -15$ K (orange line).

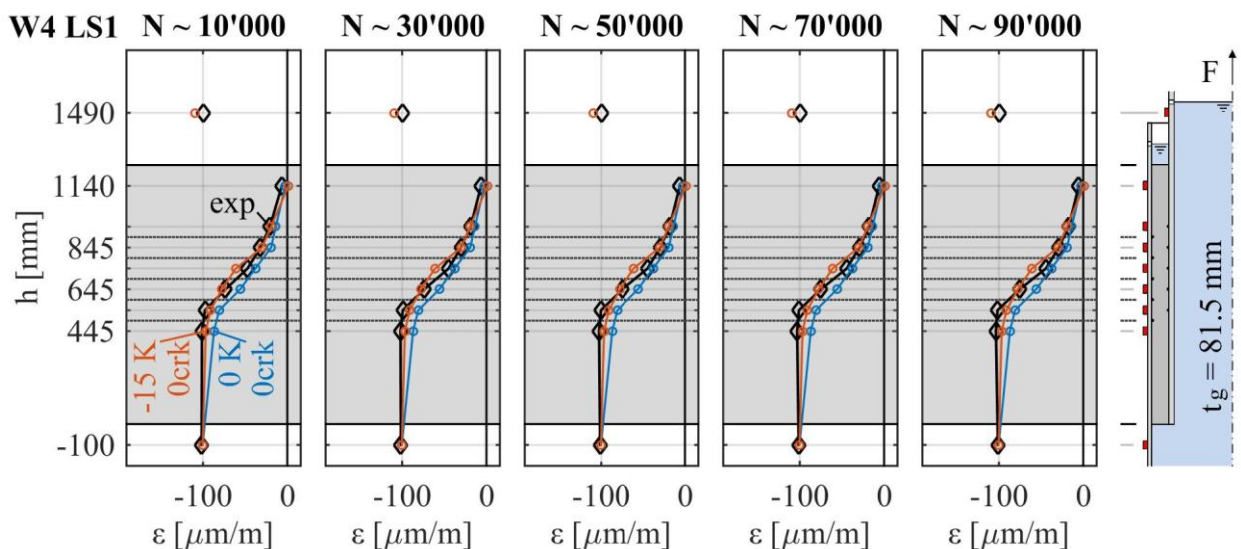


Figure 5.27: Axial strain distribution from numerical calculations and strain measurements in specimen W4 LS1 for different shrinkage rates

At $N \sim 10'000$ applied load cycles of load stage 2 (see Figure 5.28), the agreement between experimental data (black line) and numerical results improves for the calculations with 2 discrete cracks and no autogenous shrinkage (purple line). Especially the strain data at $h = 945$ mm are influenced by the uppermost diagonal shear crack. The measured strain increase at $h = 645$ mm between $N \sim 10'000$ and $N \sim 30'000$ applied load cycles of load stage 2 is best covered by the numerical calculations without autogenous shrinkage and four diagonal shear cracks (green line).

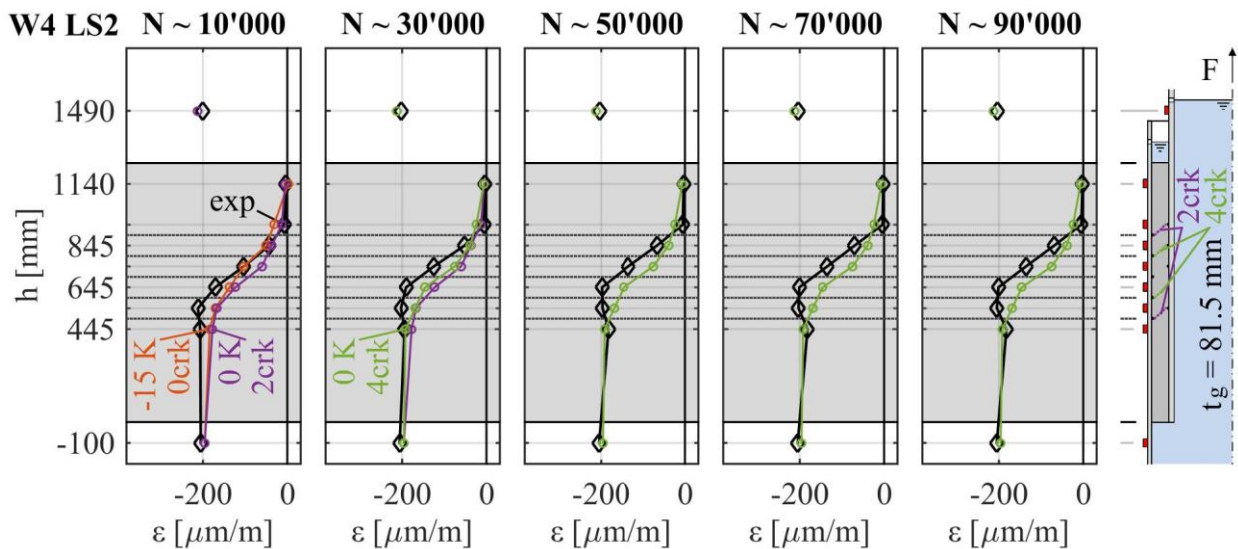


Figure 5.28: Axial strain distribution from numerical calculations and strain measurements in specimen W4 LS2 for different cracking states and shrinkage rates

At $N \sim 30'000$ applied load cycles of load stage 3, the numerical results calculated without autogenous shrinkage and an additional fifth diagonal shear crack between shear keys S1 and P2 (red line) give the best agreement with experimental strain data (black line). Especially the strain measured at $h = 445$ mm is influenced by the fifth crack.

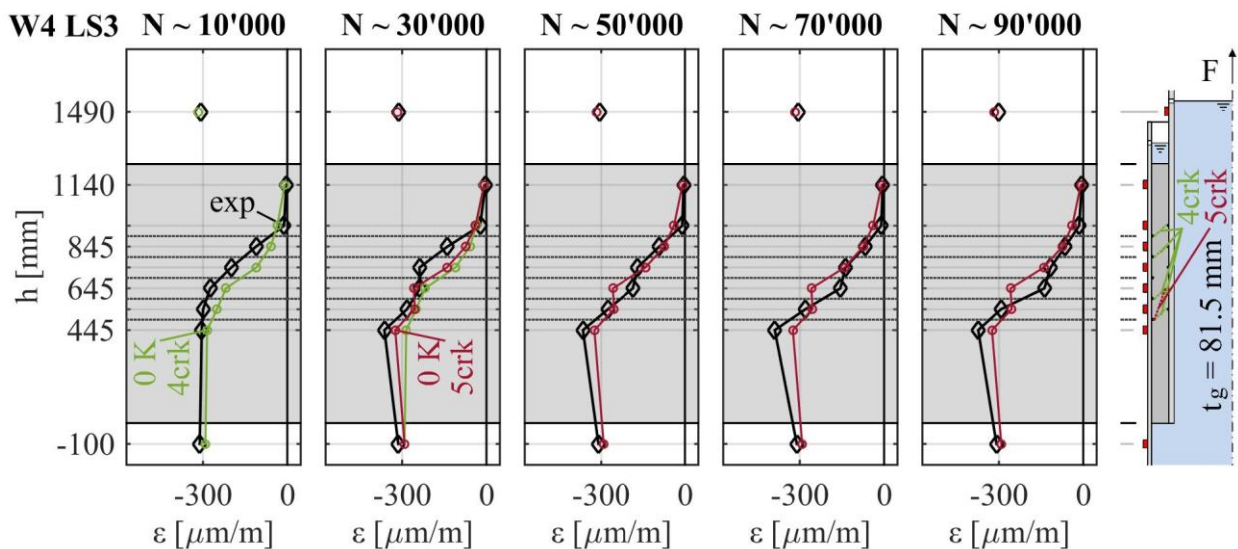


Figure 5.29: Axial strain distribution from numerical calculations and strain measurements in specimen W4 LS3 for different cracking states

The strain distribution for load stage 4 showed no additional insights. The corresponding Figure can be found in Appendix D.2.

Local stress distribution

Specimen W1

Figure 5.30 shows the minimum principal stress distribution per shear key for different values of autogenous shrinkage and a compressive load of 1 MN (LS1). The corresponding Figure for tensile

loading can be found in Appendix D.3. Without autogenous shrinkage (blue line) the main load share acts on shear keys P5 and S1. The stress level at shear key P5 almost reaches the fatigue stress level for $N = 10^5$ load cycles (upper dotted black line). Nevertheless, according to the fatigue calculation scheme (see Section 5.2.4), no displacement relevant fatigue damage occurs at this load level. At an autogenous shrinkage rate equivalent to a thermal load of $\Delta T = -10$ K (orange line) the load share per shear key on the pile reduces significantly and the main load share now acts on shear key P1. In contrast, the stress distribution at the shear keys on the sleeve concentrates towards the shear key root at $h_{sk} = 0.0$ and significantly increases up to five times of the stress level, calculated without autogenous shrinkage. At all shear keys S1 to S5 the stresses exceed the fatigue limit stress for $N = 10^0$ load cycles. Hence, from the beginning of this load stage fatigue damage must be expected at the interface between sleeve and grout in case of autogenous shrinkage. Without autogenous shrinkage fatigue damage is not likely to occur.

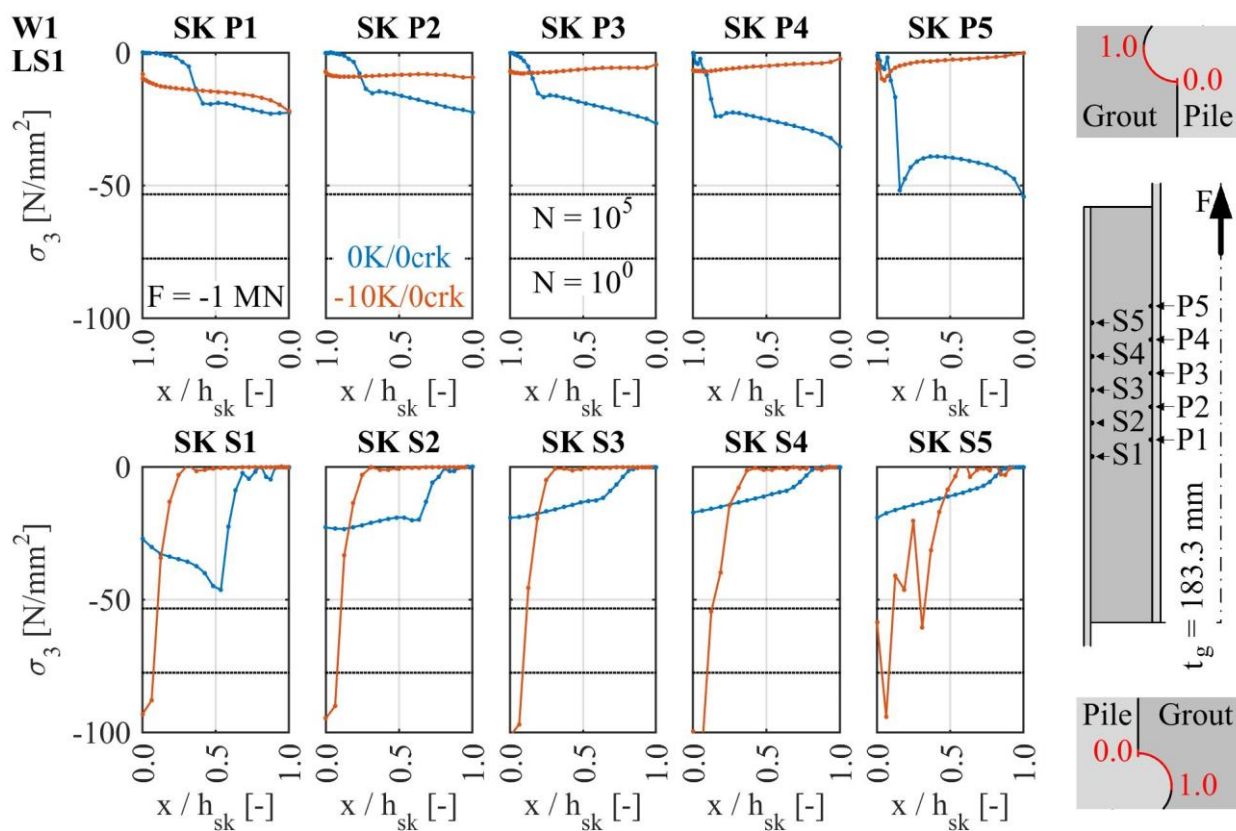


Figure 5.30: Minimum principal stress distribution from numerical calculations in specimen W1 LS1 (compression) for different measures of autogenous shrinkage

Specimen W2

The local stress distributions calculated for specimen W2 at load stage 1 and compressive loading of 1 MN are given in Figure 5.31. The corresponding stress distributions for tensile loading in load stage 1 can be found in Appendix D.3. For both calculations with (orange line) and without autogenous shrinkage (blue line), the results are similar to the ones of specimen W1. Main difference is a generally lower stress level at the pile shear keys for the larger pile diameter and lower stress concentrations towards the shear key roots ($h_{sk} = 0.0$) of the sleeve shear keys. Nevertheless, the stress concentration slightly exceeds the fatigue limit stress for $N = 10^0$ load cycles (lower dotted black line) at all shear keys S1 to S5. Hence, according to the numerical investigations, fatigue

damage has to be expected during load stage 1. In the absence of autogenous shrinkage, no fatigue damage has to be expected because all stresses are below the fatigue limit stress for $N = 10^5$ load cycles (upper dotted black line).

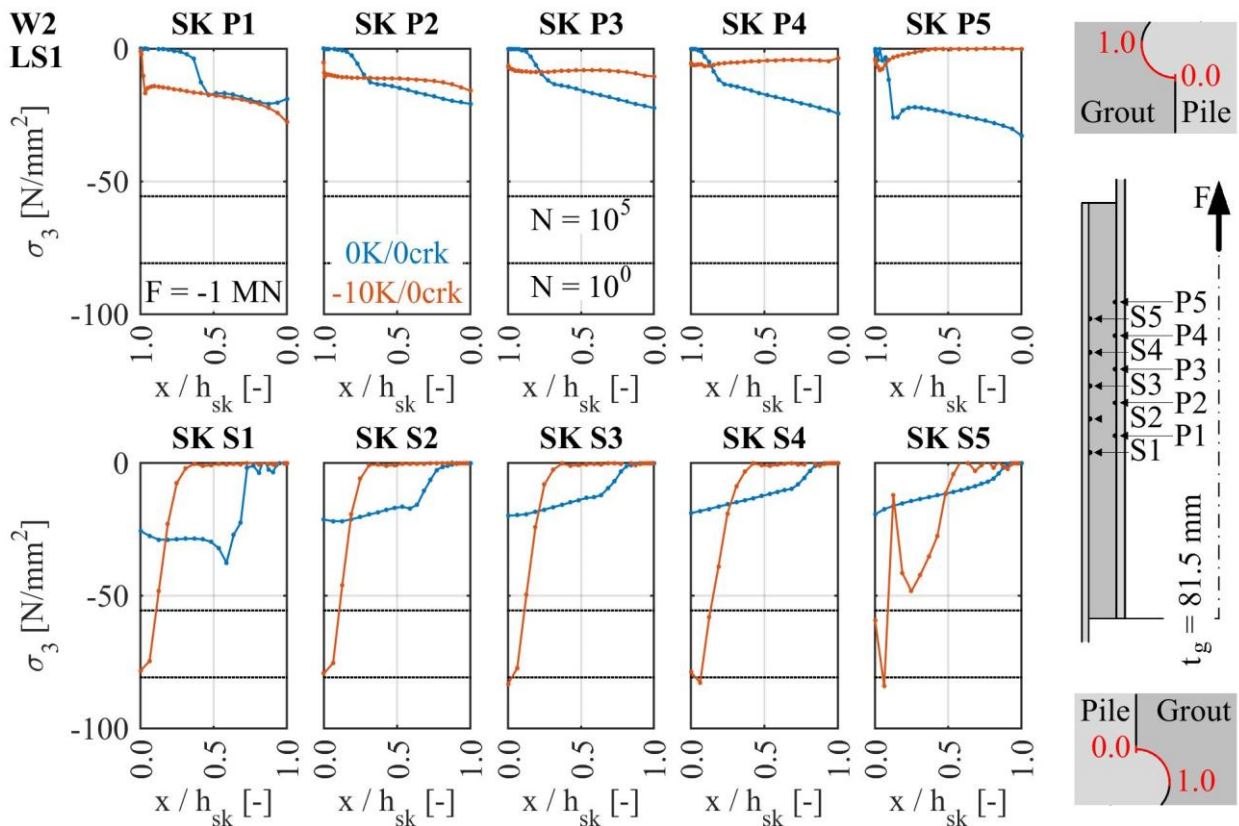


Figure 5.31: Minimum principal stress distribution from numerical calculations in specimen W2 LS1 (compression) for different autogenous shrinkage rates

Figure 5.32 and Figure 5.33 show the local minimum principal stress distributions for compressive and tensile loading at load stage 2. For the uncracked grout layer the stresses exceed the fatigue limit stress for $N = 10^0$ load cycles at all shear keys S1 to S5. In the cracked grout layer the stresses at the sleeve shear keys caused by compression loading are only slightly influenced, whereas for tensile loads shear key S2 is deactivated by the crack and the stresses at the remaining shear keys S1, S3 to S5 increase respectively. Hence, according to the numerical investigations, degradation at the sleeve shear keys must be expected for load stage 2 of specimen W2 and an increased degradation once the diagonal shear cracks have evolved.

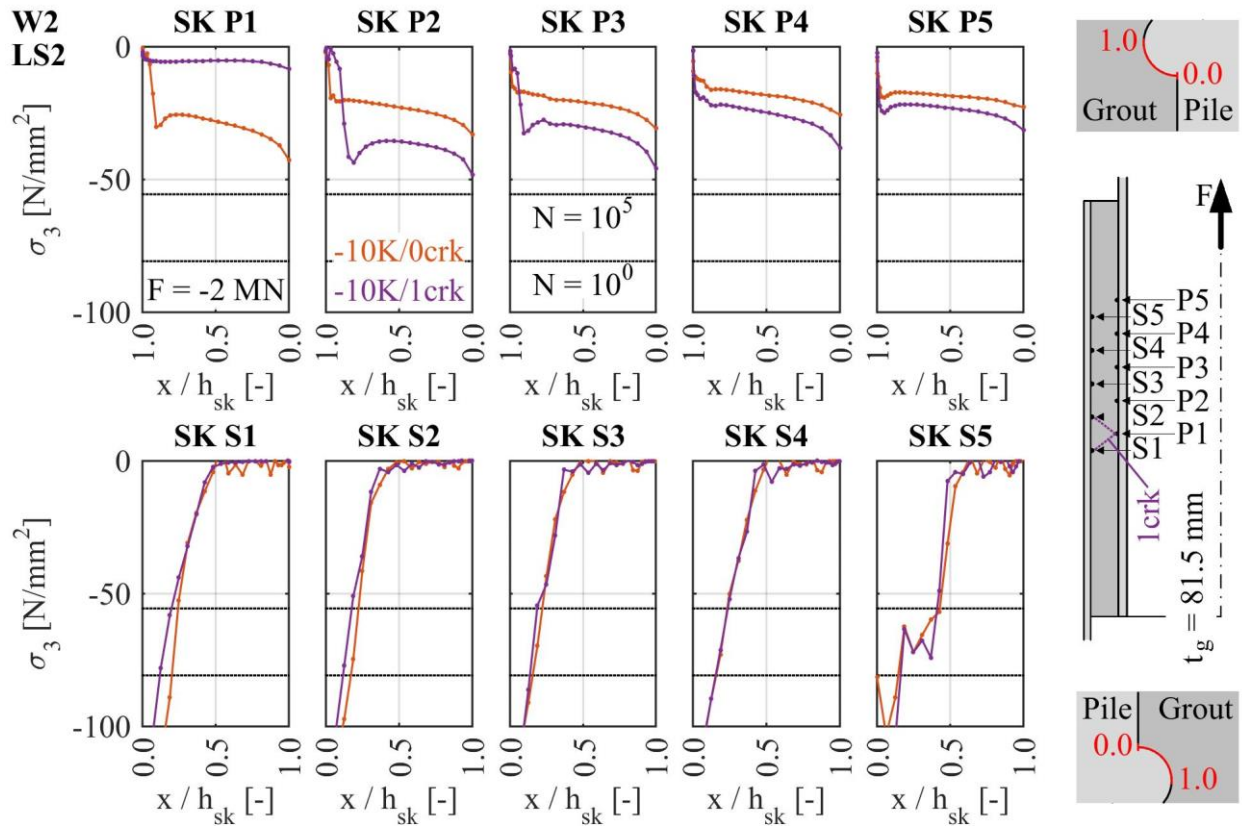


Figure 5.32: Minimum principal stress distribution from numerical calculations in specimen W2 LS2 (compression) for different cracking states

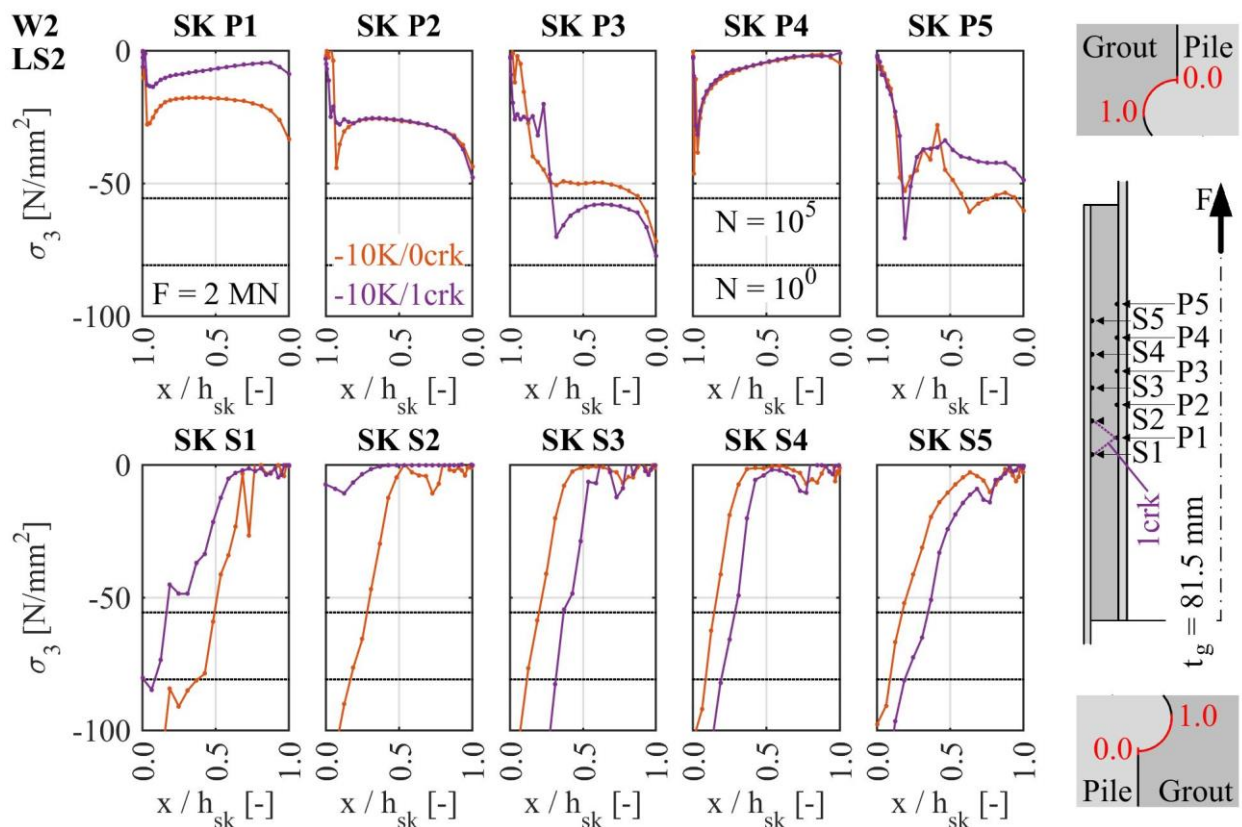


Figure 5.33: Minimum principal stress distribution from numerical calculations in specimen W2 LS2 (tension) for different cracking states

Specimen W3

At load stage 1 of specimen W3 the local minimum principal stress distribution given in Figure 5.34 and calculated with an autogenous shrinkage equivalent thermal load of $\Delta T = -15$ K (orange line) exceeds the fatigue limit stress for $N = 10^0$ load cycles at all shear keys S1 to S5. Thus, fatigue related degradation must be expected from the beginning of load stage 1. The two other local stress distributions are below the fatigue limit stress for $N = 10^5$ load cycles at all shear keys. Thus, they are not likely to cause fatigue damage in this load stage. For the stress distribution calculated with two discrete diagonal shear cracks (green line), both shear keys P1 and P2 are deactivated for the load transfer. Hence, the load share for shear keys P3 to P5 increases.

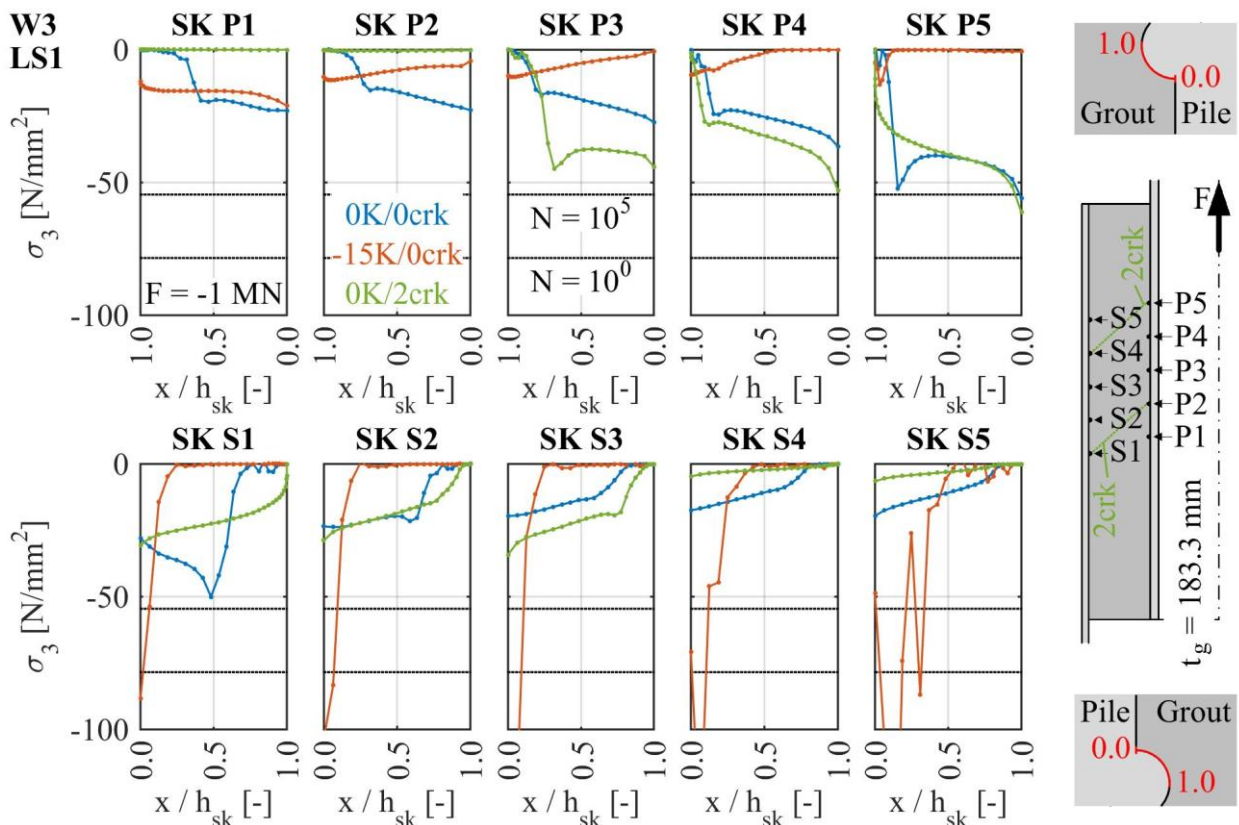


Figure 5.34: Minimum principal stress distribution from numerical calculations in specimen W3 LS1 for different cracking states and autogenous shrinkage rates

In load stage 2 (see Figure 5.35) the local stress distribution calculated with two discrete shear cracks (green line) exceeds the fatigue limit stress for $N = 10^0$ load cycles at the shear keys P3 and P5 and almost at P4. For the shear keys at the sleeve all stresses are below the fatigue limit stress for $N = 10^5$ load cycles. Hence, fatigue damage is likely to occur at the active shear keys along the pile. With an additional third diagonal shear crack (red line) the stress distributions for the remaining active shear keys P4 and P5 significantly exceed the fatigue limit stress for $N = 10^0$ load cycles. Contrarily, the stress distribution along the sleeve shear keys is just slightly influenced by the discrete cracks.

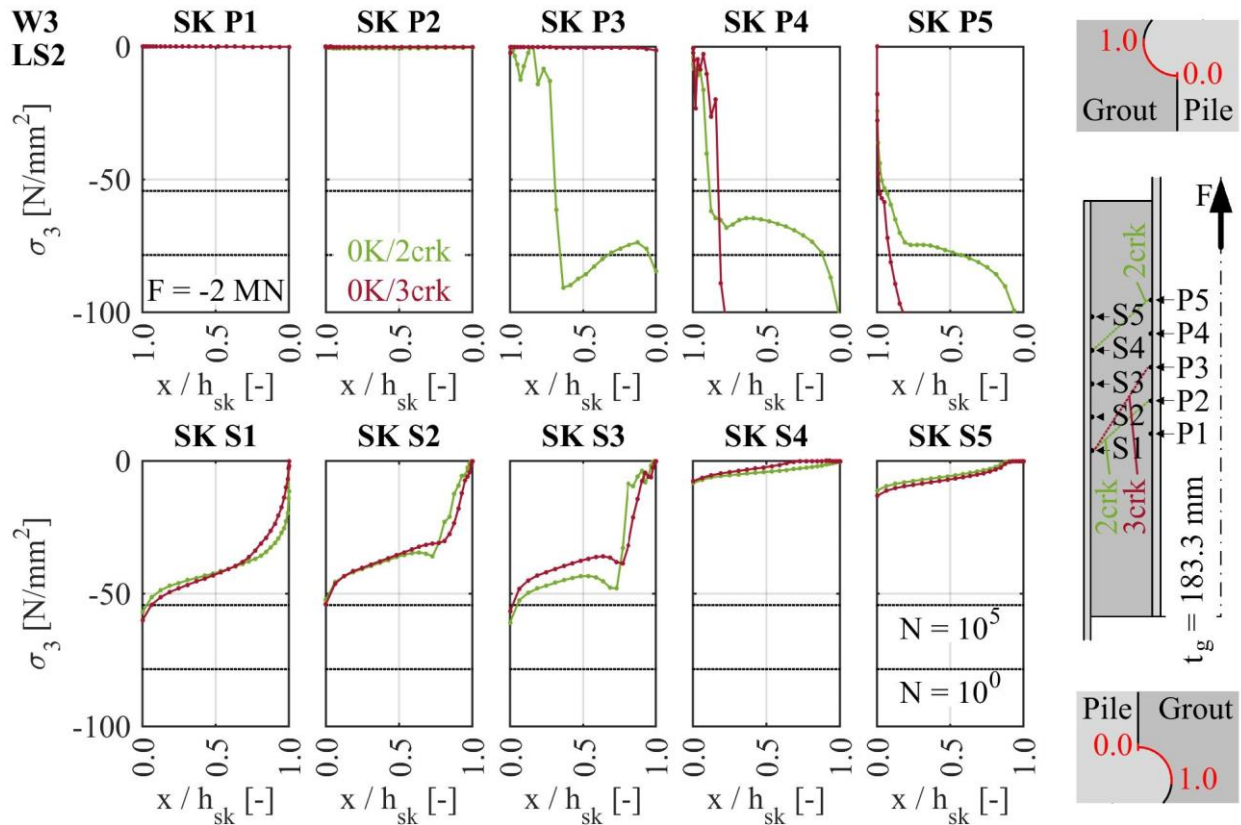


Figure 5.35: Minimum principal stress distribution from numerical calculations in specimen W3 LS2 for different cracking states

Specimen W4

The local minimum principal stress distribution (see Figure 5.36) calculated for specimen W4 at load stage 1 and without autogenous shrinkage (blue line) is below the fatigue limit stress for $N = 10^5$ load cycles at all shear keys. Thus, no fatigue damage is likely to occur in this scenario. In contrast, the local stress distribution calculated with an autogenous shrinkage equivalent thermal load of $\Delta T = -15$ K (orange line) exceeds the fatigue limit stress for $N = 10^0$ load cycles at all shear keys S1 to S5 during load stage 1. Hence, grout material degradation in load stage 1 must be expected in case of significant autogenous shrinkage.

In load stage 2 the minimum principal stresses calculated with 2 diagonal shear cracks (purple line) slightly exceed the fatigue limit stress for $N = 10^0$ load cycles at shear keys P2 and P3 (see Figure 5.37). Two additional diagonal shear cracks (green line) lead to only minor changes in the stress distribution. With introduction of the lowest diagonal shear crack, shear key P1 is deactivated. The comparison of the stress distributions for the different cracking states at shear key P2 shows that numerical cracking of the CDP material model (purple line) in front of the shear key tip ($h_{sk} = 1.0$) causes small but inhomogeneous stresses at $\sim 1/3$ of the shear key height followed by a significant stress peak. In contrast, a discretely modelled crack (green line) leads to a homogenous stress distribution along the full shear key height and a generally lower stress level. Hence, for the calculations without autogenous shrinkage, fatigue damage is not likely to occur in load stage 2.

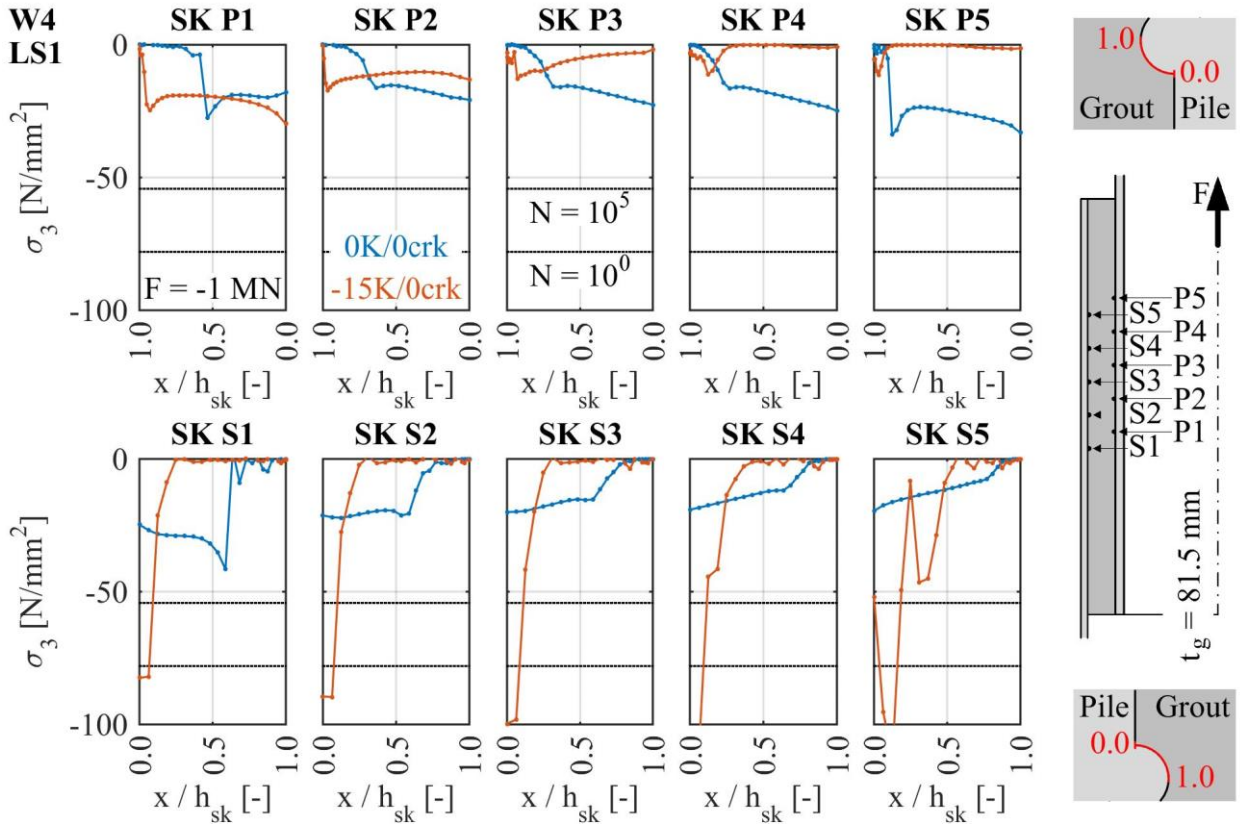


Figure 5.36: Minimum principal stress distribution from numerical calculations in specimen W4 LS1 for different autogenous shrinkage rates

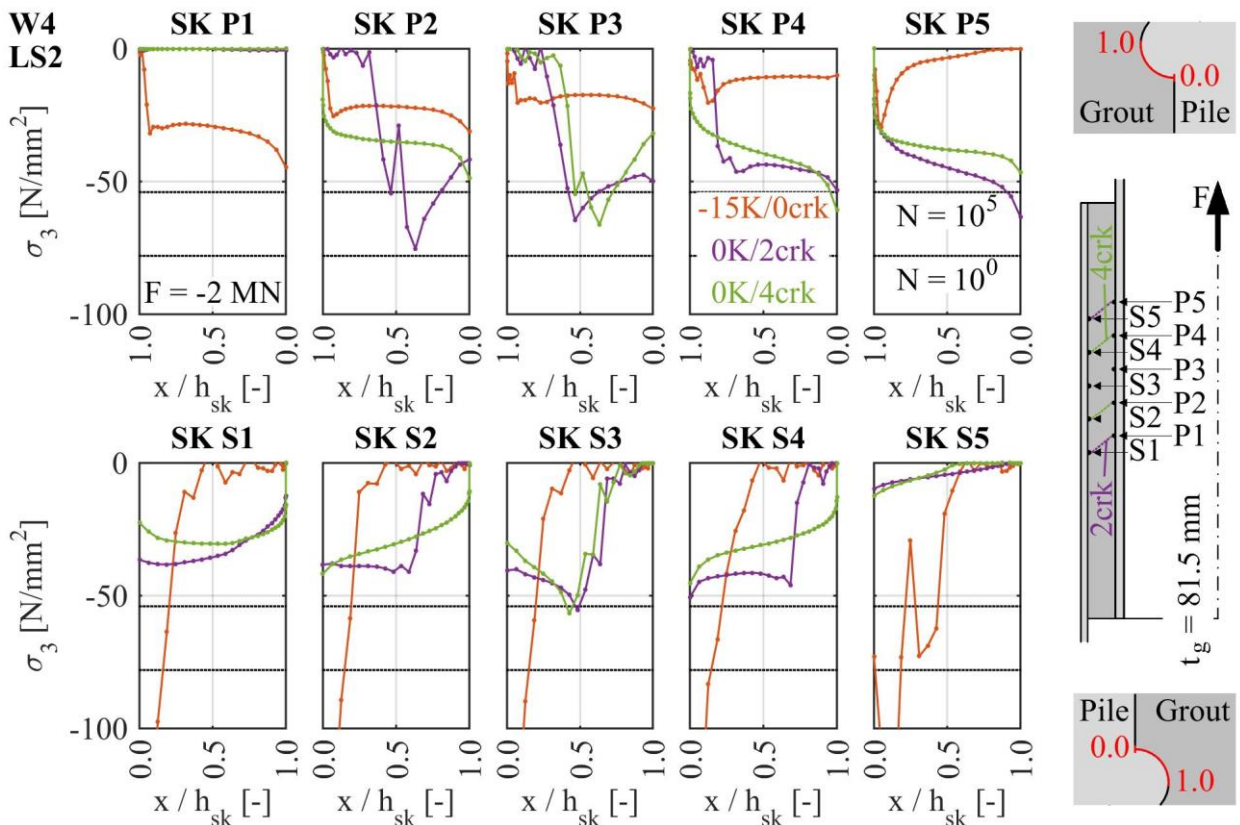


Figure 5.37: Minimum principal stress distribution from numerical calculations in specimen W4 LS2 for different cracking states and autogenous shrinkage rates

The load increase to -3 MN in load stage 3 (see Figure 5.38) causes all stresses at the pile shear keys to exceed the fatigue limit stress for $N = 10^5$ load cycles (green line). As a result, fatigue damage must be expected during load stage 3. Once a fifth additional diagonal shear crack between shear keys S1 and P2 has occurred (red line), shear key P2 is deactivated and the stress increase for the remaining shear keys leads to exceedance of the fatigue limit stress for $N = 10^0$ load cycles at shear key P3 and P4. Thus, a faster degradation is likely to occur once the fifth crack has evolved.

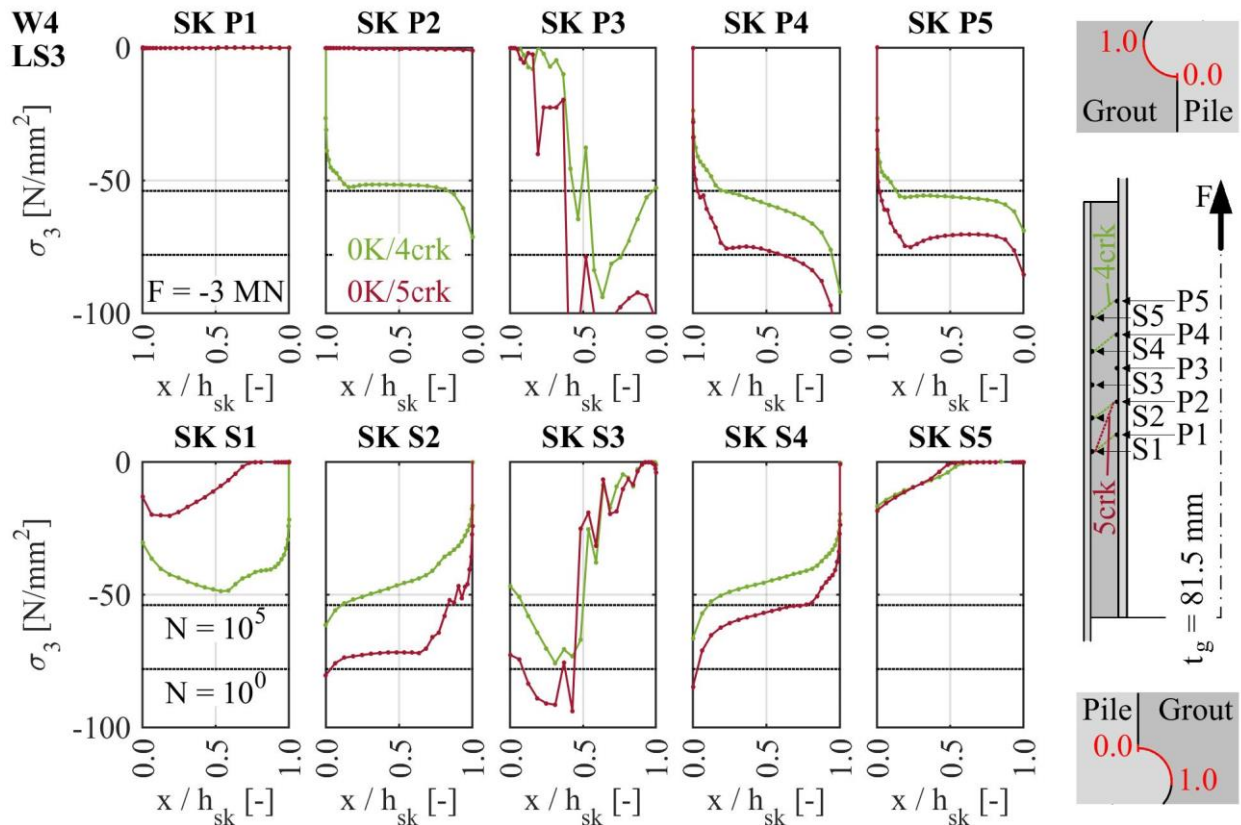


Figure 5.38: Minimum principal stress distribution from numerical calculations in specimen W4 LS3 for different cracking states

The minimum principal stresses, calculated for load stage 4, significantly exceed the fatigue limit stress for $N = 10^0$ load cycles at all relevant shear keys. The corresponding plot can be found in Appendix D.3.

5.4 Discussion

5.4.1 Grout material parameters

The investigations on the general behaviour of the “Concrete Damaged Plasticity” material model (see Section 5.3.1) showed good agreement with recommendations from the literature as well as with experimental results for HPG material. Moreover, the proposed approach for estimating all necessary material parameters (see Section 5.2.3) could be confirmed to give good results. Hence, the material model can be rated as suitable and recommendable for numerical investigations of grouted connections.

5.4.2 Fatigue Limit State (FLS)

Small-scale specimens

The comparison between experimental and numerical results according to the introduced fatigue verification approach showed big differences (see Section 5.3.2) with significantly lower fatigue capacities according to the numerical results. However, it has to be considered that by definition of the fatigue verification approach no material removal occurs for $D < 1$ and thus no displacement offset between steel and grout. In contrast, the experimental results indicate failure of the specimens after relative displacements of up to 8 mm were measured (see Section 3.5.2). Results from calculations with discretely modelled cracks underlined the importance of the influence of cracks on the fatigue behaviour of grouted connections.

Specimen W1

The comparison of strain distributions from different numerical calculations for specimen W1 (see Figure 5.22) underlines the assumption of autogenous shrinkage deformations in the grout layer. As shown in Figure 5.30 the local stresses at the shear keys on the sleeve exceed the fatigue stress limit for $N = 10^0$ load cycle when assuming an autogenous shrinkage value of $-100 \mu\text{m/m}$, which corresponds to the material characteristics stated by the grout material manufacturer (see Table 5.3). Consequently, grout crushing must be expected to occur right from the start of load stage 1. In wet AC the crushed grout material on both sides of the shear key groove is flushed out by the water and a connection backlash evolves as described in Section 4.3. On the one hand the material removal might increase the width of the load application area and thus reduce the stress peaks towards the stress distribution calculated without autogenous shrinkage. On the other hand the alternating load and the connection backlash lead to the observed load impulse (see Section 4.3.2) and thus increase the degradation mechanism.

This fatigue evaluation corresponds to the measured relative displacements presented in Figure 4.13. It is clearly visible that the degradation started right from the beginning of load stage 1. Moreover, the increase of displacement slightly slowed down after $\sim 20\%$ of applied load cycles, which would correspond to a larger load application area of the shear keys.

Specimen W2

For specimen W2 a degradation behaviour similar to specimen W1 was observed (see Section 4.3.3). Likewise, the numerical investigations also showed good agreement with experimental data for calculations with autogenous shrinkage values of $-100 \mu\text{m/m}$. However, for the thinner grout layer less deformation caused by autogenous shrinkage was calculated and therefore the stress peaks at the sleeve shear keys are lower in load stage 1 than for specimen W1. As a result, the degradation can be expected to be significantly slower at identical load levels for the thinner grout layer.

For load stage 2 the stress levels at the shear keys S1 to S5 significantly exceed the fatigue stress limit for $N = 1$. The discrete cracks and the resulting deactivation of shear key S2 lead to an increase of the stress levels at the sleeve shear keys. Hence, significant grout degradation must be expected during load stage 2.

The measured relative displacement for load stage 1 presented in Figure 4.14 showed a slight degradation during the first ~30 % of applied load cycles. This behaviour can be interpreted as a removal of the initial stress peaks caused by autogenous shrinkage. Afterwards a stable load bearing behaviour was observed (see Figure 4.14). Even though the local influence of autogenous shrinkage vanished by the degradation behaviour during load stage 1, the axial strain distribution (see Figure 5.23) shows a sustained global influence of autogenous shrinkage.

From the beginning of load stage 2, an increase of relative displacement between sleeve and grout was measured (see Figure 4.14). After approximately 10'000 load cycles the relative displacement suddenly increased and the specimen failed. Corresponding, towards the end of load stage 2 the measured strain distribution showed better agreement with the distribution, calculated with a cracked grout layer (see Figure 5.24). The discrete cracks lead to higher stress concentrations and thus a faster degradation.

Specimen W3

During the first half of load stage 1, the change of the measured axial strain distribution of specimen W3 can be explained by a reduced influence of autogenous shrinkage and formation of two cracks (see Figure 5.25). For the local stress distributions at the shear keys (see Figure 5.34) this behaviour would correspond to a reduction of stress concentrations below the fatigue limit stress for $N = 10^5$ load cycles at all shear keys. Hence, only minor degradation in the beginning of load stage 1 can be expected from the numerical investigations. This corresponds to the relative axial displacement measured during the experiments. As shown in Figure 4.16 both measurements between pile and sleeve as well as between sleeve and grout show a slight increase during the first ~40 % of applied load cycles. Afterwards, the relative axial displacement remains constant.

In load stage 2 a good compliance between measured and calculated strain distributions could not be obtained, but the formation of a third crack at ~20 % of applied load cycles can be assumed (see Figure 5.26). The local stress distributions at the shear keys given in Figure 5.35 lead to the assumption that material degradation is likely to occur from the beginning of load stage 2 and considerably increased once the third diagonal shear crack has evolved. Comparing these, numerical investigations based, expectations to the measured relative axial displacements, given in Figure 4.16, shows good compliance. A distinct increase in displacement is measured at ~20 % of applied load cycles where the formation of the third crack is expected.

Specimen W4

During load stage 1 the axial strain distribution of specimen W4 (see Figure 5.27) shows best agreement with the numerical calculations including autogenous shrinkage. The distribution is constant during the whole load stage. The corresponding local stress distributions given in Figure 5.36 show exceeded fatigue limit stresses for $N = 1$ load cycles at all shear keys along the sleeve,

caused by autogenous shrinkage. Thus, material degradation at the shear keys should be expected. Contrarily, the measured relative displacements (see Figure 4.17) do not show any degradation during the first load stage.

Similar to the observations for load stage 1 of specimen W3, in the first ~40 % of applied load cycles of load stage 2 the compliance between measured and calculated axial strain distribution changes from an uncracked grout layer with autogenous shrinkage to four diagonal shear cracks and no autogenous shrinkage (see Figure 5.28). For the local stress distributions (see Figure 5.37) this behaviour would lead to homogenised distributions with stresses slightly below the fatigue limit stress for $N = 10^5$ load cycles at all shear keys. Hence, only slight degradation is expectable during load stage 2. This is in good agreement with the measured relative axial displacement shown in Figure 4.17.

In load stage 3 the introduction of a fifth diagonal shear crack at ~ 30 % of applied load cycles improves the compliance between numerical and experimental results of the axial strain distribution (see Figure 5.29). Further changes in the strain distribution during load stage 4 cannot be explained by the chosen numerical models. From the beginning of load stage 3 the local stress distribution exceeds the fatigue limit stress for $N = 10^5$ load cycles at all shear keys along the pile (see Figure 5.38). With introduction of the fifth diagonal shear crack, stresses increase above the fatigue limit stress for $N = 1$ load cycles. Hence, significant degradation must be expected once the fifth shear crack has evolved. The numerical investigation based behaviour corresponds to the measured relative axial displacement given in Figure 4.17. During load stage 3, clear degradation is visible which increases drastically in load stage 4. In correspondence, the local stress levels at the shear keys along the pile are similar for load stage 2 of specimen W3 and load stage 4 of specimen W4. Likewise, the degradation rates for these load stages are similar (see Table 4.3).

5.4.3 Autogenous shrinkage

The results of the numerical investigations (see Section 0) showed a significant influence of autogenous shrinkage on the local stress distribution at the shear keys at both specimen scales (see e.g., Figure 5.18 and Figure 5.30). For all investigated specimens the equivalent thermal load cases caused a detachment of the grout layer from the sleeve surface. Moreover, the local stresses at the shear keys along the sleeve increased significantly because a smaller area could be activated for the load transfer between shear key and grout. In contrast, the local stresses at the shear keys along the pile reduced distinctly due to pre-stressing of the pile-grout interface and activation of surface friction capabilities between the shear keys. These results confirm similar theoretical considerations described in Section 4.4.3.

For the large-scale specimens W1 and W2 no radial cracks were observed during the experiments (see Section 4.3.1). Moreover, the grout degradation occurred at the shear key grooves facing the sleeve (see Section 4.3.3). The numerical results calculated with autogenous shrinkage are in good agreement with these observations, especially regarding the local stress distribution at the shear keys (see e.g., Figure 5.30). During fatigue loading, local grout degradation at contact singularities around the shear keys, leads to a larger grout area that can be activated for the load transfer. This reduces the local stress concentrations and has a positive effect on the grout material's fatigue behaviour. However, a growing connection backlash is inevitable. As a result, for alternating loads

the positive effect of stress concentration reduction is counteracted by the impulse load caused by connection backlash (see Section 4.3.2).

During the experiments on specimens W3 and W4, radial cracks associated with autogenous shrinkage were observed (see Section 4.3.1). Likewise to specimens W1 and W2, the numerical investigations on specimens W3 and W4 with autogenous shrinkage showed fatigue critical stress concentrations at the shear keys along the sleeve. In contrast, only minor degradation at this interface was measured during the experiments (see e.g., Figure 4.16). Nevertheless, the comparison between numerical and experimental axial strain distributions (see e.g., Figure 5.27) showed good agreement when considering autogenous shrinkage for the first load stage. It can be concluded that radial cracks caused by autogenous shrinkage release the pre-stress of the pile-grout interface and thus reduce its positive effect on the local stress distribution. Simultaneously, the stress concentrations at the shear keys along the sleeve are reduced, resulting in a positive effect regarding fatigue damage. Thus, as long as only compression-compression or tension-tension loads are applied to a grouted connection, the local stress concentrations might vanish during the first load cycles and leave a settling of the connection. If the resulting stress distribution is below the fatigue critical stress level no further degradation might occur in the grout layer.

Consequently, the investigations on autogenous shrinkage confirm the recommendation that alternating loads should be excluded from acting on grouted connections. In cases of compression-compression or tension-tension loading the effects of autogenous shrinkage can be considered in a design analysis by a slightly reduced fatigue strength and possible settlements of the connection.

5.4.4 Discrete cracks

Investigations with discrete diagonal shear cracks confirmed the assumed influence on the load transfer behaviour in the contact interfaces and especially the deactivation of specific shear keys for the load transfer between steel and grout (see Section 4.4.2). Basis for the numerical investigations were quasi-static stress calculations. Load cycle dependent material behaviour was covered in the later fatigue evaluation. Thus, expectable crack growth could only be considered in the numerical calculations by the discretely modelled cracks. Consequently, if, for example from ULS load cases, load levels must be expected which are likely to cause diagonal shear cracks, the possible influence of diagonal shear cracks shall be investigated as part of the fatigue verification.

5.4.5 Requirements for a standardisation

The previously described fatigue verification approach showed very good agreement with the experimental results and hence provides a first tool for the fatigue safe design of axially loaded grouted connections for a submerged application. Due to the complex numerical procedure necessary for a reliable calculation, several requirements must be defined to standardise this approach. In the following the major requirements are summarised.

- **Applicability**

Within this thesis, the fatigue verification approach for submerged grouted connections is validated for connections loaded with axial compression-compression and filled with cement based grout materials with aggregates.

- **Geometric model with shear keys**

First of all, the geometric model must include modelled shear keys. The shear key shape should be as realistic as possible, but in relation to the general element size. Hence, modelling geometrical changes smaller than the general element size, for example filleting of the shear key roots, is not necessary.

The geometrical model should also cover the whole overlapping length between grout and steel (see Figure 5.1) to allow a reliable depiction of the individual load share per shear key.

- **Mesh density and element size**

The appropriate element size should be investigated in a sensitivity study, which is carried out for the load transfer area at the decisive shear key as described in Section 5.2.4 (see also Section 5.3.2 and Figure 5.6 as well as Section 5.3.3 and Figure 5.21). Within this thesis, an element size of 16 elements along the shear key height gave the best results. A deviation of the mesh density should only be permissible, if its influence on the local stress distribution at the shear keys can be proven to be negligible. This is required because the cracking behaviour of the CDP material model significantly varies with element size deviations and consequently influences the local stress distribution.

- **Material model for grout**

For the grout layer a material model capable of covering the nonlinear material behaviour of grout should be utilised. This applies in particular to the low tensile strength. Within this thesis the material model “Concrete Damaged Plasticity” was used. The applicability of other material models can be proven by a comparison between the material model’s yield surface with the Ottosen (1977) yield surface as described in Section 5.3.1 and shown in Figure 5.9. Moreover a comparison between calculation results with results presented in this thesis can provide further proof.

- **Interaction between steel and grout**

Between steel and grout Coulomb friction must be applied. The effect of different friction coefficients should be investigated in a sensitivity study. By virtue of missing reliable friction values for wet friction between steel and grout, friction coefficients can be chosen between $0.0 \leq \mu \leq 0.5$ (see Section 5.2.2). Within this thesis a friction coefficient of $\mu \leq 0.4$ gave the best compliance between experimental and numerical results.

- **Cracks**

Since the cracking state of the grout layer influences the load share per shear key and also can lead to deactivation of shear keys, the effect of cracking states on the local stress distributions should be considered. Grout areas and shear keys which do not participate in the load transfer (see Figure 4.34, W3 and W4) can be identified by estimating the diagonal shear cracks in the end regions. The crack orientation can be estimated as the diagonal, between a shear key on the pile and a shear key on the sleeve, which has an orientation angle closest to 45° .

The deactivated shear keys can be considered by modelling actual cracks or by leaving out the deactivated shear keys in the model. The cracks can be modelled by splitting the grout layer along the crack orientation. Contact definition of the crack surfaces is only necessary if closing of the crack or shear deformations can occur.

- **Submodelling**

The use of submodels can be allowed if the global load share per shear key and the influence of a different cracking states of the grout layer is appropriately covered. Corresponding proof must be provided by the user.

- **Fatigue verification**

The final fatigue verification can be carried out as described in Section 5.2.5 with inclusion of the fatigue calculation procedure described in MC2010 (2013).

5.5 Summary and conclusion

Numerical investigations were carried out for all small- and large-scale geometries. Additional to different sets of material parameters, autogenous shrinkage as well as discretely modelled cracks were considered. Moreover, a general modelling approach and a fatigue verification approach for numerical investigations on grouted connections were described. The numerical results showed good agreement with the experimental results and facilitated the understanding of the critical influences on the load bearing and fatigue behaviour of grouted connections. The main findings for the defined objectives of this Chapter can be summarised as follows:

- **Development and validation of numerical models**

A general modelling approach for axially loaded grouted connections was described. The model must include discretely modelled shear keys and has to be meshed with a sufficient element size to cover the local stress distribution in front of the loaded shear key surfaces. A corresponding verification approach was presented. For the material model “Concrete Damaged Plasticity”, used for the grout layer, a way to estimate all necessary material parameters was described. The final material definition was validated by comparison to experimental results and was in very good compliance.

- **Influence of autogenous shrinkage**

Investigations on autogenous shrinkage showed good agreement with the load bearing behaviour of all large-scale specimens and the degradation behaviour of specimens W1 and W2. In cases of compression-compression loading (specimens W3 and W4) the influence of numerically estimated autogenous shrinkage on the local degradation behaviour could not be confirmed with experimental data. It is assumed that for these specimens the effects of autogenous shrinkage in tangential direction were dissolved by radial cracking. The results lead to the conclusion that alternating loads should be generally prevented. Moreover, the influence auf autogenous shrinkage on the local stress state can be neglected in cases were radial cracking, caused by autogenous shrinkage is presumable. Nevertheless, an initial settling process must be expected for the connection.

- **Influence of cracks**

The cracking capabilities of the “Concrete Damaged Plasticity” material model showed that in general, crack initiation at the shear key tips must be expected. This can be caused by the applied load but also by autogenous shrinkage. The initial cracks cause a stress increase at the load transferring interface between shear key and grout and therefore must be considered in a fatigue verification. Moreover, calculations with discretely modelled cracks proved the assumption of possible shear key deactivation in correspondence with the crack position and a resulting load share increase for the remaining active shear keys. Thus, these crack states can be covered in a fatigue verification similar to the beforehand described approach.

- **Development and validation of a fatigue verification approach for wet AC**

The fatigue behaviour of submerged grouted connections is governed by local grout crushing in front of the loaded shear key surface and subsequent flushing of the crushed grout particles due to water circulating in the contact interface. Based on the assumption that the critical particle flushing can be prevented if local crushing is excluded, a fatigue verification approach was developed. It was based on evaluating the minimum principal stresses in the grout layer in front of the loaded shear key surfaces and comparing them to uniaxial compression-compression S-N curves from MC2010 (2013). The calculated results were conservative for the small-scale specimens and showed very good agreement with the experimental results of the large-scale specimens. Requirements for a standardisation of the described fatigue verification approach for wet AC were defined.

6 Summary and Outlook

6.1 Summary

Predominantly axially loaded grouted connections, as they are applied in lattice substructures of offshore wind turbines and substations, are located in submerged ambient conditions. Prior to this thesis, very limited knowledge on interactions between connection and the surrounding water was available. This motivated the thesis in hands which deals with the influence of water on the fatigue behaviour of axially loaded grouted connections in submerged conditions.

As outlined in the state of the art, interactions between water and concrete which result in a reduced fatigue capacity were known from experimental investigations as well as degradations observed in real applications. Nonetheless, neither corresponding investigations on grouted connections had been carried out nor possible influences were considered in design approaches and recommendations. Therefore, in the scope of this thesis, a three-stage investigation was carried out. In the first stage experiments on small-scale grouted connections were performed in order to investigate the main influence of water and identify relevant parameters. In the second stage experiments on large-scale specimens were used to verify the findings from the small-scale experiments at this scale. Finally, the third stage comprised numerical investigations to supplement the experimental investigations and develop a design verification approach for the fatigue behaviour of axially loaded grouted connections in submerged ambient conditions.

In total 78 small-scale and 4 large-scale tests were conducted and evaluated. The presented experiments are the world's first investigations on submerged grouted connections. In the following, the main findings from the presented experimental and numerical investigations are summarised.

- **Surrounding water**

The experimental investigations at both scales showed a significantly reduced fatigue capacity for grouted connections loaded in submerged conditions. The main degradation mechanism was the crushing of grout material in front of the loaded shear key surfaces and subsequent flushing of the crushed grout particles by water, pumped through the grout steel interface. This resulted in widened shear key grooves in the grout layer and increasing relative displacements between steel and grout. While in dry AC the crushed grout particles stay in place and further participate in the connection's load bearing behaviour, this structure related benefit is lost in wet AC. Thus, for the verification of a grouted connection design against fatigue failure in submerged application, the influence of water has to be considered.

- **Autogenous shrinkage**

Significant influences of autogenous shrinkage were observed in the large-scale experiments. The numerical investigations, which include autogenous shrinkage, confirmed this influence. In combination with alternating loads ($R < 0$) autogenous shrinkage became severely critical, while for compression-compression loading its influence vanished over time. In the small-scale experiments autogenous shrinkage was less important because of

the smaller geometrical dimensions and less resulting shrinkage deformation. It was concluded that autogenous shrinkage affects the load bearing behaviour of grouted connections with shear keys. The radial and axial shrinkage deformations not only influence the axial load distribution but also the local stress distribution around the shear keys. In addition, autogenous shrinkage can cause initial cracking of the grout layer in radial direction as well as at the shear key tips. As a result, a form fitted connection between grout layer and sleeve cannot be expected at any time. Possible positive effects due to pre-stressing of the inner grout steel interface vanish if radial cracks occur.

- **Influence of cracks**

Diagonal shear cracking was observed in almost all specimens. The crack orientation was influenced by the shear key arrangement as well as the grout layer thickness. The cracks caused a redistribution of the load share per shear key and a deactivation of certain shear keys for the load transfer. This behaviour was in good agreement with the observed displacement behaviour of the specimens, where more cracks led to faster degradation. Moreover, the cracking behaviour was the main reason for a lower load bearing and fatigue capacity of a thicker grout layer. Since crack initiation from autogenous shrinkage must be expected in general and cracking can also occur caused by high single load peaks, the influence of cracking must be considered in a design verification by means of a limit state analysis. A corresponding approach with discretely modelled cracks was presented.

- **Scale effects**

Both small- and large-scale experiments showed comparable results for the main influence of water on the fatigue behaviour of grouted connections. A direct analysis of scale effects was not possible since neither the specimen geometries, nor the applied load levels were comparable. However, the same aggregate size resulted in less homogenous grout layers for the small-scale specimens and thus a coarser cracking behaviour. Furthermore, the influence of autogenous shrinkage was less pronounced in the small-scale specimens.

- **Influences of the grout material**

Main observed influence of the used grout materials was the size of autogenous shrinkage deformations in the large-scale experiments and resulting difference in the degradation behaviour. Effects of the material strength, as planned to be investigated in the small-scale tests, could not be rated since the actual material properties were too much alike for a statically reliable evaluation.

- **Load ratio R**

For the two investigated load ratios of alternating loads and compression-compression loads, a significant influence was attested in the large-scale experiments. In combination with effects of autogenous shrinkage, alternating loads resulted in an unfavourable load displacement behaviour of the specimens. Since autogenous shrinkage is inevitable for cement based filling materials, for the time being alternating loads on grouted connections in submerged conditions should be excluded.

- **Loading frequency**

The small-scale tests showed larger numbers of endurable load cycles for lower frequencies. This is in contrast to experimental results for plain concrete specimens. It was concluded that for the small-scale specimens mainly the pumping speed was influenced by the loading frequency and hence the amount of flushed particles per load cycle. The results of wet AC fatigue tests, carried out with higher loading frequencies (≤ 10 Hz) than expectable for real grouted connections, can be assumed to provide conservative results.

- **Analytical design approaches**

The analytical ULS design approaches gave conservative results for the small-scale geometries. With the results of the large-scale fatigue tests the ULS design approach given in DNVGL-ST-0126 (2016) could be proven as conservative for the investigated geometries. However, for an evaluation of the other approaches corresponding test results were not generated.

The analytical FLS design approach given in DNVGL-ST-0126 (2016) showed conservative results compared to the large-scale fatigue experiments with compression-compression loading and wet AC. All other approaches predicted higher fatigue capacities than achieved in the large-scale experiments. For the small-scale specimens all analytical FLS approaches gave conservative results when accepting large axial deformations of the grouted connections.

- **Numerical design approach**

Finally, a numerical design approach for the fatigue behaviour of submerged grouted connections was presented. The decisive criterion is the local stress distribution in the grout layer in front of the loaded shear key surface. Hence, the approach description included a suitable modelling procedure regarding the geometric details and an appropriate non-linear material model for the grout layer. Moreover, it included a method to evaluate the calculated results, in which the local minimum principal stresses are compared to S-N curves from MC2010 (2013). The numerical simulations also included investigations on the effects of autogenous shrinkage as well as on diagonal shear cracks. Good agreement between numerical and experimental results was found.

6.2 Outlook

Future experimental investigations on the fatigue behaviour of grouted connections should be carried out in wet AC in order to provide reliable results for submerged applications. For the presented numerical design verification approach further investigations with different specimen geometries, closer arranged load stages and higher numbers of load cycles are desirable. Additionally, tests with single peak loads and different load chronology are of interest to further proof the described influence of diagonal shear cracking, especially for connections with larger overlapping length and higher numbers of shear keys. Furthermore, additional tests with alternating loads might provide further insights on the backlash effect. In order to investigate the transferability of the presented results to combined loading, especially for connections with predominant bending loading, further tests are necessary. Moreover, research activities regarding possible sealing systems, their influence on the observed degradation mechanisms and their durability are desirable. A reliable sealing

systems might allow the grouted connection to benefit from the additional structural fatigue capacities found in dry AC tests.

For future small-scale experiments the specimen geometry ought to be revised. Circular shaped shear keys are desirable for a more realistic representation of the interlocking between steel and grout. Moreover, the stiffnesses of the steel parts should be reduced to allow a more realistic confinement of the grout layer. The ideal case would be an exactly scaled steel geometry which would allow a detailed analysis of scale effects. Certainly, a study of manufacturing possibilities and load bearing capacity will be necessary before realising such specimens. Nevertheless, the economic benefits of small-scale experiments allow the investigation of various parameters. Thus, they can provide a broader insight than a small number of expensive large-scale experiments. Complementary, large-scale experiments focusing on the influence of the loading frequency, are desirable to investigate the transferability of the corresponding small-scale test results to larger scales and to reveal possible scale effects. Likewise, further detailed investigations on the local flushing process based on small detailed specimens are of interest. These experiments will not only allow a more economic investigation of these phenomena but also allow to estimate these effects for other hybrid steel-grout or steel-concrete connections such as for example welding studs.

Finally, further investigations on numerical modelling approaches will be beneficiary if they show possibilities for further simplifications while maintaining the reliability of the results. This is especially desirable for investigating designs without rotational symmetry. Thinkable options are the use of detailed sub-models for the shear key area and a comprehensive analysis of the interaction between master- and sub-model, especially regarding cracking. The presented experimental data can be used for validation.

Bibliography

Please note that all publications not written in English language are listed with their original title and a corresponding English title. In cases where no English title was given in the publication itself, the title was translated to the best of the author's belief.

Standards, Codes of Practice and Laws

- API RP 2A-WSD (2007). *Recommended practice for planing, designing and constructing fixed offshore platforms - Working stress design*. API American Petroleum Institute. API Publishing Services, Washington, D.C., USA, August 2007.
- DIN 4766-2 (1981). *Herstellverfahren der Rauheit von Oberflächen - Erreichbare Mittenrauhwerte Ra nach DIN 4768 Teil 1 (Surface roughness associated with types of manufacturing method - Attainable arithmetical mean value Ra according to DIN 4768 Part 1)*. DIN Deutsches Institut für Normung e.V. Beuth Verlag, Berlin, Germany, March 1981.
- DIN EN 10025-4 (2005). *Warmgewalzte Erzeugnisse aus Baustählen - Teil 4: Technische Lieferbedingungen für thermomechanisch gewalzte schweißgeeignete Feinkornbaustähle (Hot rolled products of structural steels - Part 4: Technical delivery conditions for thermomechanical rolled weldable fine grain structural steels)*. DIN Deutsches Institut für Normung e.V. Beuth Verlag, Berlin, Germany, April 2005.
- DIN EN 10210-2 (2006). *Warmgefertigte Hohlprofile für den Stahlbau aus unlegierten Baustählen und aus Feinkornbaustählen - Teil 2: Grenzabmaße, Maße und statische Werte (Hot finished structural hollow sections of non-alloy and fine grain steels - Part 2: Tolerances, dimensions and sectional properties)*. DIN Deutsches Institut für Normung e.V. Beuth Verlag, Berlin, Germany, July 2006.
- DIN EN 10225 (2009). *Schweißgeeignete Baustähle für feststehende Offshore-Konstruktionen - Technische Lieferbedingungen (Weldable structural steels for fixed offshore structures - Technical delivery conditions)*. DIN Deutsches Institut für Normung e.V. Beuth Verlag, Berlin, Germany, October 2009.
- DIN EN 12495 (2000). *Kathodischer Korrosionsschutz von ortsfesten Offshore-Anlagen aus Stahl (Cathodic protection for fixed steel offshore structures)*. DIN Deutsches Institut für Normung e.V. Beuth Verlag, Berlin, Germany, April 2000.
- DIN EN ISO 19902 (2014). *Erdöl- und Erdgasindustrie - Gegründete Stahlplattformen (Petroleum and natural gas industries - Fixed steel offshore structures)*. DIN Deutsches Institut für Normung e.V. Beuth Verlag, Berlin, Germany, January 2014.
- DIN EN ISO 4287 (2010). *Geometrische Produktspezifikation (GPS) - Oberflächenbeschaffenheit: Tastschnittverfahren - Benennungen, Definitionen und Kenngrößen der Oberflächenbeschaffenheit (Geometrical Product Specifications (GPS) - Surface texture: Profile method - Terms, definitions and surface texture parameters)*. DIN Deutsches Institut für Normung e.V. Beuth Verlag, Berlin, Germany, July 2010.
- DIN EN ISO 8501-1 (2007). *Vorbereitung von Stahloberflächen vor dem Auftragen von Beschichtungsmitteln - Visuelle Beurteilung der Oberflächenreinheit - Teil 1: Rostgrade und Oberflächenvorbereitungsgrade von unbeschichteten Stahloberflächen und Stahloberflächen nach ganzflächigem Entfernen vorhandener Beschichtungen (Preparation of steel substrates before application of paints and related products - Visual assessment of surface cleanliness -*

- Part 1: Rust grades and preparation grades of uncoated steel substrates and of steel substrates after overall removal of previous coatings*). DIN Deutsches Institut für Normung e.V. Beuth Verlag, Berlin, Germany, Dezember 2007.
- DNVGL-RP-0419 (2016). *Analysis of grouted connections using the finite element method*. DNV GL, Oslo, Norway, September 2016.
- DNVGL-ST-0126 (2016). *Support structures for wind turbines*. DNV GL, Oslo, Norway, April 2016.
- DNV-OS-C502 (2012). *Offshore concrete structures*. Det Norske Veritas AS, Høvik, Norway, September 2012.
- DNV-OS-J101 (2013). *Design of offshore wind turbine structures*. Det Norske Veritas AS, Høvik, Norway, January 2013.
- DNV-OS-J101 (2014). *Design of offshore wind turbine structures*. Det Norske Veritas AS, Høvik, Norway, May 2014.
- EEG (2000). Gesetz für den Vorrang Erneuerbarer Energien sowie zur Änderung des Energiewirtschaftsgesetzes und des Mineralölsteuergesetzes (*Act on the primacy of renewable energies and the amendment of the Energy Industry Act and the Mineral Oil Tax Act*), 29 March 2000. Deutscher Bundestag, *Bundesgesetzblatt Teil 1*, pp. 305–309.
- EEG (2017). Gesetz zur Förderung von Mieterstrom und zur Änderung weiterer Vorschriften des Erneuerbare-Energien-Gesetzes (*Act for the promotion of tenant electricity and amendment of further regulations of the Renewable Energies Act*), 17 July 2017. Deutscher Bundestag, *Bundesgesetzblatt Teil 1*, pp. 2532–2539.
- GL-COWT (2012). *Guideline for the certification of offshore wind turbines*. GL Renewables Certification, Hamburg, Germany, December 2012.
- GL-TN-GC (2013). *Certification of grouted connections for offshore wind turbines*. GL Renewables Certification, Hamburg, Germany, December 2013.
- IEC 61400-3 (2009). *Wind turbines - Part 3: Design requirements for offshore wind turbines*. IEC International Electrotechnical Commission, Brussels, Belgium, April 2009.
- MC1990 (1993). *CEB-FIB Model Code 1990*. Comité Euro-International du Béton. Thomas Telford, London, England, 1993.
- MC2010 (2013). *fib Model Code for concrete structures 2010*. Fédération Internationale du Béton. Ernst & Sohn, Berlin, Germany, 2013.
- NORSOK N-004 (2013). *Design of steel structures*. Norsok Standard. Standards Norway, Lysaker, Norway, February 2013.
- OTO 2001/016 (2002). *Pile / Sleeve connections - Offshore technology report*. HSE Health & Safety Executive. HSE Books, Suffolk, United Kingdom, 2002.
- SVB-Richtlinie (2003). *DAfStb-Richtlinie - Selbstverdichtender Beton (DAfStb-Guideline - Self-compacting concrete)*. DAfStb Deutsche Ausschuss für Stahlbeton. Beuth Verlag, Berlin, Germany, November 2003.

Books, Articles and Handbooks

- 4COffshore (2018). *Offshore Wind Farms: Database of Offshore Wind Farms from Planned to Decommissioned*. URL: www.4coffshore.com [last checked 20.02.18].

- Anders, S. (2007). *Betontechnologische Einflüsse auf das Tragverhalten von Grouted Joints (Influences of concrete technology on the bearing behaviour of grouted joints)*. Dissertation. Institut für Baustoffe. Leibniz Universität Hannover, Hannover, Germany.
- Aritenang, W.; Elnashai, A.S. et al. (1990). Failure mechanisms of weld-beaded grouted pile/sleeve connections. *Marine Structures* (3), pp. 391–417. Elsevier, Amsterdam, Netherlands.
- Barrett, J.F. & Keat, N. (2004). Artifacts in CT: recognition and avoidance. *RadioGraphics* 24 (6), pp. 1679–1691. RSNA Publications, Oak Brook, IL, USA.
- BASF Construction Chemicals (2010). *Masterflow 9500: Ultra-high strength offshore windmill grout, Product Sheet*.
- Bechtel, A. (2009). Influence of the shear key geometry to the fatigue design of hybrid connections of offshore wind energy converters. Diploma Thesis (not published). Institut für Stahlbau. Leibniz Universität Hannover, Hannover, Germany.
- Bechtel, A. (2016). Fatigue behaviour of axially loaded grouted connections in jacket structures. Dissertation. Institut für Stahlbau. Leibniz Universität Hannover, Hannover, Germany.
- Billington, C.J. (1978). The integrity of jacket to pile connections, *Proceedings of the 4th International Conference for the Offshore Industries - Oceanology International*, pp. 79–88.
- Billington, C.J. & Chetwood, J. (2012). Lessons from previous research for the design of grouted connections for offshore wind foundations: A new interpretation, *Proceedings of the International Quality & Productivity Center Conference*.
- Billington, C.J. & Tebbet, I.E. (1980). The basis for new design formulae for grouted jacket to pile connections, *Proceedings of the 12th Annual Offshore Technology Conference - OTC*. Houston, TX, USA, pp. 449–458.
- Billington, C.J. & Tebbet, I.E. (1982). Fatigue strength of grouted tubular steel connections for offshore structures, *Proceedings of the IABSE Colloquium Lausanne: Fatigue of Steel and Concrete Structures - IABSE*. Lausanne, Switzerland, pp. 625–632.
- Böker, C. (2010). *Load simulation and local dynamics of support structures for offshore wind turbines, Dissertation*. Shaker Verlag, Hannover, Germany. (Schriftenreihe des Instituts für Stahlbau der Gottfried Wilhelm Leibniz Universität Hannover, Vol. 26).
- Bosse, H. (2008). Technische Aspekte bei der Sanierung von Fundamentschäden: Teil 1: Schadensbilder und mögliche Ursachen (*Technical aspects in the renovation of foundation damages - Part 1: Damage patterns and possible causes*). *Wind Kraft Journal* (6), pp. 14–19. Verlag Natürliche Energien, Seevetal, Germany.
- Bosse, H. (2009). Guter Stand gelingt nur auf festem Grund: Schäden an Fundamenten von Windenergieanlagen treten vermehrt auf (*Good balance succeeds only on firm ground: Damage on foundations of wind turbines occur frequently*). *Erneuerbare Energien* 2009 (2), pp. 24–30. SunMedia, Hannover, Germany.
- Boswell L. F. & D'Mello, C. (1986). The fatigue strength of grouted repaired tubular members, *Proceedings of the 18th Annual Offshore Technology Conference - OTC*. Houston, TX, USA, 147-152.
- Cervenka, V.; Jendele, L. & Cervenka, J. (2016). *ATENA Program Documentation: Part 1 - Theory*. Cervenka Consulting, Prague, Czech Republic. URL: http://www.cervenka.cz/assets/files/atena-pdf/ATENA_Theory.pdf [last checked 20.02.18].

- Chaboche, J.L. (1989). Constitutive equations for cyclic plasticity and cyclic viscoplasticity. *International Journal of Plasticity* 5 (3), pp. 247–302. Elsevier, Amsterdam, Netherlands.
- Chilvers, G.A. (1984). Analysis of the structural behaviour of grouted pile/sleeve connections for offshore structures. Dissertation. City University London, London, United Kingdom.
- Cierniak, R. (2011). *X-Ray computed tomography in biomedical engineering*. Springer-Verlag, London, United Kingdom.
- Clormann, U.H. & Seeger, T. (1986). Rainflow-HCM - Ein Zählverfahren für betriebsfestigkeitsnachweise auf werkstoffmechanischer Grundlage (*RAINFLOW-HCM - A counting method for fatigue strength evaluation based on material behaviour*). *Stahlbau* 55 (3), pp. 65–71. Ernst & Sohn, Berlin, Germany.
- Cotardo, D.; Lohaus, L. & Werner, M. (2017). Practical performance of OPC-grout for offshore wind turbines in large-scale execution tests, *Proceedings of the 27th International Ocean and Polar Engineering Conference - ISOPE*. San Francisco, CA, USA, pp. 997–1002.
- Dahl, K.K. (1992). A constitutive model for normal and high strength concrete. Dissertation. Technical University of Denmark, Lyngby, Denmark.
- Dallyn, P.; El-Hamalawi, A. et al. (2016). Experimental investigation on the development of wear in grouted connections for offshore wind turbine generators. *Engineering Structures* (113), pp. 89–102. Elsevier, Amsterdam, Netherlands.
- Dassault Systèmes (2015). *Abaqus 2016 Online Documentation*.
- Det Norske Veritas AS (2013). *Joint Industry Project: Capacity of Cylindrical Shaped Grouted Connections with Shear Keys (2012-0371), Summary Report*, Hoevik, Norway.
- Deutsche WindGuard GmbH (2018). *Status des Windenergieausbaus in Deutschland (Status of wind energy expansion in Germany)*. URL: http://www.windguard.de/_Resources/Persistent/005f7376fe568db6655015912203b4170c0d17c2/Factsheet-Status-Offshore-Windenergieausbau-2017.pdf [last checked 20.02.18].
- Domone, P.L. & Jefferis, S.A. (2005). *Structural grouts*. CRC Press, London, United Kingdom.
- Drucker, D.C. & Prager, W. (1952). Soil mechanics and plastic analysis or limit design. *Quarterly of Applied Mathematics* 10 (2), pp. 157–165. AMS, Providence, RI, USA.
- Dubois, J.; Thieken, K. et al. (2016). Advanced incorporation of soil-structure interaction into integrated load simulation, *Proceedings of the 26th International Ocean and Polar Engineering Conference - ISOPE*. Rhodes, Greece, pp. 754–762.
- Fehling, E. (1990). Zur Energiedissipation und Steifigkeit von Stahlbetonbauteilen unter besonderer Berücksichtigung der Rißbildung und verschieblichem Verbund (*On energy dissipation and stiffness of reinforced concrete components with special consideration of cracking and slippage*). Dissertation. Technische Hochschule Darmstadt, Darmstadt, Germany.
- Fehling, E.; Leutbecher, T. et al. (2013). Grouted connections for offshore wind turbine structures: Part 2: Structural modelling and design of grouted connections. *Steel Construction* 6 (3), pp. 216–228. Ernst & Sohn, Berlin, Germany.
- Forsyth, P. & Tebbet, I.E. (1988). New test data on the strength of grouted connections with closely spaced weld beads, *Proceedings of the 20th Annual Offshore Technology Conference - OTC*. Houston, TX, USA, pp. 237–245.
- Göhlmann, J. (2008). Zur Schädigungsberechnung an Betonkonstruktionen für Windenergieanlagen unter mehrstufiger und mehraxialer Ermüdungsbeanspruchung (*On*

- damage calculation of concrete structures for wind turbines under multi stage and multi axial fatigue loading*). Dissertation. Institut für Massivbau. Leibniz Universität Hannover, Hannover, Germany.
- Grünberg, J.; Lohaus, L. et al. (2007). Mehraxiales mechanisches Ermüdungsmodell von Ultra-Hochfestem Beton: Experimentelle und analytische Untersuchungen (*Multiaxial mechanical model of ultra-high-performance concrete*). *Beton- und Stahlbetonbau* 102 (6), pp. 388–398. Ernst & Sohn, Berlin, Germany.
- Harwood, R.G.; Billington, C.J. et al. (1996). Grouted pile to sleeves connections: Design provisions for the new ISO standard for offshore structures, *Proceedings of the 15th International Conference on Ocean, Offshore and Arctic Engineering - OMAE*. Florence, Italy, pp. 1–12.
- Holmen, J.O. (1979). Fatigue of concrete by constant and variable amplitude loading. Dissertation. Norwegian Institute of Technology. University of Trondheim, Trondheim, Norway.
- Hümme, J. (2013). Einfluss der Feuchtigkeit auf das Ermüdungsverhalten druckschwellbeanspruchter hochfester Vergussbetone (*Influence of humidity on the fatigue behaviour of compressively stressed grouts*), *Beiträge zur 1. DAfStb Jahrestagung mit 54. Forschungskolloquium*. Bochum, Germany, pp. 393–398.
- Hümme, J. (2015). Fatigue behaviour of high-strength grouting concrete tested under water, *Proceedings of the fib Symposium on Concrete - Innovation and Design*. Copenhagen, Sweden.
- Hümme, J.; Elsmeier, K. & Lohaus, L. (2016). Influence of the load frequency in dry and submerged conditions on the fatigue behaviour of high-strength concrete, *Proceedings of the 4th International Symposium on Ultra-High Performance Concrete and High Performance Construction Materials - HiPerMat*. Kassel, Germany.
- Ingebrigtsen, T.; Løset, Ø. & Nielsen, S.G. (1990). Fatigue design and overall safety of grouted pile sleeve connections, *Proceedings of the 22nd Annual Offshore Technology Conference - OTC*. Houston, TX, USA, 615-628.
- ITW Densit ApS (2012). *Data Sheet Ducorit: ultra high performance grout, Product Sheet*.
- ITW Engineered Polymers (2016). *Data Sheet Ducorit: ultra high performance grout*.
- Johansson, M. & Akesson, M. (2001). Finite element study of concrete-filled steel tubes using a new confinement-sensitive concrete compression model. *Nordic Concrete Research* (27), pp. 43–62. NCR Publications, Oslo, Norway.
- Joint Committee on Structural Safety (2001). *Probabilistic Model Code: Part 3 Resistance Models*. URL: http://www.jcss.byg.dtu.dk/-/media/Subsites/jcss/english/publications/probabilistic_model_code/steelpr.ashx?la=da [last checked 20.02.18].
- Karsan, D.I. & Krahl, N.W. (1984). New API equation for grouted pile-to-structure connections, *Proceedings of the 16th Annual Offshore Technology Conference - OTC*. Houston, TX, USA, pp. 49–56.
- Katwan, M.J. (1988). Corrosion fatigue of reinforced concrete. University of Glasgow, Glasgow, United Kingdom.
- Keindorf, C. (2010). *Tragverhalten und Ermüdungsfestigkeit von Sandwichtürmen für Windenergieanlagen (Load bearing behaviour and fatigue resistance of sandwich towers for*

- wind turbines), *Dissertation*. Shaker Verlag, Aachen, Germany. (Schriftenreihe des Instituts für Stahlbau der Gottfried Wilhelm Leibniz Universität Hannover, Vol. 25).
- Kleppmann, W. (2013). *Versuchsplanung (Design of experiments)*. Carl Hanser Verlag, München, Germany.
- Krahl, N.W. & Karsan, D.I. (1985). Axial strength of grouted pile-to-sleeve connections. *Journal of Structural Engineering* 111 (4), pp. 889–905. ASCE, New York, NY, USA.
- Kupfer, H.; Hilsdorf, H.K. & Rusch, H. (1969). Behavior of concrete under biaxial stresses. *Journal Proceedings* 66 (8), pp. 656–666. ACI, Farmington Hills, MI, USA.
- Lamport, W.B. (1988). Ultimate strength of grouted pile-to-sleeve-connections. *Dissertation*. University of Texas at Austin, Austin, Texas, USA.
- Lee, J. & Fenves, G.L. (1998). Plastic-damage model for cyclic loading of concrete structures. *Journal of Engineering Mechanics* 124 (8), 892-900. ASCE, New York, NY, USA.
- Lochte-Holtgreven, S. (2013). *Zum Trag- und Ermüdungsverhalten biegebeanspruchter Grouted Joints in Offshore-Windenergieanlagen (On load bearing and fatigue behaviour of grouted joints in offshore wind turbines subjected to bending)*, *Dissertation*. Shaker Verlag, Aachen, Germany. (Schriftenreihe des Instituts für Stahlbau der Gottfried Wilhelm Leibniz Universität Hannover, Vol. 29).
- Lohaus, L.; Cotardo, D. & Werner, M. (2014). The early-age cycling and its influence on the properties of hardened grout material, *Proceedings of the 1st International Wind Engineering Conference - IWEC*. Hannover, Germany.
- Löhning, T. & Muurholm, U. (2013). Finite Element-Based Design of Grouted Connections with Shear Keys for Offshore Wind Turbines. *Structural Engineering International* (3), pp. 295–302. IABSE, Zurich, Switzerland.
- Lotsberg, I.; Serednicki, A. et al. (2012). Design of grouted connections for Monopile Offshore Structures: Results from two Joint Industry Projects. *Stahlbau* 81 (9), pp. 695–704. Ernst & Sohn, Berlin, Germany.
- Lotsberg, I.; Serednicki, A. et al. (2013). Behaviour of grouted connections of monopile structures at ultimate static and cyclic limit states. *Structural Engineer* 91 (2), pp. 51–57. The Institution of Structural Engineers, London, United Kingdom.
- Lubliner, J.; Oliver, J. et al. (1989). A plastic-damage model for concrete. *International Journal of Solids and Structures* 25 (3), pp. 299–326. Elsevier, Amsterdam, Netherlands.
- Menetray, P. & Willam, K.J. (1995). Triaxial failure criterion for concrete and its generalization. *ACI Structural Journal* 92 (3), pp. 311–318. ACI, Farmington Hills, MI, USA.
- Mises, R.v. (1913). Mechanik der festen Körper im plastisch-deformablen Zustand (*Mechanics of solid bodies in the plastic-deformable state*). *Nachrichten von der Gesellschaft der Wissenschaften zu Göttingen* 4 (1), 582-592. Göttingen, Germany.
- Mittelstaedt, M.; Ertel, C. et al. (2014). Neue Ansätze für den Nachweis von zylindrischen Grout-Verbindungen von Offshore-Windenergieanlagen (*New approaches for the verification of cylindrical grouted connections of offshore wind energy turbines*). *Stahlbau* 83 (8), pp. 516–521. Ernst & Sohn, Berlin, Germany.
- Muguruma, H. & Watanabe, F. (1984). On the low-cycle compressive fatigue behaviour of concrete under submerged condition, *Proceedings of the 27th Japan Congress on Materials Research*. Tokyo, Japan, pp. 219–224.

- Muguruma, H. & Watanabe, F. (1986). Low-cycle fatigue behaviour of concrete and AE monitoring under submerged condition, *Proceedings of the 29th Japan Congress on Materials Research*. Tokyo, Japan, pp. 151–158.
- Nishiyama, M.; Muguruma, H. & Watanabe, F. (1987). On the low-cycle fatigue behaviours of concrete and concrete members under submerged condition pp. 319–330.
- Nygaard, K.; Petkovic, G. et al. (1992). *High Strength Concrete, SP3 - Fatigue: Report 3.1: The Influence of Moisture Conditions on the Fatigue Strength of Concrete*. SINTEF Structural Engineering - FCB, Trondheim, Norway.
- Oñate, E.; Oller, S. et al. (1988). A constitutive model for cracking of concrete based on the incremental theory of plasticity. *Engineering Computations* 5 (4), pp. 309–319. Emerald Publishing, Bingley, United Kingdom.
- Oneschkow, N. (2016). Analyse des Ermüdungsverhaltens von Beton anhand der Dehnungsentwicklung (*Analysis of the fatigue behavior of concrete on the basis of strain development*). Dissertation. Institut für Baustoffe. Leibniz Universität Hannover, Hannover, Germany.
- Ottosen, N.S. (1977). A failure criterion for concrete. *Journal of the Engineering Mechanics Division* 103 (4), pp. 527–535. ASCE, New York, NY, USA.
- Pfanner, D. (2003). Zur Degradation von Stahlbetonbauteilen unter Ermüdungsbeanspruchungen (*On degradation of reinforced concrete members under fatigue loading*). Dissertation. Institut für Konstruktiven Ingenieurbau. Ruhr-Universität Bochum, Bochum, Germany.
- Pölling, R. (2000). Eine praxisnahe, schädigungsorientierte Materialbeschreibung von Stahlbeton für Strukturanalysen (*A practical damage oriented material description of reinforced concrete for structural analysis*). Dissertation. Lehrstuhl für Statik und Dynamik. Ruhr-Universität Bochum, Bochum, Germany.
- Raba, A. (2010). Restlebensdauerermittlung von Schubrippen unter Ansatz bruchmechanischer Berechnungsmethoden (*Residual lifetime estimation of shear keys using fracture mechanics*). Project Thesis (not published). Institut für Stahlbau. Leibniz Universität Hannover, Hannover, Germany.
- Radaj, D. & Vormwald, M. (2007). *Ermüdungsfestigkeit (Fatigue resistance)*. Springer-Verlag, Berlin, Germany.
- Rücker, W.; Lüddecke, F. & Thöns, S. (2012). Tragverhalten von Offshore Gründungskonstruktionen: Rechnerische und messtechnische Untersuchungen (*Structural behaviour of offshore support structures – Computational and experimental analysis*). *Bautechnik* 89 (12), pp. 821–830. Ernst & Sohn, Berlin, Germany.
- Schaumann, P.; Bechtel, A. & Lochte-Holtgreven, S. (2010a). Fatigue performance of grouted joints for offshore wind energy converters in deeper waters, *Proceedings of the 20th International Ocean and Polar Engineering Conference - ISOPE*. Beijing, China, pp. 672–679.
- Schaumann, P.; Bechtel, A. & Lochte-Holtgreven, S. (2012). Nachweisverfahren zur Tragfähigkeit überwiegend axial beanspruchter Grouted Joints in Offshore-Tragstrukturen (*Design of axially loaded grouted joints of offshore support structures*). *Stahlbau* 81 (9), pp. 679–688. Ernst & Sohn, Berlin, Germany.

- Schaumann, P.; Dubois, J. et al. (2010b). Integrated simulation of the REpower 5 MW offshore wind turbine with alpha ventus measurement data, *Proceedings of the 10th German Wind Energy Conference - DEWEK*. Bremen, Germany.
- Schaumann, P.; Henneberg, J. & Raba, A. (2018). Axially loaded grouted connections in offshore conditions using ordinary portland cement, *Proceedings of the 12th International Conference on Advances in Steel-Concrete Composite Structures - ASCCS*. València, Spain.
- Schaumann, P.; Keindorf, C. & Lochte-Holtgreven, S. (2009). Statische und dynamische Axialdruckversuche an vergROUTETEN Rohr-in-Rohr-Verbindungen mit verschiedenen Füllmaterialien (*Static and dynamic axial compression tests on grouted tube-intube connections with various grout materials*). *Bautechnik* 86 (11), pp. 719–728. Ernst & Sohn, Berlin, Germany.
- Schaumann, P. & Lochte-Holtgreven, S. (2013). A novel plasticity-based failure model for grouts in grouted joints for offshore wind turbines with monopiles, *Proceedings of the 5th International Conference on Computational Methods in Marine Engineering - Marine*. Hamburg, Germany, pp. 35–46.
- Schaumann, P.; Lochte-Holtgreven, S. et al. (2010c). Durchrutschende Grout-Verbindungen in OWEA – Tragverhalten: Instandsetzung und Optimierung (*Sinking grouted joints in offshore wind turbines – Bearing behaviour, repair, and optimisation*). *Stahlbau* 79 (9), pp. 637–647. Ernst & Sohn, Berlin, Germany.
- Schaumann, P.; Lochte-Holtgreven, S. et al. (2013). Numerical investigations on local degradation and vertical misalignments of grouted joints in monopile foundations, *Proceedings of the 23th International Ocean and Polar Engineering Conference - ISOPE*. Anchorage, AK, USA, pp. 164–179.
- Schaumann, P.; Lochte-Holtgreven, S. & Keindorf, C. (2008). Influence of material strengths on bearing behaviour of grouted joint connections under high frequent amplitude loading, *Proceedings of the 9th German Wind Energy Conference - DEWEK*. Bremen, Germany.
- Schaumann, P. & Raba, A. (2015a). Influence of the loading frequency on the fatigue performance of submerged small-scale grouted joints, *Proceedings of the 12th German Wind Energy Conference DEWEK 2015 - DEWEK*. Bremen, Germany.
- Schaumann, P. & Raba, A. (2015b). Systematic testing of the fatigue performance of submerged small-scale grouted joints, *Proceedings of the 34th International Conference on Ocean, Offshore and Arctic Engineering - OMAE*. St. John's, NL, Canada.
- Schaumann, P. & Wilke, F. (2006a). Fatigue assessment of support structures of offshore wind energy conversion systems, in Schaumann, P. & Peinke, J. (eds.), *ForWind: Annual Report 2005*, Hannover, Germany, pp. 36–39.
- Schaumann, P. & Wilke, F. (2006b). Fatigue of grouted joint connections, *Proceedings of the 8th German Wind Energy Conference - DEWEK*. Bremen, Germany.
- Schaumann, P. & Wilke, F. (2007). Design of large diameter hybrid connections grouted with high performance concrete, *Proceedings of the 17th International Offshore and Polar Engineering Conference - ISOPE*. Lisbon, Portugal, pp. 340–347.
- Seidel, M. & Foss, G. (2006). Impact of different substructures on turbine loading and dynamic behaviour for the DOWNVInD project in 45m water depth, *Proceedings of the European Windenergy Association Conference - EWEC*. Athens, Greece.

- Sele, A.B. & Kjeoy, H. (1989). Background for the new design equations for grouted connections in the DnV draft rules for fixed offshore structures, *Proceedings of the 21st Annual Offshore Technology Conference - OTC*. Houston, TX, USA, pp. 463–474.
- Sele, A.B. & Seow, P.F. (1988). Recent developments in design and use of grouted clamps for offshore repair and strengthened of structures and pipelines, *Proceedings of the 7th Offshore South East Conference*. Singapore, pp. 561–574.
- Soerensen, E.V. (2011). Fatigue life of high performance grout in dry and wet environment for wind turbine grouted connections, *Proceedings of the European Windenergy Association Offshore Conference - EWEA Offshore*. Amsterdam, Netherlands.
- Speck, K. (2008). Beton unter mehraxialer Beanspruchung: Ein Materialgesetz für Hochleistungsbetone unter Kurzzeitbelastung (*Concrete under multiaxial stress: A material law for high-performance concretes under short term loading*). Dissertation. Institut für Massivbau. Technische Universität Dresden, Dresden, Germany.
- Tebbet, I.E. & Billington, C.J. (1985). Recent developments in the design of grouted connections, *Proceedings of the 17th Annual Offshore Technology Conference - OTC*. Houston, TX, USA, pp. 439–450.
- Voßbeck, M.; Kelm, M. & Löhning, T. (2013). Tragverhalten von Groutverbindungen bei Monopilegründungen von Offshore-Windenergieanlagen (*Structural behaviour of grouted connections for monopile foundations of offshore wind turbines*). *Stahlbau* 82 (1), pp. 55–60. Ernst & Sohn, Berlin, Germany.
- Waagaard, K. (1977). Fatigue of offshore concrete structures: Design and experimental investigations, *Proceedings of the 9th Annual Offshore Technology Conference - OTC*. Houston, TX, USA, pp. 341–350.
- Waagaard, K. (1986). Experimental investigation on the fatigue strength of offshore concrete structures, *Proceedings of the 9th Annual Energy Technology Conference - ETC*. New Orleans, LA, USA, pp. 73–81.
- Weicken, H. (2013). Einfluss von Umgebungstemperaturen auf die autogenen Schwindverformungen von Vergussmörteln in Offshore Anwendungen (*Influence of ambient temperatures on the autogenous shrinkage deformation of grouting mortar in offshore applications*), *Beiträge zur 1. DAfStb Jahrestagung mit 54. Forschungskolloquium*. Bochum, Germany, 159-164.
- Weicken, H. & Lohaus, L. (2014). Measures for autogenous shrinkage compensation and their influence on selected durability properties, *Proceedings of the International RILEM Conference on Application of Superabsorbent Polymers and Other New Admixtures in Concrete Construction*. Dresden, Germany, pp. 245–256.
- Werner, M. (2017). Realitätsnahe Materialeigenschaften von hochfesten Feinkornbetonen in Grouted Joints (*Realistic material properties of high-strength fine-grained concrete in grouted joints*). Dissertation. Institut für Baustoffe. Leibniz Universität Hannover, Hannover, Germany.
- Werner, M. & Lohaus, L. (2014). Ausführungstechnische Einflüsse auf Aspekte der Tragsicherheit von Grouted Joints (Influences of in situ production of grouted joints on aspects of structural safety) (*Influences of in situ production of grouted joints on aspects of structural safety*). *Bautechnik* 91 (8), pp. 554–560. Ernst & Sohn, Berlin, Germany.

- Wilke, F. (2014). *Load bearing behaviour of grouted joints subjected to predominant bending, Dissertation*. Shaker Verlag, Aachen, Germany. (Schriftenreihe des Instituts für Stahlbau der Gottfried Wilhelm Leibniz Universität Hannover, Vol. 31).
- Willam, K.J. & Warnke, E.P. (1974). Constitutive model for the triaxial behaviour of concrete, *Proceedings of the IABSE Seminar on Concrete Structures Subjected to Triaxial Stresses*. Bergamo, Italy, pp. 1–30.
- WindEurope Business Intelligence (2018). *Offshore Wind in Europe: Key trends and statistics 2017*, Brussels, Belgium. URL: <https://windeurope.org/wp-content/uploads/files/about-wind/statistics/WindEurope-Annual-Offshore-Statistics-2017.pdf> [last checked 20.02.18].
- Yamasaki, T.; Hara, M. & Takahashi, C. (1980). Static and dynamic tests on cement-grouted pile-to-pile connections, *Proceedings of the 12th Annual Offshore Technology Conference - OTC*. Houston, TX, USA, pp. 467–476.

Lists

List of Figures

Figure 1.1: Two offshore wind turbines with jacket substructure located at the German offshore wind farm alpha ventus (© DOTI 2011 / alpha ventus, Photo: Matthias Ibeler)	1
Figure 2.1: General geometry and geometrical parameters of a grouted connection in analogy to DIN EN ISO 19902 (2014).....	5
Figure 2.2: Typical support structures for offshore wind turbines and positions of grouted connections	6
Figure 2.3: Geometry of simplified real grouted connections	7
Figure 2.4: Schematic grouted connection designs for different installation procedures of jacket support structures	8
Figure 2.5: Schematic manufacturing process of a pre-piled grouted connection and in-situ quality of the grout material (acc. to Werner & Lohaus (2014)).....	9
Figure 2.6: Possible shear key designs (1.-3.) acc. to Karsan & Krahl (1984) and DIN EN ISO 19902 (2014) and realistic weld bead shape (4.) acc. to GL-TN-GC (2013).....	11
Figure 2.7: Schematic effects of loads (E) and reaction loads (R) in the grouted connections, depending on the type of substructure	12
Figure 2.8: Characteristic properties of load cycles in analogy to Radaj & Vormwald (2007)...	13
Figure 2.9: Classes of axial loads for a typical grouted connection of a wind turbine with jacket substructure located in the German North Sea and exemplary time series segment	14
Figure 2.10: Schematic load transfer of grouted connections for axial (left), horizontal (centre) and bending (right) loads	15
Figure 2.11: Schematic damage modes of grouted connections	16
Figure 2.12: Schematic local damage mechanisms in grouted connections	17
Figure 2.13: Schematic load displacement curve of a quasi-static loaded grouted connection with plain cement grout acc. to Billington & Tebbet (1980) (left) and with HPG acc. to Schaumann & Wilke (2006b) (right).....	18
Figure 2.14: Schematic relative displacement evolution over number of normalised load cycles and corresponding hysteresis for alternating loads acc. to Billington & Tebbet (1982) (left) and for compression loads acc. to Schaumann et al. (2010a) (right).....	19
Figure 2.15: Schematic strain evolution over number of normalised load cycles of a concrete cylinder under cyclic compression and cracking phases acc. to Pfanner (2003) (top left), schematic reduction of elasticity modulus over number of normalised load cycles acc. to Holmen (1979) (bottom left) and schematic stress strain behaviour (right).....	19
Figure 2.16: Compression strut model and corresponding free body diagram acc. to Schaumann et al. (2012)	28

Figure 2.17: Model for vertical shear failure acc. to Schaumann et al. (2012).....	30
Figure 2.18: Characteristic S-N curves for fatigue design approaches of current design standards and corresponding test results (calculations for pre-piled reference structure)	32
Figure 2.19: Schematic uniaxial stress-strain relation for grout material	34
Figure 2.20: Yield surfaces according to Drucker & Prager (1952) and Ottosen (1977)	35
Figure 2.21: Schematic representation of two simplified numerical modelling approaches for grouted connections.....	37
Figure 2.22: S-N curves for concrete and different loading ratios acc. to MC2010 (2013)	38
Figure 3.1: Set-up for small-scale grouted connection tests	46
Figure 3.2: Geometry of the two small-scale grouted connection specimens	47
Figure 3.3: Measured surface properties of small-scale specimens.....	49
Figure 3.4: Blank steel pieces and formwork of the two specimen geometries.....	50
Figure 3.5: Grout material properties according to manufacturer (M) and accompanying material test batches (1-3) at an age of 28 days (Schaumann & Raba (2015b))	51
Figure 3.6: Grout material strength evolution.....	51
Figure 3.7: Test rig for quasi-static tests.....	53
Figure 3.8: Schematic load-displacement curve of a small-scale ULS test with Geometry 1	54
Figure 3.9: Schematic load-displacement curve of a small-scale ULS test with Geometry 2	54
Figure 3.10: Summarised results of the ULS tests.....	55
Figure 3.11: Damage patterns of ULS specimens with different grout layer thickness	56
Figure 3.12: Damage patterns at shear key of ULS specimen	57
Figure 3.13: Load-displacement results of ULS step test (left) and damage pattern at different load levels (right).....	57
Figure 3.14: Characteristic load bearing capacities F_{ULS} measured in tests and calculated F_{ULS} for different material batches (1,2,3) according to current design methods.....	58
Figure 3.15: Characteristic load bearing capacities F_{slip} measured in tests and calculated F_{ULS} for different material batches (1,2,3) according to current design methods.....	58
Figure 3.16: Schematic cracking behaviour of small-scale specimens in ULS tests.....	59
Figure 3.17: Test rig for the fatigue tests	60
Figure 3.18: Automated photography system	61
Figure 3.19: Measurement of rig stiffness with dummy	62
Figure 3.20: FLS test rig and range of measured displacement.....	62
Figure 3.21: Initial displacement correction approach.....	63
Figure 3.22: Test results of specimen F127 with termination criterion runner.....	64

Figure 3.23: Test results of specimen F133 with termination criterion Δu	65
Figure 3.24: Test results of specimen F137 with termination criterion u_{\max}	65
Figure 3.25: S-N plot of small-scale test results for different AC and loading frequencies in analogy to Schaumann & Raba (2015a).....	66
Figure 3.26: S-N plot of small-scale test results for different AC and grout layer thickness	67
Figure 3.27: Deformation behaviour of two specimens tested in dry AC.....	68
Figure 3.28: Deformation behaviour of two specimens tested in dry and wet AC.....	68
Figure 3.29: Deformation behaviour of two specimens tested at different loading levels.....	69
Figure 3.30: Deformation behaviour of two specimens tested in same conditions showing different degradation behaviour.....	69
Figure 3.31: Deformation behaviour of two specimens with different grout layer thickness.....	70
Figure 3.32: Secant stiffness behaviour of three specimens with different loading conditions and AC.....	71
Figure 3.33: Distribution of stiffness K_2 for small-scale specimens with DDS2.....	72
Figure 3.34: Distribution of stiffness K_2 for small-scale specimens with BM95	72
Figure 3.35: Grout particle flushing observed during FLS tests	73
Figure 3.36: Damage patterns of FLS specimens with different grout layer thickness tested in dry ambient conditions	74
Figure 3.37: Damage patterns of FLS specimens with different grout layer thickness tested in wet ambient conditions.....	74
Figure 3.38: Damage patterns of FLS specimens with different failure modes tested in wet ambient conditions.....	75
Figure 3.39: CT-scanner set-up.....	78
Figure 3.40: Spatial model of CT-scan data of a small-scale specimen from an FLS test showing six vertical cutting planes, steel parts are coloured in black	79
Figure 3.41: CT-scan slice showing typical artifacts	79
Figure 3.42: Characteristic analytical fatigue design for grouted connections according to current design methods and comparison with small-scale fatigue test results	81
Figure 3.43: Schematic cracking behaviour of small-scale specimens in FLS tests.....	82
Figure 4.1: Geometry of the two large-scale grouted connection specimens	88
Figure 4.2: Exemplary geometry of real shear keys.....	90
Figure 4.3: Schematic water system and filter basin.....	91
Figure 4.4: Measurement set-up for large-scale specimens exemplarily for geometry 1	92
Figure 4.5: Load scenarios for large-scale fatigue tests in analogy to Bechtel (2016)	93

Figure 4.6: Grout material strength evolution of specimens W1 and W2 (left) and strength properties at first day of test (right), all samples taken before grout pump.	95
Figure 4.7: Grout material strength evolution of specimens W3 and W4 (left) and strength properties at first day of test (right), all samples taken before grout pump.	95
Figure 4.8: Mechanical grout material properties at beginning of each test, values for specimens D1 and D2 from Bechtel (2016)	96
Figure 4.9: Slump flows of BM95 measured according to SVB-Richtlinie (2003)	96
Figure 4.10: BM95 behaviour during filling process of specimens W1 and W2	97
Figure 4.11: Compilation of material quality related weak spots in specimen W1	98
Figure 4.12: Example of the distribution of measured load peaks per load cycle	100
Figure 4.13: Relative displacement behaviour of specimens W1 and D1	101
Figure 4.14: Relative displacement behaviour of specimens W2 and D2	101
Figure 4.15: Relative displacement between sleeve and grout of specimen W1	102
Figure 4.16: Relative displacement behaviour of specimen W3	102
Figure 4.17: Relative displacement behaviour of specimen W4	103
Figure 4.18: Regression analysis of mean displacement behaviour of specimen W4	104
Figure 4.19: Regression analysis of displacement range behaviour of specimen W4.....	104
Figure 4.20: Hysteresis loops of specimen W1.....	105
Figure 4.21: Hysteresis loops of specimen W3.....	106
Figure 4.22: Strain distribution in specimen W1	107
Figure 4.23: Strain distribution in specimen W2	107
Figure 4.24: Strain distribution in specimen W3	108
Figure 4.25: Strain distribution in specimen W4.....	108
Figure 4.26: Load control curve of test rig for specimens W1 and W2 (top), resulting impulse rate dp (middle) and load-displacement curve (bottom)	109
Figure 4.27: Load control curve while switching to high pressure for specimen W4 (top left), resulting displacement (bottom left) and load-displacement curve (right)	110
Figure 4.28: Compilation of grout particle flushing observations in specimens W1 (top and left) and W2 (bottom right)	111
Figure 4.29: Compilation of grout particle flushing observations in specimens W3 (left) and W4 (right).....	111
Figure 4.30: Compilation of major degradation mechanisms found in dismantled specimens W1 (left) and W2 (right)	112
Figure 4.31: Compilation of major degradation mechanisms found in dismantled specimens W3 (left) and W4 (right)	113

Figure 4.32: Characteristic ULS capacities for the large-scale specimen geometries and grout materials calculated according to current design methods	115
Figure 4.33: Characteristic FLS capacities for the large-scale specimen geometries and grout materials calculated according to current design methods	115
Figure 4.34: Overview of damage modes found in the grout layers of the specimens	116
Figure 5.1: Rotational symmetric finite element models of small- and large-scale specimens with geometry 1	129
Figure 5.2: Schematic uniaxial stress-strain relation acc. to MC2010 (2013)	131
Figure 5.3: Stress-crack opening relation for uniaxial tension acc. to MC2010 (2013)	131
Figure 5.4: Concrete damaged plasticity yield surfaces according to Lubliner et al. (1989) with different parameter sets and no plastic strains	133
Figure 5.5: Concrete damaged plasticity flow potential according to Lee & Fenves (1998) with two different parameter sets	134
Figure 5.6: Local mesh at shear key and evaluation path for stresses and sensitivity analysis ..	137
Figure 5.7: Schematic representation of the fatigue verification approach.....	139
Figure 5.8: Exemplary minimum principal stress distribution along the loaded shear key surface for two load stages (left) and corresponding damage estimation (right)	141
Figure 5.9: Concrete damaged plasticity yield surface according to Lubliner et al. (1989) compared to the yield surface according to Ottosen (1977).....	143
Figure 5.10: Nonlinear regression for plasticity number k acc. to MC2010 (2013) and linear correction proposal for brittle grout materials	144
Figure 5.11: Numerical model of grout prism (left) and comparison of numerical results with experimental results from Lochte-Holtgreven (2013) (right).....	145
Figure 5.12: Local numerical maximum principal stress results at loaded shear key surface for small-scale geometry 1 with different dilatation angles	145
Figure 5.13: Comparison between experimental cracking pattern (right) and numerical plastic strains calculated with different dilatation angles (left)	146
Figure 5.14: Local numerical minimum principal stress results at loaded shear key surface for small-scale geometry 1 with different mesh densities.....	147
Figure 5.15: Local numerical minimum principal stress results at loaded shear key surface for small-scale geometry 1 with different material models for the grout.....	147
Figure 5.16: Local numerical maximum principal stress results at loaded shear key surface for small-scale geometry 1 with different material models for the grout.....	148
Figure 5.17: Local numerical minimum principal stress results at loaded shear key surface for small-scale geometry 1 with discrete cracks	149
Figure 5.18: Local numerical minimum principal stress results at loaded shear key surface for small-scale geometry 1 with different autogenous shrinkage rates	149

Figure 5.19: F-N diagram with experimental and numerical results for small-scale geometry 1, different grout materials and discrete cracks.....	150
Figure 5.20: F-N diagram with experimental and numerical results for small-scale geometry 2, different grout materials and discrete cracks.....	151
Figure 5.21: Local numerical minimum principal stress results at loaded shear key surface for large-scale geometry 1 with different mesh densities	152
Figure 5.22: Axial strain distribution from numerical calculations and strain measurements in specimen W1 LS1 for different measures of autogenous shrinkage	152
Figure 5.23: Axial strain distribution from numerical calculations and strain measurements in specimen W2 LS1 for different autogenous shrinkage rates.....	153
Figure 5.24: Axial strain distribution from numerical calculations and strain measurements in specimen W2 LS2 for different cracking states	153
Figure 5.25: Axial strain distribution from numerical calculations and strain measurements in specimen W3 LS1 for different cracking states and shrinkage rates	154
Figure 5.26: Axial strain distribution from numerical calculations and strain measurements in specimen W3 LS2 for different cracking states	155
Figure 5.27: Axial strain distribution from numerical calculations and strain measurements in specimen W4 LS1 for different shrinkage rates.....	155
Figure 5.28: Axial strain distribution from numerical calculations and strain measurements in specimen W4 LS2 for different cracking states and shrinkage rates	156
Figure 5.29: Axial strain distribution from numerical calculations and strain measurements in specimen W4 LS3 for different cracking states	156
Figure 5.30: Minimum principal stress distribution from numerical calculations in specimen W1 LS1 (compression) for different measures of autogenous shrinkage	157
Figure 5.31: Minimum principal stress distribution from numerical calculations in specimen W2 LS1 (compression) for different autogenous shrinkage rates.....	158
Figure 5.32: Minimum principal stress distribution from numerical calculations in specimen W2 LS2 (compression) for different cracking states.....	159
Figure 5.33: Minimum principal stress distribution from numerical calculations in specimen W2 LS2 (tension) for different cracking states	159
Figure 5.34: Minimum principal stress distribution from numerical calculations in specimen W3 LS1 for different cracking states and autogenous shrinkage rates	160
Figure 5.35: Minimum principal stress distribution from numerical calculations in specimen W3 LS2 for different cracking states	161
Figure 5.36: Minimum principal stress distribution from numerical calculations in specimen W4 LS1 for different autogenous shrinkage rates.....	162
Figure 5.37: Minimum principal stress distribution from numerical calculations in specimen W4 LS2 for different cracking states and autogenous shrinkage rates	162

Figure 5.38: Minimum principal stress distribution from numerical calculations in specimen W4 LS3 for different cracking states.....	163
--	-----

List of Tables

Table 2.1: Ranges of applicability for current design codes	31
Table 3.1: Ranges of applicability for ISO 19902, N-004 and DNVGL-ST-0126 and parameters of the small-scale specimens, exceeding values are highlighted.....	48
Table 3.2: Mechanical properties of the two grout materials given by the manufacturers (ITW Densit ApS (2012); BASF Construction Chemicals (2010))	49
Table 3.3: Summarised load bearing capacities compared between grout material and specimen geometry	55
Table 3.4: Summarised stiffness compared between grout material and specimen geometry.....	56
Table 3.5: Overview of damage patterns of small-scale FLS test specimens with Geometry 1 and grout material DDS2.....	76
Table 3.6: Overview of damage patterns of small-scale FLS test specimens with Geometry 1 and grout material BM95.....	77
Table 3.7: Overview of damage patterns of small-scale FLS test specimens with Geometry 2...	77
Table 4.1: Mechanical properties of the two grout materials given by the manufacturers (ITW Engineered Polymers (2016), BASF Construction Chemicals (2010)).....	89
Table 4.2: Overview of large-scale test results	99
Table 4.3: Overview of mean displacement rate and displacement range rate	104
Table 4.4: Overview of calculated mean secant stiffnesses of large-scale specimens.....	106
Table 4.5: Ranges of applicability for DIN EN ISO 19902 (2014), NORSOK N-004 (2013) and DNVGL-ST-0126 (2016) and parameters of the large-scale specimens.....	114
Table 5.1: Used material parameters for grout.....	135
Table 5.2: Used material parameters for steel.....	136
Table 5.3: Autogenous shrinkage values for different grout materials	138

Nomenclature

Capital Latin symbols

C_L, C_P, C_S	[-]	Coefficients
D	[-]	Damage variable
D_g, D_p, D_s	[mm]	Diameter of grout, pile, sleeve, outer value
E	[N]; [N/mm ²]	Effect of action; Elastic modulus
E_0	[N/mm ²]	Elastic modulus, initial value
E_{c1}	[N/mm ²]	Elastic modulus, secant value at compressive strength
E_{ci}	[N/mm ²]	Elastic modulus, initial value
E_g	[N/mm ²]	Elastic modulus grout
E_s	[N/mm ²]	Elastic modulus steel
F	[N]; [-]	Force; Yield criterion
F_a	[N]	Force axial
$F_{a,d}$	[N]	Force axial, design value
F_F	[N]	Force from friction
F_G	[N]	Force in compression strut
F_{ges}	[N]	Force capacity of grouted connection
F_K	[N]	Force from shear key
$F_{max}, F_{mean}, F_{min}$	[N]	Force, max, mean and min value
F_N	[N]	Force from normal contact
F_{real}	[N]	Force, actual value
F_{shear}	[N]	Force from shear
F_{slip}	[N]	Force at end of linear behaviour
F_{target}	[N]	Force, target value
F_{TR}	[N]	Force measured in test rig
$F_{ULS}, F_{ULS,ISO}$	[N]	Force capacity measured and acc. to ISO 19902
$F_{V1,Shk,cap,d}$	[N]	Force capacity of grouted connection, design value
$F_{V1,Shk,d}$	[N]	Force capacity of one shear key, design value
G	[-]	Yield criterion
G_F	[Nmm]	Tensile cracking energy
H	[N/mm ²]	Hardening modulus
I	[Ns]	Impulse
I_i	[-]	Invariant i of the stress tensor
J_i	[-]	Invariant i of the deviatoric stress tensor
K	[N/mm]	Stiffness
K_1	[N/mm]	Secant stiffness between min and max
K_2	[N/mm]	Secant stiffness between mean and max
K_c	[N/mm]; [-]	Secant stiffness in compression; Shape parameter
K_{laser}	[N/mm]	Secant stiffness of specimen
K_{rig}	[N/mm]	Secant stiffness of specimen and test rig
K_t	[N/mm]	Secant stiffness in tension
L_e, L_g	[mm]	Length, geometrical and effective axial value for grout
N	[-]	Number of load cycles

N_E	[-]	Number of load cycles, acting
N_f	[-]	Number of load cycles, at failure
N_{max}	[-]	Number of load cycles, maximum value
N_R	[-]	Number of load cycles, endurable
N_{sk}	[-]	Number of shear keys
R	[N]; [-]	Reaction; Ratio between min and max load
R^2	[-]	Coefficient of determination
R_a	[μm]	Roughness arithmetic average value
S	[-]	Stress ratio regarding strength
$S_{c,max}$	[-]	Stress ratio regarding strength and max compression stress
$S_{c,min}$	[-]	Stress ratio regarding strength and min compression stress
T	[s]; [K]	Period; Temperature
U_g	[-]	Utilisation ratio grout
Y	[-]	Variable parameter

Small Latin symbols

f	[1/s]	Frequency
f_{2c}, f_{b0}	[N/mm ²]	Strength, initial biaxial compression
f_{ba}	[N/mm ²]	Strength, bonding with adhesion
f_{bt}	[N/mm ²]	Strength, bending tension
f_{bu}	[N/mm ²]	Strength, bonding
f_c	[N/mm ²]	Strength, uniaxial compression
f_{c0}	[N/mm ²]	Strength, initial uniaxial compression
f_{ck}	[N/mm ²]	Strength, characteristic compression
$f_{ck,fat}$	[N/mm ²]	Strength, fatigue limit
f_{cm}	[N/mm ²]	Strength, uniaxial compression mean
f_{ctm}	[N/mm ²]	Strength, uniaxial tension mean
$f_{ctm,fl}$	[N/mm ²]	Strength, flexural tension mean
f_{cu}	[N/mm ²]	Strength, unconfined uniaxial compression
f_d	[N/mm ²]	Strength, design value
f_g	[N/mm ²]	Strength, grout connection
$f_{g,hear}$	[N/mm ²]	Strength, grout matrix
$f_{g,sliding}$	[N/mm ²]	Strength, interface shear
f_t	[N/mm ²]	Strength, uniaxial tension
f_{t0}	[N/mm ²]	Strength, initial uniaxial tension
f_y	[N/mm ²]	Strength, yield value
h	[mm]	Height
h_b	[mm]	Prism depth
h_{sk}	[mm]	Height of shear key
k	[-]	Plasticity number
k_{red}	[-]	Early age cycling reduction factor
m	[-]	Gradient
s_{sk}	[mm]	Spacing between shear keys
t	[s], [d]	Time

t_g, t_p, t_s	[mm]	Thickness of grout, pile, sleeve, nominal value
u	[mm]	Displacement
u_0	[mm]	Displacement, initial value
u_{Ad}	[mm]	Displacement of adapter
u_{end}	[mm]	Displacement, final value
u_{Laser}	[mm]	Displacement measured with laser
u_{PS}	[mm]	Displacement measured between pile and sleeve
u_{Ri}	[mm]	Displacement of rig
u_{Rig}	[mm]	Displacement measured inside test rig
u_{SG}	[mm]	Displacement measured between sleeve and grout
u_{Sp}	[mm]	Displacement of specimen
u_{TR}	[mm]	Displacement measured in test rig
u_{ULS}	[mm]	Displacement at static load bearing capacity
w	[mm]	Crack opening width
w_{sk}	[mm]	Width of shear key
x	[-]	Variable parameter
y	[-]	Variable parameter

Greek symbols

α	[°]; [-]	Geometrical angle; Variable parameter
α_{bs}	[-]	Coefficient for cement type
α_E	[-]	Coefficient for effect of types of aggregate
α_{fl}	[-]	Coefficient for conversion
α_T	[1/K]	Coefficient of thermal expansion
β	[-]	Variable parameter
β_{cc}	[-]	Coefficient for material age
γ	[-]	Variable parameter
γ_m	[-]	Material safety factor
ε	[-]; [-]	Strain; Eccentricity parameter
$\varepsilon_{ax,i}$	[-]	Strain, axial value at position i
ε_c	[-]	Strain, total compressive value
$\varepsilon_{c,lim}$	[-]	Strain at compressive failure
ε_{cl}	[-]	Strain at compressive strength
ε_{cbs}	[-]	Strain caused by autogenous shrinkage
ε_{ct}	[-]	Strain at tensile failure
ε_{el}	[-]	Strain, elastic part
ε_f	[-]	Strain at failure
$\varepsilon_{max}, \varepsilon_{min}$	[-]	Strain, max and min value
ε_{pl}	[-]	Strain, plastic part
ε_T	[-]	Strain caused by thermal load
ε_v	[-]	Strain, viscous part
η	[-];[-]	Utilisation ratio; Normalised strain
θ	[N/mm ²]	Randulic coordinate
κ	[-]	Confinement factor

μ	[-]; [-]; [-]	Friction coefficient; Mean value; Viscosity parameter
ν	[-]	Poisson ratio
ξ	[N/mm ²]	Randulic coordinate
π	[-]	Pi
ρ	[kg/m ³]; [N/mm ²]	Density, Randulic coordinate
σ	[N/mm ²]; [-]	Stress; Standard deviation
σ_i	[N/mm ²]	Stress, principal value i
σ_a	[N/mm ²]	Stress in axial direction
σ_c	[N/mm ²]	Stress, compression
$\sigma_{c,max}, \sigma_{c,min}$	[N/mm ²]	Stress, compression max and min values
σ_{lat}	[N/mm ²]	Stress in lateral direction
ψ	[-]	Dilatancy angle

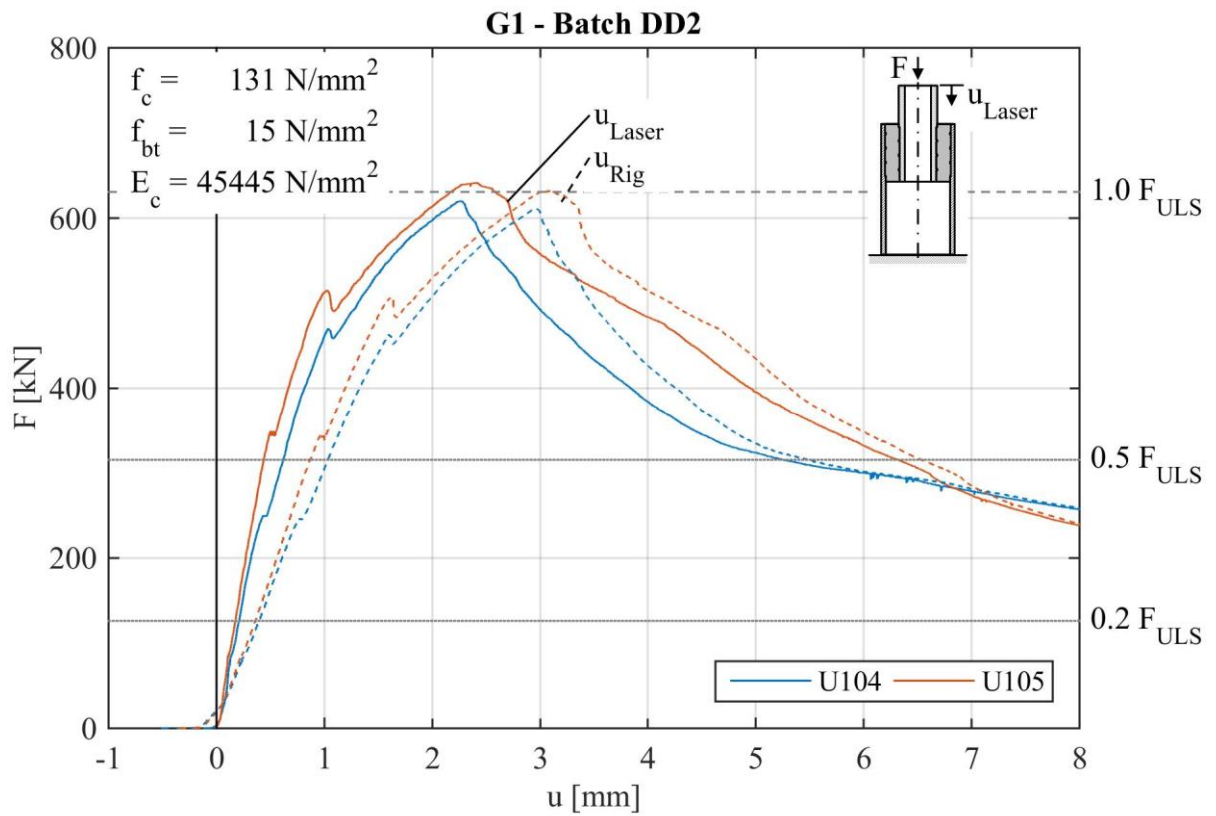
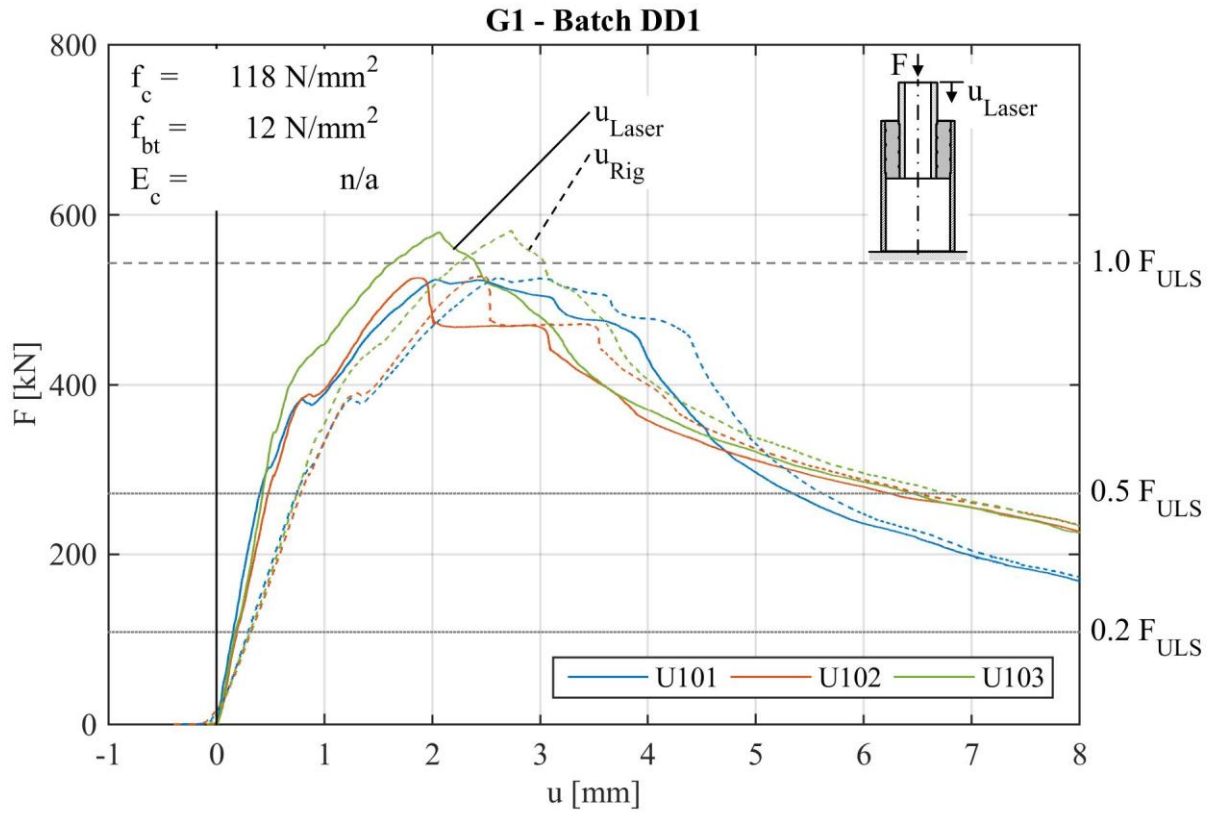
Abbreviations

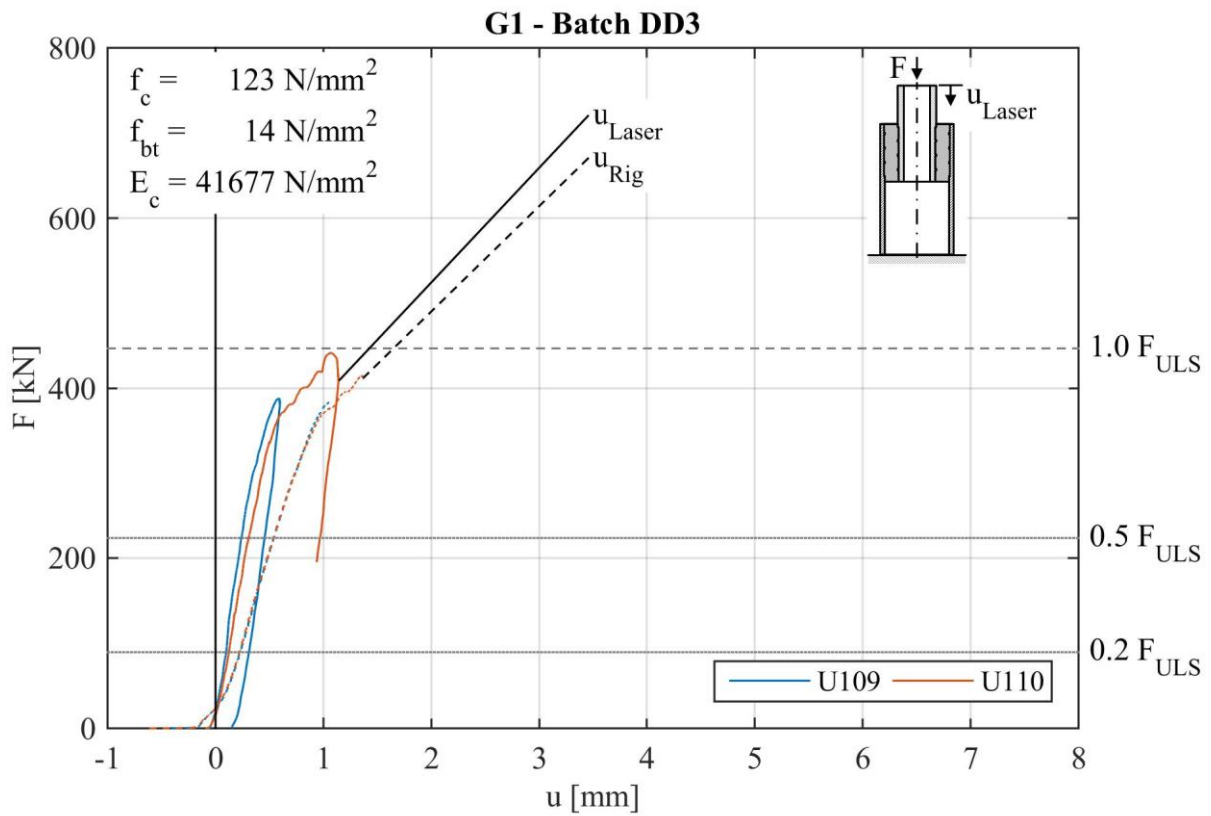
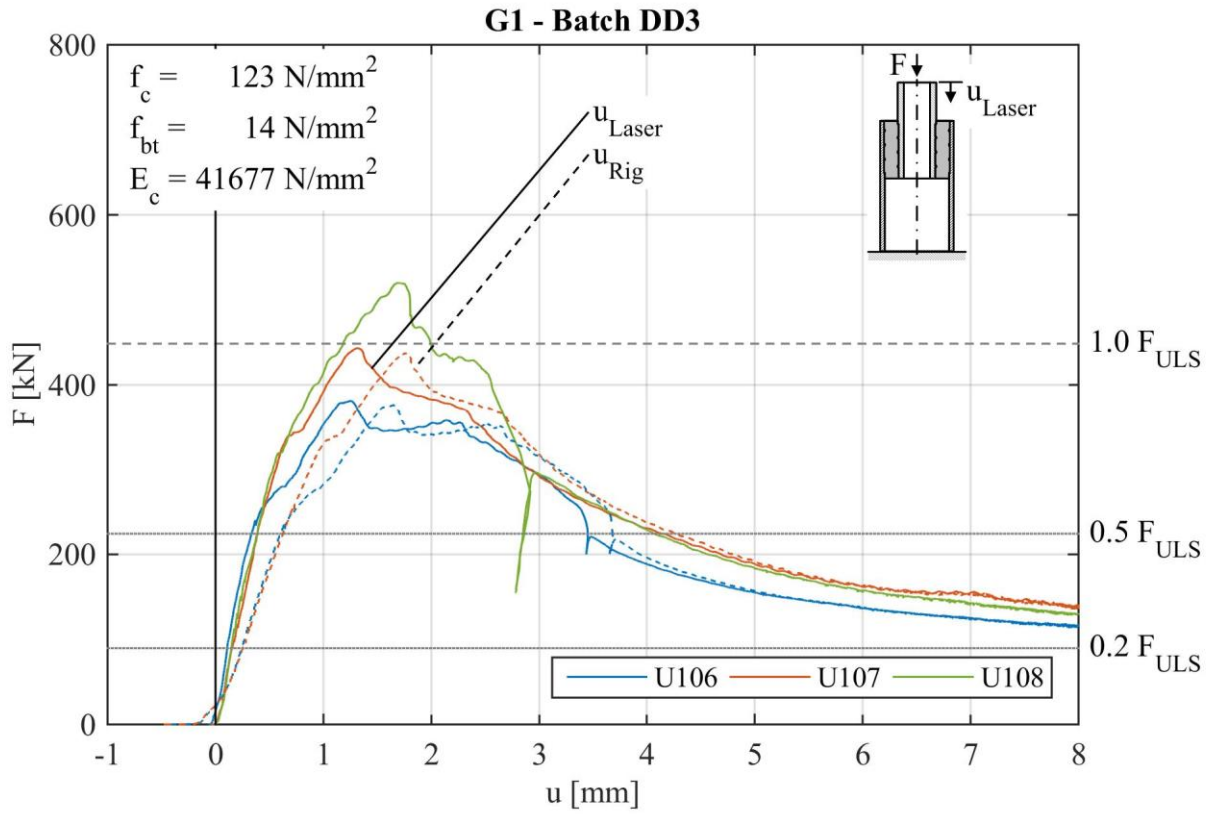
AC	Ambient condition
BM95	BASF Masterflow 9500
CDP	Concrete Damaged Plasticity
CI	Confidence Interval
DDS2	Densit Ducorit S2
DDS5	Densit Ducorit S5
D1, D2	Specimens tested in dry AC
DLC	Design Load Case
DP	Drucker-Prager
EDP	Extended-Drucker-Prager
FLS	Fatigue Limit State
GC	Grouted Connection
HAC	High Alumina Cement
HPC	High Performance Concrete
HPG	High Performance Grout
LS1...LS7	Load Stages
OIC	Oilwell B Cement
OPC	Ordinary Portland Cement
P1...P5	Shear keys on pile
S1...S5	Shear keys on sleeve
TC	Termination Criterion
UHPC	Ultra High Performance Concrete
ULS	Ultimate Limit State
W1...W4	Specimens tested in wet AC

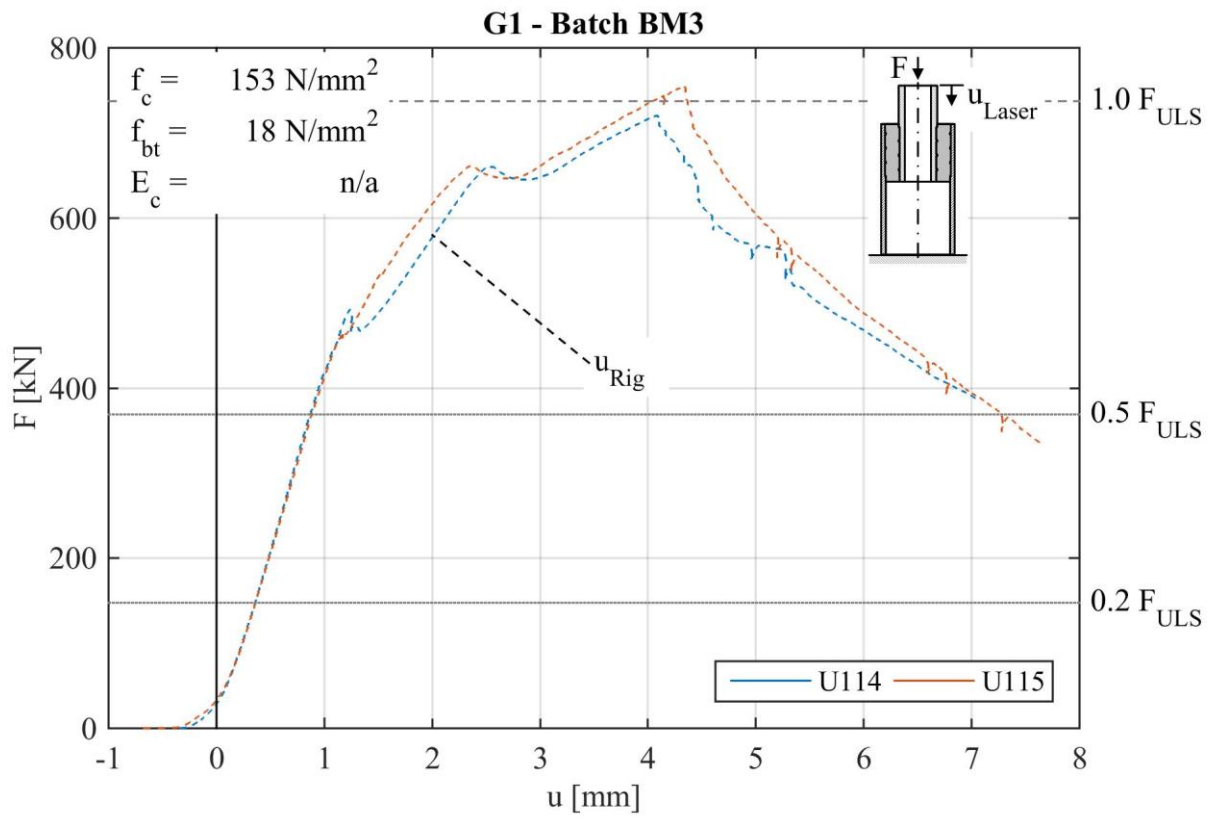
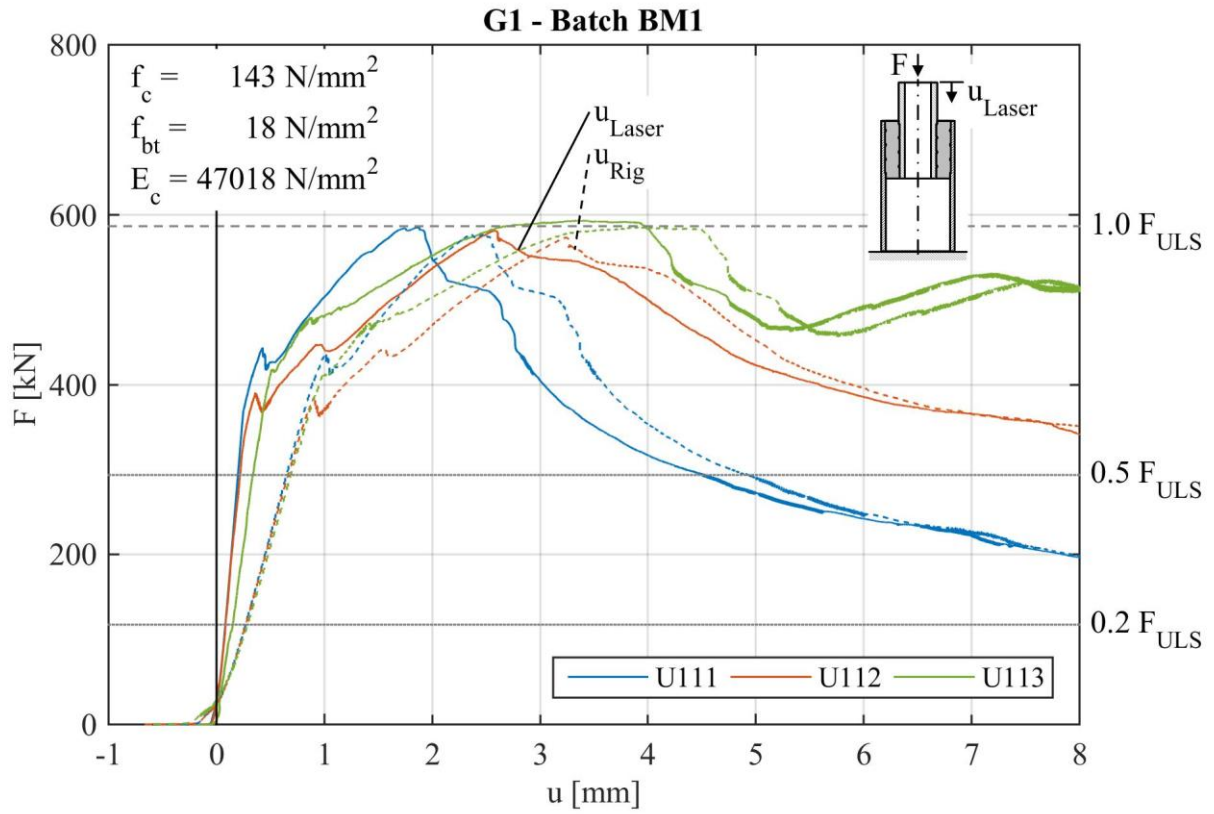
Appendix A – Small-scale test results

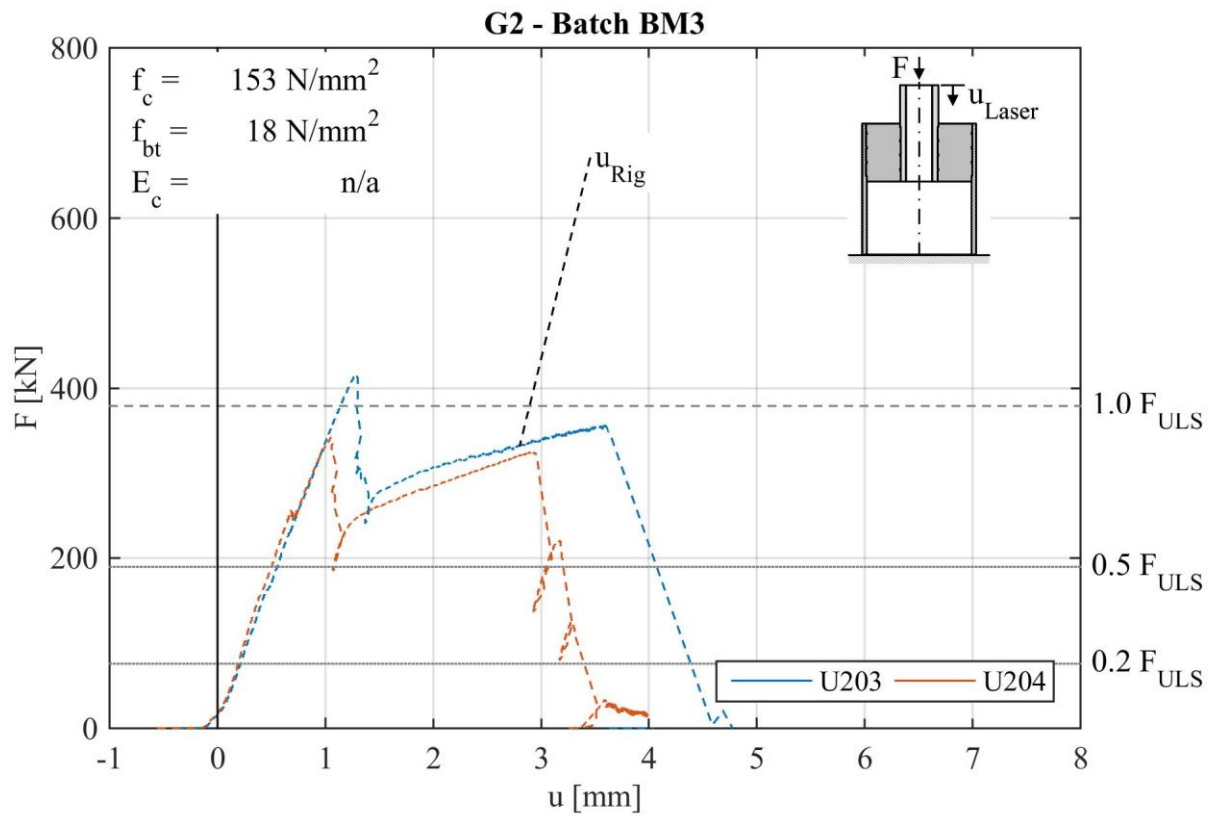
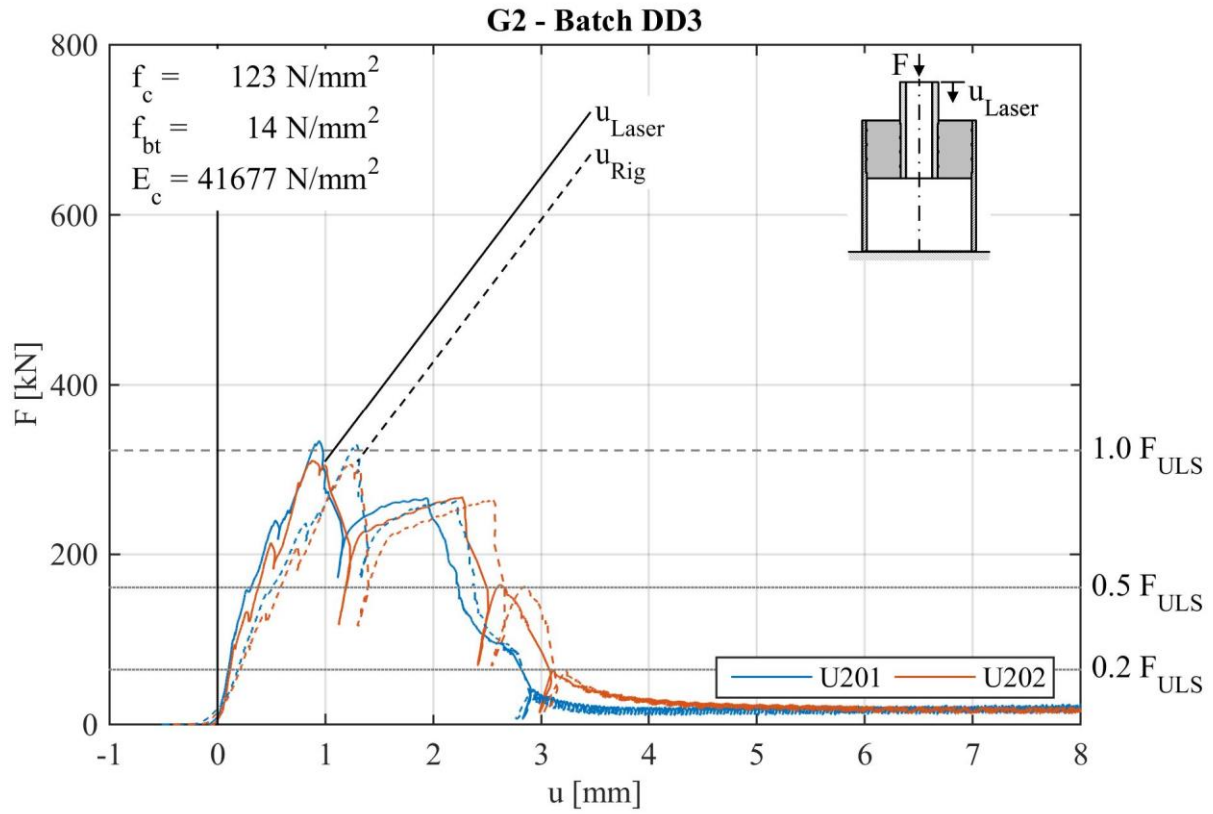
A.1 ULS results

Id	Geom	Material	Batch	F_{slip}			F_{ULS}			F_{slip} / F_{ULS}	
				i [kN]	mean [kN]	std [%]	i [kN]	mean [kN]	std [%]	i [-]	mean [-]
U101	1	Densit Ducorit S2	DD1	303			524			0.58	
U102				293	313	7.0	526	543	4.7	0.56	0.58
U103				344			579			0.59	
U104	1	Densit Ducorit S2	DD2	250			620	630	1.6	0.40	0.47
U105				348	299	16.4	640			0.54	
U106	1	Densit Ducorit S2	DD3	240			381			0.63	
U107				344	301	14.8	442	447	12.6	0.78	0.67
U108				320			519			0.62	
U109	1	Densit Ducorit S2	DD3	388			-	447	-	-	0.86
U110				381	385	0.9	-			-	
U111	1	BASF Masterflow 9500	BM1	442			576			0.77	
U112				391	417	5.0	583	585	1.3	0.67	0.71
U113				418			595			0.70	
U114	1	BASF Masterflow 9500	BM3	493			720	737	2.3	0.68	0.65
U115				465	479	2.9	754			0.62	
U201	2	Densit Ducorit S2	DD3	159	146	8.9	333	322	3.6	0.48	0.45
U202				133			310			0.43	
U203	2	BASF Masterflow 9500	BM3	161	160	0.9	417	380	9.9	0.39	0.42
U204				158			342			0.46	







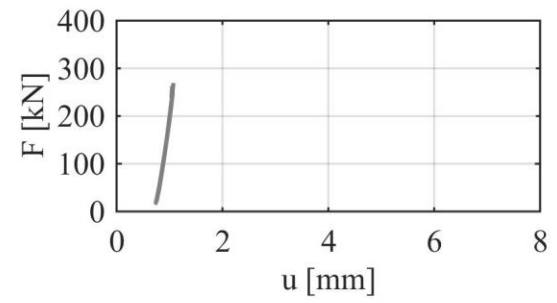
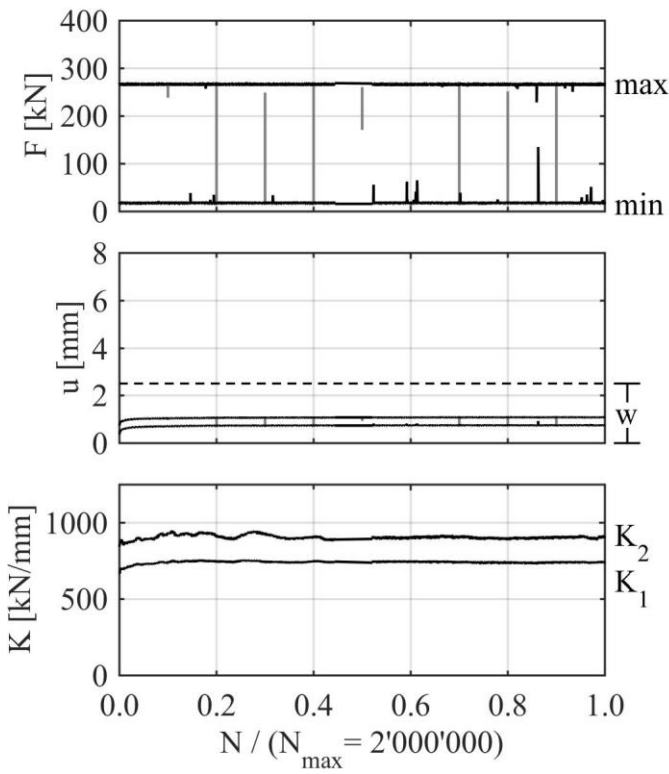


A.2 FLS results – Geometry 1, Densit Ducorit S2

Id	Geom.	Material	Test procedure						Batch	Dates		
			F _{ULS} [kN]	AC	F _{max} /F _{ULS} [-]	f [Hz]	N [-]	Term. Crit.		Grouting	Testing	Age [d]
F101	1	Densit Ducorit S2	543	dry	0.5	5.0	2000000	runner	DD1	18.07.2012	17.09.2012	60
F102	1	Densit Ducorit S2	543	dry	0.5	5.0	2000000	runner	DD1	18.07.2012	26.09.2012	69
F103	1	Densit Ducorit S2	630	dry	0.5	5.0	2000000	runner	DD2	18.03.2014	28.04.2014	41
F104	1	Densit Ducorit S2	447	wet	0.5	10.0	16685	Δu	DD3	03.07.2014	22.08.2014	50
F105	1	Densit Ducorit S2	447	wet	0.5	10.0	32435	Δu	DD3	03.07.2014	22.08.2014	50
F106	1	Densit Ducorit S2	447	wet	0.5	10.0	60937	Δu	DD3	03.07.2014	21.08.2014	49
F107	1	Densit Ducorit S2	543	wet	0.5	5.0	64125	Δu	DD1	18.07.2012	25.09.2012	68
F108	1	Densit Ducorit S2	543	wet	0.5	5.0	31392	Δu	DD1	18.07.2012	08.10.2012	81
F109	1	Densit Ducorit S2	543	wet	0.5	5.0	35307	Δu	DD1	18.07.2012	01.10.2012	74
F110	1	Densit Ducorit S2	543	wet	0.5	5.0	101221	Δu	DD1	18.07.2012	24.09.2012	67
F111	1	Densit Ducorit S2	447	wet	0.5	2.0	142148	Δu	DD3	03.07.2014	27.08.2014	55
F112	1	Densit Ducorit S2	447	wet	0.5	2.0	204282	Δu	DD3	03.07.2014	25.08.2014	53
F113	1	Densit Ducorit S2	447	wet	0.5	2.0	65298	Δu	DD3	03.07.2014	28.08.2014	56
F114	1	Densit Ducorit S2	543	wet	0.5	1.0	102735	Δu	DD1	18.07.2012	04.10.2012	77
F115	1	Densit Ducorit S2	543	wet	0.5	1.0	116482	Δu	DD1	18.07.2012	02.10.2012	75
F116	1	Densit Ducorit S2	630	wet	0.5	1.0	49349	Δu	DD2	18.03.2014	29.04.2014	42
F117	1	Densit Ducorit S2	630	wet	0.5	1.0	80146	Δu	DD2	18.03.2014	06.06.2014	79
F118	1	Densit Ducorit S2	543	wet	0.5	0.3	156307	Δu	DD1	18.07.2012	09.10.2012	82
F119	1	Densit Ducorit S2	447	wet	0.5	0.3	248450	Δu	DD3	03.07.2014	06.11.2014	124
F120	1	Densit Ducorit S2	447	wet	0.5	0.3	95250	Δu	DD3	03.07.2014	10.10.2014	98
F121	1	Densit Ducorit S2	447	wet	0.5	0.3	407951	Δu	DD3	03.07.2014	22.09.2014	80
F122	1	Densit Ducorit S2	447	wet	0.5	0.3	258350	Δu	DD3	03.07.2014	09.09.2014	67
F123	1	Densit Ducorit S2	630	wet	0.2	5.0	2000000	runner	DD2	18.03.2014	19.05.2014	62
F124	1	Densit Ducorit S2	630	wet	0.2	5.0	2000000	runner	DD2	18.03.2014	12.05.2014	55
F125	1	Densit Ducorit S2	630	wet	0.2	5.0	1038739	u _{max}	DD2	18.03.2014	02.06.2014	75
F126	1	Densit Ducorit S2	447	wet	0.2	5.0	1188273	u _{max}	DD3	03.07.2014	29.08.2014	57

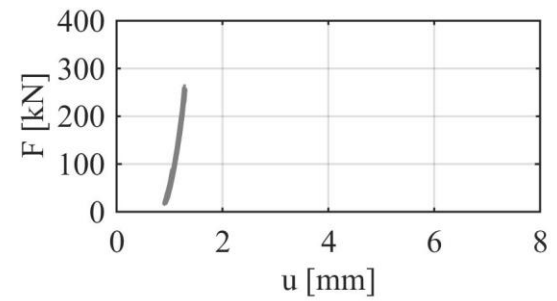
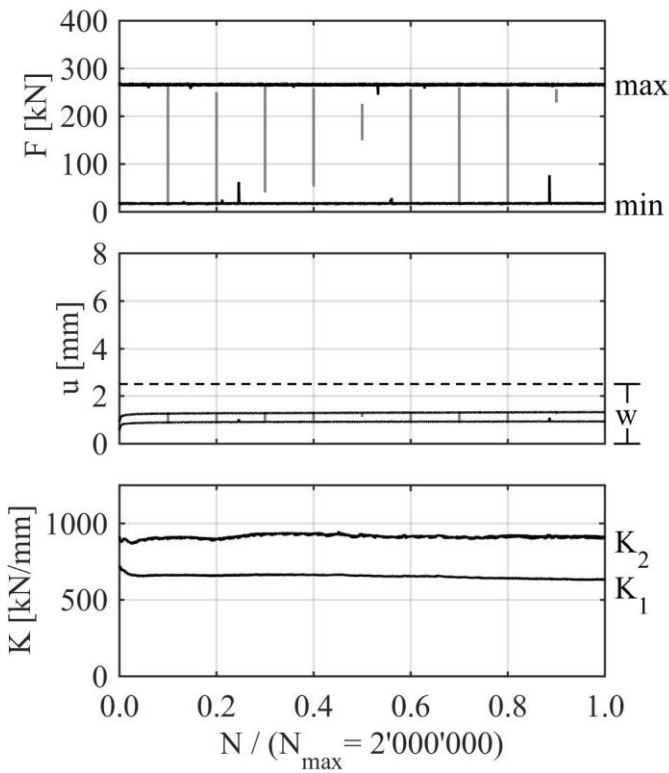
Id: 101 **Geom: 1** **Mat: Densit Ducorit S2**

AC: dry $F_{max} = 50 \% F_{ULS}$ $f = 5 \text{ Hz}$



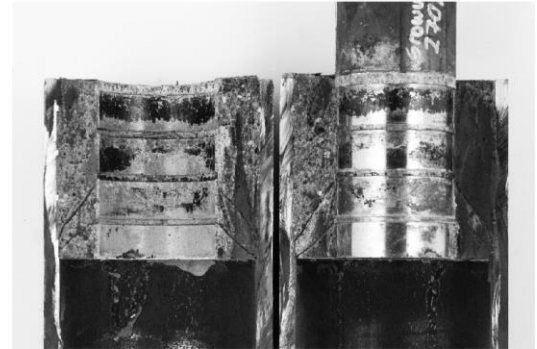
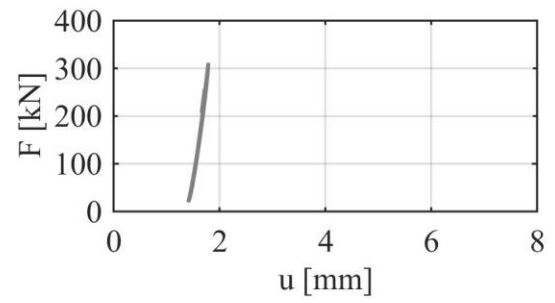
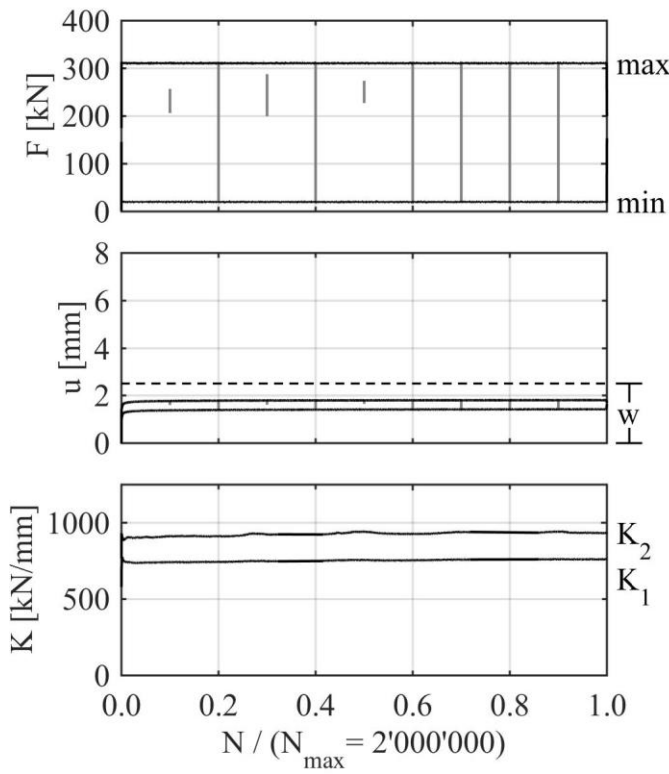
Id: 102 **Geom: 1** **Mat: Densit Ducorit S2**

AC: dry $F_{max} = 50 \% F_{ULS}$ $f = 5 \text{ Hz}$



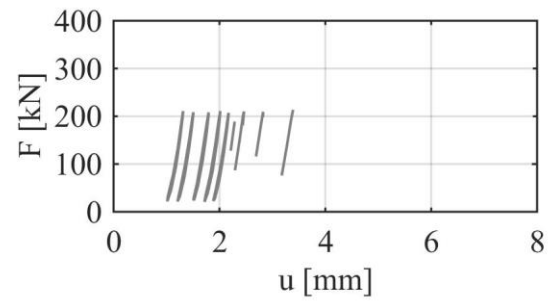
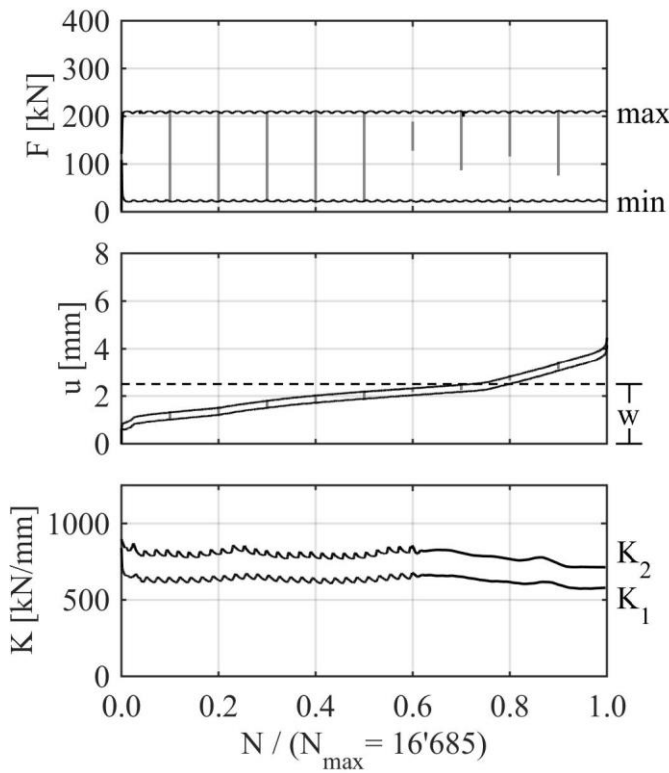
Id: 103 **Geom: 1** **Mat: Densit Ducorit S2**

AC: dry $F_{max} = 50 \% F_{ULS}$ $f = 5 \text{ Hz}$



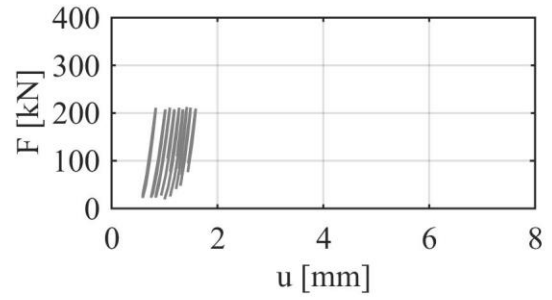
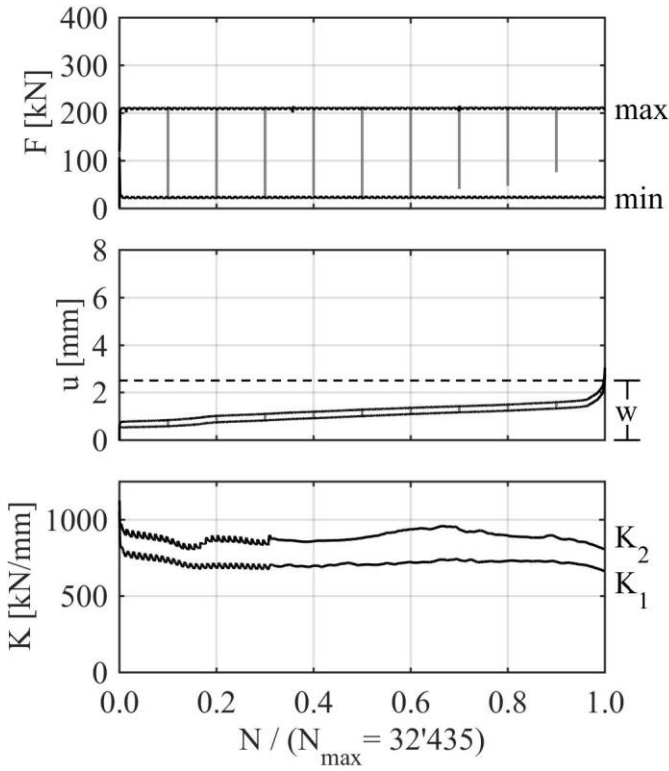
Id: 104 **Geom: 1** **Mat: Densit Ducorit S2**

AC: wet $F_{max} = 50 \% F_{ULS}$ $f = 10 \text{ Hz}$



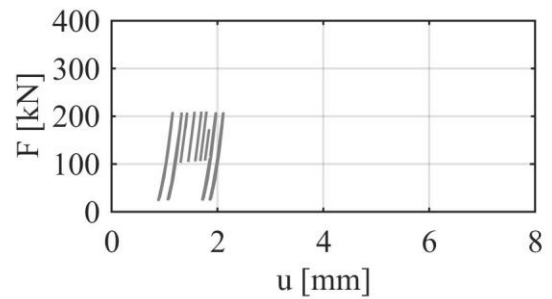
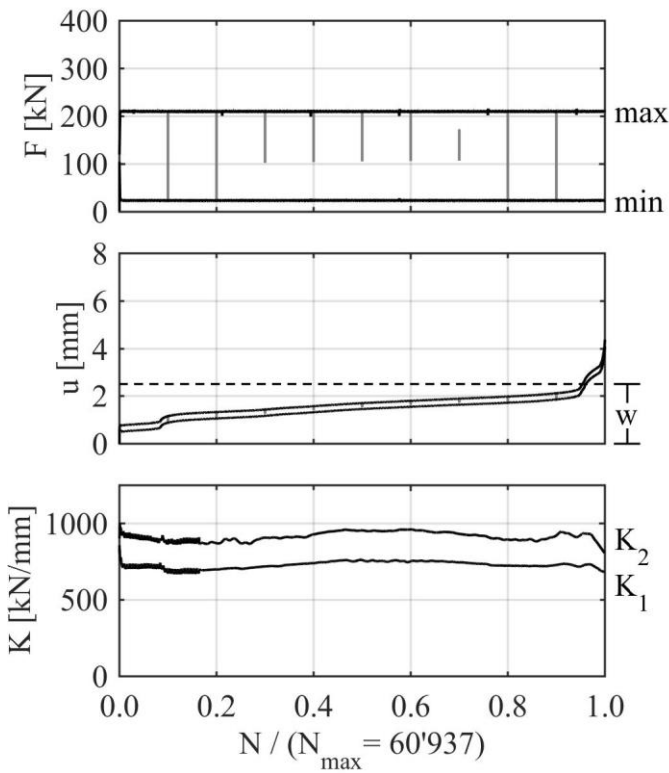
Id: 105 **Geom: 1** **Mat: Densit Ducorit S2**

AC: wet $F_{max} = 50\% F_{ULS}$ $f = 10\text{ Hz}$



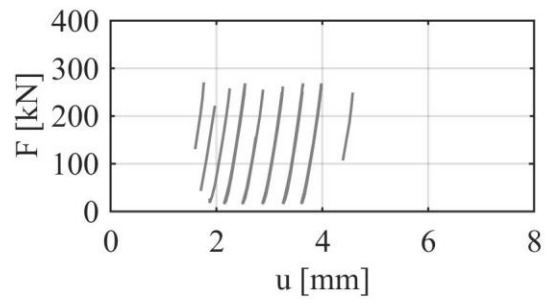
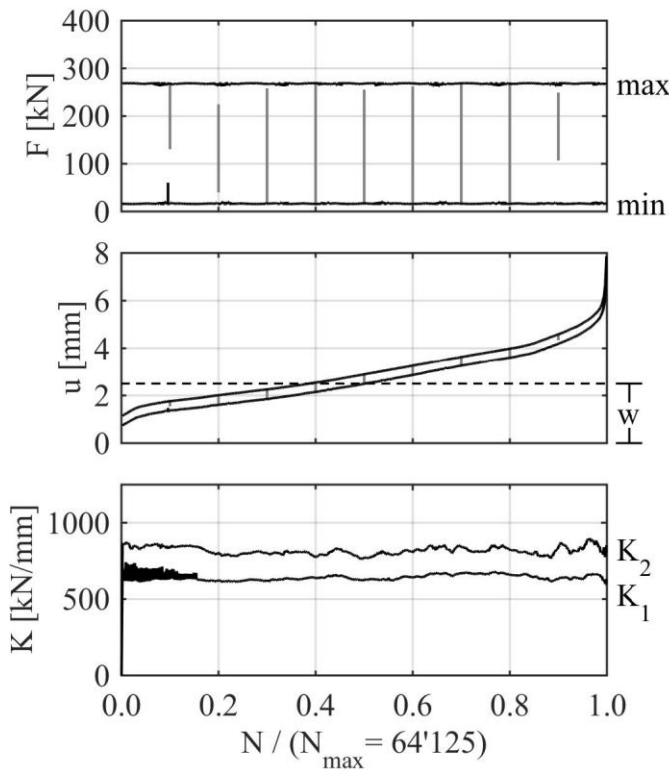
Id: 106 **Geom: 1** **Mat: Densit Ducorit S2**

AC: wet $F_{max} = 50\% F_{ULS}$ $f = 10\text{ Hz}$



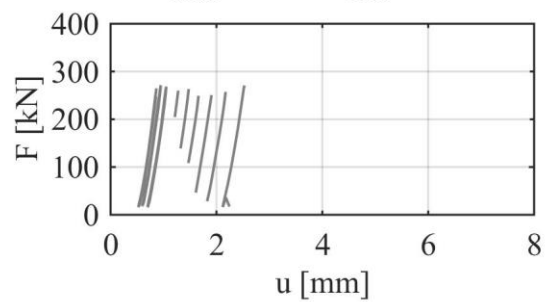
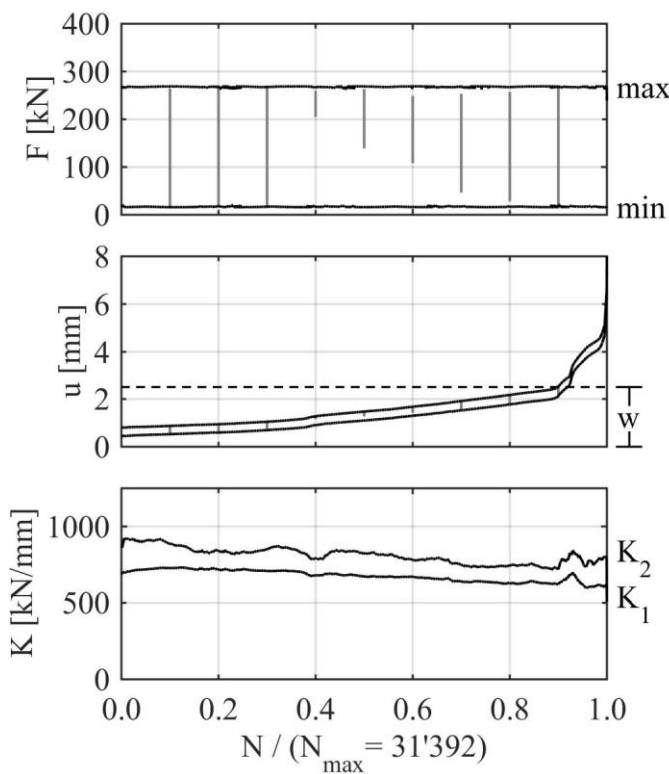
Id: 107 **Geom: 1** **Mat: Densit Ducorit S2**

AC: wet $F_{max} = 50 \% F_{ULS}$ $f = 5 \text{ Hz}$



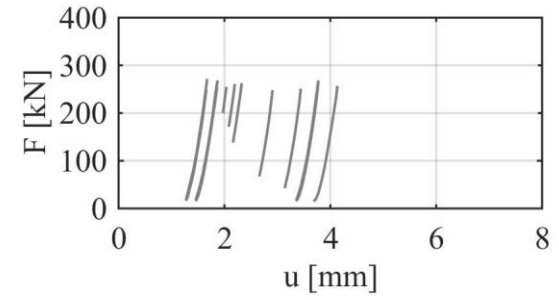
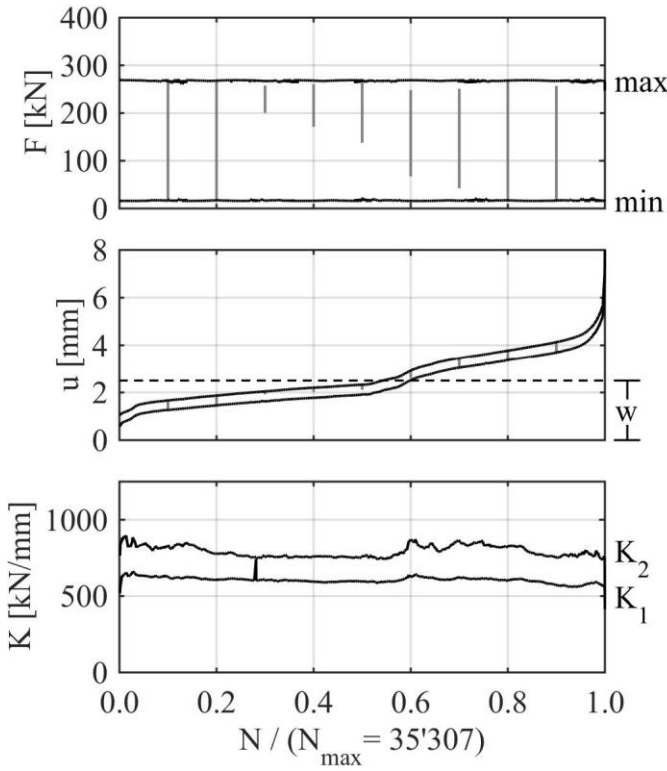
Id: 108 **Geom: 1** **Mat: Densit Ducorit S2**

AC: wet $F_{max} = 50 \% F_{ULS}$ $f = 5 \text{ Hz}$



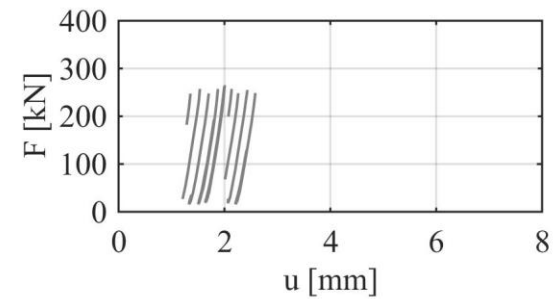
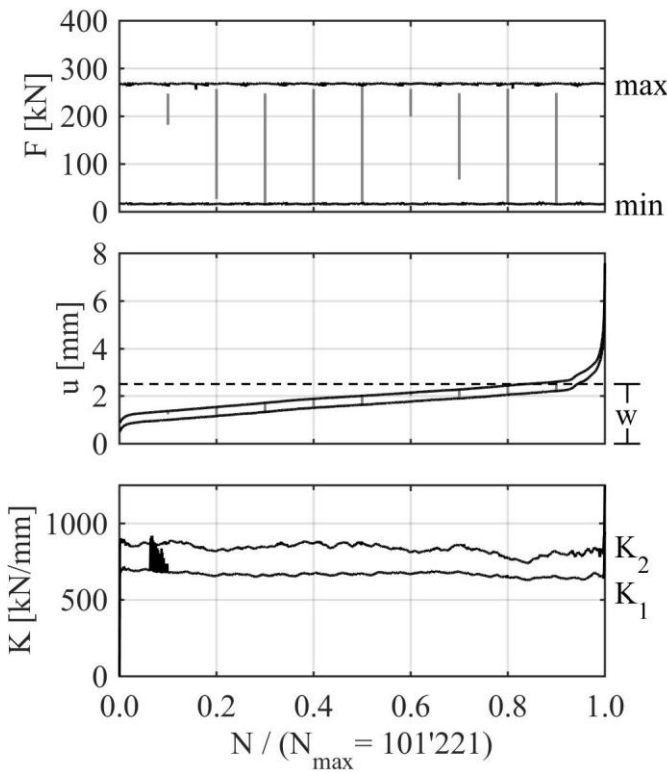
Id: 109 **Geom: 1** **Mat: Densit Ducorit S2**

AC: wet $F_{max} = 50\% F_{ULS}$ $f = 5\text{ Hz}$



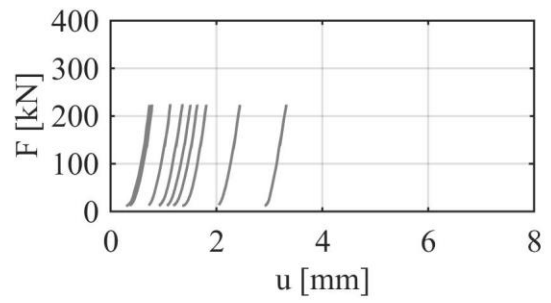
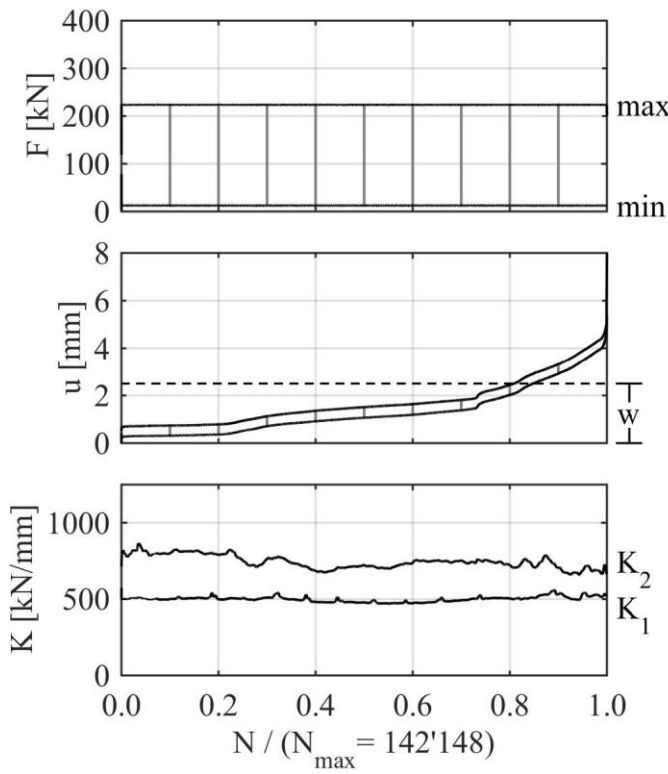
Id: 110 **Geom: 1** **Mat: Densit Ducorit S2**

AC: wet $F_{max} = 50\% F_{ULS}$ $f = 5\text{ Hz}$



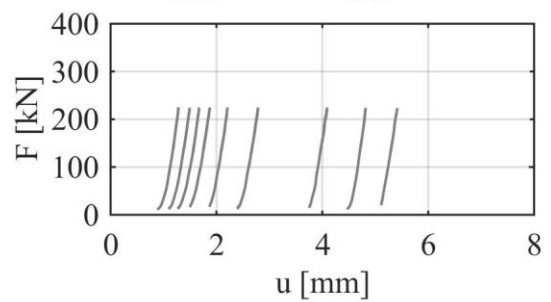
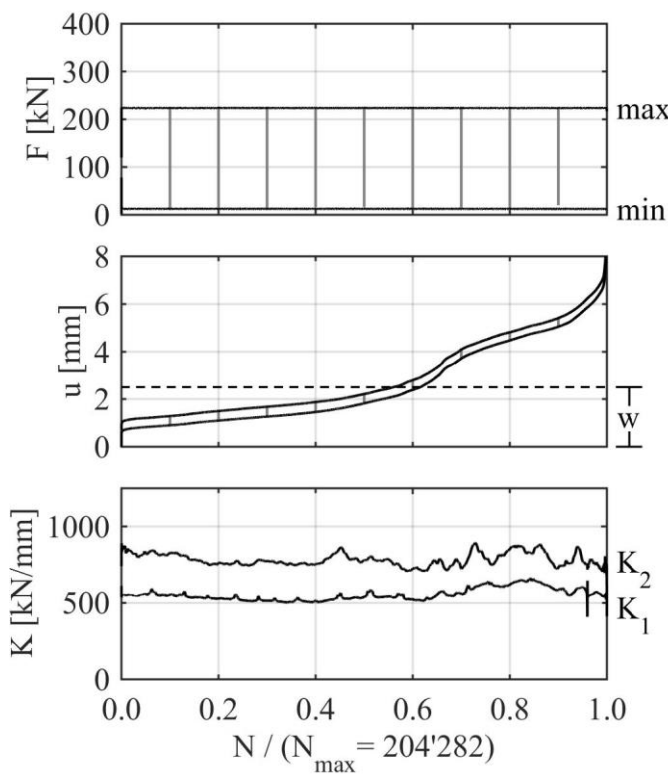
Id: 111 **Geom: 1** **Mat: Densit Ducorit S2**

AC: wet $F_{max} = 50 \% F_{ULS}$ $f = 2 \text{ Hz}$



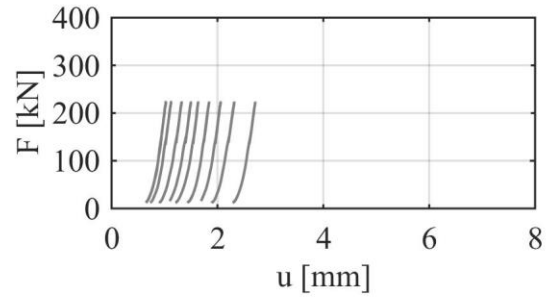
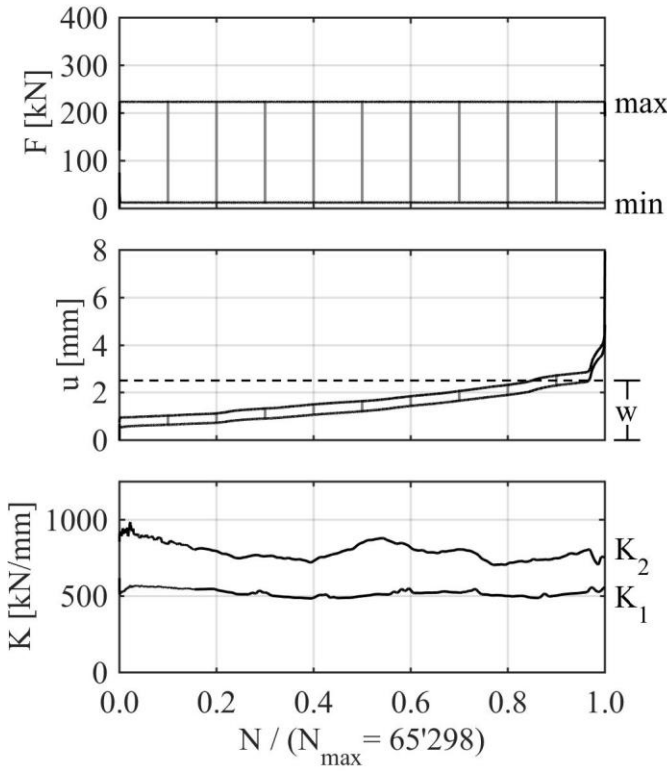
Id: 112 **Geom: 1** **Mat: Densit Ducorit S2**

AC: wet $F_{max} = 50 \% F_{ULS}$ $f = 2 \text{ Hz}$



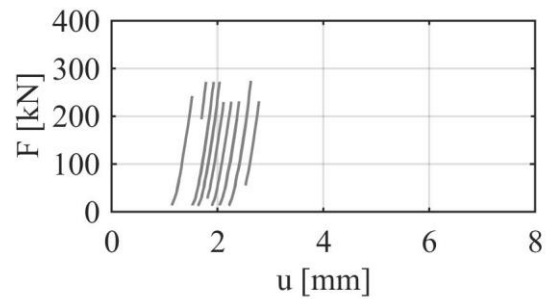
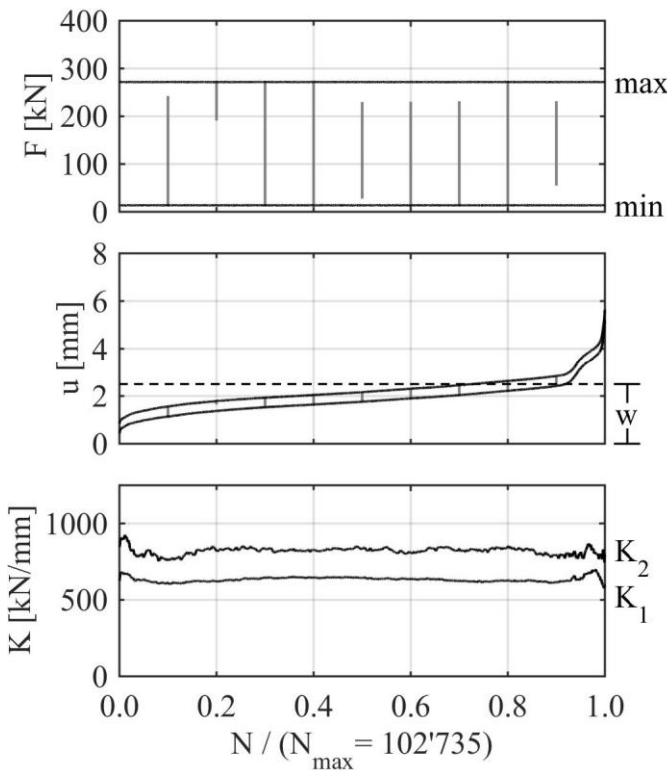
Id: 113 **Geom: 1** **Mat: Densit Ducorit S2**

AC: wet $F_{max} = 50\% F_{ULS}$ $f = 2\text{ Hz}$



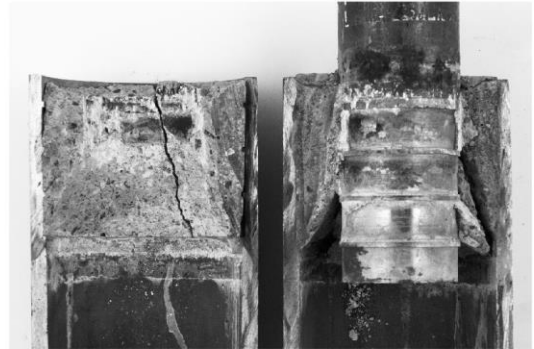
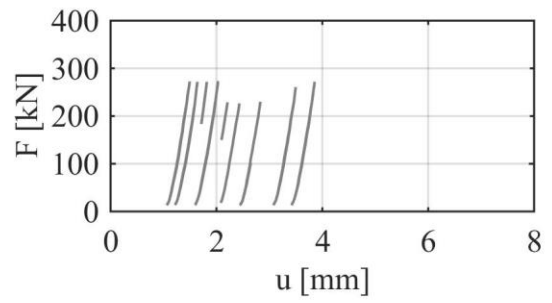
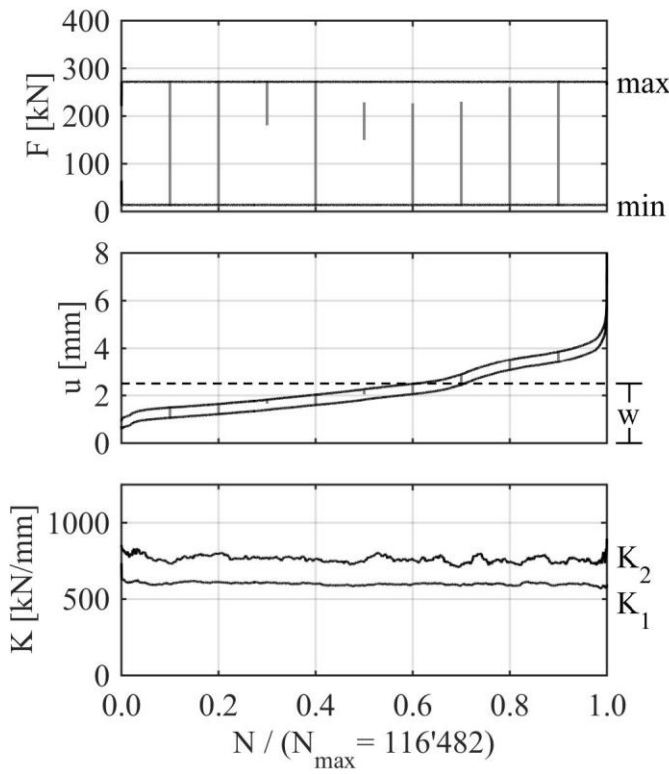
Id: 114 **Geom: 1** **Mat: Densit Ducorit S2**

AC: wet $F_{max} = 50\% F_{ULS}$ $f = 1\text{ Hz}$



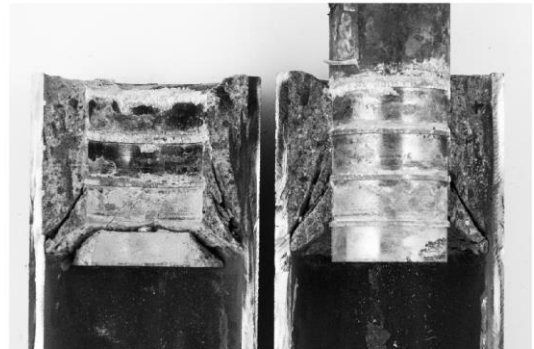
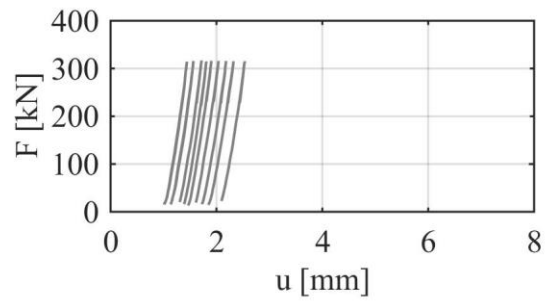
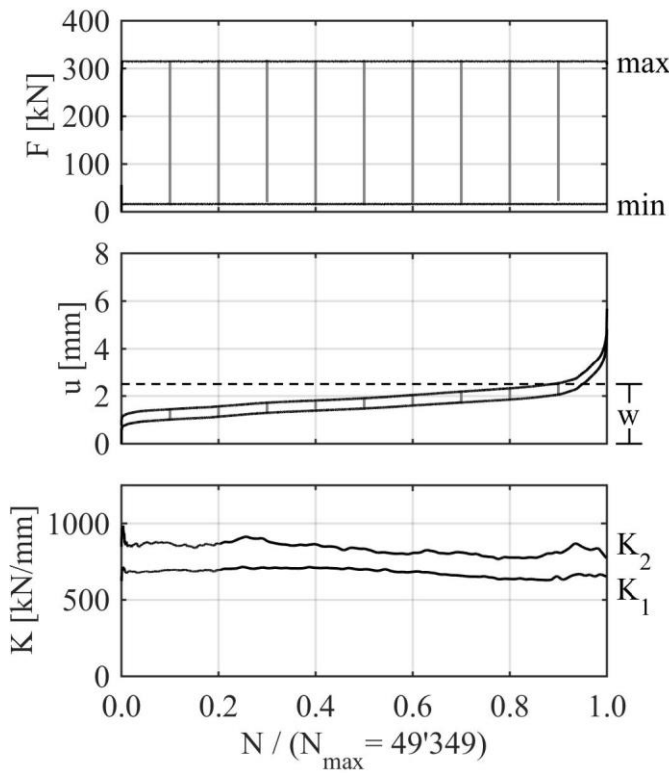
Id: 115 **Geom: 1** **Mat: Densit Ducorit S2**

AC: wet $F_{max} = 50 \% F_{ULS}$ $f = 1 \text{ Hz}$



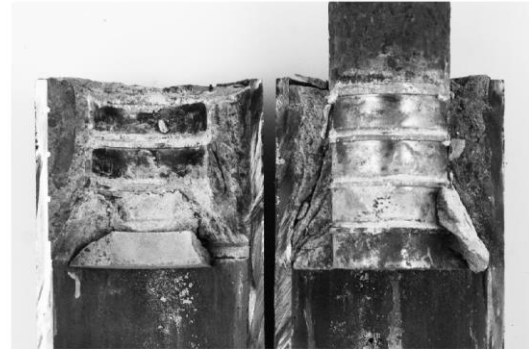
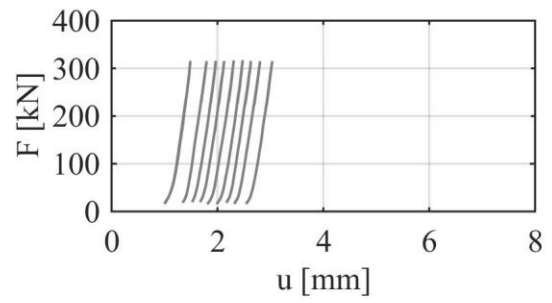
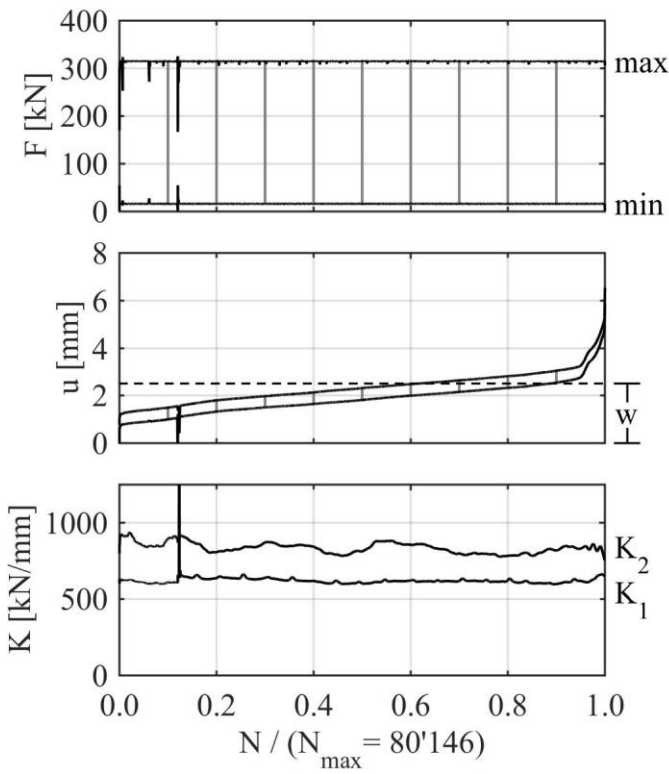
Id: 116 **Geom: 1** **Mat: Densit Ducorit S2**

AC: wet $F_{max} = 50 \% F_{ULS}$ $f = 1 \text{ Hz}$



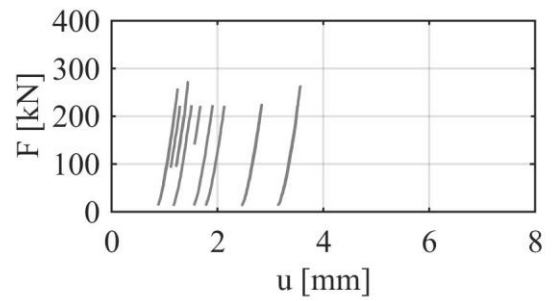
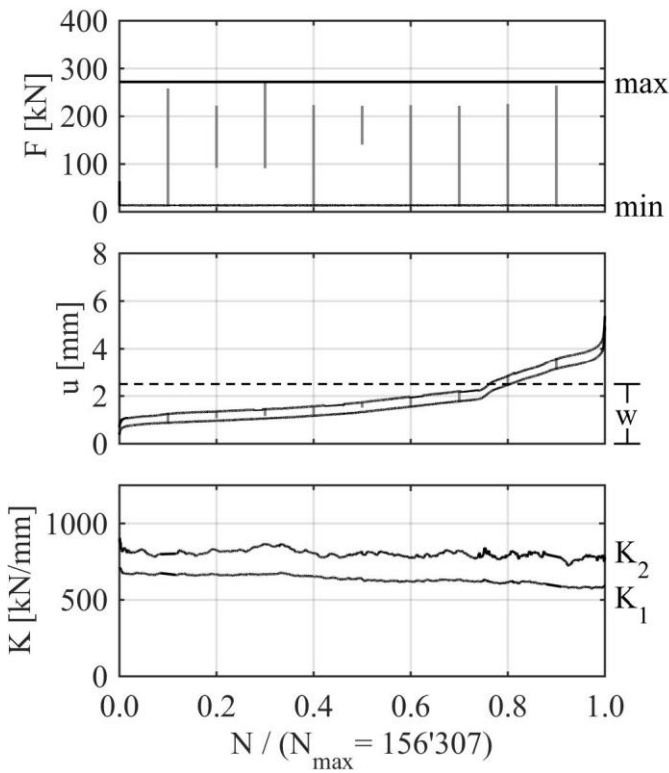
Id: 117 **Geom: 1** **Mat: Densit Ducorit S2**

AC: wet $F_{max} = 50\% F_{ULS}$ $f = 1\text{ Hz}$



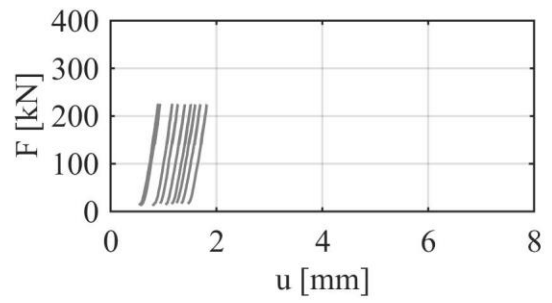
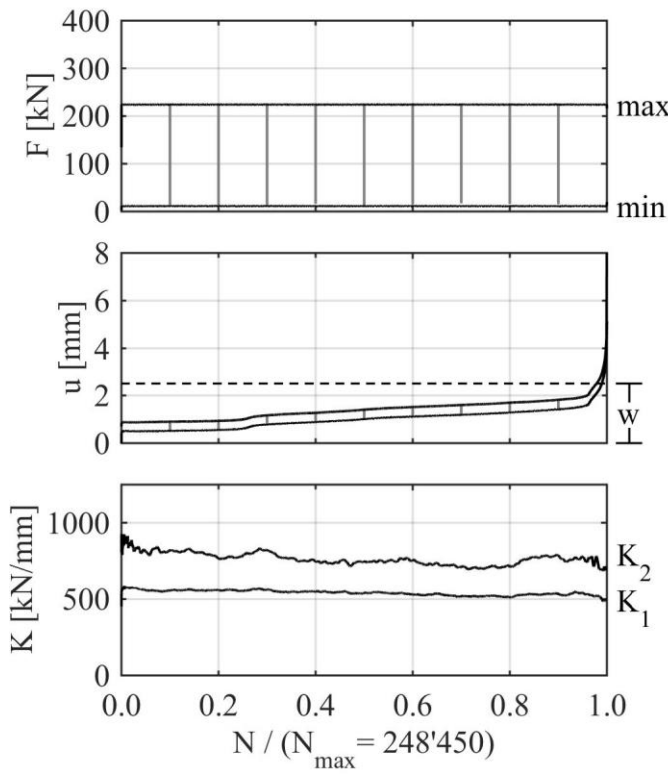
Id: 118 **Geom: 1** **Mat: Densit Ducorit S2**

AC: wet $F_{max} = 50\% F_{ULS}$ $f = 0.3\text{ Hz}$



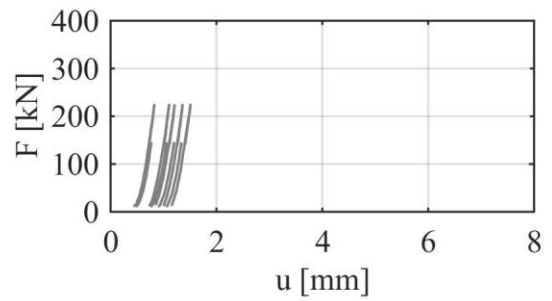
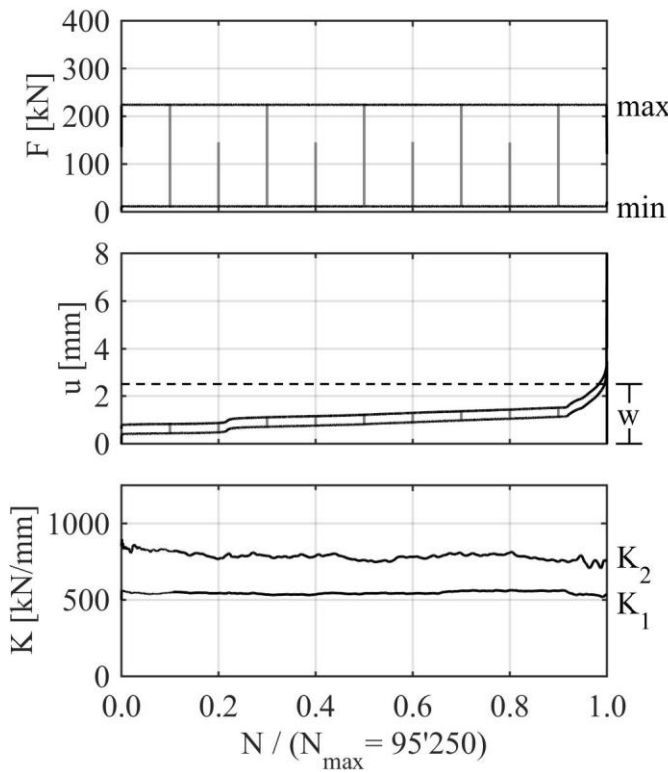
Id: 119 **Geom: 1** **Mat: Densit Ducorit S2**

AC: wet $F_{max} = 50 \% F_{ULS}$ $f = 0.3 \text{ Hz}$



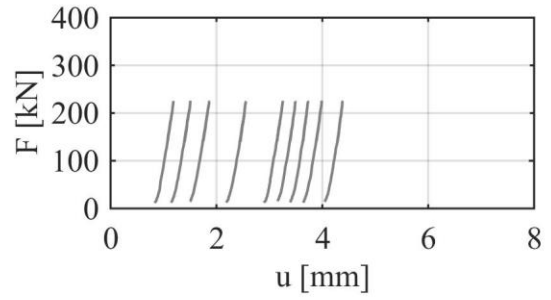
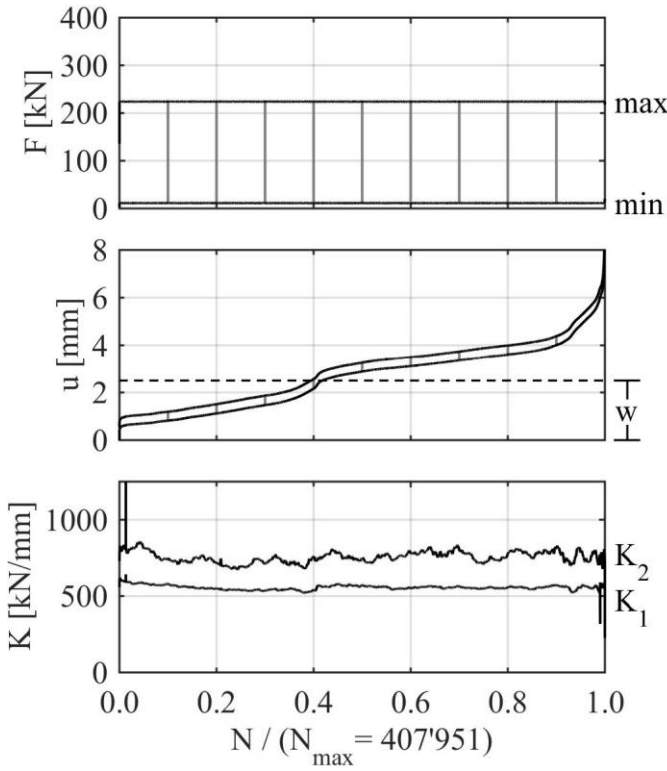
Id: 120 **Geom: 1** **Mat: Densit Ducorit S2**

AC: wet $F_{max} = 50 \% F_{ULS}$ $f = 0.3 \text{ Hz}$



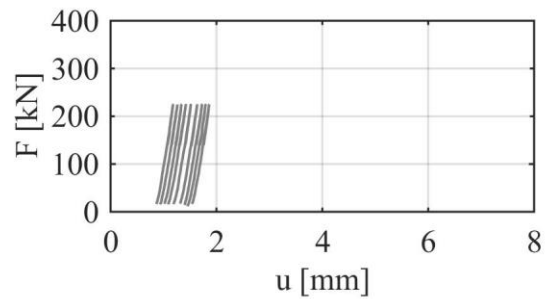
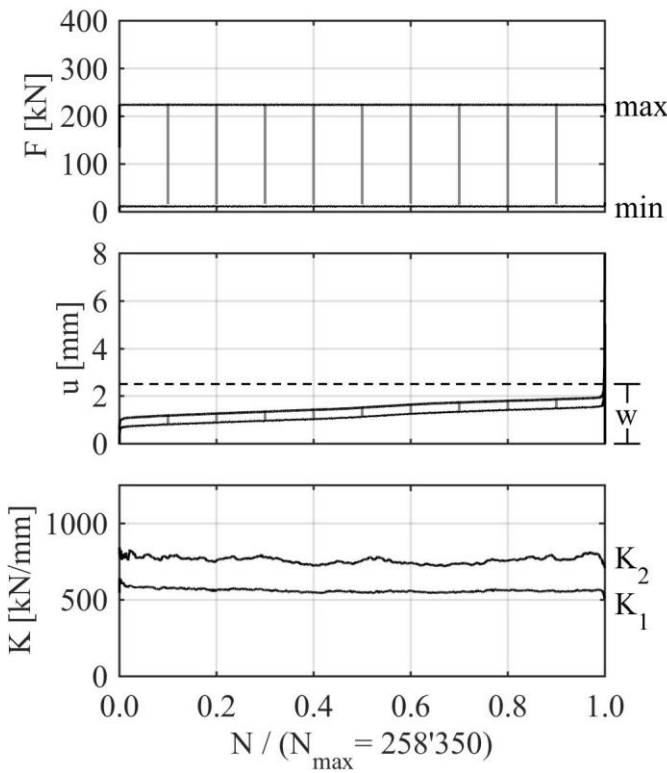
Id: 121 **Geom: 1** **Mat: Densit Ducorit S2**

AC: wet $F_{max} = 50 \% F_{ULS}$ $f = 0.3 \text{ Hz}$



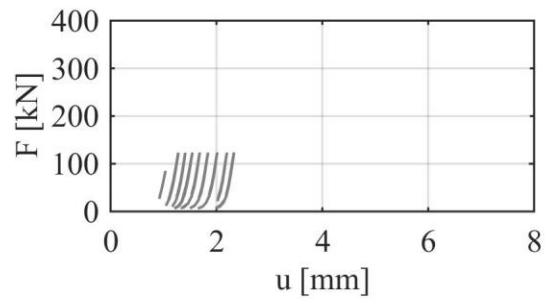
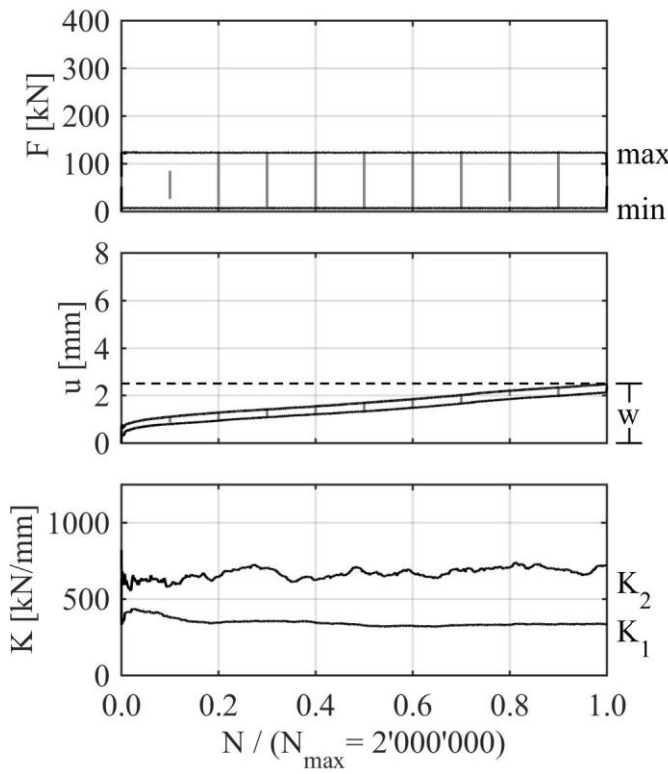
Id: 122 **Geom: 1** **Mat: Densit Ducorit S2**

AC: wet $F_{max} = 50 \% F_{ULS}$ $f = 0.3 \text{ Hz}$



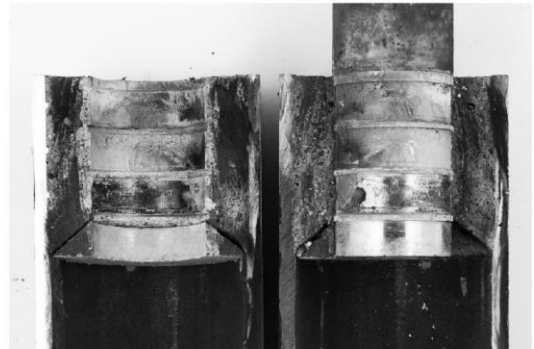
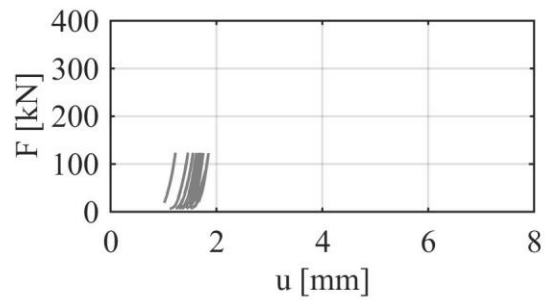
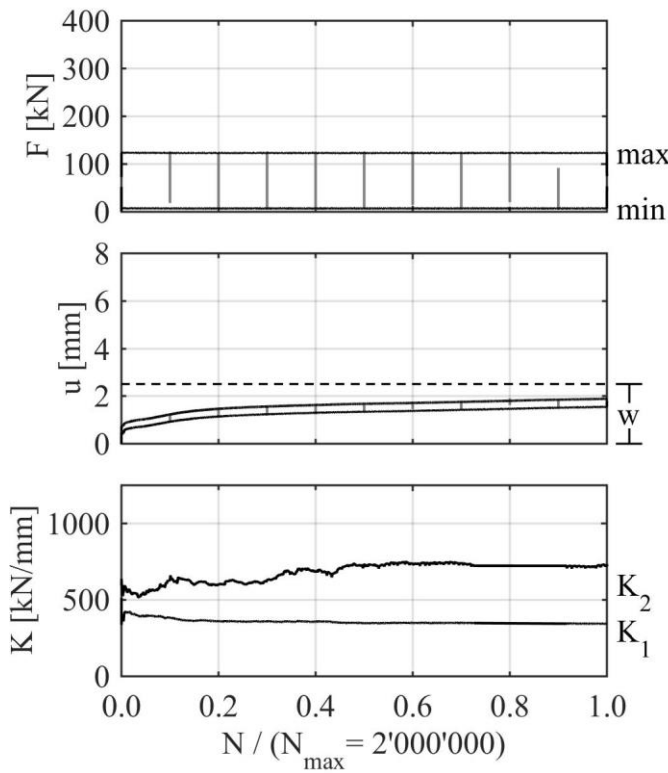
Id: 123 **Geom: 1** **Mat: Densit Ducorit S2**

AC: wet $F_{max} = 20 \% F_{ULS}$ $f = 5 \text{ Hz}$



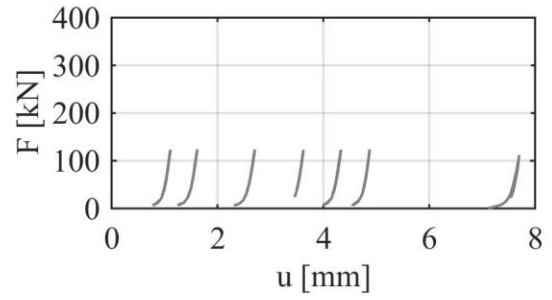
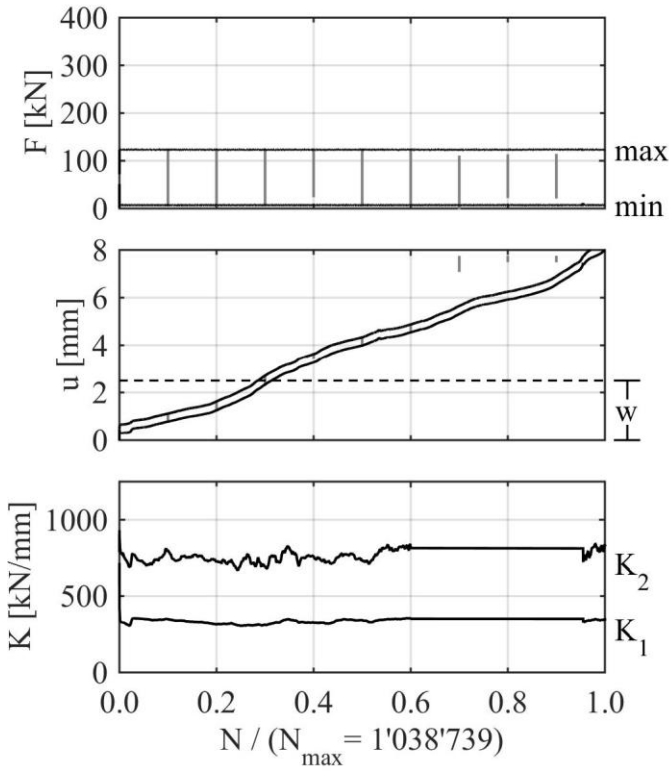
Id: 124 **Geom: 1** **Mat: Densit Ducorit S2**

AC: wet $F_{max} = 20 \% F_{ULS}$ $f = 5 \text{ Hz}$



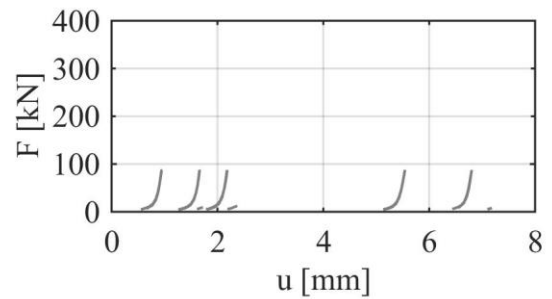
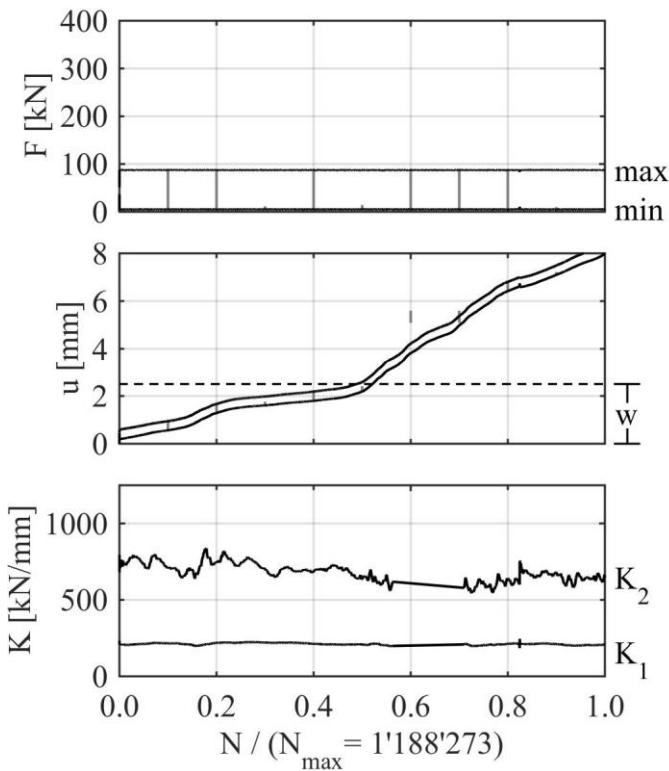
Id: 125 **Geom: 1** **Mat: Densit Ducorit S2**

AC: wet $F_{max} = 20\% F_{ULS}$ $f = 5\text{ Hz}$



Id: 126 **Geom: 1** **Mat: Densit Ducorit S2**

AC: wet $F_{max} = 20\% F_{ULS}$ $f = 5\text{ Hz}$

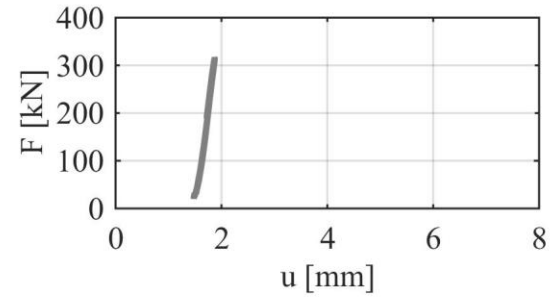
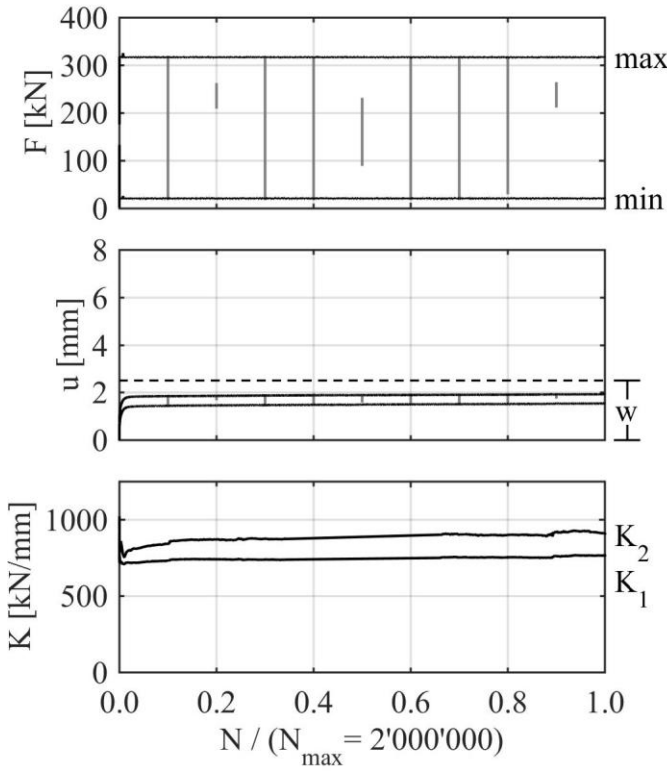


A.3 FLS results – Geometry 1, BASF Masterflow 9500

Id	Geom.	Material	Test procedure						Batch	Dates		
			F_{ULS} [kN]	AC	F_{max}/F_{ULS} [-]	f [Hz]	N [-]	Term. Crit.		Grouting	Testing	Age [d]
F127	1	BASF Masterflow 9500	737	dry	0.5	5.0	2000000	runner	BM3	14.10.2014	17.11.2014	34
F128	1	BASF Masterflow 9500	737	dry	0.5	5.0	2000000	runner	BM3	14.10.2014	24.11.2014	41
F129	1	BASF Masterflow 9500	737	dry	0.5	5.0	2000000	runner	BM3	14.10.2014	01.12.2014	48
F130	1	BASF Masterflow 9500	585	wet	0.5	5.0	30700	Δu	BM1	13.02.2013	09.04.2013	57
F131	1	BASF Masterflow 9500	585	wet	0.5	5.0	41300	Δu	BM1	13.02.2013	30.05.2013	108
F132	1	BASF Masterflow 9500	585	wet	0.5	5.0	39837	Δu	BM1	13.02.2013	22.08.2013	190
F133	1	BASF Masterflow 9500	585	wet	0.5	1.0	112150	Δu	BM1	13.02.2013	28.05.2013	106
F134	1	BASF Masterflow 9500	585	wet	0.5	1.0	41800	Δu	BM1	13.02.2013	29.08.2013	197
F135	1	BASF Masterflow 9500	585	wet	0.5	1.0	132923	Δu	BM1	13.02.2013	17.04.2013	65
F136	1	BASF Masterflow 9500	585	wet	0.2	5.0	1190005	u_{max}	BM1	13.02.2013	10.04.2013	58
F137	1	BASF Masterflow 9500	585	wet	0.2	5.0	887510	u_{max}	BM1	13.02.2013	03.06.2013	111
F138	1	BASF Masterflow 9500	585	wet	0.2	5.0	1277251	u_{max}	BM1	13.02.2013	23.08.2013	191
F139	1	BASF Masterflow 9500	585	wet	0.2	1.0	2000000	runner	BM1	13.02.2013	30.04.2013	78
F140	1	BASF Masterflow 9500	585	wet	0.2	1.0	1325875	u_{max}	BM1	13.02.2013	15.03.2013	33
F141	1	BASF Masterflow 9500	585	wet	0.2	1.0	2000000	runner	BM1	13.02.2013	03.07.2013	141

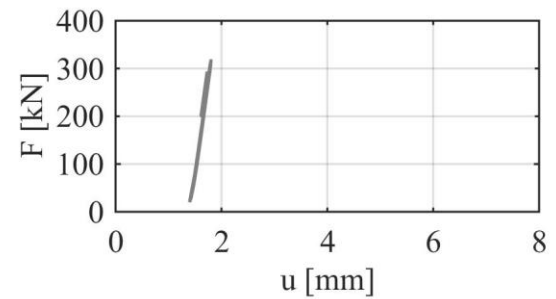
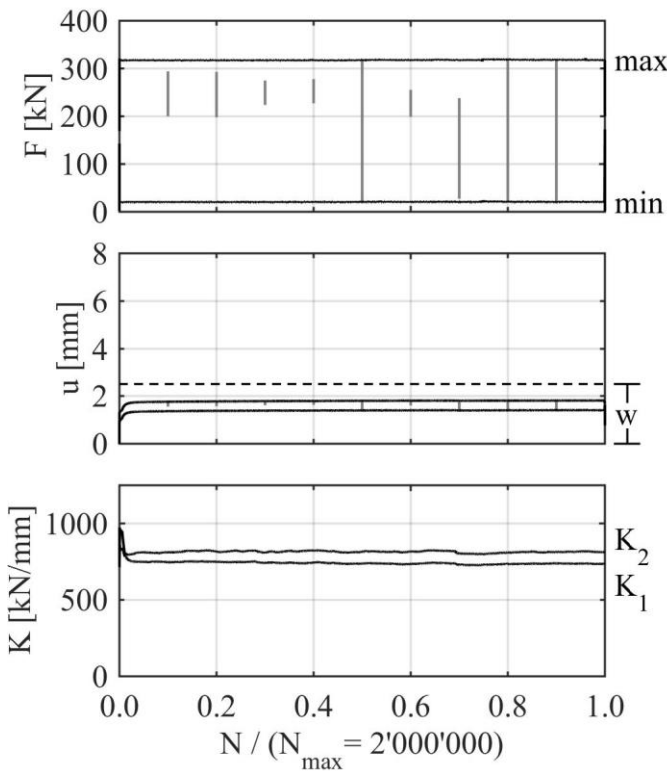
Id: 127 Geom: 1 Mat: BASF Masterflow 9500

AC: dry $F_{max} = 50 \% F_{ULS}$ $f = 5 \text{ Hz}$



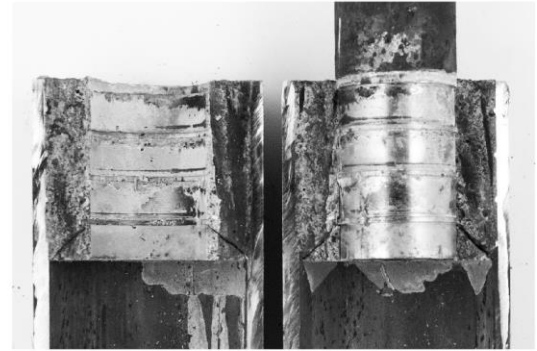
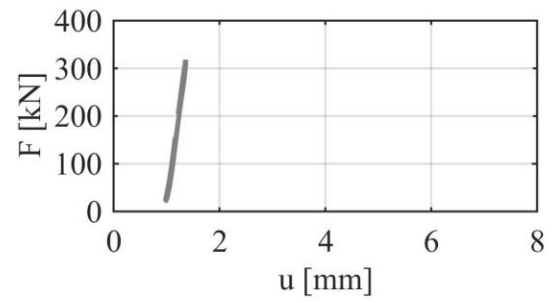
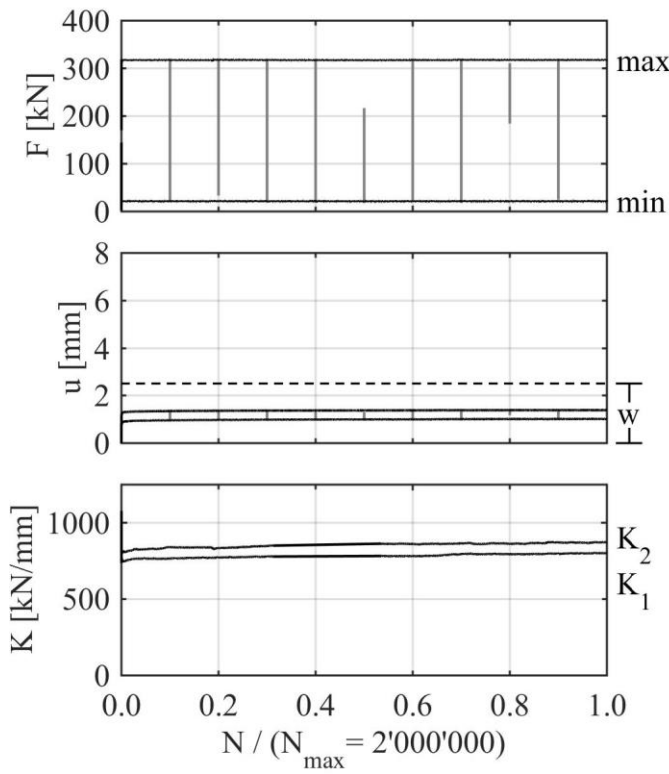
Id: 128 Geom: 1 Mat: BASF Masterflow 9500

AC: dry $F_{max} = 50 \% F_{ULS}$ $f = 5 \text{ Hz}$



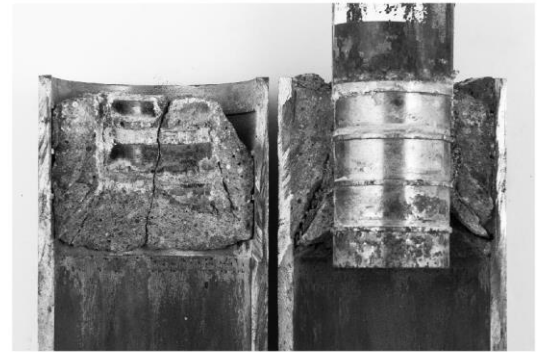
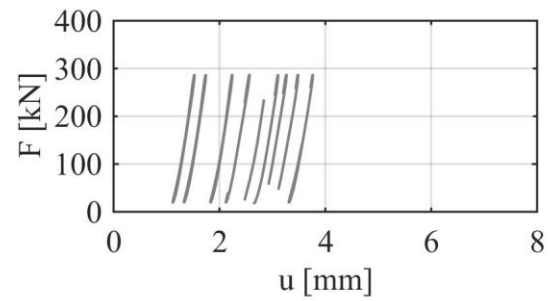
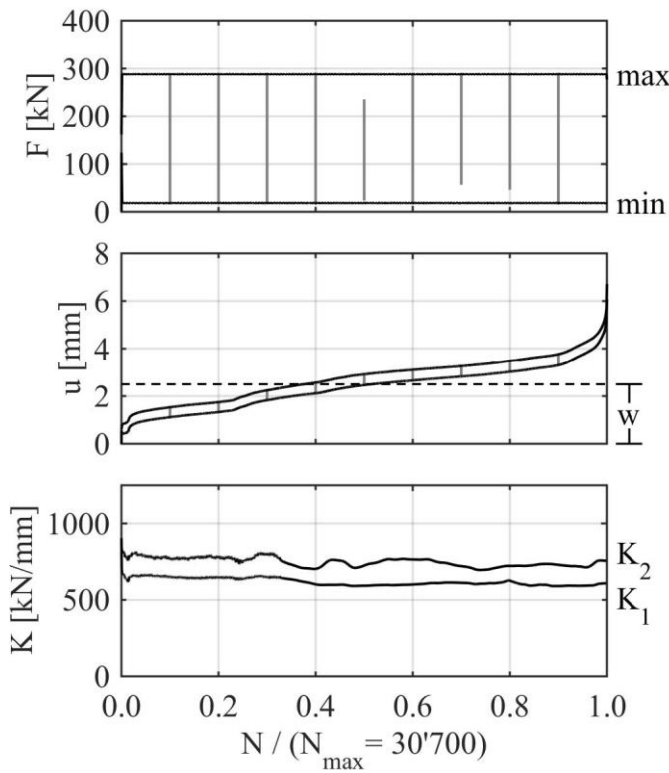
Id: 129 **Geom: 1** **Mat: BASF Masterflow 9500**

AC: dry $F_{max} = 50 \% F_{ULS}$ $f = 5 \text{ Hz}$



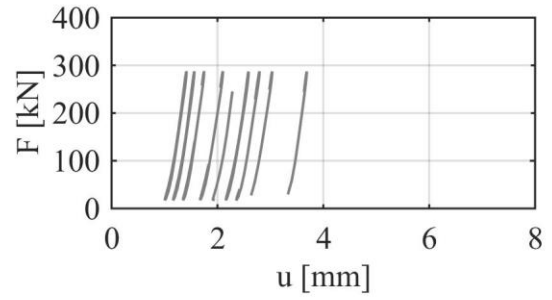
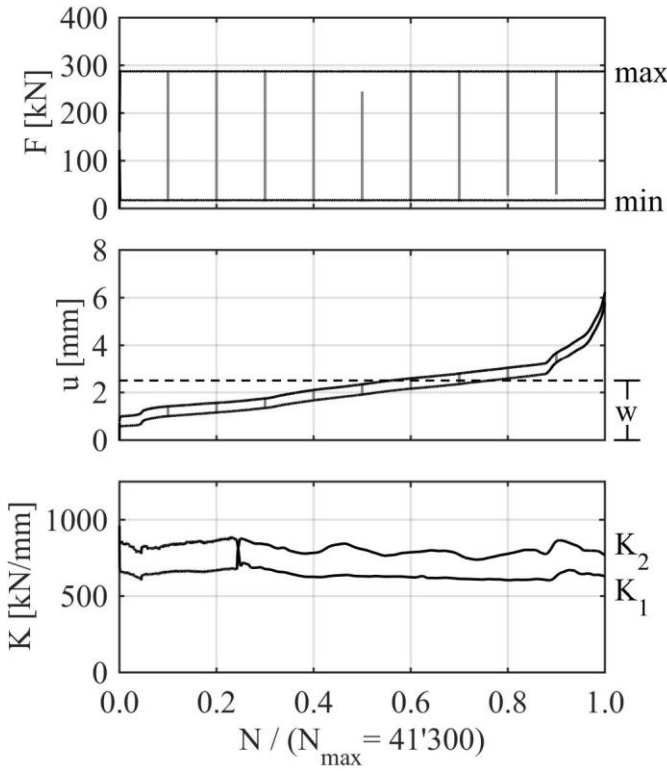
Id: 130 **Geom: 1** **Mat: BASF Masterflow 9500**

AC: wet $F_{max} = 50 \% F_{ULS}$ $f = 5 \text{ Hz}$



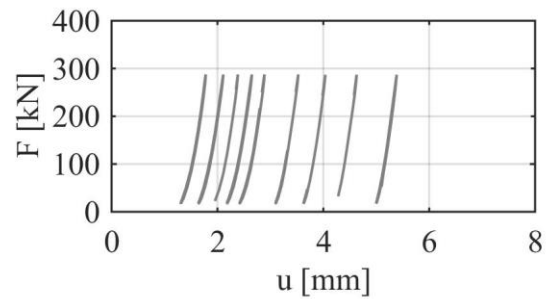
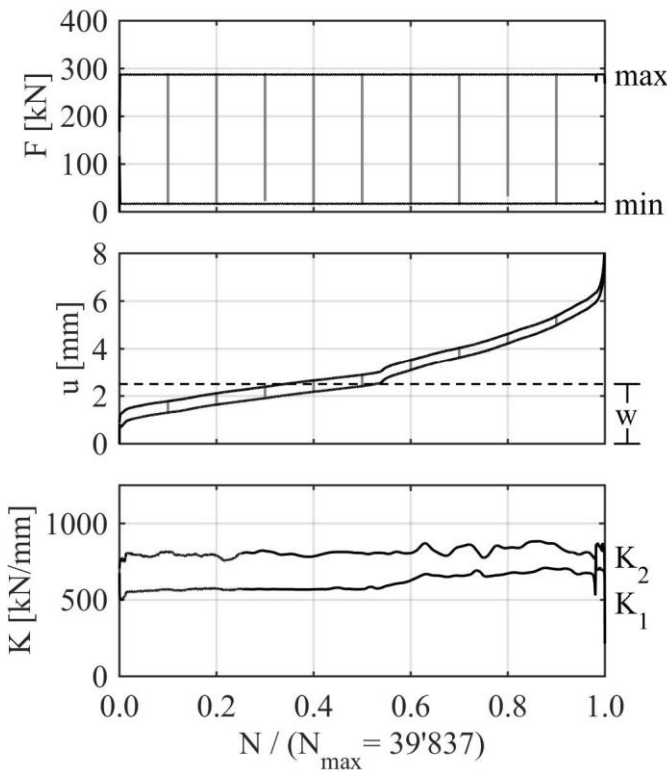
Id: 131 Geom: 1 Mat: BASF Masterflow 9500

AC: wet $F_{max} = 50 \% F_{ULS}$ $f = 5 \text{ Hz}$



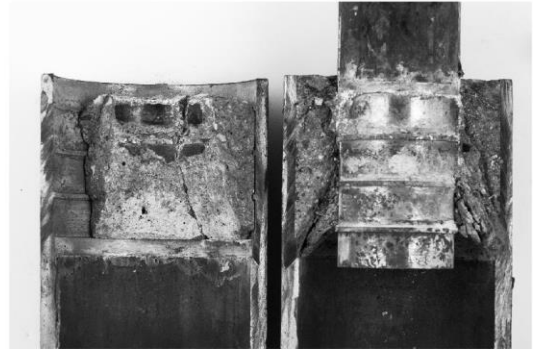
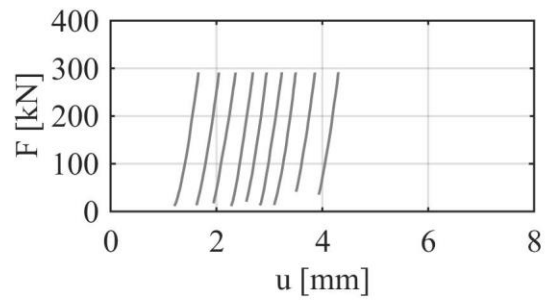
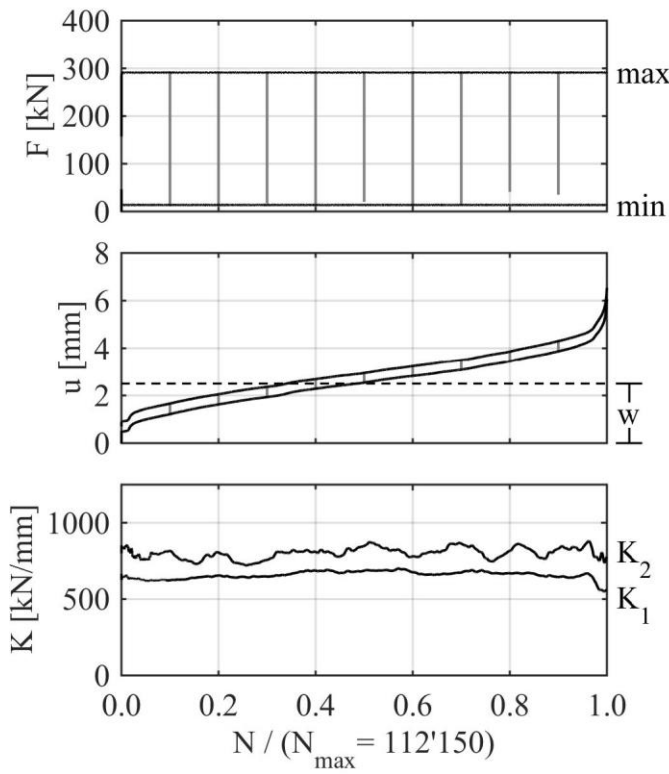
Id: 132 Geom: 1 Mat: BASF Masterflow 9500

AC: wet $F_{max} = 50 \% F_{ULS}$ $f = 5 \text{ Hz}$



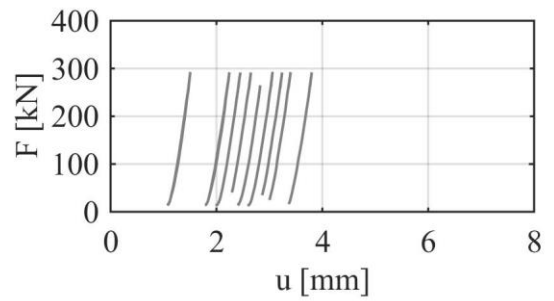
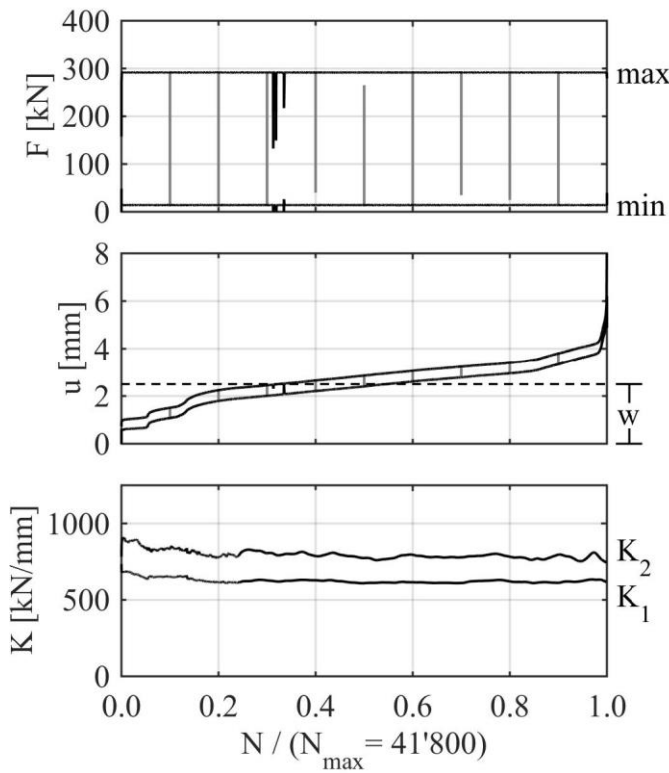
Id: 133 **Geom: 1** **Mat: BASF Masterflow 9500**

AC: wet $F_{max} = 50 \% F_{ULS}$ $f = 1 \text{ Hz}$



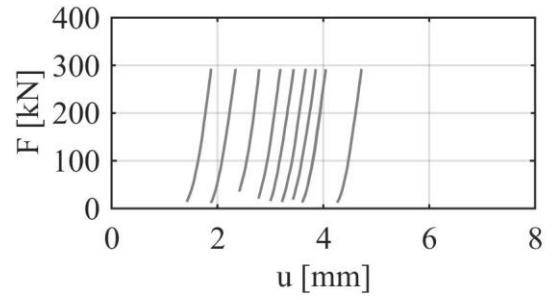
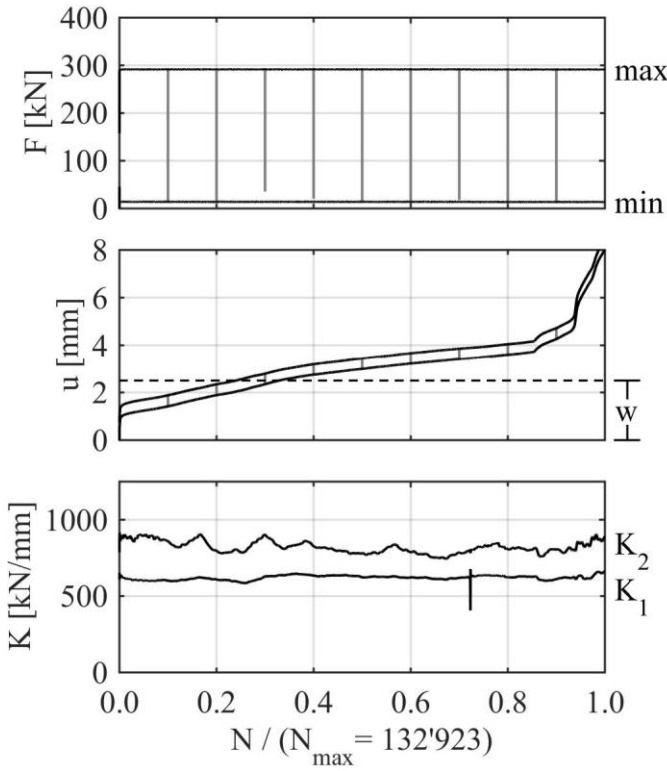
Id: 134 **Geom: 1** **Mat: BASF Masterflow 9500**

AC: wet $F_{max} = 50 \% F_{ULS}$ $f = 1 \text{ Hz}$



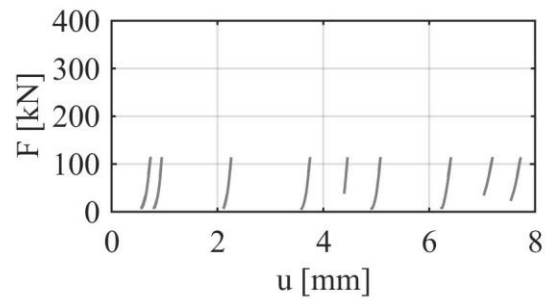
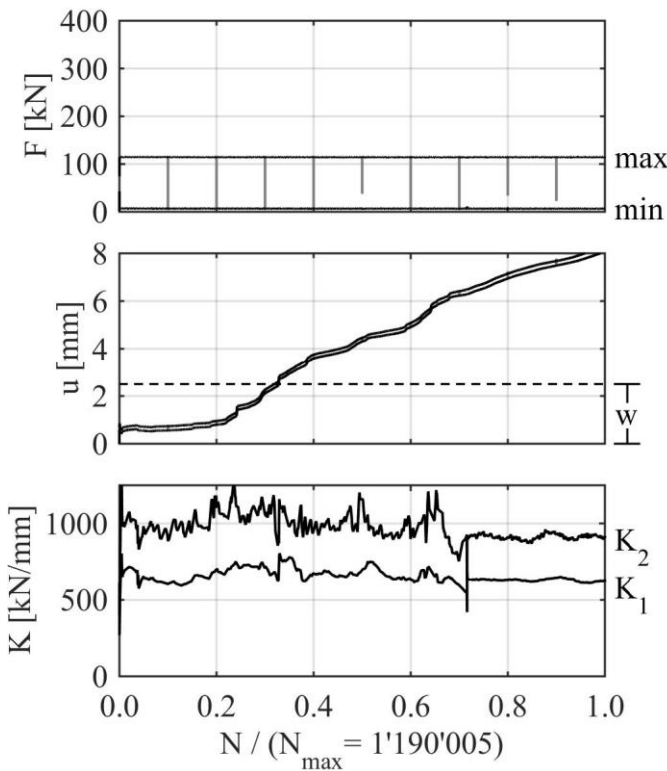
Id: 135 Geom: 1 Mat: BASF Masterflow 9500

AC: wet $F_{max} = 50 \% F_{ULS}$ $f = 1 \text{ Hz}$



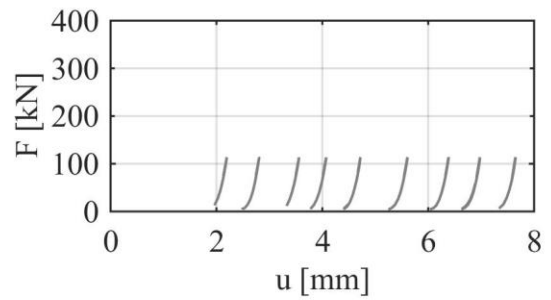
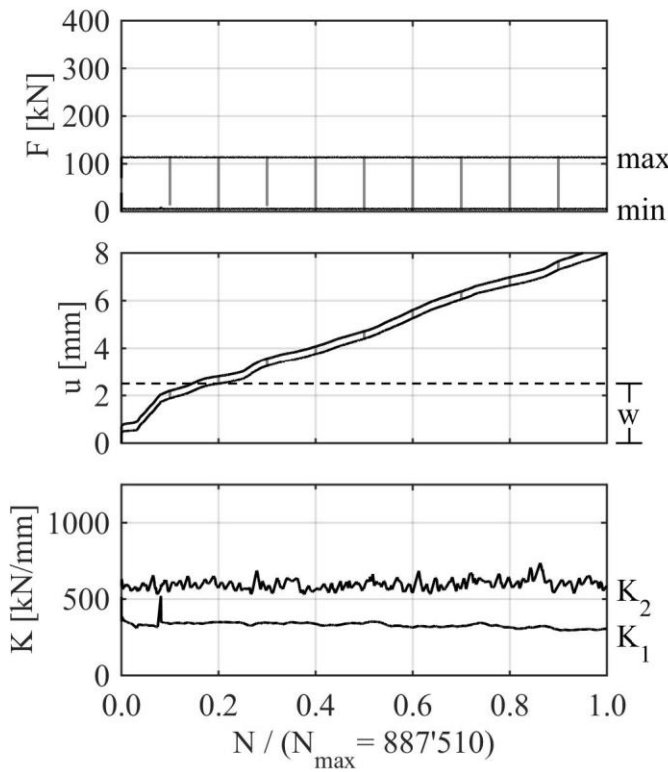
Id: 136 Geom: 1 Mat: BASF Masterflow 9500

AC: wet $F_{max} = 20 \% F_{ULS}$ $f = 5 \text{ Hz}$



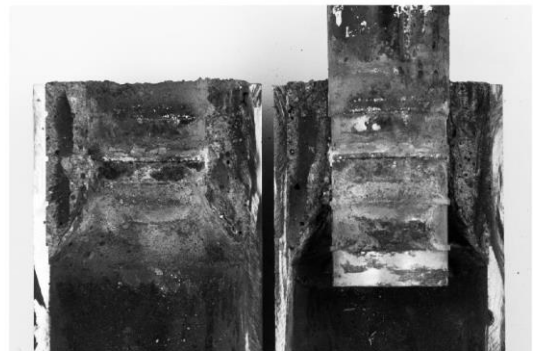
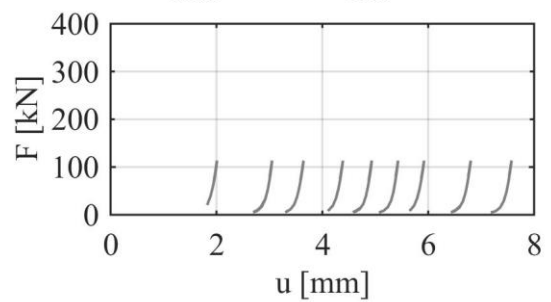
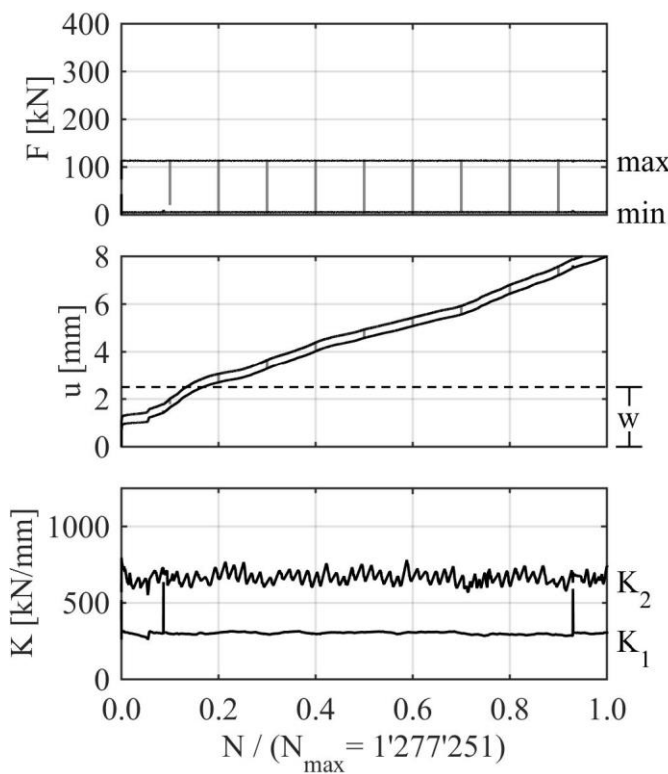
Id: 137 Geom: 1 Mat: BASF Masterflow 9500

AC: wet $F_{max} = 20 \% F_{ULS}$ $f = 5 \text{ Hz}$



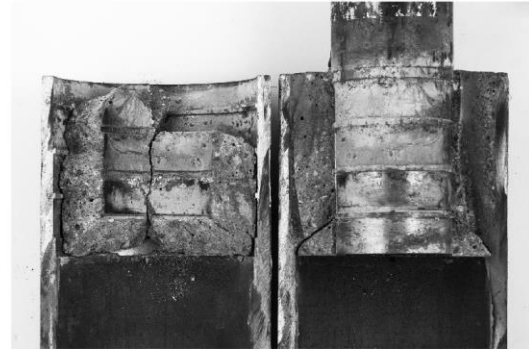
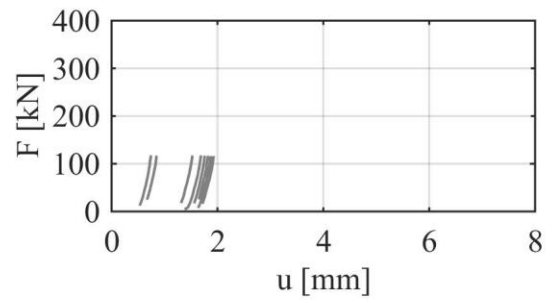
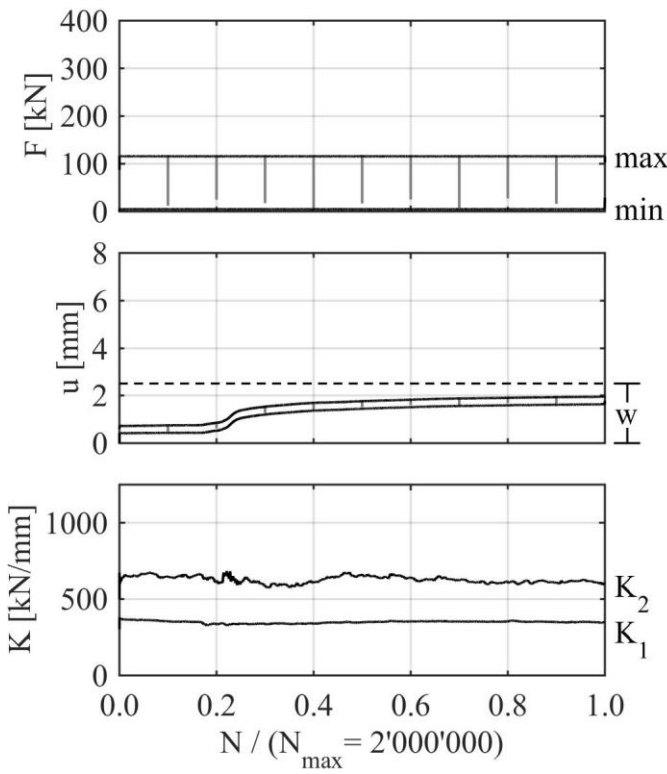
Id: 138 Geom: 1 Mat: BASF Masterflow 9500

AC: wet $F_{max} = 20 \% F_{ULS}$ $f = 5 \text{ Hz}$



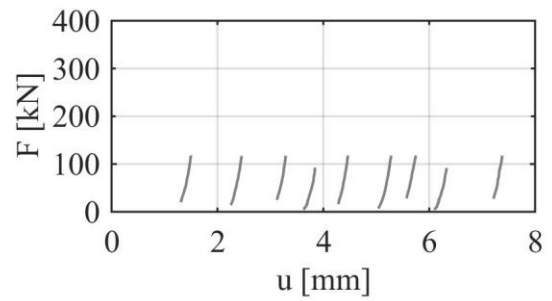
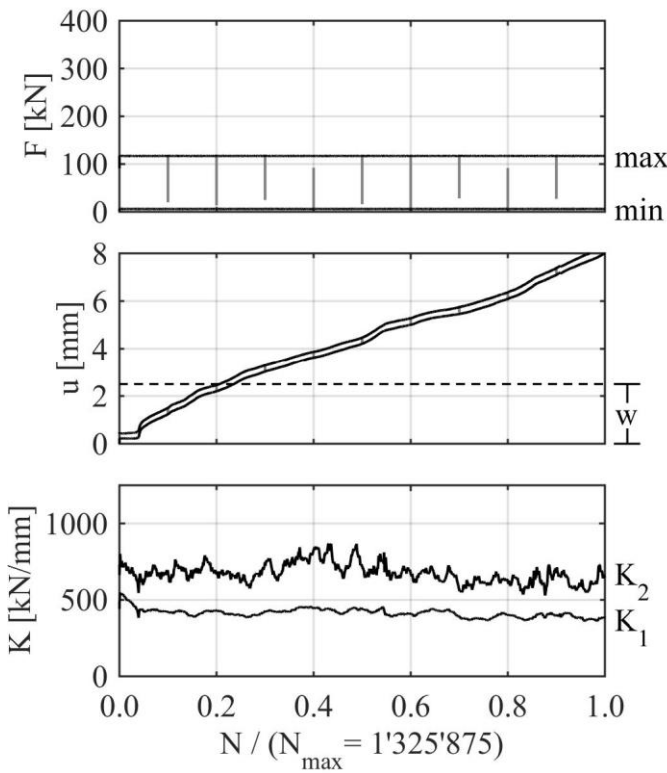
Id: 139 Geom: 1 Mat: BASF Masterflow 9500

AC: wet $F_{max} = 20\% F_{ULS}$ $f = 1$ Hz



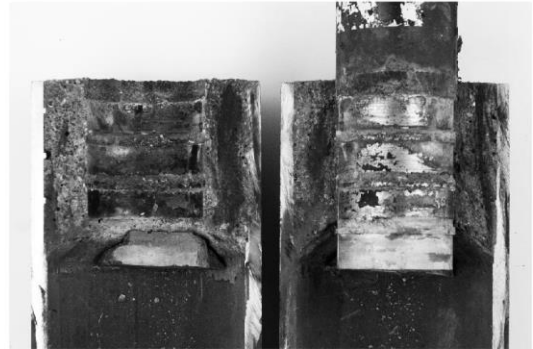
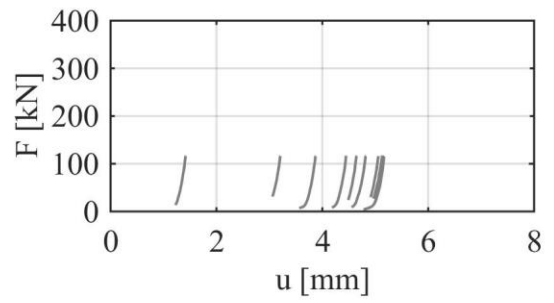
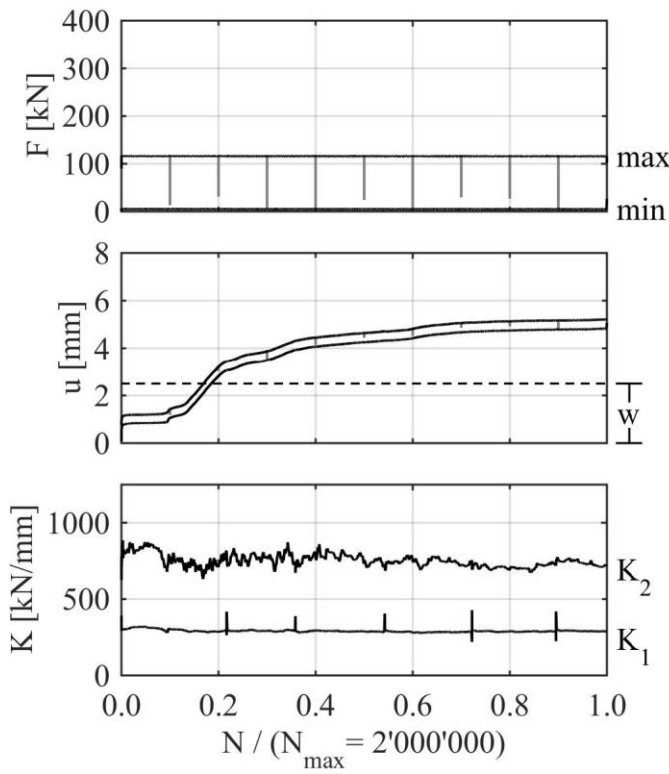
Id: 140 Geom: 1 Mat: BASF Masterflow 9500

AC: wet $F_{max} = 20\% F_{ULS}$ $f = 1$ Hz



Id: 141 **Geom: 1** **Mat: BASF Masterflow 9500**

AC: wet $F_{\max} = 20\% F_{\text{ULS}}$ $f = 1 \text{ Hz}$

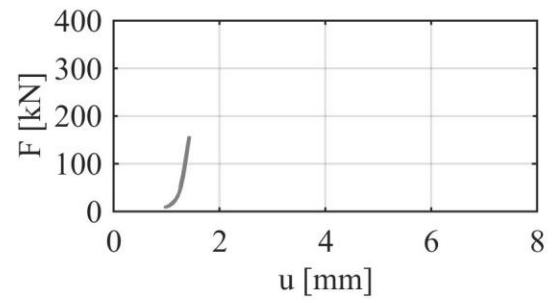
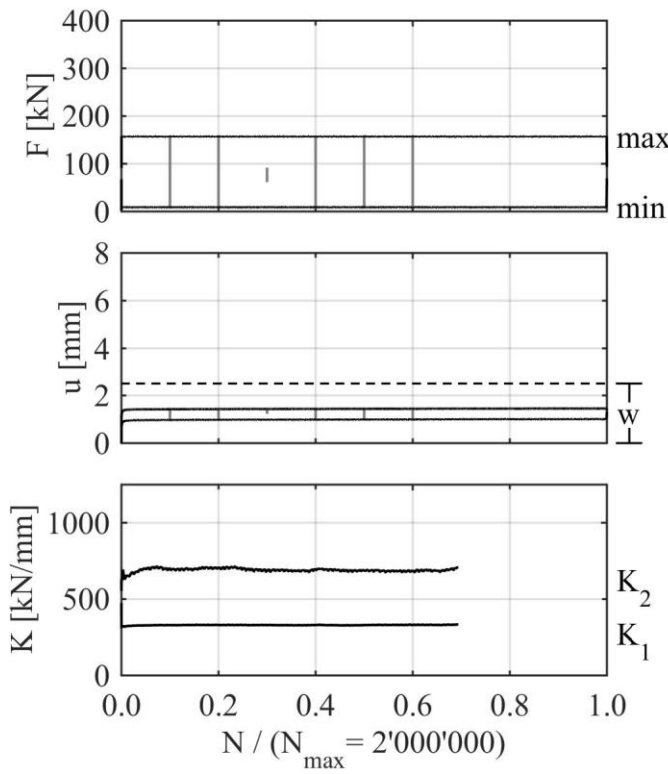


A.4 FLS results – Geometry 2, Densit Ducorit S2

Id	Geom.	Material	Test procedure							Batch	Dates		
			F_{ULS} [kN]	AC	F_{max}/F_{ULS} [-]	f [Hz]	N [-]	Term. Crit.	Grouting		Testing	Age [d]	
F201	2	Densit Ducorit S2	322	dry	0.5	5.0	2000000	runner	DD3	03.07.2014	11.08.2014	39	
F202	2	Densit Ducorit S2	322	dry	0.5	5.0	2000000	runner	DD3	03.07.2014	04.08.2014	32	
F203	2	Densit Ducorit S2	322	wet	0.5	5.0	24393	Δu	DD3	03.07.2014	19.08.2014	47	
F204	2	Densit Ducorit S2	322	wet	0.5	5.0	21743	Δu	DD3	03.07.2014	18.08.2014	46	

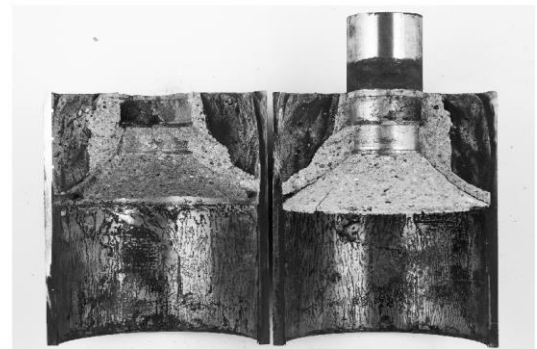
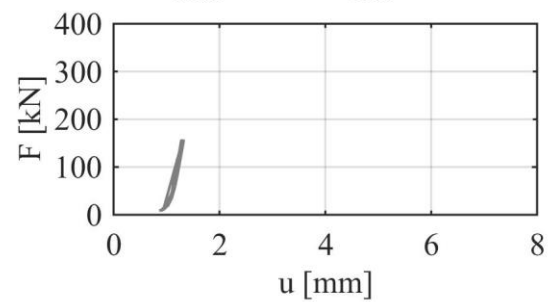
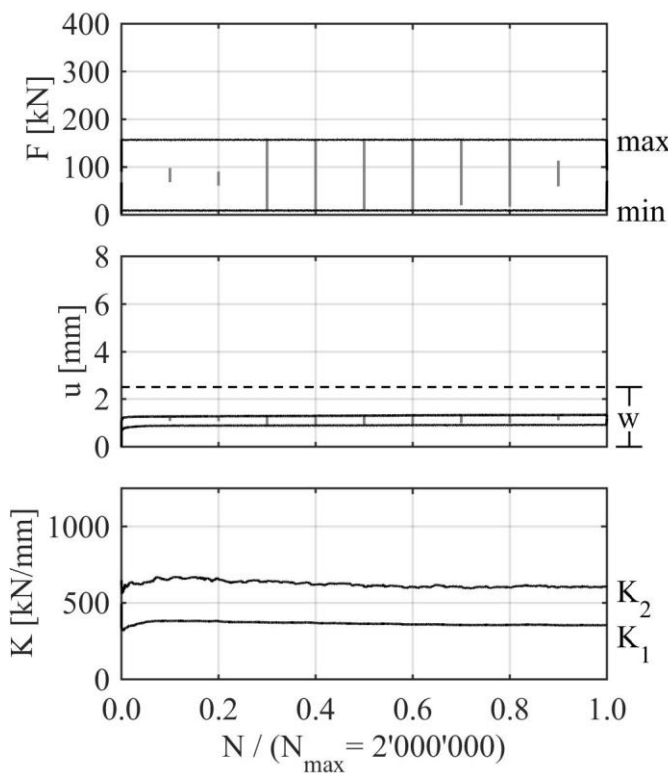
Id: 201 **Geom: 2** **Mat: Densit Ducorit S2**

AC: dry $F_{max} = 50 \% F_{ULS}$ $f = 5 \text{ Hz}$



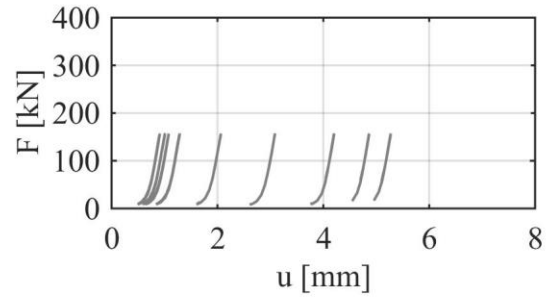
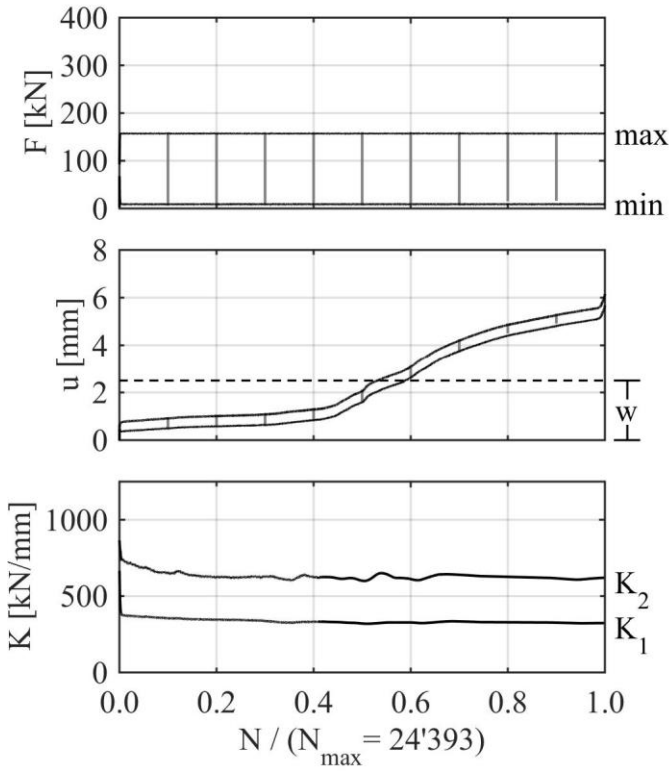
Id: 202 **Geom: 2** **Mat: Densit Ducorit S2**

AC: dry $F_{max} = 50 \% F_{ULS}$ $f = 5 \text{ Hz}$



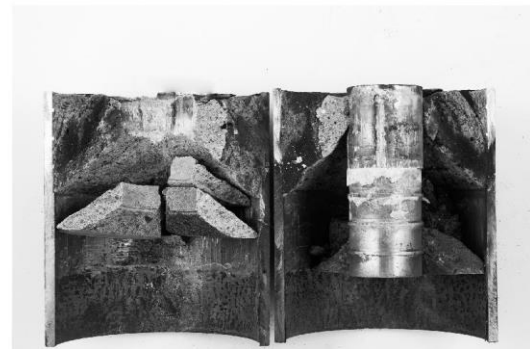
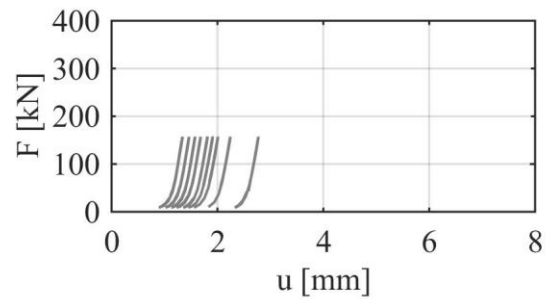
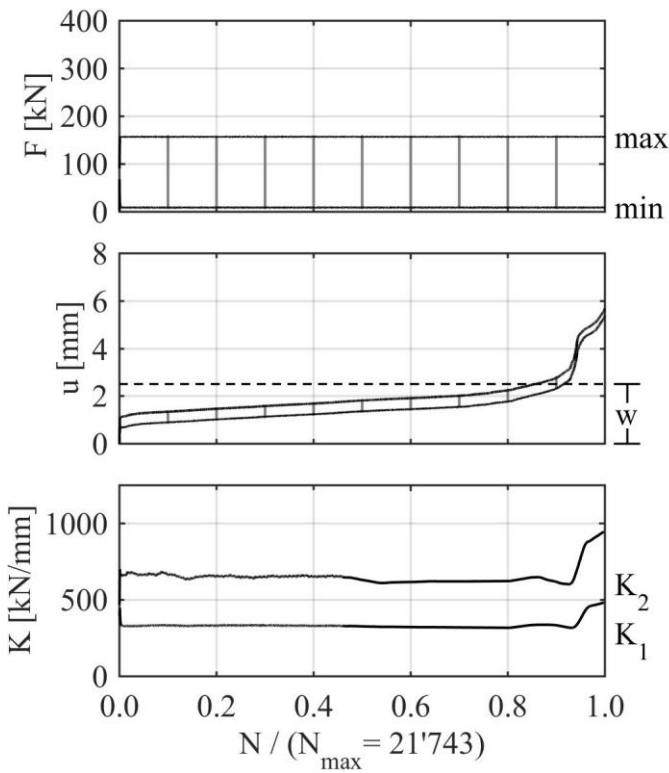
Id: 203 **Geom: 2** **Mat: Densit Ducorit S2**

AC: wet $F_{max} = 50\% F_{ULS}$ $f = 5\text{ Hz}$



Id: 204 **Geom: 2** **Mat: Densit Ducorit S2**

AC: wet $F_{max} = 50\% F_{ULS}$ $f = 5\text{ Hz}$

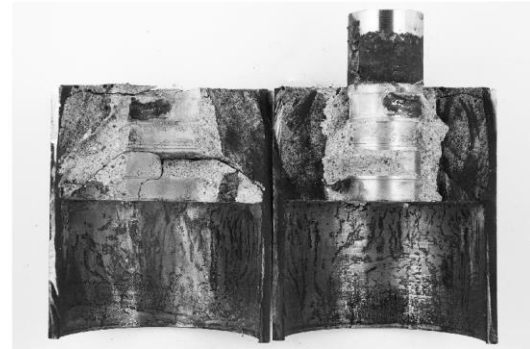
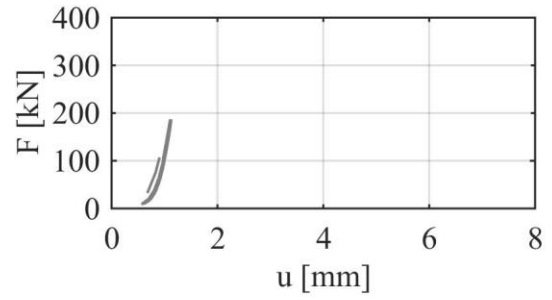
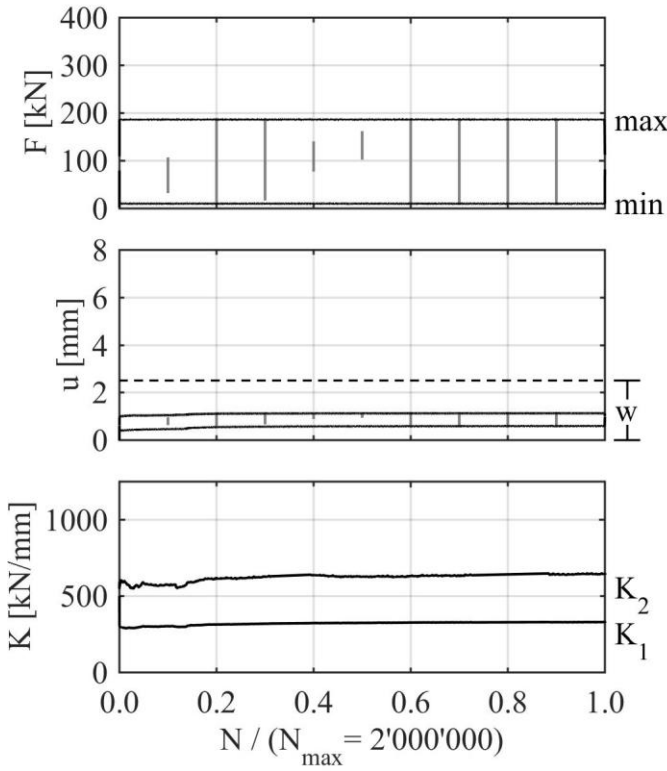


A.5 FLS results – Geometry 2, BASF Masterflow 9500

Id	Geom.	Material	Test procedure						Batch	Dates		
			F _{ULS} [kN]	AC	F _{max} /F _{ULS} [-]	f [Hz]	N [-]	Term. Crit.		Grouting	Testing	Age [d]
F205	2	BASF Masterflow 9500	379	dry	0.5	5.0	2000000	runner	BM3	14.10.2014	10.12.2014	57
F206	2	BASF Masterflow 9500	379	dry	0.5	5.0	348245	Δu	BM3	14.10.2014	08.12.2014	55
F207	2	BASF Masterflow 9500	379	wet	0.5	5.0	5310	Δu	BM3	14.10.2014	14.01.2015	91
F208	2	BASF Masterflow 9500	379	wet	0.5	5.0	5050	Δu	BM3	14.10.2014	14.01.2015	91

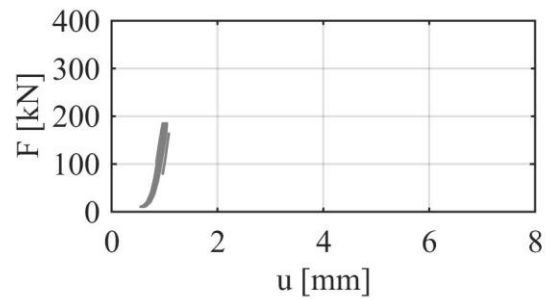
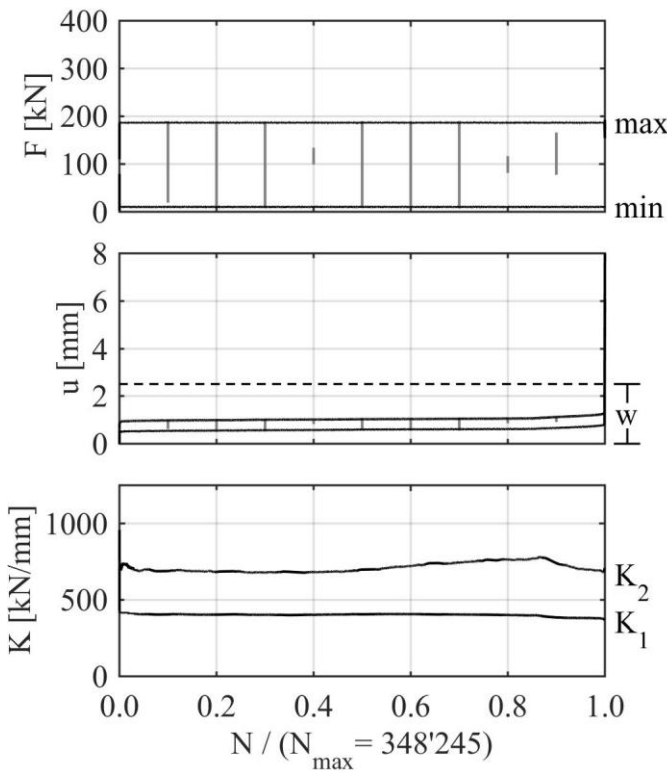
Id: 205 Geom: 2 Mat: BASF Masterflow 9500

AC: dry $F_{max} = 50 \% F_{ULS}$ $f = 5 \text{ Hz}$



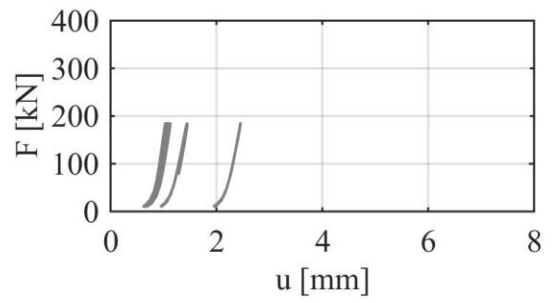
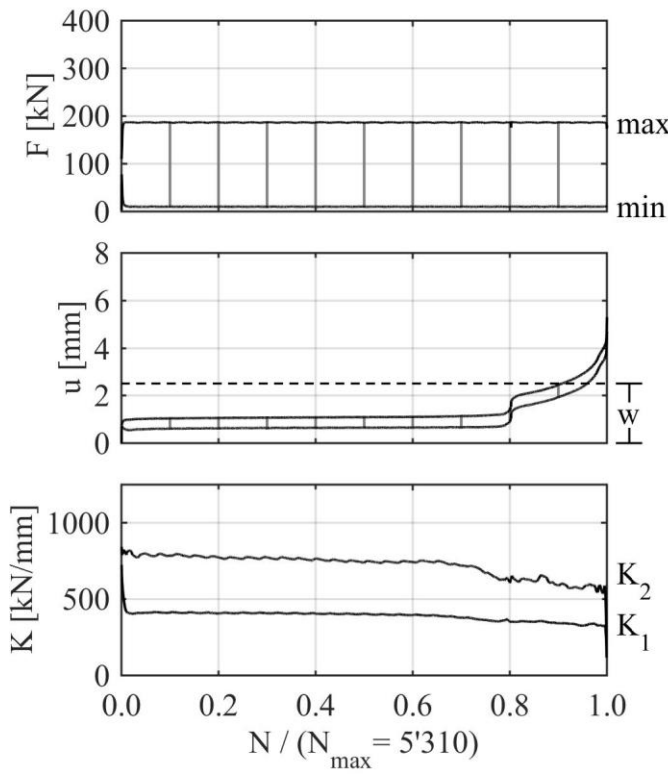
Id: 206 Geom: 2 Mat: BASF Masterflow 9500

AC: dry $F_{max} = 50 \% F_{ULS}$ $f = 5 \text{ Hz}$



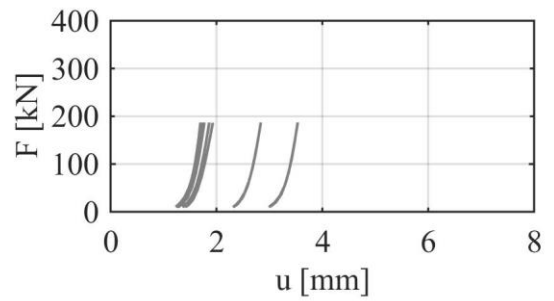
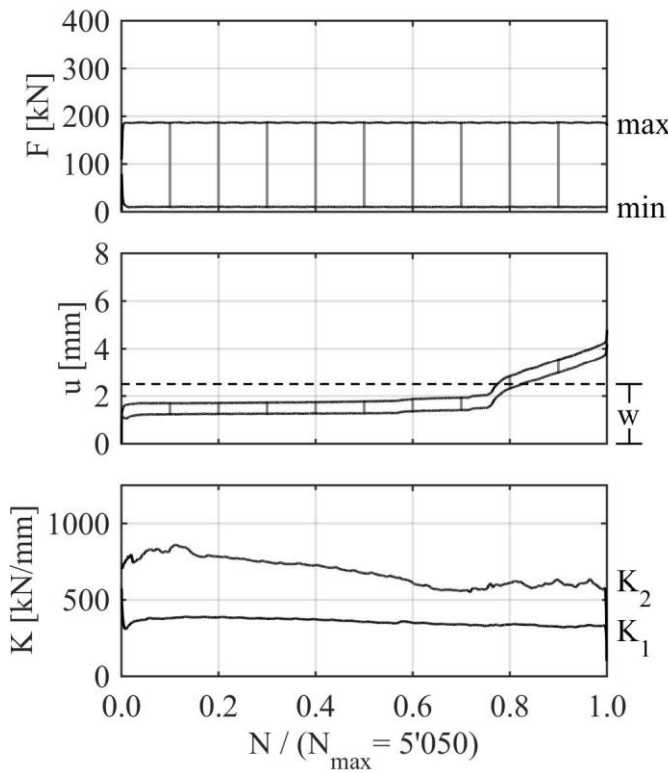
Id: 207 **Geom: 2** **Mat: BASF Masterflow 9500**

AC: wet $F_{max} = 50 \% F_{ULS}$ $f = 5 \text{ Hz}$



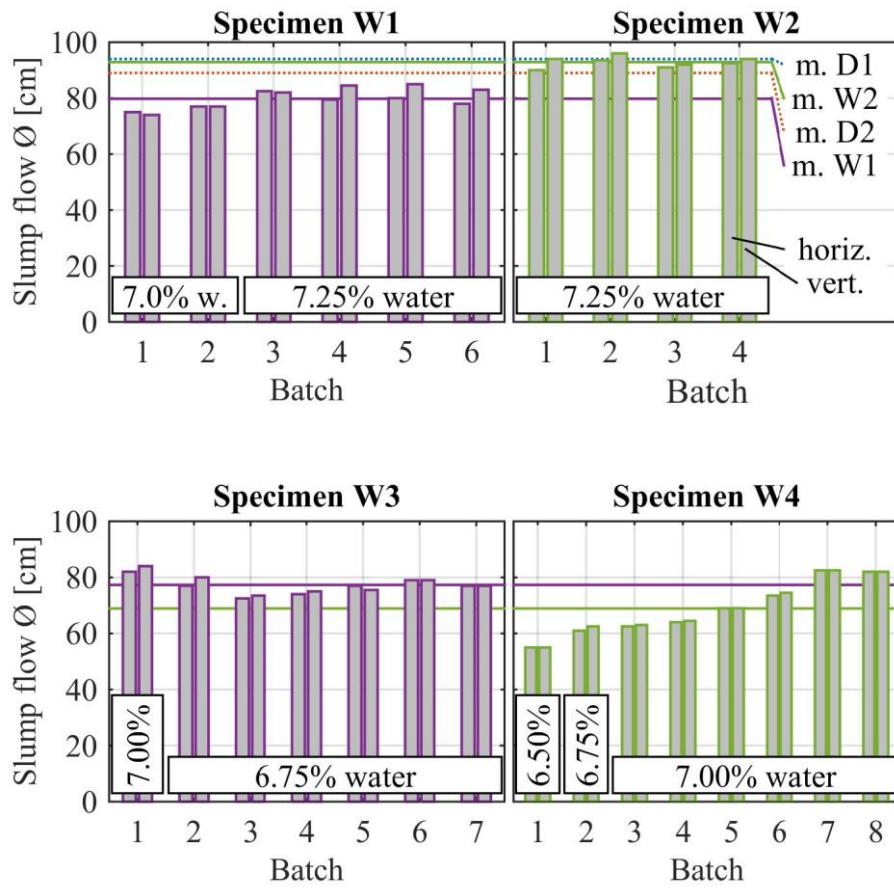
Id: 208 **Geom: 2** **Mat: BASF Masterflow 9500**

AC: wet $F_{max} = 50 \% F_{ULS}$ $f = 5 \text{ Hz}$

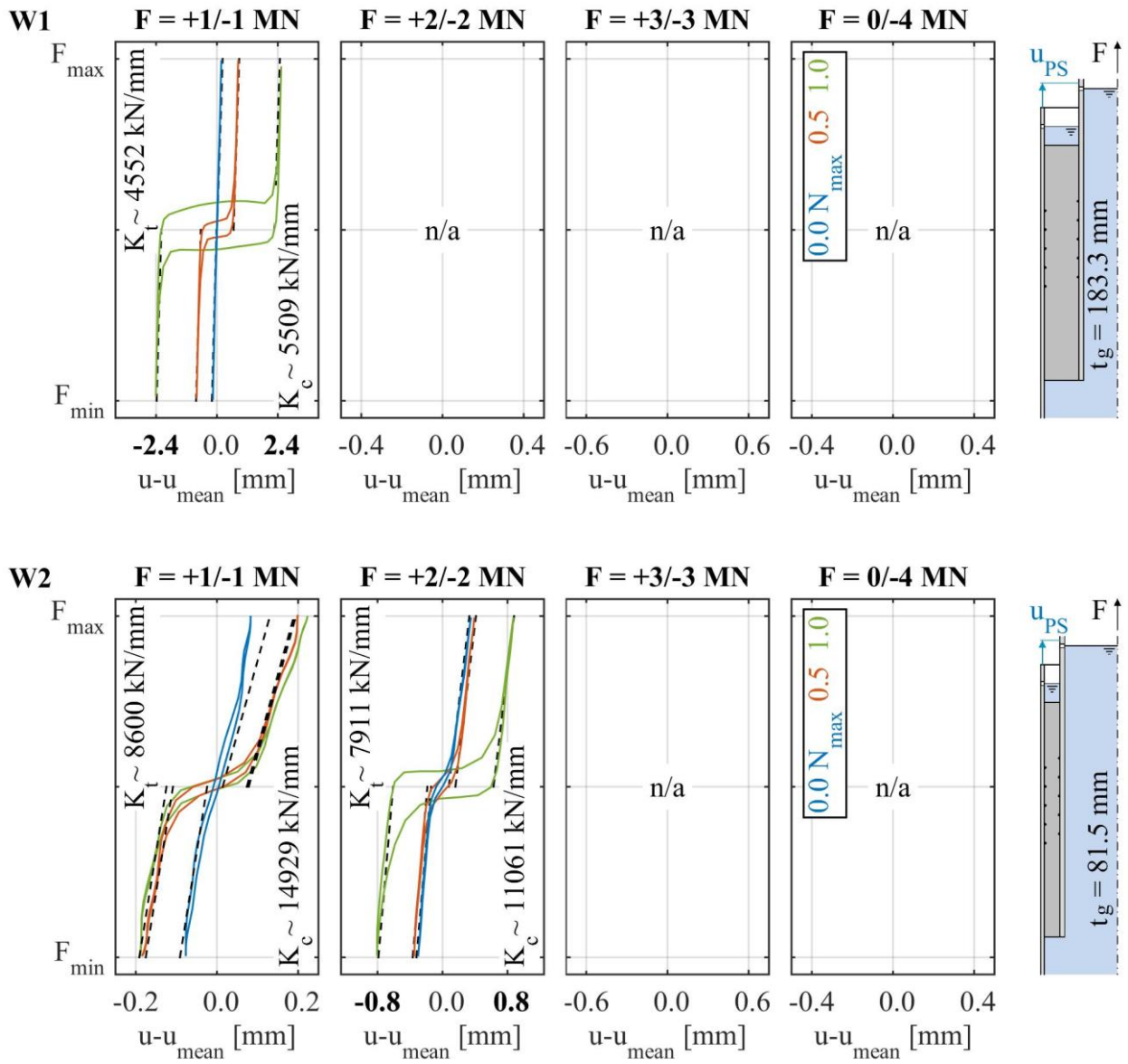


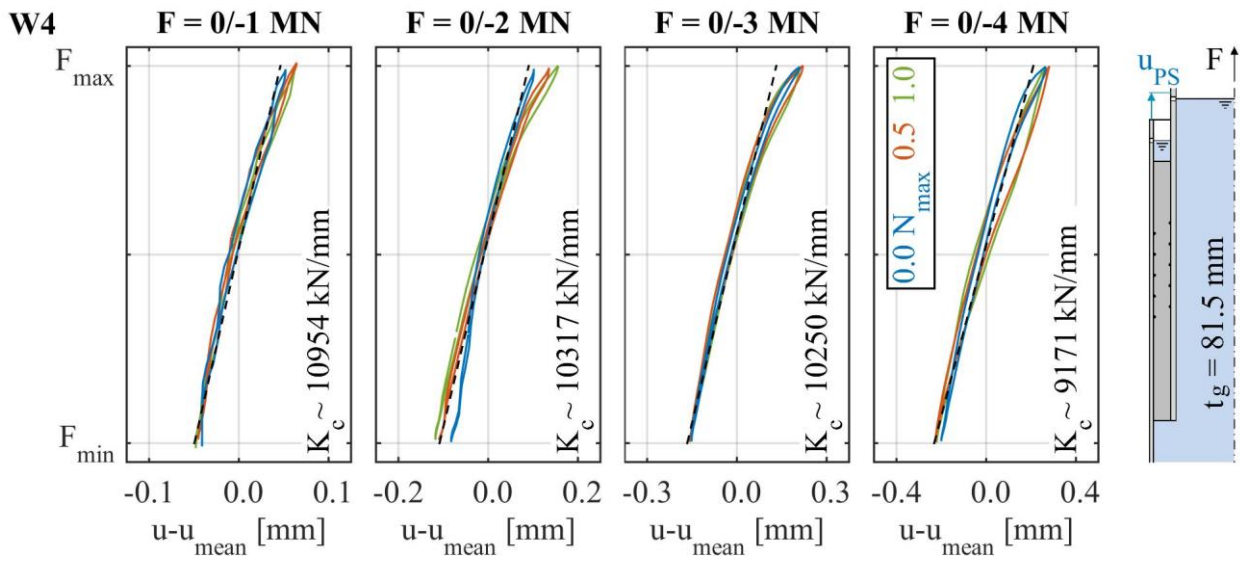
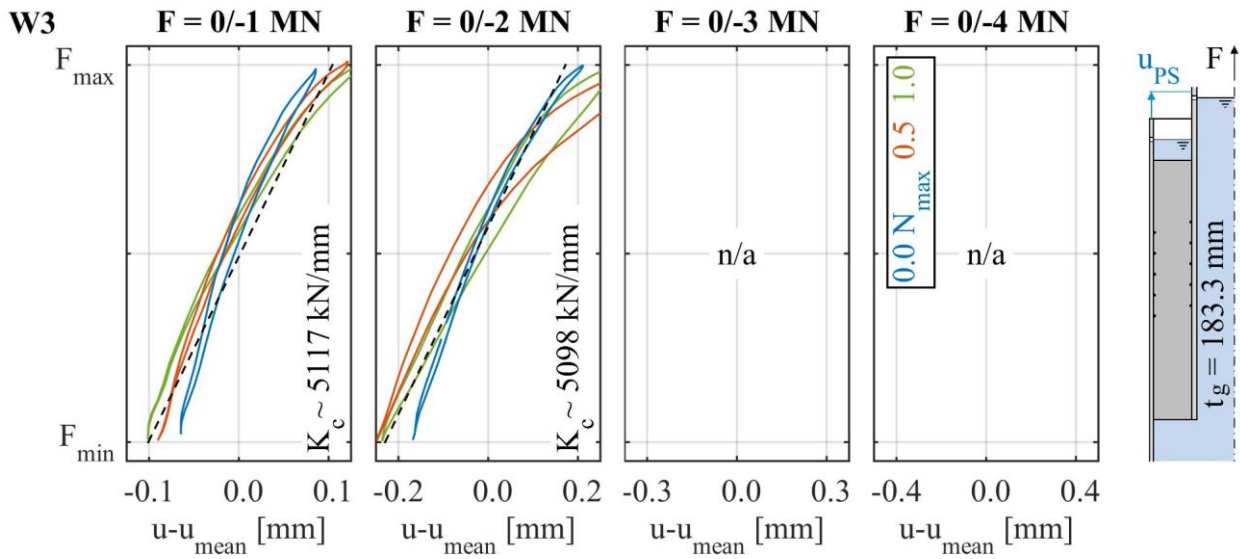
Appendix B – Large-scale test results

B.1 Grout material properties

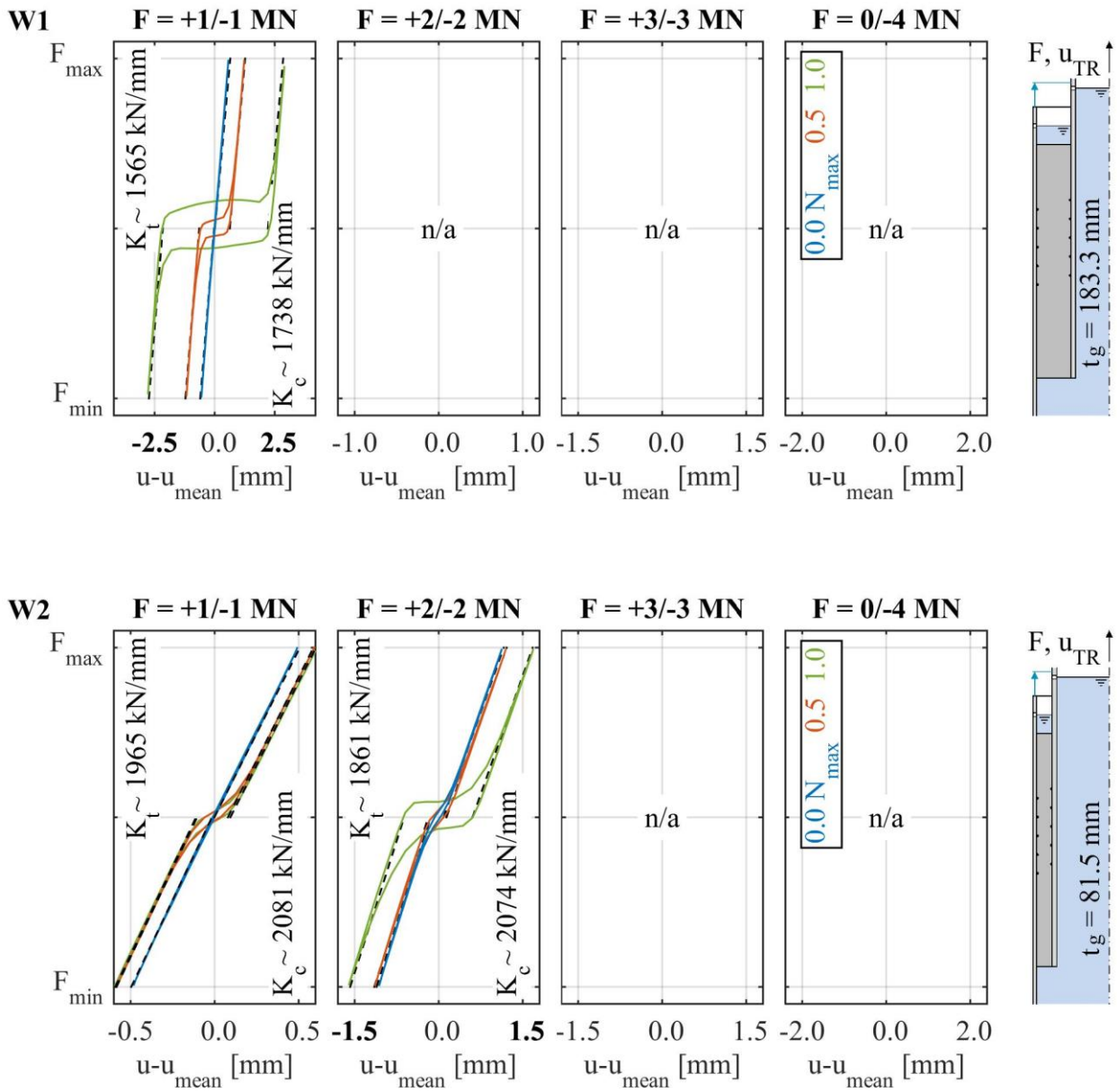


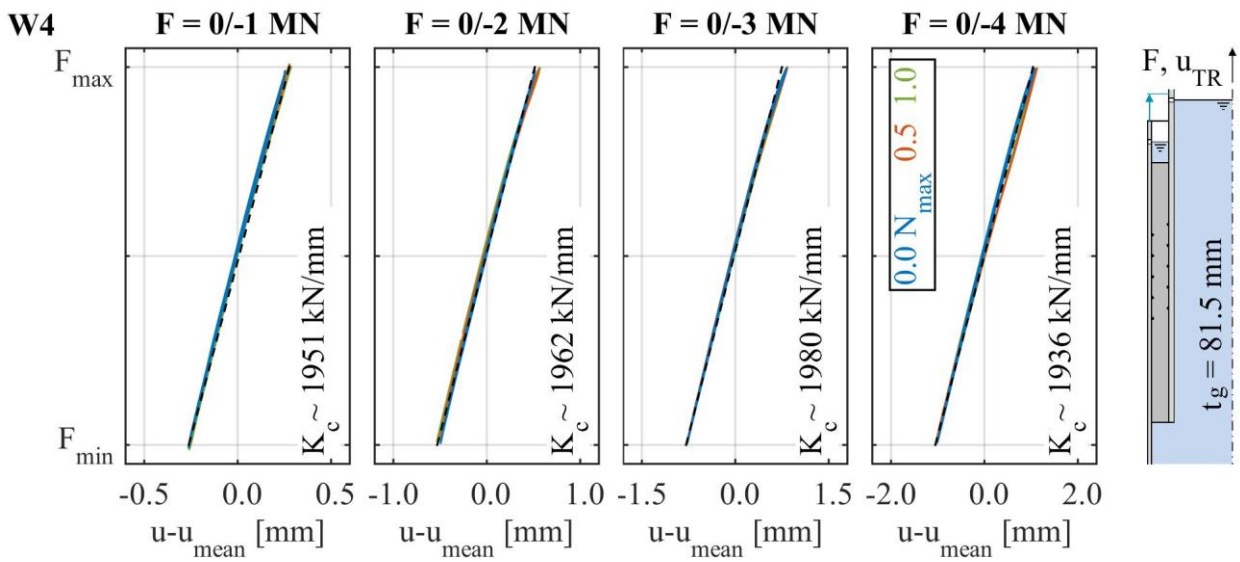
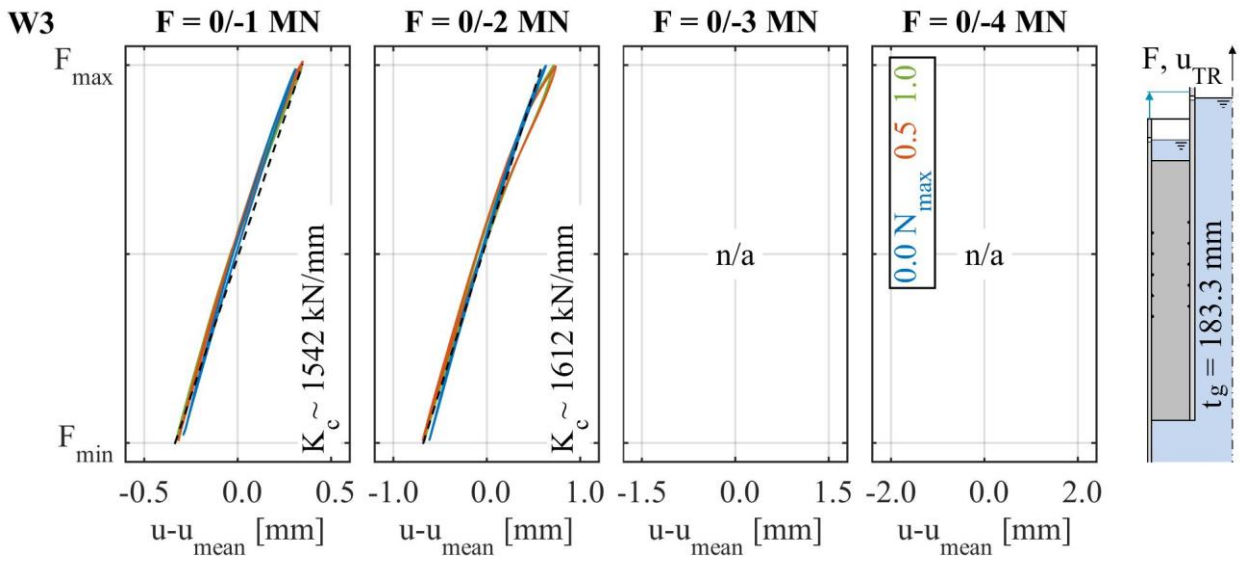
B.2 Hysteresis loops – laser data





B.3 Hysteresis loops – test rig data





Appendix C – Analytical design approaches

Design of axially loaded Grouted Connections

acc. to ISO 19902 (2014), DNVGL-ST-0126 (2016), N-004 (2013), Schaumann et al. (2012)

			Reference geometry		
			pre-piled	post-piled	
Geometry	Tubes	D_p [mm]	884.0	2480.0	
		t_p [mm]	56.0	50.0	
		D_s [mm]	1829.0	3180.0	
		t_s [mm]	50.0	56.0	
		D_g [mm]	1729.0	3068.0	
		t_g [mm]	422.5	294.0	
	Shear keys	h [mm]	10.0	15.0	
		w [mm]	25.0	30.0	
		s [mm]	200.0	300.0	
		N_c [-]	17.0	14.0	
		N_t [-]	17.0	14.0	
	Grout	L_g [mm]	4300.0	5800.0	
		Δl [mm]	845.0	588.0	
		$L_e = L_g - \Delta l$ [mm]	3455.0	5212.0	
	Material	Steel	E_s [N/mm ²]	210000.0	210000.0
f_y [N/mm ²]			355.0	355.0	
Grout		E_g [N/mm ²]	40700.0	50900.0	
		f_{cu} [N/mm ²]	60.0	140.0	
Range of validity	$20 \leq f_{cu} \leq 80$		60.000	140.000 ▼	
	$20 \leq D_p/t_p \leq 60$		15.786 ▲	49.600	
	$30 \leq D_s/t_s \leq 140$		36.580	56.786	
	$10 \leq D_g/t_g \leq 45$		4.092 ▲	10.435	
	$1 \leq L_e/D_p \leq 10$		4.864	2.339	
	$1.5 \leq w/h \leq 3$		2.500	2.000	
	$5 \leq h$		10.000	15.000	
	$h/s \leq 0.1$		0.050	0.050	
	$h/D_p \leq 0.01$		0.011 ▼	0.006	
	$D_p/s \leq 16$		4.420	8.267	
	$1 \leq s/s_{min} \leq [-]$		1.589	1.506	
	$C_p \leq 1.5$		1.013	1.000	
$K \leq 0.02$		0.066 ▼	0.033 ▼		
Ultimate Limit State (ULS)	ISO	$f_{g,sliding}$ [N/mm ²]	10.0	8.3	
		$f_{g,hear}$ [N/mm ²]	5.3 ◀	8.0 ◀	
		$F_{ISO,ULS}$ [MN]	50.5	326.7	
	NORSOK	f_{bks} [N/mm ²]	9.2	7.4 ◀	
		f_{bkg} [N/mm ²]	5.3 ◀	8.0	
		$F_{N,ULS}$ [MN]	50.5	299.7	
	DNVGL	$f_{g,sliding}$ [N/mm ²]	9.2	7.4 ◀	
		$f_{g,hear}$ [N/mm ²]	5.3 ◀	8.0	
		$F_{DNV,ULS,c}$ [MN]	49.7	241.5	
			$F_{DNV,ULS,t}$ [MN]	49.7	241.5
	Schaumann	σ_{lat} [N/mm ²]	19.4	12.5	
		κ [-]	3	3	
		f_{cc} [N/mm ²]	118.2	177.5	
		F_K [MN]	3.3	20.9	
		α [-]	45	45	
μ [-]		0.4	0.4		
F_N [MN]		5.4	33.0		
$F_{tot,c}$ [MN]		137.2	697.9		
$F_{tot,t}$ [MN]		137.2	697.9		
FLS	ISO	$f_{g,sliding}$ [N/mm ²]	1.4 ◀	1.1 ◀	
		$f_{g,hear}$ [N/mm ²]	5.8	8.9	
		$F_{ISO,FLS}$ [MN]	13.1	45.9	

Design of axially loaded Grouted Connections

acc. to ISO 19902 (2014), DNVGL-ST-0126 (2016), N-004 (2013), Schaumann et al. (2012)

			Small-scale geometry 1		Small-scale geometry 2	
			DDS2	BM95	DDS2	BM95
Geometry	Tubes	D_p [mm]	57.50	57.50	57.50	57.50
		t_p [mm]	8.25	8.25	8.25	8.25
		D_s [mm]	114.30	114.30	177.80	177.80
		t_s [mm]	5.90	5.90	5.90	5.90
		D_g [mm]	102.50	102.50	166.00	166.00
		t_g [mm]	22.50	22.50	54.25	54.25
	Shear keys	h [mm]	1.25	1.25	1.25	1.25
		w [mm]	2.50	2.50	2.50	2.50
		s [mm]	22.50	22.50	22.50	22.50
		N_c [-]	3.00	3.00	2.00	2.00
		N_t [-]	2.00	2.00	1.00	1.00
	Grout	L_g [mm]	90.00	90.00	90.00	90.00
		Δl [mm]	0.00	0.00	0.00	0.00
$L_c = L_g - \Delta l$ [mm]		90.00	90.00	90.00	90.00	
Material	Steel	E_s [N/mm ²]	210000.00	210000.00	210000.00	210000.00
		f_y [N/mm ²]	355.00	355.00	355.00	355.00
	Grout	E_g [N/mm ²]	40000.00	50900.0	40000.00	50900.00
		f_{cu} [N/mm ²]	90.00	140.0	90.00	140.00
Range of validity	$20 \leq f_{cu} \leq 80$ [N/mm ²]	90.000 ▼	140.000 ▼	90.000 ▼	140.000 ▼	
	$20 \leq D_p/t_p \leq 60$ [-]	6.970 ▲	6.970 ▲	6.970 ▲	6.970 ▲	
	$30 \leq D_s/t_s \leq 140$ [-]	19.373 ▲	19.373 ▲	30.136	30.136	
	$10 \leq D_g/t_g \leq 45$ [-]	4.556 ▲	4.556 ▲	3.060 ▲	3.060 ▲	
	$1 \leq L_c/D_p \leq 10$ [-]	1.565	1.565	1.565	1.565	
	$1.5 \leq w/h \leq 3$ [-]	2.000	2.000	2.000	2.000	
	$5 \leq h$ [mm]	1.250	1.250	1.250	1.250	
	$h/s \leq 0.1$ [-]	0.056	0.056	0.056	0.056	
	$h/D_p \leq 0.01$ [-]	0.022 ▼	0.022 ▼	0.022 ▼	0.022 ▼	
	$D_p/s \leq 16$ [-]	2.556	2.556	2.556	2.556	
	$1 \leq s/s_{min}$ [-]	1.826	1.826	1.826	1.826	
	$C_p \leq 1.5$ [-]	1.888 ▼	1.888 ▼	1.888 ▼	1.888 ▼	
$K \leq 0.02$ [-]	0.080 ▼	0.091 ▼	0.089 ▼	0.106 ▼		
Ultimate Limit State (ULS)	ISO	$f_{g,sliding}$ [N/mm ²]	25.3	31.4	27.1	34.3
		$f_{g,shear}$ [N/mm ²]	6.4 ◀	8.0 ◀	6.4 ◀	8.0 ◀
		$F_{ISO,ULS}$ [kN]	103.7	129.3	103.7	129.3
	NORSOK	f_{bks} [N/mm ²]	23.5	29.1	25.1	31.9
		f_{bkg} [N/mm ²]	6.4 ◀	8.0 ◀	6.4 ◀	8.0 ◀
		$F_{N,ULS}$ [kN]	103.7	129.3	103.7	129.3
	DNVGL	$f_{g,sliding}$ [N/mm ²]	23.5	29.1	25.1	31.9
		$f_{g,shear}$ [N/mm ²]	6.4 ◀	8.0 ◀	6.4 ◀	8.0 ◀
		$F_{DNV,ULS,e}$ [kN]	77.8	97.0	51.8	64.7
		$F_{DNV,ULS,t}$ [kN]	51.8	64.7	25.9	32.3
	Schaumann	σ_{lat} [N/mm ²]	36.6	36.6	23.6	23.6
		κ [-]	3	3	3	3
		f_{cc} [N/mm ²]	199.9	249.9	160.7	210.7
		F_K [kN]	46.1	57.7	37.1	48.6
		α [-]	45	45	45	45
		μ [-]	0.4	0.4	0.4	0.4
		F_N [MN]	72.6	90.8	60.4	79.1
		$F_{tot,c}$ [MN]	308.5	385.6	168.8	221.3
		$F_{tot,t}$ [MN]	205.7	257.1	84.4	110.6
	FLS	ISO	$f_{g,sliding}$ [N/mm ²]	3.2 ◀	4.0 ◀	3.4 ◀
$f_{g,shear}$ [N/mm ²]			7.1	8.9	7.1	8.9
$F_{ISO,FLS}$ [kN]			51.9	64.3	55.5	70.4

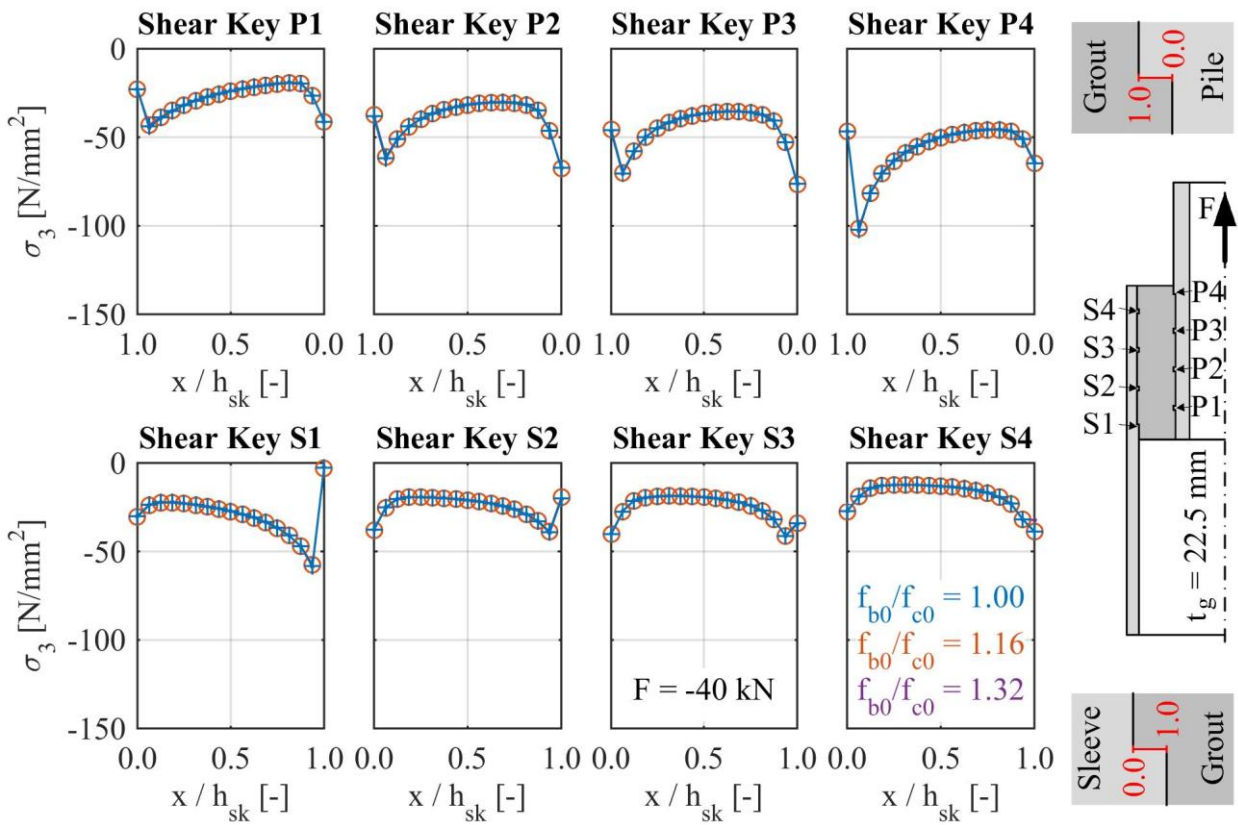
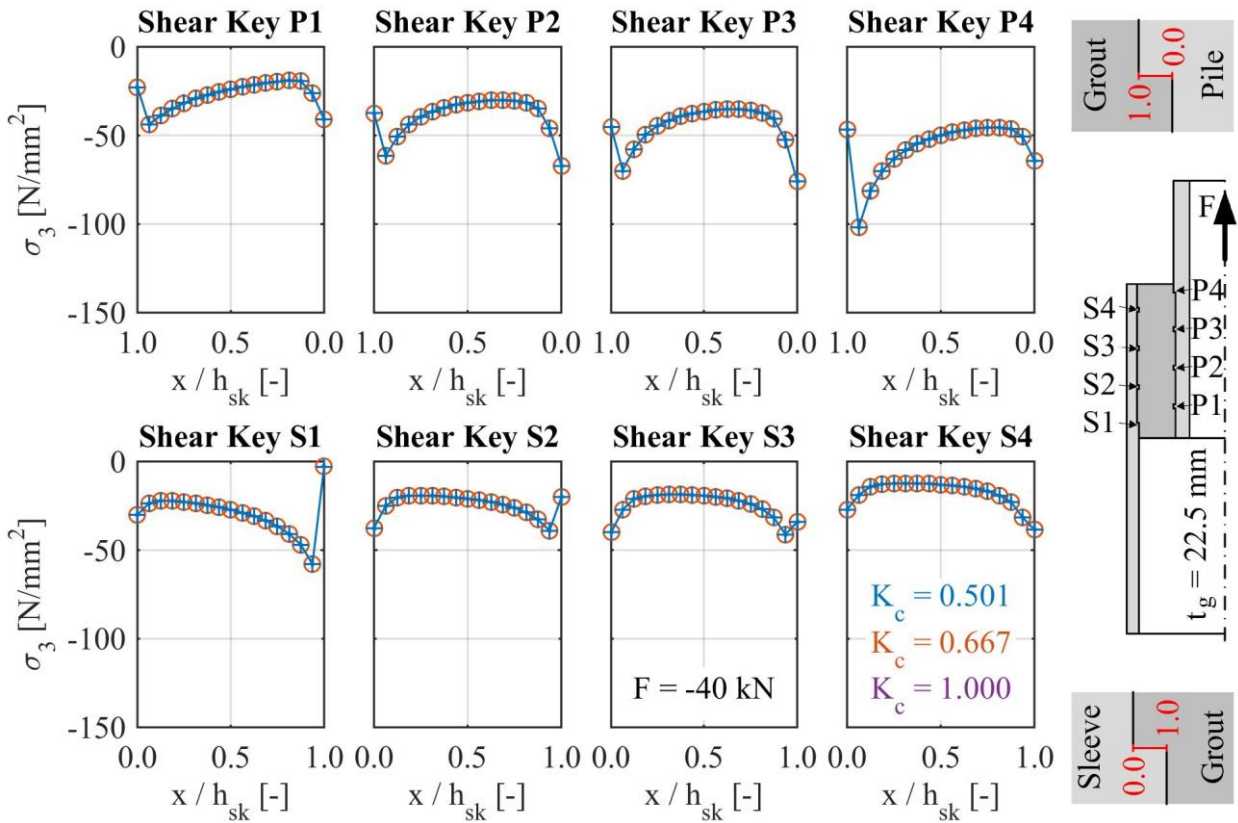
Design of axially loaded Grouted Connections

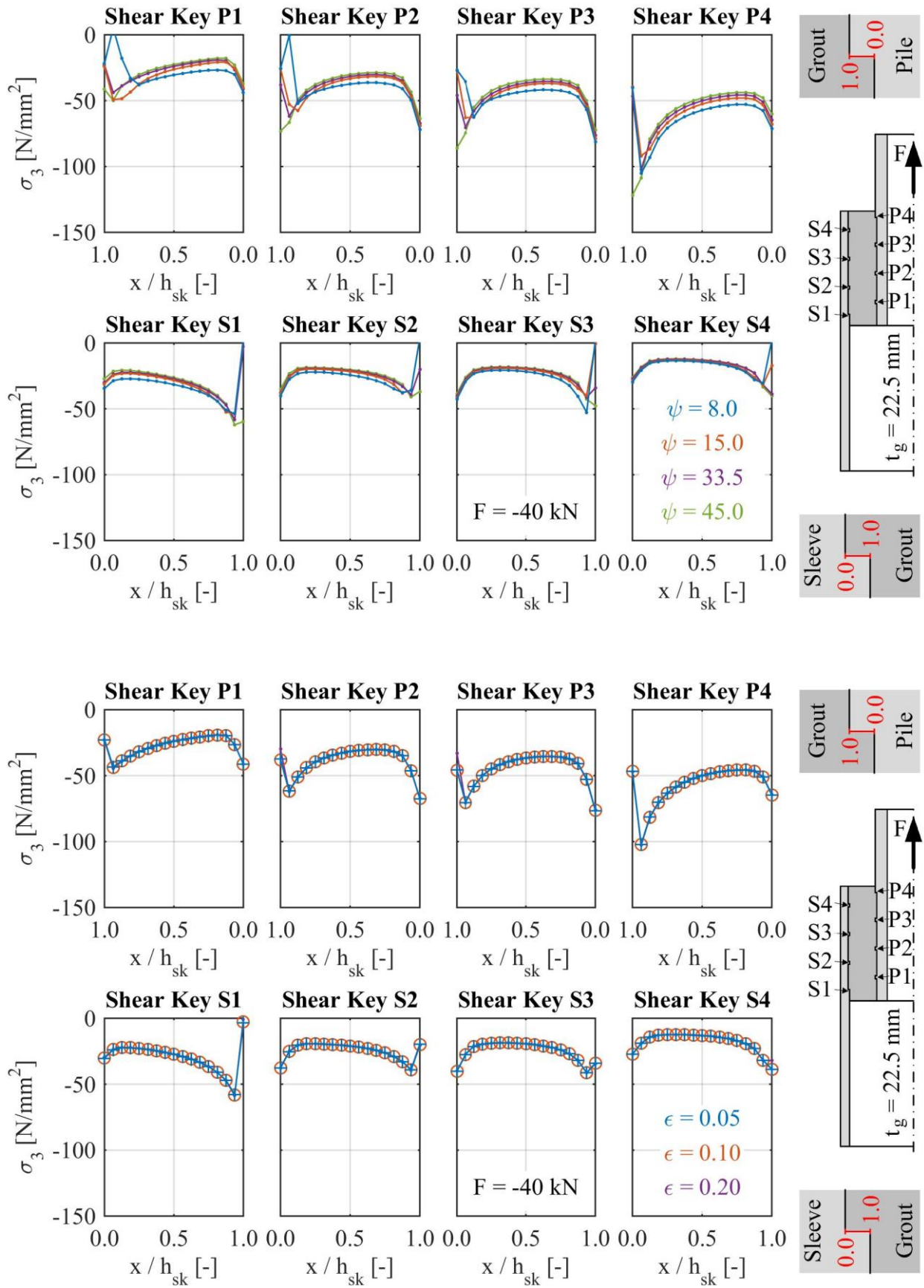
acc. to ISO 19902 (2014), DNVGL-ST-0126 (2016), N-004 (2013), Schaumann et al. (2012)

			Large-scale geometry 1		Large-scale geometry 2	
			BM95	DDS5	BM95	DDS5
Geometry	Tubes	D_p [mm]	406.4	406.4	610.0	610.0
		t_p [mm]	25.0	25.0	25.0	25.0
		D_s [mm]	813.0	813.0	813.0	813.0
		t_s [mm]	20.0	20.0	20.0	20.0
		D_g [mm]	773.0	773.0	773.0	773.0
		t_g [mm]	183.3	183.3	81.5	81.5
	Shear keys	h [mm]	6.0	6.0	6.0	6.0
		w [mm]	12.0	12.0	12.0	12.0
		s [mm]	100.0	100.0	100.0	100.0
		N_c [-]	5.0	5.0	5.0	5.0
		N_t [-]	4.0	4.0	4.0	4.0
	Grout	L_g [mm]	1240.0	1240.0	1240.0	1240.0
		Δl [mm]	366.6	366.6	163.0	163.0
		$L_c = L_g - \Delta l$ [mm]	873.4	873.4	1077.0	1077.0
	Material	Steel	E_s [N/mm ²]	210000.0	210000.0	210000.0
f_y [N/mm ²]			355.0	355.0	355.0	355.0
Grout		E_g [N/mm ²]	50900.0	55000.0	50900.0	55000.0
		f_{cu} [N/mm ²]	140.0	130.0	140.0	130.0
Range of validity		$20 \leq f_{cu} \leq 80$	140.000 ▼	130.000 ▼	140.000 ▼	130.000 ▼
		$20 \leq D_p/t_p \leq 60$	16.256 ▲	16.256 ▲	24.400	24.400
		$30 \leq D_s/t_s \leq 140$	40.650	40.650	40.650	40.650
		$10 \leq D_g/t_g \leq 45$	4.217 ▲	4.217 ▲	9.485 ▲	9.485 ▲
		$1 \leq L_c/D_p \leq 10$	3.051	3.051	2.033	2.033
		$1.5 \leq w/h \leq 3$	2.000	2.000	2.000	2.000
		$5 \leq h$	6.000	6.000	6.000	6.000
		$h/s \leq 0.1$	0.060	0.060	0.060	0.060
		$h/D_p \leq 0.01$	0.015 ▼	0.015 ▼	0.010	0.010
		$D_p/s \leq 16$	4.064	4.064	6.100	6.100
		$1 \leq s/s_{min}$ [-]	1.754	1.754	1.431	1.431
	$C_p \leq 1.5$	1.352	1.352	1.152	1.152	
	$K \leq 0.02$	0.075 ▼	0.080 ▼	0.041 ▼	0.043 ▼	
Ultimate Limit State (ULS)	ISO	$f_{g,sliding}$ [N/mm ²]	21.1	21.4	12.5	12.6
		$f_{g,shear}$ [N/mm ²]	7.9 ◀	7.6 ◀	7.9 ◀	7.6 ◀
		$F_{ISO,ULS}$ [MN]	8.8	8.5	16.3	15.7
	NORSOK	f_{bks} [N/mm ²]	15.6	15.8	10.4	10.5
		f_{bkg} [N/mm ²]	7.9 ◀	7.6 ◀	7.9 ◀	7.6 ◀
		$F_{N,ULS}$ [MN]	8.8	8.5	16.3	15.7
	DNVGL	$f_{g,sliding}$ [N/mm ²]	15.6	15.8	10.4	10.5
		$f_{g,shear}$ [N/mm ²]	7.9 ◀	7.6 ◀	7.9 ◀	7.6 ◀
		$F_{DNV,ULS,c}$ [MN]	5.0	4.8	7.6	7.3
		$F_{DNV,ULS,t}$ [MN]	4.0	3.9	6.0	5.8
	Schaumann	σ_{iat} [N/mm ²]	17.5	17.5	17.5	17.5
		κ [-]	3	3	3	3
		f_{cc} [N/mm ²]	192.4	182.4	192.4	182.4
		F_K [MN]	1.5	1.4	2.2	2.1
		α [-]	45	45	45	45
		μ [-]	0.4	0.4	0.4	0.4
		F_N [MN]	2.4	2.3	3.4	3.3
$F_{tot,c}$ [MN]		16.1	15.3	23.4	22.2	
$F_{tot,t}$ [MN]		12.9	12.2	18.8	17.8	
FLS	ISO	$f_{g,sliding}$ [N/mm ²]	2.5 ◀	2.6 ◀	1.5 ◀	1.5 ◀
		$f_{g,shear}$ [N/mm ²]	8.9	8.6	8.9	8.6
		$F_{ISO,FLS}$ [MN]	2.8	2.8	3.1	3.1

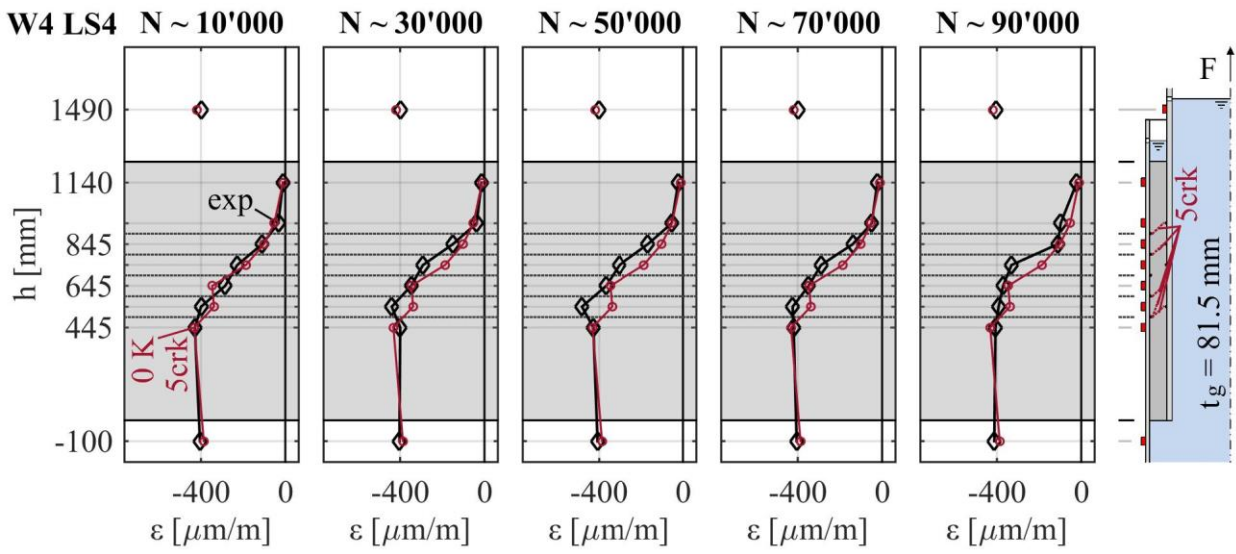
Appendix D – Numerical results

D.1 Small-scale - parameter studies

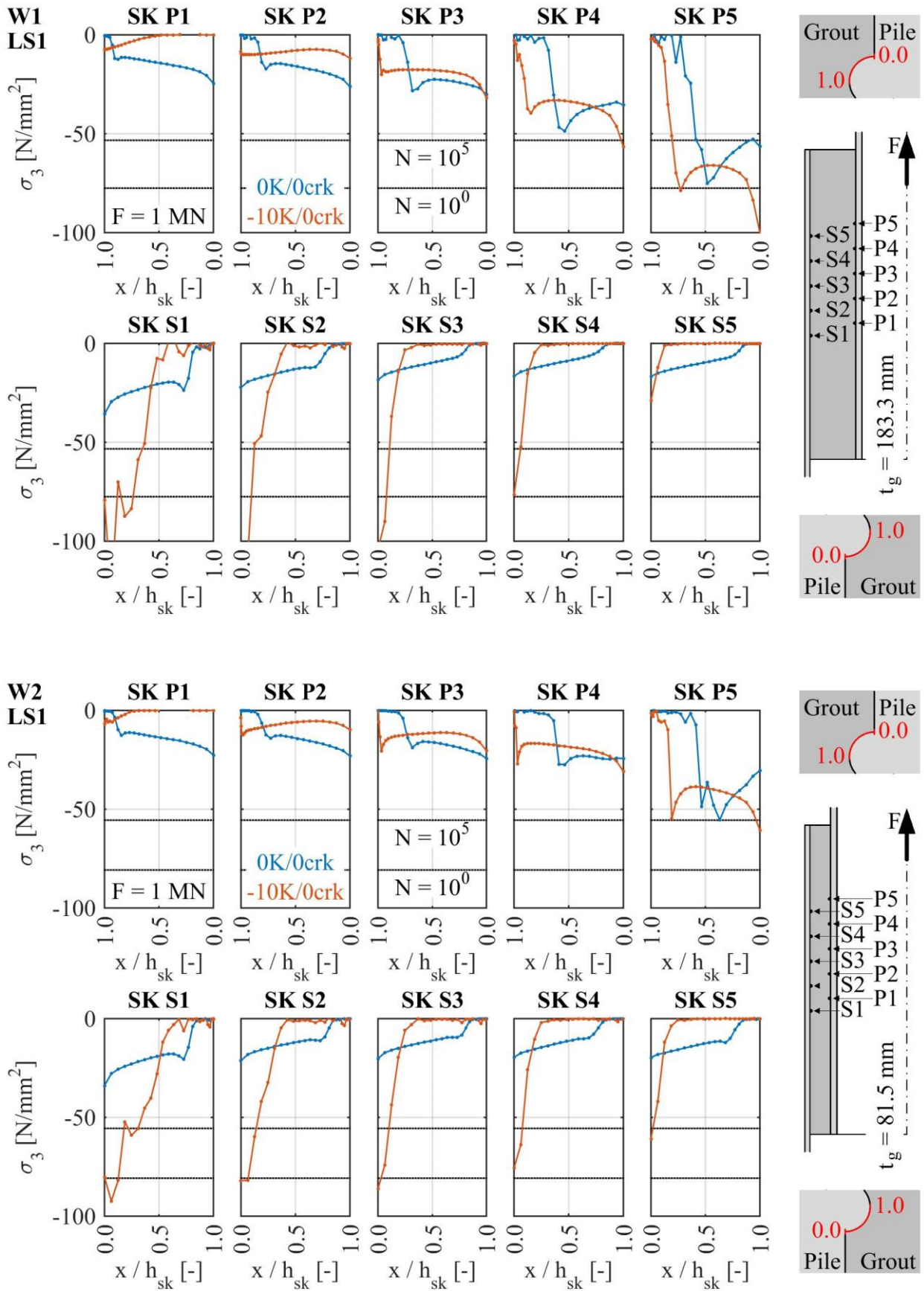


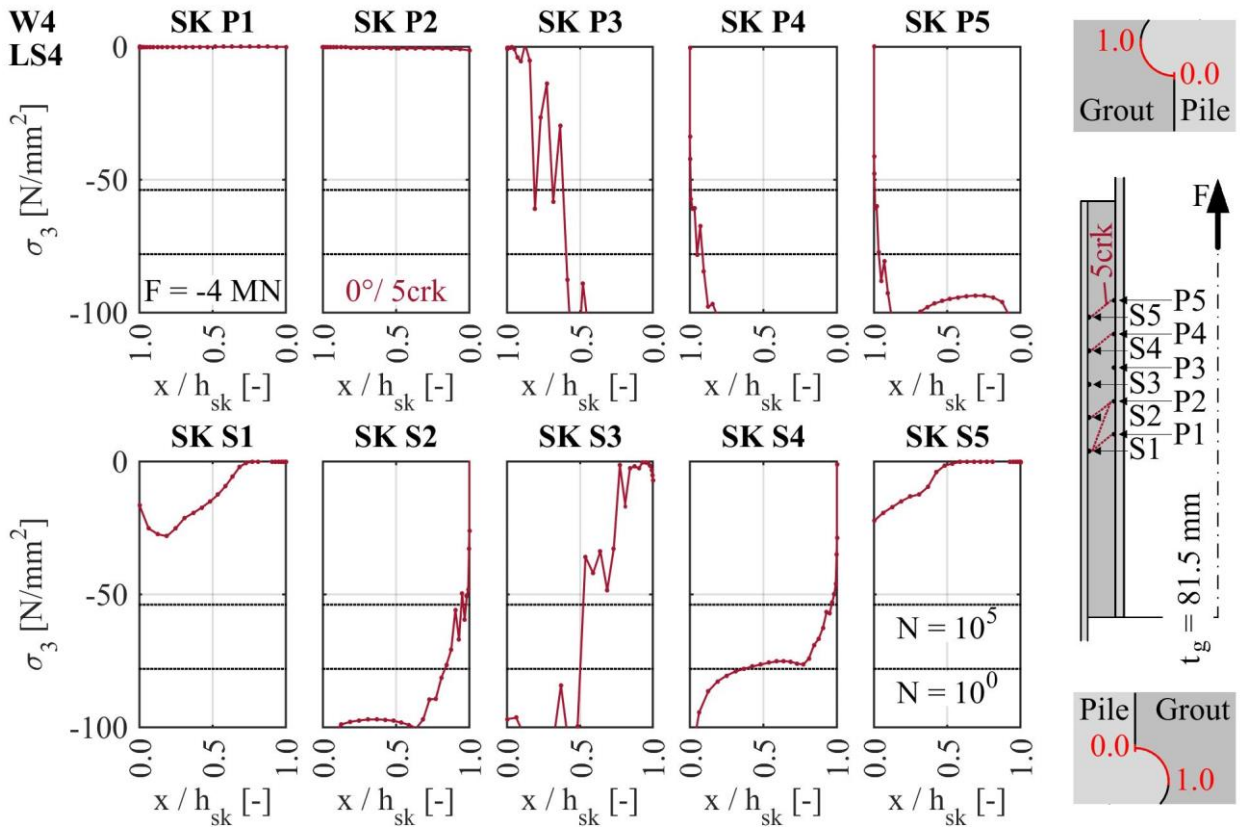


D.2 Large-scale – strain distributions



D.3 Large-scale – local stress distributions





Statement of Authorship

I hereby declare that I am the sole author of this doctoral thesis and that I have not used any sources other than those listed in the bibliography and identified as references. I further declare that I have not submitted this thesis at any other institution in order to obtain a degree.

Hannover, 28.08.2018

Curriculum Vitae

Name: Alexander Raba
Date of birth: 19.10.1982
Place of birth: Achim, Germany

Education

1995 – 2002 Cato Bontjes van Beek Gymnasium, Achim, Germany, Degree: Abitur
2002 – 2003 Civil Service
08.2003 – 06.2006 Apprenticeship Media Designer for Sound and Vision
Norddeutscher Rundfunk, Hamburg, Germany, Degree: IHK-Certificate
10.2006 – 09.2011 Study of Civil-Engineering, Leibniz Universität Hannover (LUH)
Major in Structure Design and Construction,
Degree: Diplom-Ingenieur

Internships

06.2006 – 10.2006 Carpentry Shop Die Holzverbindung,
Langenhagen, Germany
03.2009 Engineering consultancy LSM Ingenieure für Tragwerksplanung,
Hannover, Germany
05.2011 – 07.2011 Vestas Wind Systems A/S,
Offshore Support Structures Department, Århus, Denmark

Secondary Employment

05.2007 – 01.2010 Research Assistant at Institute of Structural Analysis, LUH
04.2008 – 06.2008 Research Assistant at Institute for Engineering Informatics, LUH
02.2010 – 04.2011 Research Assistant at Institute for Steel Construction, LUH

Professional Experience

10.2011 – 09.2017 Research Associate at Institute for Steel Construction,
Leibniz Universität Hannover, Germany
01.2012 – 04.2018 Freelance Structural Engineer,
diverse clients
Since 04.2018 Structural Engineer at engineering consultancy Meyer + Schubart,
Partnerschaft Beratender Ingenieure, Wunstorf, Germany